GENERATION OF LOW $\delta^{18}O$ SILICIC MAGMAS, BRUNEAU-JARBIDGE VOLCANIC CENTER, YELLOWSTONE HOTSPOT: EVIDENCE FROM ZIRCONS, INCLUDING OXYGEN ISOTOPES, U-Th-Pb DATING, AND MELT INCLUSIONS

by

Angela Nicole Seligman

A thesis submitted to the faculty of
The University of Utah
in partial fulfillment of the requirements for the degree of

Master of Science

in

Geology

Department of Geology and Geophysics

The University of Utah

May 2012

The University of Utah Graduate School

STATEMENT OF THESIS APPROVAL

The thesis of **Angela Nicole Seligman**

has been approved by the following supervisory committee members:

Barbara Nash	, Chair	**11/29/2011** Date Approved
John R. Bowman	, Member	**11/29/2011** Date Approved
Henrietta Cathey	, Member	**11/29/2011** Date Approved

and by **D. Kip Solomon** , Chair of

the Department of **Geology and Geophysics**

and by Charles A. Wight, Dean of The Graduate School.

ABSTRACT

The Yellowstone hotspot is characterized by magmas with both normal and low $^{18}O/^{16}O$ ratios. The production of isotopically light magmas at the Heise volcanic center (6.6–4.5 Ma) and on the Yellowstone volcanic plateau (2.1 Ma to present) appears to be associated with cycles of multiple caldera-forming eruptions that lead to deep burial and remelting of hydrothermally altered rhyolites. At the Miocene Bruneau-Jarbidge eruptive center in the central Snake River Plain, all of the eruptive products are isotopically light, present no evident cyclical behavior, and increase in mafic content through progressive eruptions. This study describes the results of oxygen isotopic analyses and U-Th-Pb dating on individual crystals of zircon from Bruneau-Jarbidge eruptive center (BJEC) lavas erupted between 11 and 8 Ma. These mostly post-date the large-volume ignimbrites of the Cougar Point Tuff (CPT) erupted between 12.8-10.5 Ma. 109 zircons were analyzed with the Cameca IMS-1280 ion microprobe at the University of Wisconsin to determine $\delta^{18}O$ of cores, rims, and interiors. U-Th-Pb ages for zircon spots previously analyzed for oxygen were determined on the Stanford SHRIMP together with trace element analyses including Ti. Zircons from all rhyolite lavas from the BJEC have low $\delta^{18}O$ values. The $\delta^{18}O$ analyses average 1.47 $^{o}/_{oo}$, with values ranging from -3.41 $^{o}/_{oo}$ to 8.10 $^{o}/_{oo}$. The overall eruptive series of the lavas demonstrate that the $\delta^{18}O$ of the zircons began with an average value of -0.47 $^{o}/_{oo}$ in the first erupted lava, and ultimately rose to an average value of 1.81 $^{o}/_{oo}$ with the eruption of Dorsey Creek rhyolite at the final stages of the BJEC. The rhyolite lava with the

highest average $\delta^{18}O$ in zircon was Sheep Creek rhyolite (3.3 $^{o}/_{oo}$), erupted near the end of the sequence, still nearly 1 $^{o}/_{oo}$ below nonaltered values. Ti-in-zircon temperatures average 930 °C, with values as low as 817 °C and as high as 996 °C. This indicates the sustained high temperature of the magmatic system, even following the large-volume eruptions of the CPT.

TABLE OF CONTENTS

LIST OF TABLES

ACKNOWLEDGEMENTS

I would like to thank Barbara Nash for her continual guidance and support, as well as John Bowman and Henrietta Cathey, who are also on my committee and were incredibly patient and provided me with much guidance. Henrietta Cathey also collected the samples used in this study and provided zircon mounts for the melt inclusion study, and trained me in picking zircons containing melt inclusions. A to Z, Inc. produced the zircon separations for the samples used in this study. I would also like to thank Matthew Heumann for teaching me how to mount my first set of zircons into epoxy, and for checking all my mounts to make sure they were prepared properly. Also, I would like to thank John Valley for the use of the SIMS at the University of Wisconsin, as well as Arial Strickland who patiently taught and supervised me in the use of the SIMS. I also need to thank Jorge Vasquez and Joseph Wooden for helping me analyze my zircons on the SHRIMP at Stanford University, and for their continued help with interpretation of the data. Financial support was provided in part by NSF grant EAR–0510327 and the Volcano Studies Project in the Department of Geology and Geophysics. Finally, I absolutely need to thank my wonderful family and friends for their everlasting love and support, and my dog Kayak for his company during my long days of finishing my thesis.

CHAPTER 1

INTRODUCTION

Purpose

The primary objective of this paper is to investigate low $\delta^{18}O$ rhyolites of the Bruneau-Jarbidge eruptive center (BJEC). Previous studies have been conducted on various eruptive centers of the Yellowstone-Snake River Plain (YSRP) hotspot system (i.e., Bruneau-Jarbidge, Twin Falls, Heise, and Yellowstone Plateau) to determine the $\delta^{18}O$ and chemical composition of volcanic products of each eruptive center. Eruptive centers of the YSRP exemplify some of the largest rhyolitic magmatic systems in the world, so comprehensive analysis of these systems can potentially elucidate processes responsible for producing such large igneous provinces. Recently, it has been recognized that some of the magmas generated by this hotspot have anomalously low $^{18}O/^{16}O$ ratios (Bindeman et al., 2007a; Watts et al., 2011; Boroughs et al., 2005; Cathey et al., 2007). The often complex means by which magmas acquire these low ratios is of considerable interest. Possible mechanisms include: (1) a catastrophic eruption and caldera collapse that allows for the incorporation of hydrothermally altered material from a previous eruption through remelting of that material into the magmatic system, (2) previous hydrothermal alteration of the surrounding crust that is assimilated into the magma chamber, or (3) direct influx of hydrothermal fluid into the

magma chamber (Bindeman et al., 2000; Bindeman and Valley, 2001; Watts et al., 2011; Taylor and Sheppard, 1986; Hildreth et al., 2001). Prior work on magma genesis of the Yellowstone Volcanic Plateau and the slightly older Heise volcanic center has led to a preference for the first mechanism (Bindeman and Valley, 2001; Bindeman et al., 2007a; Watts et al., 2011) however, differences in the style of volcanism of earlier volcanic centers, including the BJEC, in addition to the prevalence of low ratio magmas that have been discovered since the earliest eruptions at the BJEC validates further study of these centers. This study aims to expound on the genesis of the BJEC by analyzing the $\delta^{18}O$ of rhyolite lavas together with the chemical compositions of melt inclusions from lavas and ignimbrites erupted from the BJEC. This research can potentially aid in decreasing devastating effects of volcanic eruptions through a more extensive understanding of magma generation processes- a critical part of the build up to cataclysmic eruptions from a large-scale silicic system.

Low $\delta^{18}O$ Magmas

The oxygen isotopic composition of igneous rocks and minerals are dependent on multiple variables including their temperature of crystallization, isotopic composition and degree of fractional crystallization of the host magma, any retrograde effects due to re-equilibration at subsolidus temperature, and any interactions the material may have with aqueous solutions (Faure, 1986).

The $\delta^{18}O$ value of any object in relation to the Vienna Standard of Mean Ocean Water (VSMOW) is defined as:

$$\delta^{18}O = \left[\frac{(^{18}O/^{16}O)_{sam} - (^{18}O/^{16}O)_{VSMOW}}{(^{18}O/^{16}O)_{VSMOW}} \right] x10^{3} \quad (1)$$

where variations in stable isotope ratios are typically reported as per mil deviations from

VSMOW. The $\delta^{18}O$ values of rocks and minerals tend to be positive and most silicate rocks have $\delta^{18}O$ between +5 and +15 $^{o}/_{oo}$ (Faure, 1986). The oxygen isotopic composition of MORB ranges between 5.6 $^{o}/_{oo}$ and 5.7 $^{o}/_{oo}$, and the $\delta^{18}O$ of material erupted from the YSRP that has not been depleted in ^{18}O ranges from 6.5 $^{o}/_{oo}$ to 7.5 $^{o}/_{oo}$ (Portnayagin et al., 2005; Bindeman et al., 2007b). Zircons from these magmas that are in equilibrium with the mantle have $\delta^{18}O$ values of 5.3 ± 0.3 (Valley et al., 2005).

Isotope fractionation between melts and crystals is minimal at high temperatures, but magmatic differentiation processes at lower temperatures found closer to Earth's surface increase the ^{18}O content of silicic magmas by several per mil (Muehlenbachs and Byerly, 1982). Different minerals have varying tendencies to concentrate ^{18}O, with quartz having the strongest and magnetite having the weakest (Faure, 1986). The crystallization of titanomagnetite, olivine, and pyroxene at normal igneous temperatures, which are depleted in ^{18}O, will enrich the residual magma in ^{18}O, causing the $\delta^{18}O$ of igneous rocks to typically increase with increasing SiO_2 (Muehlenbachs and Byerly, 1982; Anderson et al., 1971).

It is known that magmas, or previously erupted igneous rocks, with whole rock $\delta^{18}O$ < 5.5 $^{o}/_{oo}$ were depleted in ^{18}O through a process involving at least 10% of the total oxygen in the rock being exchanged with meteoric water (Bindeman et al., 2001a). The formation of low-$\delta^{18}O$ magmas, which can later be erupted as a low-$\delta^{18}O$ product, is thought to require at least one of three processes: the first requires direct infiltration of water into the magma, the second option involves a gradual assimilation of hydrothermally altered rock that was brought into contact with the magma chamber through caldera collapse, and the final method involves the assimilation of previously hydrothermally altered walls and roof material of the magma chamber that have low $^{18}O/^{16}O$ ratios (Bindeman and Valley, 2000; Friedman et al., 1974; Muehlenbachs et al., 1974; Criss and Taylor, 1986; Taylor, 1987;

Hildreth et al., 1984; Taylor and Sheppard, 1986; Balsley and Gregory, 1998; Bacon et al., 1989). The last two scenarios are more likely, as the first is physically difficult to achieve. Water does not readily diffuse directly into a magma chamber because of the high lithostatic pressure in the area, decreasing permeability of progressively hotter rock near the magma chamber margin, and the limit of water solubility in magmas. If the water is able to reach the magmatic system, it is then likely to have already undergone a significant ^{18}O shift to higher $\delta^{18}O$ values due to exchange with the surrounding material (Taylor, 1986). Therefore, although meteoric water has a naturally low $\delta^{18}O$ value, it is unlikely that a direct influx of surficial water into a magmatic system could cause a dramatic lowering of magmatic $\delta^{18}O$. Although this is true, it is possible for meteoric water to interact with previously erupted material that is now at Earth's surface and lower its $\delta^{18}O$ value, even though the lava was erupted from normal $\delta^{18}O$ magma.

Low $\delta^{18}O$ Magmas Worldwide

Low $\delta^{18}O$ magmas have been recognized worldwide and occur in a variety of geologic environments. The common factor among these is the interaction of material with meteoric water, which is later incorporated into the magmatic system, lowering its $\delta^{18}O$ value.

Oxygen isotope ratios from silicic rocks of the Kamchatka Peninsula span about 3 $^{o}/_{oo}$, with many showing low $\delta^{18}O$, including eruptive material from the Eastern Volcanic Zone including the Karymsky Center and the Uzon-Shorokoy Plateau, as well as material from the Sredinny Range including the Tekletunup Volcano (Bindeman et al., 2010a). These low $\delta^{18}O$ magmas were most likely formed by low $\delta^{18}O$ glacial meltwaters interacting with

previously erupted material that was subsequently remelted and assimilated into the magma system (Bindeman et al., 2010a).

The Dongargarh Group in central India is a large basalt-rhyolite province containing low $\delta^{18}O$ magmas. $^{18}O/^{16}O$ depletions in this region are most likely due to interaction of magma with hydrothermal fluids contemporaneous with the emplacement of a large volume of komatiitic magma within the middle to lower crust, prior to the formation of the low $\delta^{18}O$ Bijli melt (Sensarma et al., 2004a).

Hawaiian lavas from the Puu Oo vent record significant variations in matrix and olivine $\delta^{18}O$, even within single eruptions. These variations are due to an exchange between the magma and a low ^{18}O source, such as meteoric water, after the growth of olivine. This is expressed in historical summit lavas from Kilauea that exhibit a range in matrix $\delta^{18}O$ (4.9-5.6 $^{o}/_{oo}$); where more depleted $\delta^{18}O$ values are found in rocks that erupted after a major collapse or break in eruptions (Garcia et al., 2008).

In Iceland, the 15-km^3 Laki eruption contains tephra and basalt with $\delta^{18}O$ values depleted below 3 $^{o}/_{oo}$ from that of the unaltered mantle. Recent eruptions over the last 800 years from the Grimsvotn central volcano, which is part of the same volcanic system as the Laki eruption, also have low $\delta^{18}O$, suggesting a low $\delta^{18}O$ magmatic system. The low $\delta^{18}O$ values suggest that both Laki and Grimsvotn require a period of deglaciation as a source of abundant meltwater to allow for the hydrothermal alteration of the basaltic crust that was later incorporated into the magma and erupted (Bindeman et al., 2006).

There is also evidence that the snowball earth period during the middle Neoproterozoic (700-800 Ma) triggered the formation of low $\delta^{18}O$ magmas. This is possibly due to the cold climates and widespread glaciers that both provide abundant meteoric water to interact with magmatic systems. The Dabie-Sulu orogenic belt of east-central China is an

example of this, where rift-magmatism in the region served as a heat source to melt the overlying glacial ice and snow, allowing the meteoric water to penetrate the system and produce hydrothermal circulation needed to form the low $\delta^{18}O$ magmas (Zheng et al., 2004).

Among the volcanic centers of the track of the Yellowstone hotspot, low $\delta^{18}O$ rhyolites have been described at the current Yellowstone Plateau eruptive center (Bindeman et al., 2000, 2001b, 2007a; Bindeman and Valley, 2001; Hildreth et al., 2001), the Heise eruptive center (Bindeman et al., 2007b; Watts et al., 2010, 2011), the Twin Falls eruptive center (Ellis et al., 2010), and the Bruneau-Jarbidge eruptive center (Boroughs et al., 2005; Cathey et al., 2007). These eruptive centers will be further discussed below.

Low $\delta^{18}O$ Magmas of the Yellowstone Hotspot

The YSRP is approximately 700 km long and runs from eastern Oregon to western Wyoming while forming a series of volcanic centers, with the active one located on the Yellowstone Plateau (Perkins and Nash, 2002; Figure 1). Rhyolites of the YSRP that were erupted to the east of the Archean crustal boundary ($^{87}Sr/^{86}Sr = 0.706$ line) were generated through basaltic intrusions into continental crust and produced these silicic magmas through partial melting of the surrounding crust (Smith and Braile, 1994; Leeman et al., 2008; Watts et al., 2010, 2011). Previous studies conducted on the rhyolites from the central Snake River Plain, the Heise eruptive center, and the Yellowstone Plateau eruptive center illustrate the presence of over 10,000 km^3 of low-$\delta^{18}O$ material (Boroughs et al., 2005; Cathey et al., 2007; Bindeman and Valley, 2000; Bindeman et al., 2001b; Watts et al., 2010; Watts et al., 2011).

Geologic Setting

Initial magmatism of the Yellowstone hotspot coincides with the timing of the primary eruptions of the Columbia Plateau flood basalts around 16.6 to 15 Ma (Camp and Ross, 2004). Volcanism from the YSRP system migrates with the 2 cm/yr movement of the North American plate above the Yellowstone mantle plume, which has produced multiple 2-4 m.y. duration eruptive centers. Total eruptive material from this system includes approximately 40 rhyolitic eruptions which produced over 300 km^3 of material each, since its initiation at 16 Ma, as well as a minimum of 142 noteworthy explosive events determined from abundant fallout tuffs (Perkins and Nash, 2002).

Seismic evidence has been established by both Peng and Humphreys (1998) and Shervais et al. (2006) for the emplacement of a mid-crustal basaltic sill complex that could provide the necessary heat to produce large-volume silicic eruptions. Peng and Humphreys (1998) utilized teleseismic receiver functions to determine the presence of a basaltic layer in the mid crust of the eastern Snake River Plain approximately 10 km thick and 90 km wide that is surrounded by crustal material ranging from primarily granulitic material in the lower crust to more felsic material in the upper crust. The study also suggests that the extra mass from the intrusions increased the density of the crust, causing the depression of the Snake River Plain (SRP), which persists today. Shervais et al. (2006) reported the presence of complex cyclic repetitions of phase assemblages and compositions in basalts of the eastern SRP, suggesting fractional crystallization, assimilation of wall rock, and recharge by primitive magmas in a mid-crustal sill complex. The elemental studies from this research inferred the presence of a series of layered mafic sills beneath the eastern SRP that are interconnected and feed multiple volcanic centers. Details of this study also suggest that basaltic melts are able to bypass the granitic and dioritic gneisses of this region with minimal interaction once

the melts have produced a hardened layer of basalt covering the surface of the sill (Shervais et al., 2006).

Leeman et al. (2008) concluded that enrichment levels of trace elements in central SRP rhyolites require 15-25% partial melting of the overlying crust. The energy required for this melting process is provided by the massive input of basalt into the crust. This takes place at depths shallower than 20 km (as suggested by phase equilibria experiments), but no shallower than 5-10 km, as these depths could not sustain the high silicic magma temperatures (>900 °C) of the central SRP (Leeman et al., 2008; Thompson, 1975).

Decreasing SiO_2 and increasing total iron and TiO_2 with time characterize rhyolites of the BJEC, which is consistent with the repeated addition of basalt into the crust and therefore an increase in mafic content of the system. This can be achieved by episodic removal of rhyolitic material from the system through eruptions, and a continued input of mafic material. This addition of mafic material also heats the system and therefore increases the degree of partial melting of the surrounding crust. When the melt is removed from the crust, the remaining crust will be left with a more overall mafic content, which could also explain the elemental trends of the BJEC (Leeman et al., 2008; Annen et al., 2006).

These large amounts of basaltic intrusions required to produce the rhyolites of the central SRP impose a significant room problem, which suggests that the crust must have been deformed to accommodate the large input of new material. One means of creating this necessary space is Basin and Range extension, which occurred during the formation of the central SRP, although the magnitude of extensional strain in this region is not well known (Leeman et al., 2008).

Much debate has been directed toward whether or not the YSRP system is fed by a deep-seated plume or various lithospheric-driven processes of fracture and volcanism (Pierce

and Morgan, 1992; Camp and Ross, 2004; Smith et al., 2009). A non-plume hypothesis is suggested to be related to regional deformation, such as crustal thinning, which then implies that the low velocity anomaly determined through geophysical studies beneath Yellowstone was formed from rising magma at a weak region of the lithosphere (Anderson, 2000; Christiansen et al., 2002).

However, recent geophysical observations (Obrebski et al., 2010; Zhdanov et al., 2011; Smith et al., 2009), along with the discovery of high $^{3}He/^{4}He$ isotopic ratios (often representative of a lower mantle source) throughout much of the YSRP (Graham et al., 2009), provide persuasive evidence for the presence of a mantle plume beneath the present day Yellowstone Volcanic Plateau. Obrebski et al. (2010) interpret the source of the YSRP system to be a mantle plume originating from the lower mantle based on tomographic modeling. Their model suggests the presence of a large volume of low-velocity material interpreted as a mantle plume (Obrebski et al., 2010). This material could account for a measured free air gravity anomaly, high heat flow and geoid high associated with a regional topographic swell observed on the Yellowstone Plateau (Smith et al., 2009). Smith et al. (2009) concluded from seismic tomography at shallower depths that there is a magma reservoir between 6 and 16 km beneath the Yellowstone caldera locally containing 8 to 15 % melt. More recently, Zhdanov et al. (2011) used EarthScope MT data to model a high-conductivity feature beneath the Yellowstone Plateau eruptive center that they believe is evidence for hot conductive material located in the upper mantle, with similar conductivity to silicate melts and their associated saline fluids (Zhdanov et al., 2011; Pommier et al., 2008; Pommier and Le Trong, 2011).

The Bruneau-Jarbidge Eruptive Center

The Bruneau-Jarbidge eruptive center (BJEC) was active between 12.8 and ~8.1 Ma, and produced large volumes of high-temperature silicic magmas consisting of between 7000 km^3 to over 10,000 km^3 of material, approximately 15% of which are rhyolitic lava flows (Figure 1.1). Explosive ashflow tuffs erupted over 2.3 m.y. from approximately 12.8 to 10.5 Ma. Rhyolite lavas began erupting before the last of these ignimbrites, with 2.4 m.y. of effusive eruptions between approximately 10.5 and 8 Ma (Cathey and Nash, 2004, 2009; Boroughs et al., 2005; Perkins and Nash, 2002; Bonnichsen et al., 2008; Leeman et al., 2008). These studies demonstrate that this eruptive material form from $^{18}O/^{16}O$-depleted magmas, as illustrated by measured $\delta^{18}O$ values of quartz ($\delta^{18}O$ = 1.3 to 4.5 $^{o}/_{oo}$), feldspar ($\delta^{18}O$ = -1.3 to 3.8 $^{o}/_{oo}$), and zircon ($\delta^{18}O_{rims}$ = -3.1 to 3.3 $^{o}/_{oo}$) (Boroughs et al., 2005; Cathey et al., 2007).

Based on petrological and geochronological evidence, the Twin Falls eruptive center (TFEC), ~100 km east of the BJEC, consists of later erupted material similar and successive to the BJEC, indicating that this may be a continuous eruptive series as suggested by (Bonnichsen et al., 2008). This is consistent with the continually high temperatures of the lavas from the BJEC that coincide with the high pre-eruptive magma and ashflow temperatures recorded by the early stages of the TFEC (Cathey and Nash, 2009).

Lavas of the Bruneau-Jarbidge Eruptive Center

The rhyolite lavas of the BJEC were first described by Bonnichsen (1982b) and details of these lava units, including physical dimensions and field locations, can be found in Bonnichsen (1982b). All $^{40}Ar/^{39}Ar$ and K/Ar ages reported below are from Bonnichsen et al.

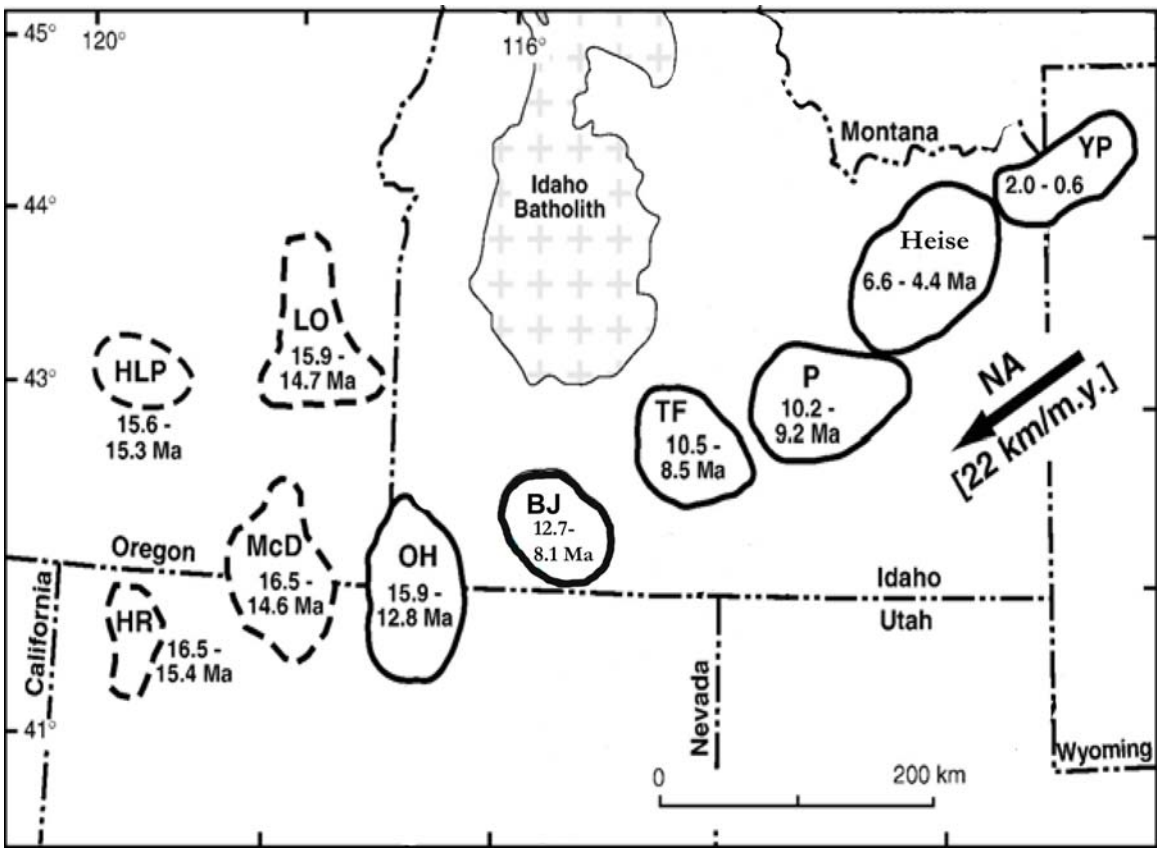

Figure 1.1. Map of the Yellowstone hotspot system showing the location and age of its various eruptive centers including High Rock (HR), High Lava Plains (HLP), McDermitt (McD), Lake Owyhee (LO), Owyhee-Humboldt (OH), Bruneau-Jarbidge (BJ), Twin Falls (TF), Picabo (P), Heise (H), and Yellowstone Plateau (YP). The arrow shows the migration of the North American plate over the Yellowstone hotspot at 22 km/m.y. (modified from Nash et al., 2006; Figure 1).

(2008), except the K/Ar age for the Dorsey Creek rhyolite (DCR), which was determined by Hart and Aronson (1982). The lavas contain a variety of minerals including plagioclase, sanidine, augite, pigeonite, quartz, titanomagnetite, ilmenite, fayalite, and accessory zircon and apatite, with crystal contents between 10% and 20%, which are higher than that of the CPT (Bonnichsen, 1982b; Cathey and Nash, 2009). Bonnichsen et al. (2008, Table 2) provide major and trace element compositions as well as Sr and Nd isotopic ratios, and Boroughs et al. (2005) provides O isotopic ratios for some of the lavas discussed here. Additionally, Cathey and Nash (2009) provide pyroxene compositions and thermometry that confirm the high temperatures for this magmatic system. Chemical analyses indicate that, in general, iron concentrations increase through the evolution of the rhyolite lavas of the BJEC, with the Bruneau-Jasper rhyolite (BJR) having the highest silica and lowest iron content and the Sheep Creek rhyolite (SCR) having the highest iron content. The continuation of the increasingly mafic trend from the CPT to the rhyolites indicates that the eruptive center is becoming overall less evolved with time (Bonnichsen et al., 2008). The multiple similarities between tuffs and lavas of the central SRP can cause them to be difficult to distinguish from one another, which has caused the Three Creek tuff (TCT) to be initially thought of as a rhyolite flow, but due to its physical characteristics and high silica content, it is now thought to be a high-temperature ashflow tuff (Bonnichsen et al., 2008).

Most lavas do not extend beyond the BJEC, and although the Sheep Creek rhyolite ($\geq$200 km^3) and Dorsey Creek rhyolite (75 km^3) have larger volumes, most lavas have volumes of approximately 10 km^3 and lengths ranging from 4 km up to 42 km. Volume estimates have not been approximated for Marys Creek rhyolite (MCR), Cedar Tree rhyolite (CTR) (100 m thick in Bruneau Canyon), the Bruneau-Jasper rhyolite (BJR) (nearly 150 m

thick), the Poison Creek rhyolite (PCR) (~100 m thick in Jarbidge Canyon), and Louse Creek rhyolite (LCR), because not enough information is available to make a valid volume estimate. The Triguero Homestead rhyolite (THR) is estimated to have a volume of 10 km^3 or more, the Indian Batt rhyolite (IBR) has a minimum volume of 12 km^3, and the Three Creek tuff (TCT) has a minimum volume of approximately 10 km^3, but could be much larger since a large portion of it is buried (Bonnichsen, 1982b).

Although eruption ages are not known for many lavas of the BJEC, previous studies on stratigraphy, tephrochronology, K/Ar dating, and $^{40}Ar/^{39}Ar$ dating have allowed for some determination of eruptive sequence (Bonnichsen, 1982b; Bonnichsen et al., 2008; Hart and Aronson, 1982; Henshaw, 2002; Perkins and Nash, 2002), and an overview of the stratigraphic relationships of the CPT and lavas is provided by Cathey and Nash (2009; Figure 2). There are three lava flows within the end stages of the CPT sequence informally referred to here as lava flow one (lava one of Cathey and Nash (2009)), lower lava flow, and upper lava flow. There is an exposure of lava flow one (LF1) between CPT units XII and XIII, indicating an eruption age between 11.3 and 11 Ma. CPT XIII is stratigraphically lower than the lower lava flow (LLF), which is in turn overlain by the upper lava flow (ULF). The upper lava flow (ULF) underlies CPT XV, which is estimated by tephrostratigraphy to be ~ 10.5 Ma (Perkins and Nash, 2002). The Triguero Homestead rhyolite (THR) underlies the Indian Batt rhyolite, overlies CPT XV, and has an age estimate of approximately 10.5 Ma based on a fallout ash associated with it. The stratigraphic position of THR in relation to MCR and all other BJEC rhyolites except DCR is unknown. Both the Indian Batt rhyolite and the Long Draw rhyolite overlie CTR, and a $^{40}Ar/^{39}Ar$ age of 10.16 ± 0.09 Ma has been determined for this unit. The Bruneau-Jasper rhyolite (BJR) has a $^{40}Ar/^{39}Ar$ age of 9.50 ± 0.06 Ma, is overlain by the Indian Springs basalt and the Sheep Creek rhyolite, and overlies

the Long Draw rhyolite. PCR overlies the Indian Springs basalt. LCR is overlain by the Sheep Creek rhyolite. SCR has a tentative age of approximately 9.3 Ma based on K/Ar dating and stratigraphic position. IBR lies below the rhyolite of Dorsey Creek. In various exposures, DCR overlies the Indian Springs basalt, PCR, and IBR, and has a tentative age of 8.1 Ma based on K/Ar dating. Location and age of TCT also suggest that it may be associated with the Twin Falls eruptive center instead of the BJEC. TCT lies above CPT XIII, but the stratigraphic relationship of this unit to other rhyolite flows of the BJEC is unknown. An age of approximately 8.6 Ma has been tentatively proposed for basal ash from the Tuff of McMullen Creek, which is possibly correlated with TCT, based on a correlation between glass compositions with regional fallout tuffs (Michael Perkins, personal communication).

CHAPTER 2

OXYGEN ISOTOPES

Zircons

The refractory nature and slow intracrystalline diffusion and growth rate of zircons allows them to incorporate and maintain valuable geochemical and geochronological information (e.g., trace elements and past $\delta^{18}O$ variations) during the evolution of igneous rocks (Fu et al., 2008; Valley, 2003). In particular, zircon's refractory nature allows it to be more resistant to hydrothermal alteration and capable of surviving melting episodes than most minerals, hence its ability to preserve the $\delta^{18}O$ of magma from which it crystallized (Bindeman et al., 2001a). Zircons are used in this study to document the oxygen isotopic composition of rhyolite magmas that produced the effusive phase of volcanism at the BJEC and to provide a basis for comparison with the earlier explosive phase. In addition, as discussed below, these zircons were dated to establish the time they acquired their oxygen isotope signature, thus confirming that they crystallized from the BJEC magmatic system as well as identifying possible xenocrystic and other inherited zircons.

Oxygen Isotope Studies of the Yellowstone Hotspot

The Yellowstone Eruptive Center

The low $\delta^{18}O$ magmas from the Yellowstone Plateau volcanic center are thought to be produced through cannibalization of previously erupted material that was hydrothermally altered and incorporated into the magma chamber during caldera collapse (Bindeman et al., 2001b). This process is described in three stages, which typically repeats itself, allowing for the continual re-incorporation into the magma chamber of previously erupted and hydrothermally altered material residing above the magmatic system (Bindeman and Valley, 2001; Figure 8). The first stage involves hydrothermal alteration of the country rock, lowering the $\delta^{18}O$ of the roof of the magma chamber, which will later become the source material for the low $\delta^{18}O$ rhyolites. Although feldspar and glass in the rock are depleted in $^{18}O/^{16}O$, the quartz and zircon, which are more resistant to oxygen isotopic exchange, remain unaffected. The second stage involves the collapse of the caldera during a catastrophic eruption, which brings the $\delta^{18}O$-depleted material closer to the magma reservoir. The final stage involves melting and incorporation of the hydrothermally altered material, which forms pockets of low-$\delta^{18}O$ magma near the roof of the reservoir, thereby providing low-$\delta^{18}O$ magmas for future eruptions. This process involves the melting of large quantities of previously altered and $^{18}O/^{16}O$-depleted rhyolites, shown by the abundance of inherited zircons in the low-$\delta^{18}O$ lavas and the exceptionally low whole rock $\delta^{18}O$ of the lavas (Bindeman et al., 2001b; Bindeman et al., 2007a; Bindeman and Valley, 2001).

The Heise Eruptive Center

Although the Heise and Yellowstone centers are similar in that they both produce high-silica, low $\delta^{18}O$ rhyolites with similar magmatic temperatures, there are two distinctions between the two eruptive centers. The first is that the low $\delta^{18}O$ rhyolites at Yellowstone are typically smaller in volume (not including the 600 km^3 Central Plateau Member) and more depleted in $\delta^{18}O$. The second is that the crystallization ages of zircons from Heise are similar to the $^{40}Ar/^{39}Ar$ eruptive ages of the individual units, which is not the case at Yellowstone where the zircon ages and the $^{40}Ar/^{39}Ar$ ages are different. Apart from the abovementioned disparities, the production of low $\delta^{18}O$ material at Heise and Yellowstone appears to be very similar, and both centers indicate that previously erupted and hydrothermally altered material was reincorporated into the magmatic system (lowering its $\delta^{18}O$) and then later erupted (Bindeman et al., 2007b; Watts et al., 2011).

The Bruneau-Jarbidge Eruptive Center

The Bruneau-Jarbidge eruptive center (BJEC) differs significantly from the younger Heise and Yellowstone centers in that all of the magmas at the BJEC are low in $\delta^{18}O$. Cathey et al. (2007) report first order estimates of the average $\delta^{18}O_{WR}$ for the total eruptive volume from the CPT ranging from 2.4 to 3.4 $^{o}/_{oo}$ for all CPT erupted material. As the depletions in $^{18}O/^{16}O$ are present throughout the eruptive episode, Cathey et al., (2007) conclude that the CPT is the largest currently known low $\delta^{18}O$ silicic province on the planet.

Boroughs et al. (2005) and Boroughs (2010) suggest that the low $\delta^{18}O$ magmas from the BJEC may have been derived from melting of low $\delta^{18}O$ hydrothermally altered material from the Idaho Batholith. This cannot be a source for the erupted material at the more

easterly Heise and Yellowstone centers because of the sharp contrast between the earlier erupted normal $\delta^{18}O$ rhyolites and the later erupted low $\delta^{18}O$ rhyolites at those centers (Watts et al., 2011). Watts et al. (2011) also suggest that the Idaho Batholith could not be a source for Snake River Plain rhyolites due to the normal to high $\delta^{18}O$ for the majority of the batholith.

Regional Isotopic Modification

Leeman et al. (2008) evaluated the theoretical isotopic response of the crust to the penetration of meteoric waters and suggested that substantial $^{18}O/^{16}O$ depletions are possible (Leeman et al., 2008; Figure 12). They suggest that $^{18}O/^{16}O$ depletion in the shallow to mid crust may be of sufficient magnitude ($\delta^{18}O$ as low as -2 $^{o}/_{oo}$) to provide an appropriate protolith for the low $\delta^{18}O$ rhyolite magmas of the central Snake River Plain. At the BJEC, fluid migration into the crust may have been enhanced through Basin and Range extension, crustal deformation associated with magmatism, and also by the presence of a large lacustrine environment (Lake Idaho) in the topographically low regions of the central Snake River Plain during the Neogene (Leeman et al., 2008).

Methods

Zircons in this study were separated from hand specimens of lavas by A to Z, Inc. and individually selected using a binocular microscope. A total of 1,229 zircons were arranged within 5 mm of the center in 3 epoxy mounts and polished to a smooth, flat surface. Each mount contained the KIM-5 oxygen standard and the R33 U-Th-Pb standard. Zircons from the CPT had been mounted in epoxy prior to this study using similar methods

(Cathey et al., 2007). Prior to SIMS analysis, all zircons were imaged by cathodoluminescence (CL) in order to select optimum grains for subsequent work (Figure 2.1; Appendix F).

Zircons were analyzed for ^{16}O and ^{18}O on the Cameca IMS 1280 ion microprobe at the University of Wisconsin, with an analytical precision of 3 $^{o}/_{oo}$. Individual zircons were analyzed using a $^{133}Cs^{+}$ primary beam, with a 20 keV impact energy and primary ion intensities of 2 nA. The analysis spot size for the two days of analysis averaged 17 μm on the sample. Eight standard analyses bracketed every 10-20 analyses of unknowns (4 before and 4 after). The standard analyses were used to correct for instrumental mass fractionation (IMF) when determining the $\delta^{18}O$ of the analysis. When possible, each zircon was analyzed on the core and rim, as well as other areas in the interiors of some larger grains to determine intracrystal variations. After analyses were completed, each spot was examined by SEM at the University of Utah to assess whether or not other phases had been encountered in the analysis and if the ablation pit appeared to be pristine. Any analyses with spots that appeared problematic were omitted.

Results

Results of the oxygen isotope analyses of zircons are provided in Table 2.1 and summarized in Figures 2.2 and 2.3. Zircon $\delta^{18}O$ averages 1.5 $^{o}/_{oo}$ for all rhyolite lavas from the BJEC, with values ranging from as low as -3.4 $^{o}/_{oo}$ and as high as 8.1 $^{o}/_{oo}$ for individual analyses (Figure 2.2). Units that have near average $\delta^{18}O$ for all BJEC lavas are LCR, BJR, DCR, LLF, and CTR (1.0 – 1.8 $^{o}/_{oo}$), although the maximum value for CTR is a rim analysis that is about 2 $^{o}/_{oo}$ higher than most other analyses from the unit. ULF, MCR, and THR all have average $\delta^{18}O$ slightly below the average for all BJEC lavas (0.2 – 1.0 $^{o}/_{oo}$), although the

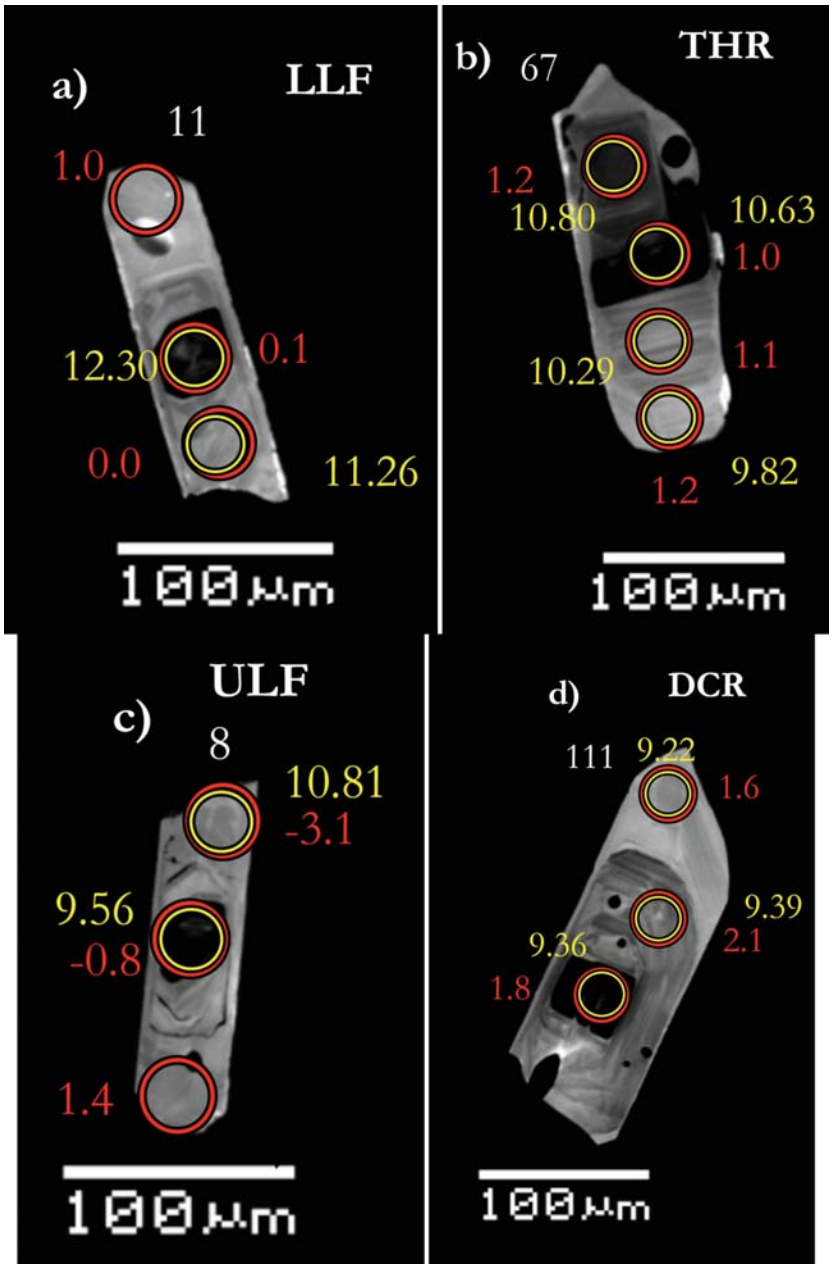

Figure 2.1. Examples of cathodoluminescence imaging of select zircons analyzed for oxygen isotopes ($\delta^{18}O$ as $^{o}/_{oo}$ in red) and U-Th-Pb dating (age as Ma in yellow) (discussed subsequently in the text). a) LLF-11 has an interior that is lower in $\delta^{18}O$ than the rim, as well as an older, inherited core; b) THR-67 is homogeneous in $\delta^{18}O$ c) ULF-8 has complex zoning, with an interior value of -3.1 $^{o}/_{oo}$ that is unusually low for volcanic systems; d) DCR-111 shows, within analytical error, no zoning throughout the grain; e) IBR-39 shows an inherited core (1.7 Ga) and inner region (175 Ma), and $\delta^{18}O$ that is heavier than average for the BJEC. The age of 7.83 Ma was discarded due to a suspected error from the unusually young age; f) LF1-2 shows complex zoning, with a rim of -2.9 $^{o}/_{oo}$; g) LF1-41 has a heavier core with a very ^{18}O-depleted rim of -3.4 $^{o}/_{oo}$; h) SCR-43 is a non-ancient grain showing unusually high $\delta^{18}O$ values for the core, interior, and rim. The age interior analysis was discarded due to its unusually young age compared to the rim (see chapter on dating).

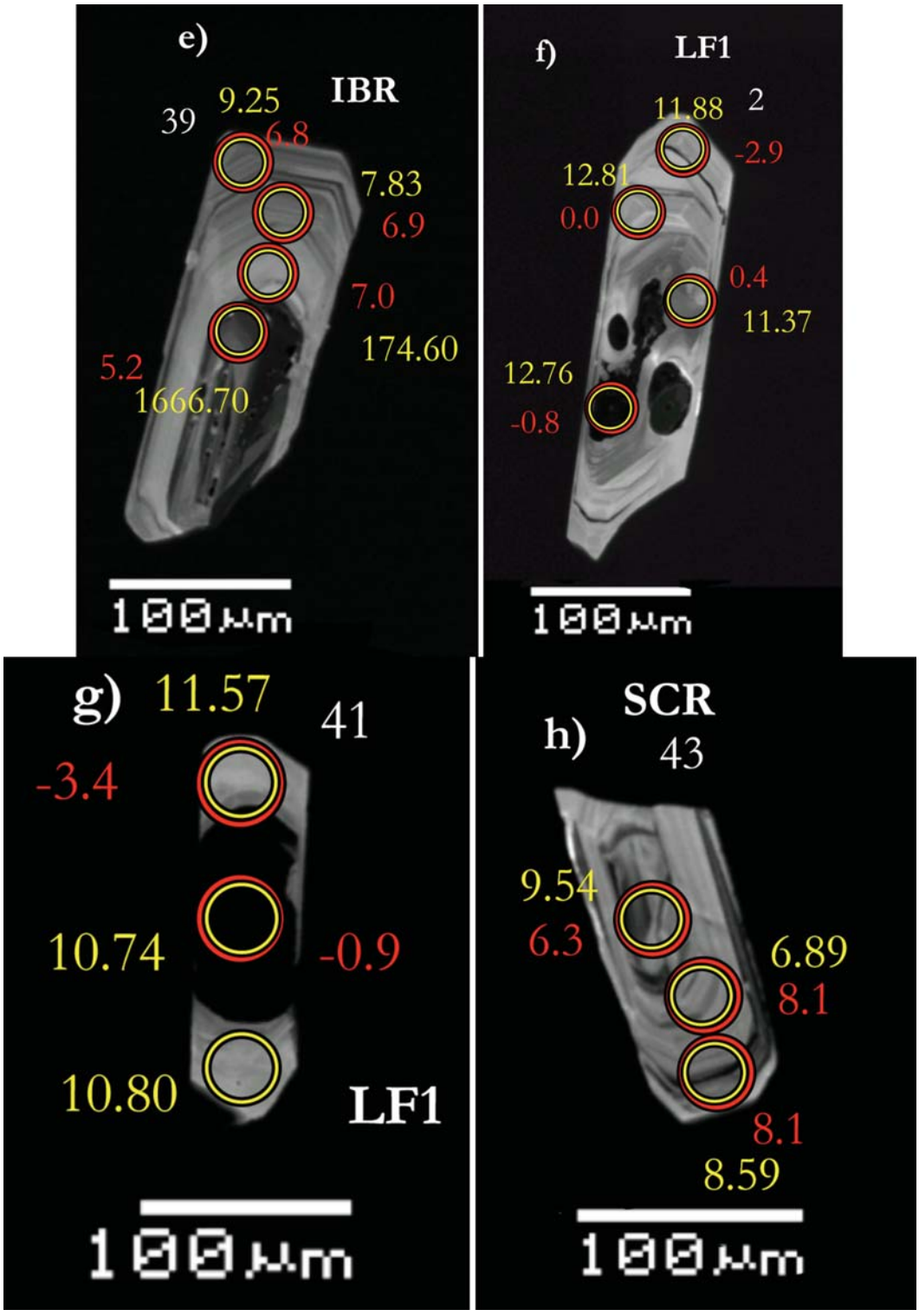

Figure 2.1 continued

Table 2.1: $\delta^{18}O$ of zircon from BJEC rhyolite lavas

SAMPLE NAME	UNIT	$\delta^{18}O$ (VSMOW)	IMF	$\delta^{18}O$ (VSMOW)*	$\delta^{18}O$ (2σ)
BJR-6-c	Bruneau-Jasper rhyolite	1.87	0.75	1.1	0.119
BJR-6-r	Bruneau-Jasper rhyolite	2.53	0.75	1.8	0.119
BJR-61-c	Bruneau-Jasper rhyolite	2.88	0.75	2.1	0.119
BJR-61-r	Bruneau-Jasper rhyolite	2.36	0.75	1.6	0.119
BJR-62-c	Bruneau-Jasper rhyolite	1.95	0.75	1.2	0.119
BJR-62-r	Bruneau-Jasper rhyolite	2.41	0.75	1.7	0.119
BJR-83-c	Bruneau-Jasper rhyolite	2.60	0.86	1.7	0.281
BJR-83-r	Bruneau-Jasper rhyolite	2.76	0.86	1.9	0.281
BJR-79-c	Bruneau-Jasper rhyolite	2.54	0.86	1.7	0.281
BJR-79-a	Bruneau-Jasper rhyolite	2.87	0.86	2.0	0.281
BJR-79-r	Bruneau-Jasper rhyolite	2.70	0.86	1.8	0.281
	Average			1.7	
	Maximum			2.1	
	Minimum			1.1	
CTR-60-c	Cedar Tree rhyolite	2.35	1.34	1.0	0.219
CTR-60-r	Cedar Tree rhyolite	2.36	1.34	1.0	0.219
CTR-53-c	Cedar Tree rhyolite	2.76	1.34	1.4	0.219
CTR-53-r	Cedar Tree rhyolite	5.08	1.34	3.7	0.219
CTR-37-c	Cedar Tree rhyolite	2.48	1.34	1.1	0.219
CTR-37-r	Cedar Tree rhyolite	2.05	1.34	0.7	0.219

IMF = Instrumental Mass Fractionation; $\delta^{18}O$ (VSMOW)* indicates $\delta^{18}O$ has been corrected for mass fractionation
c =core, r=rim, a,b=various interior regions of grain trending away from core.

Table 2.1 continued

SAMPLE NAME	UNIT	$\delta^{18}O$ (VSMOW)	IMF	$\delta^{18}O$ (VSMOW)*	$\delta^{18}O$ (2σ)
CTR-14-c	Cedar Tree rhyolite	2.30	1.34	1.0	0.219
CTR-14-r	Cedar Tree rhyolite	2.97	1.34	1.6	0.219
CTR-20-c	Cedar Tree rhyolite	2.40	1.34	1.1	0.219
CTR-20-a	Cedar Tree rhyolite	2.20	1.34	0.9	0.219
CTR-20-r	Cedar Tree rhyolite	2.70	1.34	1.4	0.219
CTR-67-c	Cedar Tree rhyolite	1.66	1.27	0.4	0.203
CTR-67-a	Cedar Tree rhyolite	2.26	1.27	1.0	0.203
CTR-67-r	Cedar Tree rhyolite	2.34	1.27	1.1	0.203
CTR-48-c	Cedar Tree rhyolite	1.76	1.34	0.4	0.219
CTR-48-a	Cedar Tree rhyolite	1.89	1.34	0.5	0.219
CTR-48-r	Cedar Tree rhyolite	2.50	1.34	1.2	0.219
CTR-64-a	Cedar Tree rhyolite	-0.40	1.34	-1.7	0.219
CTR-64-r	Cedar Tree rhyolite	2.41	1.34	1.1	0.219
	Average			1.0	
	Maximum			3.7	
	Minimum			-1.7	
DCR-12-c	Dorsey Creek rhyolite	4.18	1.26	2.9	0.156
DCR-12-r	Dorsey Creek rhyolite	2.89	1.26	1.6	0.156
DCR-20-c	Dorsey Creek rhyolite	3.39	1.26	2.1	0.156
DCR-20-r	Dorsey Creek rhyolite	3.68	1.26	2.4	0.156
DCR-57-r	Dorsey Creek rhyolite	3.30	1.26	2.0	0.156
DCR-41-c	Dorsey Creek rhyolite	2.42	1.26	1.2	0.156

Table 2.1 continued

SAMPLE NAME	UNIT	$\delta^{18}O$ (VSMOW)	IMF	$\delta^{18}O$ (VSMOW)*	$\delta^{18}O$ (2σ)
DCR-41-r	Dorsey Creek rhyolite	2.87	1.26	1.6	0.156
DCR-70-c	Dorsey Creek rhyolite	3.43	1.26	2.2	0.156
DCR-70-a	Dorsey Creek rhyolite	3.31	1.26	2.0	0.156
DCR-97-c	Dorsey Creek rhyolite	1.76	1.33	0.4	0.065
DCR-97-r	Dorsey Creek rhyolite	1.78	1.33	0.5	0.065
DCR-111-c	Dorsey Creek rhyolite	3.11	1.33	1.8	0.065
DCR-111-a	Dorsey Creek rhyolite	2.06	1.33	2.1	0.065
DCR-111-r	Dorsey Creek rhyolite	3.85	1.33	2.5	0.065
	Average			1.8	
	Maximum			2.9	
	Minimum			0.4	
IBR-62-c	Indian Batt rhyolite	2.54	0.96	1.6	0.222
IBR-62-ra	Indian Batt rhyolite	1.94	0.96	1.0	0.222
IBR-62-rb	Indian Batt rhyolite	1.94	0.96	1.0	0.222
IBR-54-c	Indian Batt rhyolite	1.95	0.96	1.0	0.222
IBR-54-r	Indian Batt rhyolite	1.53	0.96	0.6	0.222
IBR-44-c	Indian Batt rhyolite	1.84	0.92	0.9	0.201
IBR-44-a	Indian Batt rhyolite	2.12	0.92	1.2	0.201
IBR-44-r	Indian Batt rhyolite	1.62	0.92	0.7	0.201
IBR-21-c	Indian Batt rhyolite	1.84	0.92	0.9	0.201
IBR-21-a	Indian Batt rhyolite	1.80	0.92	0.9	0.201
IBR-21-r	Indian Batt rhyolite	1.99	0.92	1.1	0.201

Table 2.1 continued

SAMPLE NAME	UNIT	$\delta^{18}O$ (VSMOW)	IMF	$\delta^{18}O$ (VSMOW)*	$\delta^{18}O$ (2σ)
IBR-13-c	Indian Batt rhyolite	2.02	0.92	1.1	0.201
IBR-13-a	Indian Batt rhyolite	2.28	0.92	1.4	0.201
IBR-13-r	Indian Batt rhyolite	2.23	0.92	1.3	0.201
IBR-39-ca	Indian Batt rhyolite	6.07	0.92	5.2	0.201
IBR-39-a	Indian Batt rhyolite	7.88	0.92	7.0	0.201
IBR-39-b	Indian Batt rhyolite	7.78	0.92	6.9	0.201
IBR-39-r	Indian Batt rhyolite	7.69	0.92	6.8	0.201
	Average			2.2	
	Maximum			7.0	
	Minimum			0.6	
LF1-2-c	Lava flow one	0.58	1.33	-0.8	0.065
LF1-2-a	Lava flow one	1.77	1.33	0.4	0.065
LF1-2-b	Lava flow one	1.29	1.30	0.0	0.065
LF1-2-r	Lava flow one	-1.57	1.33	-2.9	0.065
LF1-35-c	Lava flow one	1.44	1.30	0.1	0.157
LF1-35-r	Lava flow one	-1.87	1.30	-3.2	0.157
LF1-66-c	Lava flow one	0.82	1.30	-0.5	0.157
LF1-66-a	Lava flow one	1.85	1.33	0.5	0.157
LF1-66-r	Lava flow one	2.23	1.30	0.9	0.157
LF1-76-c	Lava flow one	1.50	1.33	0.2	0.157
LF1-12-c	Lava flow one	0.70	1.33	-0.6	0.065
LF1-12-r	Lava flow one	0.63	1.30	-0.7	0.065

Table 2.1 continued

SAMPLE NAME	UNIT	$\delta^{18}O$ (VSMOW)	IMF	$\delta^{18}O$ (VSMOW)*	$\delta^{18}O$ (2σ)
LF1-41-c	Lava flow one	0.44	1.30	-0.9	0.157
LF1-41-r	Lava flow one	-2.11	1.30	-3.4	0.157
LF1-39-c	Lava flow one	2.56	1.30	1.3	0.157
LF1-39-r	Lava flow one	3.29	1.30	2.0	0.157
	Average			-0.5	
	Maximum			2.0	
	Minimum			-3.4	
LCR-18-c	Louse Creek rhyolite	2.55	0.91	1.6	0.288
LCR-18-r	Louse Creek rhyolite	2.11	0.91	1.2	0.288
LCR-17-c	Louse Creek rhyolite	2.29	0.91	1.4	0.288
LCR-17-r	Louse Creek rhyolite	1.86	0.91	1.0	0.288
LCR-40-c	Louse Creek rhyolite	2.29	0.91	1.4	0.288
LCR-40-r	Louse Creek rhyolite	2.10	0.91	1.2	0.288
LCR-10-ca	Louse Creek rhyolite	2.48	1.01	1.5	0.217
LCR-10-cb	Louse Creek rhyolite	2.33	1.01	1.3	0.217
LCR-10-a	Louse Creek rhyolite	2.13	1.01	1.1	0.217
LCR-10-r	Louse Creek rhyolite	2.32	1.01	1.3	0.217
LCR-34-c	Louse Creek rhyolite	2.59	1.01	1.6	0.217
LCR-34-r	Louse Creek rhyolite	1.89	1.01	0.9	0.217
LCR-88-c	Louse Creek rhyolite	2.20	1.01	1.2	0.217
LCR-88-r	Louse Creek rhyolite	2.12	1.01	1.1	0.217
LCR-105-c	Louse Creek rhyolite	1.70	1.01	0.7	0.217

Table 2.1 continued

SAMPLE NAME	UNIT	$\delta^{18}O$ (VSMOW)	IMF	$\delta^{18}O$ (VSMOW)*	$\delta^{18}O$ (2σ)
LCR-105-r	Louse Creek rhyolite	2.48	1.01	1.5	0.217
LCR-79-c	Louse Creek rhyolite	2.85	1.04	1.8	0.215
LCR-85-c	Louse Creek rhyolite	2.55	1.04	1.5	0.215
LCR-85-r	Louse Creek rhyolite	3.09	1.04	2.0	0.215
	Average			1.3	
	Maximum			2.0	
	Minimum			0.7	
LLF-4-c	Lower lava flow	2.37	1.22	1.2	0.189
LLF-4-r	Lower lava flow	2.29	1.22	1.1	0.189
LLF-11-c	Lower lava flow	1.30	1.22	0.1	0.189
LLF-11-a	Lower lava flow	1.26	1.22	0.0	0.189
LLF-11-r	Lower lava flow	2.22	1.22	1.0	0.189
LLF-15-c	Lower lava flow	2.03	1.22	0.8	0.189
LLF-15-r	Lower lava flow	3.17	1.22	2.0	0.189
LLF-26-c	Lower lava flow	2.24	1.24	1.0	0.197
LLF-26-r	Lower lava flow	1.82	1.24	0.6	0.197
LLF-43-c	Lower lava flow	2.86	1.24	1.6	0.197
LLF-43-r	Lower lava flow	2.43	1.24	1.2	0.197
LLF-41-c	Lower lava flow	2.39	1.24	1.2	0.197
LLF-41-r	Lower lava flow	2.52	1.24	1.3	0.197
LLF-35-c	Lower lava flow	2.52	1.24	1.3	0.197
LLF-35-r	Lower lava flow	2.53	1.24	1.3	0.197

Table 2.1 continued

Average	1.0
Maximum	2.0
Minimum	0.0

SAMPLE NAME	UNIT	$\delta^{18}O$ (VSMOW)	IMF	$\delta^{18}O$ (VSMOW)*	$\delta^{18}O$ (2σ)
MCR-87-ca	Marys Creek rhyolite	2.39	1.31	1.1	0.267
MCR-87-cb	Marys Creek rhyolite	2.76	1.31	1.5	0.267
MCR-87-a	Marys Creek rhyolite	3.01	1.31	1.7	0.267
MCR-87-ra	Marys Creek rhyolite	0.57	1.31	-0.7	0.267
MCR-87-rb	Marys Creek rhyolite	1.03	1.31	-0.3	0.267
MCR-80-c	Marys Creek rhyolite	4.39	1.31	3.1	0.267
MCR-78-a	Marys Creek rhyolite	2.44	1.31	1.1	0.267
MCR-78-r	Marys Creek rhyolite	0.25	1.31	-1.1	0.267
MCR-77-c	Marys Creek rhyolite	2.37	1.22	1.1	0.189
MCR-77-r	Marys Creek rhyolite	2.82	1.22	1.6	0.189
MCR-71-ca	Marys Creek rhyolite	2.49	1.22	1.3	0.189
MCR-71-cb	Marys Creek rhyolite	2.15	1.22	0.9	0.189
MCR-71-r	Marys Creek rhyolite	2.70	1.22	1.5	0.189
MCR-66-c	Marys Creek rhyolite	2.48	1.22	1.3	0.189
MCR-65-c	Marys Creek rhyolite	1.55	1.22	0.3	0.189
MCR-65-ra	Marys Creek rhyolite	1.18	1.22	0.0	0.189
MCR-65-rb	Marys Creek rhyolite	2.64	1.22	1.4	0.189
MCR-57-c	Marys Creek rhyolite	2.24	1.22	1.0	0.189
MCR-57-a	Marys Creek rhyolite	0.34	1.22	0.3	0.189
MCR-57-r	Marys Creek rhyolite	0.34	1.22	-0.9	0.189

Table 2.1 continued

Average	0.8
Maximum	3.1
Minimum	-1.1

SAMPLE NAME	UNIT	$\delta^{18}O$ (VSMOW)	IMF	$\delta^{18}O$ (VSMOW)*	$\delta^{18}O$ (2σ)
PCR-69-c	Poison Creek rhyolite	3.93	1.04	2.9	0.215
PCR-69-r	Poison Creek rhyolite	2.97	1.04	1.9	0.215
PCR-27-c	Poison Creek rhyolite	2.96	1.04	1.9	0.215
PCR-27-r	Poison Creek rhyolite	3.01	1.04	2.0	0.215
PCR-52-c	Poison Creek rhyolite	3.67	1.04	2.6	0.215
PCR-52-r	Poison Creek rhyolite	3.47	1.04	2.4	0.215
PCR-15-c	Poison Creek rhyolite	2.82	1.04	1.8	0.215
PCR-15-r	Poison Creek rhyolite	2.89	1.04	1.8	0.215
PCR-46-c	Poison Creek rhyolite	2.73	1.04	1.7	0.215
PCR-46-r	Poison Creek rhyolite	3.29	1.04	2.3	0.215
PCR-45-c	Poison Creek rhyolite	3.96	0.97	3.0	0.297
PCR-45-r	Poison Creek rhyolite	3.57	0.97	2.6	0.297
PCR-74-ca	Poison Creek rhyolite	5.03	0.97	4.1	0.297
PCR-74-cb	Poison Creek rhyolite	4.51	0.97	3.5	0.297
PCR-74-r	Poison Creek rhyolite	2.94	0.97	2.0	0.297
PCR-104-c	Poison Creek rhyolite	3.28	0.97	2.3	0.297
PCR-104-r	Poison Creek rhyolite	3.88	0.97	2.9	0.297
PCR-129-c	Poison Creek rhyolite	3.07	0.97	2.1	0.297
PCR-129-r	Poison Creek rhyolite	3.26	0.97	2.3	0.297
PCR-131-c	Poison Creek rhyolite	3.17	0.97	2.2	0.297

Table 2.1 continued

SAMPLE NAME	UNIT	$\delta^{18}O$ (VSMOW)	IMF	$\delta^{18}O$ (VSMOW)*	$\delta^{18}O$ (2σ)
PCR-131-r	Poison Creek rhyolite	3.67	0.97	2.7	0.297
	Average			2.4	
	Maximum			4.1	
	Minimum			1.7	
SCR-2-c	Sheep Creek rhyolite	7.99	1.30	6.7	0.157
SCR-2-a	Sheep Creek rhyolite	8.12	1.30	6.8	0.157
SCR-2-r	Sheep Creek rhyolite	7.95	1.30	6.7	0.157
SCR-14-r	Sheep Creek rhyolite	3.30	1.30	2.0	0.157
SCR-62-c	Sheep Creek rhyolite	3.67	1.30	2.4	0.157
SCR-62-r	Sheep Creek rhyolite	3.58	1.30	2.3	0.157
SCR-70-c	Sheep Creek rhyolite	1.54	1.27	0.3	0.203
SCR-101-c	Sheep Creek rhyolite	3.31	1.27	2.0	0.203
SCR-101-r	Sheep Creek rhyolite	3.27	1.27	2.0	0.203
SCR-43-c	Sheep Creek rhyolite	7.52	1.27	6.3	0.203
SCR-43-r	Sheep Creek rhyolite	9.37	1.27	8.1	0.203
SCR-43-a	Sheep Creek rhyolite	9.32	1.27	8.1	0.203
SCR-51-c	Sheep Creek rhyolite	2.52	1.27	1.2	0.203
SCR-51-r	Sheep Creek rhyolite	2.36	1.27	1.1	0.203
	Average			4.0	
	Maximum			8.1	
	Minimum			0.3	

Table 2.1 continued

SAMPLE NAME	UNIT	$\delta^{18}O$ (VSMOW)	IMF	$\delta^{18}O$ (VSMOW)*	$\delta^{18}O$ (2σ)
TCT-1-c	Three Creek tuff	2.81	0.86	1.9	0.281
TCT-1-r	Three Creek tuff	3.56	0.86	2.7	0.281
TCT-5-c	Three Creek tuff	1.43	0.86	0.6	0.281
TCT-5-r	Three Creek tuff	0.27	0.86	-0.6	0.281
TCT-13-c	Three Creek tuff	2.12	0.86	1.3	0.281
TCT-13-a	Three Creek tuff	3.50	0.86	2.6	0.281
TCT-13-r	Three Creek tuff	2.13	0.86	1.3	0.281
TCT-76-c	Three Creek tuff	7.36	0.86	6.5	0.281
TCT-76-r	Three Creek tuff	3.90	0.86	3.0	0.281
TCT-61-c	Three Creek tuff	3.71	0.86	2.8	0.281
TCT-71-c	Three Creek tuff	2.93	0.96	2.0	0.222
TCT-71-a	Three Creek tuff	3.48	0.96	2.5	0.222
TCT-71-b	Three Creek tuff	3.26	0.96	2.3	0.222
TCT-71-ra	Three Creek tuff	2.25	0.96	1.3	0.222
TCT-71-rb	Three Creek tuff	2.90	0.96	1.9	0.222
TCT-87-c	Three Creek tuff	3.89	0.96	2.9	0.222
TCT-87-r	Three Creek tuff	3.71	0.96	2.8	0.222
TCT-91-c	Three Creek tuff	4.30	0.96	3.3	0.222
TCT-91-r	Three Creek tuff	3.40	0.96	2.4	0.222
	Average			2.3	
	Maximum			6.5	
	Minimum			-0.6	

Table 2.1 continued

SAMPLE NAME	UNIT	$\delta^{18}O$ (VSMOW)	IMF	$\delta^{18}O$ (VSMOW)*	$\delta^{18}O$ (2σ)
THR-9-c	Triguero Homestead rhyolite	2.83	1.24	1.6	0.197
THR-9-r	Triguero Homestead rhyolite	1.98	1.24	0.7	0.197
THR-20-c	Triguero Homestead rhyolite	0.27	1.24	-1.0	0.197
THR-20-a	Triguero Homestead rhyolite	2.11	1.24	0.9	0.197
THR-20-r	Triguero Homestead rhyolite	2.27	1.24	1.0	0.197
THR-23-c	Triguero Homestead rhyolite	2.55	1.24	1.3	0.197
THR-23-r	Triguero Homestead rhyolite	2.50	1.24	1.3	0.197
THR-29-c	Triguero Homestead rhyolite	2.39	1.24	1.2	0.197
THR-29-r	Triguero Homestead rhyolite	2.34	1.24	1.1	0.197
THR-30-c	Triguero Homestead rhyolite	1.55	1.24	0.3	0.197
THR-30-a	Triguero Homestead rhyolite	1.67	1.24	0.4	0.197
THR-30-r	Triguero Homestead rhyolite	2.58	1.24	1.3	0.197
THR-31-c	Triguero Homestead rhyolite	2.68	1.24	1.4	0.197
THR-31-a	Triguero Homestead rhyolite	1.86	1.24	0.6	0.197
THR-31-r	Triguero Homestead rhyolite	1.96	1.24	0.7	0.197
THR-52-c	Triguero Homestead rhyolite	2.72	1.29	1.4	0.159
THR-52-a	Triguero Homestead rhyolite	2.76	1.29	1.5	0.159
THR-52-r	Triguero Homestead rhyolite	2.47	1.29	1.2	0.159
THR-85-c	Triguero Homestead rhyolite	0.88	1.29	-0.4	0.159
THR-85-a	Triguero Homestead rhyolite	2.90	1.29	1.6	0.159
THR-85-r	Triguero Homestead rhyolite	2.54	1.29	1.3	0.159
THR-67-c	Triguero Homestead rhyolite	2.47	1.29	1.2	0.159
THR-67-a	Triguero Homestead rhyolite	2.24	1.29	1.0	0.159
THR-67-b	Triguero Homestead rhyolite	2.40	1.29	1.1	0.159
THR-67-r	Triguero Homestead rhyolite	2.46	1.29	1.2	0.159

Table 2.1 continued

	Average			1.0	
	Maximum			1.6	
	Minimum			-1.0	

SAMPLE NAME	UNIT	$\delta^{18}O$ (VSMOW)	IMF	$\delta^{18}O$ (VSMOW)*	$\delta^{18}O$ (2σ)
ULF-42-c	Upper lava flow	0.60	1.29	-0.7	0.159
ULF-42-ra	Upper lava flow	0.81	1.29	-0.5	0.159
ULF-42-rb	Upper lava flow	1.38	1.29	0.1	0.159
ULF-16-c	Upper lava flow	1.45	1.29	0.2	0.159
ULF-16-r	Upper lava flow	2.34	1.29	1.1	0.159
ULF-13-c	Upper lava flow	2.22	1.29	0.9	0.159
ULF-4-c	Upper lava flow	0.77	1.29	-0.5	0.159
ULF-39-r	Upper lava flow	2.19	1.29	0.9	0.159
ULF-8-c	Upper lava flow	0.48	1.29	-0.8	0.159
ULF-8-a	Upper lava flow	-1.80	1.29	-3.1	0.159
ULF-8-r	Upper lava flow	2.65	1.29	1.4	0.159
ULF-19-c	Upper lava flow	1.96	1.29	0.7	0.159
ULF-19-r	Upper lava flow	2.28	1.29	1.0	0.159
ULF-11-c	Upper lava flow	2.79	1.29	1.5	0.159
ULF-11-r	Upper lava flow	2.20	1.29	0.9	0.159
	Average			0.2	
	Maximum			1.5	
	Minimum			-3.1	

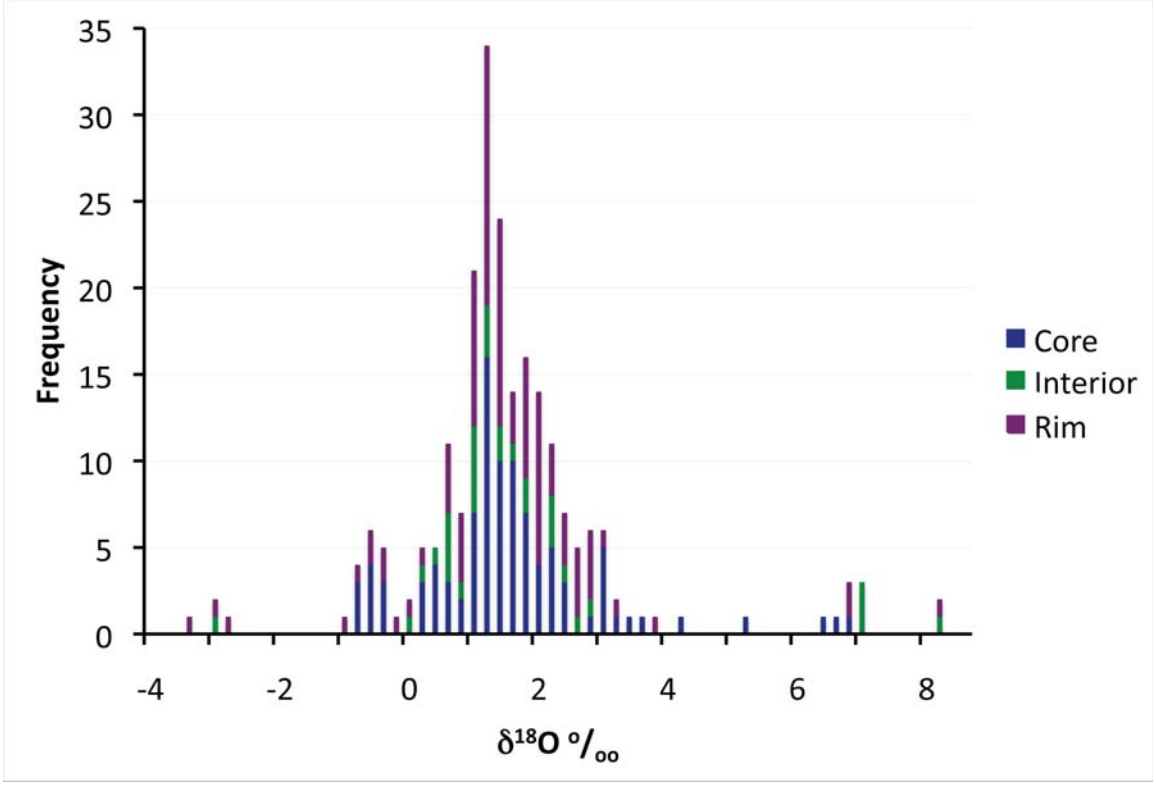

Figure 2.2. $\delta^{18}O$ for cores, rims, and interiors of zircons in lavas from the BJEC.

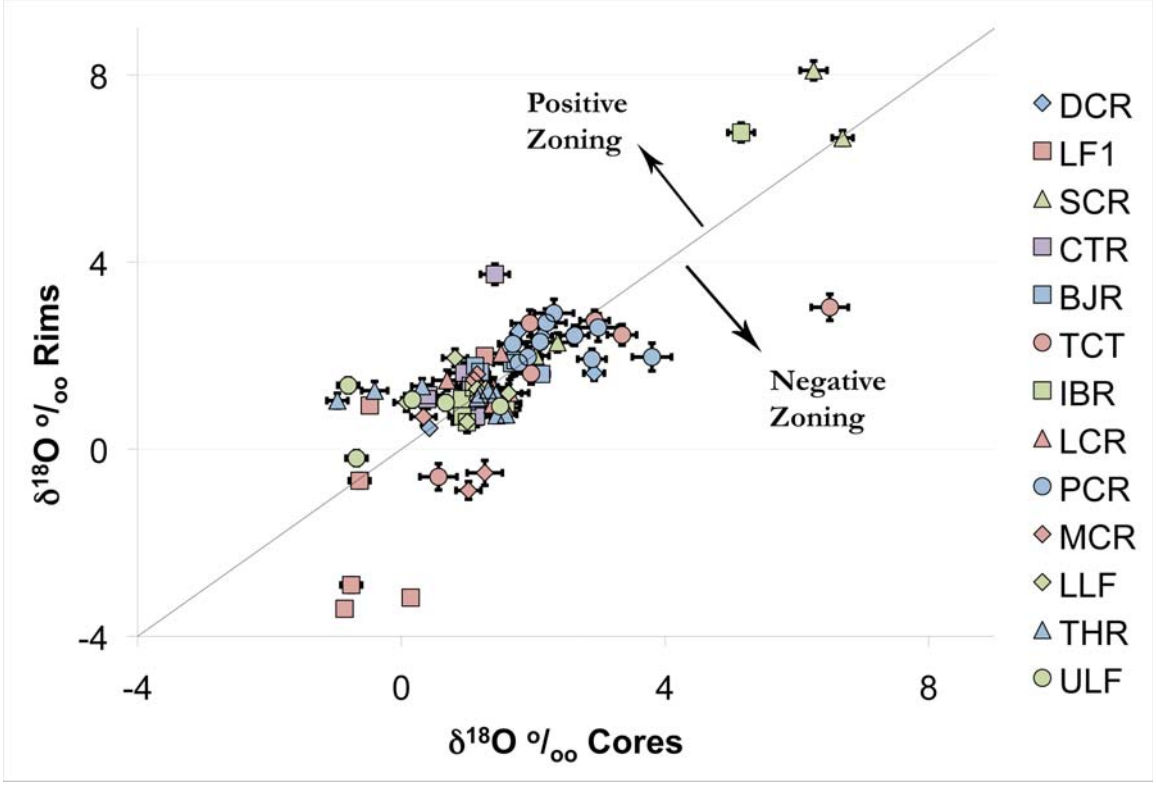

Figure 2.3. $\delta^{18}O$ in zircon rims vs. cores showing zoning in zircon from BJEC lavas. Error bars are 2σ.

lowest value for ULF is an interior analysis that is over 2 $^{o}/_{oo}$ lower than all other analyses from that unit. IBR, PCR, SCR, and TCT all have average $\delta^{18}O$ heavier than average for most BJEC lavas (2.2 – 4.0 $^{o}/_{oo}$). Although these units have unusually heavy values, there are grains included in some of these units that bias their averages. There are three analyses that are above average for IBR that are all from the same grain and cluster within the same range of $\delta^{18}O$ even though the rest of the analyses from IBR have $\delta^{18}O$ values that are near average for BJEC lavas. There are six analyses above average from SCR that are all from two grains, and from TCT there is one anomalously high core value that is approximately 3 $^{o}/_{oo}$ heavier than most other analyses from this unit. LF1 includes some of the lowest $\delta^{18}O$ of all lavas from the BJEC, with a $\delta^{18}O$ average of -0.5 $^{o}/_{oo}$, and the lowest $\delta^{18}O$ values of the unit, which are significantly lower than many other values, are all from zircon rims which average -1.2 $^{o}/_{oo}$.

Intracrystal Variation in $\delta^{18}O$

Zoning was determined on individual grains by assessing whether the difference between $\delta^{18}O$ of the core and rim (or interior region) was greater than the combination of the analytical uncertainty from the two analyses. If the inner regions of the grain have a higher $\delta^{18}O$ than the rim, the zoning was designated to be negative, and if the outer regions of the grain were heavier, the zoning was determined to be positive, the convention adopted by Cathey et al., unpublished. There are 41 grains that are unzoned between the core and rim, where the difference in $\delta^{18}O$ is less than that of the uncertainties of the analyses. This is illustrated in Figure 2.3, where there are 20 grains with negative zonation, and 26 grains showing positive zonation based on their trends between the core and rim. In greater detail,

9 grains have positive zonations from the core to interior A region (the outer core), while 4 grains have negative zonation and 13 grains are unzoned from the core to interior A. Four grains were analyzed further to allow for the determination of the zonation from the interior A to the interior B (inner rim) region of the grain. These grains are IBR-39, LF1-2, TCT-71, and THR-67, and will be discussed later in the text.

Units DCR, BJR, and LCR show the least variation between the $\delta^{18}O$ of cores and rims. Zoning trends of DCR grains show a larger number of heavier rims than cores but all but one of the rim values are within 1 $^{o}/_{oo}$ of the core values, where the one grain showing a larger zonation has a lighter rim than core. Two of the three zircons with small variations in BJR show a trend towards heavier rims than cores, with only one grain having a heavier core than rim, while the other two grains are unzoned. LCR shows an equal number of negative and unzoned grains (three each), while there are two grains showing positive zonation, with no zonations reaching above 1 $^{o}/_{oo}$.

Most zircons from LLF, IBR, and SCR show little zoning, except a few outliers. Three grains from LLF have no zoning, while two grains show slight negative zonation (~0.4 $^{o}/_{oo}$), and two grains show positive zonation, with one having zonation greater than 1 $^{o}/_{oo}$. All but one grain from IBR (IBR-39) show little to no zoning (less than 1 $^{o}/_{oo}$). One grain with a high core $\delta^{18}O$ of 5.2 $^{o}/_{oo}$ (ancient) and a rim $\delta^{18}O$ of 6.8 $^{o}/_{oo}$, shows a heavier rim than core by 1.6 $^{o}/_{oo}$. This is one of the grains that was also analyzed in multiple interior regions. The patterns here show that from the core to the nearest interior region there was positive zonation. Then, from the outer core to the inner rim and from the inner rim to the rim, there was no zonation (zonation within the range of the uncertainty). Four of the five SCR grains are nearly homogeneous, with core and rim variations of less than 0.3 $^{o}/_{oo}$. The

fifth grain has a heavier rim than core. This grain also has a high $\delta^{18}O$ for the core (6.3 $^{o}/_{oo}$) and rim (8.1 $^{o}/_{oo}$).

MCR, PCR, and TCT all show some grains with small positive zoning, with a few grains having much heavier cores than rims. Three of the six zircons in MCR have less than 1 $^{o}/_{oo}$ positive zonation, with the other three having much heavier cores than rims (greater than 1 $^{o}/_{oo}$ difference). Four of the ten grains from PCR show no zonation, while three grains show positive zonation of ~0.6 $^{o}/_{oo}$, and three show negative zonation with one of the negatively zoned grains having a nearly 2 $^{o}/_{oo}$ difference between the core and rim, and one having nearly a 1 $^{o}/_{oo}$ difference. Two grains from TCT show no zonation between the core and rim, while two grains show positive zonation, with one having a less than 1 $^{o}/_{oo}$ zonation and one having greater than 1 $^{o}/_{oo}$ zonation. Three grains have negative zonation, with one being less than 1 $^{o}/_{oo}$ and two greater than 1 $^{o}/_{oo}$ (one being -3.5 $^{o}/_{oo}$). TCT-71 (analyzed for multiple interior regions but no core analysis) is unzoned from the outer core to the inner rim, and has negative zonation from the inner rim to the rim (Appendix F).

ULF, THR, and CTR all have predominantly positive zonation. ULF has one zircon with a slight negative zonation (-0.6 $^{o}/_{oo}$), but the other four have heavier rims than cores. Three zircons from THR show no zonation, while three other grains have negative zonation of less than 1 $^{o}/_{oo}$. The remaining three grains from THR have positive zonation, with 2 of the 3 having zonation of greater than 1 $^{o}/_{oo}$. One of the grains from THR (67) has multiple analyses in the interior region of the grain. This grain has no zonation from the core to the interior nearest the core as well as to the inner rim and also from the inner rim to the rim. Most CTR zircons show only slight zonation between cores and rims. One grain from CTR has a slight negative zonation (-0.4 $^{o}/_{oo}$) and another shows no zoning, but the rest have heavier rims than cores, and one of these has a much heavier rim than core (2.3 $^{o}/_{oo}$).

LF1 zircons exhibit the most zoning of any lava, with only one unzoned grain. Two grains have positive zonation of less than 1 $^{o}/_{oo}$, and three grains show negative zonation of greater than 2 $^{o}/_{oo}$. One grain (LF1-2) had multiple analyses conducted on its interior. This zoning trend shows that from the core to interior A there was positive zonation, but from interior A to interior B there was negative zonation. From interior B (the inner rim) to the rim there was a significant depletion in ^{18}O, with a negative zonation of -2.9 $^{o}/_{oo}$.

Although 53% of grains show zoning of either positive or negative, only 22%, or 19 grains, have zoning above 1 $^{o}/_{oo}$. Of these 19 grains that have zonations greater than 1 $^{o}/_{oo}$, 9 show positive zonation and 10 show negative zonation. When considering all zonations in these zircons (even those below 1 $^{o}/_{oo}$) there does not appear to be any definite trends of zonation with time in relation to positive or negative zonation.

CHAPTER 3

U-Th-Pb DATING OF ZIRCON

Background

U-Th-Pb dating is based on the rate of radioactive decay of multiple isotopes of uranium (^{238}U, ^{235}U, and ^{234}U) and thorium (^{232}Th) isotopes to various lead isotopes (^{208}Pb, ^{207}Pb, and ^{206}Pb) along with various other intermediate daughters, including ^{234}U as an intermediate daughter product from the decay of ^{238}U. This method uses the measured ratios of various elements such as U/Pb, U/Th, and Th/Pb to determine a precise age of crystallization of minerals such as zircon (Ireland and Williams, 2003). Zircons are useful for this method of dating because of their moderate incorporation of U and Th, and their near exclusion of common ^{204}Pb, which allows for the precise determination of ages due to the high initial U/Pb and Th/Pb ratios (Speer, 1982). The refractory nature of zircons, which allows them to survive many extreme environments that most other minerals cannot also allows them to be a useful mineral for this technique of dating (Ireland and Williams, 2003). The zircons from the BJEC lavas were dated by the U-Th-Pb technique in order to determine the timing for acquisition of the oxygen isotope signatures in the zircon grains that were analyzed earlier using the Wisconsin SIMS.

Methods

Analyses for U-Th-Pb dating were conducted using the SHRIMP-RG at the USGS-Stanford University SUMAC laboratory. It was not possible to analyze all of the same locations that were previously analyzed for $\delta^{18}O$, so locations were chosen to include zircons exhibiting a variety of zonations in $\delta^{18}O$. Most of the time, the U-Th-Pb analysis was placed directly over the previous $\delta^{18}O$ analysis, although when possible the same CL region was used instead of overlapping multiple analyses. Most CL regions were too small to allow for the analysis of the ages to be adjacent to those of the $\delta^{18}O$ (Appendix F). R33, a zircon from the 419 Ma quartz diorite from the Braintree complex in Vermont, was used as a standard and analyzed approximately once every 4 unknown analyses (Black et al., 2004). A beam diameter of 25 μm was used, along with a 6-7 nA O^{2-} primary beam. The procedure provided a mass resolution of 8,000 at a 10% peak height. The primary beam was rastered over the spot for 3 minutes prior to analysis to remove any surficial common Pb. To correct for any ^{230}Th deficiency due to the slightly greater ionic radius of Th relative to U in the octahedral site in zircon, a ^{230}Th correction for a U/Th ratio of 0.25 was used.

Results

The ages determined from this study are based on the $^{206}Pb/^{238}U$ ratio of the individual analysis spot of the zircon. Results of the age determinations of zircons are provided in Tables 3.1 and 3.2 and summarized in Figure 3.1. All analyses with high common lead were removed at the start of assessment of the results, and were not considered for any ages. Weighted average mean ages (WAMA) as well as unmixed ages were determined using Isoplot (Ludwig, 2003) for each lava unit. A mean square of the weighted

Table 3.1: Age at which zircons acquired their oxygen isotopic ratios, showing possible inheritance of $\delta^{18}O$ values from from previously erupted units, as well as any analyses that were discarded due to discrepancies between core and rim ages, or ages that are too old to have been acquired from the BJEC.

UNIT	SAMPLE	$\delta^{18}O$ (VSMOW)	2σ	$^{206}P/^{238}U$ AGE (Ma)	2σ	INHERITED	DISCARD
Lava flow one	LF1-41-c	-0.9	0.157	10.74	0.40		
Lava flow one	LF1-41-r	-3.4	0.157	11.57	0.62		
Lava flow one	LF1-66-c	-0.5	0.157	10.44	0.45		
Lava flow one	LF1-66-a	0.5	0.157	10.92	0.68		
Lava flow one	LF1-66-r	0.9	0.157	10.71	0.66		
Lava flow one	LF1-35-c	0.1	0.157	11.17	0.45		
Lava flow one	LF1-39-c	1.3	0.157	11.35	0.63		
Lava flow one	LF1-39-r	2.0	0.157	11.08	0.61		
Lava flow one	LF1-12-c	-0.6	0.065	12.41	0.56	Y	
Lava flow one	LF1-12-r	-0.7	0.065	12.11	0.67	Y	
Lava flow one	LF1-2-c	-0.8	0.065	12.76	0.47	Y	
Lava flow one	LF1-2-a	0.4	0.065	11.37	0.58		
Lava flow one	LF1-2-b	0.0	0.065	12.81	0.72	Y	
Lava flow one	LF1-2-r	-2.9	0.065	11.88	0.56		
Eruption Age Determination							
Weighted Average Mean Age (±2σ)	11.42±0.43 Ma	8.0 MSWD					
Unmixed Age	10.97±0.18 Ma *	0.321 Relative Misfit	2 Ages				
Manual Exclusions	0						
Inheritance	Yes						

*** = selected magmatic age (also highlighted). c =core, r=rim, a,b=various interior regions of grain trending away from core. Y=discarded analysis if under discard column, or inherited grain if under the inherited column.**

Table 3.1 continued

UNIT	SAMPLE	$\delta^{18}O$ (VSMOW)	2σ	$^{206}P/^{238}U$ AGE (Ma)	2σ	INHERITED	DISCARD
Lower lava flow	LLF-4-c	1.2	0.189	11.11	0.47		
Lower lava flow	LLF-4-r	1.1	0.189	10.30	0.56		
Lower lava flow	LLF-11-c	0.1	0.189	12.30	0.39	Y	
Lower lava flow	LLF-11-a	0.0	0.189	11.26	0.60		
Lower lava flow	LLF-26-c	1.0	0.197	11.43	0.43		
Lower lava flow	LLF-26-r	0.6	0.197	12.06	0.37		
Lower lava flow	LLF-15-r	2.0	0.189	10.21	0.55		
Eruption Age Determination							
Weighted Average Mean Age (±2σ)	11.45±0.72	11.5 MSWD					
Unmixed Age	10.93±0.23 Ma *	0.341 Relative Misfit	2 Ages				
Manual Exclusions	0						
Inheritance	Yes						
Upper lava flow	ULF-42-c	-0.7	0.159	10.69	0.44		
Upper lava flow	ULF-42-ra	-0.5	0.159	10.59	0.55		
Upper lava flow	ULF-42-rb	0.1	0.159	11.51	0.40		
Upper lava flow	ULF-16-c	0.2	0.159	10.99	0.34		
Upper lava flow	ULF-16-r	1.1	0.159	11.09	0.56		
Upper lava flow	ULF-19-c	0.7	0.159	10.82	0.50		
Upper lava flow	ULF-19-r	1.0	0.159	9.38	0.50		Y
Upper lava flow	ULF-11-c	1.5	0.159	10.54	0.42		
Upper lava flow	ULF-11-r	0.9	0.159	10.63	0.64		

Table 3.1 continued

UNIT	SAMPLE	$\delta^{18}O$ (VSMOW)	2σ	$^{206}P/^{238}U$ AGE (Ma)	2σ	INHERITED	DISCARD
Upper lava flow	ULF-8-c	-0.8	0.159	9.56	0.41		Y
Upper lava flow	ULF-8-a	-3.1	0.159	10.81	0.57		
Eruption Age Determination							
Weighted Average Mean Age (±2σ)	10.89±0.25 Ma *	2.0 MSWD					
Unmixed Age	10.79±0.17	0.295 Relative Misfit	2 Ages				
Manual Exclusions	2						
Inheritance	No						
Triguero Homestead rhyolite	THR-9-c	1.6	0.197	10.86	0.45		
Triguero Homestead rhyolite	THR-23-c	1.3	0.197	10.99	0.39		
Triguero Homestead rhyolite	THR-23-r	1.3	0.197	8.86	0.59		
Triguero Homestead rhyolite	THR-52-c	1.4	0.159	10.59	0.47		
Triguero Homestead rhyolite	THR-85-c	-0.4	0.159	12.76	0.26	Y	
Triguero Homestead rhyolite	THR-85-a	1.6	0.159	10.17	0.61		
Triguero Homestead rhyolite	THR-85-r	1.3	0.159	10.56	0.54		
Triguero Homestead rhyolite	THR-67-c	1.2	0.159	10.80	0.37		
Triguero Homestead rhyolite	THR-67-a	1.0	0.159	10.63	0.28		
Triguero Homestead rhyolite	THR-67-b	1.1	0.159	10.29	0.57		
Triguero Homestead rhyolite	THR-67-r	1.2	0.159	9.82	0.70		
Triguero Homestead rhyolite	THR-20-c	-1.0	0.197	11.65	0.62	Y	
Triguero Homestead rhyolite	THR-20-a	0.9	0.197	11.78	0.66	Y	
Triguero Homestead rhyolite	THR-20-r	1.0	0.197	10.62	0.55		

Table 3.1 continued

UNIT	SAMPLE	$\delta^{18}O$ (VSMOW)	2σ	$^{206}P/^{238}U$ AGE (Ma)	2σ	INHERITED	DISCARD
Triguero Homestead rhyolite	THR-30-c	0.3	0.197	11.33	0.55	Y	
Triguero Homestead rhyolite	THR-30-a	0.4	0.197	11.73	0.54	Y	
Triguero Homestead rhyolite	THR-30-r	1.3	0.197	9.17	0.58		
Eruption Age Determination							
Weighted Average Mean Age (±2σ)	11.03±0.53	20.0 MSWD					
Unmixed Age	10.52±0.13 Ma *	0.331 Relative Misfit	2 Ages				
Manual Exclusions	0						
Inheritance	Yes						
Marys Creek Rhyolite	MCR-87-ca	1.1	0.267	9.68	0.55		
Marys Creek Rhyolite	MCR-87-cb	1.5	0.267	10.90	0.63		
Marys Creek rhyolite	MCR-87-a	1.7	0.267	9.55	0.46		
Marys Creek rhyolite	MCR-87-ra	-0.7	0.267	11.45	0.67		Y
Marys Creek rhyolite	MCR-87-rb	-0.3	0.267	9.82	0.92		
Marys Creek rhyolite	MCR-77-c	1.1	0.189	10.52	0.23		
Marys Creek rhyolite	MCR-77-r	1.6	0.189	9.79	0.50		
Marys Creek rhyolite	MCR-71-ca	1.3	0.189	10.47	0.50		
Marys Creek rhyolite	MCR-71-cb	0.9	0.189	10.78	0.61		
Marys Creek rhyolite	MCR-71-r	1.5	0.189	10.87	0.56		
Marys Creek rhyolite	MCR-65-c	0.3	0.189	10.22	0.24		
Marys Creek rhyolite	MCR-65-ra	0.0	0.189	10.19	0.56		
Marys Creek rhyolite	MCR-65-rb	1.4	0.189	9.76	0.57		

Table 3.1 continued

UNIT	SAMPLE	$\delta^{18}O$ (VSMOW)	2σ	$^{206}P/^{238}U$ AGE (Ma)	2σ	INHERITED	DISCARD
Marys Creek rhyolite	MCR-57-c	1.0	0.189	10.48	0.39		
Marys Creek rhyolite	MCR-57-a	0.3	0.189	10.45	0.45		
Marys Creek rhyolite	MCR-57-r	-0.9	0.189	10.27	0.50		
Eruption Age Determination							
Weighted Average Mean Age (±2σ)	10.29±0.20 Ma *	2.9 MSWD					
Unmixed Age	9.71±0.28	0.533 Relative Misfit	2 Ages				
Manual Exclusions	1						
Inheritance	No						
Cedar Tree rhyolite	CTR-67-c	0.4	0.203	11.08	0.66		
Cedar Tree rhyolite	CTR-67-a	1.0	0.203	10.33	0.72		
Cedar Tree rhyolite	CTR-67-r	1.1	0.203	10.64	0.73		
Cedar Tree rhyolite	CTR-48-c	0.4	0.219	10.31	0.47		
Cedar Tree rhyolite	CTR-48-a	0.5	0.219	9.44	0.62		
Cedar Tree rhyolite	CTR-48-r	1.2	0.219	10.62	0.58		
Cedar Tree rhyolite	CTR-20-c	1.1	0.219	9.51	0.53		
Cedar Tree rhyolite	CTR-20-a	0.9	0.219	10.52	0.67		
Cedar Tree rhyolite	CTR-20-r	1.4	0.219	10.02	0.51		
Cedar Tree rhyolite	CTR-53-c	1.4	0.219	10.30	0.42		
Cedar Tree rhyolite	CTR-37-c	1.1	0.219	10.80	0.54		
Cedar Tree rhyolite	CTR-14-c	1.0	0.219	10.57	0.57		
Cedar Tree rhyolite	CTR-64-r	1.1	0.219	9.87	0.80		

Table 3.1 continued

Eruption Age Determination								
Weighted Average Mean Age (±2σ)	10.29±0.28 Ma *	2.6 MSWD						
Unmixed Age	9.57±0.48	0.608 Relative Misfit	2 Ages					
Manual Exclusions	0							
Inheritance	No							

UNIT	SAMPLE	$\delta^{18}O$ (VSMOW)	2σ	$^{206}P/^{238}U$ AGE (Ma)	2σ	INHERITED	DISCARD
Bruneau-Jasper rhyolite	BJR-6-c	1.1	0.119	9.13	0.18		
Bruneau-Jasper rhyolite	BJR-6-r	1.8	0.119	8.97	0.34		
Bruneau-Jasper rhyolite	BJR-62-c	1.2	0.119	9.54	0.88		
Bruneau-Jasper rhyolite	BJR-62-r	1.7	0.119	9.78	0.49		
Bruneau-Jasper rhyolite	BJR-83-c	1.7	0.281	9.52	0.71		
Bruneau-Jasper rhyolite	BJR-83-r	1.9	0.281	9.76	0.48		
Bruneau-Jasper rhyolite	BJR-79-c	1.7	0.281	9.10	0.24		
Bruneau-Jasper rhyolite	BJR-79-a	2.0	0.281	9.27	0.30		
Bruneau-Jasper rhyolite	BJR-61-c	2.1	0.119	1095.50	24.00	Ancient	Y
Bruneau-Jasper rhyolite	BJR-61-r	1.6	0.119	8.62	0.45		

Eruption Age Determination								
Weighted Average Mean Age (±2σ)	9.17±0.21 Ma *	2.8 MSWD						
Unmixed Age	9.11±0.12	0.407 Relative Misfit	2 Ages					

Table 3.1 continued

Manual Exclusions	1
Inheritance	Yes

UNIT	SAMPLE	$\delta^{18}O$ (VSMOW)	2σ	$^{206}P/^{238}U$ AGE (Ma)	2σ	INHERITED	DISCARD
Poison Creek rhyolite	PCR-69-c	2.9	0.215	9.18	0.23		
Poison Creek rhyolite	PCR-69-r	1.9	0.215	8.96	0.79		
Poison Creek rhyolite	PCR-15-c	1.8	0.215	8.54	0.53		
Poison Creek rhyolite	PCR-15-r	1.8	0.215	6.80	0.60		Y
Poison Creek rhyolite	PCR-74-ca	4.1	0.297	9.40	0.67		
Poison Creek rhyolite	PCR-74-cb	3.5	0.297	9.30	0.61		
Poison Creek rhyolite	PCR-104-c	2.3	0.297	9.35	0.40		
Poison Creek rhyolite	PCR-104-r	2.9	0.297	7.66	0.84		Y
Eruption Age Determination							
Weighted Average Mean Age (±2σ)	9.16±0.26 Ma *	1.5 MSWD					
Unmixed Age	8.59±0.62	0.286 Relative Misfit	2 Ages				
Manual Exclusions	2						
Inheritance	No						
Louse Creek rhyolite	LCR-10-ca	1.5	0.217	9.75	0.68		
Louse Creek rhyolite	LCR-10-cb	1.3	0.217	8.58	0.59		
Louse Creek rhyolite	LCR-10-a	1.1	0.217	7.13	0.77		Y
Louse Creek rhyolite	LCR-10-r	1.3	0.217	9.11	0.71		

Table 3.1 continued

UNIT	SAMPLE	$\delta^{18}O$ (VSMOW)	2σ	$^{206}P/^{238}U$ AGE (Ma)	2σ	INHERITED	DISCARD
Louse Creek rhyolite	LCR-88-c	1.2	0.217	10.27	0.16	Y	
Louse Creek rhyolite	LCR-88-r	1.1	0.217	9.07	0.73		
Louse Creek rhyolite	LCR-105-c	0.7	0.217	8.57	0.58		
Louse Creek rhyolite	LCR-105-r	1.5	0.217	8.69	0.80		
Louse Creek rhyolite	LCR-85-c	1.5	0.215	9.91	0.46	Y	
Louse Creek rhyolite	LCR-85-r	2.0	0.215	9.84	0.84		
Louse Creek rhyolite	LCR-34-r	0.9	0.217	9.32	0.46		
Eruption Age Determination							
Weighted Average Mean Age (±2σ)	9.87±0.45	9.7 MSWD					
Unmixed Age	8.98±0.27 Ma *	0.209 Relative Misfit	2 Ages				
Manual Exclusions	1						
Inheritance	Yes						
Sheep Creek rhyolite	SCR-43-c	6.3	0.203	9.54	0.46		
Sheep Creek rhyolite	SCR-43-a	8.1	0.203	6.89	0.39		Y
Sheep Creek rhyolite	SCR-43-r	8.1	0.203	8.59	0.38		
Sheep Creek rhyolite	SCR-101-c	2.0	0.203	8.24	0.33		Y
Sheep Creek rhyolite	SCR-101-R	2.0	0.203	9.07	0.38		
Sheep Creek rhyolite	SCR-51-c	1.2	0.203	9.18	0.49		
Sheep Creek rhyolite	SCR-51-r	1.1	0.203	8.71	0.53		
Sheep Creek rhyolite	SCR-62-r	2.3	0.157	9.42	0.46		
Sheep Creek rhyolite	SCR-2-r	6.7	0.157	587.90	10.80	Ancient	Y

Table 3.1 continued

UNIT	SAMPLE	$\delta^{18}O$ (VSMOW)	2σ	$^{206}P/^{238}U$ AGE (Ma)	2σ	INHERITED	DISCARD
Sheep Creek rhyolite	SCR-2-c	6.7	0.157	621.20	12.20	Ancient	Y
Sheep Creek rhyolite	SCR-2-a	6.8	0.157	690.20	13.20	Ancient	Y
Eruption Age Determination							
Weighted Average Mean Age (±2σ)	9.06±0.40 Ma *	3.0 MSWD					
Unmixed Age	8.65±0.38	0.399 Relative Misfit	2 Ages				
Manual Exclusions	5						
Inheritance	Yes						
Indian Batt rhyolite	IBR-54-c	1.0	0.222	10.03	0.37		
Indian Batt rhyolite	IBR-54-r	0.6	0.222	9.57	0.85		
Indian Batt rhyolite	IBR-21-c	0.9	0.201	10.11	0.50		
Indian Batt rhyolite	IBR-21-a	0.9	0.201	7.89	0.43		
Indian Batt rhyolite	IBR-39-ca	5.2	0.201	1666.70	16.60	Ancient	Y
Indian Batt rhyolite	IBR-39-a	7.0	0.201	174.60	3.20	Ancient	Y
Indian Batt rhyolite	IBR-39-b	6.9	0.201	7.83	0.46		Y
Indian Batt rhyolite	IBR-39-r	6.8	0.201	9.25	0.37		
Indian Batt rhyolite	IBR-44-a	1.2	0.201	9.92	0.59		
Indian Batt rhyolite	IBR-44-r	0.7	0.201	10.77	0.72		
Indian Batt rhyolite	IBR-62-c	1.6	0.222	8.61	0.64		
Indian Batt rhyolite	IBR-62-ra	1.0	0.222	7.99	0.65		

Table 3.1 continued

Eruption Age Determination				
Weighted Average Mean Age (±2σ)	9.32±0.73 Ma *	14 MSWD		
Unmixed Age	8.09±0.31	0.268 Relative Misfit	2 Ages	
Manual Exclusions	3			
Inheritance	Yes			

UNIT	SAMPLE	$\delta^{18}O$ (VSMOW)	2σ	$^{206}P/^{238}U$ AGE (Ma)	2σ	INHERITED	DISCARD
Dorsey Creek rhyolite	DCR-12-c	2.9	0.156	8.40	0.33		
Dorsey Creek rhyolite	DCR-12-r	1.6	0.156	8.47	0.49		
Dorsey Creek rhyolite	DCR-20-c	2.1	0.156	9.21	0.47		
Dorsey Creek rhyolite	DCR-20-r	2.4	0.156	9.40	0.45		
Dorsey Creek rhyolite	DCR-41-c	1.2	0.156	8.90	0.61		
Dorsey Creek rhyolite	DCR-41-r	1.6	0.156	9.22	0.56		
Dorsey Creek rhyolite	DCR-111-c	1.8	0.065	9.36	0.41		
Dorsey Creek rhyolite	DCR-111-a	2.1	0.065	9.39	0.53		
Dorsey Creek rhyolite	DCR-111-r	2.5	0.065	7.82	0.54		
Dorsey Creek rhyolite	DCR-97-c	0.4	0.065	10.43	0.45	Y	
Dorsey Creek rhyolite	DCR-97-r	0.5	0.065	8.87	0.53		
Dorsey Creek rhyolite	DCR-70-a	2.0	0.156	7.85	0.36		
Eruption Age Determination							
Weighted Average Mean Age (±2σ)	8.88±0.49 Ma *	11.4 MSWD					
Unmixed Age	8.18±0.22	0.349 Relative Misfit	2 Ages				

Table 3.1 continued

Manual Exclusions	0
Inheritance	Yes

UNIT	SAMPLE	$\delta^{18}O$ (VSMOW)	2σ	$^{206}P/^{238}U$ AGE (Ma)	2σ	INHERITED	DISCARD
Three Creek Tuff	TCT-1-c	1.9	0.281	8.46	0.20		
Three Creek Tuff	TCT-1-r	2.7	0.281	8.53	0.52		
Three Creek Tuff	TCT-5-c	0.6	0.281	7.81	0.75		
Three Creek Tuff	TCT-5-r	-0.6	0.281	7.50	0.72		
Three Creek Tuff	TCT-76-c	6.5	0.281	9.33	0.24	Y	
Three Creek Tuff	TCT-76-r	3.0	0.281	7.82	0.63		
Three Creek Tuff	TCT-71-a	2.5	0.222	9.14	0.49	Y	
Three Creek Tuff	TCT-71-b	2.3	0.222	9.18	0.57	Y	
Three Creek Tuff	TCT-71-rb	1.9	0.222	9.68	0.83	Y	
Three Creek Tuff	TCT-13-c	1.3	0.281	951.1	6.7	Ancient	Y
Three Creek Tuff	TCT-13-d	NA	NA	8.01	0.76		
Eruption Age Determination							
Weighted Average Mean Age (±2σ)	8.73±0.41	8.2 MSWD					
Unmixed Age	8.31±0.17 Ma *	0.294 Relative Misfit	2 Ages				
Manual Exclusions	1						
Inheritance	Yes						

Table 3.2: Age determination of individual rhyolite units

UNIT	Number Analyses	Number Crystals Analyzed	Number Discarded Ages	Weighted Average Mean Age (Ma)	MSWD	Unmixed Age (Ma)	Relative Misfit	% Analyses Contributed	Number Analyses Contributed
Lava flow one	15	6	0	11.42±0.43	8	10.97±0.18	0.321	66	10
						12.41±0.28		34	5
Lower lava flow	11	5	4	11.45±0.72	11.5	10.93±0.23	0.341	71	5
						12.17±0.28		29	2
Upper lava flow	12	5	3	10.89±0.25	2	10.79±0.17	0.295	88	8
						11.48±0.44		12	1
Triguero Homestead rhyolite	20	7	3	11.03±0.53	20	10.52±0.13	0.331	77	13
						12.38±0.22		23	4
Marys Creek rhyolite	16	5	1	10.29±0.20	2.9	9.71±0.28	0.533	29	4
						10.42±0.13		71	11
Cedar Tree rhyolite	19	8	6	10.29±0.28	2.6	9.57±0.48	0.608	20	3
						10.459±0.19		80	10

Table 3.2 continued

UNIT	Number Analyses	Number Crystals Analyzed	Number Discarded Ages	Weighted Average Mean Age (Ma)	MSWD	Unmixed Age (Ma)	Relative Misfit	% Analyses Contributed	Number Analyses Contributed
Bruneau-Jasper rhyolite	10	5	1	9.17±0.21	2.8	9.11±0.12	0.407	70	6
						9.73±0.34		30	2
Poison Creek rhyolite	8	4	2	9.16±0.26	1.5	8.59±0.62	0.286	17	1
Louse Creek rhyolite	12	5	2	9.87±0.45	9.7	8.98±0.27	0.209	65	7
						10.20±0.15		35	3
Sheep Creek rhyolite	12	5	6	9.06±0.40	3	8.65±0.38	0.399	32	2
						9.27±0.25		68	4
Indian Batt rhyolite	15	5	6	9.32±0.73	14	8.09±0.31	0.268	33	3
						9.83±0.20		67	6
Dorsey Creek rhyolite	13	6	1	8.88±0.49	11.4	8.18±0.22	0.349	35	4
						9.42±0.22		65	8
Three Creek tuff	11	5	1	8.73±0.41	8.2	8.31±0.17	0.294	60	6
						9.3±0.20		40	4

deviates (MSWD) ≤ 3.0, instead of the standard use of ≤ 2.0, was used to indicate a unimodal, homogeneous age spectrum for which a single age is appropriate due to the general larger span in ages from these lavas. Larger values of the MSWD are indicative of either underestimated analytical errors or scatter in the data due to multiple age components that may be extracted from the spectrum by "unmixing" (Ludwig, 2003). These multiple ages are often discernable on a probability density plot. Unmixed ages are derived by deconvolution of all zircon analyses from a single lava flow and involves guessing the number of age components and assessing the optimum number by evaluating the Relative Misfit parameter, which decreases with increasing likelihood of a particular number of ages. Once the relative misfit of the ages that are placed into the calculation no longer decreases with an increased number of input ages, that age is the preferred value (Sambridge and Compston, 1994). In some cases, although the relative misfit was at its minimum, the percentage of grains used for the preferred age from the unmixed age determination was below 40%, which does not constitute a meaningful age (Ludwig, 2003). When this was the case, the WAMA with the large MSWD was used as the preferred age, with its large uncertainty, and with the knowledge that there is a significant portion of inherited grains associated with that age. This was done so an age would not be based on only a few grains, and a more robust age would be used as a best age estimate for a particular unit. Unmixed ages for units with MSWD smaller than 3.0 are provided in Table 3.2. In the cases where rims were older than cores, or interiors older than cores, etc., the problematic ages were discarded, as were ages of units that were suspected to be unusually young based on geologic evidence. All ages that were determined to be ancient (older than the age of the eruptive center) were not included in the calculation to determine the age for an individual unit. Zircons are defined as being inherited if their age minus their uncertainty is still older than

the magma age for their lava unit plus its uncertainty. If the rim age is similar to the age of the core, but the rim has a larger uncertainty, these criteria may determine that a rim is inherited when its core is not, and if this is the case the rim was not determined to be inherited. If the unmixed age includes a considerable portion of grains comprising an older age, or if the MSWD was significantly large, this could also suggest the presence of inherited grains. Age and $\delta^{18}O$ data on CPT zircons used to assess possible sources for inherited zircons was provided by H. E. Cathey (personal communication). Ages that are inferred to be too young for individual eruptive units and are excluded from the age calculations are interpreted to have incorporated error in the analysis. The sequence of eruptions was determined using a combination of the newly determined U-Th-Pb ages, previously known stratigraphic order, and previously determined K-Ar and $^{40}Ar/^{39}Ar$ eruptive ages from Bonnichsen (1982b), Bonnichsen et al. (2008), and Hart and Aronson (1982). Ages range from LF1 as the oldest, at 10.97 ±0.18 Ma, to either DCR or SCR as the youngest, at 8.88 ± 0.49 and 9.06 ± 0.40 Ma. TCT (possibly from the TFEC) is considered as a separate unit due to it being a tuff and not a lava and has an age of 8.31 ±0.17 Ma.

Figure 3.1 compares U-Th-Pb dates on zircon to independently determined ages based on $^{40}Ar/^{39}Ar$, K/Ar, or stratigraphy. The figure shows each unit as being associated with a position on the y-axis and includes its U-Th-Pb age with uncertainty, as well as any previously determined age for that unit, with its uncertainty. All units overlap in their multiple age determinations or are close in age when considering their uncertainties. There is evidence in large volume, ashflow producing systems, of prolonged intervals of zircon crystallization and growth prior to eruption on the order of 350 k.y. (Reid, 2008; Vazquez and Reid, 2002), but this resolution is beyond the precision available for Miocene magmas. It

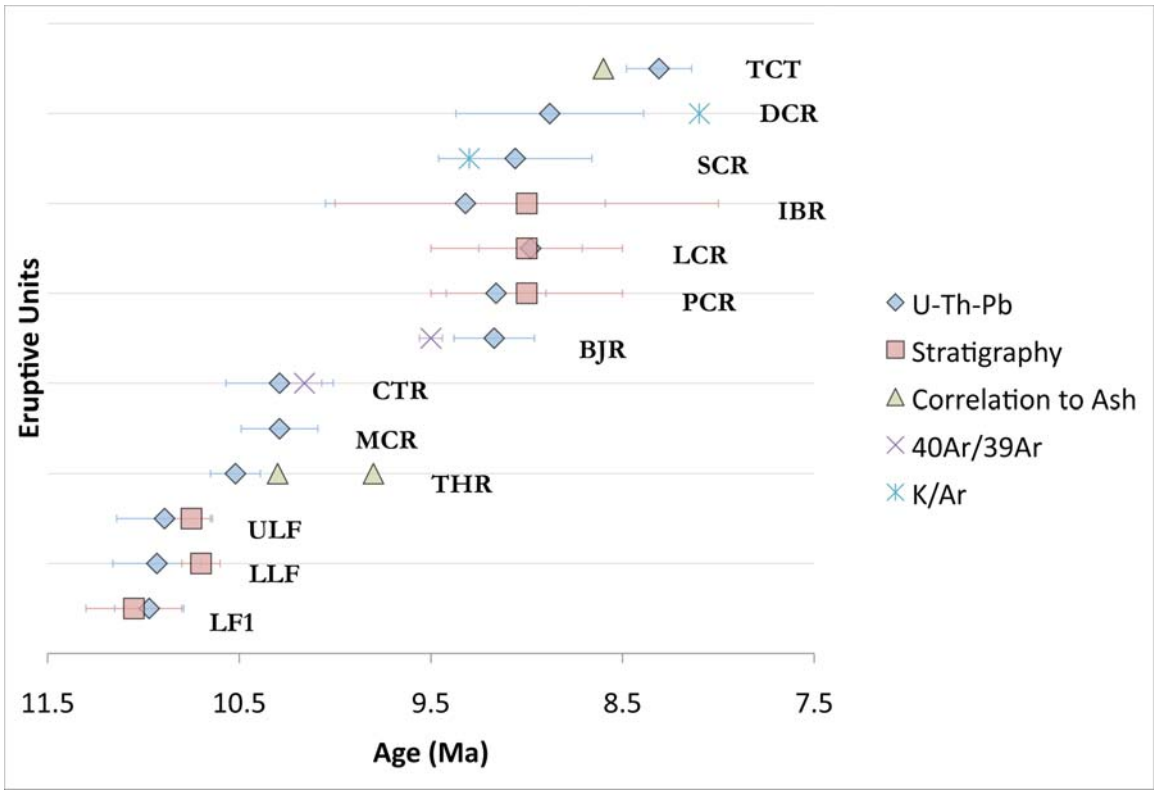

Figure 3.1. U-Th-Pb ages for the magmatic system as compared to those determined through stratigraphic order, tephrostratigraphy, $^{40}Ar/^{39}Ar$, or K/Ar dating. The units are arranged in a proposed stratigraphic order from oldest to youngest, except for the possible uncertainty in stratigraphic order between multiple units, which is discussed in the text.

is also unlikely that smaller magma volumes had prolonged residence times prior to eruption. For these reasons, the zircon magma age, or the age of the zircon at the time it was forming in the magmatic system, is taken to also represent the eruption age, again within the limit of analytical precision.

In the following sections, the lavas are described in the order of eruption from oldest to youngest, with the consideration that U-Th-Pb age uncertainties negate the possibility to establish sequentially between the relative eruptive orders of THR, CTR, and MCR, as well as those of BJR, LCR, PCR, IBR, and SCR, except for the field evidence showing that the eruption of SCR follows that of BJR and LCR, and the eruption of PCR follows BJR. The eruptive orders of DCR and TCT as well as those of SCR and DCR are also indistinguishable, but TCT is not included in any trends of the BJEC since it is a tuff and may have been erupted from the Twin Falls eruptive center.

Lava flow one (LF1) lies between Cougar Point Tuff members XII and XIII. No U-Th-Pb analyses were problematic, and all ages were accepted. A weighted average mean age of 11.42 ±0.43 Ma with a mean square of the weighted deviates (MSWD) of 8.0 and unmixed ages of 10.97 ±0.18 Ma (66% of analyses) and 12.41 ±0.28 Ma (34% of analyses) with a relative misfit of 0.321 were calculated (Table 3.2). The unmixed age of 10.97 ±0.18 Ma is thought to be the best magmatic age for this unit based on stratigraphy as well as precision of the age determination, where the percent of analyses for the unmixed age is above 40 %, and the MSWD from the WAMA is high. The age is consistent with the stratigraphic position of LF1 between CPT XII (11.3 Ma) and CPT XIII (11 Ma). Inheritance of older zircons from the BJEC magmatic system is indicated for this unit based the high MSWD and the older unmixed age (four ages from two zircons) (Tables 3.1 and

3.2). LF1 has two grains that overlap in age and $\delta^{18}O$ with the typical age and $\delta^{18}O$ of both CPT VII and CPT XII.

The Lower lava flow (LLF) has no U-Th-Pb analyses that were determined to be problematic. A weighted average mean age of 11.45 ±0.72 Ma with a large MSWD of 11.5 and unmixed ages of 10.93 ±0.23 Ma (71% of analyses) and 12.17 ±0.28 Ma (29% of analyses) with a relative misfit of 0.341 were calculated. The unmixed age of 10.93 ±0.23 Ma was determined to be the best fit for the magmatic age due to the high MSWD from the WAMA, and the unmixed age is consistent with the stratigraphic order and a high percentage of analyses were used. Inheritance is shown for this unit based on one core analysis, which overlaps in uncertainty of both the age and $\delta^{18}O$ with CPT V and CPT VII (Tables 3.1 and 3.2).

The upper lava flow (ULF) is the youngest flow within the CPT sequence, situated above LLF and below CPT XV. Two U-Th-Pb analyses are problematic, and were eliminated from the age calculation. Both of these ages were rim analyses with ages of 9.38 ± 0.50 Ma and 9.56 ±0.41 Ma and are too young for this early rhyolite flow. A weighted average mean age of 10.89 ±0.25 Ma with a MSWD of 2.0 was determined, and given the low MSWD, it was accepted as the magmatic age for this eruptive unit, which is consistent with its position above LLF and below CPT XV (~10.5 Ma). ULF shows no sign of zircon inheritance (Tables 3.1 and 3.2).

The Triguero Homestead rhyolite (THR) has a weighted average mean age of 11.03 ±0.53 Ma with a large MSWD of 20.0 with unmixed ages of 10.52 ±0.13 Ma (77% of analyses) and 12.38 ±0.22 Ma (23% of analyses) with a relative misfit of 0.331. The younger unmixed age of 10.52 ±0.13 Ma is consistent with the age of an associated fallout tuff with similar glass compositions (Mike Perkins, personal communication) and is adopted for this

lava. This age was also taken because of the high MSWD of 20 from the WAMA age. Inheritance is indicated for this unit based on five analyses conducted on three separate grains that overlap with both previously erupted lavas and various units of the CPT (Tables 3.1 and 3.2).

In the Marys Creek rhyolite (MCR) one U-Th-Pb rim analysis had an age of 11.45 ± 0.67 Ma that is older than the core and interior, and was eliminated from the age calculation. The weighted average mean age (WAMA) of 10.29 ±0.20 Ma is adopted for this eruptive unit based on the relatively small MSWD (2.9). No definite inheritance was determined for this unit (Tables 3.1 and 3.2).

The Cedar Tree rhyolite (CTR), had no problematic U-Th-Pb analyses and has a weighted average mean age of 10.29 ±0.28 Ma with a MSWD of 2.6 that is accepted as the magmatic age of the eruptive unit, and is within error of the $^{40}Ar/^{39}Ar$ eruption age of 10.16 ± 0.09 Ma (Bonnichsen et al., 2008). No distinct inheritance was determined for this unit (Tables 3.1 and 3.2).

The Bruneau-Jasper rhyolite (BJR) had one zircon with an inherited core with an age of 1095 ±24.00 Ma and a $\delta^{18}O$ of 2.1 $^{o}/_{oo}$. The remaining zircons provide a weighted average mean age of 9.17 ±0.21 Ma with a MSWD of 2.8. This age is slightly younger than the $^{40}Ar/^{39}Ar$ age of 9.50 ± 0.06 reported by Bonnichsen et al. (2008). Zircon inheritance is not suspected for this unit due to its young zircon ages and small MSWD, except for the ancient grain (Tables 3.1 and 3.2).

The Poison Creek rhyolite (PCR) includes two zircon rims of 6.80 ±0.60 Ma and 7.66 ±0.84 Ma too young for this eruptive unit and are not included in the age calculation. The remainder of analyses provided a weighted average mean age of 9.16 ±0.26 Ma with a

MSWD of 1.5. Given the low MSWD, the weighted average mean age of 9.16 ±0.26 Ma is preferred for PCR. PCR shows no signs of zircon inheritance (Tables 3.1 and 3.2).

Louse Creek rhyolite (LCR) yielded a weighted average mean age of 9.87 ±0.45 Ma with a MSWD of 9.7 and unmixed ages of 8.98 ±0.27 Ma (65% of analyses) and 10.20 ±0.15 Ma (35% of analyses) with a relative misfit of 0.209; the younger unmixed age of 8.98 ±0.27 Ma is accepted as the best fit for LCR based on the high MSWD from the WAMA and the high percentage of analyses associated with the unmixed age. An analysis on the interior of a zircon with an age of 7.13 ±0.77 Ma is inconsistent with stratigraphy and determined to be too young for this eruptive unit. Inheritance is shown for this unit based on overlapping ages and $\delta^{18}O$ values with MCR, CTR, THR and CPT XVj (Tables 3.1 and 3.2).

The Indian Batt Rhyolite (IBR) contains an inherited zircon with ages of 1666.70 ± 16.60 (core) and 174.60 ±3.20 (interior) Ma and $\delta^{18}O$ of 5.2 and 7.0 $^{o}/_{oo}$. An additional date that was not included in the magmatic age calculation is an interior age of 7.83 ±0.46 Ma that is younger than the rim. The rim analysis was preferred, as it is closer to the average age of the unit. A weighted average mean age of 9.32 ±0.73 Ma with a large MSWD of 14 and unmixed ages of 8.09 ±0.31 Ma (33% of analyses) and 9.83 ±0.20 Ma (67% of analyses) with a relative misfit of 0.268 were calculated. The WAMA of 9.32 ±0.73 Ma was adopted for IBR because of the small number of grains associated with the younger unmixed age. Inheritance suspected for this unit includes the ancient grains, although no definite inherited grains were determined through the analysis of the individual grains used for the age calculation. This is in contrast to the high MSWD and the large number of grains associated with the older unmixed age, which suggests a large population of inherited grains from this unit, possibly near 10 Ma in age (Tables 3.1 and 3.2).

Sheep Creek Rhyolite (SCR) contains a xenocryst zircon with core, interior and rim ages ranging from 587 ±9.0 to 690.20 ±13.20 Ma with $\delta^{18}O$ ranging from 6.7 to 6.8 $^{o}/_{oo}$. Problematic dates include a zircon interior with an age of 6.89 ±0.39 Ma that is too young for this eruptive unit, and a core in another zircon with an age of 8.24 ±0.33 Ma that is younger than the rim. The rim analysis was retained, as it is close to the average age of the unit. The remaining ages yield a weighted average mean age of 9.06 ±0.40 Ma with a MSWD of 3.0, and is considered the best fit for this eruptive unit, and is within error of the K-Ar age of 9.3 Ma determined by Bonnichsen et al. (2008). Zircon inheritance is illustrated for SCR based on the ancient zircon, although other inheritance is not evident based on the small MSWD (Tables 3.1 and 3.2).

The Dorsey Creek Rhyolite (DCR) yielded a weighted average mean age of 8.88 ± 0.49 Ma with a large MSWD of 11.4. Unmixing provided ages of 8.18 ±0.22 Ma (35% of analyses) and 9.42 ±0.18 Ma (65% of analyses) with a relative misfit of 0.349. The older WAMA of 8.88 ±0.49 Ma was accepted as the best fit for this eruptive unit because of the small percentage (35) of grains associated with the younger unmixed age. Zircons from this unit suggest inheritance based on the large MSWD (11.4) as well as one grain that is located in the $\delta^{18}O$ and age range of multiple lava and CPT units (Tables 3.1 and 3.2).

As mentioned earlier, the Three Creek Tuff (TCT) may be derived from the Twin Falls eruptive center. Although a stratigraphic relationship between TCT and DCR has not been determined, U-Th-Pb ages suggest that TCT erupted towards the end of the eruptive sequence of the BJEC. One zircon has an inherited core with an age of 951.1 ±6.7 Ma and a $\delta^{18}O$ of 1.3 $^{o}/_{oo}$. The remaining ages provide a weighted average mean age of 8.73 ±0.41 Ma with a MSWD of 8.2 and unmixed ages of 8.31 ±0.17 Ma (60% of analyses) and 9.3 ±0.20 Ma (40% of analyses) with a relative misfit of 0.294. The unmixed age of 8.31 ±0.17 Ma is

adopted as the best fit for this eruptive unit based on the large MSWD and the high percentage of analyses associated with this age. The age is comparable to an age of 8.6 Ma based on tephrostratigraphy by Henshaw (2002). If TCT is not actually associated with the Twin Falls eruptive center, then inheritance could be suspected for this unit based on three inherited grains that overlap with ranges from CTR, PCR, DCR, and SCR (Tables 3.1 and 3.2).

CHAPTER 4

ZIRCON THERMOMETRY

Background

The Ti-in-zircon geothermometer is one of the many geochemical uses of zircons, and is used to constrain growth and re-equilibration temperatures of zircons. Zircon's durability allows it to be especially useful in determining pre-eruptive magmatic temperatures when other minerals have been altered or destroyed (Hofmann et al., 2009).

Watson et al. (2006) discuss the first Ti-in-zircon thermometer that describes the temperature dependency on the concentration of titanium in zircon and has a precision of ±5°C:

$$\log Ti(ppm)_{zircon} = 6.01 - \left[\frac{5080}{T(K)}\right] \quad (1)$$

where T(K) is temperature in Kelvins. Ferry and Watson (2007) show that this thermometer is based on the substitution of Ti for Si in zircon, represented as:

$$TiO_2 + ZrSiO_4 = ZrTiO_4 + SiO_2 \quad (2)$$

and since this substitution is dependant on temperature the thermometer's results will be very precise.

Ferry and Watson (2007) account for the dependence of Ti substitution on the activities of both TiO_2 and SiO_2, giving an even more precise calculation:

$$\log Ti(ppm)_{zircon} = 5.711 - \left[\frac{4800}{T(K)}\right] - \log(a_{SiO_2}) + \log(a_{TiO_2}) \quad (3)$$

They estimate that temperatures calculated from the above equation will be underestimated by no more than 70 °C if $a_{TiO_2} < 1$ and overestimated to the same degree if $a_{SiO_2} < 1$. It has also been suggested that pressure may have an effect on the thermometer, which is something that merits further study (Anderson et al., 2008). Ti-in-zircon temperatures for rocks at greater than 10 kbar are thought to be underestimated using the current equation due to the smaller amount of Ti able to be incorporated into the zircon at higher pressures. This theory also suggests that Ti-in-zircon temperatures at low pressures will be overestimated due to the larger amount of Ti incorporated into the zircon (Fu et al., 2008). High-pressure experiments by Ferry and Watson (2007) suggest a pressure correction of ~5 °C/kbar at 750 °C, and a more recent estimate from Ferriss et al (2008) suggests a larger pressure correction of ~10 °C/kbar.

Methods

Titanium concentrations in zircon were determined *in situ* on the SHRIMP-RG, at the USGS-Stanford University SUMAC laboratory using a standard trace element routine. As was done for the U-Th-Pb analysis, when possible, a new location on the zircon within the same region, as shown by the CL image, was analyzed, although some spots were analyzed over the previous spot for $\delta^{18}O$ and U-Th-Pb ages (Appendix F). Madagascar Green Zircon (MAD) was used as a standard, and was analyzed approximately once for every 20 unknowns (Barth & Wooden, 2010). A beam diameter of 19 μm was used, along

with a 6-7 nA O^{2-} primary beam, with a mass resolution of approximately 10,000 at a 10% peak height. The primary beam was rastered over the spot for 3 minutes prior to analysis to remove any surficial material.

Results

Temperatures determined by the Ti-in-zircon thermometer depend upon an estimate of the activities of TiO_2 and SiO_2 in the melt (Equation 3). The TiO_2 activity used here of 0.4 is calculated from Fe-Ti oxide equilibria and TitaniQPT, using titanomagnetite and ilmenite compositions in the CPT (Cathey et al., unpublished). An SiO_2 activity of 1.0 was used since there is quartz present in all lava units. The lavas have a higher concentration of TiO_2 than members of the CPT (Bonnichsen et al., 2008), which may suggest that the temperatures reported here might be overestimated based on a resulting higher activity. Temperatures would be 20 to 30 °C less for a_{TiO_2} of 0.5 and 40 to 60 °C less for a_{TiO_2} of 0.6. The experimental calibration of the thermometer was conducted at 10 kbar (Ferry and Watson, 2007; Ferriss et al., 2008), a significantly higher pressure than appropriate for the mid to upper crustal BJEC magmatic system. If the pressure correction suggested by previous studies is applied to the BJEC (4-5 kbar), this may also decrease the temperatures determined from this study on the rhyolite lavas by 25-30 °C (Ferry and Watson, 2007) or 50-60 °C (Ferriss et al., 2008), depending on the pressure dependency that is estimated in each study. The results from this study are not shown with a pressure or activity correction, as the correction is not accurately known. This suggests that the temperatures reported here should be regarded as maximum temperatures for the rhyolite lavas of the BJEC, and could be

overestimated by as much as 120 °C if the maximum corrections are used, or 45 °C if the minimum corrections are used.

All Ti-in-zircon results for rhyolite lavas from the BJEC are provided in Table 4.1. Ti-in-zircon temperatures determined on inherited grains were not included in the average for individual lava unit temperatures. A total of 112 analyses were conducted on zircons from the rhyolite lavas, yielding an average rim temperature of 933 °C, an average core temperature of 929 °C, and an average interior temperature of 922 °C (Table 4.1). The overall range in average temperatures from individual units extends from 855 °C (SCR interiors) up to 986 °C (LCR interiors).

Zoning trends of Ti-in-zircon thermometry are based on whether the difference between the temperature of the core and that of the rim (or interior region) is greater than the combined uncertainties of the two temperatures. If this is the case and the rim is hotter than the core, then the trend is referred to as positive zonation, and if the rim is cooler than the core, then it is referred to as negative zonation. A total of 64 grains were analyzed for their Ti-in-zircon temperature, and 40 of these grains were analyzed for at least their core to rim temperature variations. Zoning trends in the lavas show that 17 grains have a hotter rim than core, 12 grains have a hotter core than rim, and 11 grains show no zonation (Figure 4.1). Six grains were also analyzed for their interior temperatures, and these analyses show that, from the core to the interior, two grains show positive zonation (increase in temperature), two grains show negative zonation (decrease in temperature), and two grain shows no zonation. Figure 4.1 also shows that grains with a hotter core than rim tend to have slightly lower temperatures, and those with higher rims than cores tend to have elevated temperatures. For the purposes of the core-rim zoning figures in appendix D, if a core could not be analyzed, but an interior region could, then the interior analysis was used

Table 4.1: Ti-in-zircon temperatures from rhyolite lavas of the BJEC.

Sample Number	^{49}Ti (ppm)	Ferry Temperature (°C)	2σ
CTR-60-c	15.9	894	10.2
CTR-60-r	23.6	945	10.2
CTR-48-c	23.5	945	10.2
CTR-48-r	20.7	928	10.2
CTR-48-a	20.7	928	10.2
CTR-53-c	24.4	950	10.2
CTR-53-r	16.5	899	10.2
CTR-37-c	15.4	890	10.2
CTR-37-r	19.4	919	10.2
CTR-14-c	17.9	909	10.2
CTR-14-r	23.5	945	10.2
CTR-20-c	16.5	899	10.2
CTR-20-r	27.0	964	10.2
CTR-67-c	22.3	938	10.2
CTR-67-a	23.8	946	10.2
CTR-67-r	22.4	938	10.2
CTR-64-a	21.1	931	10.2
CTR-64-r	21.9	935	10.2
CTR-85-c	31.8	987	10.2
CTR-85-r	22.5	939	10.2
Average	**21.6**	**932**	
Standard Deviation	**3.2**	**20.4**	
Maximum	**27.0**	**964**	
Minimum	**15.4**	**890**	
DCR-12-c	27.0	964	10.2
DCR-12-r	20.5	927	10.2
DCR-41-c	24.8	952	10.2
DCR-41-r	27.3	965	10.2
DCR-97-c	34.4	998	10.2
DCR-97-r	25.3	955	10.2
DCR-111-c	21.0	930	10.2
DCR-111-r	25.9	958	10.2
DCR-11-c	20.3	925	10.2
DCR-68-c	41.9	1027	10.2
DCR-68-r	22.0	936	10.2
DCR-57-r	21.4	933	10.2

including a melt inclusion based on high Fe, Al, P, or K). All analyses in blue were determined to be ancient based on U-Th-Pb ages. Neither were not included in any averages or trends for this study. Continued on next page.

Table 4.1 continued

Sample Number	^{49}Ti (ppm)	Ferry Temperature (°C)	2σ
DCR-58-c	19.7	921	10.2
DCR-20-c	11.2	852	10.2
DCR-43-r	33.9	996	10.2
DCR-5-r	22.4	938	10.2
DCR-79-c	30.8	982	10.2
DCR-79-r	26.5	961	10.2
DCR-70-c	19.1	917	10.2
DCR-70-r	153.3	1262	10.2
Average	**23.5**	**942**	
Standard Deviation	**5.2**	**31.9**	
Maximum	**33.9**	**996**	
Minimum	**11.2**	**852**	
LF1-2-c	129.3	1226	10.2
LF1-2-a	19.0	917	10.2
LF1-2-r	23.9	947	10.2
LF1-12-c	27.4	966	10.2
LF1-12-r	28.2	970	10.2
LF1-41-c	173.3	1288	10.2
LF1-41-r	18.3	912	10.2
LF1-39-c	16.4	898	10.2
LF1-39-r	14.2	881	10.2
LF1-35-c	36.5	1007	10.2
LF1-35-r	19.8	922	10.2
LF1-66-c	40.1	1021	10.2
LF1-66-a	31.4	985	10.2
LF1-66-r	17.2	904	10.2
Average	**21.6**	**930**	
Standard Deviation	**5.8**	**34.6**	
Maximum	**31.4**	**985**	
Minimum	**14.2**	**881**	
SCR-2-c	24.7	952	10.2
SCR-2-a	24.6	951	10.2
SCR-2-r	4.9	766	10.2
SCR-14-r	21.6	934	10.2
SCR-62-c	1246.6	1892	10.2
SCR-70-c	23.8	946	10.2
SCR-101-r	16.5	899	10.2
SCR-43-c	13.9	878	10.2

Table 4.1 continued

Sample Number	^{49}Ti (ppm)	Ferry Temperature (°C)	2σ
SCR-43-a	11.4	855	10.2
SCR-43-r	9.2	831	10.2
SCR-51-c	23.9	947	10.2
SCR-51-r	15.8	894	10.2
SCR-7-r	24.2	949	10.2
SCR-9-r	28.4	970	10.2
Average	**18.9**	**910**	
Standard Deviation	**6.4**	**46.0**	
Maximum	**28.4**	**970**	
Minimum	**9.2**	**831**	
MCR-87-ca	20.4	926	6.2
MCR-87-a	11.9	860	6.2
MCR-87-ra	19.6	921	6.2
MCR-77-r	19.2	918	6.2
Average	**17.8**	**906**	
Standard Deviation	**3.9**	**30.9**	
Maximum	**20.4**	**926**	
Minimum	**11.9**	**860**	
LLF-15-c	19.6	921	6.2
LLF-15-r	18.5	913	6.2
LLF-26-c	17.0	903	6.2
LLF-26-r	20.2	925	6.2
Average	**18.8**	**915**	
Standard Deviation	**1.4**	**9.6**	
Maximum	**20.2**	**925**	
Minimum	**17.0**	**903**	
THR-9-c	20.1	924	6.2
THR-9-r	22.6	939	6.2
THR-20-c	22.1	936	6.2
THR-20-r	20.8	929	6.2
THR-23-c	19.9	923	6.2
THR-23-r	23.2	943	6.2

Table 4.1 continued

Average	**21.5**	**932**
Standard Deviation	**1.3**	**8.3**
Maximum	**23.2**	**943**
Minimum	**19.9**	**923**

Sample Number	^{49}Ti (ppm)	Ferry Temperature (°C)	2σ
ULF-42-c	20.6	928	6.2
ULF-42-ra	23.3	944	6.2
ULF-42-rb	24.5	950	6.2
ULF-8-c	20.6	927	6.2
ULF-8-a	23.6	945	6.2
ULF-8-r	117.2	1207	6.2
Average	**22.5**	**939**	
Standard Deviation	**1.8**	**10.7**	
Maximum	**24.5**	**950**	
Minimum	**20.6**	**927**	
BJR-6-c	17.8	908	6.6
BJR-6-r	17.2	904	6.6
BJR-61-c	20.1	924	6.6
BJR-61-r	14.1	880	6.6
BJR-62-c	22.1	937	6.6
BJR-62-r	17.3	905	6.6
BJR-79-c	12.5	866	6.6
BJR-79-r	11.1	852	6.6
Average	**16.0**	**893**	
Standard Deviation	**3.7**	**28.8**	
Maximum	**22.1**	**937**	
Minimum	**11.1**	**852**	
TCT-76-c	24.4	950	6.6
TCT-76-r	20.1	924	6.6
TCT-5-c	23.4	944	6.6
TCT-5-r	25.7	957	6.6
TCT-13-c	26.5	961	6.6
TCT-1-r	20.7	928	6.6
TCT-1-c	28.2	970	6.6

Table 4.1 continued

Average	**24**	**945**
Standard Deviation	**3.1**	**17.3**
Maximum	**28.2**	**970**
Minimum	**20.1**	**924**

Sample Number	^{49}Ti (ppm)	Ferry Temperature (°C)	2σ
IBR-62-c	29.4	975	6.6
IBR-62-ra	33.6	995	6.6
IBR-54-c	15.7	893	6.6
IBR-54-r	20.2	925	6.6
IBR-21-c	24.5	950	6.6
IBR-21-r	28.2	970	6.6
IBR-39-ca	55.8	1073	6.6
IBR-39-a	26.7	962	6.6
IBR-39-b	12.8	868	6.6
IBR-39-r	8.1	817	6.6
Average	**21.6**	**924**	
Standard Deviation	**8.9**	**60.9**	
Maximum	**33.6**	**995**	
Minimum	**8.1**	**817**	
LCR-10-ca	20.7	928	6.6
LCR-10-cb	23.6	945	6.6
LCR-10-a	31.6	986	6.6
LCR-10-r	25.7	957	6.6
LCR-34-c	26.7	962	6.6
LCR-34-r	33.2	993	6.6
LCR-105-c	26.9	963	6.6
LCR-105-r	32.5	990	6.6
Average	**27.6**	**965**	
Standard Deviation	**4.5**	**22.9**	
Maximum	**33.2**	**993**	
Minimum	**20.7**	**928**	
PCR-104-c	22.9	941	6.6
PCR-104-r	30.6	981	6.6
PCR-15-c	10.5	846	6.6
PCR-15-r	26.5	961	6.6
PCR-74-ca	22.4	939	6.6

Table 4.1 continued

Sample Number	^{49}Ti (ppm)	Ferry Temperature (°C)	2σ
PCR-74-r	26.2	960	6.6
Average	**21.4**	**926**	
Standard Deviation	**7.5**	**54.6**	
Maximum	**26.5**	**961**	
Minimum	**10.5**	**846**	

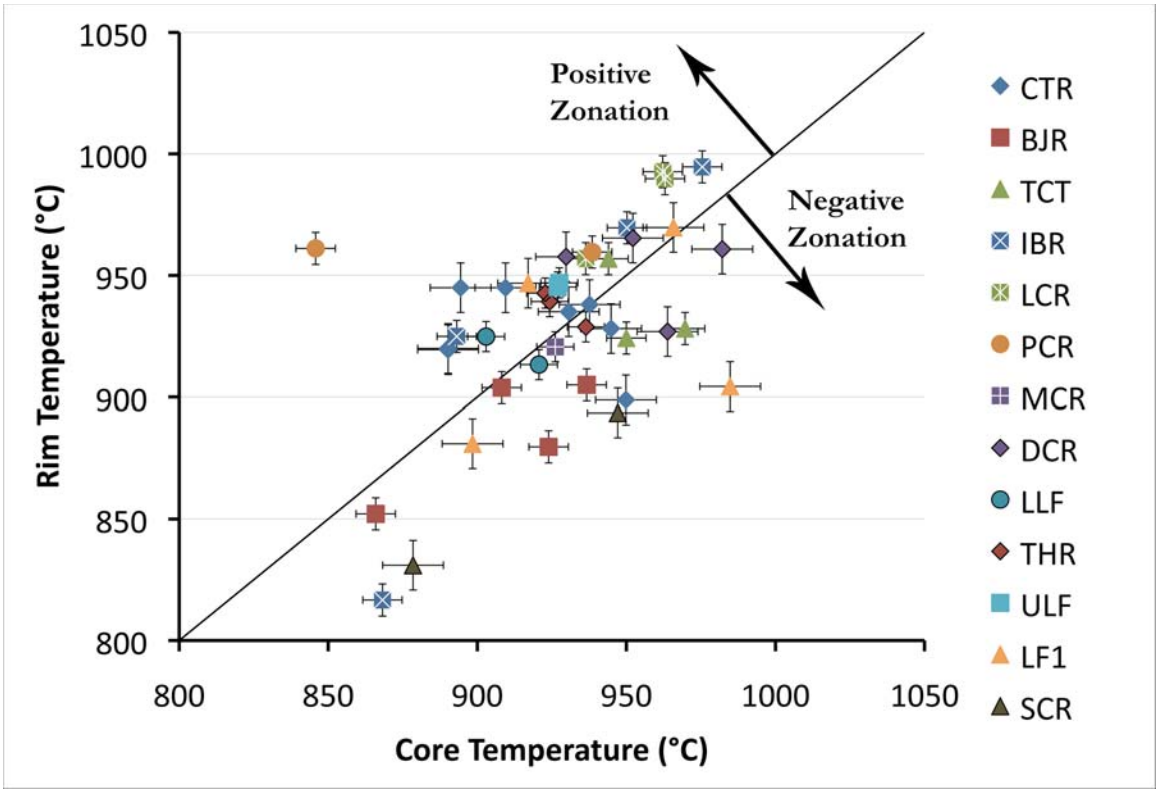

Figure 4.1. Matched core-rim temperatures for zircons in lavas from the Bruneau-Jarbidge eruptive center: All Units. Line represents 1:1 ratio. Error bars are 2σ.

as a core analysis. AD.1, PCR, ULF, and LCR have hotter rim temperatures than core temperatures by 21-115 °C, ~18 °C, and ~25 °C respectively. The interior analyses in ULF-8 as well as LCR-10 both show positive zonation as well. SCR and BJR have hotter core than rim temperatures. One grain in BJR also shows no zonation, but the remaining two grains show clear negative zonation of 15-45 °C. The negative zonation in SCR for all grains is near 50 °C. There is only one data point for MCR and the core temperature is within the uncertainty of the rim temperature. IBR, LLF, DCR, LF1, TCT, THR, and CTR all have varying core and rim temperatures, with some grains showing hotter cores than rims and some grains showing hotter rims than cores, while some grains show no zonation.

The average temperature for all lavas is 930 °C, with a minimum average temperature of 817 °C (IBR) and a maximum average temperature of 996 °C (DCR) (Figure 4.2). Rims record the two lowest temperatures, but in general, the cores, interiors, and rims all have extensive ranges that overlap.

Results for individual rhyolite units can be grouped into four categories including units with a large range in temperatures, and units having temperatures near average, hotter than average, or cooler than average for the BJEC. IBR, LF1, and SCR have large ranges in temperatures (817 – 995 °C), and the rims of IBR have a higher overall temperature than the core. It should be noted in SCR that the rims appear to have a greater span in temperatures than the cores, but this could be due to the smaller number of core analyses than rim analyses. LLF, THR, ULF, TCT, and CTR all have average temperatures close to the average of all lavas from the BJEC (915 – 945 °C). LCR, PCR, and DCR have hotter than the average temperatures (942 – 965 °C). An additional note for LCR is that the rim temperatures are slightly hotter than the core temperatures, and the one interior analysis is

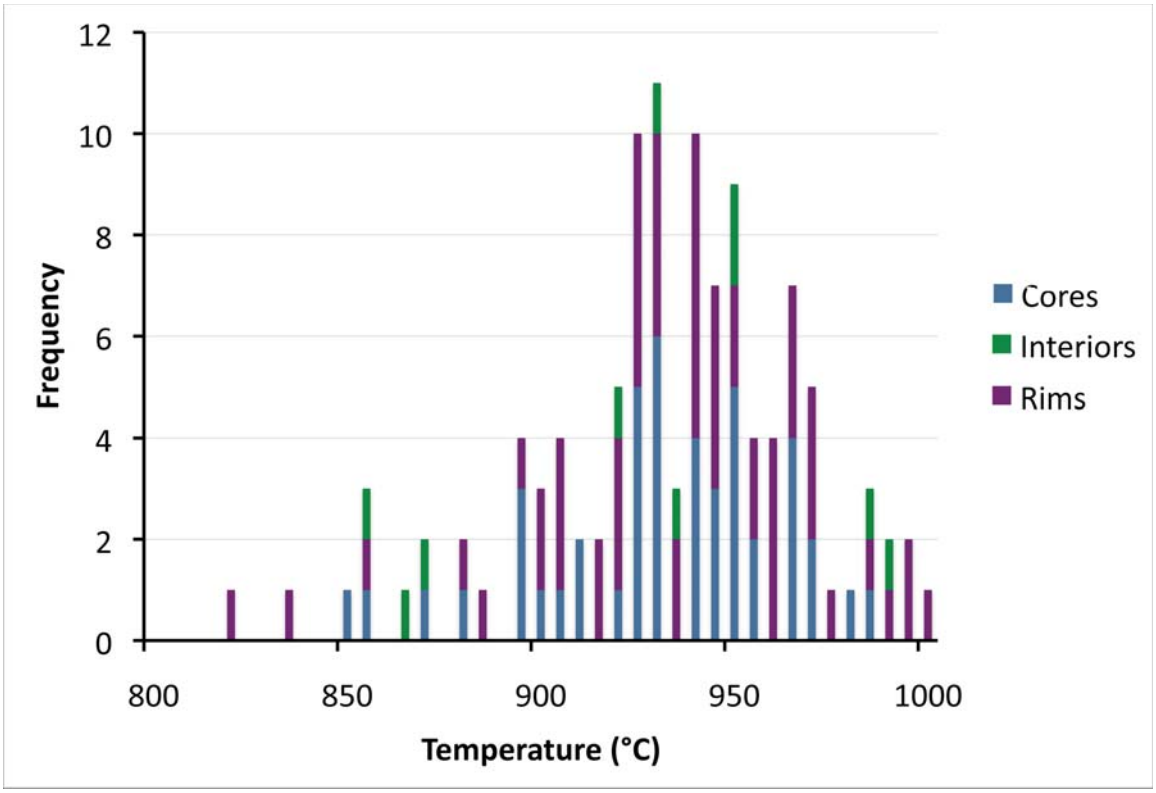

Figure 4.2. Temperatures for cores, rims, and interiors of zircon from all rhyolite units from the BJEC.

hotter than average for the unit. Also, in PCR there is one unusually low temperature recorded that is 93 °C lower than all other values, and if this analysis is excluded it would raise the average temperature for the unit to 960 °C, significantly higher than average for the BJEC lavas. In addition, the minimum recorded temperature for DCR is 65 °C below the next highest temperature, and if this analysis were excluded, it would greatly increase the average temperature for the unit. MCR (906 °C) and BJR (893 °C) have lower than average temperatures, with BJR having the lowest average temperature of any BJEC lava. An additional note for MCR is that its lowest temperature, an interior analysis, is 58 °C lower than the next highest value, and if this analysis were excluded, the average temperature would be in the range of that for average BJEC lavas.

As is shown in Figure 4.3, there appears to be a weak correlation between age and the temperature of eruptions, where there is a slight decrease in average temperature through the first half of eruptions, which is followed by a slight increase in temperature through the second half of eruptions. This is in addition to the persisting trend that shows a continuation of an unusually hot rhyolitic system, with average temperatures regularly exceeding 900 °C through all eruptions of the rhyolite lavas.

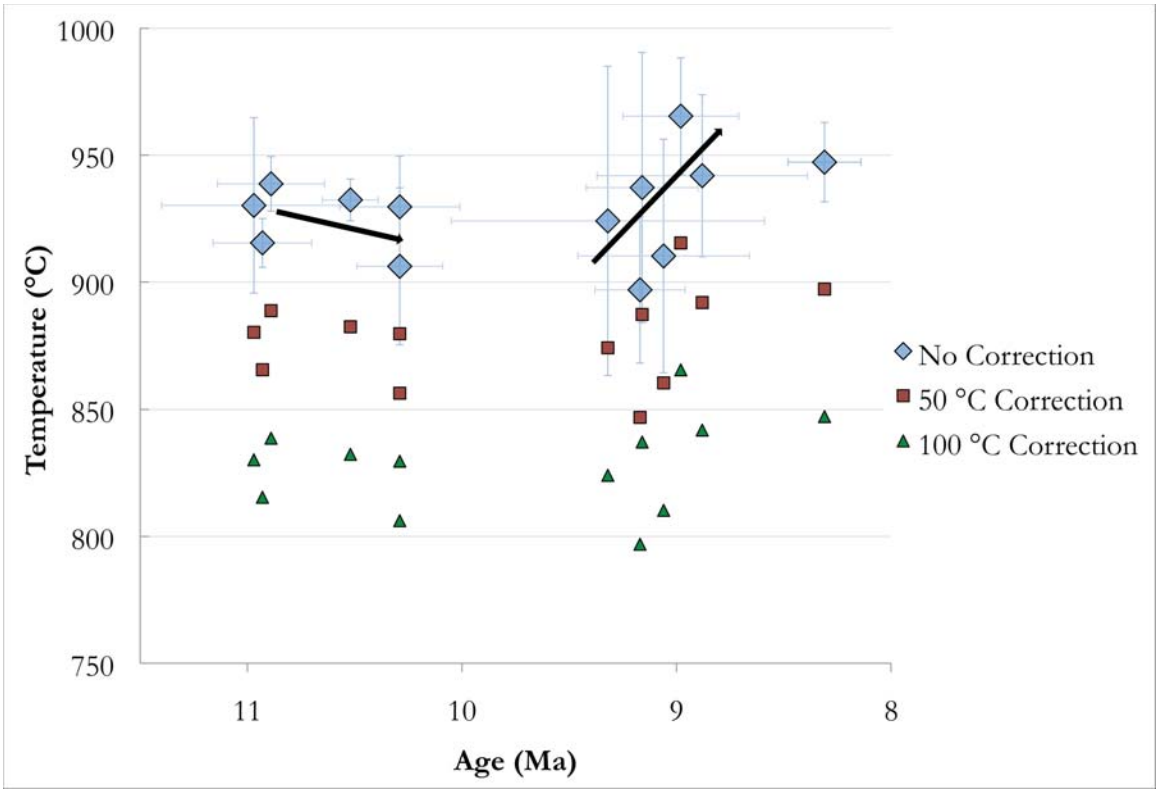

Figure 4.3. Average Ti-in-zircon temperature versus U-Th-Pb magmatic age for rhyolite lavas of the BJEC (WAMA or unmixed depending on the unit). Error bars for average temperature for each unit is shown as one standard deviation, and error bars for U-Th-Pb ages are given as two standard deviations. Trendlines are shown for the possible correlation between magmatic temperature and time, with TCT (data point to the far right) not included in any trends. Temperatures for a 50°C and 100°C correction are also shown.

CHAPTER 5

DISCUSSION

$\delta^{18}O$ Trends of the Rhyolite Lavas

There is a clear trend in $\delta^{18}O$ in zircons from the rhyolite lavas of the BJEC that begins with zircons depleted in $\delta^{18}O$ as low as -3.4 $^{o}/_{oo}$ (LF1), and gradually increases in $\delta^{18}O$ throughout the eruption sequence (Figures 5.1-5.3). The lowest average $\delta^{18}O$ (-0.5 $^{o}/_{oo}$) and $\delta^{18}O_{rims}$ (-1.2 $^{o}/_{oo}$) grains are in lava flow one, LF1, the first lava to be erupted. The highest average $\delta^{18}O$ (3.3 $^{o}/_{oo}$) and $\delta^{18}O_{rims}$ (3.1 $^{o}/_{oo}$) are found in SCR, which is one of the later rhyolites to erupt, possibly the last. DCR may also be the last rhyolite to erupt from the BJEC and has an average $\delta^{18}O$ of 1.8 $^{o}/_{oo}$ ($\delta^{18}O_{rims}$ 1.8 $^{o}/_{oo}$). There are episodic dips or spikes in $\delta^{18}O$ throughout the evolution of the rhyolite lavas, such as the increase in $\delta^{18}O$ between LF1 and LLF, BJR and PCR, IBR and SCR, and maybe DCR and SCR and the decrease in $\delta^{18}O$ between PCR and LCR, and possibly SCR and DCR. The overall trend, though, shows that the eruption of the lavas begins with depleted $\delta^{18}O$ that slowly recovers to values closer to those of the mantle or unaltered crust (Figures 5.1-5.3). This is also illustrated by the slightly larger number of zircons that are zoned towards heavier rims than cores (26 positive vs. 20 negative). In the following section, the lavas are described in the order of eruption from oldest to youngest, except that the uncertainties from the U-Th-Pb dating and some

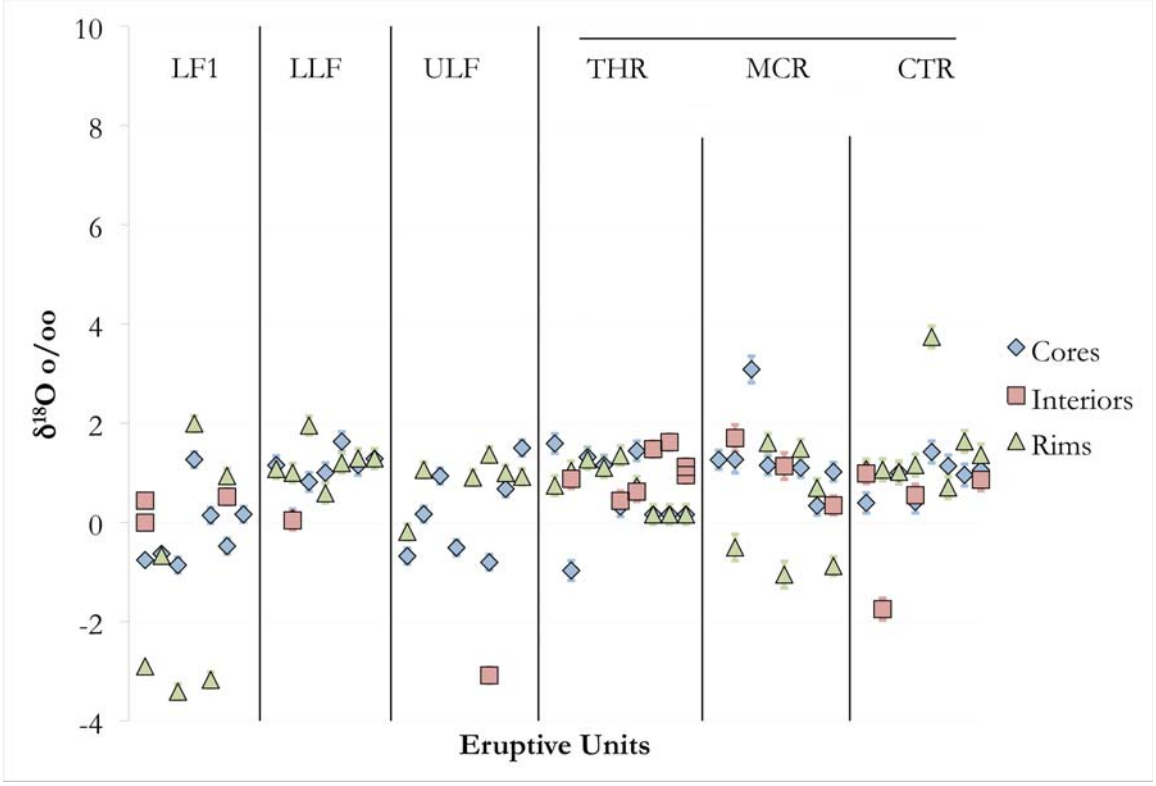

Figure 5.1. $\delta^{18}O$ vs. age for zircon in rhyolite lavas of the BJEC. U-Th-Pb analyses are shown with their respective $\delta^{18}O$ values. Cores, interiors and rims of individual zircons are aligned with the same X-value to illustrate how $\delta^{18}O$ varies in individual crystals. Error bars are 2σ, and stratigraphic order increases to the right, except for the uncertainty in eruptive order, which is detailed in the text. The bar above multiple units indicates an uncertain eruptive order among those units.

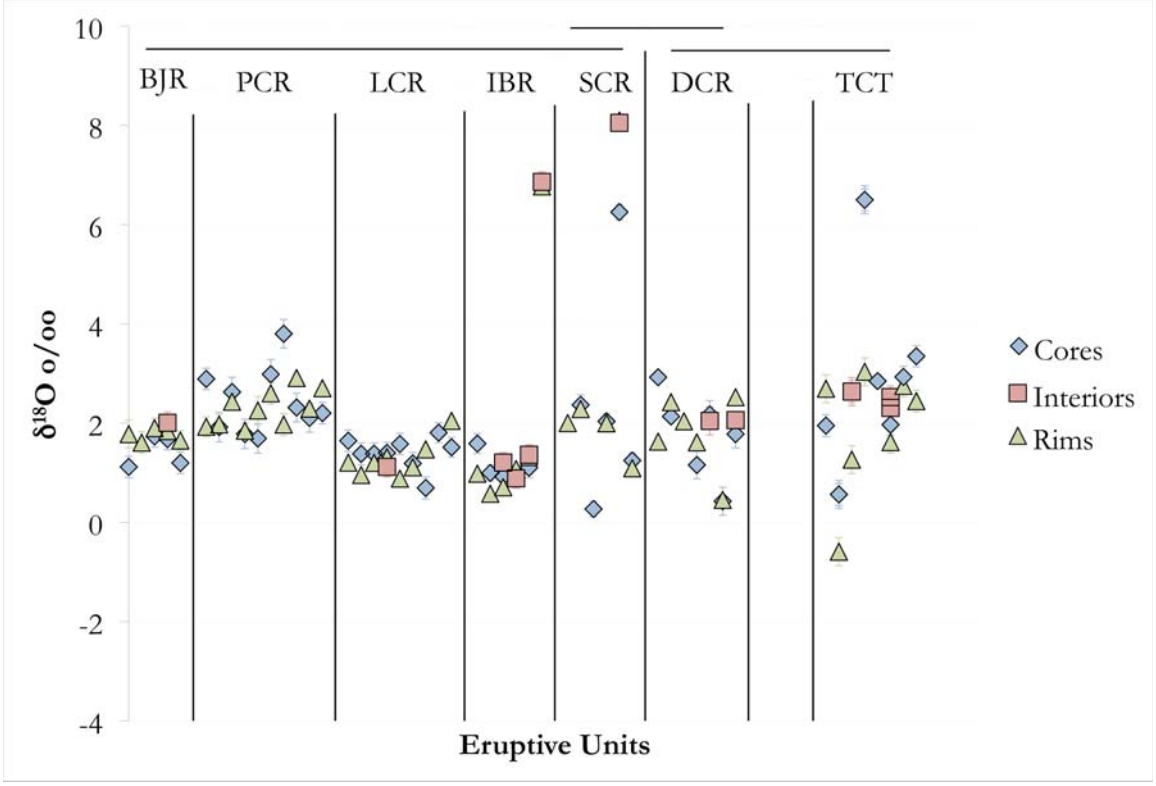

Figure 5.1 continued

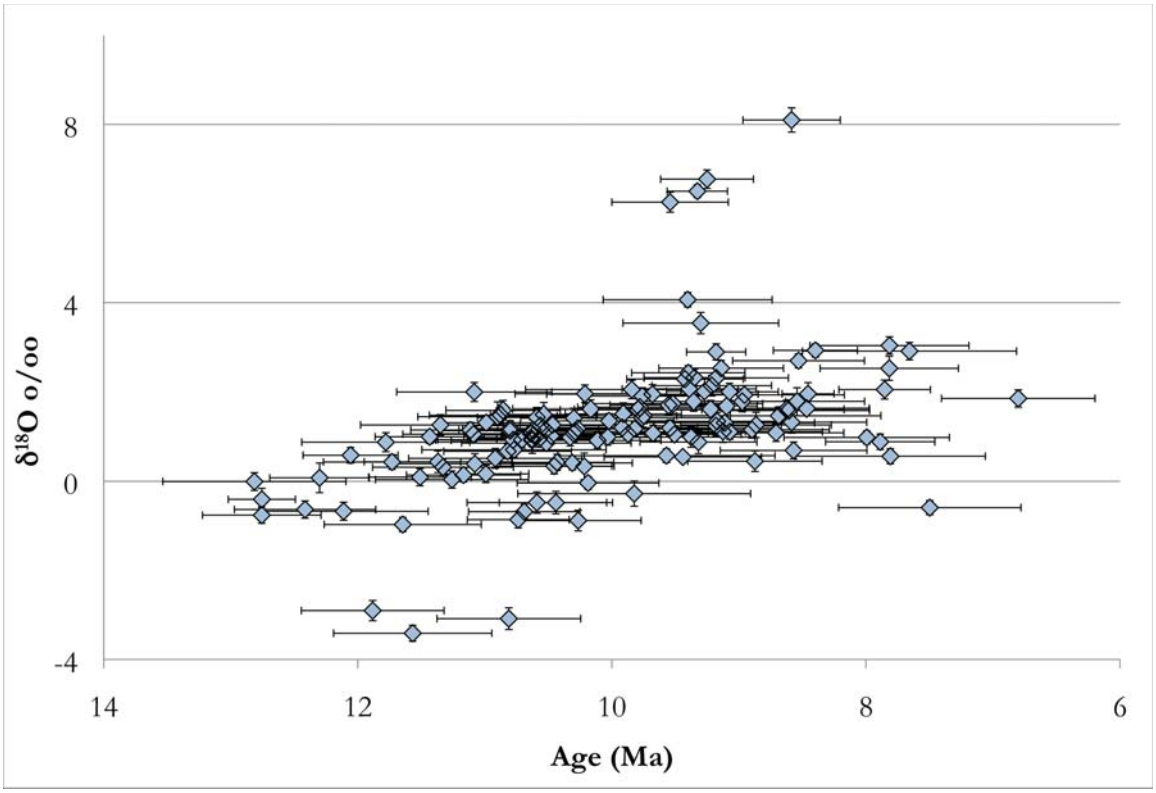

Figure 5.2. $\delta^{18}O$ vs. age for zircon in rhyolite lavas of the BJEC. All U-Th-Pb analyses are shown with their respective $\delta^{18}O$ values. Error bars are 2σ.

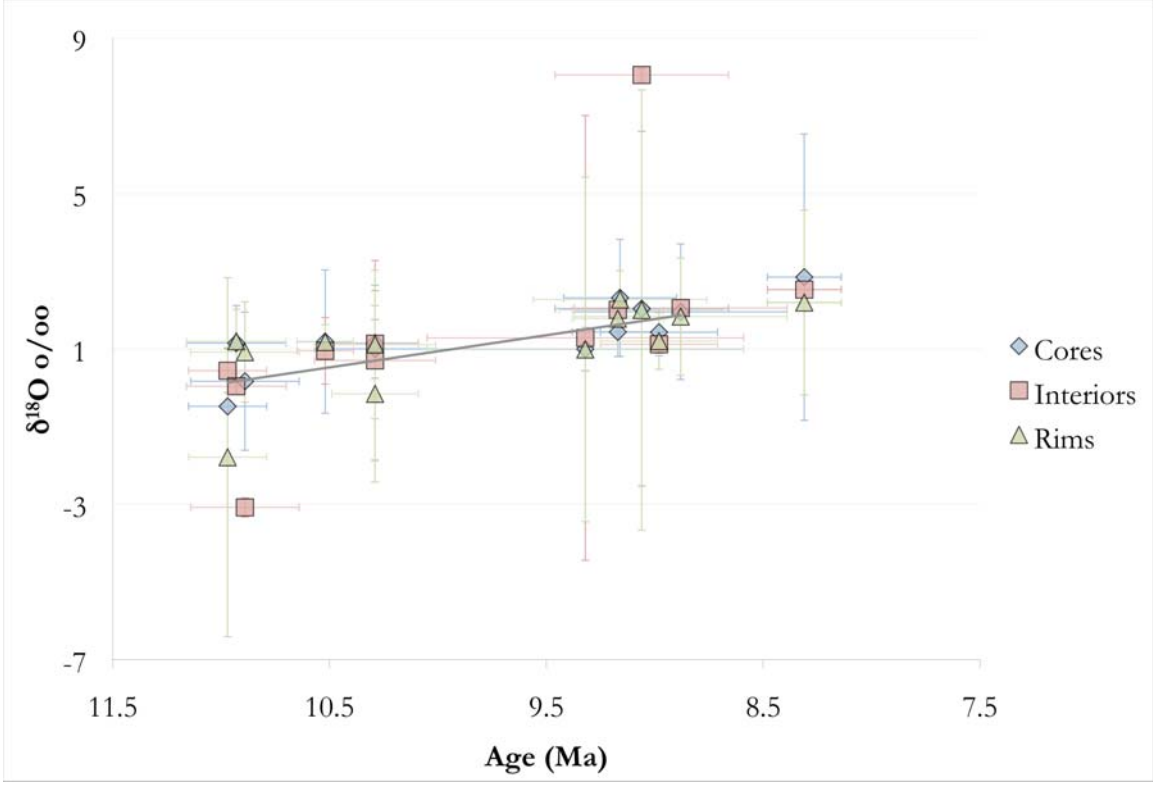

Figure 5.3. Average $\delta^{18}O$ in zircon vs. U-Th-Pb age (WAMA or unmixed age, depending on the unit) for rhyolite lavas of the BJEC. This plot shows average $\delta^{18}O$ values with one standard deviation for the average $\delta^{18}O$ of the unit and two standard deviations for the U-Th-Pb ages of the cores, interiors, and rims of each eruptive unit.

unknown stratigraphic order make it not possible to distinguish between the eruptive orders of THR, CTR, and MCR, as well as those of BJR, LCR, PCR, IBR, and SCR, except for field evidence showing that the eruption of SCR follows that of BJR and LCR, and the eruption of BJR occurred prior to that of PCR. The eruptive orders of DCR and TCT as well as those of SCR and DCR are also indistinguishable, but TCT is not included in any trends of the BJEC since it is a tuff and may have been erupted from the Twin Falls eruptive center.

Volcanism at the BJEC began with the eruption of the first seven units of the CPT between approximately 12.80 and 11.13 Ma (Bonnichsen et al., 2008; Cathey and Nash, 2004). LF1 is the oldest lava that has been found and has an age of 10.97 ±0.18 Ma. It also has the lowest average $\delta^{18}O$ (-0.5 $^{0}/_{00}$) and the lowest average $\delta^{18}O_{rims}$ (-1.2 $^{o}/_{oo}$) of any other known rhyolite lava erupted from the BJEC. There are two grains from LF1 that may have been inherited from previously erupted units of the CPT, and if these analyses are not included in the average for LF1, its average $\delta^{18}O$ remains the same. The subsequent eruption of CPT XIII (11 Ma) was followed by rhyolite lava LLF, which has a heavier average $\delta^{18}O$ than LF1 (1.0 $^{o}/_{oo}$; $\delta^{18}O_{rims}$ of 1.2 $^{o}/_{oo}$) and an eruption age of 10.93 ±0.23 Ma. There is one inherited grain in the LLF analyses, which was possibly inherited either from CPT V or CPT VII, and if the inherited grain is discarded from the average, the average remains the same. ULF, stratigraphically above LLF, has an eruption age of 10.89 ±0.25 Ma, within error of LLF. Average $\delta^{18}O$ values indicate a slight decrease in $\delta^{18}O$ with an average $\delta^{18}O$ of 0.2 $^{o}/_{oo}$ ($\delta^{18}O_{rims}$ of 0.8 $^{o}/_{oo}$) compared to 1.0 $^{o}/_{oo}$ for LLF ($\delta^{18}O_{rims}$ of 1.2 $^{o}/_{oo}$). The eruption of ULF was followed by the eruption of the last two CPT members, XVb and XVj, at approximately 10.5 Ma. The first post-CPT rhyolite is unknown, as the eruptions of THR, CTR, and MCR are all within each other's range of age uncertainty. Due to this uncertainty, these lavas will be assessed within one group of $\delta^{18}O$ and age. The average $\delta^{18}O$ of THR is 1.0 $^{o}/_{oo}$ ($\delta^{18}O_{rims}$

of 1.1 $^{o}/_{oo}$; 1.2 $^{o}/_{oo}$ if inherited grains possibly from LF1 or various units from the CPT are excluded), MCR's average is 0.8 $^{o}/_{oo}$ ($\delta^{18}O_{rims}$ of 0.2 $^{o}/_{oo}$), and the average for CTR is 1.0 $^{o}/_{oo}$ ($\delta^{18}O_{rims}$ of 1.5 $^{o}/_{oo}$). All these units (THR, CTR, and MCR) have similar average $\delta^{18}O$, which show an increase from the previous average $\delta^{18}O$ of ULF. Following this set of lavas, there is another set of lavas, whose ages overlap, including BJR, LCR, PCR, IBR, and SCR, where SCR is known to be stratigraphically above BJR and LCR. BJR has an average $\delta^{18}O$ of 1.7 $^{o}/_{oo}$ ($\delta^{18}O_{rims}$ of 1.8 $^{o}/_{oo}$). PCR's average $\delta^{18}O$ is higher, at 2.4 $^{o}/_{oo}$ ($\delta^{18}O_{rims}$ of 2.3 $^{o}/_{oo}$), and LCR has average $\delta^{18}O$ of 1.3 $^{o}/_{oo}$ ($\delta^{18}O_{rims}$ of 1.3 $^{o}/_{oo}$), closer to that of BJR. Two grains from LCR have inherited cores that may be sourced from MCR, CTR, or CPT XVj, and if these analyses are not included in the average $\delta^{18}O$ for the unit it remains at 1.3 $^{o}/_{oo}$, showing that the average $\delta^{18}O$ of LCR is not affected by the inherited grains. The average $\delta^{18}O$ for IBR is 1.8 $^{o}/_{oo}$ ($\delta^{18}O_{rims}$ of 1.9 $^{o}/_{oo}$) (excluding inherited zircons at 174.60 ±3.20 Ma (7.0 $^{o}/_{oo}$) and 1666.70 ±16.60 Ma (5.2 $^{o}/_{oo}$)). If the two outliers from this unit (6.9 and 6.8 $^{o}/_{oo}$), which are both from the same grain, are excluded, the average for the unit decreases to 1.0 $^{o}/_{oo}$. SCR has an average $\delta^{18}O$ of 3.3 $^{o}/_{oo}$ ($\delta^{18}O_{rims}$ of 3.1 $^{o}/_{oo}$), excluding inherited zircons with high $\delta^{18}O$ values ranging from 6.3 $^{o}/_{oo}$ up to 8.1 $^{o}/_{oo}$ (587.90 ±10.80 to 690.20 ±13.20 Ma*)*. If the one grain from SCR, which includes the only nonancient $\delta^{18}O$ values from the unit that are above 3 $^{o}/_{oo}$ is excluded, this drops the average $\delta^{18}O$ of SCR to 1.7 $^{o}/_{oo}$. This group of eruptive units shows an increase in $\delta^{18}O$ from the previous set, with all the units having average $\delta^{18}O$ above 1 $^{o}/_{oo}$, with some being well above 1 $^{o}/_{oo}$ depending on the exclusion of outlying grains. Possibly the last lava erupted from the BJEC, DCR, has an average $\delta^{18}O$ of 1.8 $^{o}/_{oo}$ ($\delta^{18}O_{rims}$ of 1.8 $^{o}/_{oo}$). This is within the range of the previous set of units as well as that for the average for the eruptive center. The core of one grain from DCR was possibly inherited from MCR, CPT XVj, or CPT XVb and if this analysis is not included, the average

$\delta^{18}O$ for DCR increases to 1.9 $^{o}/_{oo}$. TCT, an ashflow tuff that may have been erupted from the Twin Falls center, has an average $\delta^{18}O$ of 2.3 $^{o}/_{oo}$ ($\delta^{18}O_{rims}$ of 1.9 $^{o}/_{oo}$). Age determinations for TCT zircons reveal that one of the $\delta^{18}O$ values (1.3 $\pm$0.178 $^{o}/_{oo}$) of this unit is xenocrystic (951.10 $\pm$6.70 Ma*)*. When this value is excluded, the average $\delta^{18}O$ for the unit increases slightly to 2.4 $^{o}/_{oo}$. Three grains from TCT were determined to be inherited from an older source. If these analyses are excluded from the average $\delta^{18}O$, then it decreases to 2.1 $^{o}/_{oo}$. If TCT is actually from the BJEC, then possible sources for this inherited material include PCR, DCR, or SCR.

Inheritance

The inheritance results from this research suggest that there is an abundance of zircons that are inherited from previously erupted units that are incorporated into younger magmas (Table 3.2; Figures 5.4 and 5.5). Possible sources for zircons that are inherited by a younger unit include members of the CPT, LF1, MCR, and CTR. The predominant lavas to include inherited material are LF1, LLF, THR, LCR, and DCR. Although IBR is not shown to have definitely inherited material based on the criteria used in this study, the large MSWD and the significant group of older grains from the unmixed age suggest the presence of inherited grains in this unit. Inherited grains have lower $\delta^{18}O$ values than those that grew with the currently forming magmatic system of each particular eruptive unit, with the exception of LF1, LLF, LCR and TCT, where the average $\delta^{18}O$ value of the inherited grains from LF1, LLF, and LCR are similar to that of the noninherited grains.

As is shown in Figure 5.4, the low $\delta^{18}O$ inherited grains from LF1, LLF, and THR have a similar age to CPT III and CPT V, but their $\delta^{18}O$ values are too low to have been

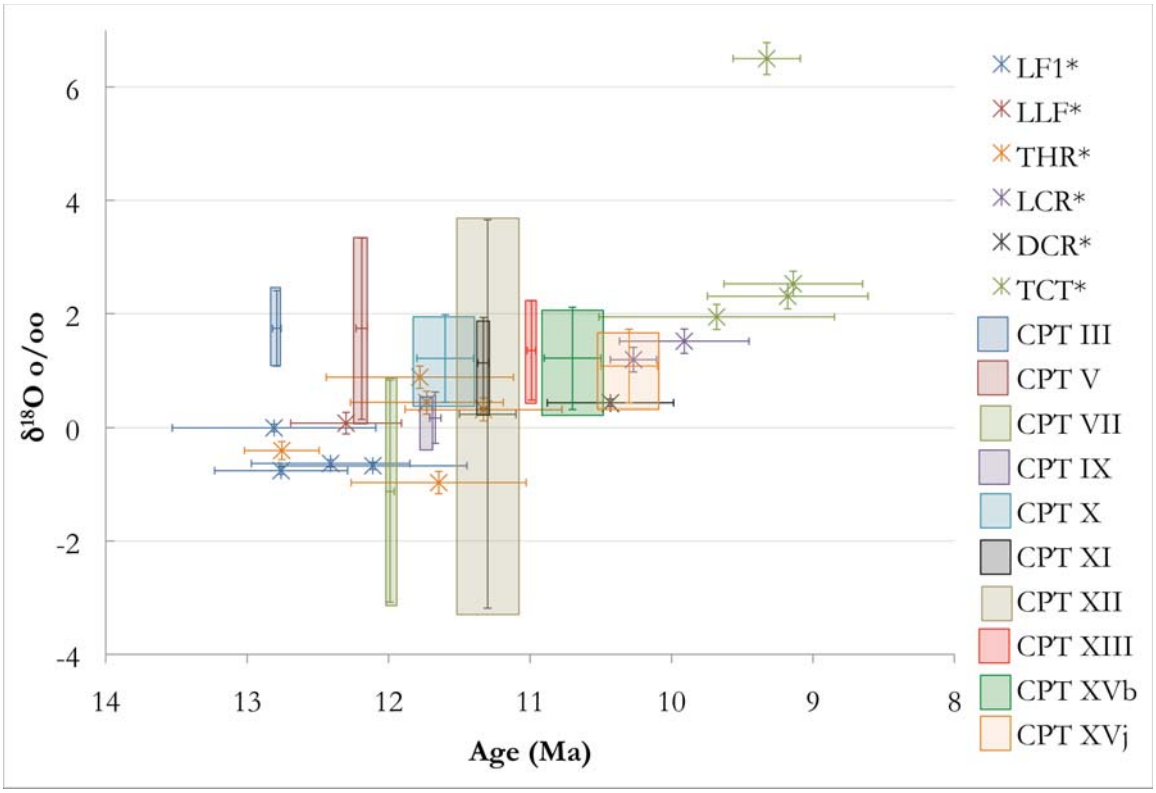

Figure 5.4. Possible sources of inheritance for grains from lava units of the BJEC. Lava units followed by "*" are units including inherited grains. When the inherited grain or its uncertainty overlaps with one of the units of the CPT, that unit is a possible source for the inherited grain. Uncertainties for the lava ages and $\delta^{18}O$ averages are 2σ. Data from the CPT are from H.E. Cathey (personal communication) with ages being 1σ and $\delta^{18}O$ averages being 2σ.

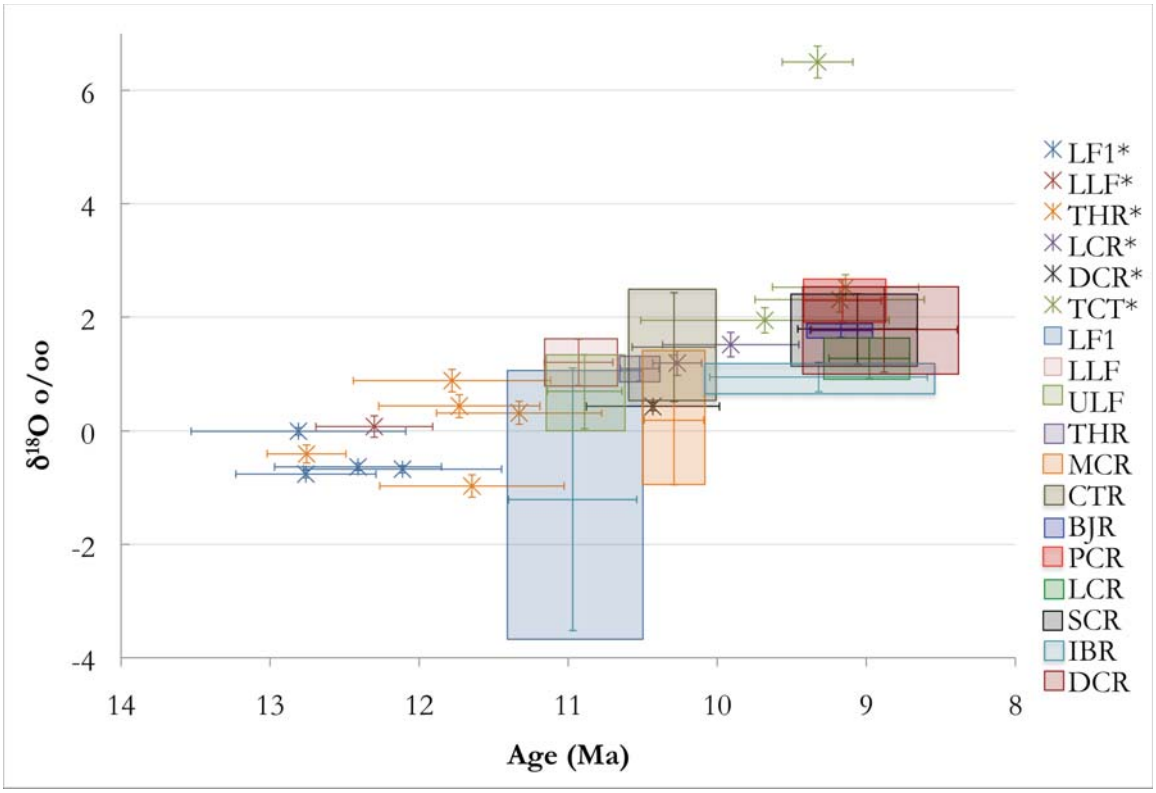

Figure 5.5. Possible sources of inheritance for grains from lava units from the BJEC. Lava units followed by "*" are units including inherited grains. When the inherited grain or its uncertainty overlaps with one of the lava units, that unit is a possible source for the inherited grain. Uncertainties for the ages and $\delta^{18}O$ averages are 2σ.

sourced from these eruptive units, which supports the hypothesis for a $\delta^{18}O$ depleted protolith in this region during the early eruptions from the BJEC. Although CPT III and CPT V are too heavy to be sources for the inherited grains from these lavas, CPT VII and CPT XII, as well as LF1, appear to be better suited for some of the younger inherited grains. It is also important to note that, as is shown in Figure 5.5, inherited grains from later erupted units of the rhyolite lavas (DCR and LCR) do not have ages old enough to be inherited from any CPT units erupted prior to XVb and XVj. Instead, the common sources for inherited material from DCR and LCR are the magmatic systems that produced the lava units of MCR and CTR, in addition to the later erupted CPT units. This suggests that material is not being continually recycled from eruption to eruption. This is in contrast to the continual recycling documented from eruptions at Heise and Yellowstone that utilize the caldera collapse model to produce eruptions depleted in ^{18}O. These systems commonly incorporate previously erupted, hydrothermally altered material into the magmatic system that will later erupt as inherited low $\delta^{18}O$ material. Another intriguing result of inherited material of the BJEC is the similar $\delta^{18}O$ and ages of inherited grains from TCT and typical values of erupted material from CTR, DCR, PCR, and SCR. This is also suggestive of either TCT being sourced from the Bruneau-Jarbidge eruptive center instead of the Twin Falls eruptive center, or continual eruptions stretching from the Bruneau-Jarbidge eruptive center to the Twin Falls eruptive center.

Two low $\delta^{18}O$ ancient zircons were found during this study, one from BJR at 1095 Ma with a $\delta^{18}O$ of 2.1 $^{o}/_{oo}$ and one from TCT at 951 Ma with a $\delta^{18}O$ of 1.3 $^{o}/_{oo}$. The U-Th-Pb analysis conducted on BJR was directly over the $\delta^{18}O$ analysis, but this was not the case for TCT, where the U-Th-Pb analysis was conducted at a location adjacent to the $\delta^{18}O$ analysis. No definite conclusions can be made based on the presence of two zircons,

although this does suggest the possibility that there may have been a low $\delta^{18}O$ protolith prior to the emplacement of the Y-SRP plume, but also warrants further study. This, of course, is complicated by the normal $\delta^{18}O$, 600 Ma inherited grain from SCR, as well as the normal $\delta^{18}O$ grains from IBR at 174 and 1666 Ma. Therefore, the presence of two low $\delta^{18}O$ grains at 1095 and 951 Ma does not constitute a strong argument for the definite existence of a low $\delta^{18}O$ protolith in the continental crust of this region that was intruded by the Y-SRP plume. Work by Valley et al. (2005) have described the existence of low $\delta^{18}O$ Proterozoic crust in various regions of the world, but these are rare occurrences, and the predominant $\delta^{18}O$ value of the crust during the Proterozoic is 7.3 $^{o}/_{oo}$, although values do range from 1 to 13 $^{o}/_{oo}$ (Valley et al., 2005).

Ti-in-zircon Temperatures in the Rhyolite Lavas

There is a weak trend of decreasing temperature through the first half of eruptions at the BJEC, with a weak increase in temperature throughout the second half of eruptions. (Figure 4.3). The temperatures remain hot throughout the eruption of all rhyolite units, with an average temperature of 933 °C for zircon rims, 929 °C for cores, 922 °C for interiors, and 930 °C for all analyses (Table 4.1). If a temperature correction is included in the results, this could dramatically decrease the temperatures by 45-120 °C, although temperatures reported and discussed here do not include any correction. The minimum temperature for all lavas from the BJEC is 817 °C (IBR) and the maximum is 996 °C (DCR). Average temperatures for individual units range from 897 °C for the BJR up to 965 °C for LCR. Both units that show the lowest temperatures (BJR) and the highest temperatures (LCR) also show clear zoning in zircons from core to rim that reflects a cooling trend (BJR ~15-45 °C) or a heating

trend (LCR ~25 °C). Excluding the zoning trends illustrated in BJR and LCR, the zoning trends from the core to the rim in relation to temperature trends is not consistent from unit to unit. The two zircons analyzed from ULF both show hotter rim than core temperatures (~18 °C), which is consistent with the hotter temperature of ULF than LLF, suggesting a heating of the system. SCR also shows clear negative zoning of ~50 °C, which suggests a cooling of the system from the previously erupted unit. Temperatures determined for BJR are similar to those determined for MCR; both of which were erupted temporally close to each other.

Comparisons to the CPT

Average temperatures remain high for the entire evolution of the BJEC. CPT temperatures, based on augite and pigeonite thermometry range primarily from 900 °C to 1000 °C, with augite temperatures having a larger range, from 755 to 969 °C and pigeonite temperatures ranging from 900 to 971 °C (Cathey and Nash, 2004). This indicates that temperatures from the commencement of eruptions from the BJEC, through the end of the effusive phase continued to be close to or above 900 °C.

The sustained high temperatures throughout the evolution of both the CPT and younger rhyolite lavas have been accompanied by an increase in mafic character (Nash et al., 2006; Figure 2; Bonnichsen et al., 2008). Total Fe (as FeO) wt. % increases from an average concentration of 1.14 % for CPT III up to 3.54 % for DCR. There are fluctuations in the increasingly mafic trend throughout the evolution of the system, as shown from FeO, but the trend is clear. The increase in Nd and Hf isotopic ratios suggests an increased input of mantle basalt into the system that may contribute to the increase in mafic content (Nash et al., 2006; Figure 3).

Pyroxene Thermometry

Pyroxene thermometry shows that magmatic temperatures of the BJEC vary between 900 and 1000 °C (Cathey and Nash, 2004; 2009) (Table 5.1). These thermometry studies on the lava flows of the BJEC demonstrate that pre-eruptive temperatures were often in excess of 950 °C, which suggest a large input of mafic material, allowing for the continued heating the system through the final eruptions (Cathey and Nash, 2009). These studies also indicate that the rhyolite lavas represented a generally higher temperature and more mafic system than that of the earlier erupted tuffs (Bonnichsen et al., 2008; Cathey and Nash, 2009). The most compositionally evolved lavas (BJR and CTR) are similar in composition to some of the least evolved and later erupted units of the CPT (CPT XVj and XVb). Moreover, high temperatures persisted in the ashflow tuffs that were erupted from the younger Twin Falls center (Ellis et al, 2010). These trends are only a general view of the evolution of the BJEC, and when examined in more detail the trends vary somewhat between eruptive units (Table 5.1).

Comparisons with Pyroxene Thermometry

In general, the Ti-in-zircon thermometer appears to correlate well with pyroxene thermometry from Cathey and Nash (2009) (Figure 5.6 and Table 5.1). Although this is true, the results from the Ti-in-zircon thermometer are typically more variable than those from pyroxene thermometry. This may be due to the slower diffusion of Ti relative to that of Ca, Mg, and Fe (Cherniak and Watson, 2007; Table 1; Huebner and Nord, 1981; Table 1).

The Ti-in-zircon thermometer tends to produce lower temperatures than the use of pigeonite for pyroxene thermometry (Figure 5.6). The interior analysis from SCR does not correlate well between the two thermometers, but has only one analysis from Ti-in-zircon

Table 5.1. Ti-in-zircon temperatures for BJEC lavas and comparative pyroxene temperatures from Cathey and Nash (2009).

Unit	n (Ti)	^{49}Ti (ppm)	1 σ	T (°C)	1 σ	Pigeonite	1 σ	Augite	1 σ
Lava flow one cores	2	21.9	8	932	48	962	19	913	
Lava flow one interiors	2	25.2	9	951	48	959	6	908	
Lava flow one rims	6	20.3	5	923	32	961	6	911	
Lower lava flow cores	2	18.3	2	912	13				
Lower lava flow rims	2	19.4	1	919	8				
Upper lava flow cores	2	20.6	0	927	0				
Upper lava flow interiors	1	23.6		945					
Upper lava flow rims	2	23.9	1	947	4				
Triguero Homestead Rhyolite cores	3	20.7	1	928	7	966	10	1016	24
Triguero Homestead Rhyolite rims	3	22.2	1	937	7	971	13	1010	28
Marys Creek Rhyolite cores	1	20.4		926					
Marys Creek Rhyolite interiors	1	11.9		860					
Marys Creek Rhyolite rims	2	19.4	0	919	2				
Cedar Tree Rhyolite cores	6	19.9	4	921	26	926	20	915	27
Cedar Tree Rhyolite interiors	3	21.9	2	935	10	921	16		
Cedar Tree Rhyolite rims	9	21.9	3	935	18	931	14	905	20
Bruneau-Jasper Rhyolite cores	3	17.5	5	904	37	905	17	888	22
Bruneau-Jasper Rhyolite rims	4	14.9	3	885	25	904	18	864	18
Poison Creek Rhyolite cores	2	16.5	8	892	66	969	18		
Poison Creek Rhyolite rims	3	27.8	2	967	12	969	20		
Louse Creek Rhyolite cores	4	24.5	3	949	17	966	11		
Louse Creek Rhyolite interiors	1	31.6		986					
Louse Creek Rhyolite rims	3	30.5	4	980	20				
Sheep Creek Rhyolite cores	3	20.5	6	924	39	964	8	971	20
Sheep Creek Rhyolite interiors	1	11.4		855		955	6	962	

Table 5.1 continued

Unit	n (Ti)	^{49}Ti (ppm)	1 σ	T (°C)	1 σ	Pigeonite	1 σ	Augite	1 σ
Sheep Creek Rhyolite rims	6	19.3	7	913	50	966	13	970	20
Indian Batt Rhyolite cores	3	23.2	7	940	42	977	11	942	9
Indian Batt Rhyolite interiors	1	12.8		868					
Indian Batt Rhyolite rims	4	22.5	11	926	79	974	7	937	7
Dorsey Creek Rhyolite cores	8	21.7	6	931	39	949	21	993	24
Dorsey Creek Rhyolite rims	9	25.0	4	952	21	951	20	987	16
Three Creek Tuff cores	3	25.3	3	955	13	972	15	946	22
Three Creek Tuff rims	3	22.2	3	936	18	976	13	936	24
All cores	42	22.2	6	974	202	956	23	948	43
All interiors	10	20.7	7	922	48	953	23	966	60
All rims	56	22.6	6	950	118	956	24	940	48
All analyses	109	21.7	5	931	37	955	23	949	46

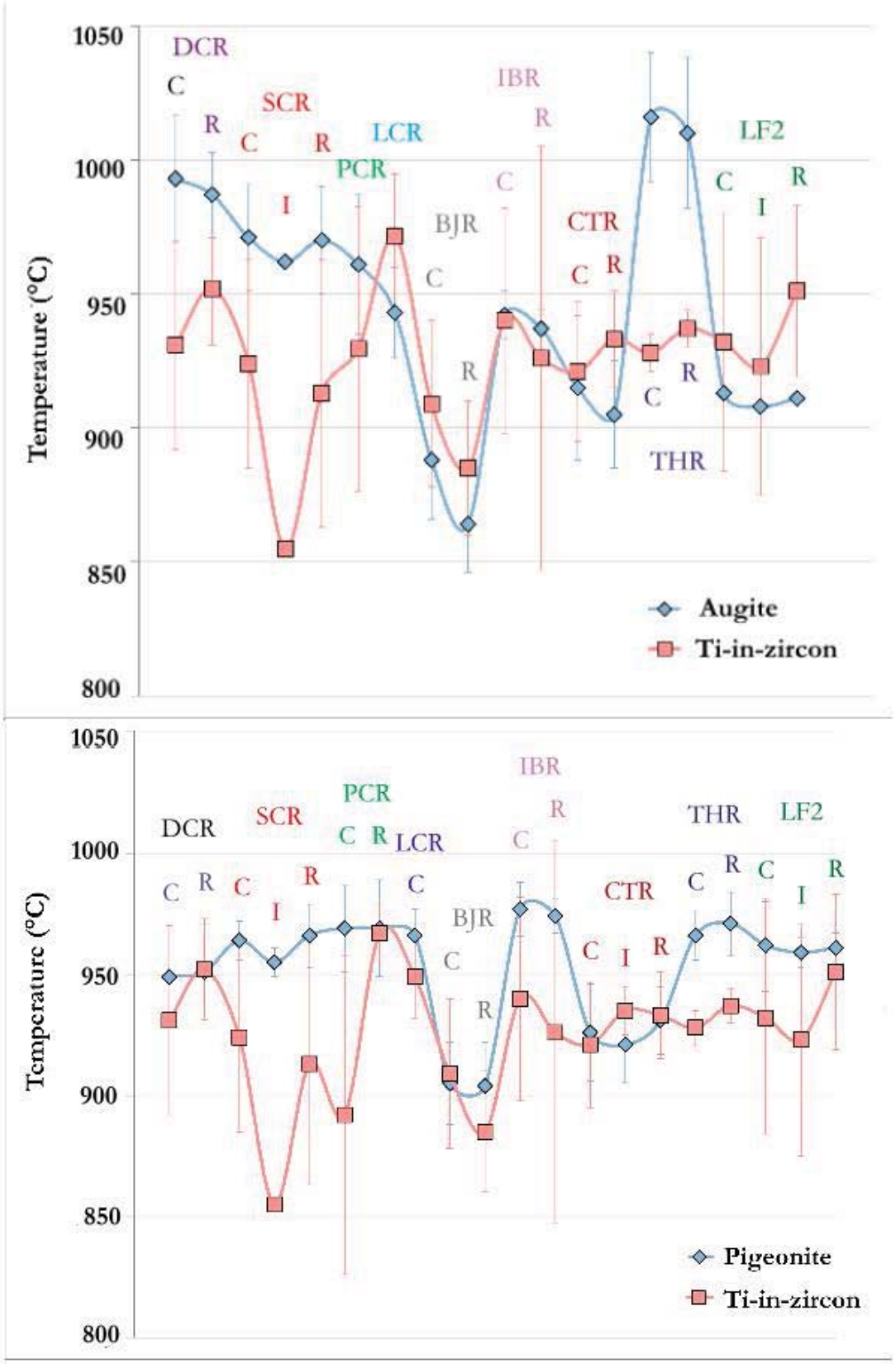

Figure 5.6. Comparisons of thermometry for lavas of the Bruneau-Jarbidge eruptive center using pigeonite, augite, and Ti-in-Zircon thermometry. Each lava unit is labeled with a different color, where C = core, I = interior, and R = rim analysis. Temperatures were determined as averages for each group; pigeonite and augite data are from Cathey and Nash (2009).

thermometry and this may be the reason for the lack of correlation, causing a 100 °C difference between the two thermometers.

The Ti-in-zircon temperatures correlate better with the results of pyroxene thermometry based on augite compositions (Figure 5.6). The interior analysis from SCR still does not correlate well with the augite thermometer, and the cores and rims of IBR do not correlate well (a greater than 70 °C difference), but otherwise the two thermometers appear to agree. The large range in Ti-in-zircon temperatures for each unit causes most values between the two thermometers to overlap, as occurs with pigeonite.

Heise and Yellowstone as a Model

As discussed earlier, the generally accepted mechanism for producing low $\delta^{18}O$ magmas at the Yellowstone and Heise volcanic centers involves a caldera collapse model. The model involves the hydrothermal alteration of previously erupted material, which is followed by a catastrophic eruption and a subsequent caldera collapse, allowing the ^{18}O depleted material to be incorporated into the magmatic system, lowering the $\delta^{18}O$ of the later erupted magma (Bindeman et al., 2001b; Bindeman et al., 2008; Watts et al., 2011). Eruptions from both the Heise and Yellowstone volcanic centers show episodic fluctuations of their magmatic $\delta^{18}O$ between depleted (as low as +3 $^{o}/_{oo}$ at Heise and +1 $^{o}/_{oo}$ at Yellowstone) and near-normal $\delta^{18}O$ (approximately +6 to +8 $^{o}/_{oo}$), where the earliest erupted units always consists of material having normal $\delta^{18}O$. This is not the case for the BJEC, where the average of the earlier erupted CPT members ranges from 0.9 to 3.4 $^{o}/_{oo}$ (Cathey et al., 2007, 2011a,b). Eruptions from the BJEC also do not show recovery to normal $\delta^{18}O$ values, and there is no evidence of near-normal $\delta^{18}O$ in zircons from the

rhyolite lavas until the eruption of the largest lava (SCR) near or at the end of the sequence of eruptions, suggesting there must be a large low $\delta^{18}O$ source for the BJEC that existed prior to the first eruptions from the BJEC and was present throughout the entire volcanic cycle. Although the eruptions of the rhyolite lavas from the BJEC show minor recoveries toward higher $\delta^{18}O$, average $\delta^{18}O$ for zircons from all BJEC rhyolites does not exceed 2.4 $^{o}/_{oo}$ if the one heavy grain from SCR is excluded from consideration.

The overall trends shown at both Heise and Yellowstone begin with the eruption of normal $\delta^{18}O$ material, followed by a decrease and later recovery in $\delta^{18}O$ in a more rapid and dramatic manner than is shown in the rhyolite lavas of the BJEC (Watts et al., 2011; Figure 7). At Heise and Yellowstone, the increases in $\delta^{18}O$ span as much as 5 $^{o}/_{oo}$ over less than 1 m.y. at Yellowstone, and just over 2 $^{o}/_{oo}$ in less than 1 m.y. at Heise. The decreases in $\delta^{18}O$ from normal values at Heise and Yellowstone are also much greater, with changes of as much as 5 $^{o}/_{oo}$ at Yellowstone, and those at Heise up to 2 $^{o}/_{oo}$ (Watts et al., 2011). The gradual rise in $\delta^{18}O$ of the BJEC rhyolite lavas, in contrast, span ~3 m.y. where normal values are never reached, and decreases in $\delta^{18}O$ from one unit to the next never exceed 1.5 $^{o}/_{oo}$.

In general, through the evolution of the Yellowstone-Snake River Plain system the amount of total Fe increased through the evolution of the BJEC, as discussed above, but there was a measurable decrease of iron in glass from fallout tuffs erupted after Bruneau-Jarbidge, that was followed by a small increase to the present (Nash et al., 2006; Figure 2). Nd and Hf isotopes show a similar trend with the amount of mantle input increasing through the evolution of the BJEC and Twin Falls eruption centers, but this input has been variably decreasing since the closing stages of the eruptions at the Twin Falls eruptive center (Nash et al., 2006). This variable input at Heise and Yellowstone versus the increasing input

at Bruneau-Jarbidge and Twin Falls suggests that the contribution of mantle material to the Heise and Yellowstone magma generation systems may be less than to the BJEC (Nash et al., 2006; Figure 3).

Other significant differences between the eruptive centers include the temperature, frequency, and volume of eruptions (Perkins and Nash, 2002). The temperature of eruptions at the BJEC range from 900 to 1000 °C, whereas those at Heise and Yellowstone are cooler, ranging typically from 800 to 900 °C (see summary by Watts et al., 2011). The higher temperatures at Bruneau-Jarbidge suggest that the source of the eruptions at Bruneau-Jarbidge may also be deeper than those at Heise and Yellowstone. The caldera-collapse model for Heise and Yellowstone would also suggest relatively shallow depths as a means to develop the nested caldera complexes that characterize these eruptive centers. The catastrophic eruptions from the BJEC are also more frequent than those from Heise and Yellowstone (Perkins and Nash, 2002). Eruptions from Heise average ~3 explosive events every m.y., and there were four major caldera-forming events between 6.6 and 4.5 m.y. at Yellowstone, whereas the explosive phase at BJEC had 10 major eruptions in as little as 2 m.y. (Nash et al., 2006). Perkins and Nash (2002), based on the abundance of fallout tuffs of BJEC age, estimated that the long-term frequency of explosive eruptions was ~10 $m.y.^{-1}$ In addition to the high frequency of explosive events at BJEC, the total erupted volume is also greater. The total erupted volume from Yellowstone is at least 6000 km^3, with greater than 2500 km^3 from the Huckleberry Ridge tuff and 1000 km^3 from the Lava Creek tuff (Christiansen, 2002). At Heise, at least 4000 km^3 of rhyolite was erupted, including approximately 1800 km^3 from the Kilgore Tuff (Watts et al., 2011). A larger volume was erupted from the BJEC (8000 km^3), with at least 7000 km^3 from the CPT and at least 1000

km^3 from the rhyolite lavas (Perkins and Nash, 2002; Bonnichsen et al., 2008; Leeman et al., 2008).

Some aspects of the eruptions at Heise and Yellowstone are similar to those of the BJEC. The prolonged episodes of large volume explosive eruptions during the CPT sequence are similar to those at Heise and Yellowstone, as both of these explosive sequences have the ability to produce large complexes of calderas. The large volume explosive eruptions of the CPT could have formed calderas that are currently hidden by a veneer of younger basalt and sediment. If this is the case, then the rhyolite lavas that are erupted at the BJEC may be analogous to the postcaldera low $\delta^{18}O$ lavas of Yellowstone. The extensive amount of inherited grains found in the rhyolite lavas would also be consistent with this model, as cannibalization of previously erupted material would incorporate earlier erupted zircons into the newly formed magma volume. However, an important difference is that none of these inherited zircons (except one ancient zircon in SCR and one from IBR) have $\delta^{18}O$ values above 6 $^{o}/_{oo}$. In contrast, at Yellowstone, normal $\delta^{18}O$ zircons from the Huckleberry Ridge tuff and the Lava Creek are incorporated into later magmas, not including the Central Plateau Member.

An important complication from this study is in comparing the BJEC to Heise and Yellowstone due to the extended duration of lavas at Bruneau-Jarbidge and the shorter episodes of lavas erupted at Yellowstone and Heise. This is compounded by the lack of large caldera forming eruptions of ignimbrite material during the latter half of the BJEC. Although there are large ignimbrite eruptions interspersed within the earlier erupted lavas, details of the $\delta^{18}O$ values of these ignimbrites are not available to this study. Collectively, these differences suggest that there are some aspects of the low-$\delta^{18}O$ eruptions at the BJEC that cannot be explained by the caldera collapse model. There must have been an earlier low-

$\delta^{18}O$ source to produce the earlier erupted CPT, and the collapse of a caldera cannot explain a gradual rise in $\delta^{18}O$ noted in these lavas. The similarity that extensive explosive volcanism is followed by low $\delta^{18}O$ rhyolite lava flows suggests there are some overall parallels between the eruptive centers, and this leads to the possibility that caldera collapses may at least aid in the explanation of the episodic dips in $\delta^{18}O$ that are seen interspersed within the gradual increase in $\delta^{18}O$ of the rhyolite lavas, as caldera collapses have been shown at Heise and Yellowstone to cause a reduction in ^{18}O of magmatic systems. This also suggests the possibility that the rise in $\delta^{18}O$ throughout the eruption of the lavas from the BJEC may simply be a progressive reduction of $\delta^{18}O$-depleted material throughout eruptions, causing an increase in leftover material that is closer to normal $\delta^{18}O$ values, as is seen in eruptions at Heise and Yellowstone.

The Idaho Batholith

Boroughs et al. (2005) and Boroughs (2010) argue for the existence of a source that was depleted in $\delta^{18}O$ prior to the commencement of eruptions in the central Snake River Plain (cSRP). Boroughs (2010) suggests that hydrothermally altered material from the Idaho Batholith may have mixed with primitive basalt to form this low $\delta^{18}O$ source. Watts et al. (2011) argue that this cannot be the case, as the average $\delta^{18}O$ of the Idaho Batholith, including the $^{18}O/^{16}O$-depleted segments, is too high for it to produce the low, measured $\delta^{18}O$ values of zircons from the BJEC. Boroughs (2010) acknowledges the predominance of $\delta^{18}O$ above 6 $^{o}/_{oo}$ in the Idaho Batholith, but argues for a similar alteration scenario to that of the Lake City Caldera, where deeper, more centralized regions of the caldera are more highly altered, and depleted in $^{18}O/^{16}O$. In this case, Boroughs (2010) suggests that there

would be sufficiently large amounts of highly altered material (<5 $^{o}/_{oo}$) to produce $\delta^{18}O$ values low enough to account for what has been observed in the central Snake River Plain. Although, this may not account for the exceptionally low $\delta^{18}O_{zircon}$ (as low as -3.4 $^{o}/_{oo}$) values measured in this study, as the depleted source must have $\delta^{18}O$ values not just below 5 $^{o}/_{oo}$, but also well below 0 $^{o}/_{oo}$.

Regional Isotopic Modification

Leeman et al. (2008) suggest that migration of meteoric water into the crust of the central Snake River Plain may have been widespread and enhanced through Basin and Range extension, crustal deformation associated with magmatism, and the presence of a large lacustrine environment (Lake Idaho) in topographically low regions of the central Snake River Plain during the Neogene. The calculated isotopic response of the crust to this deep infiltration of meteoric water, as proposed by Leeman et al. (2008), suggests that various minerals (anorthite, albite, k-feldspar, and biotite) will demonstrate maximum ^{18}O depletions at depths ranging between 10 and 15 km, with $\delta^{18}O$ as low as -2 $^{o}/_{oo}$ (Leeman et al., 2008; Figure 12). H. E. Cathey (Cathey et al., 2011a,b, manuscript) has demonstrated that oxygen isotopes in zircon from the CPT record systematic variations and intra-crystal zonation in $\delta^{18}O$ consistent with progressively shallowing partial melting of a source region with an isotopic gradient, such as that modeled by Leeman et al. (2008).

The interpretation by Cathey et al. (2011a,b) predicts a systematic increase of $\delta^{18}O$ through time in younger CPT members with the production of melts from successively shallower levels in the crust. The BJEC lavas generally follow this trend (Figure 5.7), but there are episodic small decreases in $\delta^{18}O$ that require some variability in the source.

Movement of the magma system in the crust as it migrates to the east with the mantle plume, as well as stagnations in the level of magma generation, perhaps related to complexities of the rising magmatic system, and incorporation of isotopically heterogeneous surrounding material are possible mechanisms to account for minor isotopic fluctuations (Cathey et al., unpublished). Additionally, one cannot rule out the possibility of complexities that could be superposed by caldera-forming processes similar to those that have produced low $\delta^{18}O$ magmas at Heise and Yellowstone.

Low $\delta^{18}O$ Ancient Zircons

The abundance of low $\delta^{18}O$ material from the onset of eruptions at the BJEC suggests the presence of a low $\delta^{18}O$ protolith for the BJEC, but the refractory nature of zircon suggests that any original zircons from the source rock, prior to any hydrothermal alteration, would not be altered to a lower $\delta^{18}O$ value. The lack of abundance of normal $\delta^{18}O$ ancient zircons suggests that either there were few or no zircons present in the BJEC protolith, or the melt produced from the protolith was undersaturated with respect to zircons and any zircons originating from the source were melted upon arrival of the heat source of the BJEC.

Implications From the Ti-in-zircon Temperatures

Ti-in-zircon thermometry indicates an unusually high temperature magma system that persisted through the entire evolution of the rhyolite lavas, although these temperatures may be lower if pressure and activity corrections are included. The lavas also appear to be slightly hotter than the earlier erupted CPT, which indicates a lack of cooling of the system

throughout its evolution (Cathey and Nash, 2009). These high temperatures do not allow for the magma to have resided for long periods at shallow depths before eruption, or they would have cooled and possibly fractionated. The high temperatures are also consistent with the temporal increase in mafic content of the erupted material from the BJEC.

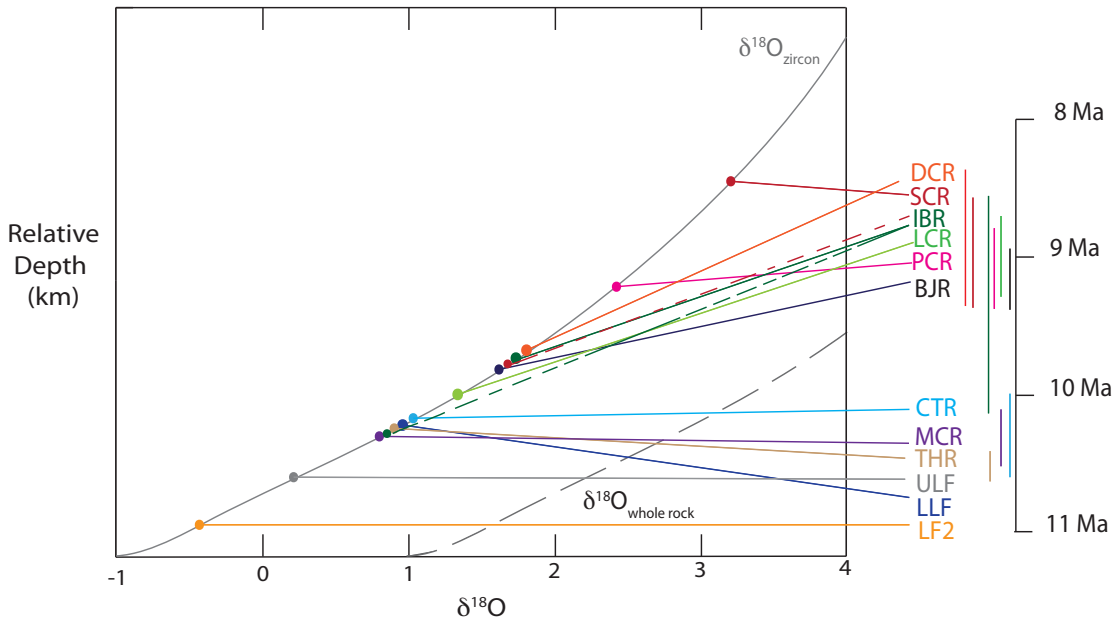

Figure 5.7. Scenario for variation in $\delta^{18}O$ of magma as a function of depth and eruption age along a hypothetical isotopic profile. Lavas are arranged in age sequence with uncertainties for individual units indicated by color bars. The dashed line for SCR and IBR indicates an assemblage exclusive of the single high $\delta^{18}O$ zircon in each unit. The $\delta^{18}O_{whole\ rock}$ is also shown for reference as 2 $^{o}/_{oo}$ lower than that of the zircon values (Adapted from Leeman et al., 2008 calculations).

CHAPTER 6

CONCLUDING REMARKS

This study reveals that a continually $\delta^{18}O$ depleted and hot eruptive center persisted in the central Snake River Plain from 12.8 to 8 Ma. Models incorporating the regional isotopic modification of the source region (Leeman et al., 2008; Cathey et al., 2011; Boroughs, 2010) as well as the well-accepted caldera collapse model for the Heise and Yellowstone centers provide possible mechanisms to explain the depletion in $\delta^{18}O$ of the rhyolites erupted from the BJEC. The earliest rhyolite lava, erupted at approximately 11 Ma had the lowest average zircon $\delta^{18}O$ (-0.5 $^{o}/_{oo}$) of any other rhyolite lava erupted from the BJEC. Following the initial eruption of LF1, oxygen isotope ratios in subsequent eruptions trend toward heavier values, with minor variation, culminating with one of the two youngest lavas of the BJEC, the Dorsey Creek rhyolite with an average $\delta^{18}O_{Zrc}$ of 1.8 $^{o}/_{oo}$, or the Sheep Creek rhyolite having an average $\delta^{18}O_{zrc}$ of 3.3 $^{o}/_{oo}$ (1.7 $^{o}/_{oo}$ not including outlying grain). Inheritance of zircons from prior magmatic units is common. Eruptive units that contributed the most zircons to later magmas include several members of the CPT as well as rhyolites LF1, MCR, and CTR, where inherited grains tend to have lighter $\delta^{18}O$ than the average for the unit, so that when the inherited grains are removed from the average, the average $\delta^{18}O$ for the unit will typically increase. Deviations from the trend of a gradual rise in

$\delta^{18}O$ over time could be explained through possible caldera collapses as well as migration of the magmatic system to the east as it shallows, stagnations from the rising of the magmatic system, and incorporation of surrounding material, which are all likely in any natural magmatic system.

Throughout this process, the temperature of the magmatic system remained extremely high, at over 900 °C, with variations in temperature during the evolution of the system being primarily between 900 and 1000 °C. Temperature trends may include a decrease in temperature through earlier rhyolitic lava eruptions, with an increase in temperature through the second half of eruptions. Temperatures as high as these cannot be sustained for long periods at shallow depths, suggesting that magmas were erupted from considerable depth and that shallow residence times, if any, for each erupted unit must have been short to avoid cooling and fractionation.

APPENDIX A

MELT INCLUSIONS

Background

Melt inclusions (MI) are useful for determining the original composition of a melt in that they theoretically should not be altered once they are fully enclosed in the crystal, especially if they are contained within a resistant phenocryst. Results that are obtained through the analyses of MI may not be possible when using whole rock or matrix glass, as these may not be a true analysis of the original magma. Although MI should contain the original composition of the melt once they are enclosed within a crystal, if the system begins to cool after entrapment, crystallization may occur along the walls of the inclusion, which will deplete the MI of the elements that are incorporated into the newly growing crystal (Kent, 2008). This cooling process may also lead to thermal contraction of the melt, which can form vapor bubbles that deplete the MI of CO_2 (Metrich et al., 2008). Another setback of the analyses of MI is that they rarely preserve the full composition of the original melt because they are not able to encompass the complete range of melt compositions due to some of the compositions being trapped in preference of others. This is because MI are more likely to form in cooler regions of the magmatic system. This preference can skew the inattentive researcher's data due to the selection of larger inclusions that are better for analyses (Kent, 2008).

Methods

Melt inclusions in zircons from both CPT and rhyolite lavas from the BJEC were analyzed using the electron microprobe (EPMA) at the University of Utah. Prior to analysis, MI were analyzed under a binocular microscope to distinguish between solid mineral and glass inclusions. Cracks that ran through the inclusion were also identified, and these inclusions were not analyzed for chemical composition since these cracks could allow secondary solutions to enter the MI and for volatile components to escape. Samples were then analyzed by EPMA to determine their major and minor element compositions. Analytical parameters were 15 keV accelerating voltage, 25 nA beam current, and a beam diameter ranging from 2 μm to 5 μm due to the beam diameter being adjusted in response to the size of the MI, with the majority of spot sizes being 2 μm. Standards used during analysis include a combination of natural mineral and obsidian standards. Melt inclusions were analyzed for Si, Al, Fe, Mn, Mg, Ca, Na, K, Ba, F, and Cl. When possible, multiple analyses were done on a single MI to determine homogeneity of the inclusion, and multiple MI were analyzed in single zircons to determine variations in the magma composition during growth of a particular crystal. A range of MI were also checked using BSE images, EDS, and a binocular microscope for secondary growth.

Results

H_2O

H_2O concentrations were estimated by difference; i.e., by taking 100 (the theoretically expected total) and subtracting the analytical total. It should be noted that only

three analyses could be conducted on CPT XIII, CPT XII, and PCR which does not give as accurate an average for these three units as was allowed for other units. LF1, DCR, CPT III, and CPT XI have a wide range in H_2O. H_2O contents of CPT V, CPT X, CPT XIII, and CPT XVb are slightly above the average of 1.6% for the CPT units. H_2O in CPT VII and CPT XII is lower than most other units for the CPT. H_2O of CPT IX and CPT XVj are similar to that of the average for all CPT units. Lava units that have near average H_2O for the rhyolites of approximately 2.1% include ULF and SCR. Lava units that have slightly above average H_2O for the rhyolites include LCR, TCT, and PCR. Lava units that have significantly higher than average H_2O for the rhyolites include CTR, IBR, and BJR. Lava units that have below average H_2O include LLF, MCR, and THR.

Elemental Trends for the Rhyolite Lavas

Many of the MI contain secondary growth crystals, with the most common minerals to grow inside the melt inclusions being ilmenite, magnetite, pyrrhotite, plagioclase, apatite, augite, and alkali feldspar.

There are two distinct modes of Fe in MI from lavas that are evident on the FeO vs. SiO_2 plot. The majority of data points from DCR, CTR, BJR, TCT, LCR, PCR, and ULF have less than 1.0% total Fe as FeO, and the majority of data points from LF1, SCR, IBR, MCR, LLF, and THR have over 1.0% FeO. LLF and IBR both have a large range in FeO.

The major secondary phases in the MI include Fe- and Fe-Ti oxides that may account for low Fe concentrations in the glass. In some units, the absence of post-entrapment crystallization was determined through microscopic analysis of the melt

inclusion. Using only MI with no secondary growth raises the FeO average for melt inclusions in all lavas from 1.23 ± 0.90 to 1.83 ± 0.49 weight %.

There are two modes of CaO that are evident on the SiO_2 vs. CaO plot. The majority of data points from DCR, CTR, SCR, BJR, TCT, LCR, PCR, IBR, MCR, and ULF have less than 0.6 wt. % CaO, and the majority of MI from LF1 and THR have over 0.6 wt. % CaO. IBR, LF1, LLF, and MCR both have a large range in CaO. The two distinct groups of CaO could also be due to secondary mineral growth in the MI, because apatite and plagioclase occur in some MI, and one MI (LCR-37) with secondary growth of plagioclase has a distinctly lower CaO (0.19 %) than average for LCR (0.36 %). Elimination of MI with secondary growth raises the total CaO weight percent average for MI for all lavas from 0.44 ± 0.22 to 0.54 ± 0.26. No other elements show a distinct difference between pristine MI and those showing secondary growth. The FeO vs. CaO plot shows a slight positive correlation between FeO and CaO.

The average Al_2O_3 is 11.9 ± 0.36. LLF and PCR both have the highest Al_2O_3 at 12.2 ± 0.45 and 12.2 ± 0.24 respectively. BJR has the lowest Al_2O_3 at 11.2 ± 0.29. The average SiO_2 is 75.4 ± 1.1 and the average TiO_2 is 0.2 ± 0.1 for all lavas. IBR has the lowest SiO_2, as well as the largest range, at 73.6 ± 1.45. ULF has the highest SiO_2 at 76.8 ± 0.59.

The average Na_2O is 2.58 ± 0.32. TCT has the highest Na_2O in MI of all other rhyolite lavas at 2.84 ± 0.24. ULF has the lowest Na_2O, with a weight percent of 2.20 ± 0.40. The average concentration of K_2O is 5.82 ± 0.33. ULF and BJR both have the highest K_2O at 6.21 ± 0.28 and 6.21 ± 0.83 respectively. TCT has the lowest K_2O at 5.52 ±0.19.

The SiO_2 vs. MgO plot shows a spike in MgO up to 0.18 weight percent, where all analyses with a high MgO have lower SiO_2. All data points with high MgO are from LF1 and

IBR. The average MgO for MI in all lavas is 0.02 ± 0.04. The FeO vs. MgO plot shows that all analyses with high MgO have moderate FeO.

The average Cl is 0.04 ± 0.02. No significant trends are shown in the FeO vs. F plot, and the average F in MI is 0.07 ± 0.04.

Unit CTR has abundant fresh glass that has been analyzed by EPMA, allowing a comparison between the glass and MI analyses (Nash, unpublished). The MI analyses have generally lower FeO, MnO, and MgO, higher SiO_2, Al_2O_3, Cl, and Na_2O, and similar F, TiO_2, K_2O, and CaO. The MI with higher Fe are similar to most Fe of glass analyses. Although, when they were checked for secondary growth two of the three MI having higher Fe values contain secondary growth, suggesting that an Fe-oxide was analyzed instead of the MI. The third MI showed no secondary growth under the petrographic microscope, and could therefore provide a reliable Fe concentration for this unit of approximately 1.7 wt. %.

Elemental Trends for the Cougar Point Tuff

The plot of SiO_2 vs. FeO shows a clear separation of different CPT units in FeO. This is most likely because, similar to the lavas, many MI analyzed from the CPT had post-entrapment growth. CPT IX, CPT V, CPT XVj, and CPT XVb have the lowest FeO. CPT X and CPT III have slightly higher concentrations, and CPT VII has even higher FeO. CPT XI has bimodal FeO, with both modes having higher concentrations than average for the CPT. As was done for the lavas, MI showing higher Fe were visually inspected under the microscope to determine if they showed post-entrapment growth to establish if their Fe concentrations could provide reliable Fe concentrations for the unit. Only MI from CPT XI

are pristine. This suggests that MI without secondary growth have an average FeO of 1.28 ± 0.26.

The SiO_2 vs. Al_2O_3 plot shows an increase in Al_2O_3 associated with lower SiO_2. This increase in Al_2O_3 is found mainly in MI from CPT IX. CPT XIII has the highest Al_2O_3 at 12.4 ± 0.31 and CPT XI has the lowest Al_2O_3 at 11.9 ± 0.22. The average Al_2O_3 for all tuffs is 12.1 ± 0.45.

Multiple trends are shown on the SiO_2 vs. TiO_2 plots. MI from CPT III and CPT X both have higher than average SiO_2 and lower than average TiO_2. MI from CPT V, CPT VII, CPT XII, CPT XVb, and CPT XVj all have higher SiO_2 and TiO_2, whereas MI from CPT IX have low SiO_2 and TiO_2 concentrations. MI from CPT XIII and CPT XI have low SiO_2 and high TiO_2 whereas MI from CPT IX, CPT XII, and CPT XIII have a large range in values for both SiO_2 and TiO_2. SiO_2 averages 76.2 ± 0.94 and TiO_2 averages 0.14 ± 0.09. Similar trends are shown in the FeO vs. TiO_2 plot.

There are two distinct compositional modes evident in the SiO_2 vs. CaO plot. MI from CPT III, CPT IX, CPT V, CPT X, CPT XII, CPT XVb, and CPT XVj have predominantly lower CaO concentrations, and MI from CPT VII and CPT XI have primarily higher CaO concentrations. As was determined for the lavas, these two distinct modes of Ca concentrations could be due to secondary mineral growth in the MI, because apatite was found in some MI. The determination of MI without secondary growth for the CPT also yields higher CaO in some MI, and raises the total CaO average for all MI in the CPT from 0.56 ± 0.16 to 0.61 ± 0.04.

MI with higher FeO have higher MgO. As CPT XI has the highest FeO, it also has the highest MgO, based on this trend, with an average MgO weight percent of 0.04 ± 0.02.

Average MgO for the CPT are 0.01 ± 0.02 which is at or below the limit of detection by EPMA.

The average Na_2O for MI from all CPT units is 2.78 ± 0.32. The average K_2O is 6.00 ± 0.25. The average Cl is 0.04 ± 0.02. The average F is 0.08 ± 0.06. The average MnO for all CPT units is 0.01 ± 0.01 which is below the limit of detection.

Analyses have also been conducted on airfall glass from the CPT and can be compared to the MI analyses (Nash, unpublished). All units have lower FeO in MI than airfall glass, and most MI analyses have higher SiO_2 and lower MgO than the airfall glass. Otherwise, there are no consistent trends between the MI from the zircons and that of the airfall glass.

Discussion

H_2O

Lavas

If all analyses are considered, since secondary growth should not significantly affect the determination of H_2O, there appears to be a general increase in H_2O throughout the evolution of the eruptive center (from 0.6 to 2.3 % if LF1 and TCT are excluded), with episodic spikes in H_2O (CTR, BJR, IBR) that are followed by smaller decreases, allowing for a gradual increase in H_2O (Figure A.1). The increase in H_2O through the evolution of the lavas is suggestive; however, it would be clearly preferable to use a method for the direct determination of H_2O. There are occasional decreases in H_2O (CPT VII, CPT XII) during the evolution of the CPT, and these decreases are followed by rapid increases during the

next eruption. These data suggest that volatile content may have increased throughout the evolution of the CPT.

Comparisons

The lava units appear to have a higher H_2O than the CPT units, although both show a gradual increase of volatile content throughout their respective evolutions (Figure A.1). The wider range in H_2O of the lava units aides in them having an overall higher average concentration than the CPT units. Episodic spikes accompany the gradual increase in H_2O in the lava units, and the gradual increase of the CPT is accompanied by occasional decreases.

If all analyses are used to determine the evolution of the entire eruptive center through both the CPT and the lavas, then there is an overall increase in H_2O weight percent.

Cougar Point Tuff

There appears to be a general trend of increasing H_2O throughout the evolution of the CPT as well (Figure A.1). Instead of episodic spikes that were seen with the lavas, for the entire eruptive center that is accompanied by both episodic increases and decreases, suggesting clear open system behavior of the magma generation system, accompanied by a gradual increase in volatile content. The higher H_2O of the lavas would therefore be suspected, as the increasing H_2O of the lavas appears to be a continuation from the CPT.

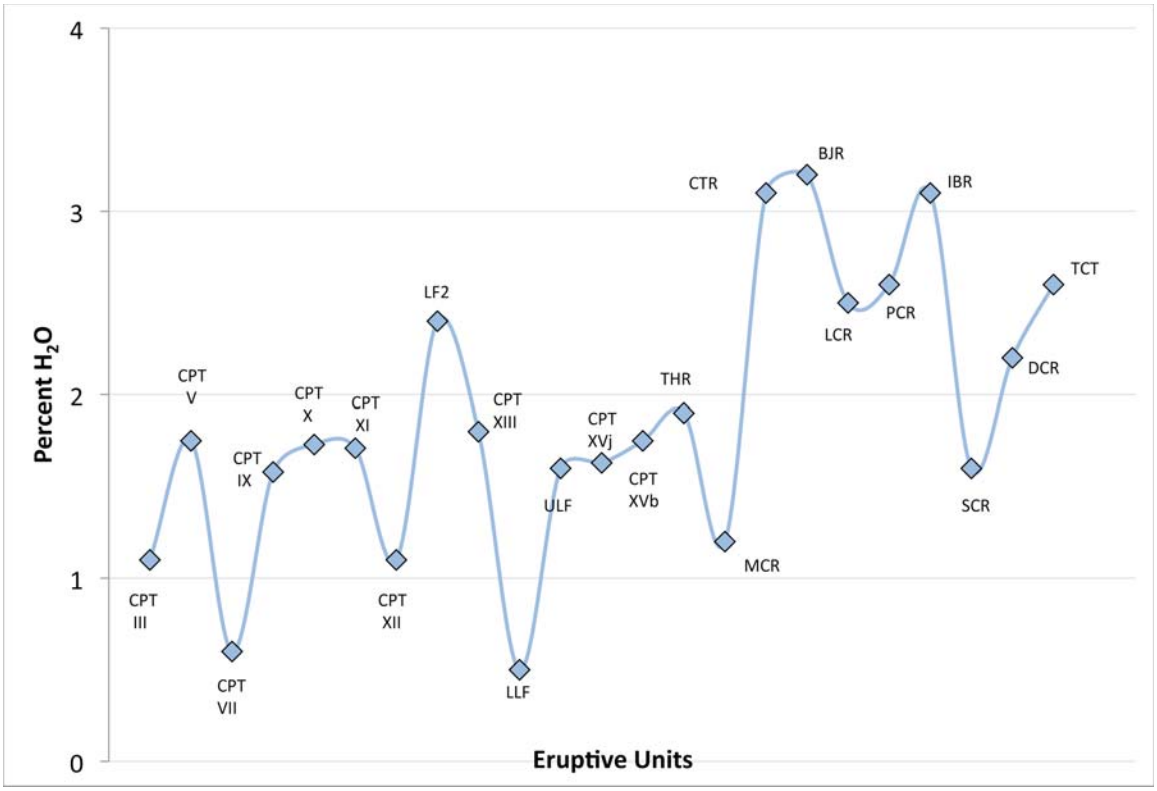

Figure A.1. Average H_2O in MI for the CPT and the rhyolite lavas through the evolution of the BJEC.

Other High-Silica Magmas

This research suggests that H_2O content of the BJEC is slightly lower than that for other high-silica magmas, including the magmas that produced the Bishop tuff and those that feed the current Yellowstone Plateau system. H_2O determined through analyses of MI from quartz crystals from the Bishop tuff range from 3.2 to 6 wt % (Hildreth and Wilson, 2007). Rhyolites from the eastern Snake River Plain have slightly lower H_2O than the Bishop tuff, at approximately 3 wt. % (Gansecki, 1998), which is still higher than those of the BJEC.

Elemental Trends

Lavas

If only MI with no evidence of post-entrapment crystallization are used to determine elemental trends for the lavas, there appears to be a general decrease in SiO_2 through their evolution, with a dramatic drop at the CTR, and a relatively low SiO_2 for LF1, the first lava erupted. There does not appear to be any other elemental trends throughout the evolution of the lavas, nor does there appear to be any elemental trends with relation to age for the lavas when all MI are used.

The clear distinction between the iron content of the MI and that of the glass analyses discussed earlier signifies the loss of iron through secondary crystallization of ilmenite, magnetite, and pyrrhotite, which were all found within the MI. The multiple sets of Fe concentrations could also be due to this phenomenon. This could also be the case for the two distinct modes of Ca that suggests the secondary crystallization of apatite, augite, or plagioclase, which was found, but was not as prominent as the secondary growth of various iron oxides. The decreased MgO, SiO_2, Al_2O_3, and Na_2O found in the MI relative to the

glass analyses could be explained by the secondary crystallization of plagioclase, alkali feldspar, or pyroxene in the MI.

Cougar Point Tuff

There does not appear to be any elemental trends in MI with respect to age throughout the eruptive center for the CPT when data from all MI are considered; however, only MI in one eruptive unit of the CPT showed no evidence of post-entrapment crystallization.

The spike in Al_2O_3 associated with lower FeO could be due to secondary crystallization of iron oxides. As was shown in the lavas, there is a clear distinction between the iron content of the MI and that of the glass analyses, which signifies the loss of iron through secondary crystallization of ilmenite, magnetite, and pyrrhotite. This, again, can explain the multiple modes of Fe. As was suggested for the lavas, this could also be the case for the two modes of Ca, suggesting secondary growth of apatite, augite, or plagioclase. All other trends in relation to MI and airfall analyses are not consistent between multiple MI, which suggests variability in secondary growth.

Comparisons

When using all analyses, there are no compositional differences between MI in the CPT and the lavas. This is the same when only MI without post-entrapment crystallization are evaluated, although it must be noted that only CPT XI can be used when determining the average for clean analyses for the entire CPT. There does not appear to be any elemental trends with age throughout the entire evolution of the BJEC when all analyses are used, or when only the clean analyses are used.

Future Research

Since this study was done as a preliminary analysis of melt inclusions trapped in erupted material from the BJEC, not all steps were taken to determine the pristine composition of the melt. In the future, melt inclusions from this eruptive center should be analyzed after heating and homogenization techniques have been used to determine the original composition of the melt. This would allow the elements that were removed from the melt due to post-entrapment growth of the pyrrhotite, ilmenite, magnetite, and feldspars to be incorporated back into the melt, and included in the analyses. Another improvement to this study would be to determine H_2O by measuring hydrogen directly by ion microprobe (SIMS) that would allow for more accurate results.

APPENDIX B

OXYGEN ISOTOPE FIGURES

SEE SUPPLEMENTAL MATERIAL

APPENDIX C

U-Th-Pb DATING FIGURES

SEE SUPPLEMENTAL MATERIAL

APPENDIX D

THERMOMETRY FIGURES

SEE SUPPLEMENTAL MATERIAL

APPENDIX E

MELT INCLUSION FIGURES AND TABLES

SEE SUPPLEMENTAL MATERIAL

APPENDIX F

CATHODOLUMINESCENCE AND BACKSCATTER ELECTRON IMAGING OF ANALYZED ZIRCONS

SEE SUPPLEMENTAL MATERIAL

The following are CL and BSE images of zircons analyzed for $\delta^{18}O$ by the SIMS, U-Th-Pb ages and thermometry analyzed by the SHRIMP, and melt inclusions analyzed by EPMA, as well as EDS qualitative analysis of a select MI that are not shown earlier in chapter 2. Analysis spots for $\delta^{18}O$ are marked in red, and BSE images accompanying these CL images show the ablation pits from the SIMS analyses; U-Th-Pb analysis spots are marked in yellow; thermometry analysis spots are marked in blue; MI analysis spots are marked with the sample number in white, and BSE images following any CL images of MI analyses show EPMA analysis spots. Zircon sample numbers are in white. Although spot locations for the $\delta^{18}O$, U-Th-Pb ages, and thermometry are accurate, the spot sizes are not to scale, and were made different sizes so all spot locations could be seen. CL and BSE images of zircons from rhyolites were imaged by Barbara Nash and CL and BSE images of zircons from CPT units were imaged by Henrietta Cathey.

REFERENCES

Anderson, A., Clayton, R., Mayeda, T., 1971, Oxygen isotope thermometry of mafic igneous rock, Journal of Geology, v. 79, p. 715-729.

Anderson, D., 2000, The thermal state of the upper mantle: no role for mantle plumes: Geophysical Research Letters, v. 27, p. 3623-3626.

Anderson, J., Barth, A., Wooden, J., Mazdab, F., 2008, Thermometers and thermobarometers in granitic systems: Reviews in Mineralogy and Geochemistry, v. 69, p. 121-142.

Annen, C., Blundy, J., Sparks, R., 2006, The genesis of calcalkaline intermediate and silicic magmas in deep crustal hot zones: Journal of Petrology, v. 47, p. 505-539.

Bachmann, O., Bergantz, G. 2008, Deciphering magma chamber dynamics from styles of compositional zoning in large silicic ash flow sheets: Reviews in Mineralogy and Geochemistry, v. 69, p. 651-674.

Bachmann, O., Bergantz, G., 2008, The magma reservoirs that feed supereruptions: Elements, v. 4, p. 17-21.

Bacon, C. Adami, L., Lanphere, M., 1989, Direct evidence for the origin of low-$\delta^{18}O$ silicic magmas: Quenched samples of a magma chamber's partially fused granitoid walls, Crater Lake, Oregon: Earth and Planetary Science Letters, v. 96, p. 199-208.

Balsley, S., Gregory , R., 1998, Low-$\delta^{18}O$ magmas: Why are they so rare?: Earth and Planeary Science Letters, v. 168, p. 123-136.

Barth, A., Wooden, J., 2010, Coupled elemental and isotopic analyses of polygenetic zircons from granitic rocks by ion microprobe, with implications for melt evolution and the sources of granitic magmas: Chemical Geology, v. 277, p. 149-159.

Bindeman, I., Valley, J., 2000, Formation of low-$\delta^{18}O$ rhyolites after caldera collapse at Yellowstone, Wyoming, USA: Geology, v. 28, p. 719-722.

Bindeman, I., Valley, J., 2001a, Low-$\delta^{18}O$ rhyolites from Yellowstone: Magmatic evolution based on analyses of zircons and individual phenocrysts: Journal of Petrology, v. 42, p. 1491-1517.

Bindeman, I., Valley, J., Wooden, J., Persing, H., 2001b, Post-caldera volcanism: in situ measurement of U-Pb age and oxygen isotope ratio in Pleistocene zircons from Yellowstone caldera: Earth and Planetary Science Letters, v. 189, p. 197-206.

Bindeman, I., Sigmarsson, O., Eiler, J., 2006, Time constraints on the origin of large volume basalts derived from O-isotope and trace element mineral zoning and U-series disequilibria in the Laki and Grimsvotn volcanic system: Earth and Planetary Science Letters, v. 245, p. 245-259.

Bindeman, I., Fu, B., Kita, N., Valley, J., 2007a, Origin and evolution of silicic magmatism at Yellowstone based on ion microprobe analysis of isotopically zoned zircons: Journal of Petrology, v. 00, p. 1-31.

Bindeman, I., Watts, K., Schmitt, A., Morgan, L., Shanks, P., 2007b, Voluminous low $\delta^{18}O$ magmas in the lat Miocene Heise volcanic field, Idaho: Implications for the fate of Yellowstone hotspot calderas: Geology, v. 35, p. 1019-1022.

Bindeman, I., 2008a, Oxygen isotopes in mantle and crustal magmas as revealed by single crystal analysis: Reviews in Mineralogy and Geochemistry, v. 69, p. 445-478.

Bindeman, I., Brooks, C., McBirney, A., Taylor, H., 2008b, The low-$\delta^{18}O$ late-stage ferrodiorite magmas in the Skaergaard intrusion: Result of liquid immiscibility, thermal metamorphism, or meteoric water incorporation into the magma?: Journal of Geology, v. 116, p. 571-586.

Bindeman, I., Leonov, V., Izbekov, P., Ponomareva, V., Watts, K., Shipley, N., Perepelov, A., Bazanova, L., Jicha, B., Singer, B., Schmitt, A., Portnyagin, M., Chen, C., 2010a, Large-volume silicic volcanism in Kamchatka: Ar-Ar and U-Pb ages, isotopic, and geochemical characteristics of major pre-Holocene caldera-forming eruptions: Journal of Volcanology and Geothermal Research, v. 189, p. 57-80.

Bindeman, I., Schmitt, A., Evans, D., 2010b, Limits of hydrosphere-lithosphere interaction: Origin of the lowest-known $\delta^{18}O$ silicate rock on Earth in the Paleoproterozoic Karelian rift: Geology, v. 38, p. 631-634.

Black, L., Kamo, S., Allen, C., Davis, D., Aleinikoff, J., Valley, J., Mundil, R., Campbell, I., Korsch, R., Williams, I., Foudoulis, C., 2004, Improved $^{206}Pb/^{238}U$ microprobe geochronology by the monitoring of trace-element-related matrix effect; SHRIMP, ID-TIMS, ELA-ICP-MS and oxygen isotope documentation for a series of zircon standards: Chemical Geology, v. 205, p. 115-140.

Bonnichsen, B., 1982a, The Bruneau-Jarbidge eruptive center, southwestern Idaho: Idaho Bureau of Mines and Geology Bulletin 26, p. 237-254.

Bonnichsen, B., 1982b, Rhyolite Lava Flows in the Bruneau-Jarbidge Eruptive Center, Southwestern Idaho: Idaho Bureau of Mines and Geology Bulletin 26, p. 283-320.

Bonnichsen, B., Leeman, W., Honjo, N., McIntosh, W., Godchaux, M., 2008, Miocene silicic volcanism in southwestern Idaho: geochronology, geochemistry, and evolution of the central Snake River Plain: Bulletin of Volcanology, v. 70, p. 315-342.

Blundy, J., Cashman, K., 2008, Petrologic reconstruction of magmatic system variables and processes: Reviews in Mineralogy and Geochemistry, v. 69, p. 179-239.

Boroughs, S., Wolff, J., Bonnichsen, B., Godchaux, M., Larson, P., 2005, Large-volume, low-$\delta^{18}O$ rhyolites of the central Snake River Plain, Idaho, USA: Geology, v. 33, p. 821-824.

Boroughs, S., 2010, Low $\delta^{18}O$ rhyolites of southwestern Idaho and vicinity: PhD Thesis, Pullman, WA, Washington State University.

Bowring, S., Schmitz, M., 2003, High-precision U-Pb zircon geochronology and the stratigraphic record: Reviews in Mineralogy and Geochemistry, v. 53, p. 305-326.

Camp, V., Ross, M., 2004, Mantle dynamics and genesis of mafic magmatism in the intermontane Pacific Northwest: Journal of Geophysical Research, v. 109, p. 1-14.

Cathey, H., Nash, B., 2004, The Cougar Point Tuff: Implications for thermochemical zonation and longevity of high-temperature, large-volume silicic magmas of the Miocene Yellowstone hotspot: Journal of Petrology, v. 45, p. 27-58.

Cathey, H., Nash, B, Valley, J., Kita, N., Ushikubo, T., Spicuzza, M., 2007, Pervasive and persistent large-volume, low $\delta^{18}O$ silicic magma generation at the Yellowstone hotspot, 12.7-10.5 Ma: ion microprobe analyses of zircon in the Cougar Point Tuff, Eos Trans. AGU, 88(52), Fall Meet. Suppl., Abstract V51C-0708.

Cathey, H., Nash, B., 2009, Pyroxene thermometry of rhyolite lavas of the Bruneau-Jaridge eruptive center, central Snake River Plain: Journal of Volcanology and Geothermal Research, v. 188, p. 173-185.

Cathey, H., Nash, B., Valley, J., Kita, N., Allen, C., Campbell, I., 2011a, A new model for large-volume low $\delta^{18}O$ silicic magmas? Insights from zircons of the Cougar Point Tuff: Geological Society of America Annual Meeting, Abstracts with Programs, Vol. 44.

Cathey, H., Nash, B., Seligman, A., Valley, J., Kito, N., Allen, C., Campbell, I., Vazquez, J., Wooden, J., 2011b, Low $\delta^{18}O$ from the Bruneau-Jarbidge eruptive center: a key to crustal anatexis along the track of the Yellowstone hotspot: Abstract presented at 2011 Fall Meeting, AGU, in press.

Cervantes, P., Wallace, P., 2003, Role of H_2O in subduction-zone magmatism: New insights from melt inclusions in high-Mg basalts from central Mexico: Geology, v. 31, p. 235-238.

Cherniak, D., Watson, E., 2007, Ti diffusion in zircon: Chemical Geology, v. 242, p. 470-483.

Costa, F., Dohmen, R., Chakraborty, S., 2008, Time scales of magmatic processes from modeling the zoning patterns of crystals: Reviews in Mineralogy and Geochemistry, v. 69, p. 545-594.

Criss, R., Taylor, H., 1986, Meteoric-Hydrothermal Systems: Reviews in Mineralogy and Geochemistry, v. 16, p. 373-424.

Eiler, J., 2001, Oxygen isotope variations of basaltic lavas and upper mantle rocks: Reviews in Mineralogy and Geochemistry, v. 43, p. 319-364.

Ellis, B., Barry, T., Branney, M., Wolff, J., Bindeman, I., Wilson, R., Bonnichsen, B., 2010, Petrologic constraints on the development of a large-volume, high temperature, silicic magma system: The Twin Falls eruptive centre, central Snake River Plain: Lithos, v. 120, p. 475-489.

Faure, G., 1986, Principles of Isotope Geology: New York, New York, John Wiley & Sons, Inc., p. 1-63, 282-340, 429-490.

Ferriss E., Essene E., Becker U., 2008, Computational study of the effect of pressure on the Ti-in-zircon geothermometer: European Journal of Mineralogy, v. 20, p. 745-755.

Ferry, J., Watson, E., 2007, New thermodynamic models and revised calibrations for the Ti-in-Zircon and Zr-in-Rutile thermometers: Contributions to Mineralogy and Petrology, v. 154, p. 429-437.

Friedman, I., Lipman, P., Obradovich, J., Gleason, J., Christiansen, R., 1974, Meteoric water in magmas: Science, v. 184, p. 1069-1072.

Fu, B., Page, F., Cavosie, A., Fournelle, J., Kita, N., Lackey, J., Wilde, S., Valley, J., 2008, Ti-in-zircon thermometry: applications and limitations: Contributions to Mineralogy and Petrology, v. 156(2), p. 197-215.

Gansecki, C., 1998, $^{40}Ar/^{39}Ar$ geochronology and pre-eruptive geochemistry of the Yellowstone Plateau volcanic field rhyolites, PhD thesis, Stanford University, Stanford, CA p. 213.

Garcia, M., Ito, E., Eiler, J., Pietruszka, A., 1998, Crustal contamination of Kilauea Volcano magmas revealed by oxygen isotope analyses of glass and olivine from Puu Oo eruption lavas: Journal of Petrology, v. 39, p. 803-817.

Garcia, M., Ito, E., Eiler, J., 2008, Oxygen isotope evidence for chemical interaction of Kilauea historical magmas with basement rocks: Journal of Petrology, v. 49, p. 757-769.

Girard, G. and Stix, J., 2009, Magma recharge and crystal mush rejuvenation associated with early post-collapse Upper Basin Member rhyolites, Yellowstone Caldera, Wyoming: Journal of Petrology, v. 50, p. 2095-2125.

Girard, G. and Stix, J., 2010, Rapid extraction of discete magma batches from a large differentiating magma chamber: the Central Plateau Member rhyolites, Yellowston Caldera, Wyoming: Contributions to Mineralogy and Petrology, v. 160, p. 441-465.

Graham, D., Reid, M., Jordan, B., Grunder, A., Leeman, W., Lupton, J., 2009, Mantle source provinces beneath the northwestern USA delimited by helium isotopes in young basalts, Journal of Volcanology and Geothermal Research, v. 188, p. 128-140.

Hammer, J., 2008, Experimental studies of the kinetics and energetics of magma crystallization: Reviews in Mineralogy and Geochemistry, v. 69, p. 9-59.

Hart, W., Aronson, J., 1982, K-Ar ages of rhyolites from the western Snake River Plain area, Oregon, Idaho, and Nevada: Isochron West, v. 36, p. 17-19.

Henshaw, N.D., 2002, Temperature of silicic magmas from the Yellowstone hotspot: unpublished M.S. Thesis, Salt Lake City, UT, University of Utah, 181 p.

Hildreth, W., Christiansen, R., O'Neil, J., 1984, Catastrophic isotopic modification of rhyolitic magma at times of caldera subsidence, Yellowstone Plateau Volcanic Field: Journal of Geophysical Research, v. 89, p. 8339-8369.

Hildreth, W., Halliday, A., Christiansen, R., 2001, Isotopic and chemical evidence concerning the genesis and contamination of basaltic and rhyolitic magma beneath the Yellowstone Plateau volcanic field: Journal of Petrology, v. 32, p. 63-138.

Hildreth, W., Wilson, C., 2007, Compositional zoning of the Bishop Tuff: Journal of Petrology, v. 48, p. 951-999.

Hofmann, A., Valley, J., Watson, E., Cavosie, A., Eiler, J., 2009, Sub-micron scale distributions of trace elements in zircon: Contributions to Mineralogy and Petrology, v. 158(3), p. 317-335.

Huebner, J., Nord, L., 1981, Assessment of diffusion in pyroxenes: what we do and do not know: Lunar and Planetary Science XII, p. 479-481: Abstract 1981Pl….12..479H.

Ireland, T., Williams, I., 2003, Considerations in zircon geochronology by SIMS: Reviews in Mineralogy and Geochemistry, v. 53, p. 215-241.

Kent, A., 2008, Melt inclusions in basaltic and related volcanic rocks: Reviews in Mineralogy and Geochemistry, v. 69, p. 273-331.

Leeman, W., Annen, C., Dufek, J., 2008, Snake River Plain-Yellowstone silicic volcanism: Implications for magma genesis and magma fluxes: The Geological Society of London Special Publication 304, p. 235-259.

Ludwig, K., 2003, User's manual for isoplot 3.00; A geochronological toolkit for Microsoft Excel: Berkeley Geochronology Center Special Publication No. 4.

Metrich, N., Wallace, P., 2008, Volatile abundances in basaltic magmas and their degassing paths tracked by melt inclusions: Reviews in Mineralogy and Geochemistry, v. 69, p. 363-402.

Muehlenbachs, K., Anderson, A., Sigvaldsson, G., 1974, Low-$\delta^{18}O$ basalts from Iceland: Geochimica et Cosmochimica Acta, v. 38, p. 577-588.

Muehlenbachs, K., Byerly, G., 1982, ^{18}O-Enrichment of silicic magmas by crystal fractionation at the Galapagos spreading center: Contributions to Mineralogy and Petrology, v. 79, p. 76-79.

Nash, B., Perkins, M., Christensen, J., Lee, D., Halliday, A., 2006, The Yellowstone hotspot in space and time: Nd and Hf isotopes in silicic magmas: Earth and Planetary Science Letters, v. 247, p. 143-156.

Nash, W., 1992, Analysis of oxygen with the electron microprobe: Applications to hydrated glass and minerals: American Mineralogist, v. 77, p. 453-457.

Obrebski, M., Allen, R., Xue, M., Hung, S., 2010, Slab-plume interaction beneath the Pacific Northwest: Geophysical Research Letters, v. 37, p. 1-6.

Parrish, R., Noble, S., 2003, Zircon U-Th-Pb geochronology by Isotope Dilution – Thermal Ionization Mass Spectrometry (ID-TIMS): Reviews in Mineralogy and Geochemistry, v. 53, p. 183-213.

Peng, X., Humphreys, E., 1998, Crustal velocity structure across the eastern Snake River Plain and the Yellowstone Swell: Journal of Geophysical Research, v. 103, p. 7171-7186.

Perkins, M., Nash, B., 2002, Explosive silicic volcanism of the Yellowstone hotspot: The ash fall tuff record: Geological Society of America Bulletin, v. 114, p. 367-381.

Pierce, K., Morgan, L., 1992, The track of the Yellowstone hot spot: Volcanism, faulting, and uplift: Geological Society of America, Memoir 179, p. 1-52.

Pommier, A., Le Trong, E., 2011, "SIGMELTS": A web portal for electrical conductivity calculations in geosciences, Computers in Geosciences, in press.

Pommier, A., Gaillard, F., Pichavant, M., Scaillet, B., 2008, Laboratory measurements of electrical conductivities of hydrous and dry Mt. Vesuvius melts under pressure, Journal of Geophysical Research, v. 113.

Portnayagin, M., Hoernle, K., Avdeiko, G., Hauff, F., Werner, R., Bindeman, I., Uspensky, V., Garbe-Schonberg, D., 2005, Transition from arc to magmatism at the Kamchatka-Aleutian junction: Geology, v. 33, p. 25-28.

Putirka, K., 2008, Thermometers and barometers for volcanic systems: Reviews in Mineralogy and Geochemistry, v. 69, p. 61-120.

Reid, M., 2008, How long does it take to supersize an eruption?: Elements, v. 4, p. 23-28.

Reid, M., Vasquez, J., Schmitt, A., 2010, Zircon-scale insights into the history of a supervolcano, Bishop Tuff, Long Valley, California, with implications for the Ti-in-zircon geothermometer: Contributions to Mineralogy and Petrology, v. 161, p. 293-311.

Roberge, J., Delgado-Granados, H., Wallace, P., 2009, Mafic magma recharge supplies high CO_2 and SO_2 gas fluxes from Popcatepetl volcano, Mexico: Geology, v. 37, p. 107-110.

Rutherford, M., Magma ascent rates: Reviews in Mineralogy and Geochemistry, v. 69, p. 241-271.

Sambridge, M., Compston, W., 1994, Mixture modeling of multi-component data sets with application to ion-probe zircon ages: Earth and Planetary Science Letters, v. 128, p. 373-390.

Saunders, K., Baker, J., Wysoczanksi, R., 2010, Microanalysis of large volume silicic magma in continental and oceanic arcs: Melt inclusions in Taupo Volcanic Zone and Kermadec Arc rocks, South West Pacific: Journal of Volcanology and Geothermal Research, v. 190, p. 203-218.

Sensarma, S., Hoernes, S., Mukhopadhyay, D., 2004a, Low-$\delta^{18}O$, high-silica rhyolite in the palaeoproterozoic Dongargarh group, central India: 32nd International Geological Congress; Florence, Italy; Abracts: v. 32, QE1; .I60, 245-46.

Sensarma, S., Hoernes, S., Mukhopadhyay, D., 2004b, Relative contributions of crust and mantle to the origin of the Bijli rhyolite in a palaeoproterozoic bimodal volcanic sequence (Dongargarh group), central India: Proceedings of the Indian Academy of Science (Earth and Planetary Science, v. 113, p. 619-648.

Shervais, J., Vetter, S., Hanan, B., 2006, Layered mafic sill complex beneath the eastern Snake river Plain: Evidence from cyclic geochemical variations in basalt: Geology, v. 34, p. 365-368.

Smith, R., Braile, L., 1994, The Yellowstone hotspot: Journal of Volcanology and Geothermal Research, v. 61, p. 121-187.

Smith, R., Jordan, M., Steinberger, B., Puskas, C., Farrell, J., Waite, G., Husen, S., Change, W., O'Connell, R., 2009, Geodynamics of the Yellowstone hotspot and mantle plume: Seismic and GPS imaging, kinematics, and mantle flow: Journal of Volcanology and Geothermal Research, v. 188, p. 26-56.

Speer, J., 1982, Zircon, Reviews in Mineralogy and Geochemistry, v. 5, p. 67-112.

Streck, M. 2008, Mineral textures and zoning as evidence for open system processes: Reviews in Mineralogy and Geochemistry, v. 69, p. 595-622.

Taylor, H., Sheppard, S., 1986, Igneous Rocks: I. Processes of isotopic fractionation and isotope systematics: Reviews in Mineralogy, v. 16, p. 227-271.

Taylor, H., 1987, Comparison of hydrothermal systems in layered gabbros and granites, and the origin of low-$\delta^{18}O$ magmas, *in* Mysen, B.O., ed., Magmatic processes: Physicochemical principles: Geochemical Society Special Publication I, p. 337-357.

Thomas, J., Bodnar, R., Shimizu, N., Chesner, C., 2003, Melt inclusions in zircon: Reviews in Mineralogy and Geochemistry, v. 53, p. 63-87.

Thomas, J., Watson, E., Spear, F., Shemella, P., Nayak, S., Lanzirotti, A., 2010, TitaniQ under pressure: the effect of pressure and temperature on the solubility of Ti in quartz: Contributions to Mineralogy and Petrology, v. 160, p. 743-759.

Turner, S., Tonarini, S., Bindeman, I., Leeman, W., Schaefer, B., 2007, Boron and oxygen isotope evidence for recycling of subducted components over the past 2.5 Gyr: Nature, v. 447, p.702-705.

Valley, J., 2003, Oxygen isotopes in zircon: Reviews in Mineralogy and Geochemistry, v. 53, p. 343-385.

Valley, J., Lackey, J., Cavosie, A, Clechenko, C., Spicuzza, M., Basei, M., Bindeman, I., Ferreira, V., Sial, A., King, E., Peck, W., Sinha, A., Wei, C., 2005, 4.4 billion years of crustal maturation: oxygen isotope ratios of magmatic zircon: Contributions to Mineralogy and Petrology, v. 150, p. 561-580.

Vazquez, J., Reid, M., 2002, Time scales of magma storage and differentiation of voluminous high-silica rhyolites at Yellowstone caldera, Wyoming: Contributions to Mineralogy and Petrology, v. 144, p. 274-285.

Vazquez, J., Kyriazis, S., Reid, M., Sehler, R., Ramos, F., 2009, Thermochemical evolution of young rhyolites at Yellowstone: Evidence for a cooling but periodically replenished postcaldera magma reservoir: Journal of Volcanology and Geothermal Research, v. 188, p. 186-196.

Wallace, P., 1998, Water and partial melting in mantle plumes: Inferences from the dissolved H_2O concentrations of Hawaiian basaltic magmas: Geophysical Research Letters, v. 25, p. 3639-3642.

Watson E. B., Wark D. A., Thomas J. B., 2006, Crystallization thermometers for zircon and rutile: Contributions to Mineralogy and Petrology, v. 151, p. 413-433.

Watts, K., Leeman, W., Bindeman, I., Larson, P., 2010, Supereruptions of the Snake River Plain: Two-stage derivation of low-$\delta^{18}O$ rhyolites from normal-$\delta^{18}O$ crust as constrained by Archean xenoliths: Geology, v. 38, p. 503-506.

Watts, K., Bindeman, I., Schmitt, A., 2011, Large-volume rhyolite genesis in caldera complexes of the Snake River Plain: Insights from the Kilgore Tuff of the Heise Volcanic Field, Idaho, with comparison to Yellowstone and Bruneau-Jarbidge rhyolites: Journal of Petrology, v. 52, p. 1-34.

Zhdanov, M., Smith, R., Gribenko, A., Cuma, M., Green, M., 2011, Three-dimensional inversion of large-scale EarthScope magnetotelluric data based on the integral equation method: Geoelectrical imaging of the Yellowstone conductive mantle plume: Geophysical Research Letters, v. 38, p. 1-7.

Zheng, Y., Wu, Y., Chen, F., Gong, B., Bi, L., Zhao, Z., 2004, Zircon U-Pb and oxygen isotope evidence for a large-scale ^{18}O depletion event in igneous rocks during the Neoproterozoic: Geochimica et Cosmochimica Acta, v. 68, p. 4145-4165.

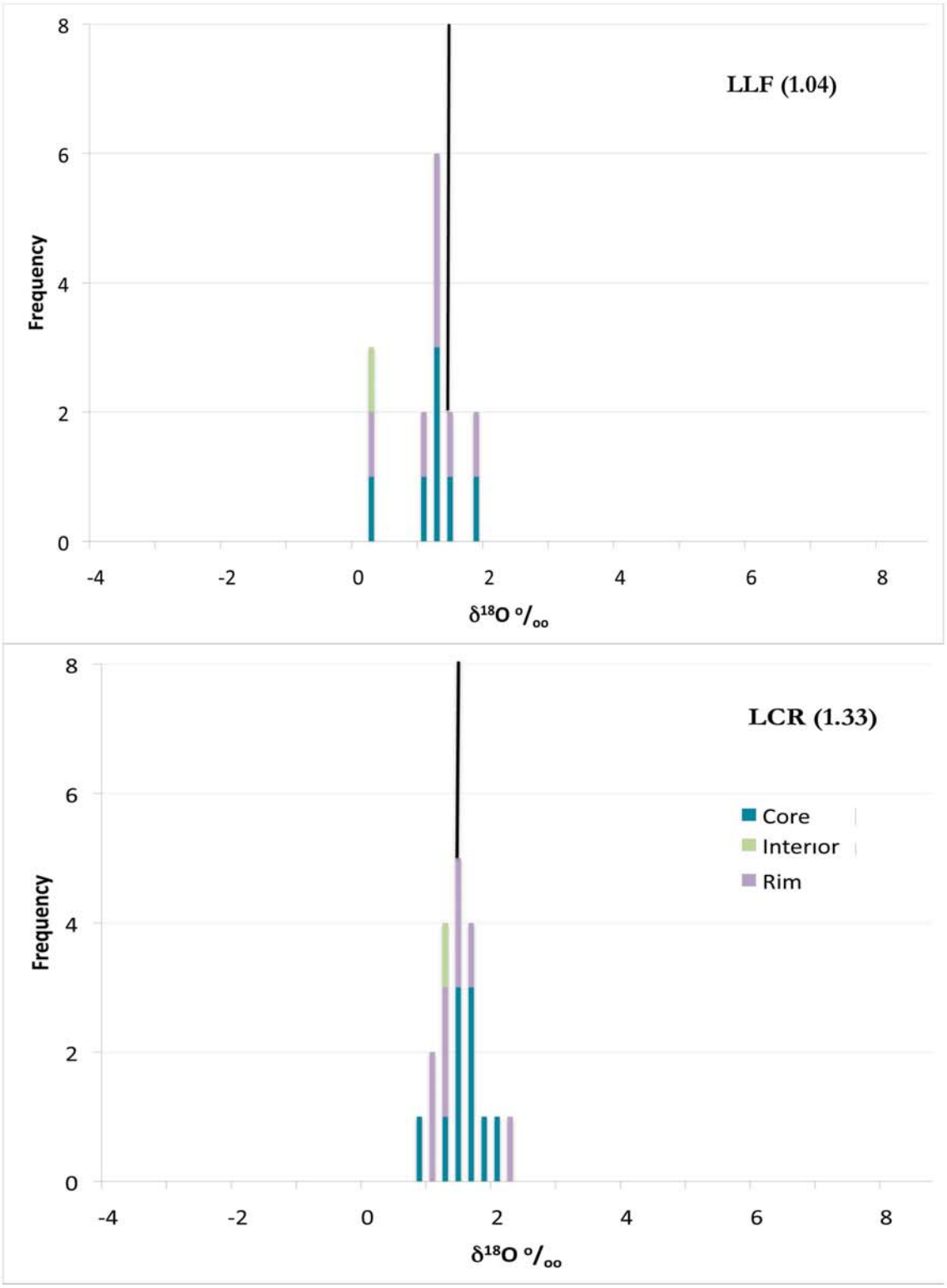

Figure B.1. $\delta^{18}O$ in cores, rims, and interiors of zircons in lavas from the BJEC that show average $\delta^{18}O$ values for the BJEC. For reference, the average for all zircons from the BJEC is 1.47 ‰ and is shown by the vertical black line. The number in parenthesis following the unit label is the unit's average $\delta^{18}O$ in per mil.

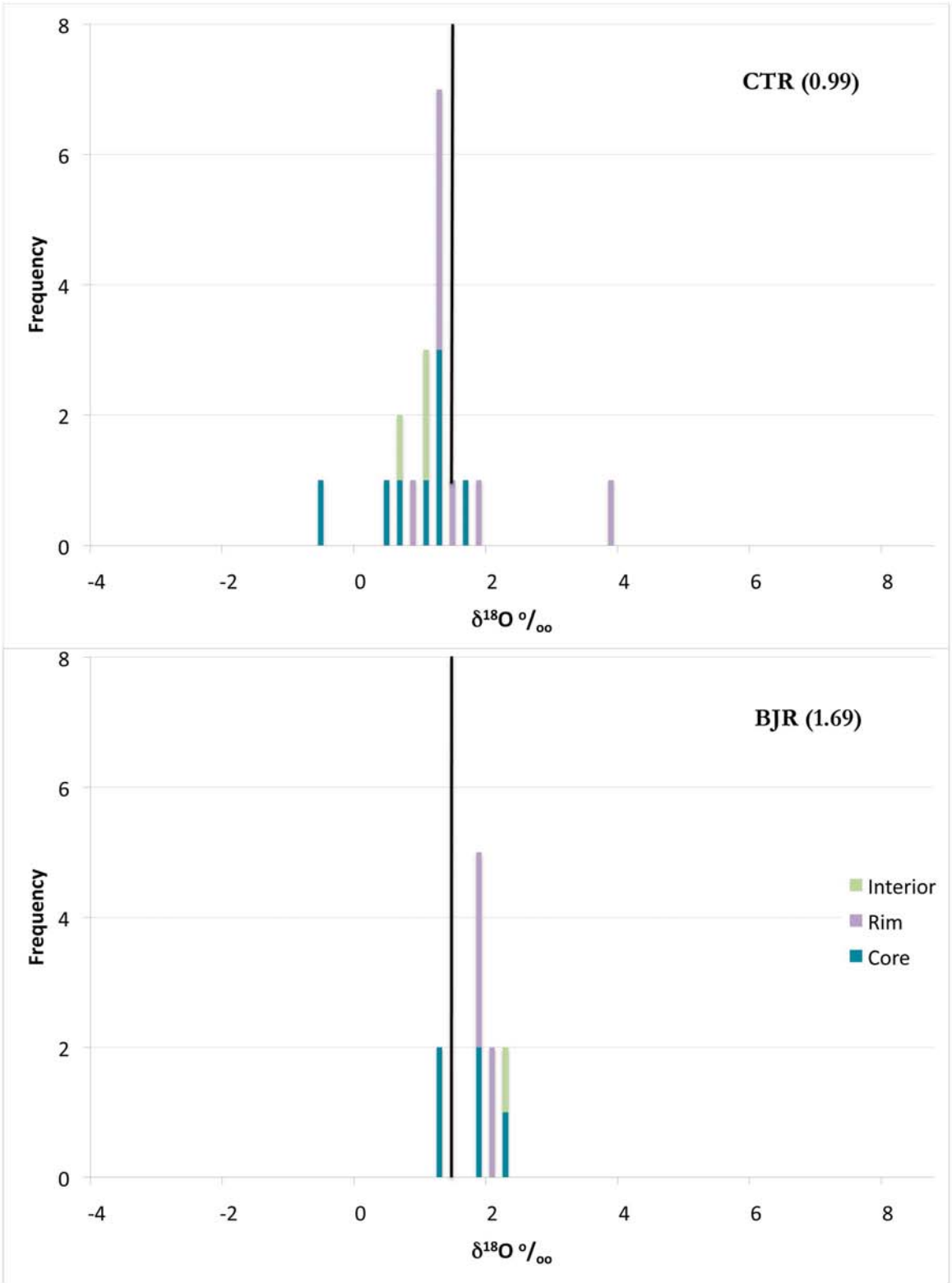

Figure B.1 continued

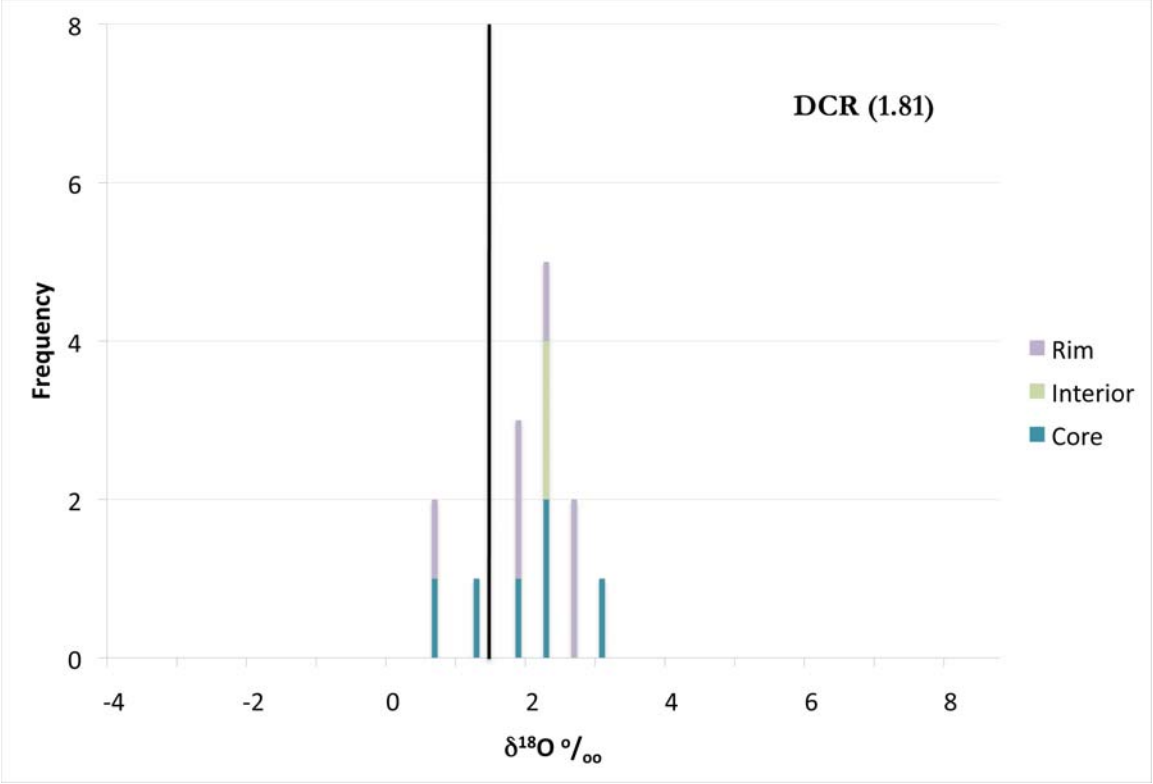

Figure B.1 continued

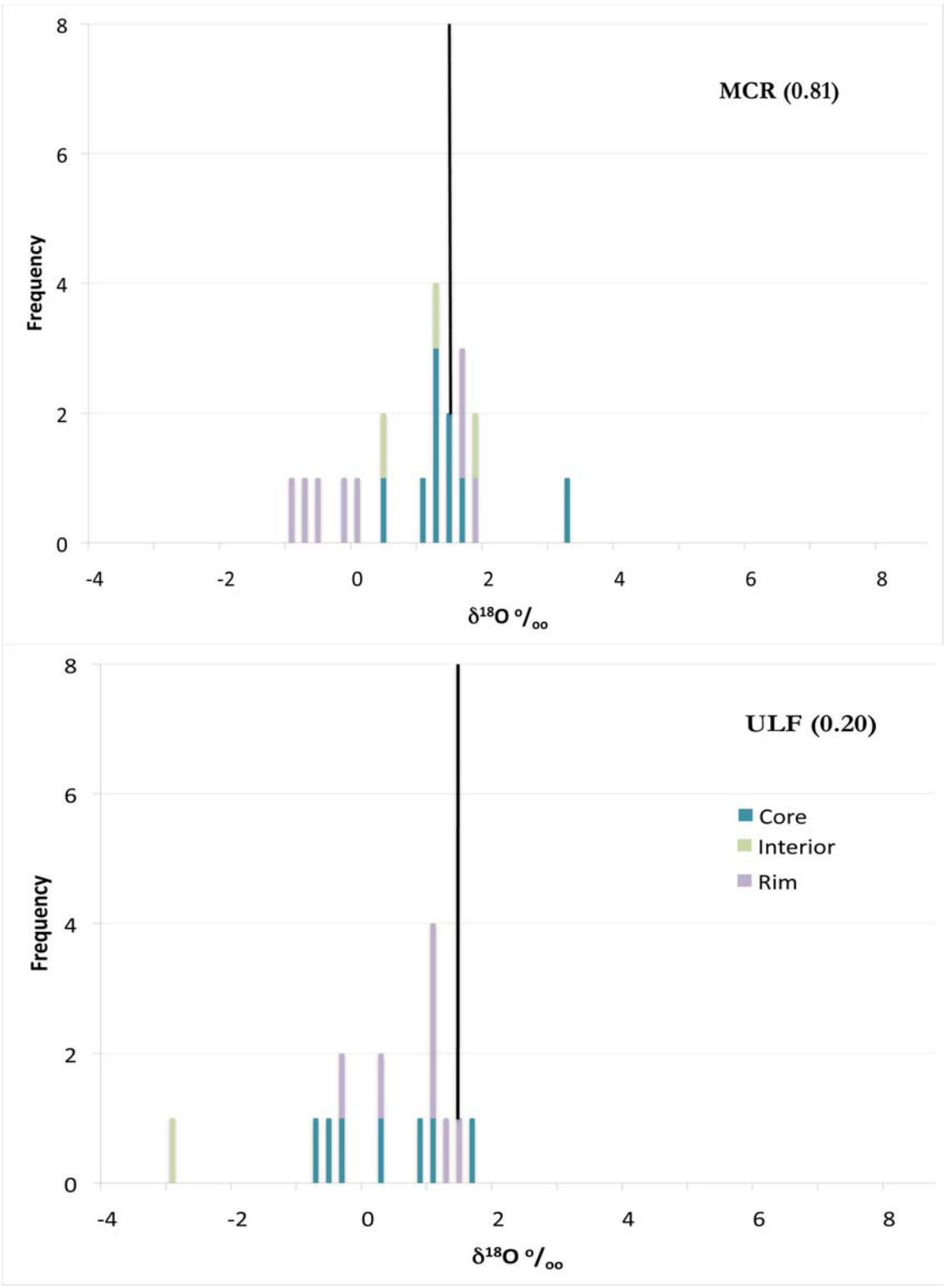

Figure B.2. $\delta^{18}O$ in cores, rims, and interiors of zircons in lavas from the BJEC showing slightly below average $\delta^{18}O$ values. For reference, the average for all zircons from the BJEC is 1.47 ‰ and is shown by the vertical black line. The number in parenthesis following the unit label is the unit's average $\delta^{18}O$ in per mil.

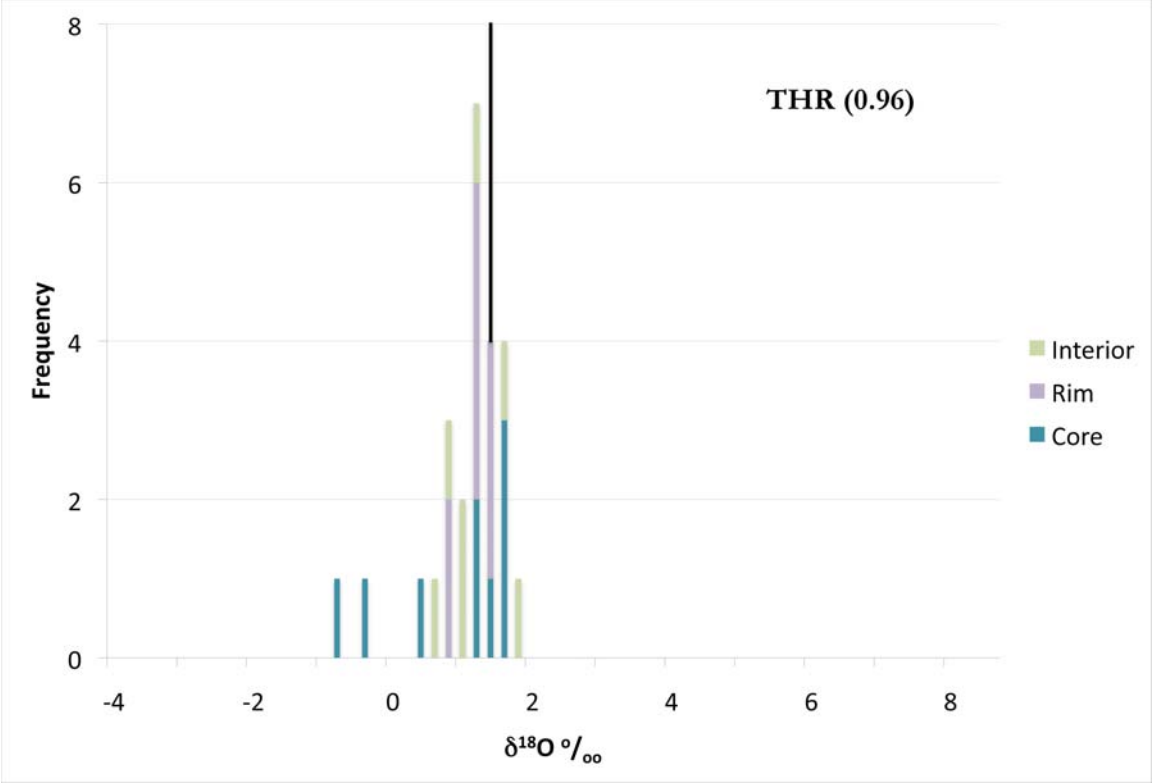

Figure B.2 continued

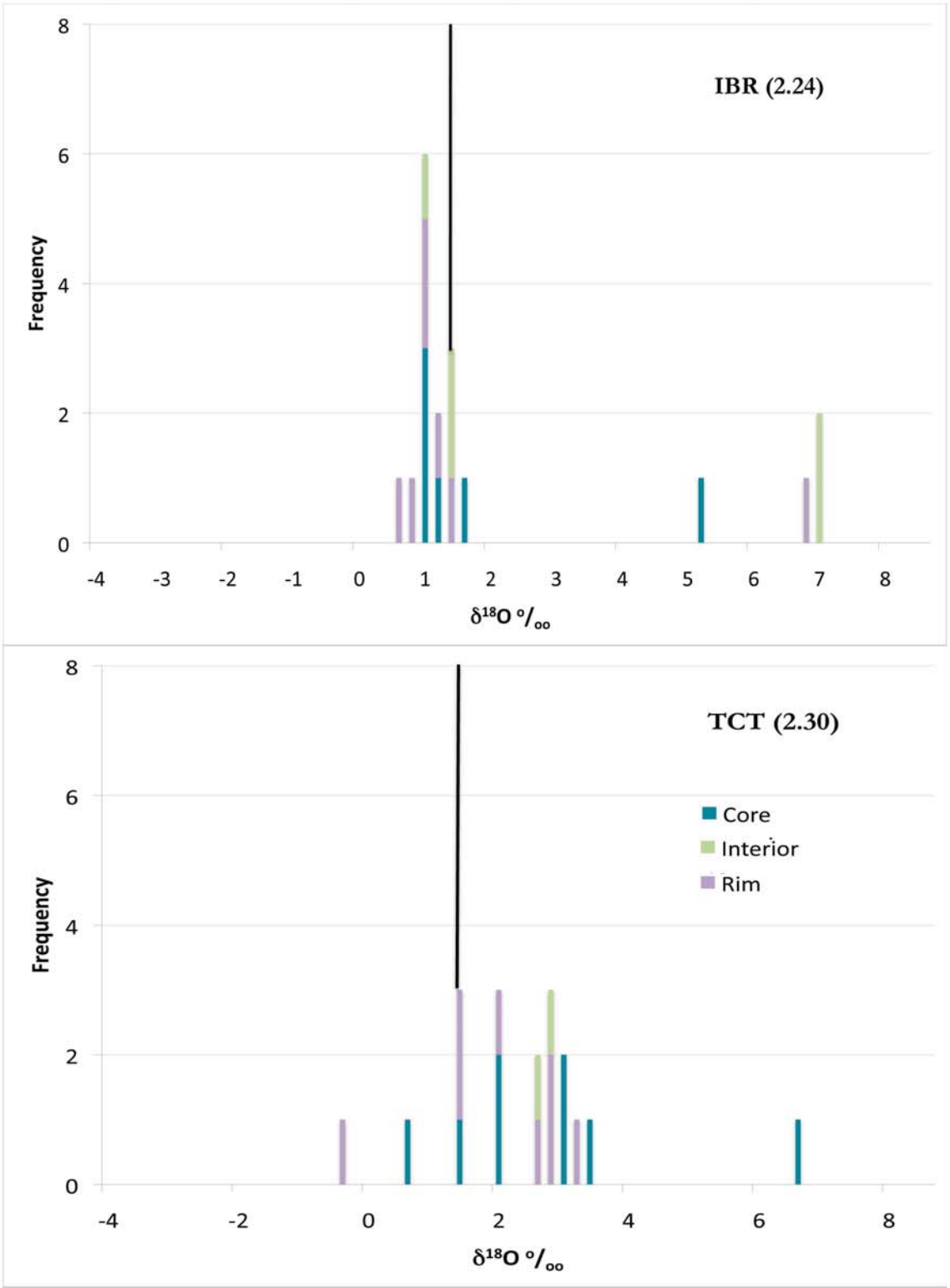

Figure B.3. $\delta^{18}O$ in cores, rims, and interiors of zircons in lavas from the BJEC showing heavier than average $\delta^{18}O$ values. . For reference, the average for all zircons from the BJEC is 1.47 ‰ and is shown by the vertical black line. The number in parenthesis following the unit label is the unit's average $\delta^{18}O$ in per mil.

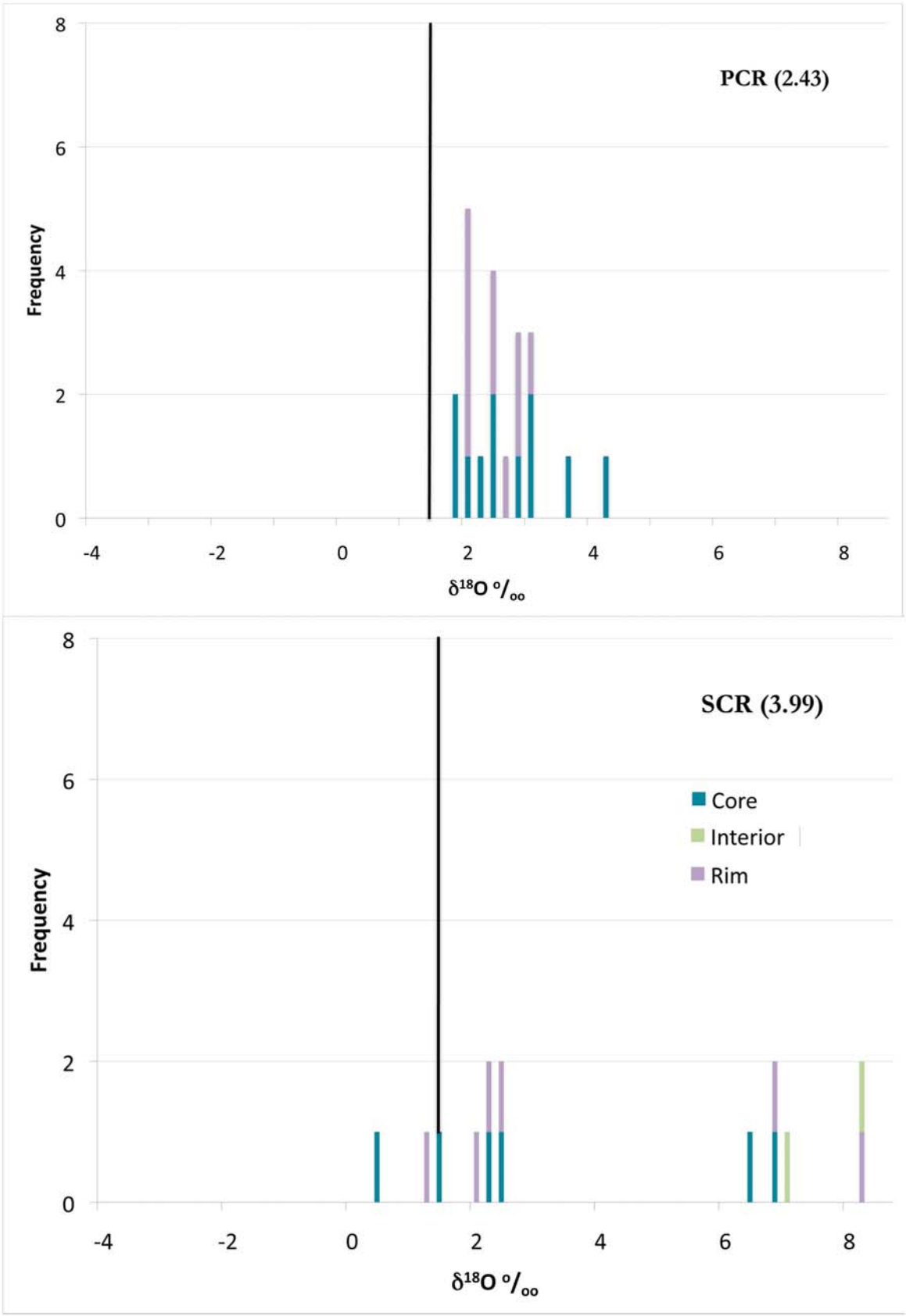

Figure B.3 continued

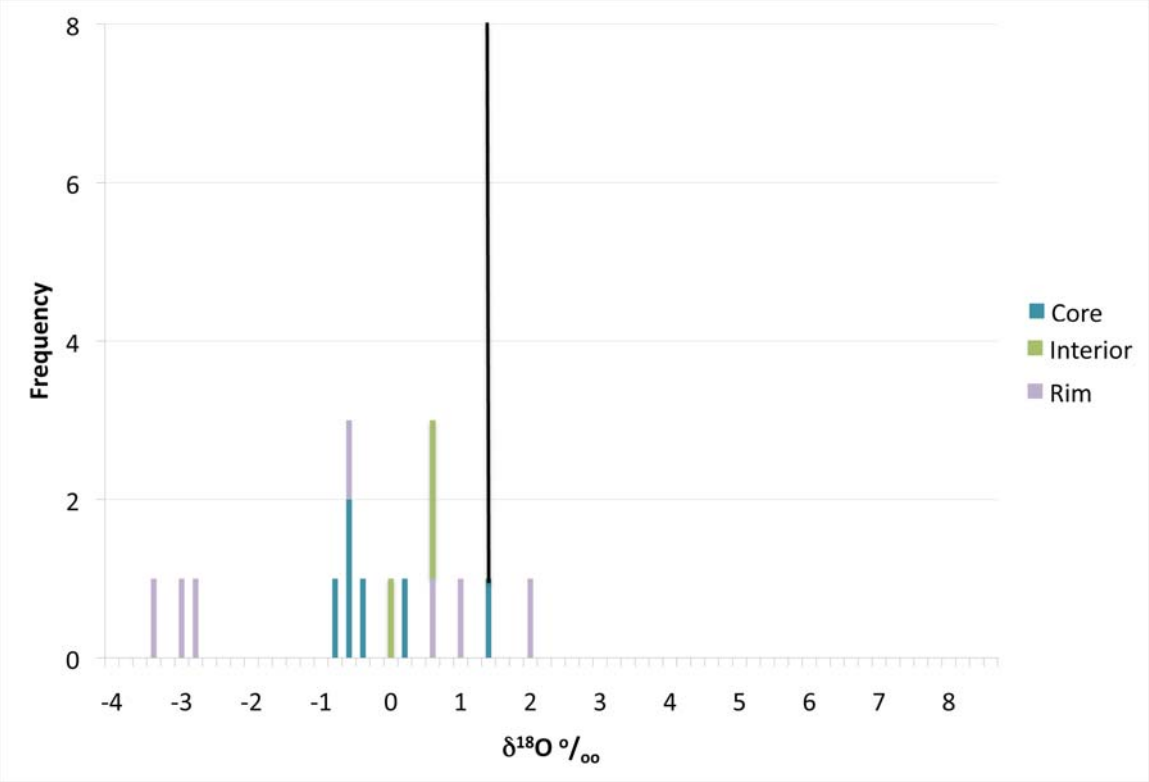

Figure B.4. $\delta^{18}O$ in cores, rims, and interiors of zircons from LF1 that shows lighter than average $\delta^{18}O$ values than other BJEC lavas. For reference, the average for all zircons from the BJEC is 1.47 ‰ and is shown by the vertical black line. The number in parenthesis following the unit label is the unit's average $\delta^{18}O$ in per mil.

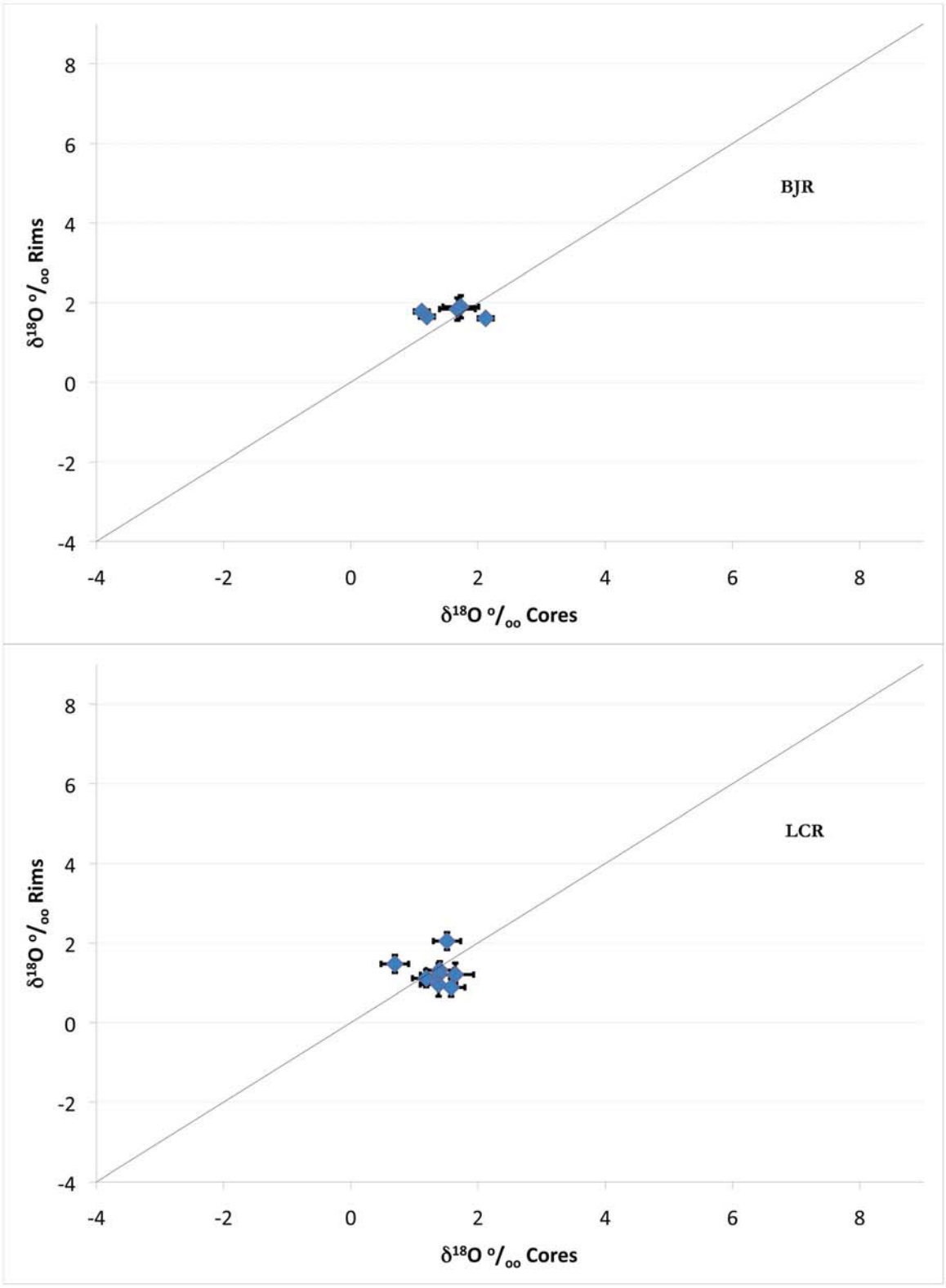

Figure B.5. δ18O in zircon rims vs. cores showing zoning in zircon with minimal zoning between cores and rims. Error bars are 2σ. Line represents 1:1 ratio.

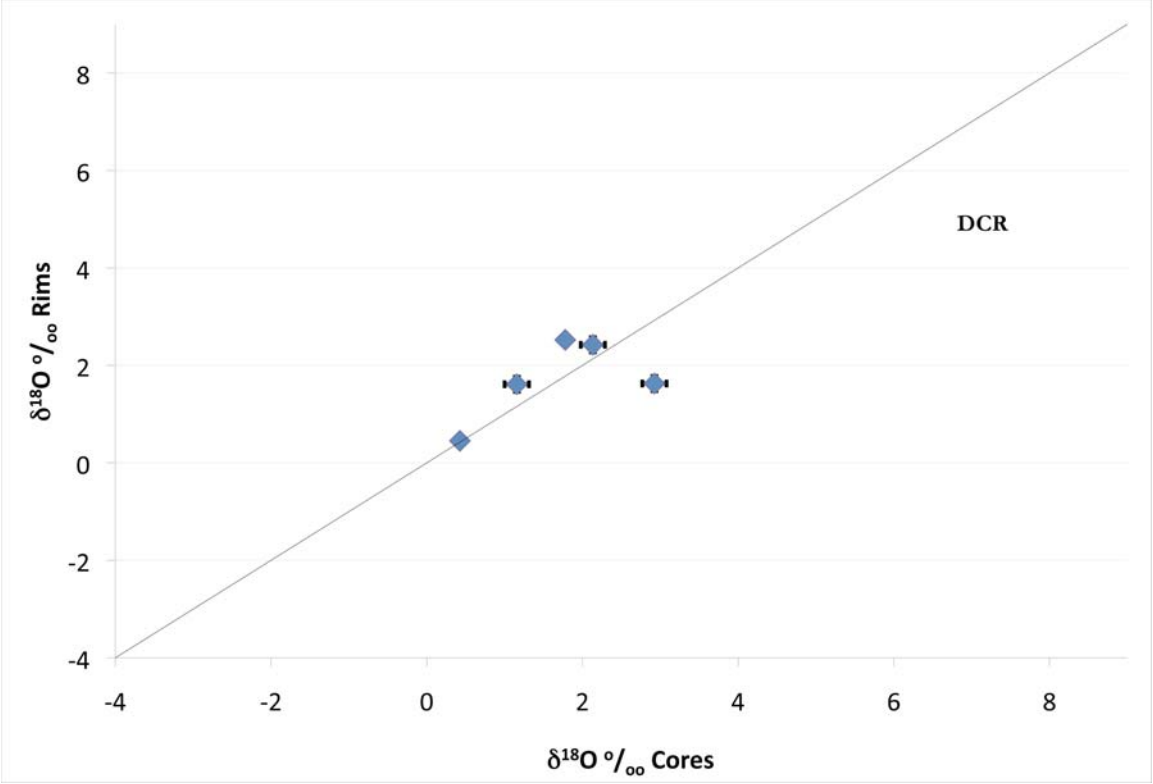

Figure B.5 continued

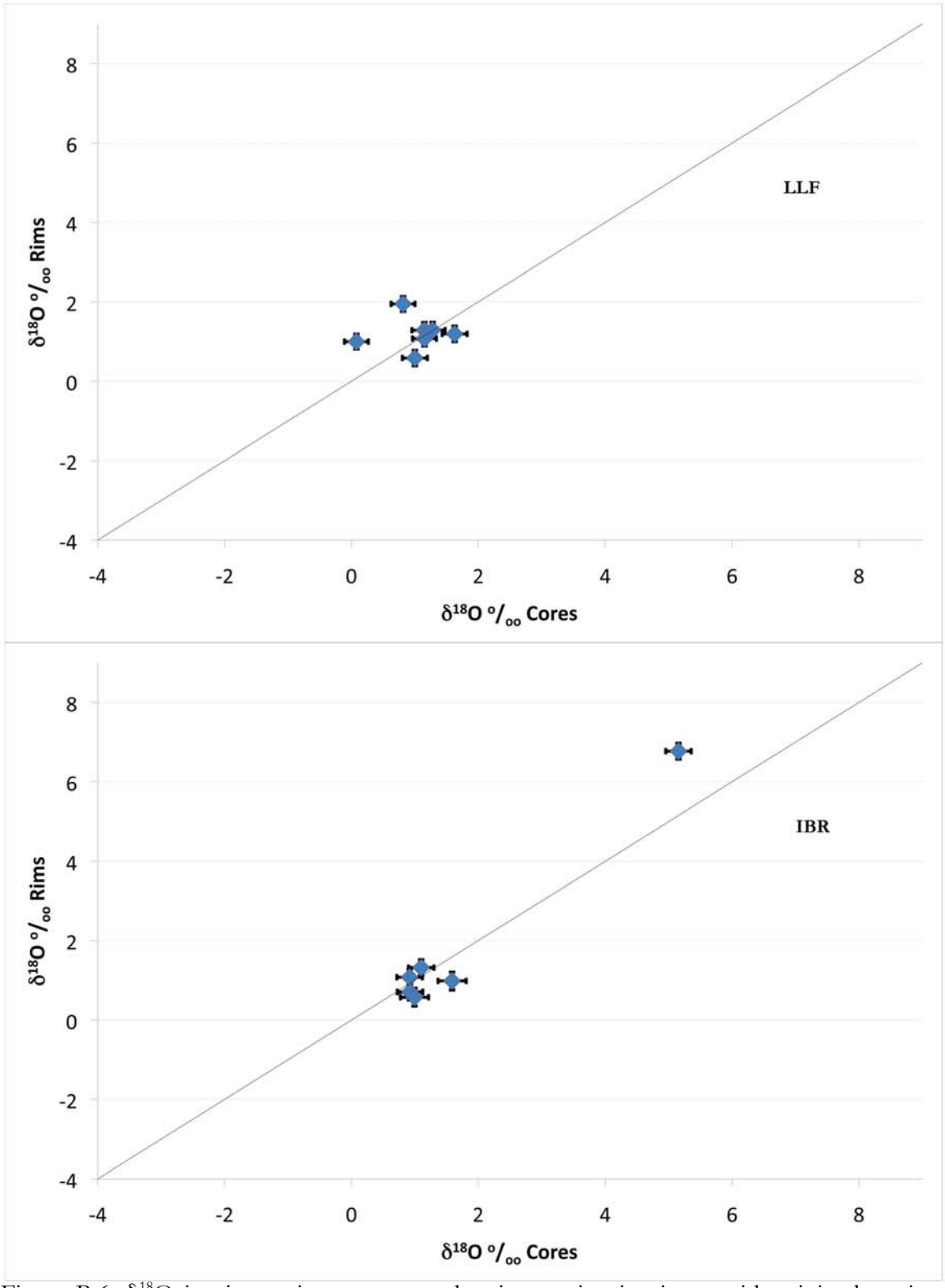

Figure B.6. $\delta^{18}O$ in zircon rims vs. cores showing zoning in zircon with minimal zoning between cores and rims except for a few outliers. Error bars are 2σ. Line represents 1:1 ratio.

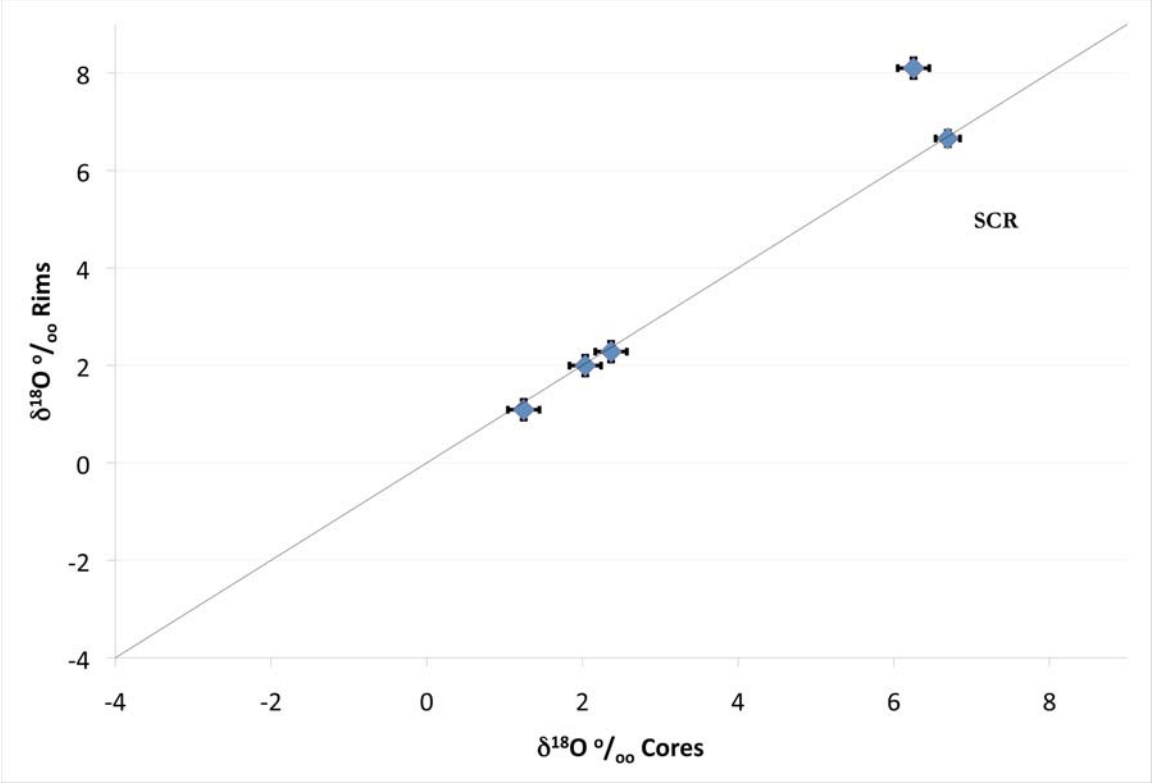

Figure B.6 continued

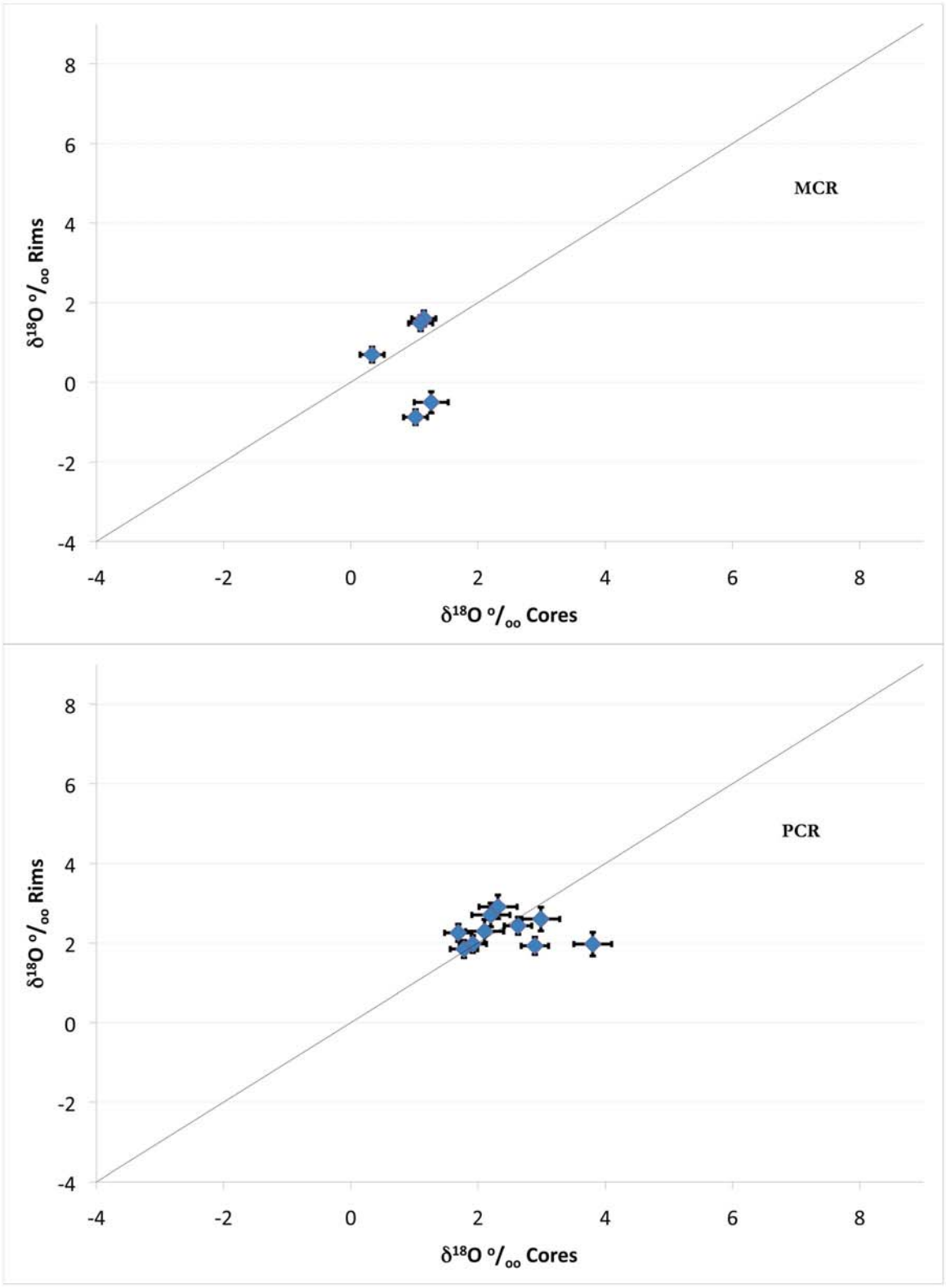

Figure B.7. $\delta^{18}O$ in zircon rims vs. cores showing zoning in zircon having slight zoning with heavier rims than cores, and a few grains with much heavier cores than rims. Error bars are 2σ. Line represents 1:1 ratio.

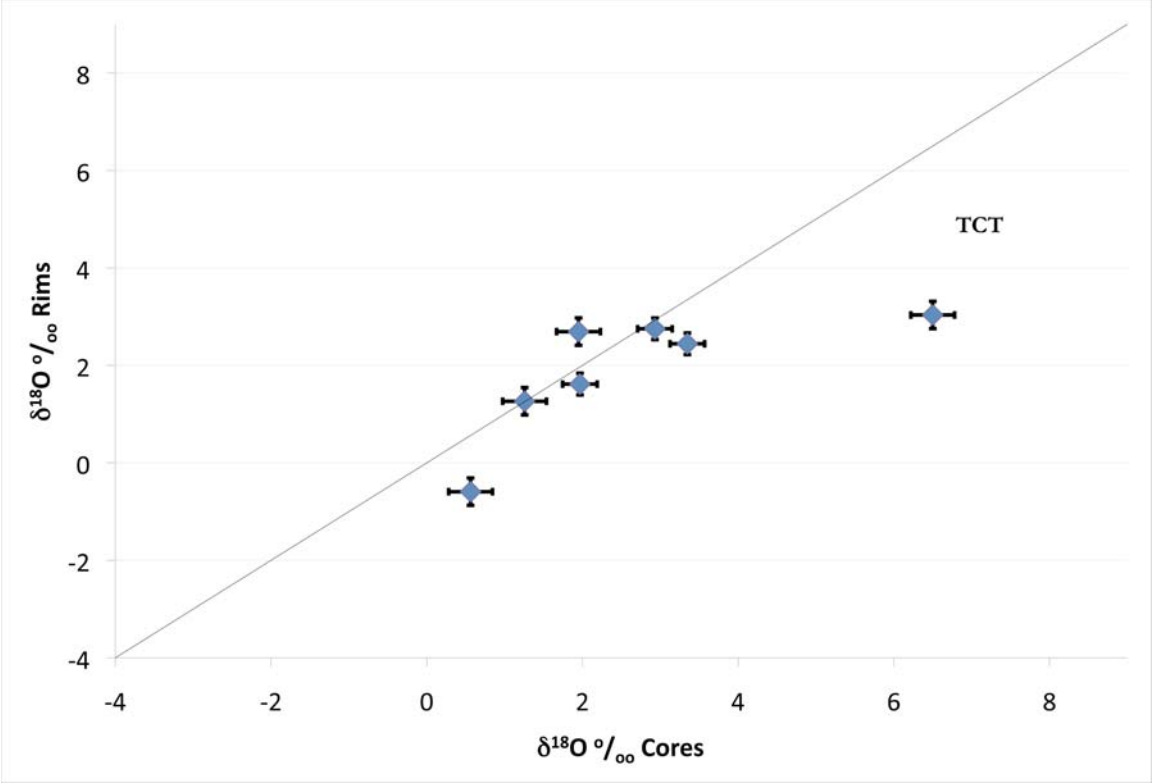

Figure B.7 continued

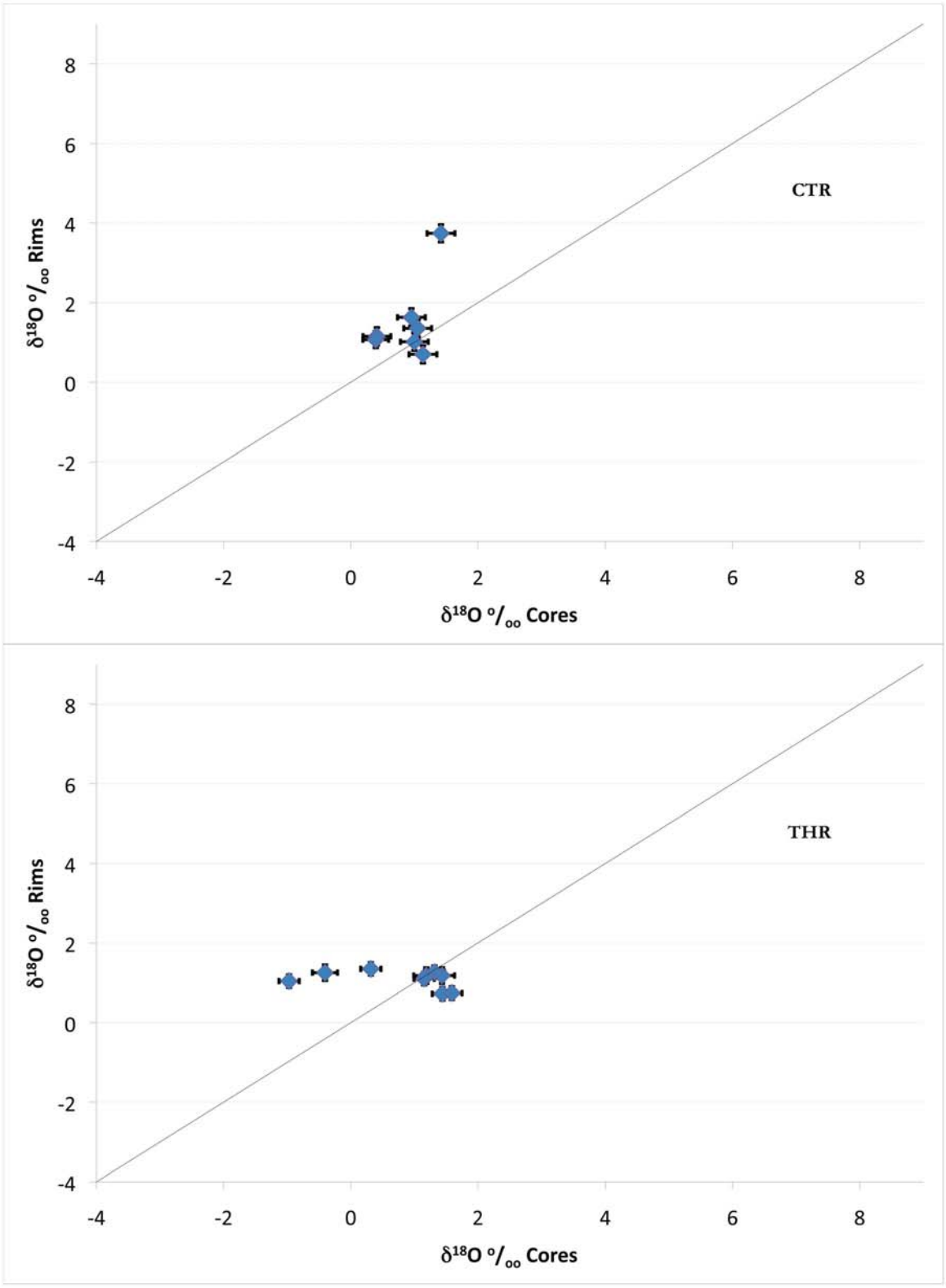

Figure B.8. $\delta^{18}O$ in zircon rims vs. cores showing zoning in zircons with predominantly heavier rims than cores. Error bars are 2σ. Line represents 1:1 ratio. Continued on next page.

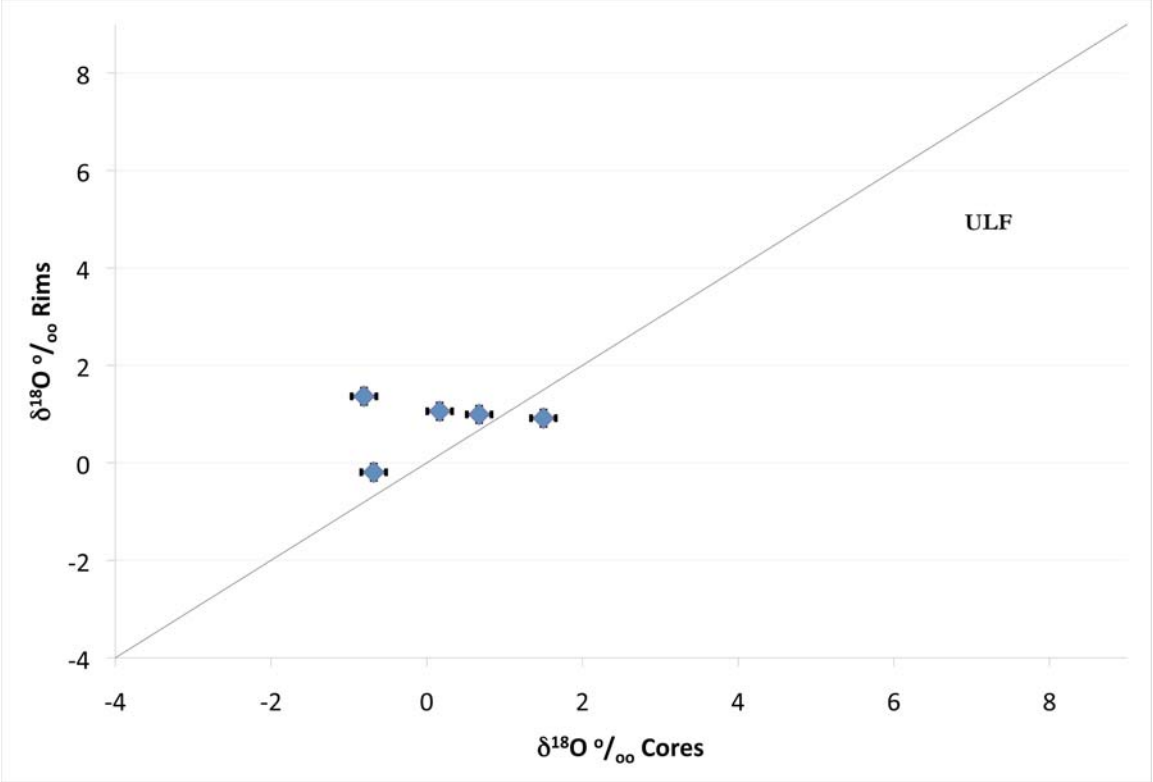

Figure B.8 continued

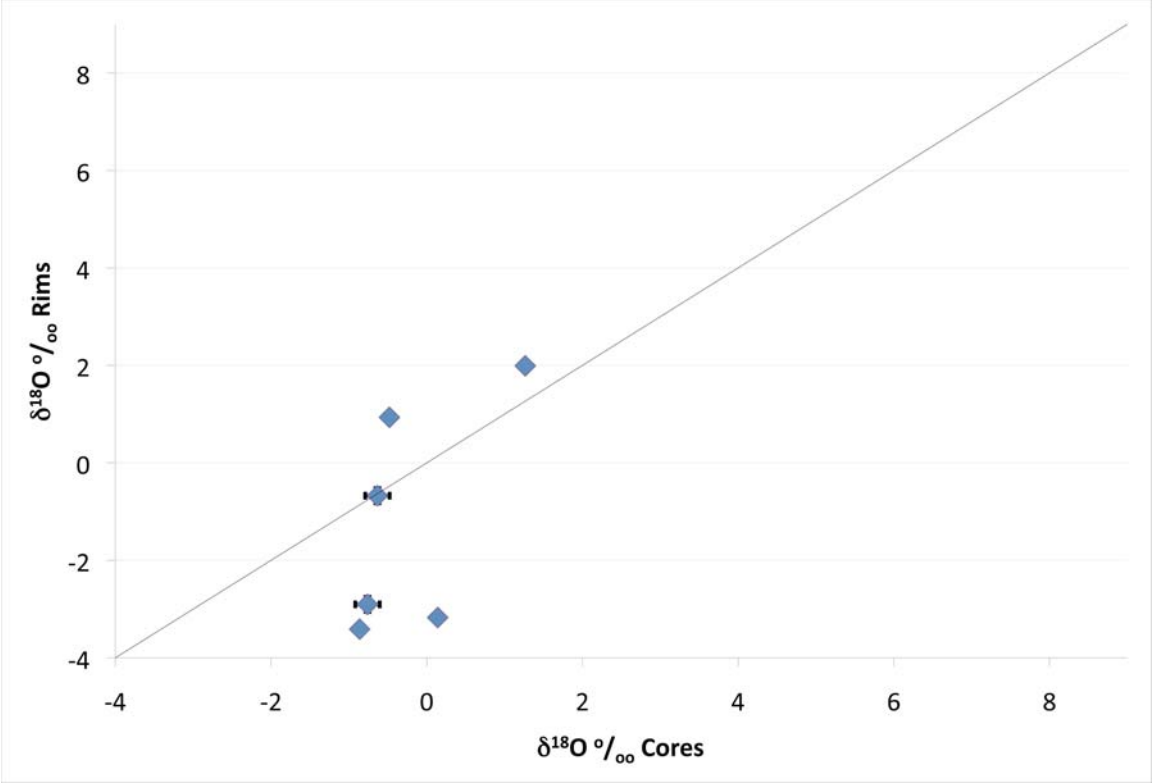

Figure B.9. $\delta^{18}O$ in zircon rims vs. cores showing large variations of lava unit LF1. Error bars are 2σ. Line represents 1:1 ratio.

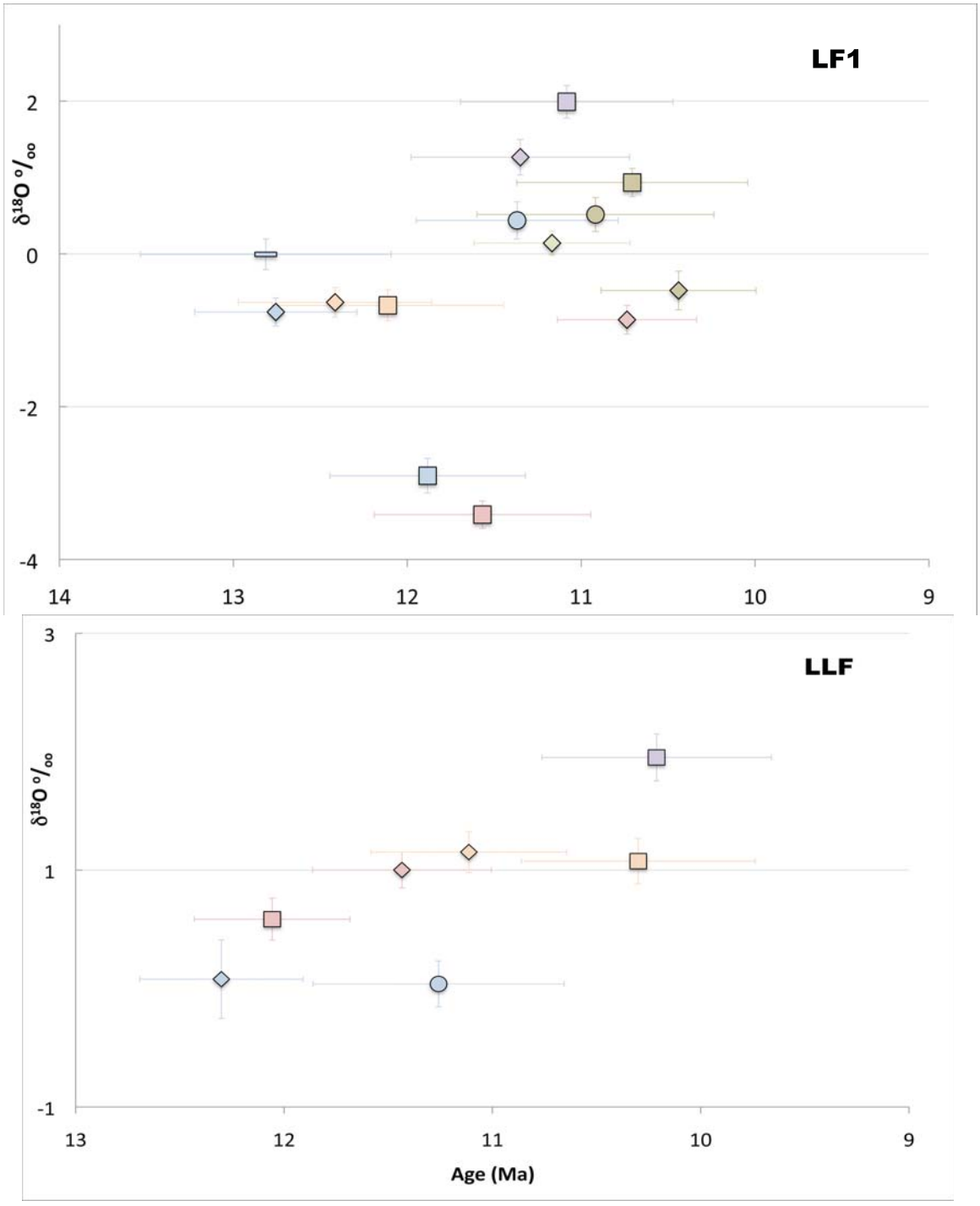

Figure C.1. $\delta^{18}O$ vs. U-Th-Pb age for each lava. Diamonds are cores, circles (A) and rectangles (B) are interior analyses, where interior A is closer to the core than interior B, and squares are rims. Data points with the same color are from the same zircon grain. Error bars are 2σ. Continued on next page.

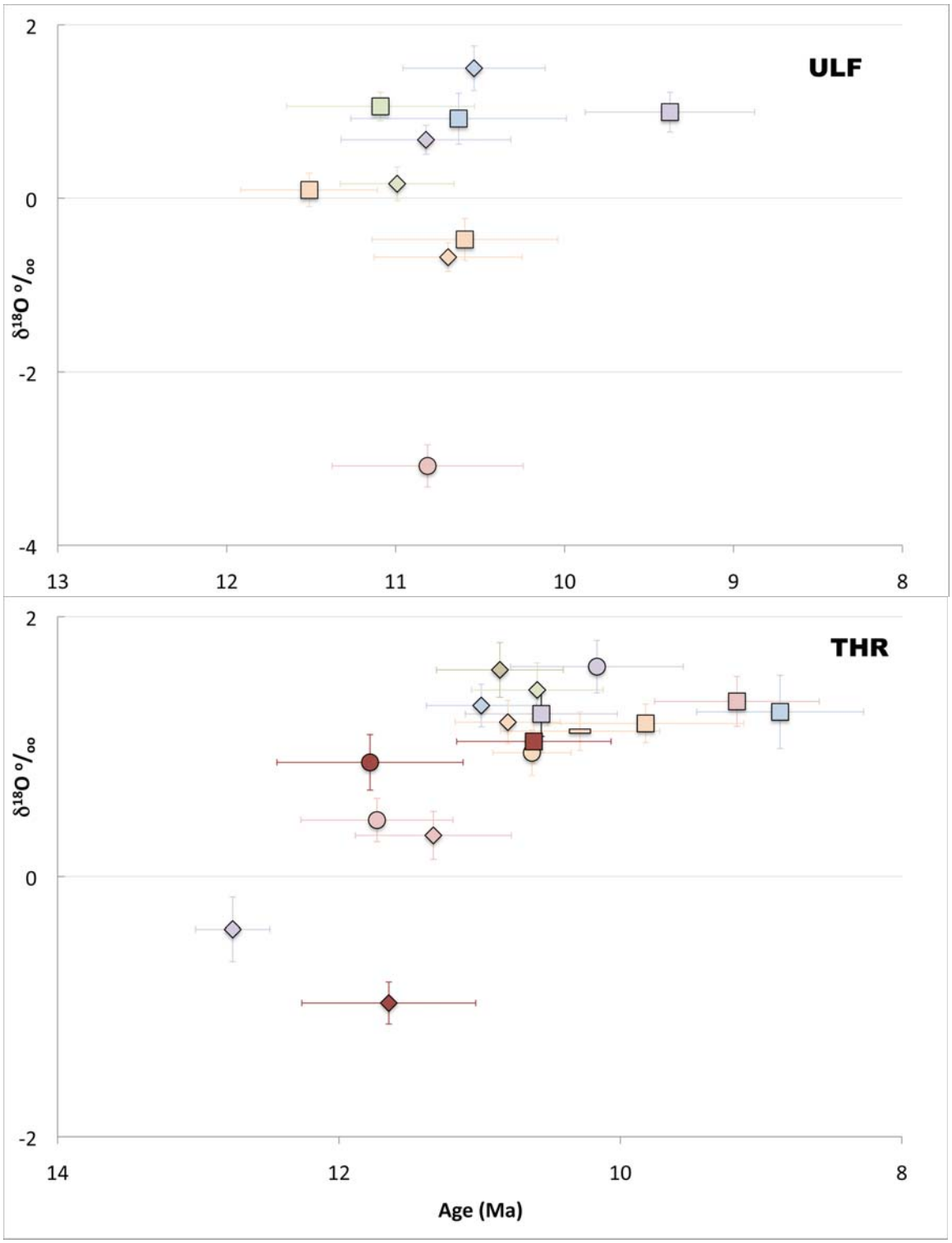

Figure C.1 continued

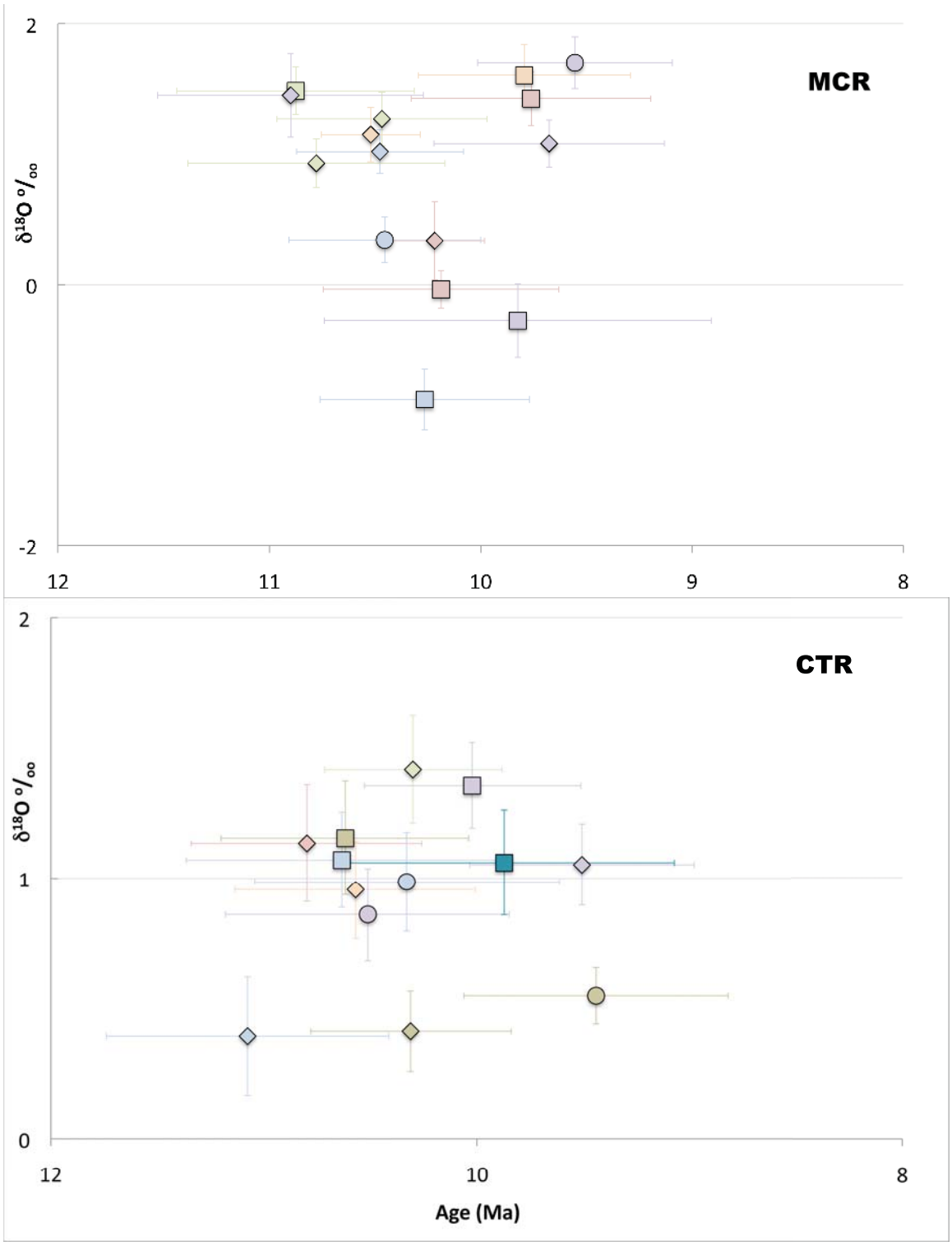

Figure C.1 continued

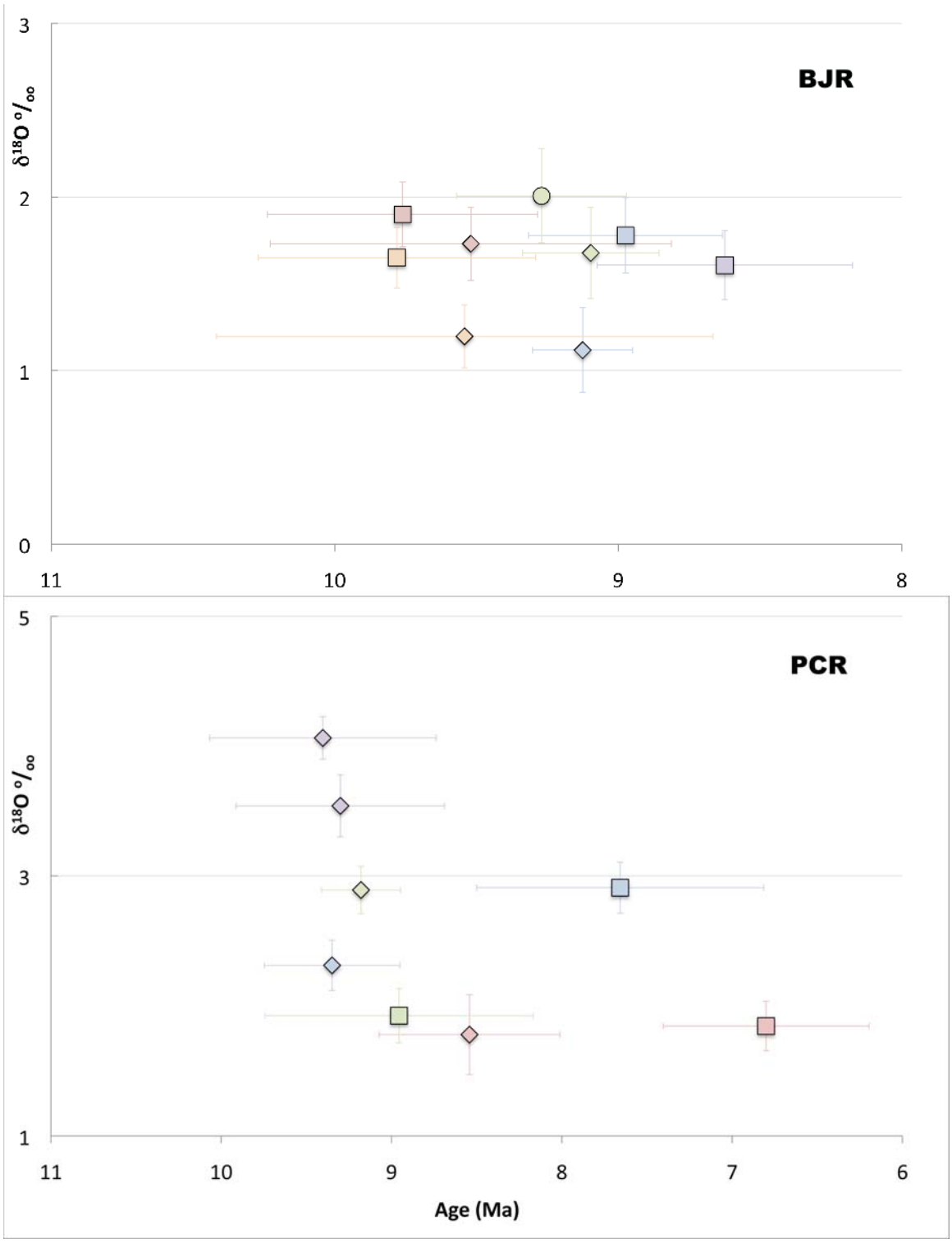

Figure C.1 continued

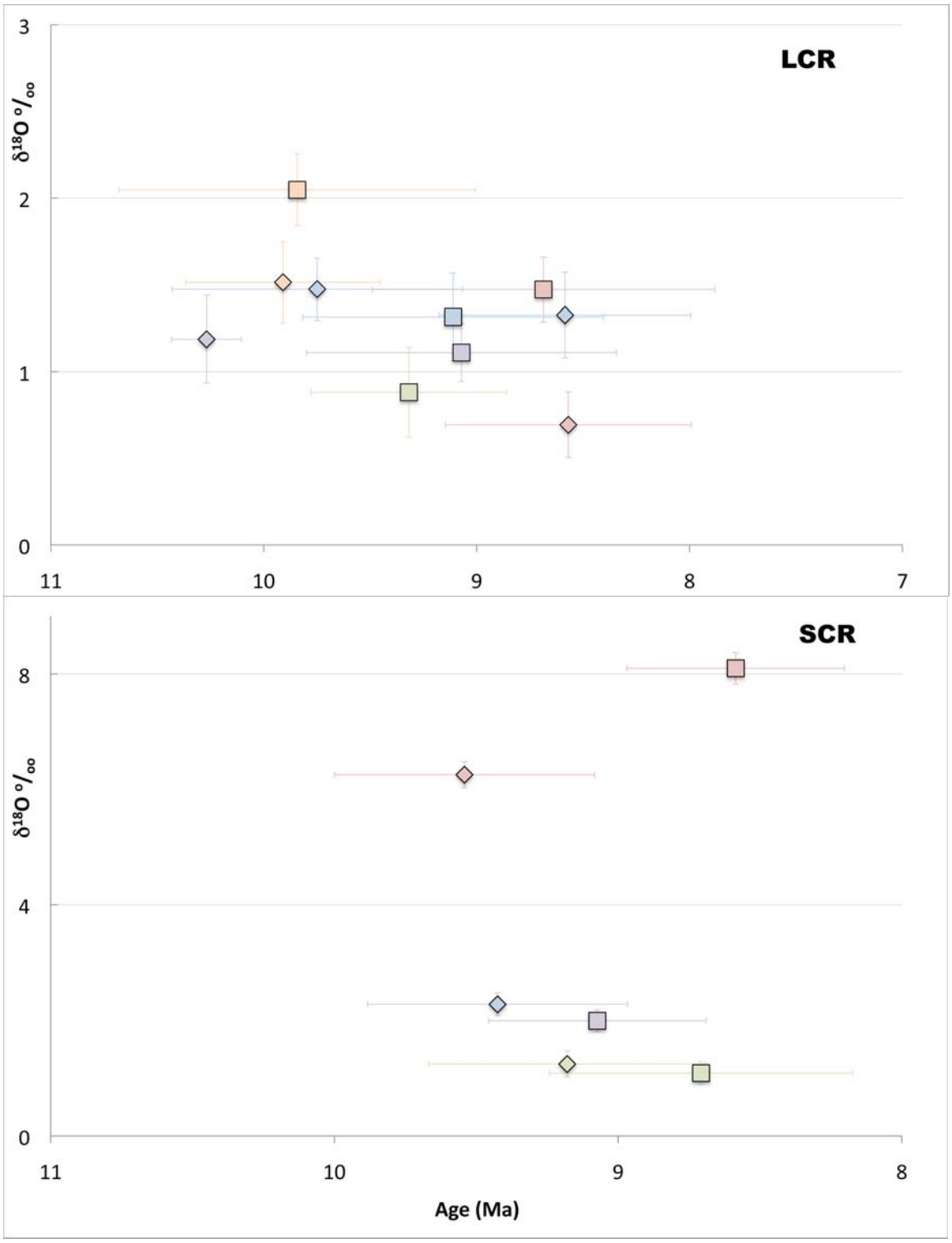

Figure C.1 continued

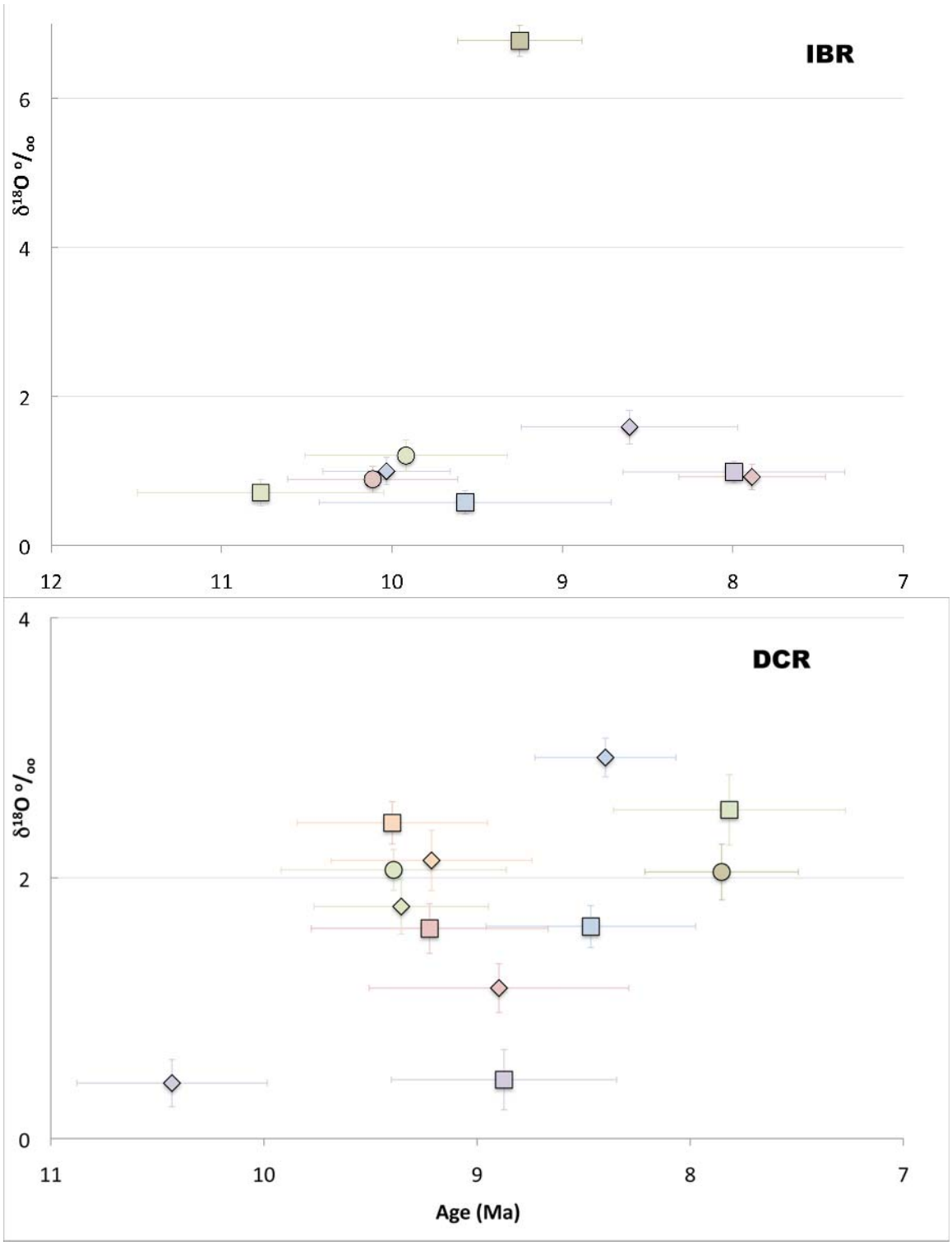

Figure C.1 continued

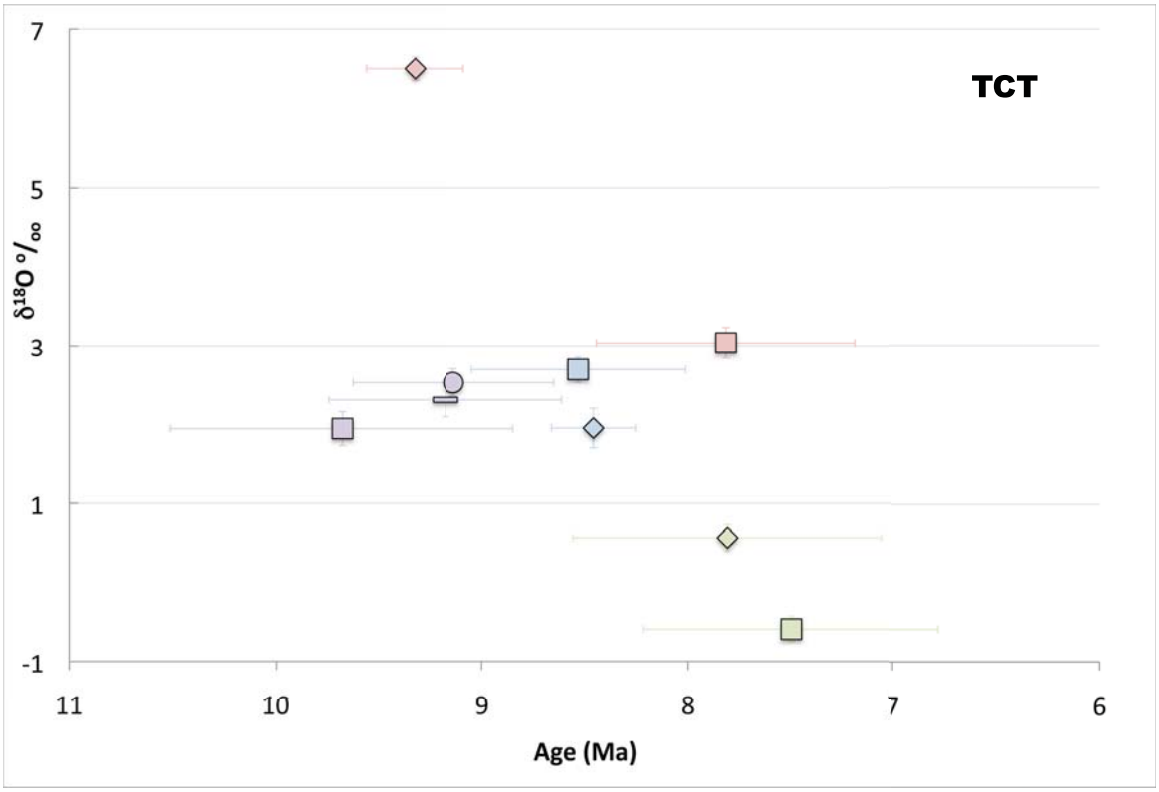

Figure C.1 continued

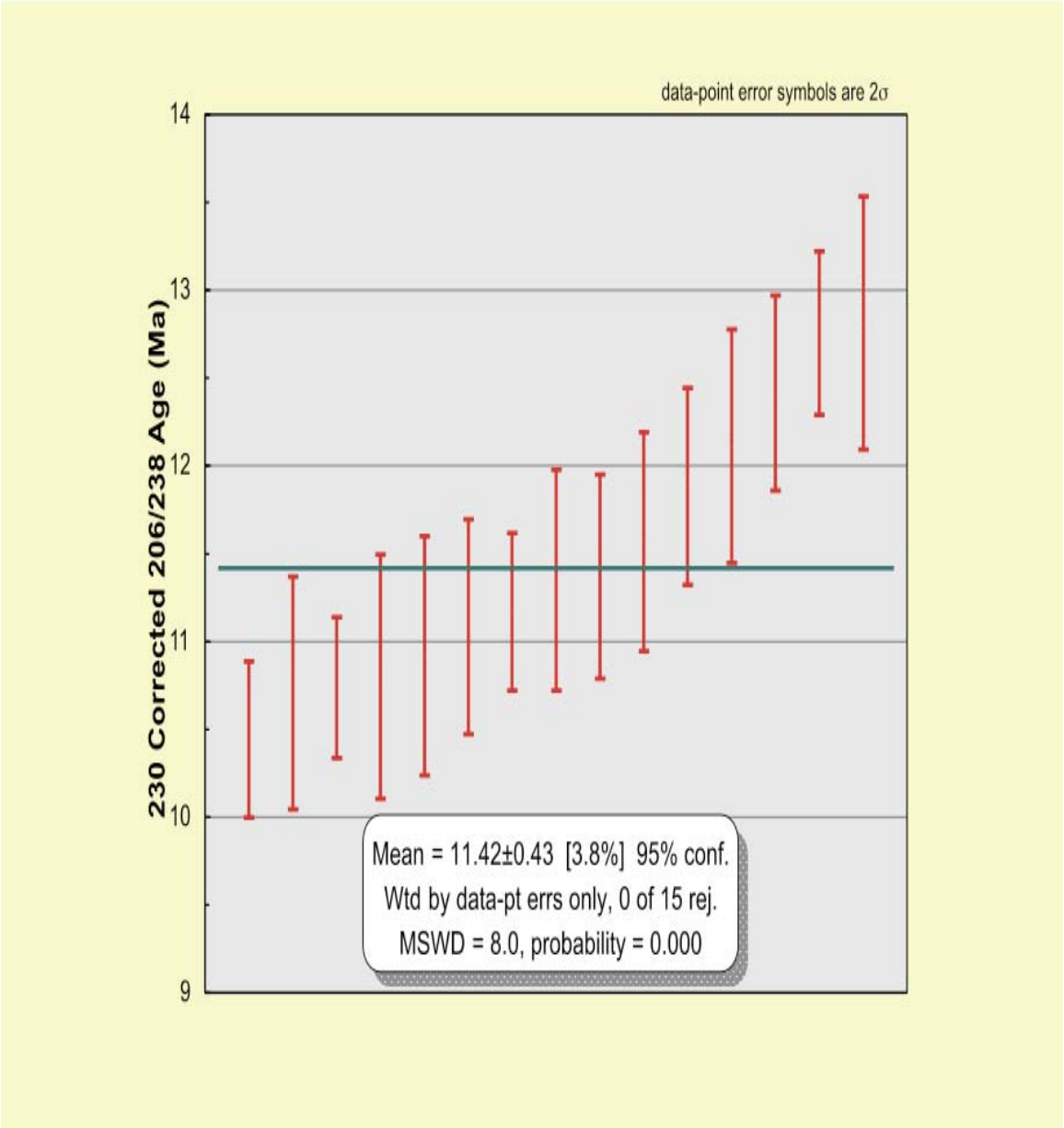

Figure C.2. Weighted Average Mean age (top) and unmixed age (bottom) results for lava flow one. Continued on next page.

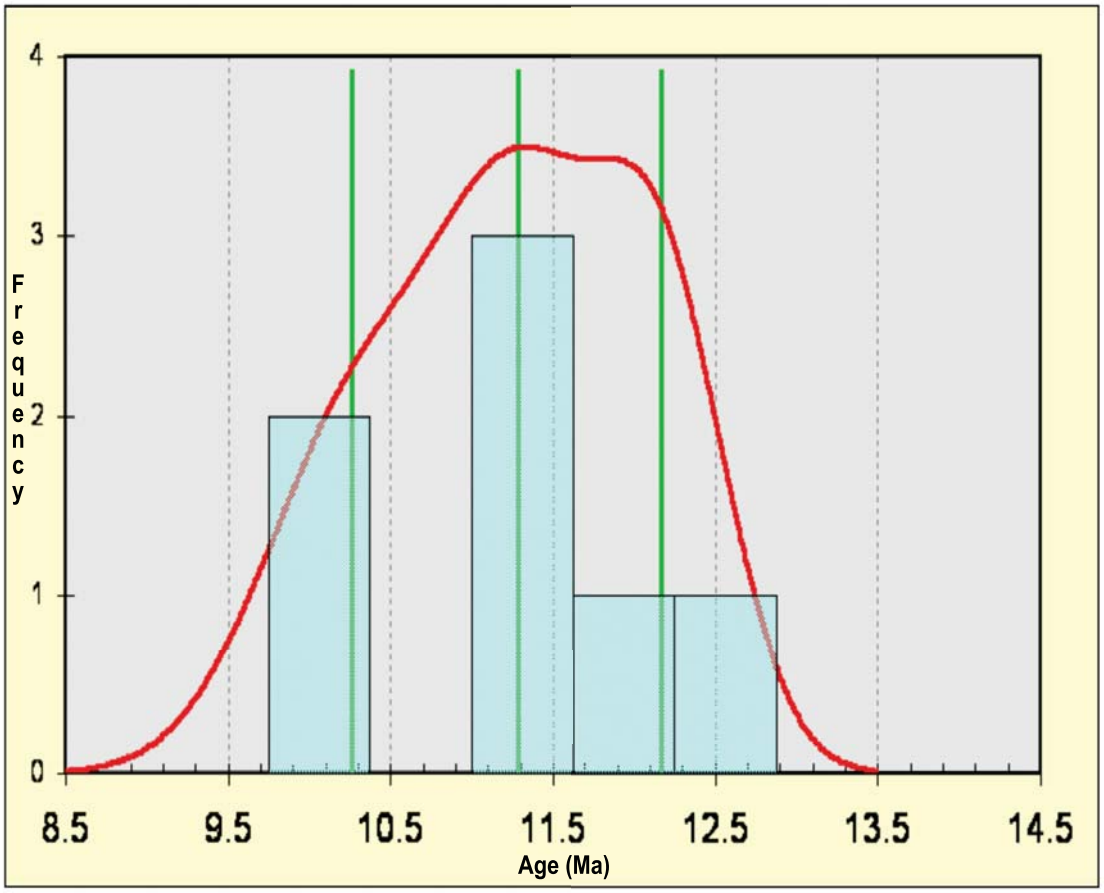

Sigma-Rho Matrix

	f1	f2	t1	t2	t3
f1	0.202	-0.003	0.007	0.006	0.000
f2	-0.003	0.248	-0.006	-0.004	0.008
t1	0.007	-0.006	.199	0.002	0.000
t2	0.006	-0.004	0.002	.142	0.003
t3	0.000	0.008	0.000	0.003	.137

Age	±2σ	fraction	±2σ
10.26	0.4	0.29	0.40
11.28	0.28	0.43	0.50
12.17	0.27	0.29	---

relative misfit = 0.157

Figure C.2 continued

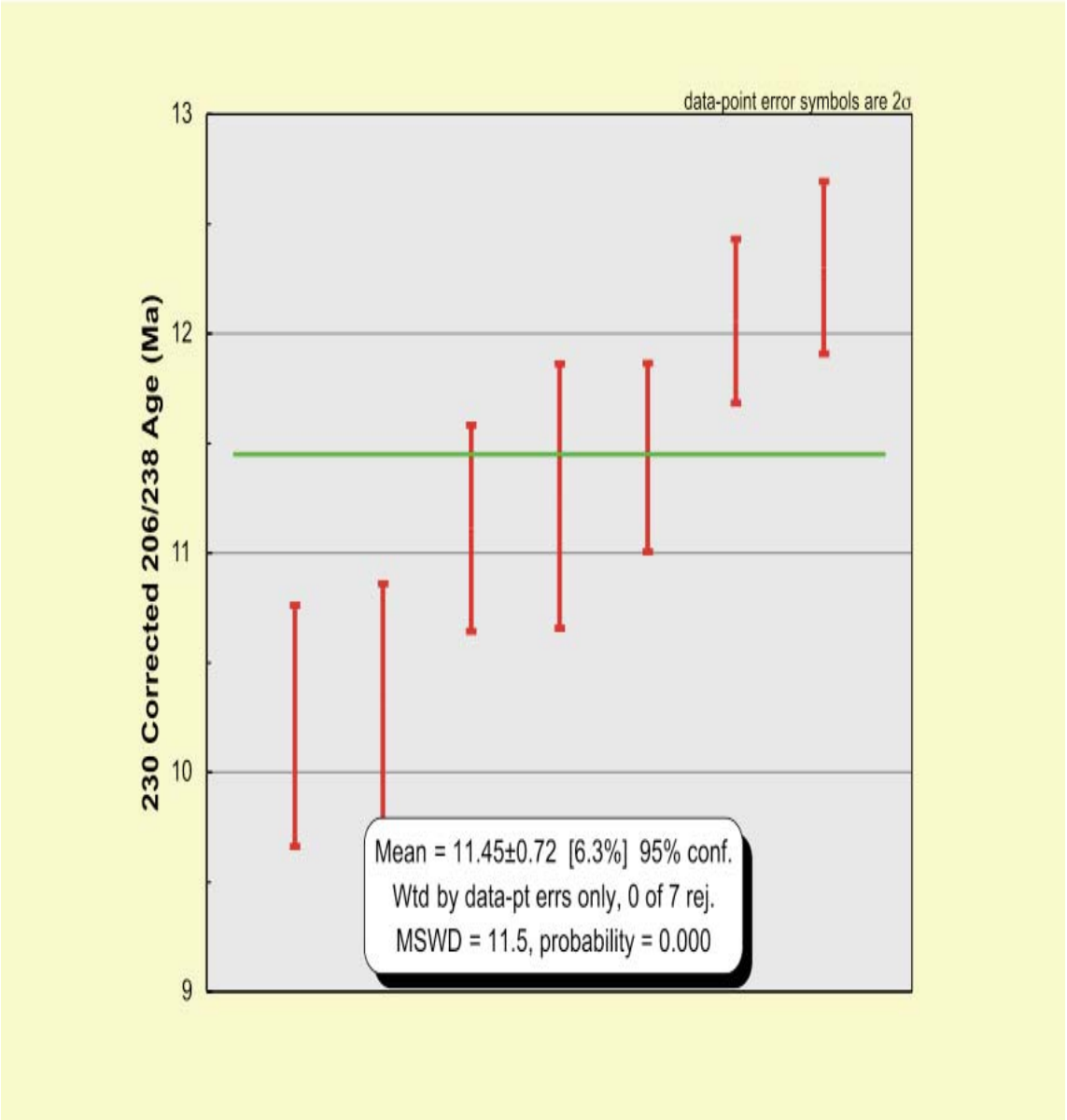

Figure C.3. Weighted Average Mean age (top) and unmixed age (bottom) results for lower lava flow. Continued on next page.

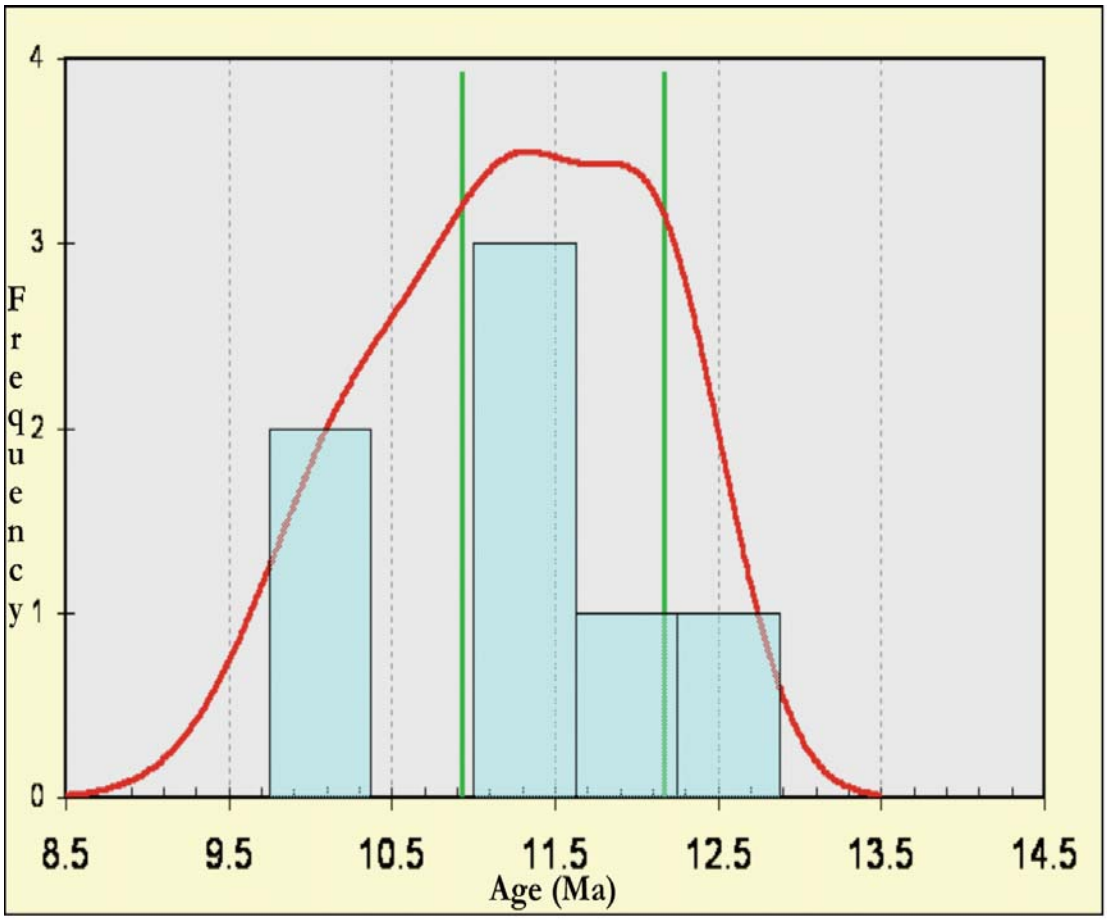

Sigma-Rho Matrix

	f1	t1	t2
f1	0.320	0.013	0.024
t1	0.013	.116	0.056
t2	0.024	0.056	.142

Age	±2σ	fraction	±2σ
10.93	0.23	0.71	0.64
12.17	0.28	0.29	---

relative misfit = 0.341

Figure C.3 continued

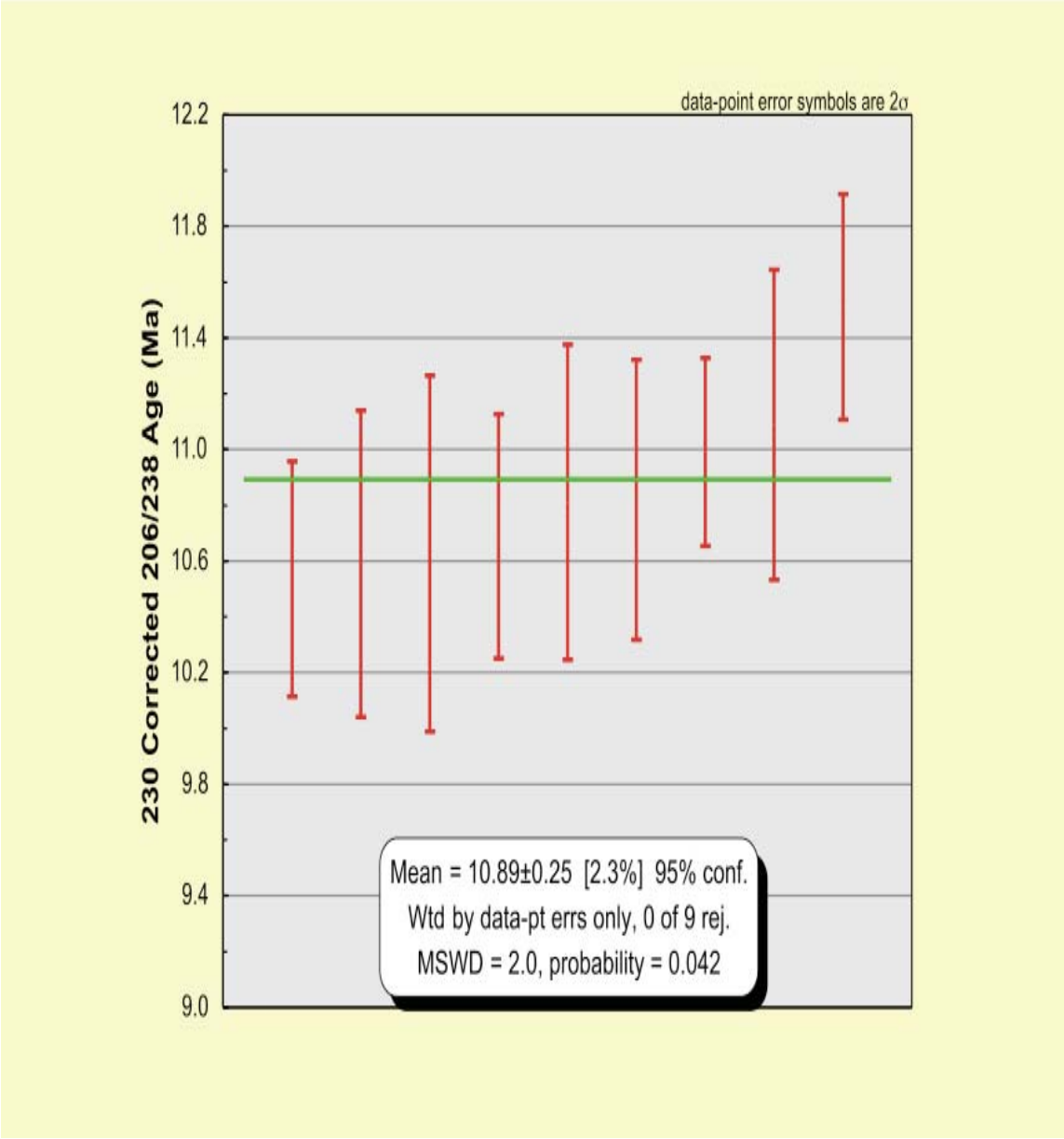

Figure C.4. Weighted Average Mean age (top) and unmixed age (bottom) results for upper lava flow. Continued on next page.

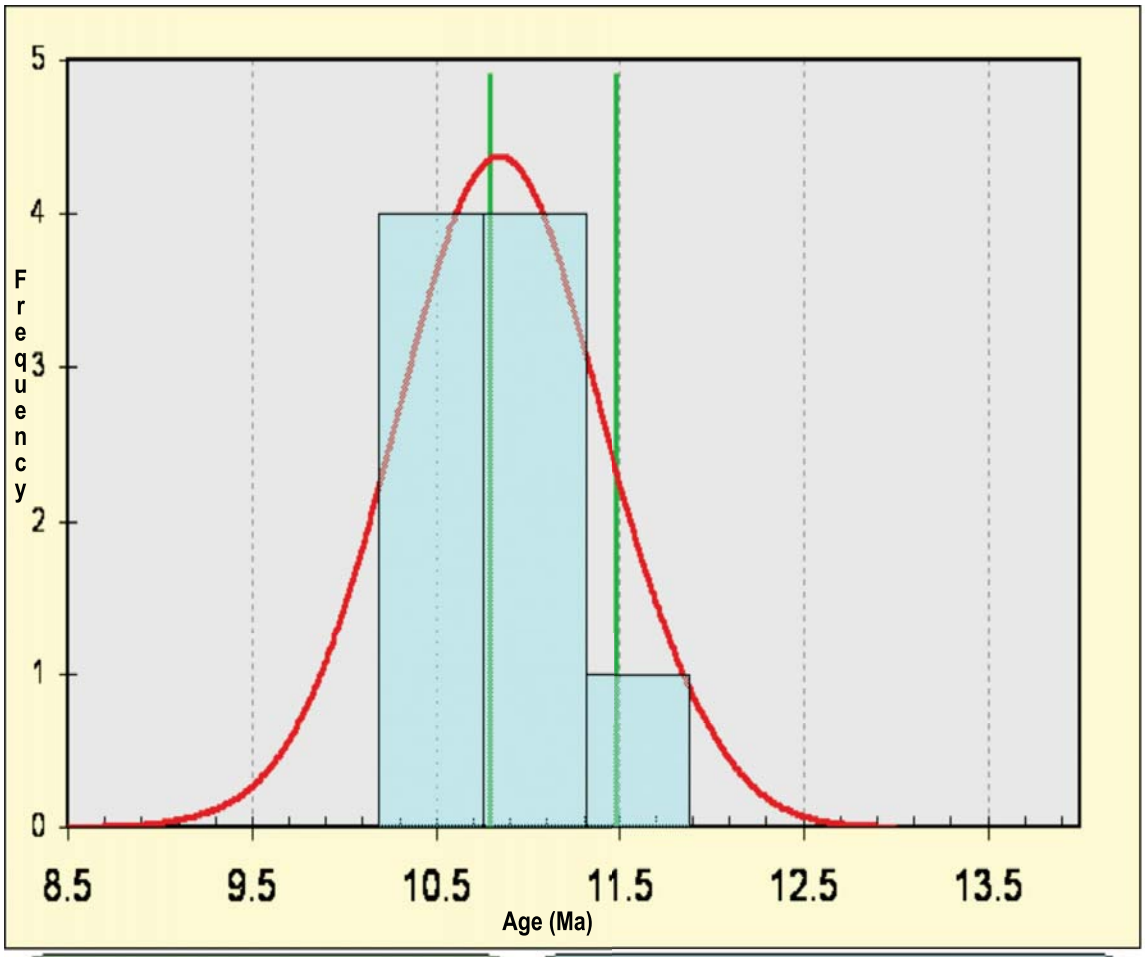

Sigma-Rho Matrix			
	f1	t1	t2
f1	0.315	0.018	0.049
t1	0.018	.0856	0.036
t2	0.049	0.036	.219

Age	±2σ	fraction	±2σ
10.786	0.17	0.88	0.63
11.48	0.44	0.12	---

relative misfit = 0.295

Figure C.4 continued

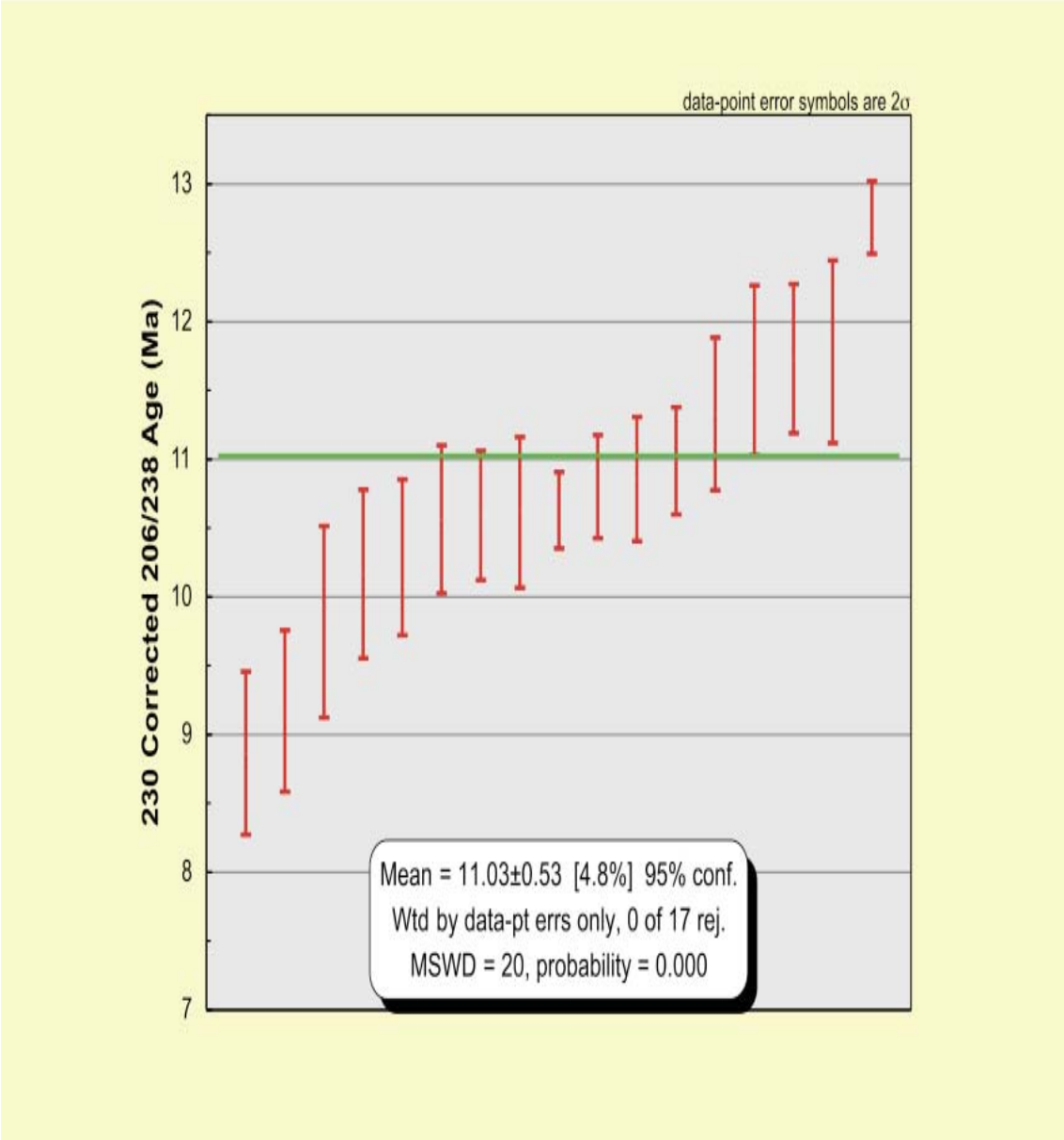

Figure C.5. Weighted Average Mean age (top) and unmixed age (bottom) results for Triguero Homestead rhyolite. Continued on next page.

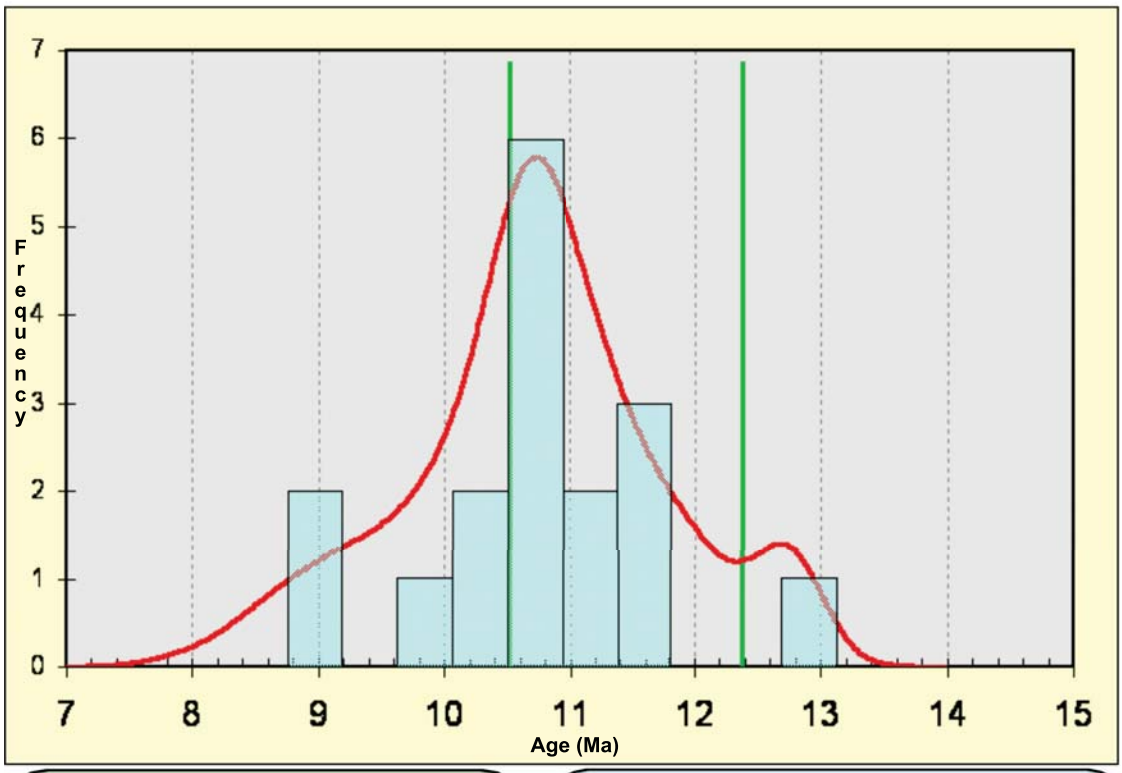

Sigma-Rho Matrix

	f1	t1	t2
f1	0.214	0.022	0.026
t1	0.022	.0665	0.067
t2	0.026	0.067	.11

Age	±2σ	fraction	±2σ
10.52	0.13	0.77	0.43
12.38	0.22	0.23	---

relative misfit = 0.331

Figure C.5 continued

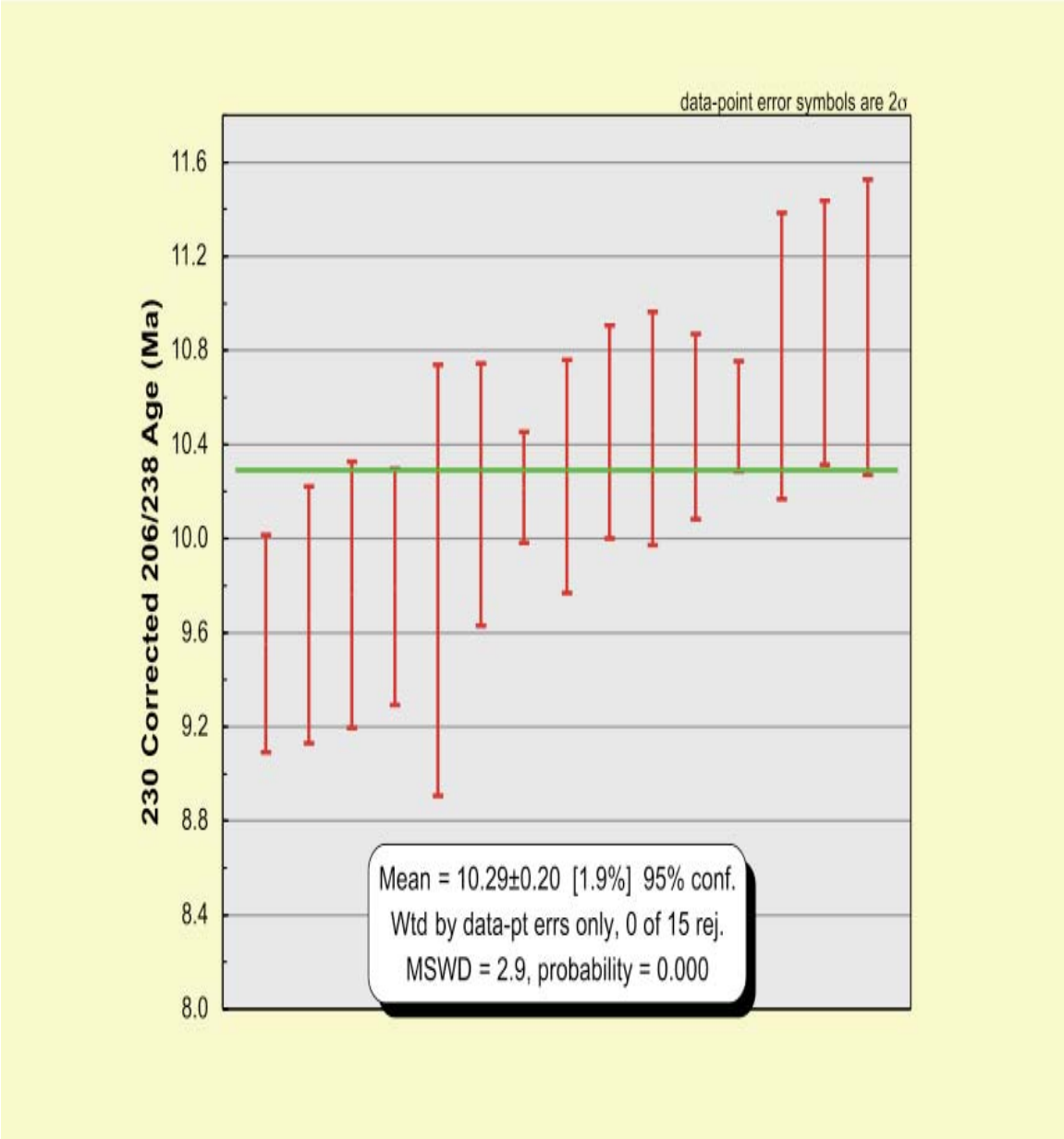

Figure C.6. Weighted Average Mean age (top) and unmixed age (bottom) results for Marys Creek rhyolite. Continued on next page.

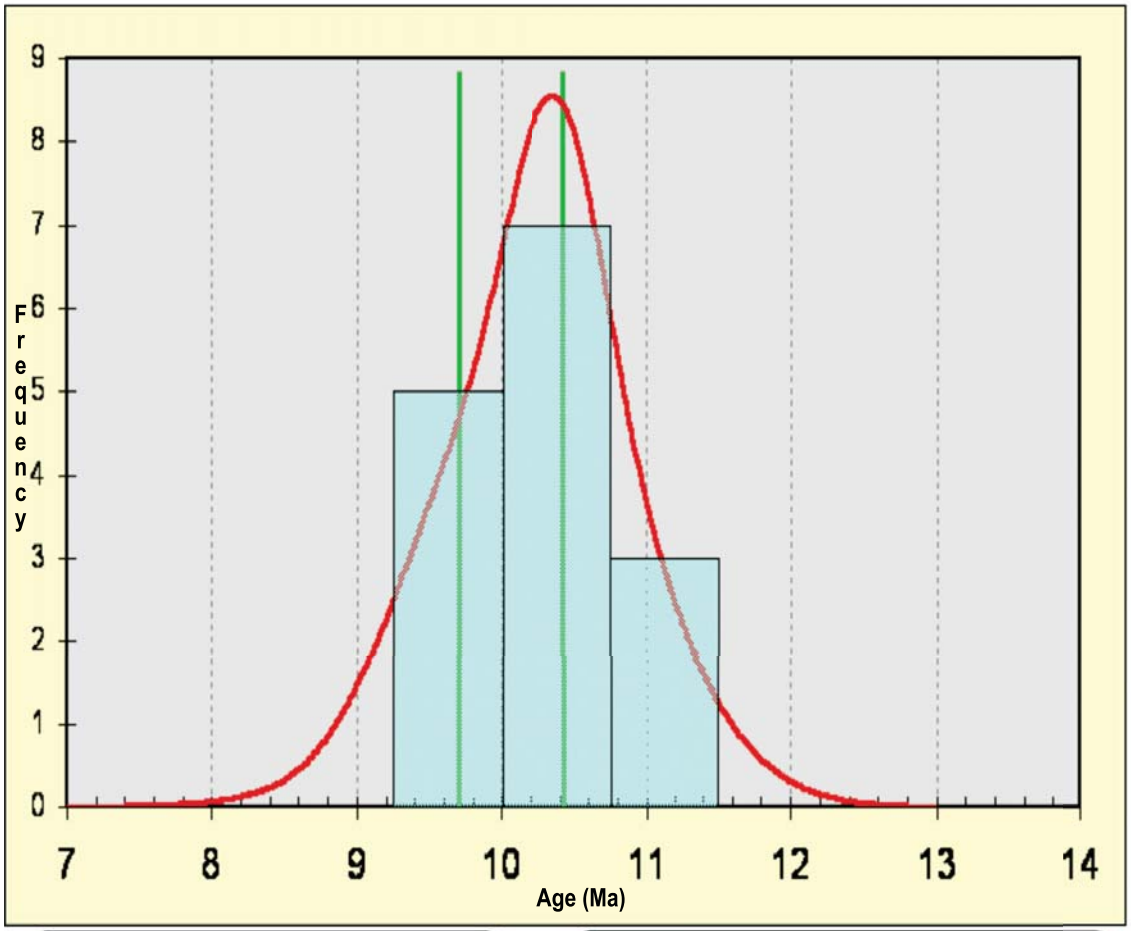

Sigma-Rho Matrix			
	f1	t1	t2
f1	0.153	0.107	0.123
t1	0.107	.139	0.053
t2	0.123	0.053	.0641

Age	±2σ	fraction	±2σ
9.71	0.28	0.29	0.31
10.423	0.13	0.71	---

relative misfit = 0.533

Figure C.6 continued

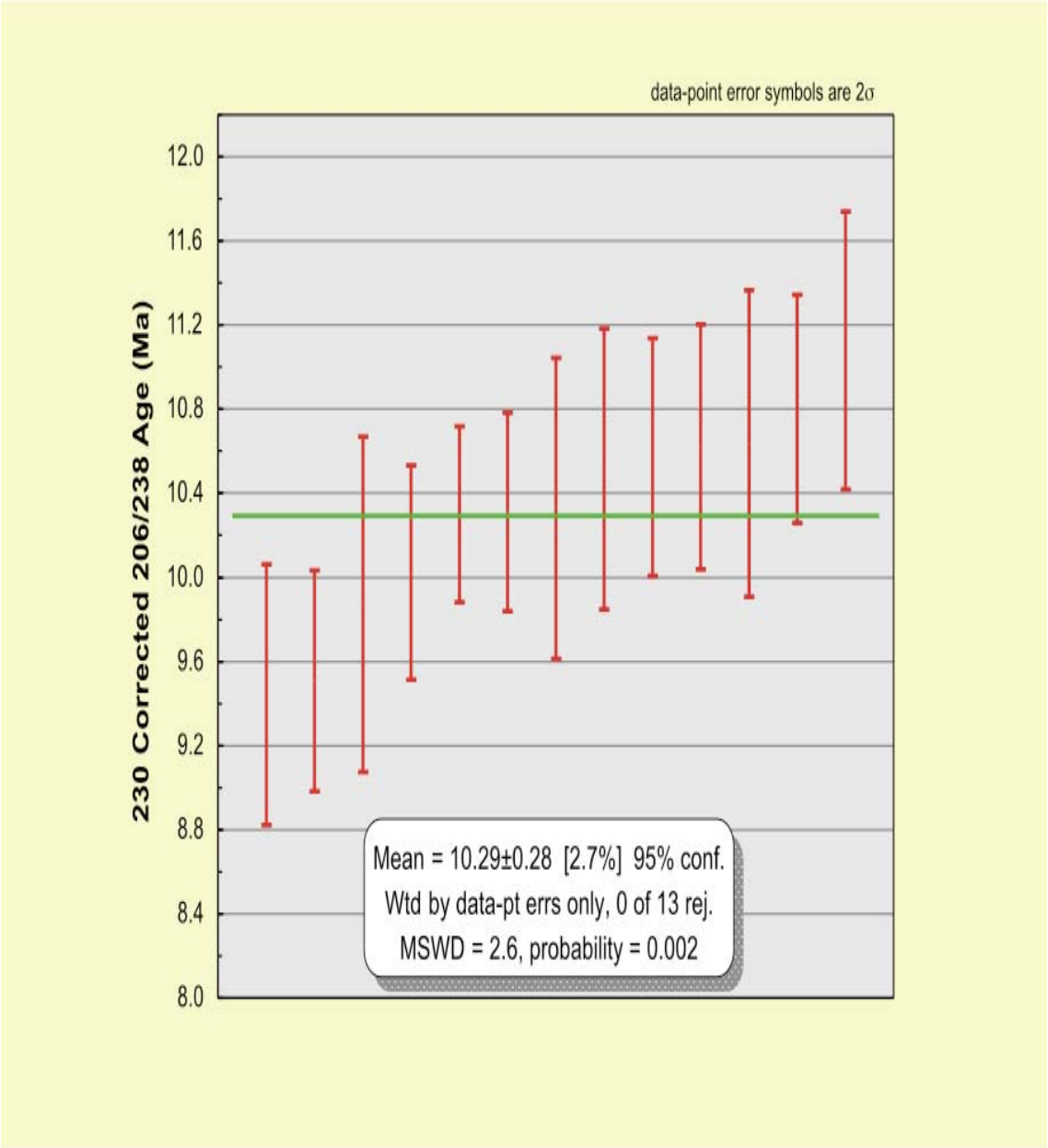

Figure C.7. Weighted Average Mean age (top) and unmixed age (bottom) results for Cedar Tree rhyolite. Continued on next page.

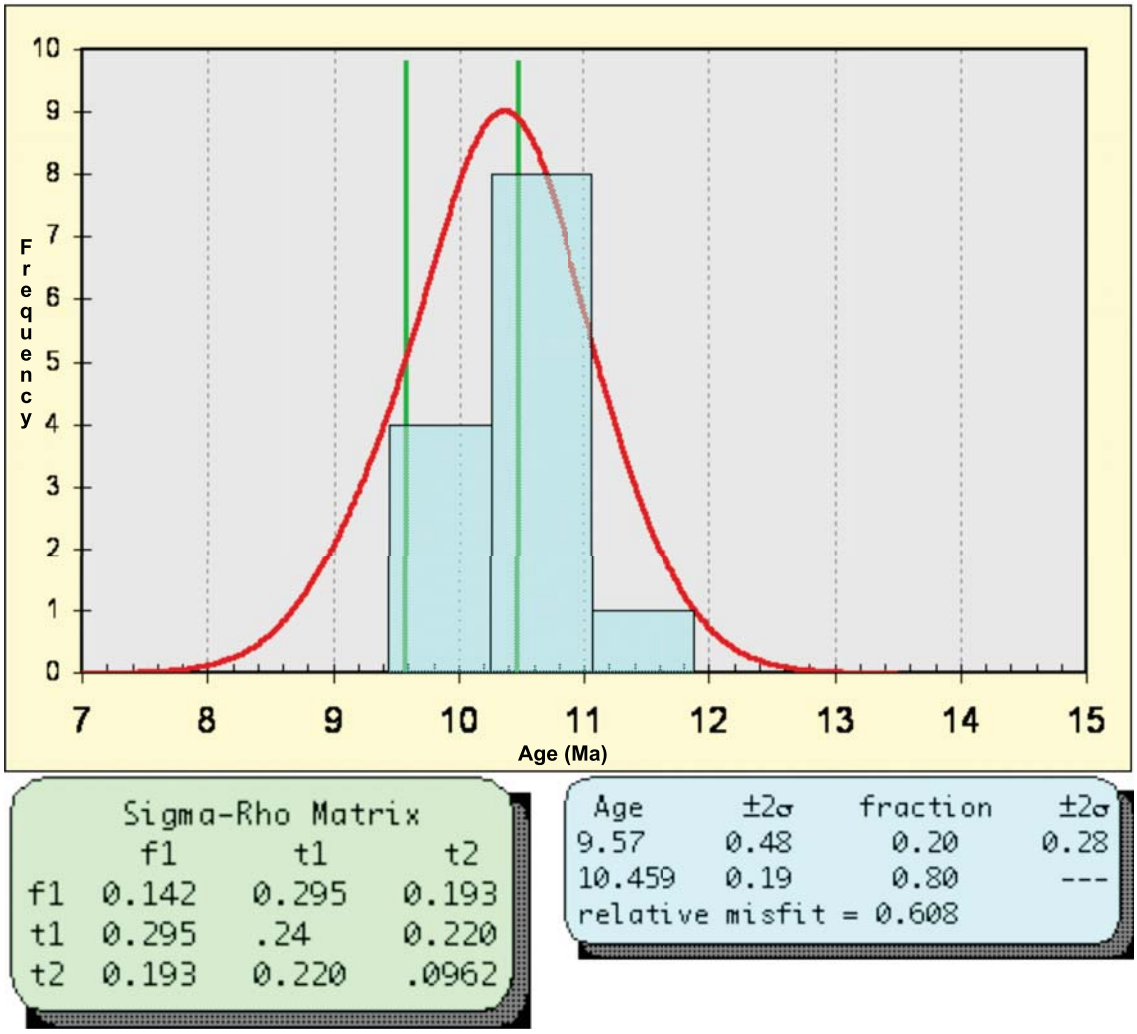

Sigma-Rho Matrix

	f1	t1	t2
f1	0.142	0.295	0.193
t1	0.295	.24	0.220
t2	0.193	0.220	.0962

Age	±2σ	fraction	±2σ
9.57	0.48	0.20	0.28
10.459	0.19	0.80	---

relative misfit = 0.608

Figure C.7 continued

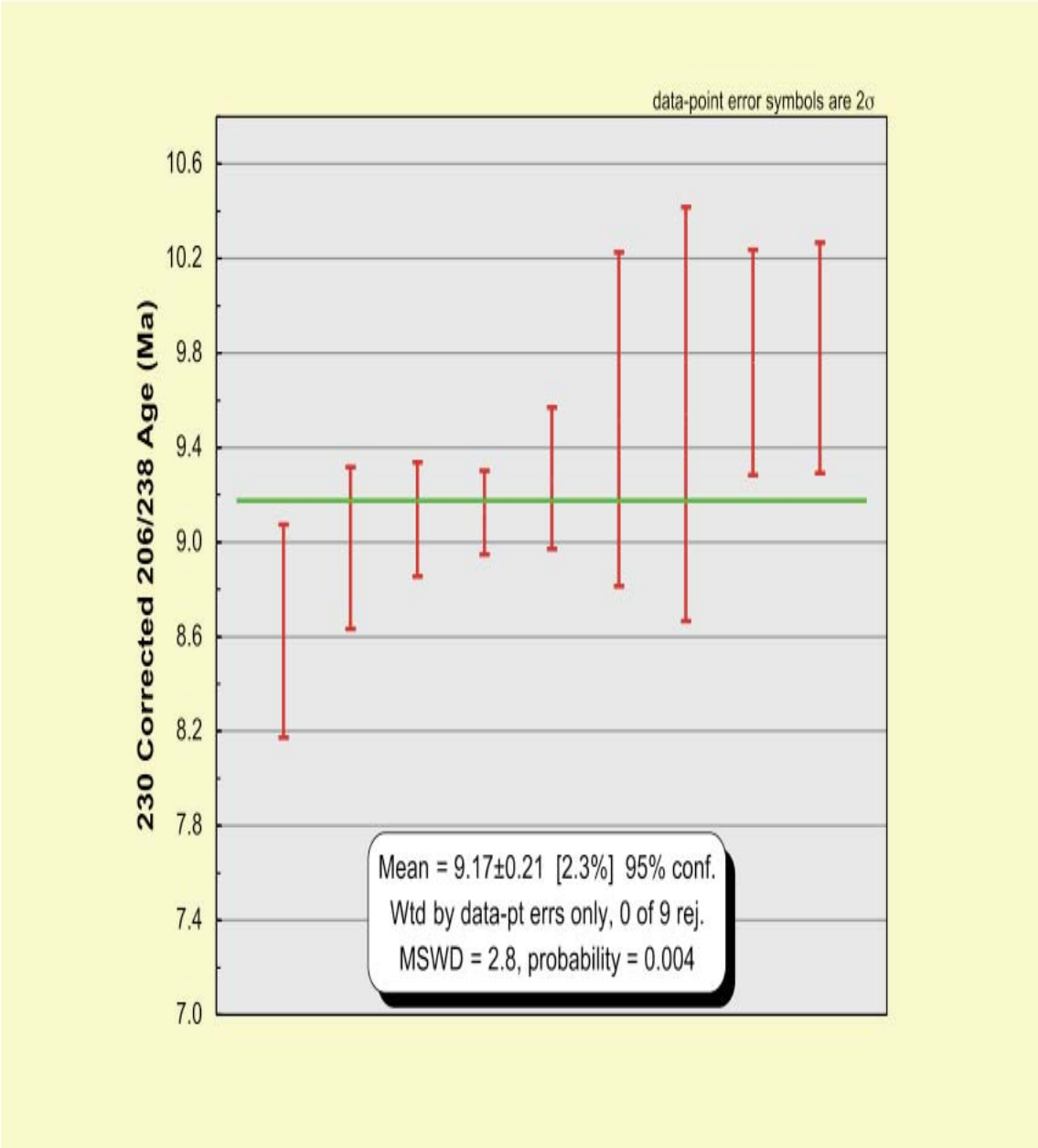

Figure C.8. Weighted Average Mean age (top) and unmixed age (bottom) results for Bruneau-Jasper rhyolite. Continued on next page.

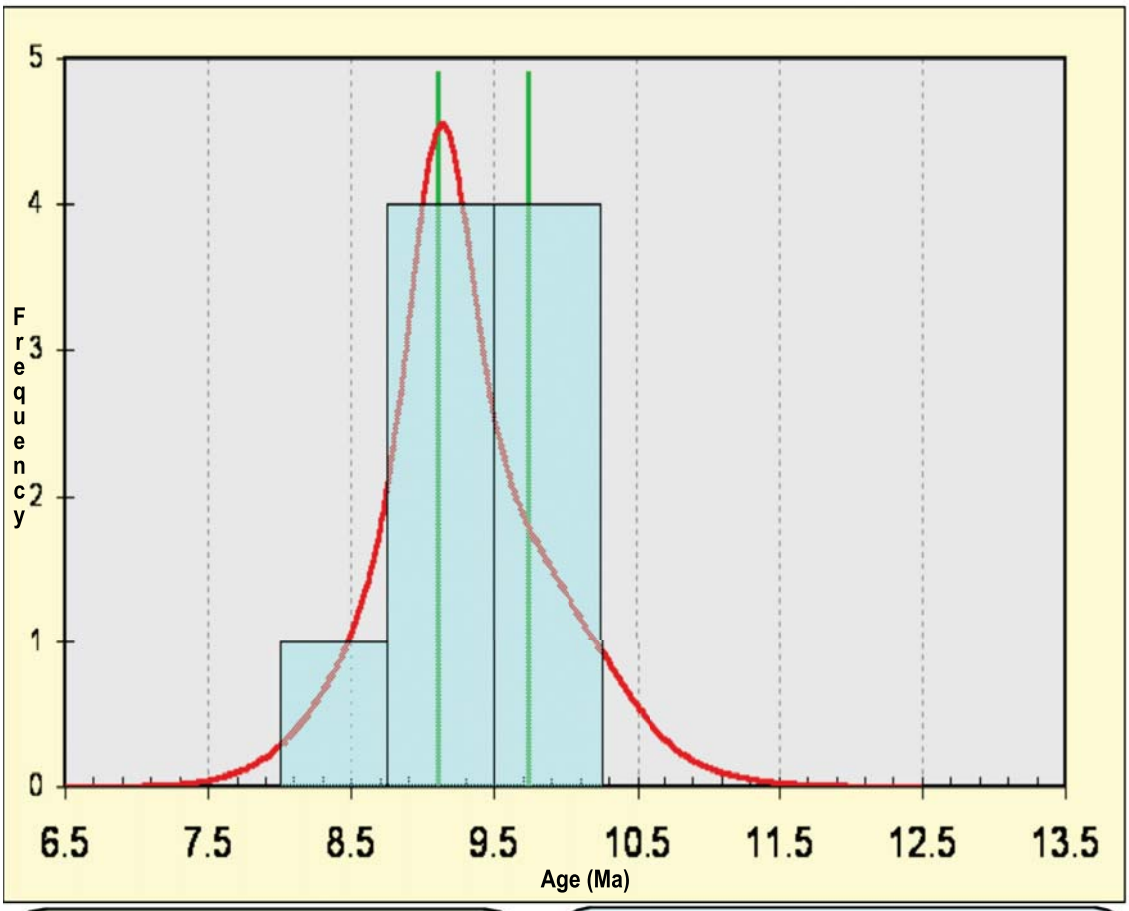

Sigma-Rho Matrix

	f1	t1	t2
f1	0.293	0.063	0.054
t1	0.063	.0591	0.026
t2	0.054	0.026	.171

Age	±2σ	fraction	±2σ
9.105	0.12	0.70	0.59
9.73	0.34	0.30	---

relative misfit = 0.407

Figure C.8 continued

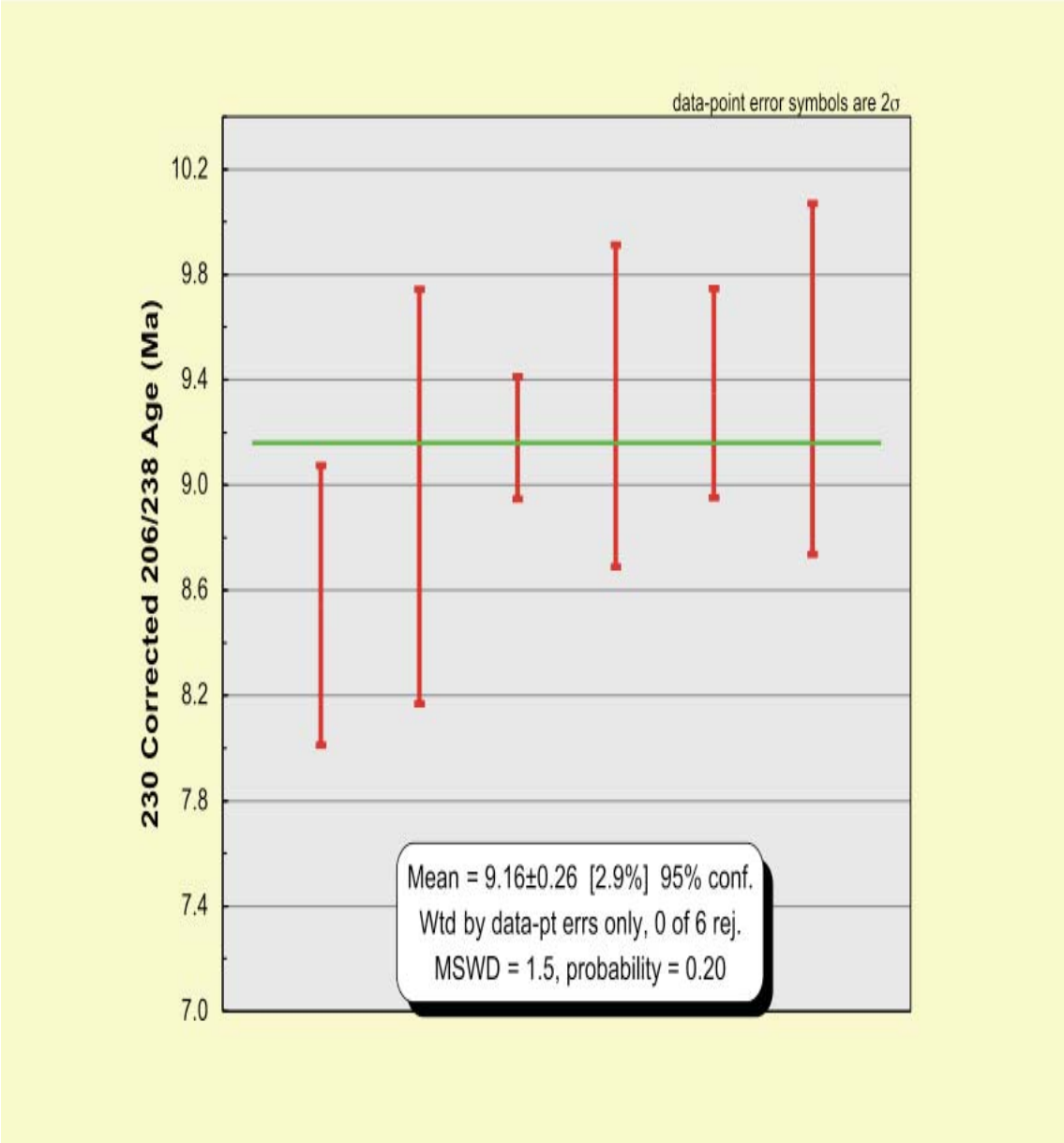

Figure C.9. Weighted Average Mean age (top) and unmixed age (bottom) results for Poison Creek rhyolite. Continued on next page.

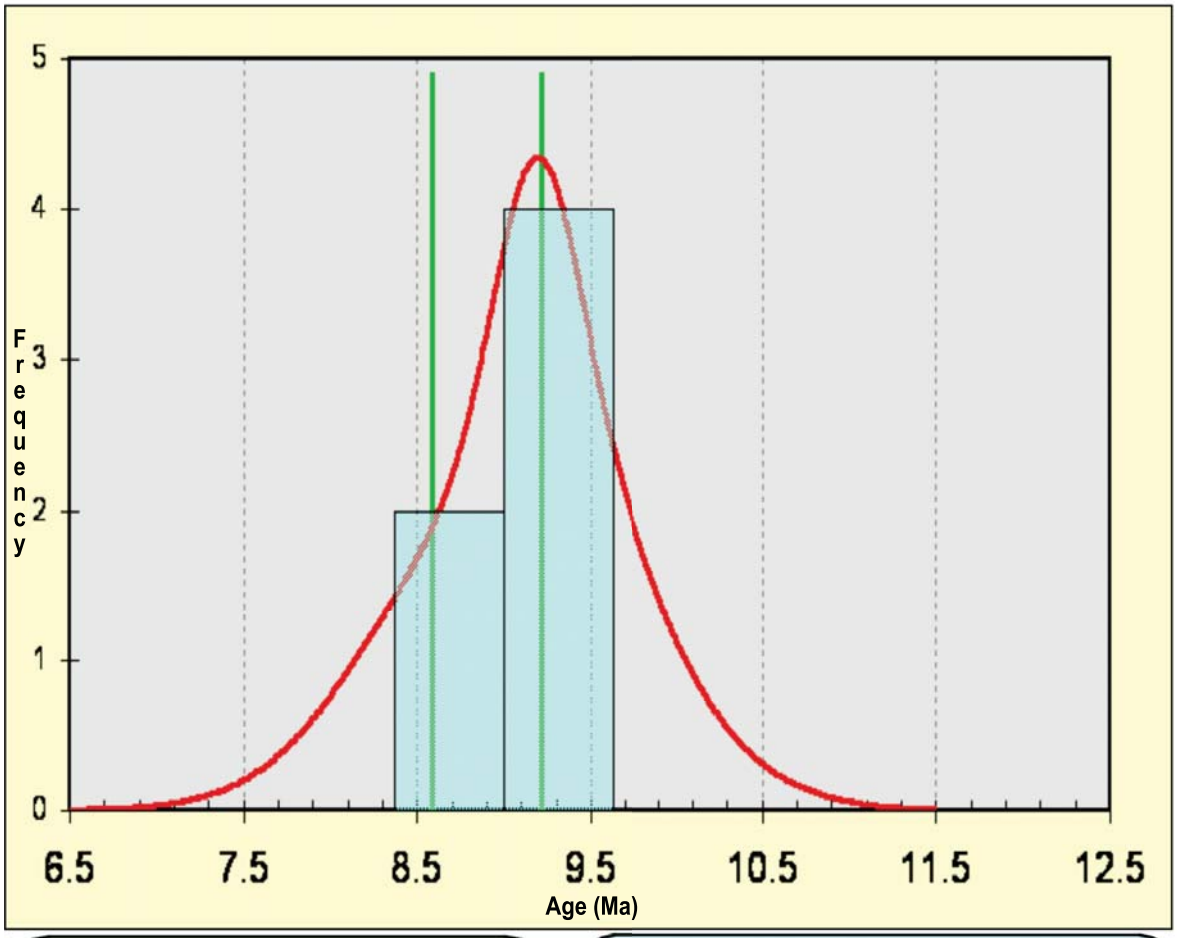

Sigma-Rho Matrix

	f1	t1	t2
f1	0.201	0.137	0.167
t1	0.137	.308	0.006
t2	0.167	0.006	.0953

Age	±2σ	fraction	±2σ
8.59	0.62	0.17	0.40
9.217	0.19	0.83	---

relative misfit = 0.286

Figure C.9 continued

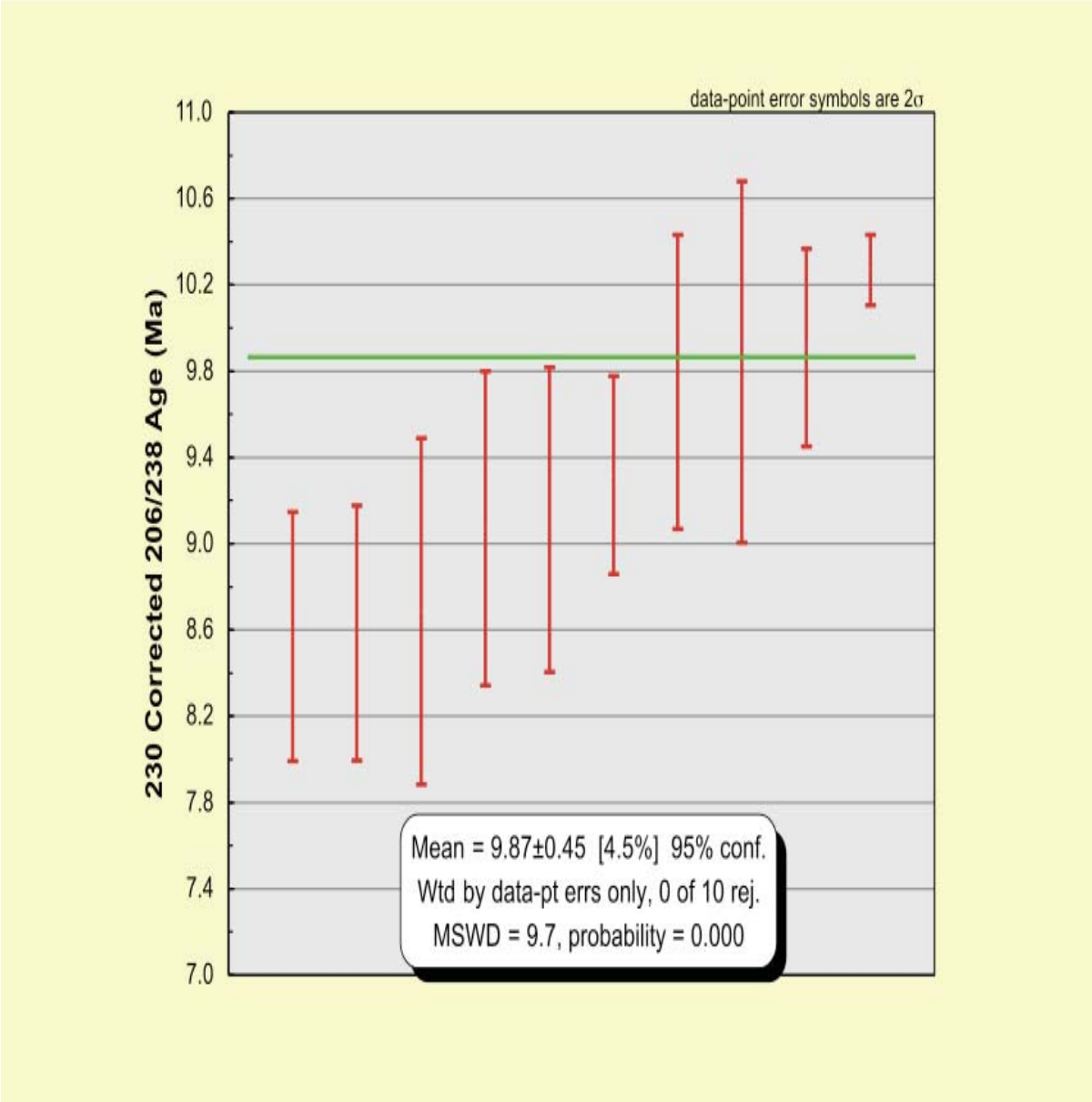

Figure C.10. Weighted Average Mean age (top) and unmixed age (bottom) results for Louse Creek rhyolite. Continued on next page.

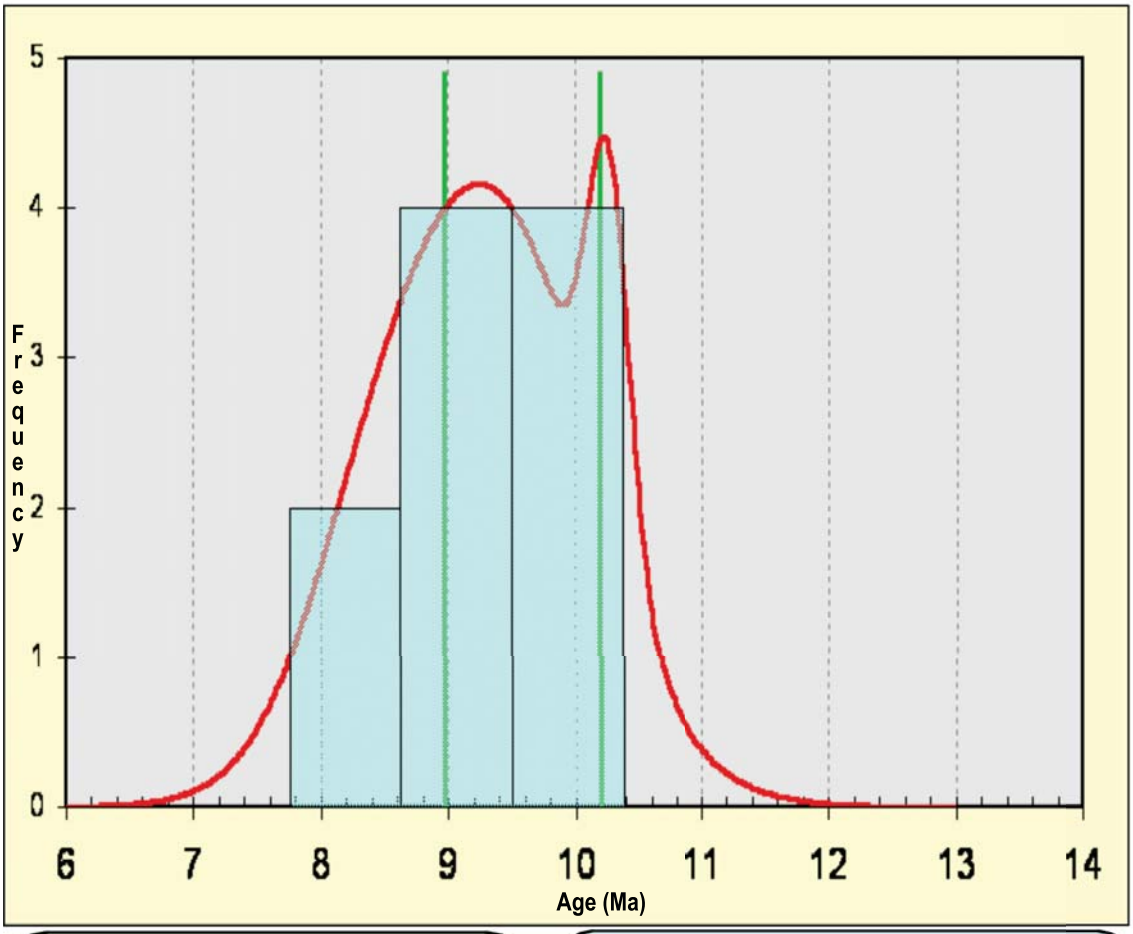

Sigma-Rho Matrix

	f1	t1	t2
f1	0.265	0.123	0.046
t1	0.123	.137	0.077
t2	0.046	0.077	.076

Age	±2σ	fraction	±2σ
8.98	0.27	0.65	0.53
10.201	0.15	0.35	---

relative misfit = 0.209

Figure C.10 continued

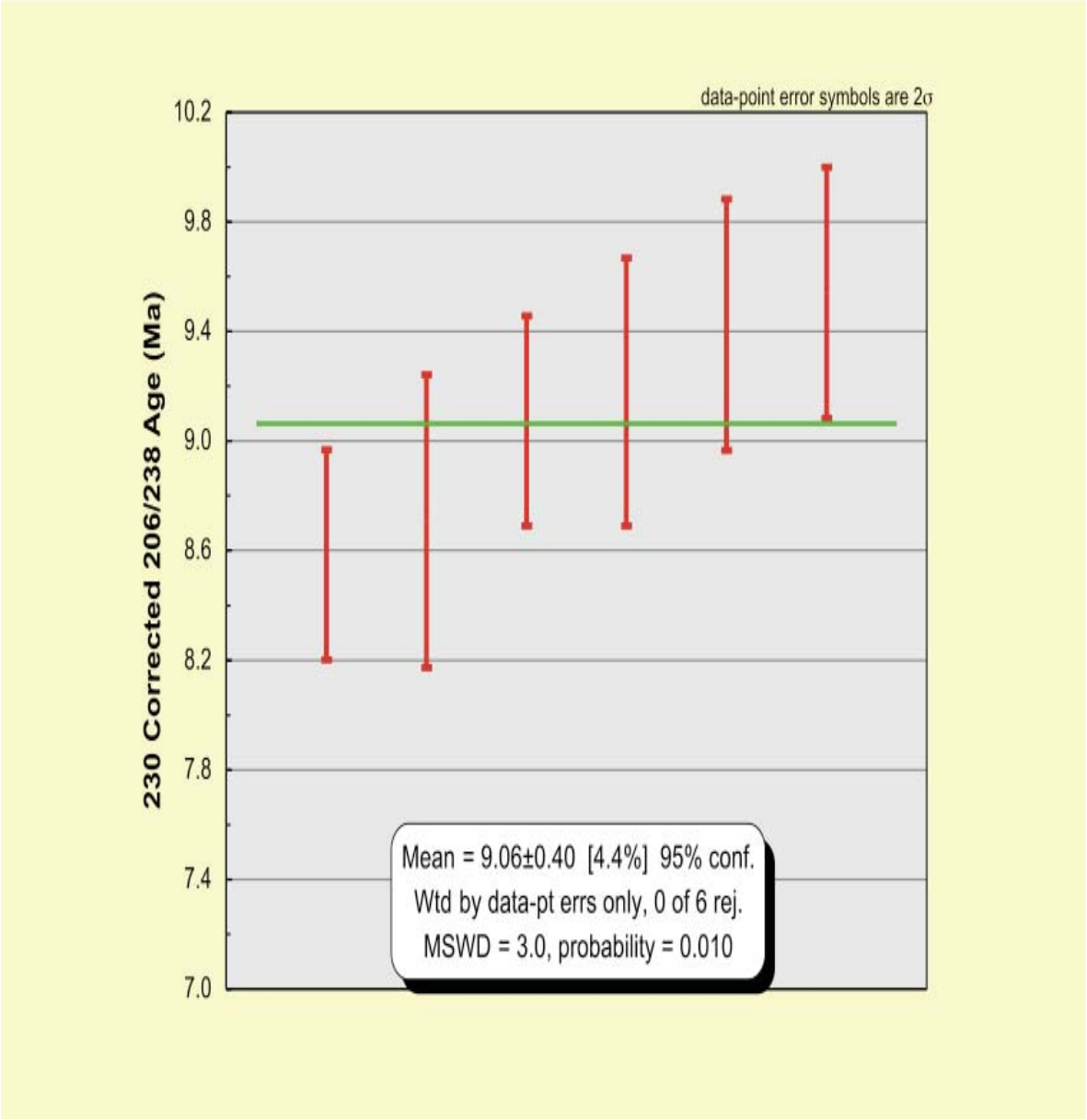

Figure C.11. Weighted Average Mean age (top) and unmixed age (bottom) results for Sheep Creek rhyolite. Continued on next page.

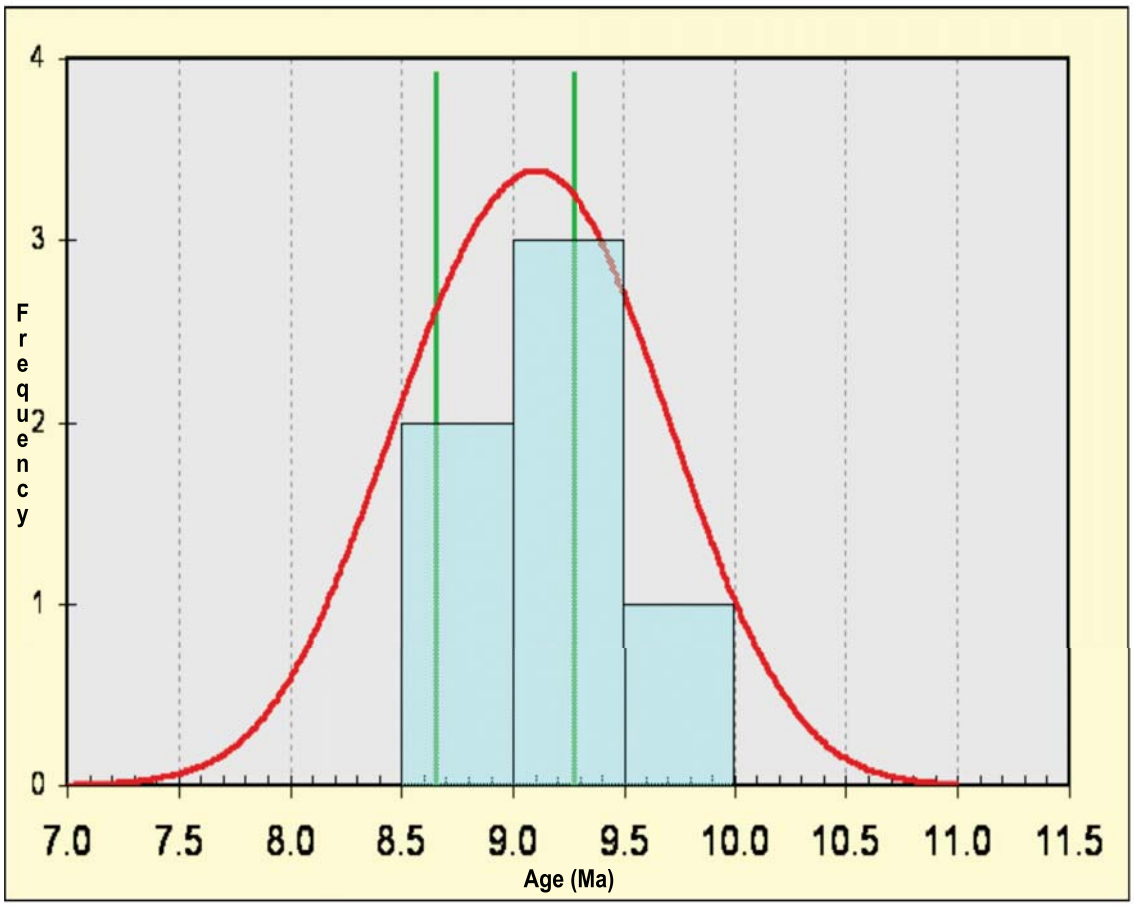

Sigma-Rho Matrix

	f1	t1	t2
f1	0.258	0.207	0.183
t1	0.207	.192	0.150
t2	0.183	0.150	.123

Age	±2σ	fraction	±2σ
8.65	0.38	0.32	0.52
9.27	0.25	0.68	---

relative misfit = 0.399

Figure C.11 continued

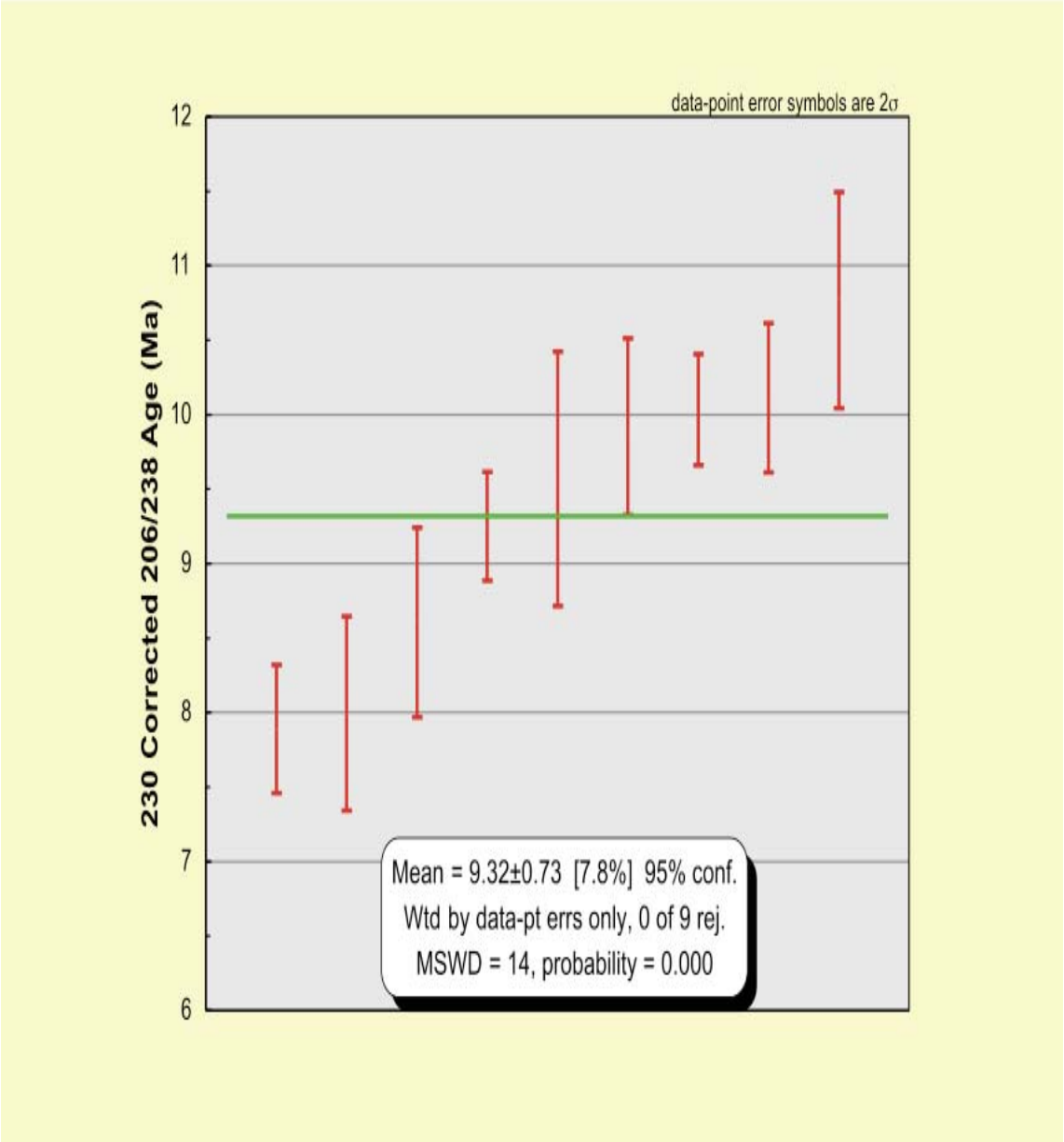

Figure C.12. Weighted Average Mean age (top) and unmixed age (bottom) results for Indian Batt rhyolite. Continued on next page.

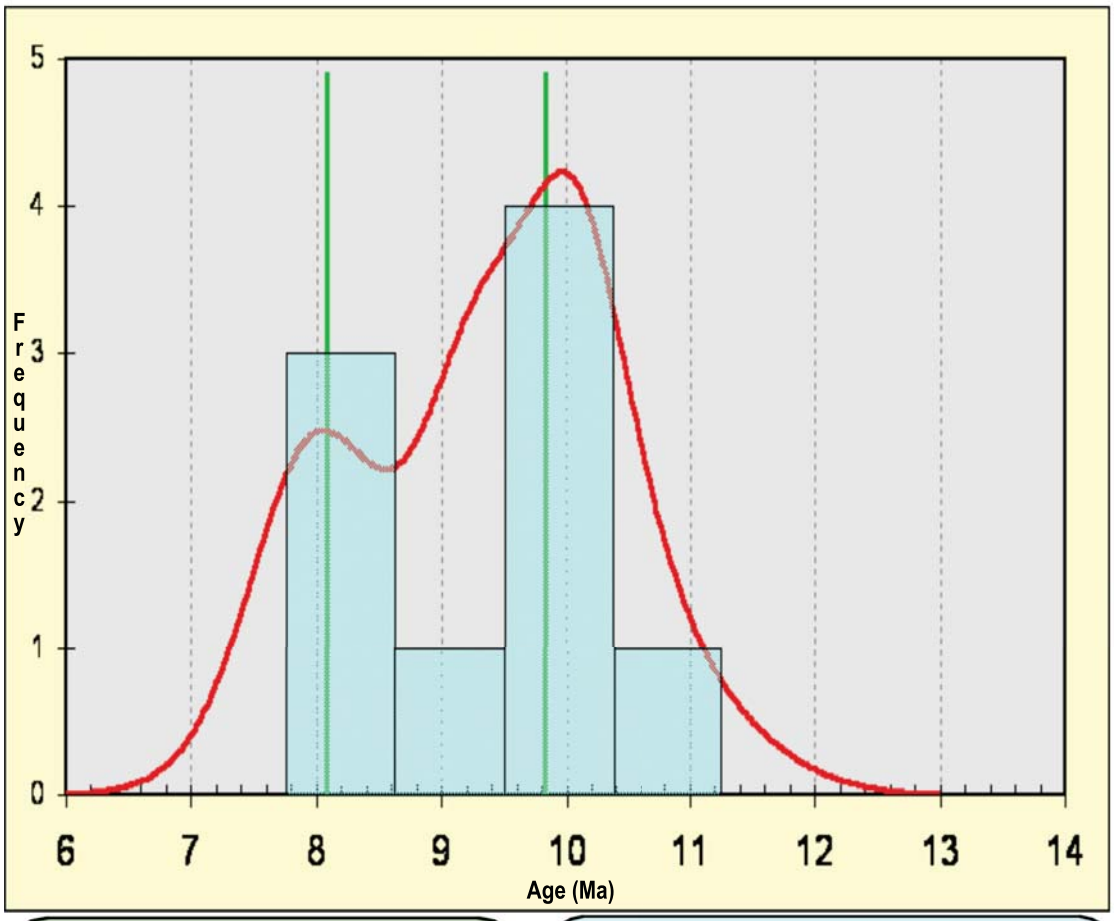

Sigma-Rho Matrix

	f1	t1	t2
f1	0.193	0.003	0.003
t1	0.003	.157	0.005
t2	0.003	0.005	.101

Age	±2σ	fraction	±2σ
8.09	0.31	0.33	0.39
9.83	0.2	0.67	---

relative misfit = 0.268

Figure C.12 continued

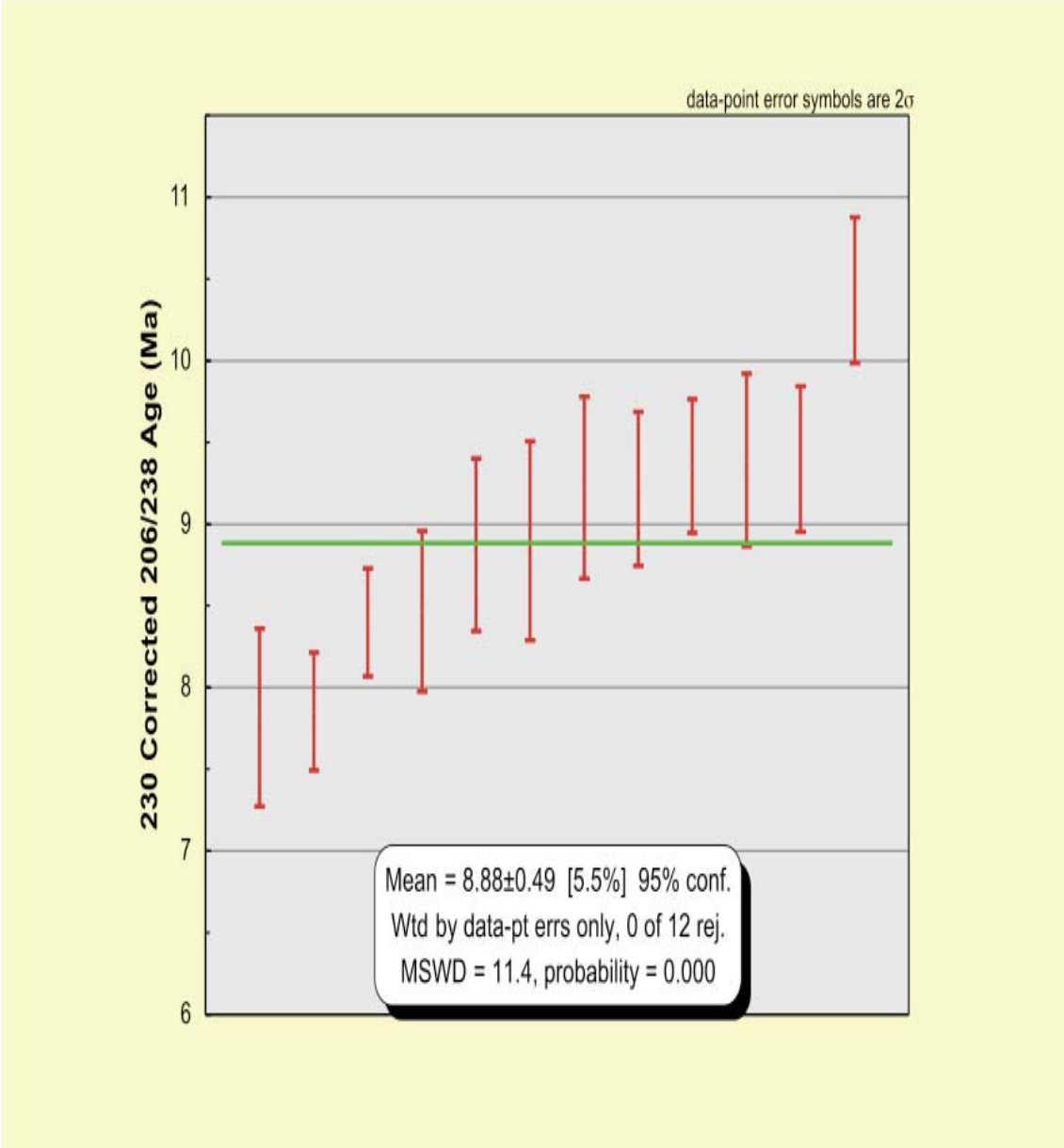

Figure C.13. Weighted Average Mean age (top) and unmixed age (bottom) results for Dorsey Creek rhyolite. Continued on next page.

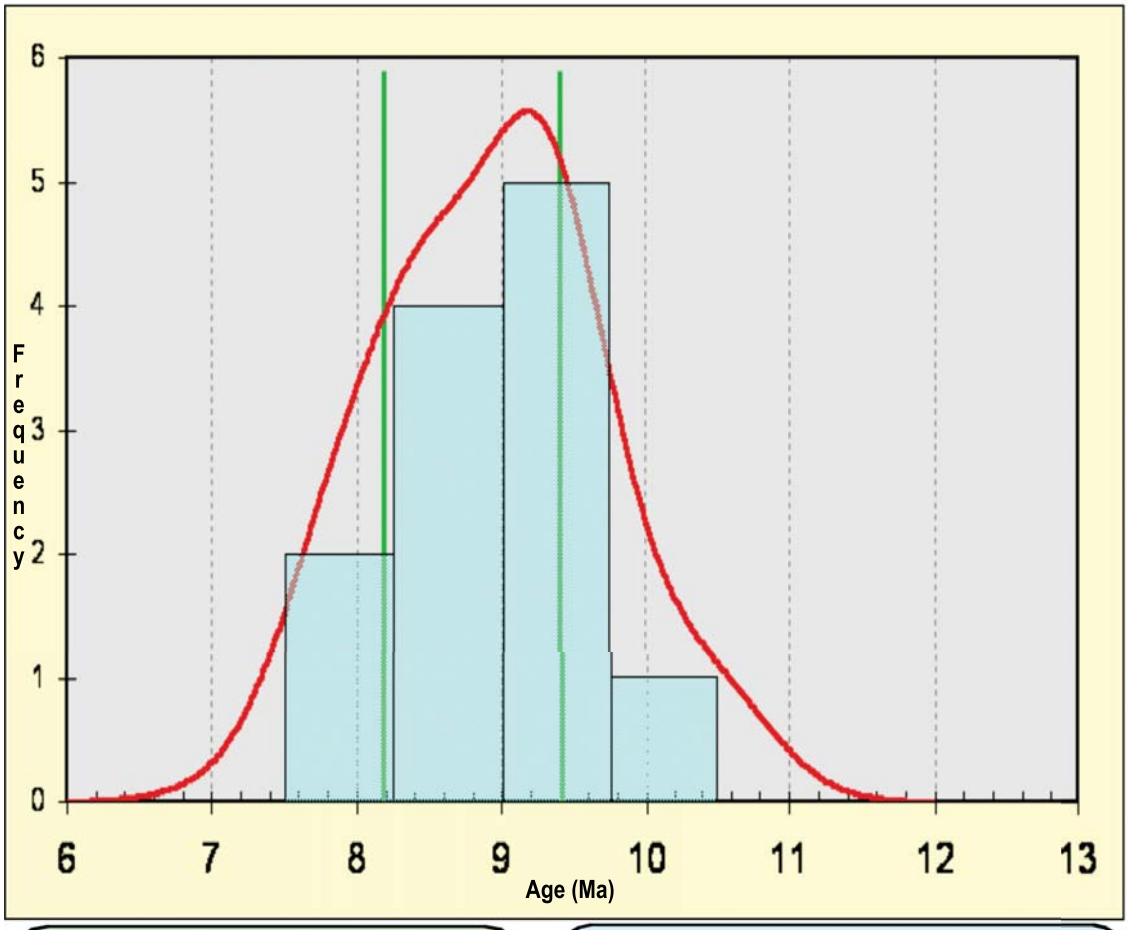

Sigma-Rho Matrix

	f1	t1	t2
f1	0.178	0.120	0.086
t1	0.120	.112	0.146
t2	0.086	0.146	.0923

Age	±2σ	fraction	±2σ
8.18	0.22	0.35	0.36
9.419	0.18	0.65	---

relative misfit = 0.349

Figure C.13 continued

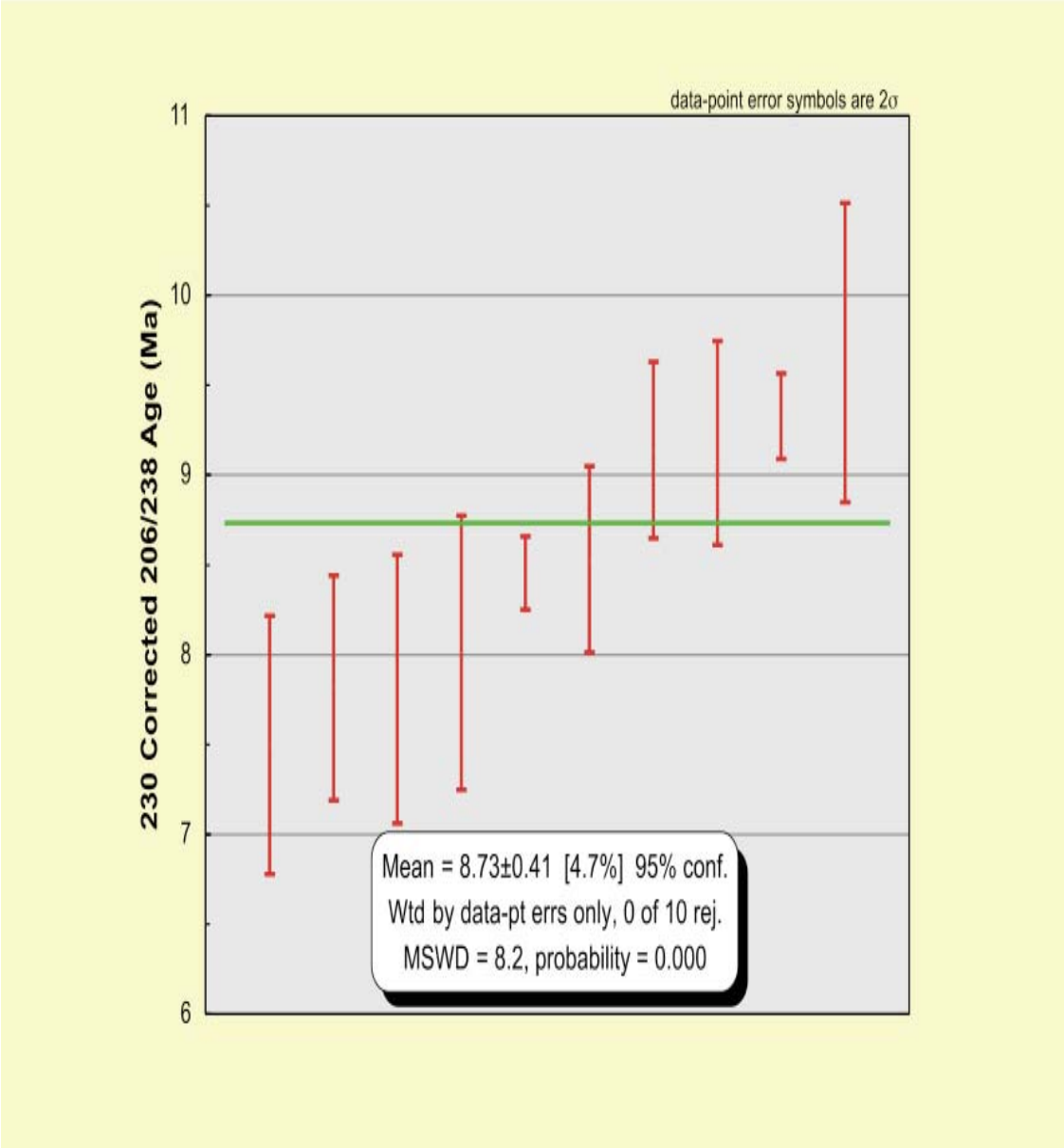

Figure C.14. Weighted Average Mean age (top) and unmixed age (bottom) results for Three Creek tuff. Continued on next page.

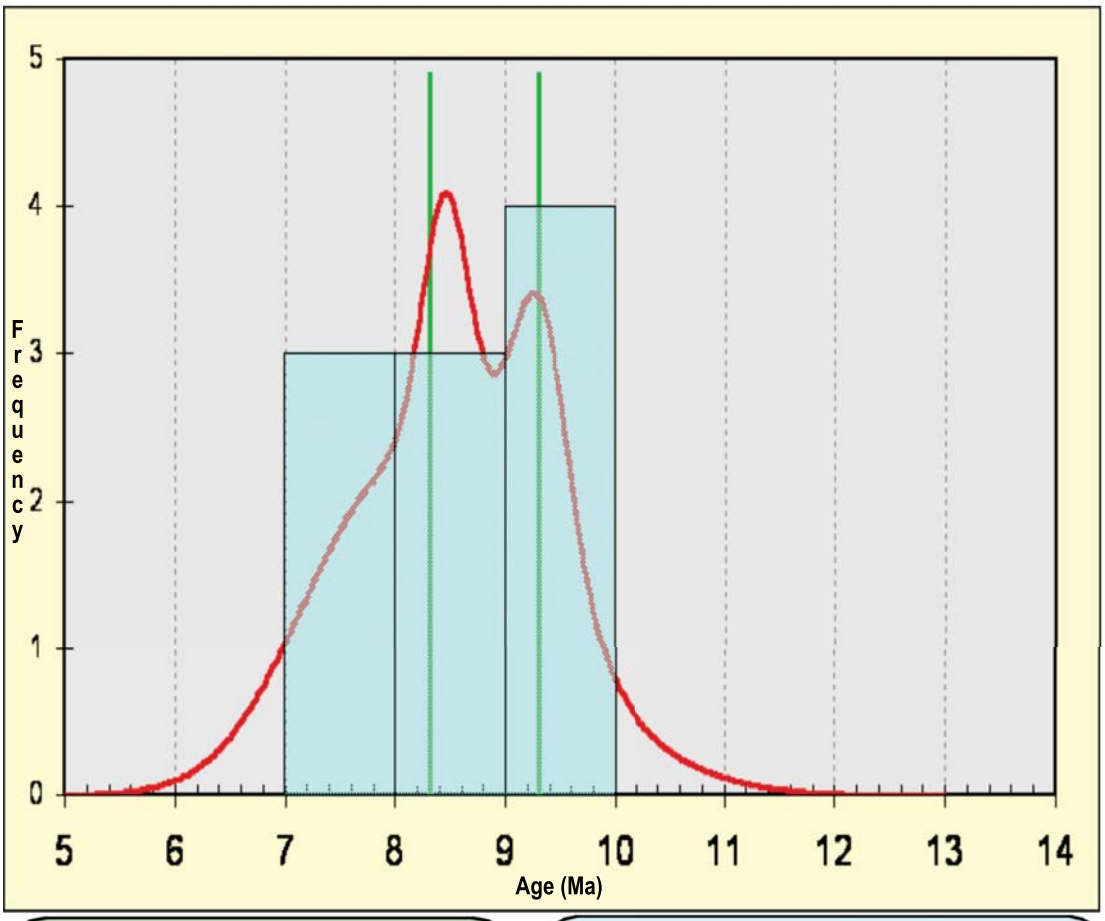

Sigma-Rho Matrix

	f1	t1	t2
f1	0.246	0.013	0.007
t1	0.013	.0848	0.005
t2	0.007	0.005	.0982

Age	±2σ	fraction	±2σ
8.314	0.17	0.60	0.49
9.298	0.2	0.40	---

relative misfit = 0.294

Figure C.14 continued

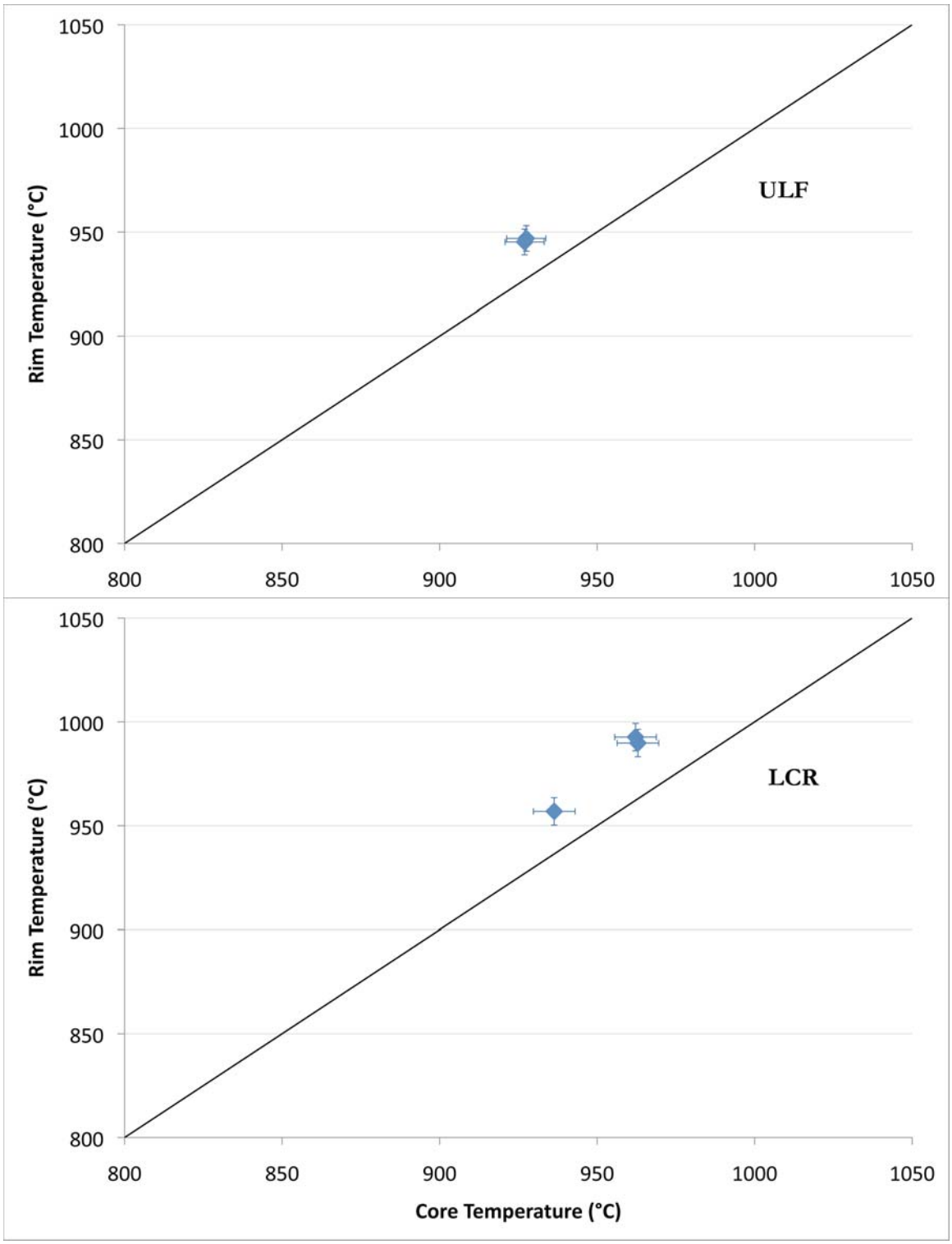

Figure D.1. Paired core-rim temperatures for zircons in lavas from the Bruneau-Jarbidge eruptive center: hotter rims than cores. Line represents 1:1 ratio.

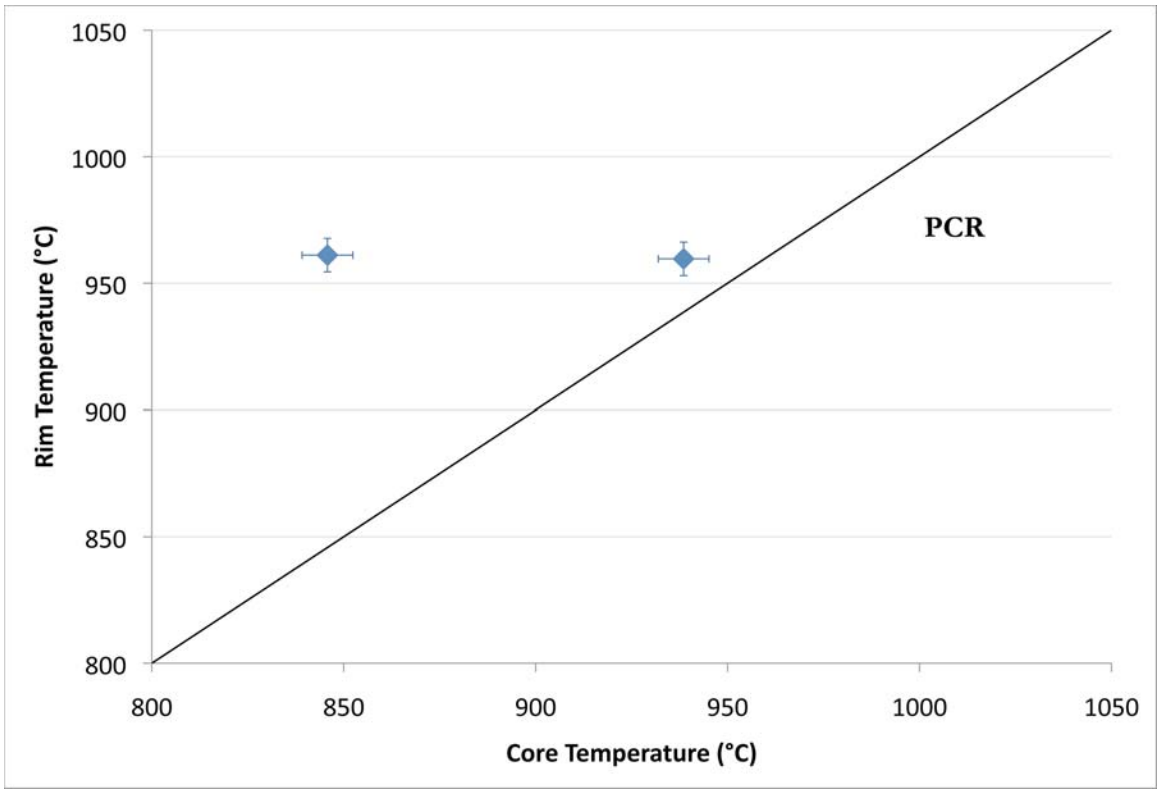

Figure D.1 continued

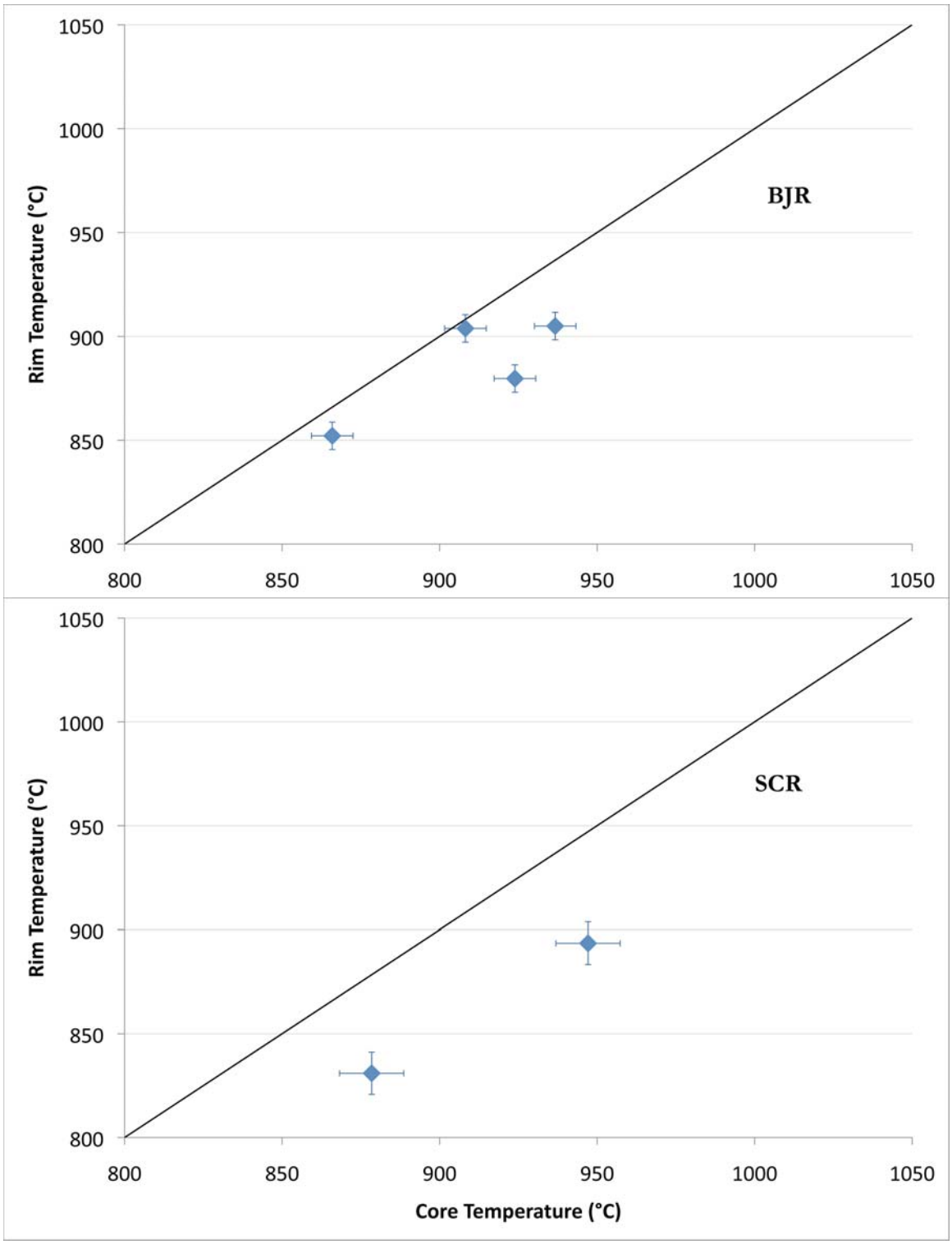

Figure D.2. Paired core-rim temperatures for zircons in lavas from the Bruneau-Jarbidge eruptive center: Hotter cores than rims. Line represents 1:1 ratio.

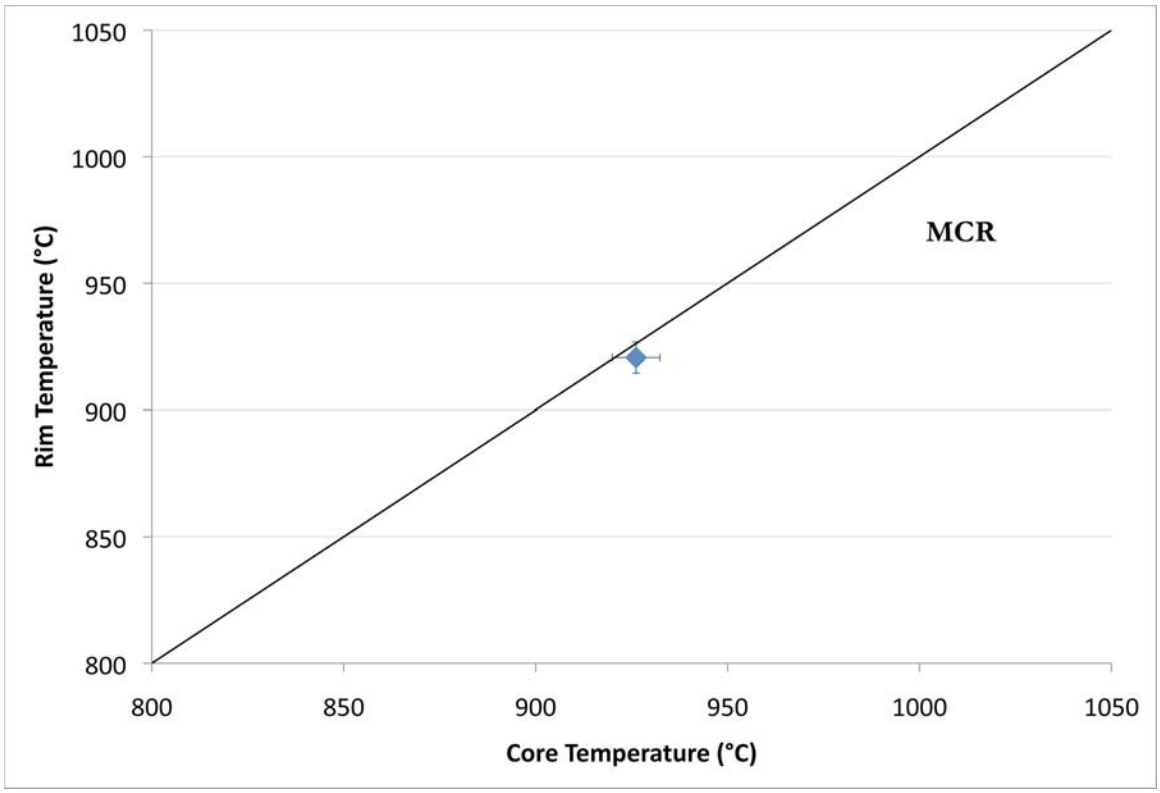

Figure D.3. Paired core-rim temperatures for zircons in lavas from the Bruneau-Jarbidge eruptive center: Cores temperatures within uncertainty of the rim temperatures. Line represents 1:1 ratio.

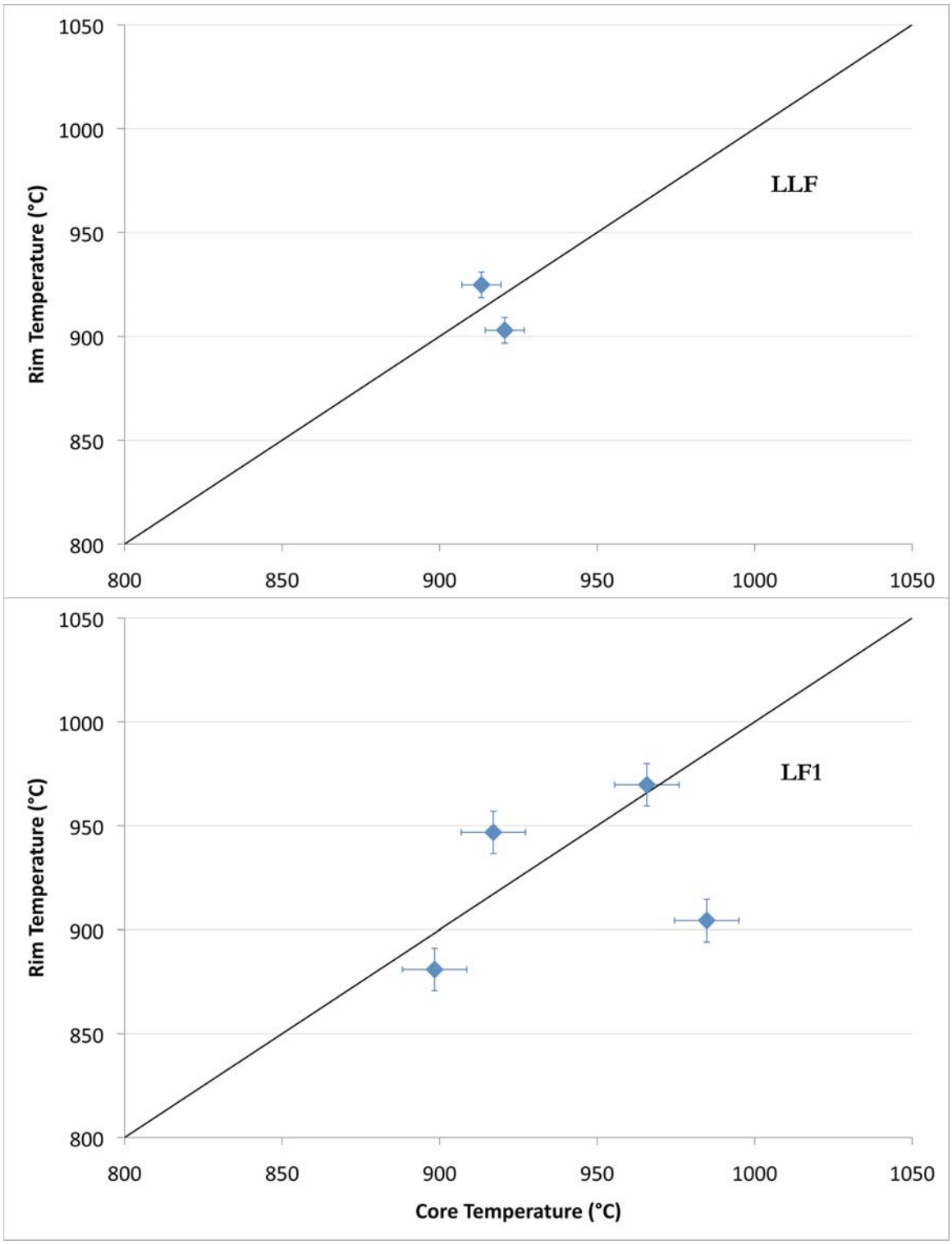

Figure D.4. Paired core-rim temperatures for zircons in lavas from the Bruneau-Jarbidge eruptive center: Ranging core and rim temperatures. Line represents 1:1 ratio.

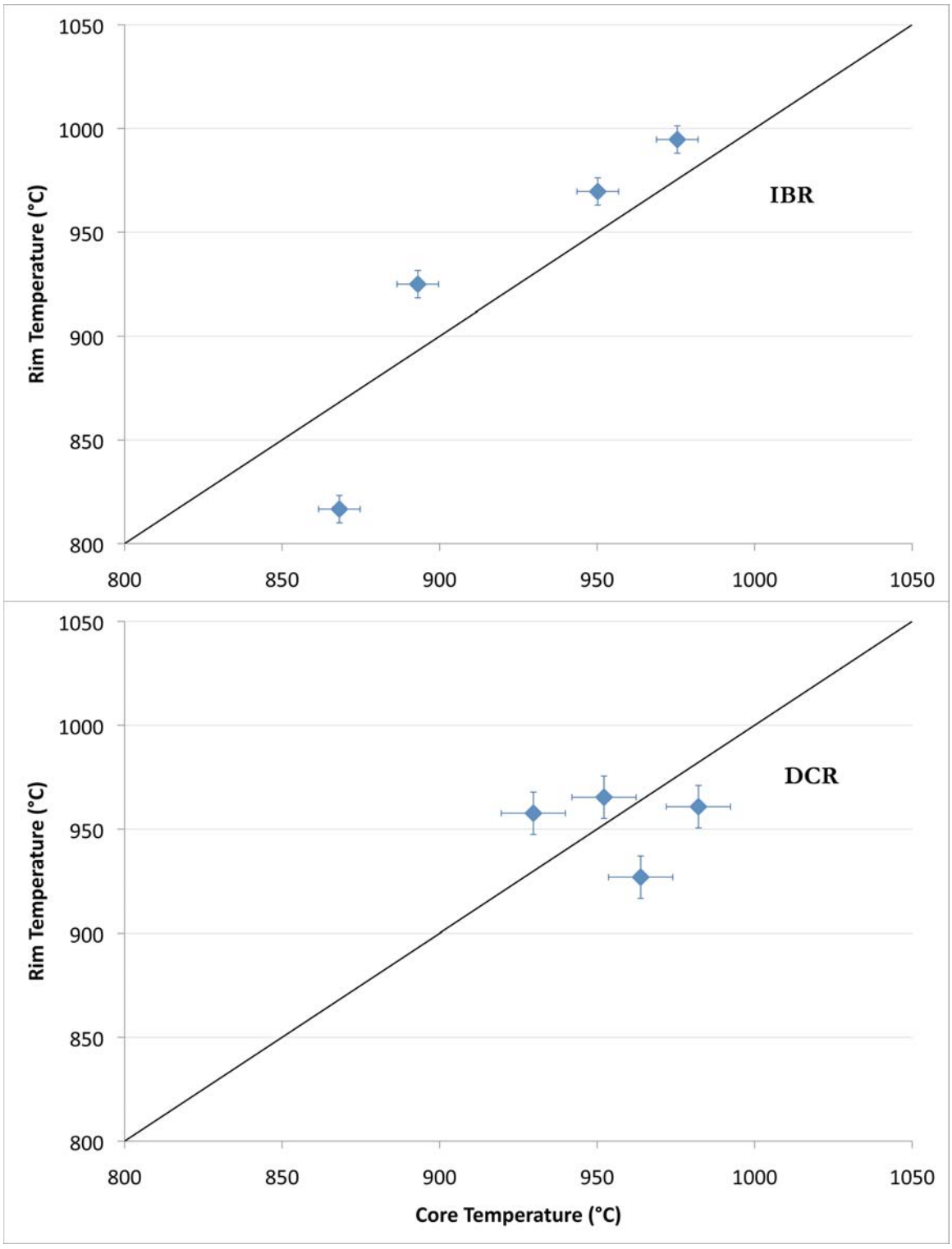

Figure D.4 continued

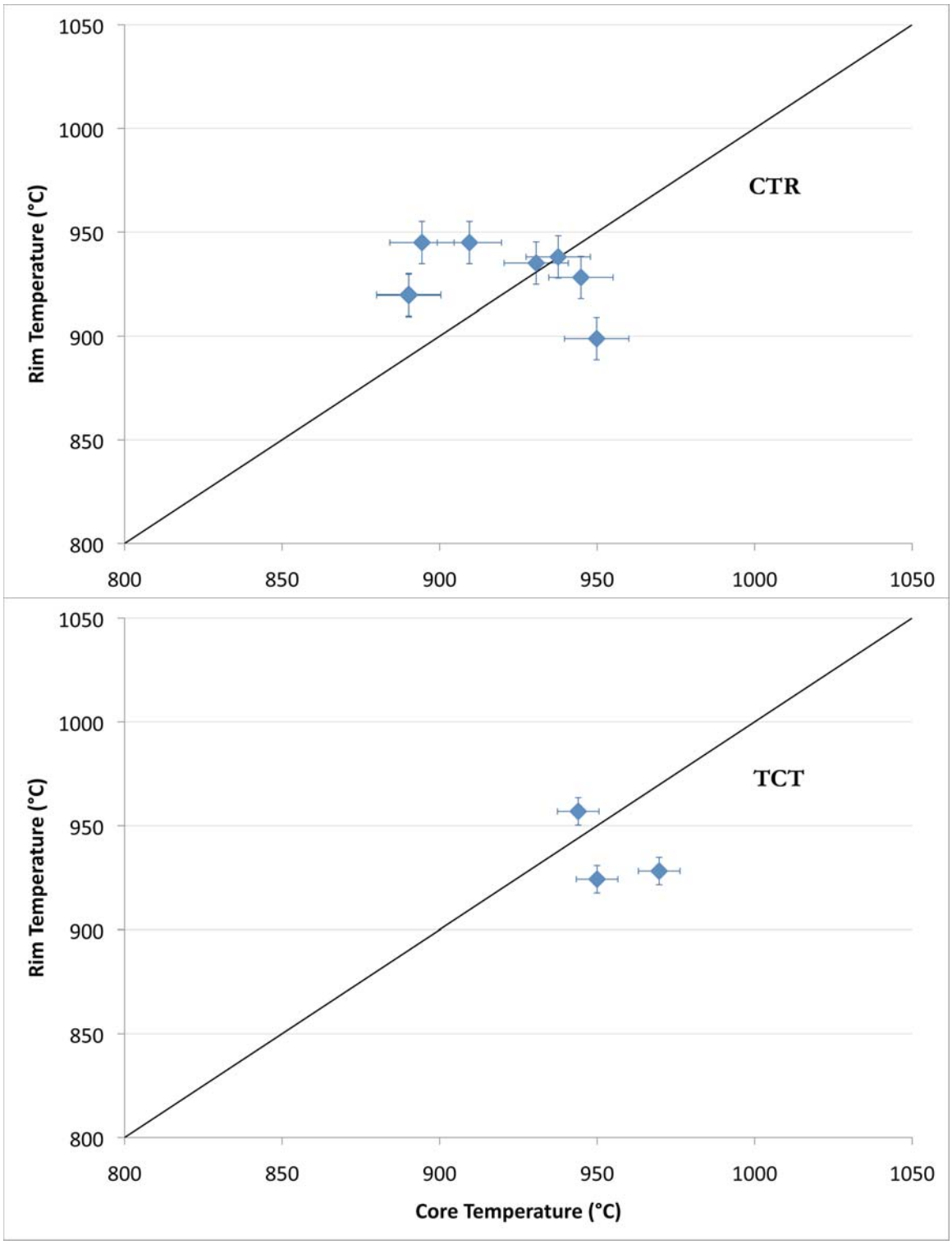

Figure D.4 continued

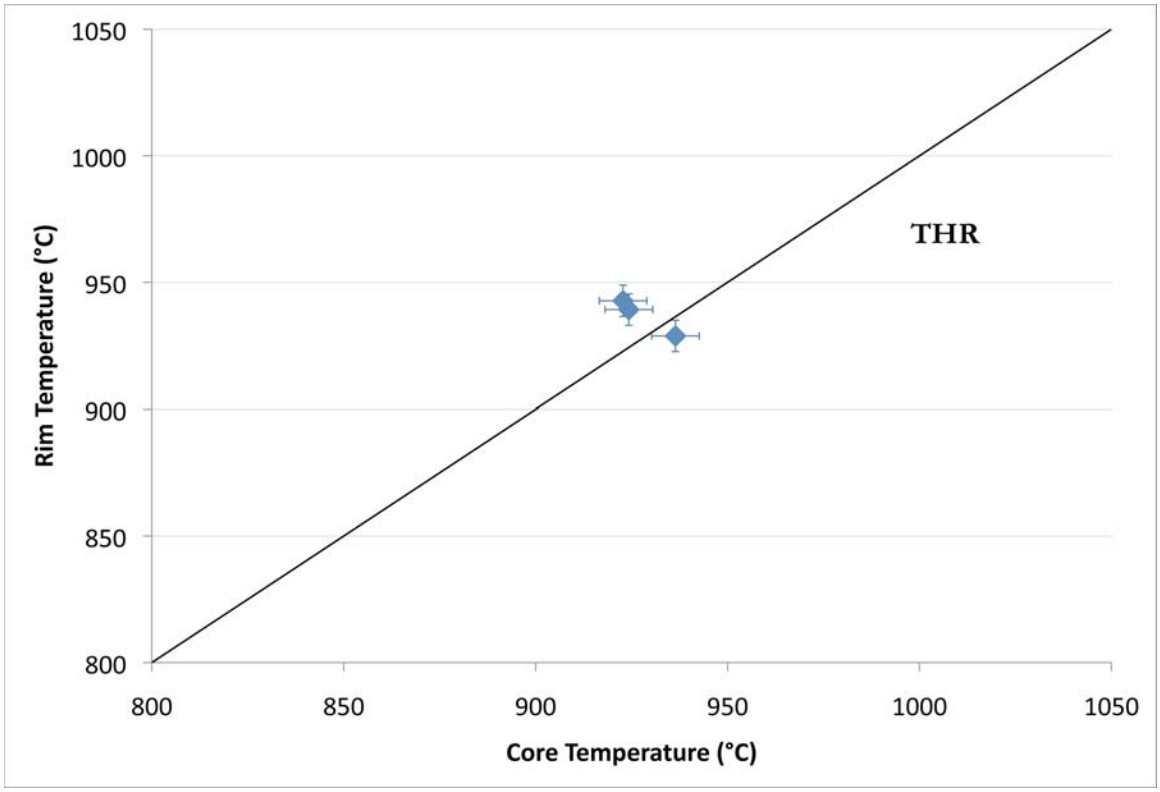

Figure D.4 continued

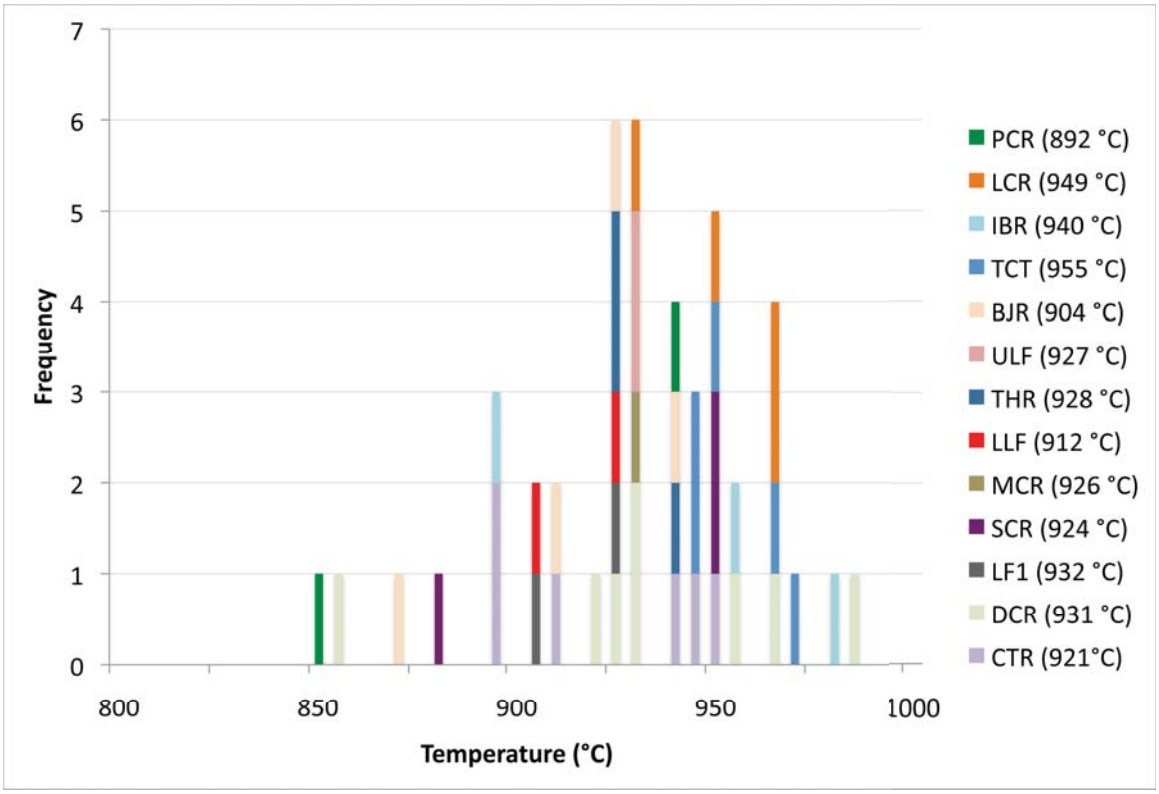

Figure D.5. Frequency of temperatures for cores of each unit from the rhyolite lavas of the BJEC.

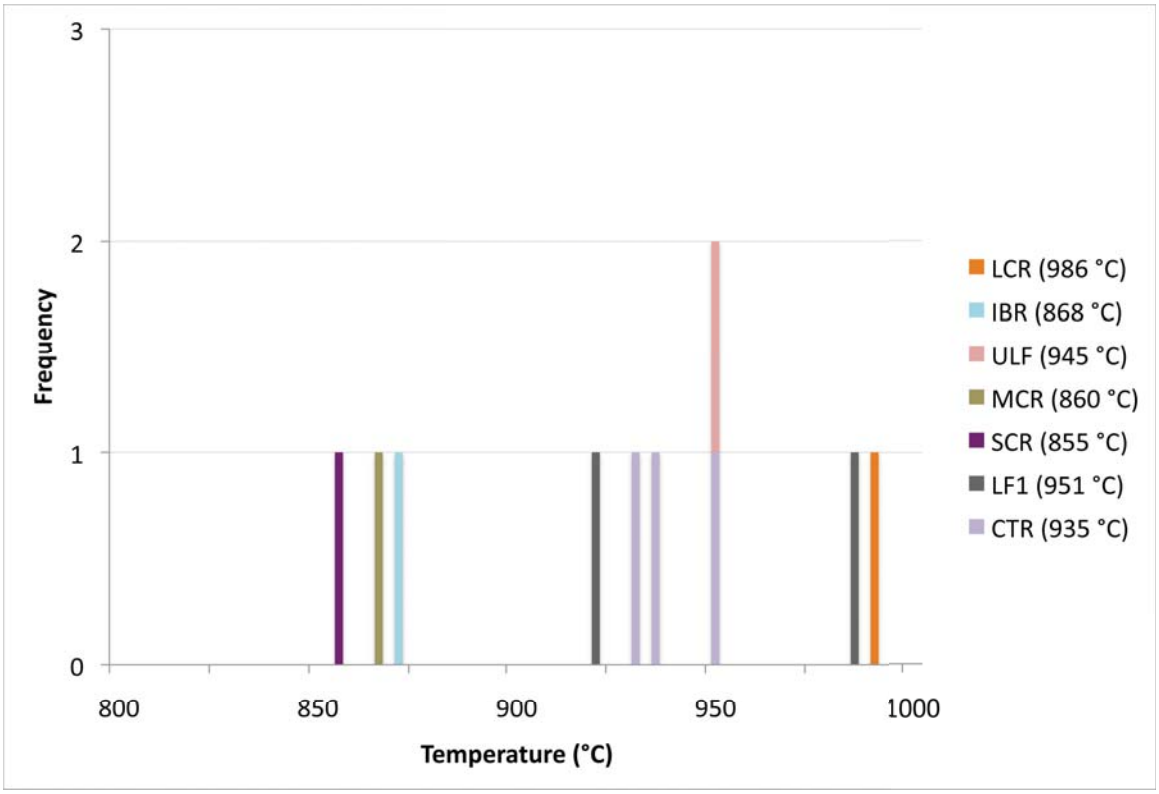

Figure D.6. Frequency of temperatures for interiors of each unit from the rhyolite lavas of the BJEC.

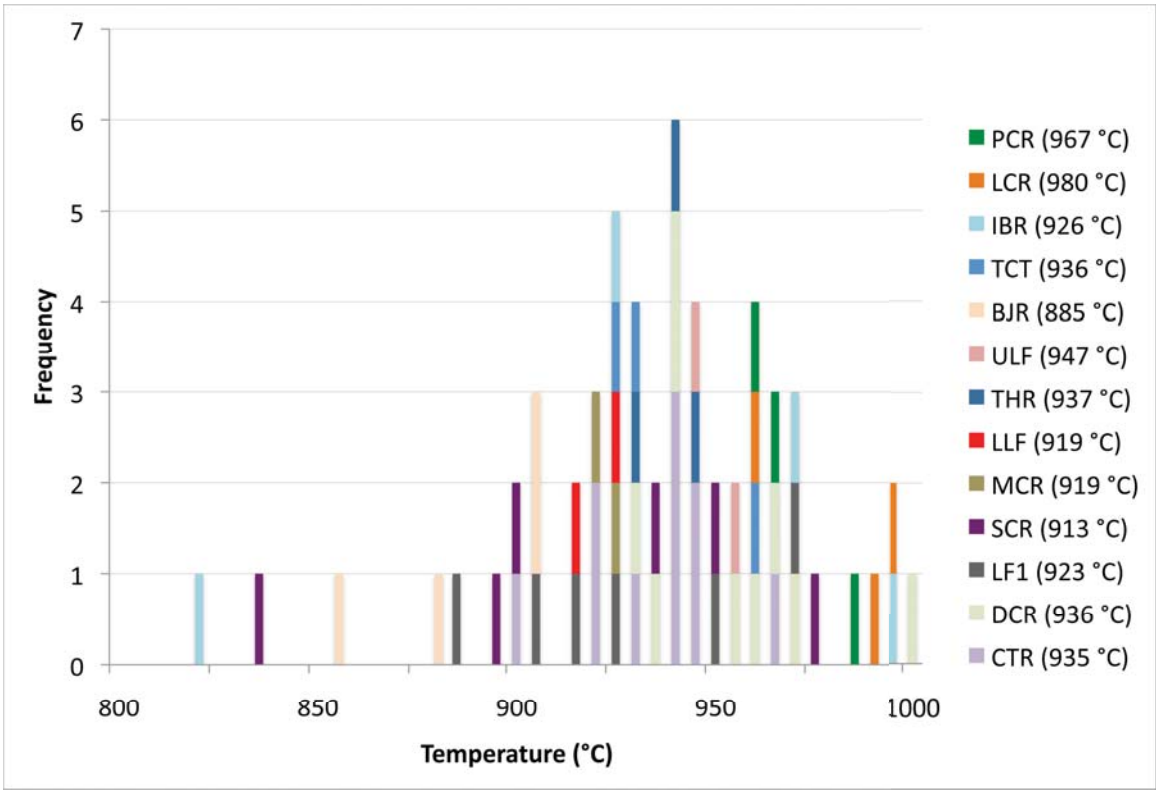

Figure D.7. Frequency of temperatures for rims of each unit from the rhyolite lavas of the BJEC.

Table E.1. EPMA analyses of melt inclusions in zircon from the CPT (H_2O by difference)

Sample Name	Notes	SiO_2	TiO_2	ZrO_2	Al_2O_3	FeO	MnO	MgO	CaO	BaO	Na_2O	K_2O	F	Cl	Sum	H_2O
CPTIII-41-1	growth in melt	76.9	0.07	0.05	12.8	0.41	0.00	0.02	0.33	0.03	2.98	6.32	0.10	0.07	100.0	0.0
CPTIII-31-1		77.7	0.07	0.13	12.1	0.24	0.02	0.00	0.24	0.02	2.63	5.94	0.18	0.07	99.3	0.7
CPTIII-53-1		77.1	0.15	0.09	12.2	0.43	0.00	0.01	0.27	0.00	2.60	6.07	0.12	0.07	99.1	0.9
CPTIII-26-1		75.6	0.05	0.08	12.4	0.33	0.00	0.00	0.04	0.00	3.04	6.26	0.36	0.06	98.2	1.8
CPTIII-59-1		76.1	0.04	0.38	11.9	0.56	0.01	0.00	0.29	0.00	2.61	5.80	0.22	0.12	98.1	1.9
Average CPT III		76.7	0.08	0.15	12.3	0.39	0.01	0.01	0.23	0.01	2.77	6.08	0.20	0.08	99.0	1.0
Standard Deviation		0.81	0.05	0.13	0.33	0.12	0.01	0.01	0.11	0.01	0.22	0.22	0.11	0.02	0.81	0.81
CPTV-17-1	growth in melt	77.0	0.29	0.19	11.9	0.79	0.00	0.00	0.01	0.03	3.05	6.12	0.05	0.09	99.5	0.5
CPTV-10-1	growth in melt	77.3	0.21	0.16	12.1	0.14	0.01	0.00	0.30	0.00	2.68	5.91	0.00	0.04	98.9	1.1
CPTV-47-1	growth in melt	76.6	0.21	0.38	11.7	0.42	0.00	0.00	0.09	0.00	3.06	6.20	0.09	0.06	98.8	1.2
CPTV-29-1	growth in melt	77.2	0.17	0.00	11.9	0.23	0.00	0.01	0.34	0.03	2.88	5.93	0.07	0.05	98.8	1.2
CPTV-47-2	growth in melt	76.8	0.17	0.00	13.2	0.13	0.04	0.00	0.36	0.00	2.51	5.28	0.03	0.06	98.6	1.4
CPTV-24-1		76.8	0.18	0.00	11.9	0.18	0.03	0.00	0.28	0.00	2.91	5.98	0.05	0.08	98.4	1.6
CPTV-24-3		77.7	0.13	0.00	12.0	0.15	0.00	0.00	0.30	0.03	1.91	5.93	0.00	0.07	98.2	1.8
CPTV-52-1		76.3	0.17	0.00	12.0	0.20	0.00	0.00	0.31	0.00	3.08	5.92	0.01	0.07	98.1	1.9
CPTV-15-1		76.3	0.19	0.00	12.0	0.16	0.00	0.01	0.33	0.00	2.80	5.96	0.06	0.05	97.8	2.2
CPTV-24-2		76.4	0.14	0.14	11.9	0.17	0.00	0.00	0.25	0.00	2.66	5.95	0.05	0.05	97.7	2.3
CPTV-29-2	growth in melt	75.9	0.16	0.14	11.9	0.20	0.04	0.01	0.55	0.03	2.72	5.93	0.01	0.04	97.6	2.4
CPTV-22-1		76.5	0.11	0.14	11.6	0.17	0.03	0.00	0.23	0.03	2.50	5.90	0.07	0.07	97.4	2.6

Any notes taken for the MI are shown in the notes column.

Table E.1 continued

Sample Name	Notes	SiO_2	TiO_2	ZrO_2	Al_2O_3	FeO	MnO	MgO	CaO	BaO	Na_2O	K_2O	F	Cl	Sum	H_2O
CPTV-17-2		75.5	0.15	1.13	11.6	0.12	0.00	0.00	0.23	0.00	2.66	5.88	0.05	0.06	97.4	2.6
Average CPT V		76.6	0.18	0.18	12.0	0.24	0.01	0.00	0.28	0.01	2.73	5.91	0.04	0.06	98.2	1.8
Standard Deviation		0.60	0.05	0.31	0.40	0.18	0.02	0.00	0.13	0.01	0.31	0.21	0.03	0.01	0.66	0.66
CPTVII-19-1	growth in melt	76.2	0.08	0.18	12.7	0.55	0.02	0.00	0.90	0.13	3.15	5.77	0.06	0.08	99.8	0.2
CPTVII-30-2	growth in melt	76.8	0.19	0.13	11.9	0.80	0.01	0.04	0.60	0.09	2.96	6.12	0.01	0.01	99.6	0.4
CPTVII-11-1		77.2	0.22	0.00	11.9	0.74	0.01	0.02	0.61	0.01	2.60	6.12	0.13	0.02	99.6	0.4
CPTVII-46-1	growth in melt	77.0	0.07	0.09	12.0	0.56	0.00	0.02	0.66	0.11	2.79	6.18	0.05	0.01	99.5	0.5
CPTVII-23-1		76.6	0.17	0.02	12.3	0.68	0.03	0.01	0.80	0.00	2.75	5.89	0.09	0.08	99.5	0.5
CPTVII-30-1	growth in melt	76.4	0.23	0.21	12.0	0.73	0.04	0.04	0.63	0.08	2.82	6.14	0.07	0.03	99.3	0.7
CPTVII-23-2		77.2	0.08	0.02	12.3	0.80	0.01	0.00	0.66	0.00	2.18	5.70	0.16	0.07	99.2	0.8
CPTVII-10-1		76.9	0.14	0.11	12.0	0.62	0.00	0.03	0.61	0.11	2.40	6.15	0.07	0.02	99.1	0.9
CPTVII-30-4		76.4	0.19	0.29	12.1	0.82	0.04	0.00	0.66	0.00	2.17	6.18	0.09	0.05	99.0	1.0
Average CPT VII		76.7	0.2	0.1	12.1	0.70	0.0	0.0	0.7	0.1	2.6	6.0	0.1	0.0	99.4	0.6
Standard Deviation		0.36	0.06	0.10	0.26	0.10	0.02	0.02	0.10	0.05	0.34	0.19	0.05	0.03	0.27	0.27
CPTIX-45-1	possible growth in melt	77.6	0.13	0.03	12.1	0.08	0.00	0.00	0.11	0.04	2.82	6.13	0.00	0.03	99.1	0.9
CPTIX-1-3		75.7	0.03	0.14	13.2	0.07	0.00	0.02	0.05	0.03	2.95	6.57	0.00	0.05	98.9	1.1
CPTIX-48-1	possible growth in melt	77.6	0.03	0.00	12.0	0.08	0.00	0.00	0.12	0.07	2.90	5.99	0.10	0.02	98.8	1.2

Table E.1 continued

Sample Name	Notes	SiO_2	TiO_2	ZrO_2	Al_2O_3	FeO	MnO	MgO	CaO	BaO	Na_2O	K_2O	F	Cl	Sum	H_2O
CPTIX-32-1	possible growth in melt	74.6	0.04	0.08	13.9	0.13	0.00	0.01	0.08	0.00	3.66	6.15	0.11	0.05	98.7	1.3
CPTIX-45-2		74.7	0.09	0.02	13.2	0.19	0.00	0.00	0.12	0.08	3.10	6.95	0.09	0.04	98.6	1.4
CPTIX-16-3		75.7	0.08	0.09	12.7	0.10	0.00	0.00	0.38	0.08	3.09	6.24	0.10	0.04	98.6	1.4
CPTIX-38-1	possible growth in melt	76.0	0.14	0.02	12.5	0.29	0.03	0.00	0.10	0.00	3.31	6.02	0.07	0.04	98.5	1.5
CPTIX-33-1	possible growth in melt	76.2	0.03	0.00	12.4	0.14	0.00	0.00	0.06	0.08	3.29	6.05	0.03	0.02	98.3	1.7
CPTIX-3-2		73.7	0.06	0.00	13.7	0.11	0.03	0.00	0.08	0.00	3.47	6.96	0.04	0.06	98.3	1.7
CPTIX-3-1	growth in melt	73.9	0.11	0.04	13.4	0.14	0.00	0.00	0.09	0.01	3.60	6.54	0.06	0.04	97.9	2.1
CPTIX-16-1-2	growth in melt	76.5	0.14	0.09	11.7	0.12	0.01	0.00	0.19	0.05	2.71	6.21	0.03	0.02	97.8	2.2
CPTIX-16-1-1	growth in melt	75.7	0.19	0.93	11.6	0.16	0.00	0.01	0.22	0.01	2.71	6.10	0.06	0.03	97.8	2.2
Average CPT IX		75.7	0.09	0.12	12.7	0.14	0.01	0.00	0.13	0.04	3.13	6.32	0.06	0.04	98.4	1.6
Standard Deviation		1.26	0.05	0.26	0.77	0.06	0.01	0.01	0.09	0.03	0.33	0.35	0.04	0.01	0.43	0.43
CPTX-6-1	growth in melt	77.6	0.03	0.01	11.8	0.34	0.02	0.00	0.17	0.03	3.07	6.04	0.11	0.04	99.3	0.7
CPTX-23-1	growth in melt	77.1	0.05	0.08	12.0	0.36	0.01	0.02	0.19	0.12	2.83	6.01	0.11	0.03	98.9	1.1
CPTX-47-2	growth in melt	77.2	0.06	0.13	11.9	0.37	0.01	0.00	0.15	0.11	2.94	5.99	0.00	0.03	98.9	1.1
CPTX-21-1	growth in melt	76.7	0.12	0.29	12.2	0.39	0.00	0.00	0.23	0.06	2.70	6.07	0.10	0.04	98.9	1.1
CPTX-47-1	growth in melt	76.7	0.02	0.07	12.3	0.31	0.01	0.00	0.20	0.14	2.88	5.97	0.12	0.05	98.8	1.2
CPTX-24-1		76.5	0.08	0.05	12.3	0.33	0.03	0.00	0.20	0.12	2.69	6.09	0.18	0.05	98.6	1.4
CPTX-34-1	growth in melt	77.8	0.03	0.07	12.1	0.27	0.00	0.01	0.16	0.01	2.05	5.95	0.12	0.03	98.6	1.4
CPTX-83-1	growth in melt	76.2	0.09	0.00	12.6	0.31	0.00	0.02	0.26	0.01	3.13	5.69	0.16	0.10	98.6	1.4

Table E.1 continued

Sample Name	Notes	SiO_2	TiO_2	ZrO_2	Al_2O_3	FeO	MnO	MgO	CaO	BaO	Na_2O	K_2O	F	Cl	Sum	H_2O
CPTX-47-4	growth in melt	77.0	0.00	0.17	11.8	0.38	0.02	0.00	0.28	0.06	2.74	5.92	0.00	0.02	98.3	1.7
CPTX-56-2		77.0	0.03	0.03	11.9	0.24	0.02	0.00	0.15	0.13	2.83	5.95	0.07	0.06	98.4	1.6
CPTX-32-1	growth in melt	76.2	0.05	0.11	12.4	0.32	0.00	0.00	0.20	0.09	2.69	6.15	0.08	0.06	98.4	1.6
CPTX-51-1		76.7	0.04	0.05	11.8	0.36	0.01	0.02	0.16	0.08	2.95	6.06	0.05	0.04	98.3	1.7
CPTX-56-1	growth in melt	74.4	0.02	0.44	12.2	1.27	0.00	0.09	0.72	0.02	2.99	5.91	0.08	0.06	98.2	1.8
CPTX-48-2		76.6	0.04	0.32	11.8	0.30	0.00	0.00	0.16	0.06	2.63	6.04	0.09	0.03	98.0	2.0
CPTX-49-1		76.7	0.03	0.06	11.8	0.27	0.00	0.00	0.16	0.06	2.85	5.91	0.08	0.06	97.9	2.1
CPTX-51-3		76.4	0.02	0.43	11.7	0.29	0.05	0.00	0.15	0.11	2.64	5.92	0.07	0.05	97.8	2.2
CPTX-48-1	growth in melt	75.0	0.06	0.19	11.9	0.76	0.00	0.01	0.02	0.07	3.27	6.26	0.21	0.05	97.8	2.2
CPTX-47-3	growth in melt	75.9	0.10	0.02	11.7	0.93	0.01	0.00	0.19	0.04	2.74	5.84	0.13	0.04	97.6	2.4
CPTX-51-2		76.1	0.02	0.02	11.9	0.32	0.00	0.00	0.19	0.07	2.77	6.03	0.12	0.05	97.6	2.4
CPTX-49-3		75.7	0.02	0.44	11.8	0.38	0.01	0.01	0.20	0.09	2.79	5.91	0.09	0.05	97.6	2.4
CPTX-49-2	growth in melt	76.2	0.04	0.03	11.8	0.40	0.01	0.01	0.19	0.11	2.60	5.94	0.07	0.04	97.5	2.5
Average CPT X		76.4	0.04	0.14	12.0	0.42	0.01	0.01	0.21	0.08	2.80	5.98	0.10	0.05	98.3	1.7
Standard Deviation		0.79	0.03	0.15	0.26	0.25	0.01	0.02	0.13	0.04	0.24	0.12	0.05	0.02	0.52	0.52
CPTXI-37-2	growth in melt	75.8	0.21	0.20	12.4	1.19	0.00	0.04	0.78	0.14	3.16	5.68	0.06	0.05	99.7	0.3
CPTXI-32-1	no growth	76.1	0.17	0.11	11.8	1.70	0.01	0.04	0.59	0.00	2.93	5.77	0.08	0.04	99.3	0.7
CPTXI-36-1	large trapped mineral in melt	76.0	0.17	0.09	12.3	1.17	0.03	0.03	0.71	0.05	2.50	5.84	0.09	0.03	99.0	1.0
CPTXI-29-2	growth in melt	75.5	0.21	0.48	11.8	1.73	0.00	0.04	0.63	0.02	2.59	5.70	0.11	0.05	98.9	1.1
CPTXI-29-1	no growth	75.9	0.22	0.11	11.8	1.66	0.01	0.07	0.65	0.01	2.37	5.80	0.16	0.03	98.7	1.3
CPTXI-26-1	no growth	75.7	0.24	0.41	12.1	1.17	0.03	0.02	0.58	0.03	2.44	5.84	0.08	0.07	98.7	1.3
CPTXI-42-1	no growth	74.6	0.24	0.14	12.3	1.49	0.01	0.02	0.66	0.07	2.89	5.92	0.01	0.05	98.3	1.7

Table E.1 continued

Sample Name	Notes	SiO_2	TiO_2	ZrO_2	Al_2O_3	FeO	MnO	MgO	CaO	BaO	Na_2O	K_2O	F	Cl	Sum	H_2O
CPTXI-18-1		76.6	0.14	0.04	11.9	0.43	0.00	0.00	0.23	0.02	2.97	6.02	0.09	0.04	98.5	1.5
CPTXI-5-1		77.9	0.00	0.08	11.6	0.07	0.00	0.02	0.25	0.08	2.67	5.67	0.10	0.05	98.5	1.5
CPTXI-42-2	no growth	75.5	0.19	0.27	11.7	1.15	0.02	0.05	0.63	0.02	2.79	5.73	0.11	0.04	98.1	1.9
CPTXI-17-1	no growth	76.0	0.15	0.04	11.7	1.10	0.01	0.04	0.66	0.00	2.47	5.65	0.07	0.04	97.9	2.1
CPTXI-43-1	growth in melt	74.1	0.19	0.48	11.9	1.62	0.01	0.03	0.62	0.00	2.57	6.17	0.12	0.04	97.8	2.2
CPTXI-11-1	no growth	75.2	0.26	0.09	12.0	1.07	0.04	0.04	0.55	0.07	2.73	5.74	0.03	0.04	97.9	2.1
CPTXI-25-2		75.7	0.25	0.15	11.9	0.65	0.01	0.04	0.22	0.07	2.59	5.91	0.12	0.03	97.7	2.3
CPTXI-6-1	growth in melt	75.1	0.21	0.22	11.6	1.18	0.03	0.01	0.53	0.05	2.85	5.67	0.02	0.03	97.6	2.4
CPTXI-11-3	no growth	75.0	0.22	0.08	11.7	1.16	0.00	0.05	0.62	0.03	2.74	5.77	0.11	0.06	97.6	2.4
CPTXI-11-2	no growth	74.5	0.14	0.07	11.9	1.04	0.01	0.05	0.55	0.06	3.11	5.90	0.03	0.04	97.4	2.6
CPTXI-25-1	growth in melt	74.6	0.17	0.01	12.0	0.98	0.04	0.04	0.55	0.03	2.97	5.74	0.05	0.04	97.2	2.8
CPTXI-12-1	growth in melt	74.2	0.23	0.02	11.9	1.42	0.00	0.04	0.62	0.07	2.67	5.74	0.07	0.05	97.0	3.0
Average CPT XI		75.5	0.19	0.16	11.9	1.16	0.01	0.04	0.56	0.04	2.74	5.80	0.08	0.04	98.2	1.8
Standard Deviation		0.91	0.06	0.15	0.22	0.43	0.01	0.02	0.16	0.03	0.23	0.13	0.04	0.01	0.74	0.74
CPTXII-24-1		77.3	0.11	0.05	12.2	0.45	0.00	0.00	0.30	0.11	2.99	6.19	0.02	0.02	99.7	0.3
CPTXII-15-1		76.9	0.29	0.10	12.2	0.13	0.01	0.00	0.37	0.00	2.76	5.97	0.00	0.03	98.7	1.3
CPTXII-43-1		74.6	0.02	0.40	12.7	0.85	0.02	0.06	0.45	0.12	2.92	5.89	0.08	0.03	98.2	1.8
Average CPT XII		76.3	0.1	0.2	12.4	0.48	0.0	0.0	0.4	0.1	2.9	6.0	0.0	0.0	98.9	1.1
Standard Deviation		1.41	0.14	0.19	0.31	0.36	0.01	0.04	0.08	0.07	0.12	0.16	0.04	0.01	0.79	0.79

Table E.1 continued

Sample Name	Notes	SiO_2	TiO_2	ZrO_2	Al_2O_3	FeO	MnO	MgO	CaO	BaO	Na_2O	K_2O	F	Cl	Sum	H_2O
CPTXIII-48-1	growth in melt	74.0	0.07	0.15	13.5	0.22	0.01	0.00	0.25	0.10	3.23	6.89	0.10	0.03	98.5	1.5
CPTXIII-43-1	growth in melt	76.1	0.21	0.00	11.7	0.77	0.05	0.03	0.59	0.00	2.69	6.06	0.00	0.04	98.2	1.8
CPTXIII-28-1		75.9	0.33	0.03	11.9	0.35	0.03	0.03	0.55	0.03	2.49	6.12	0.01	0.06	97.8	2.2
Average CPT XIII		75.3	0.20	0.06	12.4	0.44	0.03	0.02	0.46	0.04	2.80	6.36	0.04	0.05	98.2	1.8
Standard Deviation		1.19	0.13	0.08	1.01	0.29	0.02	0.01	0.19	0.05	0.38	0.46	0.05	0.02	0.36	0.36
CPTXVj-14-1	growth and trapped mineral in melt	76.8	0.26	0.30	12.1	0.21	0.02	0.00	0.19	0.02	2.92	5.87	0.07	0.04	98.8	1.2
CPTXVj-30-1		76.2	0.16	0.11	12.3	0.48	0.00	0.00	0.27	0.08	2.76	6.04	0.14	0.03	98.6	1.4
CPTXVj-25-1	growth in melt	76.3	0.33	0.00	12.4	0.17	0.00	0.00	0.29	0.11	2.84	6.02	0.03	0.03	98.5	1.5
CPTXVj-35-2		75.9	0.10	0.28	12.2	0.14	0.00	0.00	0.23	0.08	3.04	6.03	0.00	0.03	98.1	1.9
CPTXVj-14-2		76.5	0.27	0.10	12.0	0.15	0.02	0.00	0.27	0.01	2.76	5.79	0.14	0.04	98.0	2.0
Average CPT XVj		76.3	0.22	0.16	12.2	0.23	0.01	0.00	0.25	0.06	2.86	5.95	0.08	0.03	98.4	1.6
Standard Deviation		0.33	0.09	0.13	0.16	0.14	0.01	0.00	0.04	0.05	0.12	0.12	0.06	0.01	0.33	0.33
CPTXVb-9-1	growth in melt	75.1	0.26	0.13	11.9	1.57	0.02	0.00	0.36	0.10	3.34	5.93	0.00	0.04	98.8	1.2
CPTXVb-72-1		76.7	0.19	0.13	12.4	0.17	0.03	0.00	0.43	0.04	2.78	5.91	0.06	0.03	98.9	1.1
CPTXVb-6-1		77.0	0.29	0.16	12.1	0.12	0.00	0.00	0.32	0.04	2.53	6.00	0.00	0.02	98.6	1.4

Table E.1 continued

Sample Name	Notes	SiO_2	TiO_2	ZrO_2	Al_2O_3	FeO	MnO	MgO	CaO	BaO	Na_2O	K_2O	F	Cl	Sum	H_2O
CPTXVb-34-1		77.0	0.24	0.05	12.1	0.14	0.00	0.00	0.38	0.02	2.37	6.18	0.02	0.01	98.5	1.5
CPTXVb-59-3		76.8	0.29	0.05	12.1	0.14	0.00	0.01	0.35	0.10	2.56	5.92	0.08	0.04	98.4	1.6
CPTXVb-48-1		75.7	0.26	0.41	12.3	0.47	0.00	0.00	0.05	0.12	2.82	6.10	0.08	0.03	98.3	1.7
CPTXVb-59-1		76.3	0.10	0.09	12.2	0.44	0.00	0.00	0.03	0.03	2.95	5.98	0.05	0.04	98.2	1.8
CPTXVb-1-1		77.1	0.23	0.12	12.2	0.16	0.01	0.01	0.35	0.03	1.75	6.05	0.14	0.05	98.3	1.7
CPTXVb-59-2		76.8	0.21	0.09	12.1	0.08	0.00	0.00	0.37	0.03	2.09	6.05	0.01	0.02	97.8	2.2
CPTXVb-3-1		75.7	0.18	0.24	12.3	0.16	0.02	0.00	0.42	0.19	2.80	5.61	0.10	0.04	97.8	2.2
CPTXVb-62-1		75.8	0.30	0.47	12.1	0.15	0.02	0.01	0.37	0.08	2.56	5.70	0.07	0.03	97.7	2.3
CPTXVb-62-2		76.1	0.26	0.06	12.1	0.12	0.00	0.00	0.29	0.03	2.40	6.10	0.09	0.04	97.6	2.4
Average CPT XVb		76.4	0.23	0.17	12.2	0.31	0.01	0.00	0.31	0.07	2.58	5.96	0.06	0.03	98.2	1.8
Standard Deviation		0.65	0.06	0.14	0.14	0.42	0.01	0.00	0.13	0.05	0.41	0.17	0.04	0.01	0.43	0.43
Total Average		76.2	0.14	0.15	12.1	0.50	0.01	0.01	0.34	0.05	2.78	6.00	0.08	0.04	98.4	1.6
Standard Deviation		0.94	0.09	0.18	0.45	0.44	0.01	0.02	0.21	0.04	0.32	0.25	0.06	0.02	9.63	0.65

Table E.2. EPMA analyses of melt inclusions in zircon from BJEC lavas (H_2O by difference)

Sample Name	Notes	SiO_2	TiO_2	ZrO_2	Al_2O_3	FeO	MnO	MgO	CaO	BaO	Na_2O	K_2O	F	Cl	Sum	H_2O
LF1-68-1	possible growth in melt	77.9	0.18	0.09	10.9	1.38	0.03	0.02	0.41	0.07	2.62	5.73	0.10	0.03	99.5	0.5
LF1-52-2	growth in melt	75.4	0.44	0.07	11.6	1.55	0.03	0.13	1.19	0.00	2.60	5.70	0.01	0.03	98.7	1.3
LF1-81-1	growth in melt	76.1	0.32	0.16	12.1	0.89	0.01	0.00	0.30	0.03	2.41	5.98	0.08	0.02	98.3	1.7
LF1-72-1	no growth	73.8	0.30	0.24	12.4	1.16	0.05	0.17	0.76	0.03	2.41	6.65	0.12	0.03	98.1	1.9
LF1-50-1	possible growth in melt	72.0	0.21	0.07	13.0	1.83	0.02	0.17	0.79	0.06	2.81	6.63	0.12	0.03	97.8	2.2
LF1-34-1	growth in melt	76.7	0.16	0.00	10.3	1.72	0.03	0.08	0.52	0.05	2.43	5.35	0.09	0.01	97.5	2.5
LF1-64-1	no growth	73.5	0.32	0.12	11.9	1.89	0.05	0.11	0.98	0.09	2.70	5.70	0.02	0.02	97.5	2.5
LF1-75-4	no growth	72.0	0.35	0.10	12.8	1.81	0.06	0.12	1.01	0.05	2.75	6.38	0.07	0.01	97.5	2.5
LF1-57-1	growth in melt	73.1	0.38	0.10	11.7	2.01	0.06	0.09	0.86	0.06	2.14	6.45	0.08	0.01	97.0	3.0
LF1-61-1	no growth	74.5	0.10	0.03	11.7	1.68	0.01	0.08	0.71	0.06	2.19	5.96	0.02	0.03	97.0	3.0
LF1-57-2	growth in melt	72.9	0.37	0.32	11.7	1.98	0.04	0.14	0.80	0.08	2.14	6.19	0.11	0.02	96.8	3.2
LF1-71-1	growth in melt	73.4	0.36	0.12	11.7	1.79	0.02	0.10	0.69	0.00	2.05	6.37	0.11	0.01	96.7	3.3
LF1-8-1		75.7	0.18	0.00	11.0	0.86	0.00	0.07	0.42	0.08	2.62	5.58	0.05	0.03	96.6	3.4
LF1-37-1	growth in melt	72.9	0.13	0.31	11.9	1.89	0.05	0.01	0.36	0.05	2.63	5.63	0.11	0.04	96.0	4.0
Average LF2		74.3	0.27	0.12	11.8	1.60	0.03	0.09	0.70	0.05	2.46	6.02	0.08	0.02	97.5	2.5
Standard Deviation		1.81	0.11	0.10	0.70	0.39	0.02	0.05	0.27	0.03	0.25	0.42	0.04	0.01	0.93	0.93
LLF-24-1	growth in melt	75.3	0.11	0.00	11.9	2.60	0.03	0.03	1.03	0.03	2.64	5.60	0.03	0.03	99.4	0.6

Any notes taken for the MI are shown in the notes column.

Table E.2 continued

Sample Name	Notes	SiO_2	TiO_2	ZrO_2	Al_2O_3	FeO	MnO	MgO	CaO	BaO	Na_2O	K_2O	F	Cl	Sum	H_2O
LLF-37-1	growth in melt	76.4	0.02	0.07	11.7	2.19	0.05	0.03	0.69	0.06	2.58	5.61	0.12	0.04	99.6	0.4
LLF-59-1	no growth	76.3	0.14	0.07	12.2	1.89	0.02	0.01	0.35	0.01	2.68	5.86	0.06	0.05	99.6	0.4
LLF-60-1	growth in melt	77.6	0.06	0.11	12.9	0.13	0.01	0.00	0.44	0.10	2.69	5.81	0.08	0.03	99.9	0.1
LLF-60-2		77.0	0.09	0.10	12.4	0.42	0.02	0.00	0.27	0.06	2.26	6.00	0.00	0.02	98.6	1.4
Average LLF		76.5	0.08	0.07	12.2	1.45	0.03	0.01	0.56	0.05	2.57	5.77	0.06	0.03	99.4	0.6
Standard Deviation		0.85	0.04	0.04	0.45	1.10	0.01	0.02	0.31	0.03	0.18	0.17	0.04	0.01	0.49	0.49
ULF-7-1		76.0	0.24	0.18	12.1	0.62	0.03	0.00	0.29	0.01	2.45	5.99	0.05	0.03	98.1	1.9
ULF-43-1		77.7	0.16	0.02	12.2	0.26	0.00	0.01	0.26	0.05	2.45	6.27	0.15	0.04	99.5	0.5
ULF-47-1		76.8	0.06	0.17	11.9	0.29	0.02	0.00	0.22	0.05	2.44	5.94	0.09	0.02	98.0	2.0
ULF-49-2		77.1	0.33	0.12	11.8	0.72	0.03	0.00	0.23	0.00	2.47	6.03	0.13	0.05	99.0	1.0
ULF-49-3		76.9	0.17	0.19	12.5	0.24	0.01	0.01	0.26	0.13	2.49	6.02	0.08	0.03	99.1	0.9
ULF-55-1	growth in melt	76.5	0.22	0.05	12.0	0.34	0.00	0.00	0.20	0.06	1.69	6.49	0.04	0.02	97.6	2.4
ULF-55-2	growth in melt	76.0	0.14	0.13	12.0	0.61	0.00	0.00	0.18	0.00	1.63	6.46	0.05	0.04	97.3	2.7
ULF-57-1	growth in melt	76.3	0.31	0.00	12.1	0.77	0.01	0.01	0.27	0.03	1.70	6.68	0.08	0.05	98.4	1.6
ULF-57-2		77.4	0.21	0.00	12.1	0.41	0.01	0.00	0.24	0.02	2.53	5.97	0.07	0.04	99.1	0.9
Average ULF		76.8	0.20	0.10	12.1	0.47	0.01	0.00	0.24	0.04	2.20	6.21	0.08	0.04	98.4	1.6
Standard Deviation		0.59	0.08	0.08	0.21	0.21	0.01	0.00	0.04	0.04	0.40	0.28	0.04	0.01	0.75	0.75
THR-10-1	growth in melt	74.6	0.17	0.00	11.9	2.71	0.05	0.04	0.84	0.10	2.65	5.70	0.06	0.03	98.8	1.2

Table E.2 continued

Sample Name	Notes	SiO_2	TiO_2	ZrO_2	Al_2O_3	FeO	MnO	MgO	CaO	BaO	Na_2O	K_2O	F	Cl	Sum	H_2O
THR-10-2	growth in melt	74.6	0.17	0.18	11.8	2.49	0.02	0.04	0.94	0.10	2.46	5.44	0.07	0.02	98.3	1.7
THR-17-1	growth in melt	75.4	0.35	0.00	11.8	2.80	0.06	0.01	0.66	0.08	2.25	5.64	0.08	0.03	99.1	0.9
THT-17-2	no growth	75.8	0.28	0.03	12.1	1.53	0.02	0.03	0.81	0.08	2.59	5.84	0.07	0.03	99.2	0.8
THR-17-3	possible growth in melt	75.6	0.35	0.01	12.3	1.53	0.04	0.00	0.86	0.07	2.17	6.02	0.06	0.02	99.0	1.0
THR-21-1	no growth	75.6	0.17	0.12	11.9	2.55	0.05	0.02	0.93	0.11	2.48	5.32	0.07	0.02	99.3	0.7
THR-22-1	growth in melt	76.1	0.24	0.00	11.9	1.74	0.06	0.03	0.75	0.07	2.23	5.70	0.14	0.02	98.9	1.1
THR-22-2	growth in melt	76.2	0.15	0.05	11.7	1.68	0.03	0.02	0.81	0.11	2.44	5.73	0.08	0.03	99.0	1.0
THR-22-3	growth in melt	75.3	0.33	0.01	11.8	1.66	0.05	0.01	0.81	0.13	2.53	5.53	0.12	0.03	98.3	1.7
THR-25-1	no growth	75.2	0.07	0.09	11.8	2.68	0.06	0.02	0.79	0.08	2.41	5.59	0.14	0.03	98.9	1.1
THR-27-1	growth in melt	74.0	0.29	0.27	11.6	2.97	0.02	0.03	0.70	0.07	2.41	5.52	0.06	0.04	98.1	1.9
THR-63-1		76.6	0.28	0.00	12.1	1.98	0.06	0.01	0.86	0.08	2.48	5.48	0.04	0.02	100.0	0.0
THR-61-1	growth in melt	76.4	0.13	0.13	11.9	2.26	0.02	0.04	0.65	0.11	2.50	5.55	0.07	0.03	99.8	0.2
THR-61-2	no growth	75.5	0.10	0.15	12.1	2.21	0.00	0.02	0.62	0.05	2.67	5.58	0.12	0.04	99.2	0.8
THR-63-1	growth in melt	74.7	0.10	0.15	12.0	2.85	0.03	0.02	0.87	0.03	2.34	5.54	0.11	0.05	98.8	1.2
THR-63-2	growth in melt	74.9	0.12	0.00	11.8	2.60	0.06	0.02	0.80	0.12	2.29	5.59	0.07	0.03	98.5	1.5
THR-63-3	growth in melt	75.1	0.36	0.16	12.0	2.47	0.01	0.00	0.56	0.07	2.20	5.54	0.08	0.04	98.6	1.4
Average THR		75.4	0.22	0.08	11.9	2.28	0.04	0.02	0.78	0.09	2.42	5.61	0.08	0.03	98.9	1.1
Standard Deviation		0.70	0.10	0.08	0.17	0.50	0.02	0.01	0.11	0.03	0.15	0.16	0.03	0.01	0.51	0.51
MCR-15-1	growth in melt	75.2	0.10	0.12	12.1	1.25	0.00	0.00	0.37	0.07	2.82	5.96	0.07	0.03	98.1	1.9
MCR-20-1	growth in melt	75.8	0.10	0.31	12.0	1.15	0.02	0.00	0.86	0.11	2.35	5.59	0.14	0.04	98.4	1.6

Table E.2 continued

Sample Name	Notes	SiO_2	TiO_2	ZrO_2	Al_2O_3	FeO	MnO	MgO	CaO	BaO	Na_2O	K_2O	F	Cl	Sum	H_2O
MCR-21-1	no growth	75.2	0.08	0.00	12.2	2.22	0.00	0.00	0.40	0.11	2.29	5.70	0.11	0.04	98.3	1.7
MCR-26-1		76.3	0.35	0.13	12.5	0.55	0.01	0.00	0.26	0.06	2.69	5.97	0.09	0.04	98.9	1.1
MCR-28-1	no growth	76.1	0.04	0.02	12.0	1.56	0.02	0.00	0.24	0.18	2.64	5.72	0.09	0.04	98.7	1.3
MCR-30-1	no growth	75.5	0.06	0.00	11.7	1.57	0.03	0.00	0.27	0.12	2.88	5.63	0.13	0.05	97.9	2.1
MCR-33-1	growth in melt	75.7	0.13	0.01	12.1	1.82	0.01	0.01	0.35	0.08	2.42	5.76	0.10	0.03	98.5	1.5
MCR-33-2	growth in melt	76.6	0.41	0.00	12.0	1.49	0.00	0.00	0.70	0.00	2.42	5.57	0.08	0.05	99.3	0.7
MCR-34-1	growth in melt	76.4	0.08	0.02	12.5	0.60	0.01	0.01	0.33	0.24	2.48	5.49	0.05	0.06	98.3	1.7
MCR-38-1	growth in melt	76.2	0.23	0.00	11.6	1.45	0.00	0.03	0.32	0.00	2.52	6.22	0.13	0.02	98.7	1.3
MCR-38-2	growth in melt	75.4	0.23	0.00	11.8	1.18	0.01	0.02	0.41	0.00	2.69	6.45	0.15	0.04	98.3	1.7
MCR-38-3	growth in melt	75.6	0.20	0.07	11.9	1.14	0.03	0.00	0.36	0.00	2.48	6.35	0.04	0.05	98.3	1.7
MCR-39-1	growth in melt	75.3	0.29	0.02	12.0	2.84	0.00	0.02	0.06	0.09	2.65	5.78	0.10	0.02	99.2	0.8
MCR-40-1		76.3	0.13	0.01	12.4	0.64	0.02	0.00	0.68	0.11	2.25	5.99	0.02	0.06	98.6	1.4
MCR-51-1	growth in melt	74.5	0.13	0.12	12.0	1.80	0.03	0.00	0.43	0.04	2.67	5.76	0.08	0.03	97.6	2.4
MCR-64-1	growth in melt	76.2	0.20	0.03	12.0	2.02	0.04	0.01	0.48	0.12	2.32	5.71	0.07	0.03	99.3	0.7
MCR-64-2	growth in melt	76.3	0.14	0.00	11.8	1.50	0.01	0.00	0.40	0.11	2.40	5.83	0.07	0.03	98.6	1.4
MCR-72-1	growth in melt	75.9	0.20	0.06	11.8	2.43	0.07	0.00	0.41	0.00	2.30	5.64	0.08	0.05	98.9	1.1
MCR-72-2	growth in melt	75.6	0.11	0.00	11.8	3.25	0.04	0.01	0.44	0.05	2.23	5.49	0.10	0.07	99.1	0.9
MCR-72-3	growth in melt	76.3	0.19	0.28	12.2	0.92	0.00	0.01	0.27	0.00	2.36	5.84	0.10	0.06	98.5	1.5
MCR-76-1	growth in melt	76.5	0.20	0.00	11.9	1.36	0.02	0.00	0.55	0.07	2.44	5.87	0.07	0.03	98.9	1.1
MCR-76-2	growth in melt	76.4	0.16	0.03	12.0	1.43	0.03	0.01	0.59	0.11	2.52	5.84	0.09	0.03	99.2	0.8
MCR-90-1	growth in melt	75.4	0.20	0.12	11.9	2.19	0.07	0.01	0.39	0.19	2.51	5.84	0.08	0.04	99.0	1.0
MCR-90-2	growth in melt	75.4	0.26	0.07	11.9	2.81	0.05	0.00	0.48	0.16	2.59	6.02	0.08	0.04	99.8	0.2
MCR-90-3	growth in melt	74.6	0.29	0.00	11.9	3.10	0.05	0.02	0.45	0.14	2.64	5.91	0.06	0.06	99.3	0.7

Table E.2 continued

Average MCR		75.8	0.18	0.06	12.0	1.69	0.02	0.01	0.42	0.09	2.50	5.84	0.09	0.04	98.7	1.3
Standard Deviation		0.58	0.09	0.08	0.22	0.76	0.02	0.01	0.17	0.07	0.18	0.24	0.03	0.01	0.51	0.51

Sample Name	**Notes**	**SiO_2**	**TiO_2**	**ZrO_2**	**Al_2O_3**	**FeO**	**MnO**	**MgO**	**CaO**	**BaO**	**Na_2O**	**K_2O**	**F**	**Cl**	**Sum**	**H_2O**
CTR-51-1	growth in melt	74.5	0.33	0.06	11.3	2.10	0.04	0.05	0.41	0.00	2.74	6.39	0.09	0.03	98.0	2.0
CTR-51-2	growth in melt	74.2	0.35	0.18	11.3	2.06	0.00	0.06	0.32	0.00	2.97	6.34	0.09	0.02	97.9	2.1
CTR-82-1		75.7	0.35	0.13	11.9	0.39	0.05	0.02	0.43	0.00	2.42	6.18	0.12	0.03	97.8	2.2
CTR-4-1		75.9	0.21	0.00	11.6	0.59	0.00	0.02	0.48	0.10	2.92	5.84	0.07	0.04	97.7	2.3
CTR-43-1		75.1	0.24	0.14	11.5	0.74	0.01	0.02	0.72	0.06	2.92	5.79	0.07	0.02	97.3	2.7
CTR-69-1		74.8	0.28	0.06	12.0	0.48	0.00	0.00	0.48	0.12	2.90	5.72	0.10	0.04	97.1	2.9
CTR-82-2		74.9	0.17	0.10	12.0	0.36	0.01	0.00	0.58	0.01	2.45	6.27	0.04	0.04	96.9	3.1
CTR-41-1		74.8	0.25	0.09	11.7	0.54	0.01	0.00	0.58	0.01	2.68	5.79	0.08	0.03	96.6	3.4
CTR-45-1		74.7	0.28	0.02	12.1	0.24	0.00	0.00	0.51	0.03	2.56	5.89	0.11	0.02	96.5	3.5
CTR-40-1		74.4	0.21	0.27	11.8	0.39	0.01	0.00	0.46	0.07	2.54	5.93	0.12	0.04	96.2	3.8
CTR-69-2		75.3	0.24	0.14	12.1	0.21	0.01	0.00	0.42	0.07	1.74	5.57	0.01	0.03	95.9	4.1
CTR-70-1	no growth	72.5	0.28	0.12	11.4	1.69	0.03	0.07	0.48	0.00	1.94	6.25	0.00	0.02	94.8	5.2
Average CTR		74.7	0.27	0.11	11.7	0.82	0.01	0.02	0.49	0.04	2.57	6.00	0.07	0.03	96.9	3.1
Standard Deviation		0.88	0.06	0.07	0.31	0.71	0.02	0.03	0.10	0.04	0.39	0.27	0.04	0.01	0.97	0.97
BJR-77-1		77.3	0.03	0.03	11.5	0.25	0.03	0.01	0.29	0.00	3.17	5.18	0.00	0.05	97.8	2.2
BJR-63-1		76.1	0.10	0.06	10.9	0.18	0.00	0.02	0.20	0.88	1.58	7.25	0.00	0.10	97.4	2.6

Table E.2 continued

Sample Name	Notes	SiO_2	TiO_2	ZrO_2	Al_2O_3	FeO	MnO	MgO	CaO	BaO	Na_2O	K_2O	F	Cl	Sum	H_2O
BJR-31-1		74.9	0.23	0.00	11.6	0.61	0.00	0.03	0.05	0.03	2.81	6.52	0.03	0.04	96.8	3.2
BJR-63-2		76.4	0.12	0.13	11.1	0.13	0.01	0.00	0.28	0.00	2.96	5.57	0.00	0.06	96.7	3.3
BJR-77-2		74.4	0.03	0.32	11.0	0.03	0.02	0.00	0.44	0.24	2.18	6.53	0.00	0.02	95.2	4.8
Average BJR		75.8	0.10	0.11	11.2	0.24	0.01	0.01	0.25	0.23	2.54	6.21	0.01	0.05	96.8	3.2
Standard Deviation		1.16	0.09	0.13	0.29	0.22	0.01	0.01	0.14	0.37	0.65	0.83	0.01	0.03	0.98	0.98
PCR-16-1		76.7	0.05	0.00	12.1	0.24	0.00	0.01	0.29	0.13	2.94	5.55	0.00	0.05	98.1	1.9
PCR-31-2		75.8	0.04	0.10	12.5	0.31	0.04	0.01	0.29	0.09	2.55	5.84	0.06	0.04	97.7	2.3
PCR-31-1		74.8	0.11	0.35	12.0	0.23	0.04	0.00	0.35	0.09	2.87	5.53	0.09	0.05	96.5	3.5
Average PCR		75.8	0.07	0.15	12.2	0.26	0.02	0.01	0.31	0.11	2.79	5.64	0.05	0.05	97.4	2.6
Standard Deviation		0.97	0.03	0.18	0.24	0.04	0.02	0.01	0.03	0.02	0.21	0.18	0.05	0.01	0.82	0.82
LCR-32-1		76.8	0.08	0.02	12.2	0.35	0.00	0.02	0.39	0.14	2.66	6.01	0.07	0.02	98.7	1.3
LCR-62-2	vapor bubble in melt	76.6	0.13	0.21	12.1	0.65	0.00	0.00	0.52	0.09	2.41	5.82	0.01	0.03	98.6	1.4
LCR-77-1		75.4	0.13	0.16	12.4	0.72	0.00	0.00	0.41	0.10	2.81	5.97	0.07	0.02	98.1	1.9
LCR-20-1		76.3	0.20	0.06	11.9	0.54	0.03	0.00	0.35	0.07	2.66	5.90	0.06	0.03	98.1	1.9
LCR-3-1	vapor bubble in melt	76.2	0.24	0.47	12.0	0.43	0.00	0.01	0.30	0.08	2.24	5.97	0.08	0.03	98.0	2.0
LCR-3-2		75.4	0.19	0.07	12.2	0.56	0.00	0.04	0.32	0.08	2.82	6.17	0.05	0.05	98.0	2.0

Table E.2 continued

Sample Name	Notes	SiO_2	TiO_2	ZrO_2	Al_2O_3	FeO	MnO	MgO	CaO	BaO	Na_2O	K_2O	F	Cl	Sum	H_2O
LCR-62-1		75.1	0.29	0.08	12.4	0.65	0.00	0.02	0.44	0.10	2.82	5.85	0.01	0.02	97.8	2.2
LCR-69-1	vapor bubble in melt	75.9	0.11	0.13	12.0	0.65	0.02	0.01	0.34	0.09	2.58	5.99	0.08	0.04	97.9	2.1
LCR-31-2		75.4	0.14	0.25	12.2	0.59	0.03	0.02	0.36	0.08	2.80	5.72	0.05	0.05	97.7	2.3
LCR-89-1		75.7	0.28	0.03	11.9	0.61	0.00	0.01	0.34	0.09	2.51	6.03	0.00	0.04	97.6	2.4
LCR-37-1	vapor bubble in melt	76.3	0.36	0.02	11.3	0.58	0.01	0.00	0.19	0.00	2.41	6.39	0.06	0.03	97.6	2.4
LCR-47-1		75.8	0.20	0.11	11.8	0.46	0.00	0.00	0.31	0.10	2.32	5.87	0.00	0.03	97.0	3.0
LCR-31-1		75.0	0.08	0.22	12.2	0.60	0.01	0.00	0.39	0.11	2.54	5.72	0.11	0.04	97.0	3.0
LCR-30-1		72.4	0.15	0.15	13.2	0.71	0.00	0.02	0.48	0.00	3.17	6.48	0.08	0.04	97.0	3.0
LCR-64-1		74.5	0.20	0.70	11.5	0.53	0.00	0.00	0.25	0.13	2.58	6.10	0.00	0.02	96.5	3.5
LCR-36-1		73.8	0.17	0.11	12.1	0.63	0.01	0.00	0.34	0.12	2.40	6.29	0.03	0.05	96.0	4.0
LCR-36-2		74.4	0.15	0.04	12.2	0.53	0.04	0.00	0.33	0.11	2.14	5.90	0.08	0.05	96.0	4.0
Average LCR		75.3	0.18	0.17	12.1	0.58	0.01	0.01	0.36	0.09	2.58	6.01	0.05	0.03	97.5	2.5
Standard Deviation		1.11	0.08	0.18	0.42	0.10	0.01	0.01	0.08	0.04	0.26	0.22	0.03	0.01	0.82	0.82
SCR-84-1	growth in melt	76.6	0.20	0.09	11.9	1.13	0.04	0.00	0.32	0.10	3.05	5.72	0.06	0.05	99.2	0.8
SCR-99-2	no growth	75.3	0.33	0.11	12.1	1.74	0.03	0.01	0.24	0.00	3.17	5.61	0.10	0.05	98.8	1.2
SCR-109-2	growth in melt	74.6	0.44	0.19	12.8	1.81	0.04	0.04	0.68	0.00	3.18	4.92	0.10	0.01	98.8	1.2
SCR-87-1	growth in melt	75.0	0.19	0.05	11.7	2.50	0.01	0.10	0.54	0.13	2.65	5.67	0.12	0.07	98.7	1.3
SCR-89-1		76.0	0.13	0.10	11.9	1.46	0.01	0.03	0.30	0.14	3.07	5.50	0.06	0.06	98.8	1.2
SCR-109-1	growth in melt	75.0	0.20	0.13	11.9	2.04	0.05	0.08	0.48	0.03	2.89	5.74	0.07	0.06	98.7	1.3

Table E.2 continued

Sample Name	Notes	SiO_2	TiO_2	ZrO_2	Al_2O_3	FeO	MnO	MgO	CaO	BaO	Na_2O	K_2O	F	Cl	Sum	H_2O
SCR-4-1	possible growth in melt	75.6	0.16	0.18	11.6	2.02	0.04	0.06	0.37	0.06	2.59	5.76	0.09	0.02	98.6	1.4
SCR-22-1	growth in melt	75.2	0.14	0.13	12.2	1.93	0.00	0.02	0.35	0.09	2.98	5.42	0.07	0.04	98.6	1.4
SCR-49-1	no growth	75.1	0.11	0.10	11.7	2.46	0.03	0.09	0.46	0.10	2.64	5.53	0.10	0.06	98.5	1.5
SCR-99-1	growth in melt	76.2	0.12	0.11	12.1	1.12	0.00	0.03	0.39	0.09	2.82	5.48	0.06	0.06	98.6	1.4
SCR-4-2	possible growth in melt	75.8	0.17	0.13	11.7	1.67	0.02	0.03	0.32	0.03	2.57	5.90	0.07	0.04	98.5	1.5
SCR-108-1	growth in melt	75.6	0.36	0.00	11.9	1.73	0.00	0.00	0.36	0.06	2.84	5.52	0.04	0.06	98.4	1.6
SCR-7-1	growth in melt	74.5	0.03	0.13	11.9	2.33	0.02	0.08	0.43	0.00	3.05	5.70	0.08	0.08	98.3	1.7
SCR-18-1	growth in melt	75.5	0.23	0.21	12.1	1.35	0.01	0.02	0.14	0.08	3.09	5.49	0.02	0.04	98.3	1.7
SCR-74-1	growth in melt	75.1	0.45	0.08	11.7	1.87	0.04	0.05	0.27	0.00	2.29	6.30	0.04	0.04	98.2	1.8
SCR-17-1	no growth	76.2	0.18	0.13	11.9	1.01	0.04	0.02	0.26	0.11	2.39	5.88	0.05	0.05	98.2	1.8
SCR-88-1	growth in melt	74.3	0.39	0.21	12.1	1.90	0.02	0.03	0.45	0.05	2.62	5.96	0.10	0.04	98.1	1.9
SCR-88-2	growth in melt	74.1	0.35	0.20	12.1	1.87	0.01	0.04	0.48	0.01	2.71	6.04	0.13	0.06	98.1	1.9
SCR-3-1	growth in melt	74.0	0.24	0.11	12.5	1.39	0.05	0.02	0.37	0.03	3.16	6.01	0.11	0.08	98.1	1.9
SCR-111-1	growth in melt	75.9	0.17	0.09	12.0	0.98	0.00	0.00	0.34	0.10	2.79	5.58	0.09	0.05	98.1	1.9
SCR-45-1	growth in melt	75.4	0.15	0.13	12.0	1.26	0.06	0.02	0.42	0.14	2.86	5.40	0.03	0.08	98.0	2.0
SCR-40-1	growth in melt	74.8	0.28	0.18	12.3	1.12	0.02	0.02	0.47	0.03	2.85	5.83	0.01	0.03	98.0	2.0
SCR-87-2	growth in melt	76.3	0.12	0.07	12.0	0.93	0.02	0.01	0.38	0.09	2.67	5.30	0.09	0.06	98.0	2.0
SCR-67-1	no growth	75.4	0.37	0.13	11.9	1.48	0.01	0.01	0.32	0.00	2.09	5.69	0.08	0.03	97.5	2.5
SCR-89-2	no growth	74.9	0.08	0.13	11.8	1.70	0.02	0.03	0.29	0.07	2.65	5.59	0.10	0.04	97.4	2.6
SCR-104-1	no growth	73.4	0.35	0.24	11.8	2.01	0.01	0.03	0.36	0.00	2.78	5.25	0.06	0.06	96.4	3.6
Average SCR		75.2	0.23	0.13	12.0	1.65	0.02	0.03	0.38	0.06	2.79	5.65	0.07	0.05	98.3	1.7
Standard Deviation		0.77	0.12	0.05	0.26	0.45	0.02	0.03	0.11	0.05	0.27	0.28	0.03	0.02	0.56	0.56

Table E.2 continued

Sample Name	Notes	SiO_2	TiO_2	ZrO_2	Al_2O_3	FeO	MnO	MgO	CaO	BaO	Na_2O	K_2O	F	Cl	Sum	H_2O
IBR-2-1	growth in melt	75.4	0.21	0.10	12.2	1.33	0.04	0.03	0.24	0.04	2.65	5.87	0.00	0.02	98.1	1.9
IBR-18-1	no growth	73.2	0.24	0.34	11.6	2.27	0.04	0.18	0.75	0.02	3.15	5.74	0.09	0.03	97.7	2.3
IBR-63-1		75.5	0.35	0.09	12.2	0.26	0.00	0.00	0.40	0.07	2.59	5.87	0.09	0.02	97.4	2.6
IBR-2-2	vapor bubble in melt	72.5	0.39	0.21	11.4	3.28	0.05	0.06	0.12	0.02	2.46	5.75	0.06	0.05	96.4	3.6
IBR-30-2		72.6	0.37	0.14	11.7	1.92	0.07	0.16	0.89	0.01	2.32	5.65	0.02	0.02	95.9	4.1
IBR-30-1	growth in melt	72.4	0.36	0.00	11.8	1.77	0.07	0.14	0.80	0.00	1.95	5.85	0.03	0.04	95.2	4.8
Average IBR		73.6	0.32	0.15	11.8	1.80	0.05	0.10	0.53	0.03	2.52	5.79	0.05	0.03	96.8	3.2
Standard Deviation		1.45	0.08	0.12	0.30	1.00	0.03	0.08	0.32	0.03	0.40	0.09	0.04	0.01	1.13	1.13
DCR-34-1	growth in melt	74.9	0.29	0.10	11.9	2.44	0.06	0.09	0.60	0.04	2.77	5.65	0.05	0.03	99.0	1.0
DCR-48-1		76.9	0.15	0.10	12.0	0.56	0.00	0.01	0.23	0.15	3.05	5.79	0.02	0.03	98.9	1.1
DCR-61-1		76.2	0.09	0.12	11.8	1.06	0.00	0.04	0.28	0.07	2.62	6.05	0.11	0.03	98.5	1.5
DCR-61-2		76.4	0.14	0.09	11.9	0.69	0.02	0.01	0.26	0.03	2.80	6.01	0.09	0.05	98.5	1.5
DCR-40-1		76.2	0.14	0.10	12.0	0.54	0.02	0.00	0.25	0.10	3.09	5.86	0.06	0.06	98.5	1.5
DCR-15-1		76.2	0.10	0.00	12.5	0.56	0.00	0.00	0.29	0.14	2.58	5.91	0.09	0.07	98.4	1.6
DCR-80-3		76.7	0.07	0.19	12.1	0.56	0.03	0.00	0.15	0.07	2.69	5.55	0.05	0.04	98.2	1.8
DCR-34-2		75.9	0.35	0.10	11.8	0.85	0.04	0.00	0.31	0.04	2.83	5.74	0.04	0.03	98.0	2.0
DCR-95-1		76.0	0.33	0.34	11.9	0.51	0.02	0.00	0.31	0.05	2.71	5.84	0.11	0.04	98.1	1.9
DCR-78-1		76.2	0.41	0.11	12.0	0.50	0.00	0.00	0.31	0.05	2.68	5.64	0.14	0.05	98.1	1.9
DCR-39-2		76.5	0.28	0.20	12.0	0.51	0.00	0.00	0.28	0.06	2.28	5.76	0.05	0.04	98.0	2.0
DCR-39-1		75.7	0.11	0.41	12.1	0.51	0.03	0.01	0.32	0.13	2.87	5.56	0.11	0.05	97.8	2.2
DCR-107-1		75.7	0.08	0.11	12.0	0.58	0.02	0.00	0.30	0.13	3.09	5.52	0.11	0.04	97.7	2.3

Table E.2 continued

Sample Name	Notes	SiO_2	TiO_2	ZrO_2	Al_2O_3	FeO	MnO	MgO	CaO	BaO	Na_2O	K_2O	F	Cl	Sum	H_2O
DCR-46-1		76.4	0.17	0.29	11.8	0.46	0.00	0.00	0.14	0.10	2.49	5.76	0.02	0.05	97.7	2.3
DCR-106-1		76.3	0.11	0.43	11.8	0.47	0.01	0.00	0.26	0.11	2.58	5.57	0.08	0.03	97.7	2.3
DCR-89-1		75.5	0.09	0.46	11.5	0.63	0.00	0.00	0.27	0.10	2.92	5.91	0.14	0.05	97.6	2.4
DCR-90-2		75.5	0.30	0.08	12.0	0.68	0.00	0.00	0.33	0.08	2.97	5.61	0.00	0.04	97.5	2.5
DCR-89-2		75.4	0.33	0.19	12.1	0.56	0.02	0.00	0.41	0.11	2.79	5.53	0.07	0.03	97.6	2.4
DCR-80-2		75.4	0.35	0.10	12.3	0.46	0.00	0.00	0.44	0.02	2.65	5.56	0.11	0.05	97.5	2.5
DCR-84-1		76.1	0.04	0.24	11.5	0.49	0.00	0.00	0.18	0.07	2.55	6.01	0.08	0.08	97.3	2.7
DCR-103-1		75.6	0.23	0.07	11.6	0.46	0.03	0.00	0.13	0.04	2.80	5.95	0.07	0.05	97.0	3.0
DCR-90-1		75.3	0.41	0.07	11.9	0.51	0.01	0.00	0.36	0.02	2.18	5.82	0.09	0.04	96.7	3.3
DCR-80-1		74.9	0.05	0.13	11.8	0.55	0.02	0.00	0.35	0.13	2.27	5.43	0.13	0.05	95.8	4.2
DCR-71-1		75.0	0.17	0.09	11.6	0.39	0.00	0.00	0.23	0.08	2.03	5.57	0.07	0.06	95.3	4.7
Average DCR		75.9	0.20	0.17	11.9	0.65	0.01	0.01	0.29	0.08	2.68	5.73	0.08	0.04	97.7	2.3
Standard Deviation		0.55	0.12	0.13	0.24	0.41	0.02	0.02	0.10	0.04	0.28	0.18	0.04	0.01	0.86	0.86
TCT-3-1	growth in melt	76.5	0.17	0.17	12.0	0.55	0.04	0.00	0.33	0.09	2.69	5.47	0.01	0.04	98.1	1.9
TCT-3-2	growth in melt	75.7	0.10	0.16	12.0	1.13	0.05	0.06	0.51	0.06	2.83	5.29	0.06	0.05	98.1	1.9
TCT-54-1	vapor bubble in melt	75.6	0.24	0.05	12.0	0.57	0.00	0.00	0.32	0.12	3.19	5.82	0.04	0.07	98.1	1.9
TCT-48-1	growth in melt	74.7	0.23	0.11	11.9	1.53	0.03	0.00	0.41	0.05	2.95	5.33	0.04	0.07	97.4	2.6
TCT-84-2	vapor bubble in melt	76.7	0.17	0.15	11.8	0.31	0.01	0.01	0.29	0.11	2.45	5.42	0.03	0.06	97.5	2.5
TCT-18-1		75.4	0.53	0.22	11.5	0.40	0.01	0.01	0.32	0.00	2.80	5.78	0.00	0.06	97.1	2.9

Table E.2 continued

Sample Name	Notes	SiO_2	TiO_2	ZrO_2	Al_2O_3	FeO	MnO	MgO	CaO	BaO	Na_2O	K_2O	F	Cl	Sum	H_2O
TCT-50-1	no growth	73.9	0.09	0.13	12.2	1.35	0.03	0.02	0.39	0.00	3.17	5.49	0.08	0.11	97.0	3.0
TCT-48-2	growth in melt	75.4	0.23	0.09	11.9	0.48	0.00	0.02	0.36	0.02	3.01	5.36	0.02	0.04	96.9	3.1
TCT-39-1		75.2	0.27	0.51	11.5	0.43	0.02	0.02	0.23	0.06	2.57	5.72	0.06	0.05	96.6	3.4
TCT-84-1	vapor bubble in melt	75.4	0.33	0.09	11.6	0.26	0.03	0.00	0.35	0.06	2.78	5.56	0.09	0.05	96.6	3.4
Average TCT		75.5	0.23	0.17	11.9	0.70	0.02	0.01	0.35	0.06	2.84	5.52	0.04	0.06	97.3	2.7
Standard Deviation		0.80	0.13	0.13	0.26	0.46	0.02	0.02	0.08	0.04	0.24	0.19	0.03	0.02	0.59	0.59
Total Average		75.4	0.21	0.12	11.9	1.23	0.02	0.02	0.44	0.07	2.58	5.82	0.07	0.04	98.0	2.0
Standard Deviation		1.12	0.11	0.11	0.36	0.81	0.02	0.04	0.22	0.08	0.32	0.33	0.04	0.02	1.01	1.01

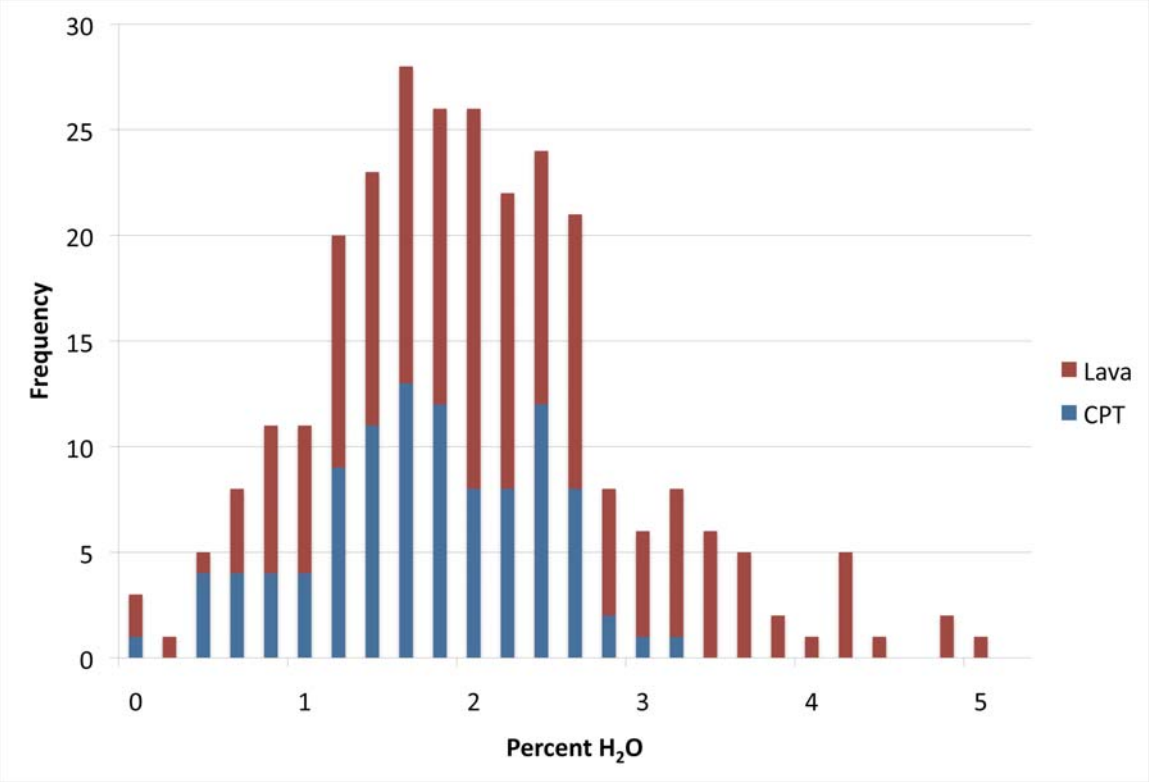

Figure E.1. H_2O in MI for both the CPT and lavas of the BJEC.

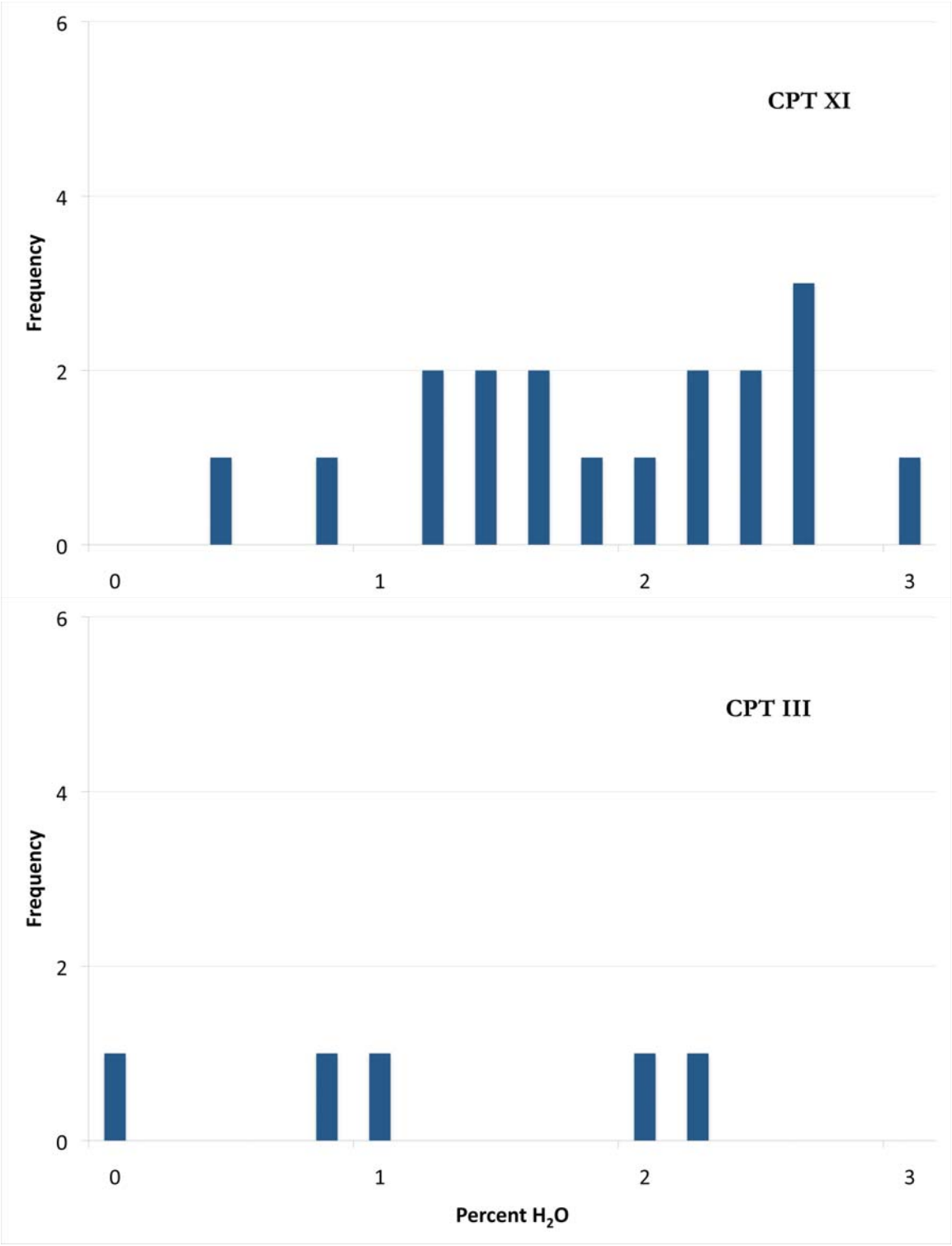

Figure E.2. H_2O in melt inclusions for CPT units showing a wide range in H_2O.

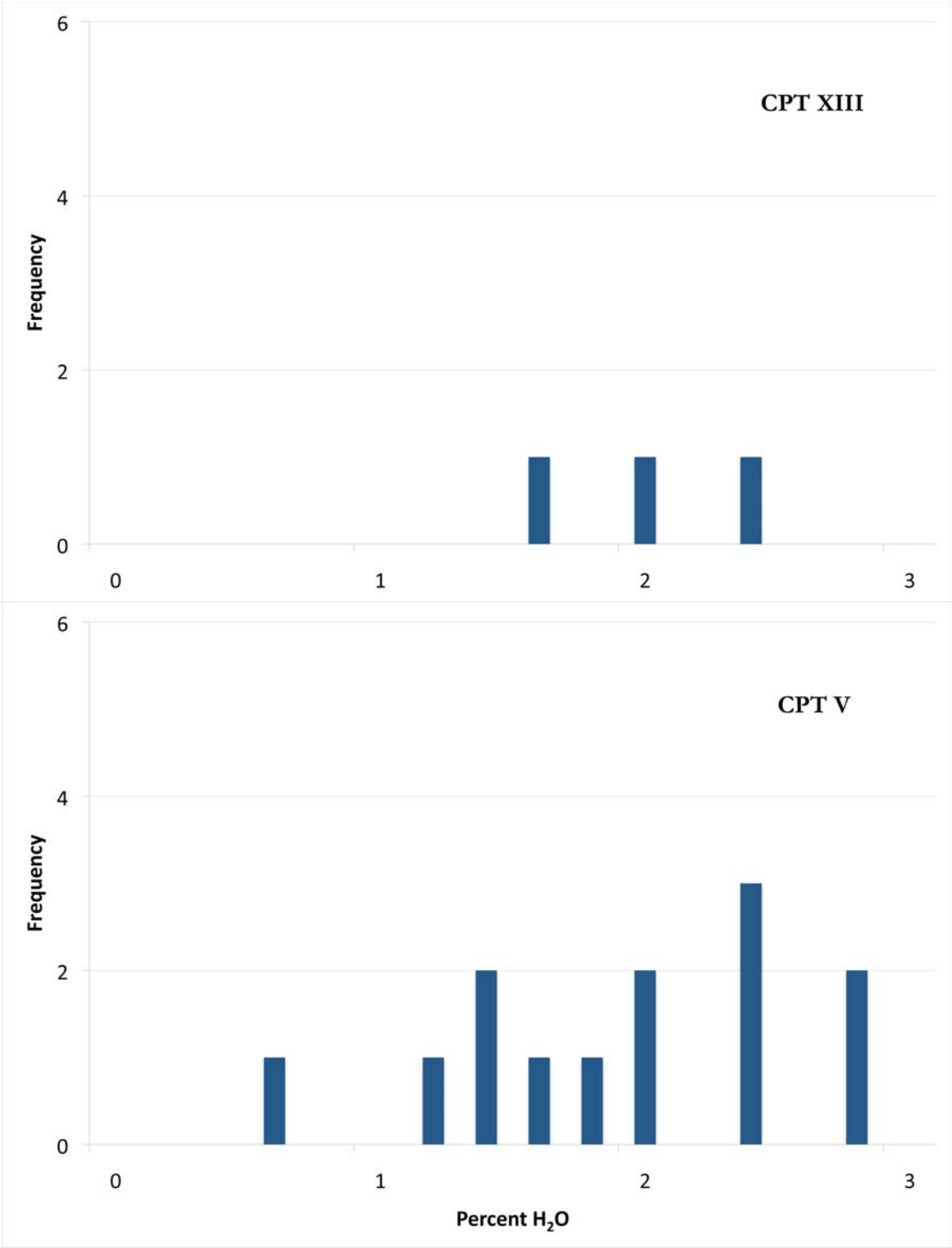

Figure E.3. H_2O in melt inclusions for CPT units showing above average H_2O.

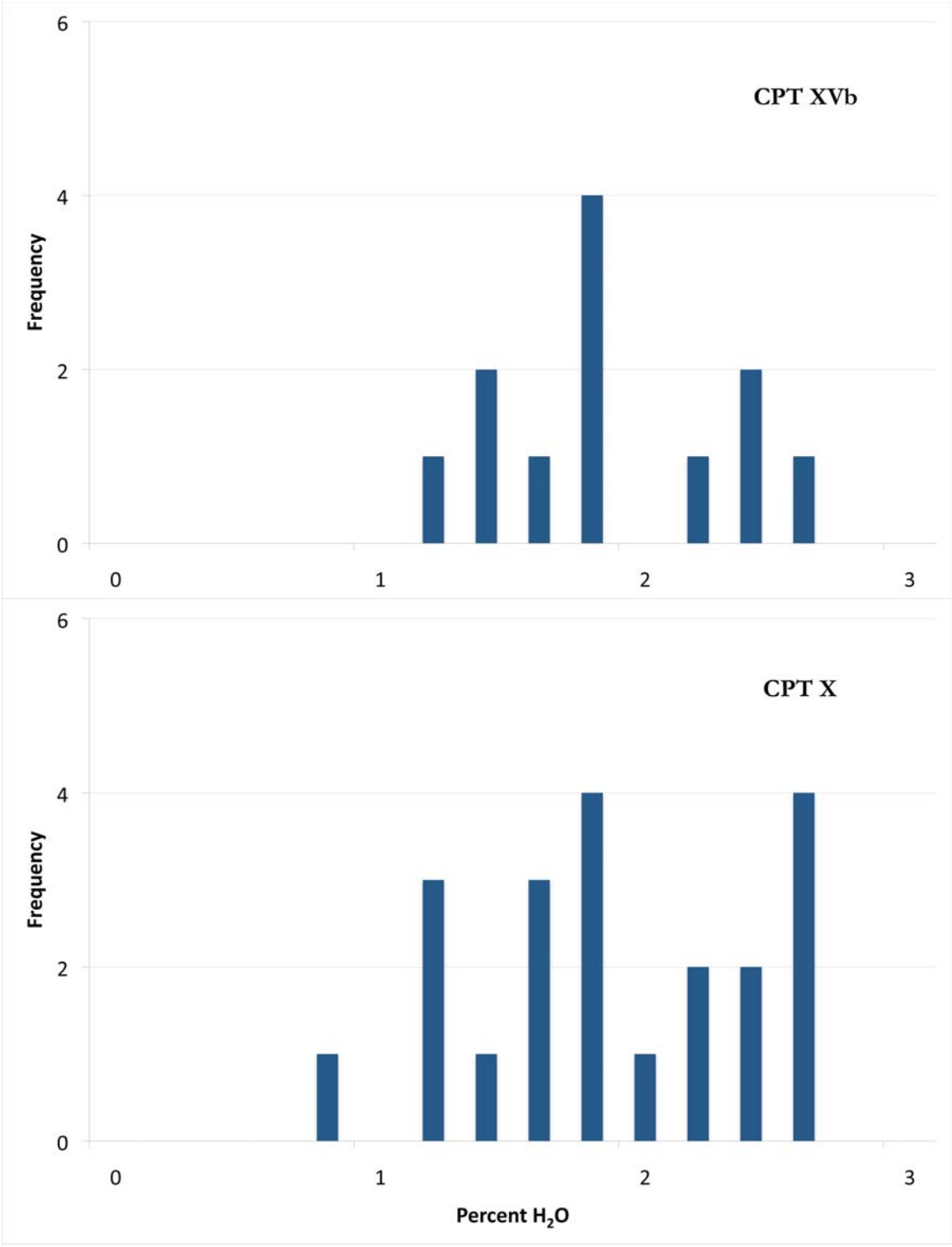

Figure E.3 continued

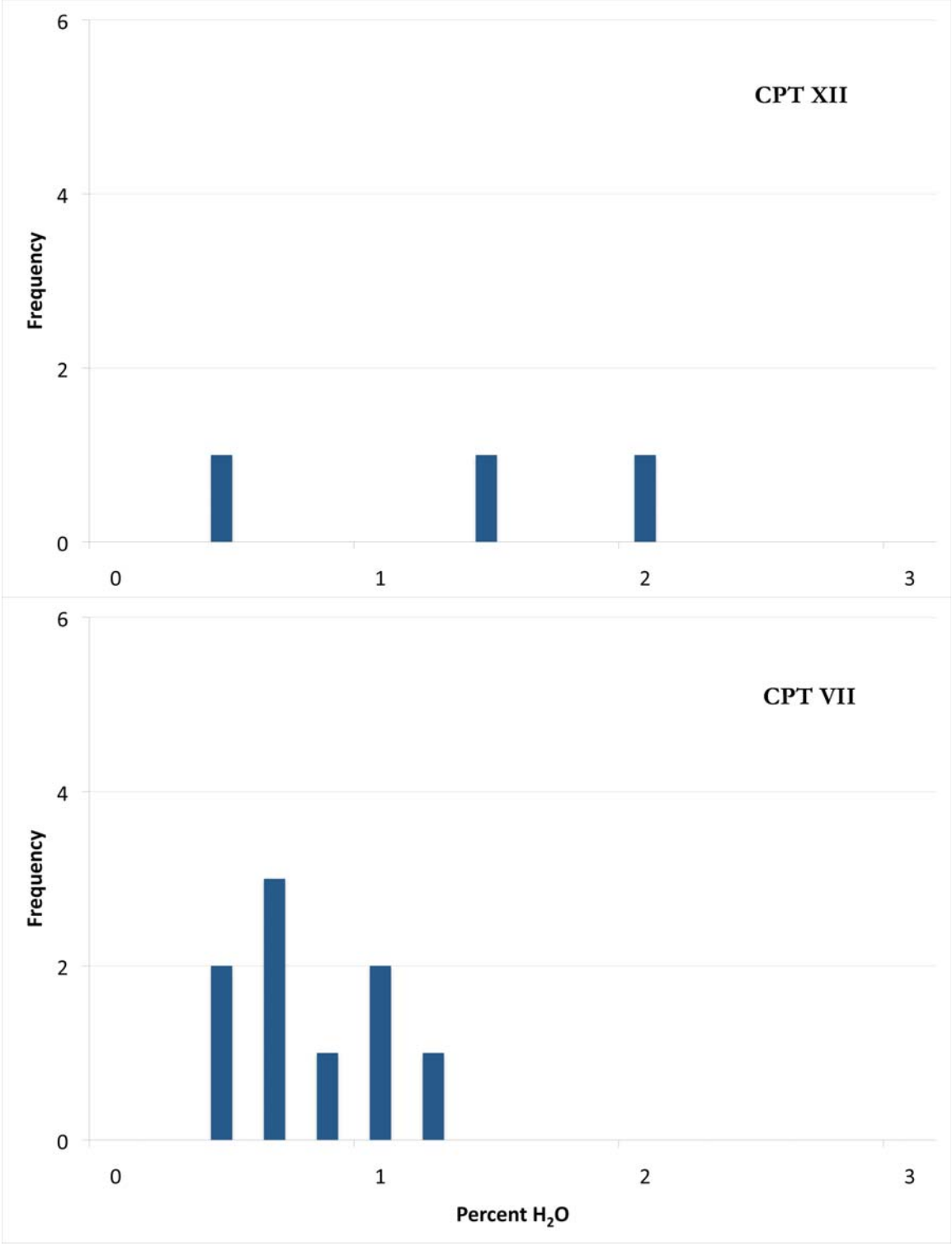

Figure E.4. H_2O in melt inclusions for CPT units showing below average H_2O.

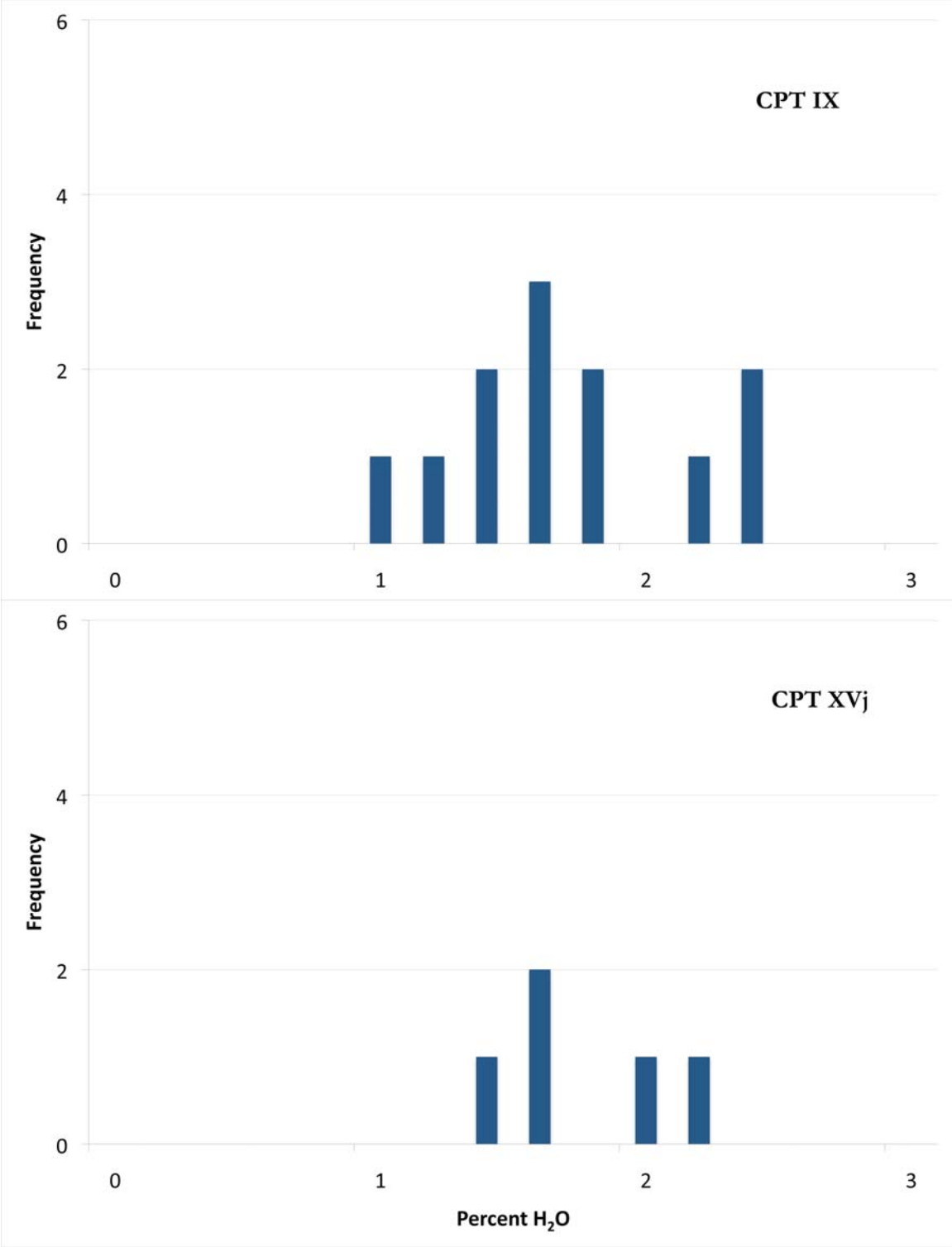

Figure E.5. H_2O in melt inclusions for CPT units showing average H_2O.

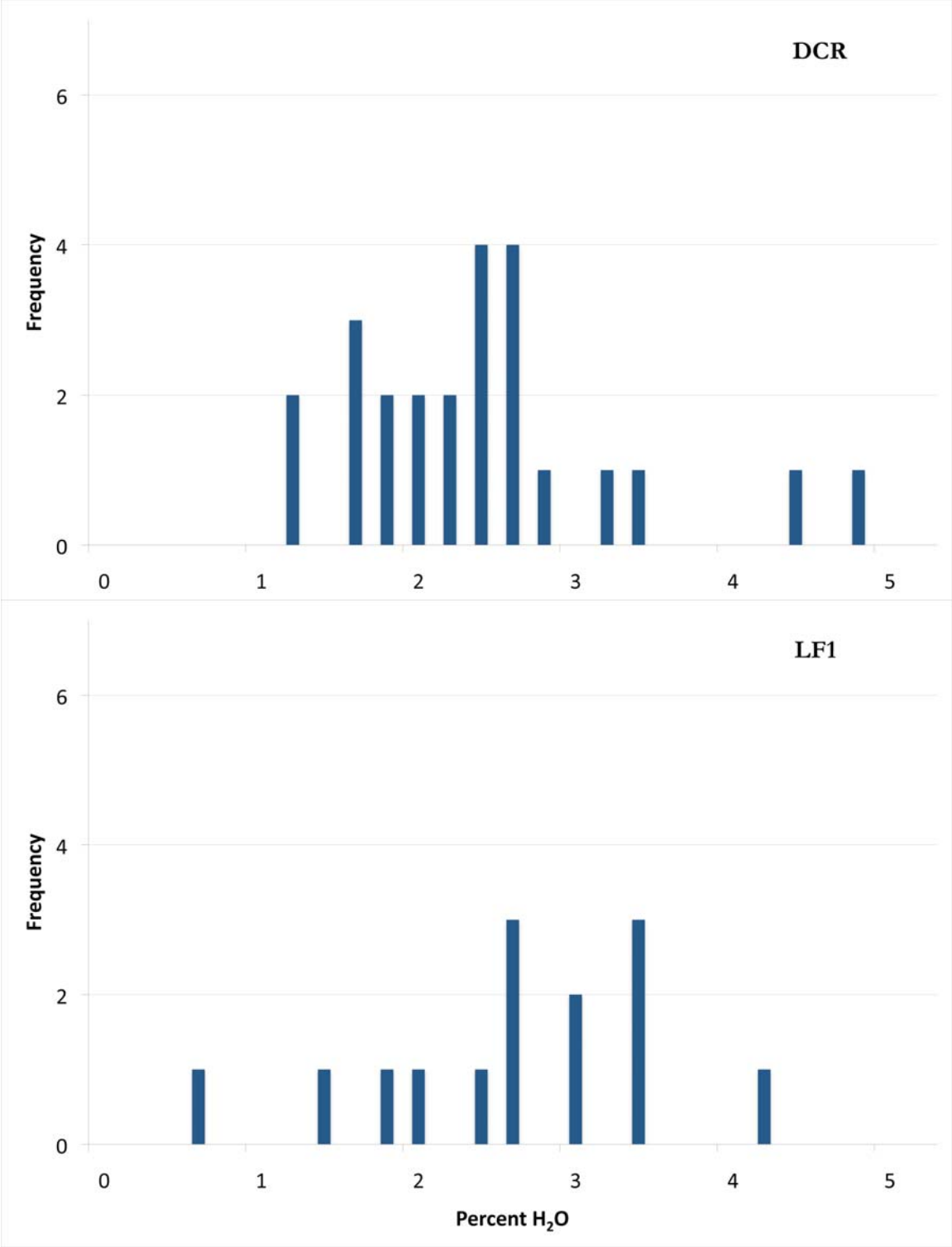

Figure E.6. H_2O in melt inclusions for lava units showing a wide range in H_2O.

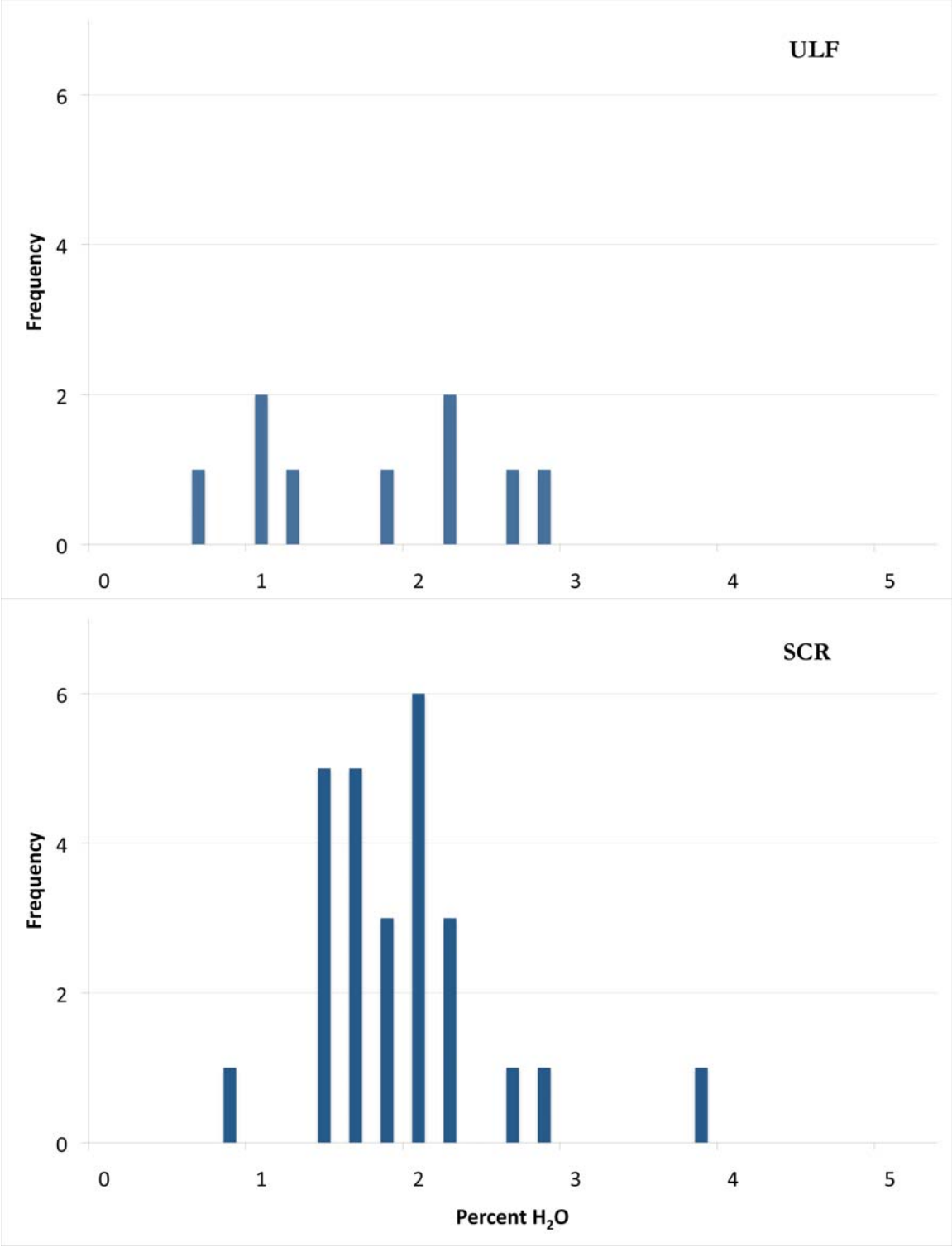

Figure E.7. H_2O in melt inclusions for lava units showing average H_2O.

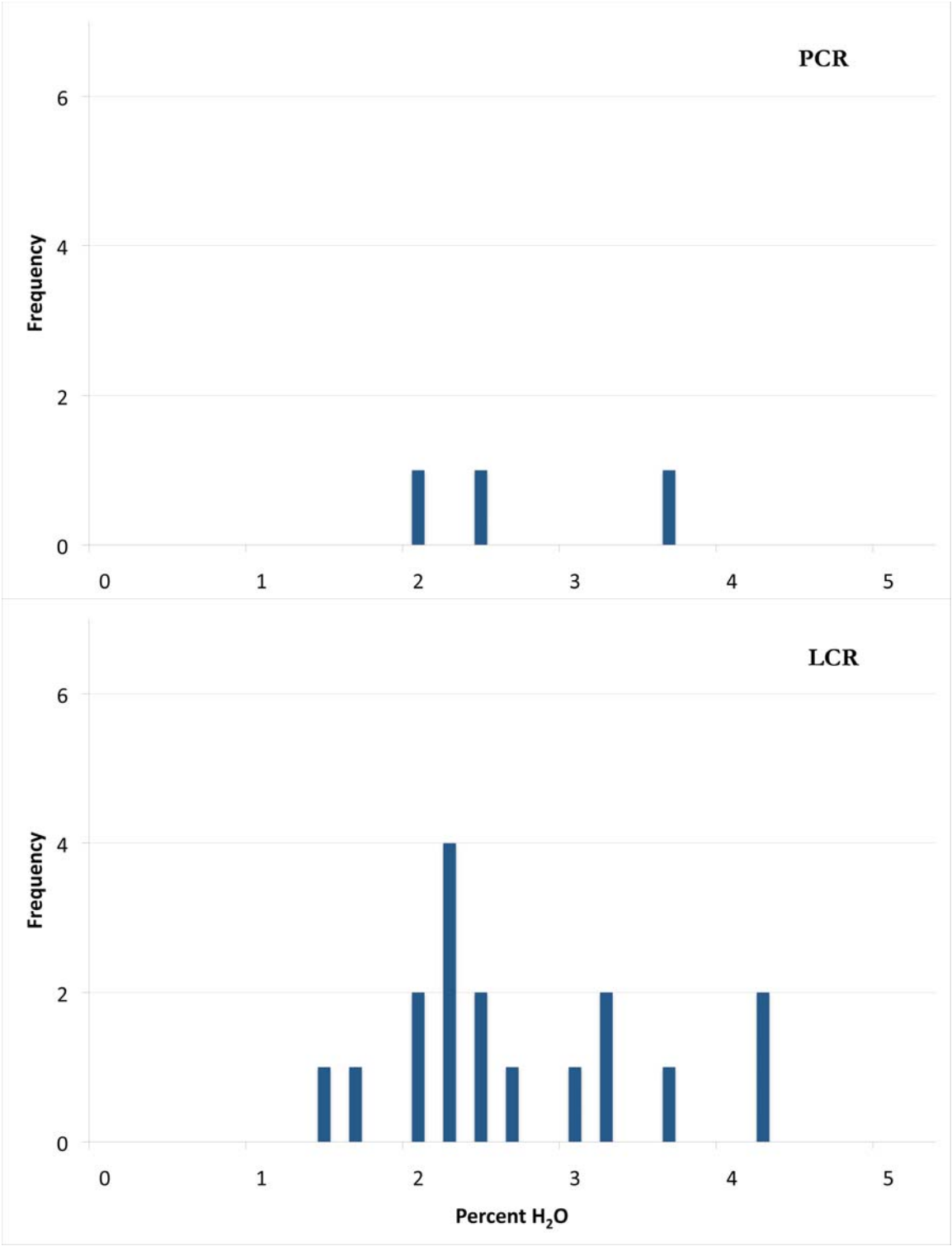

Figure E.8. H_2O in melt inclusions for lava units showing slightly above average H_2O.

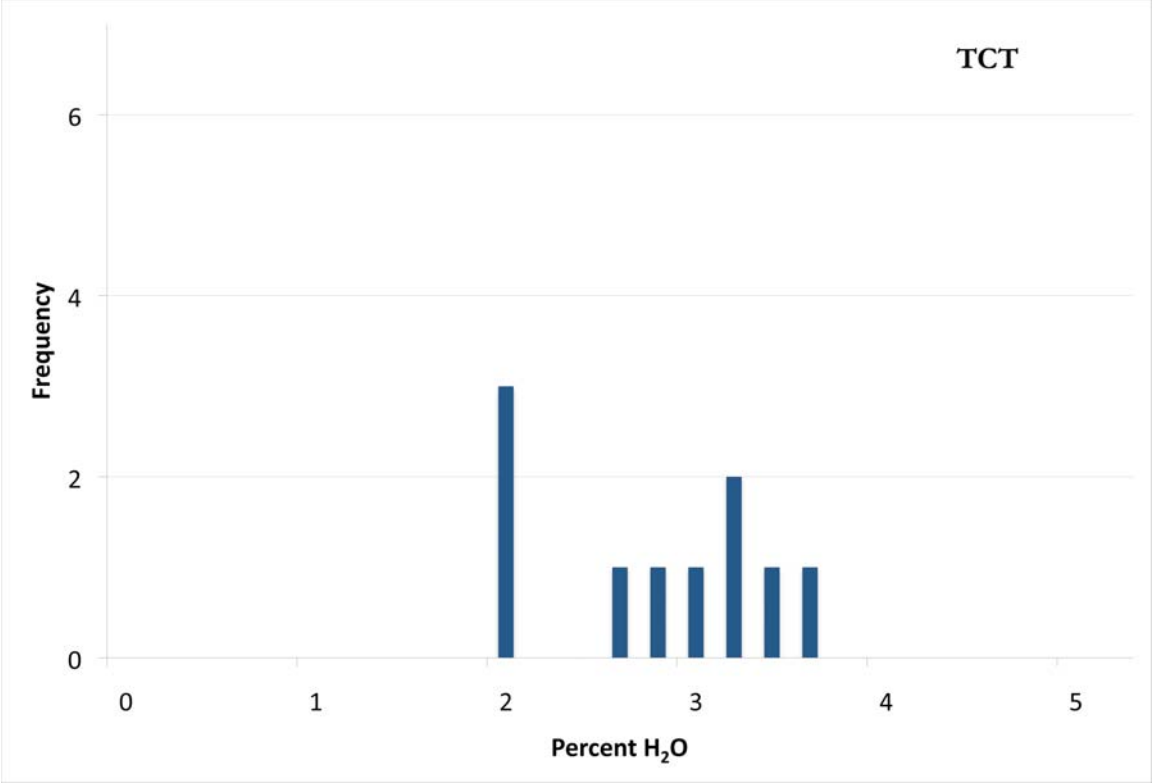

Figure E.8 continued

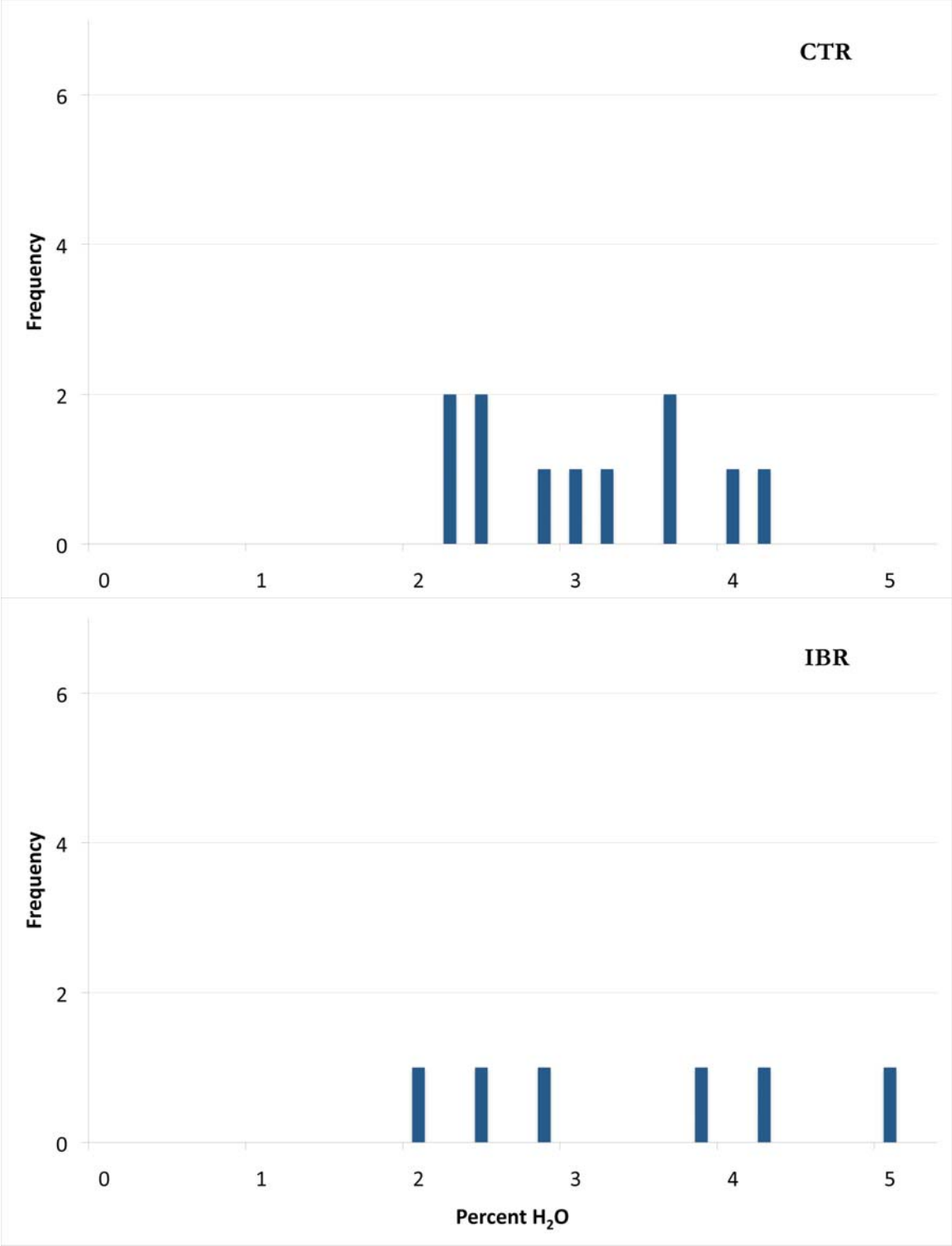

Figure E.9. H_2O in melt inclusions for lava units showing well above average H_2O.

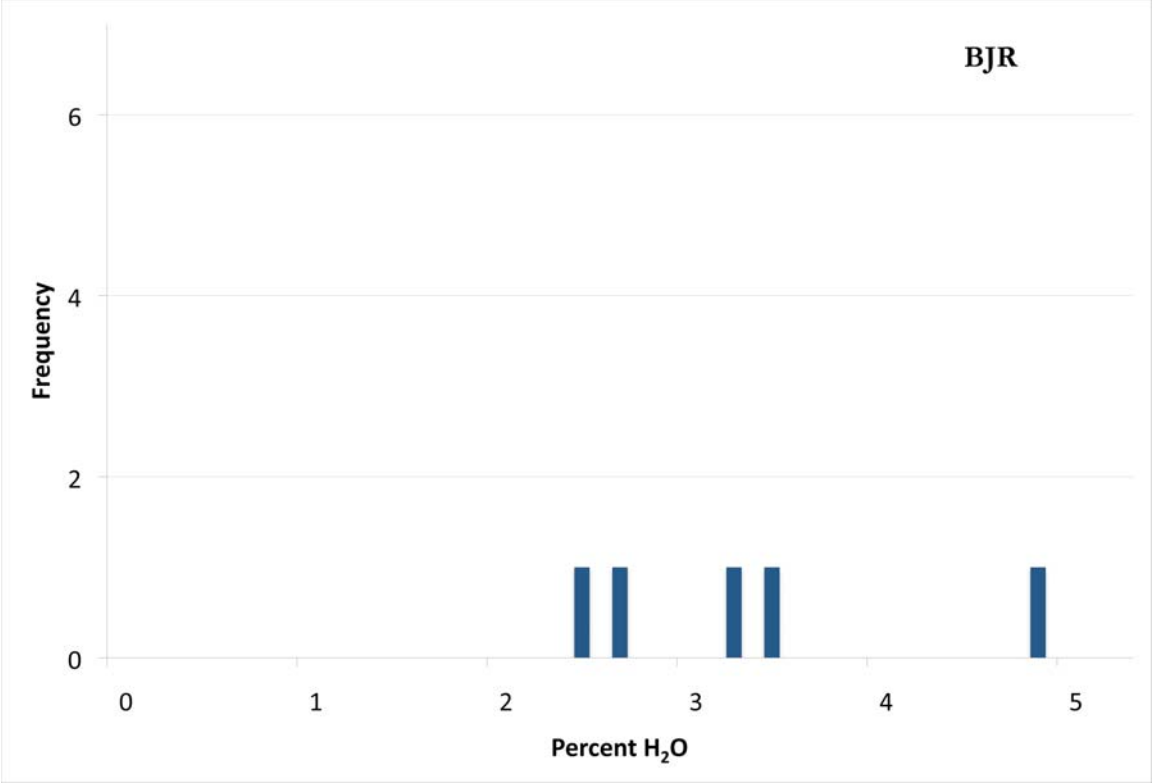

Figure E.9 continued

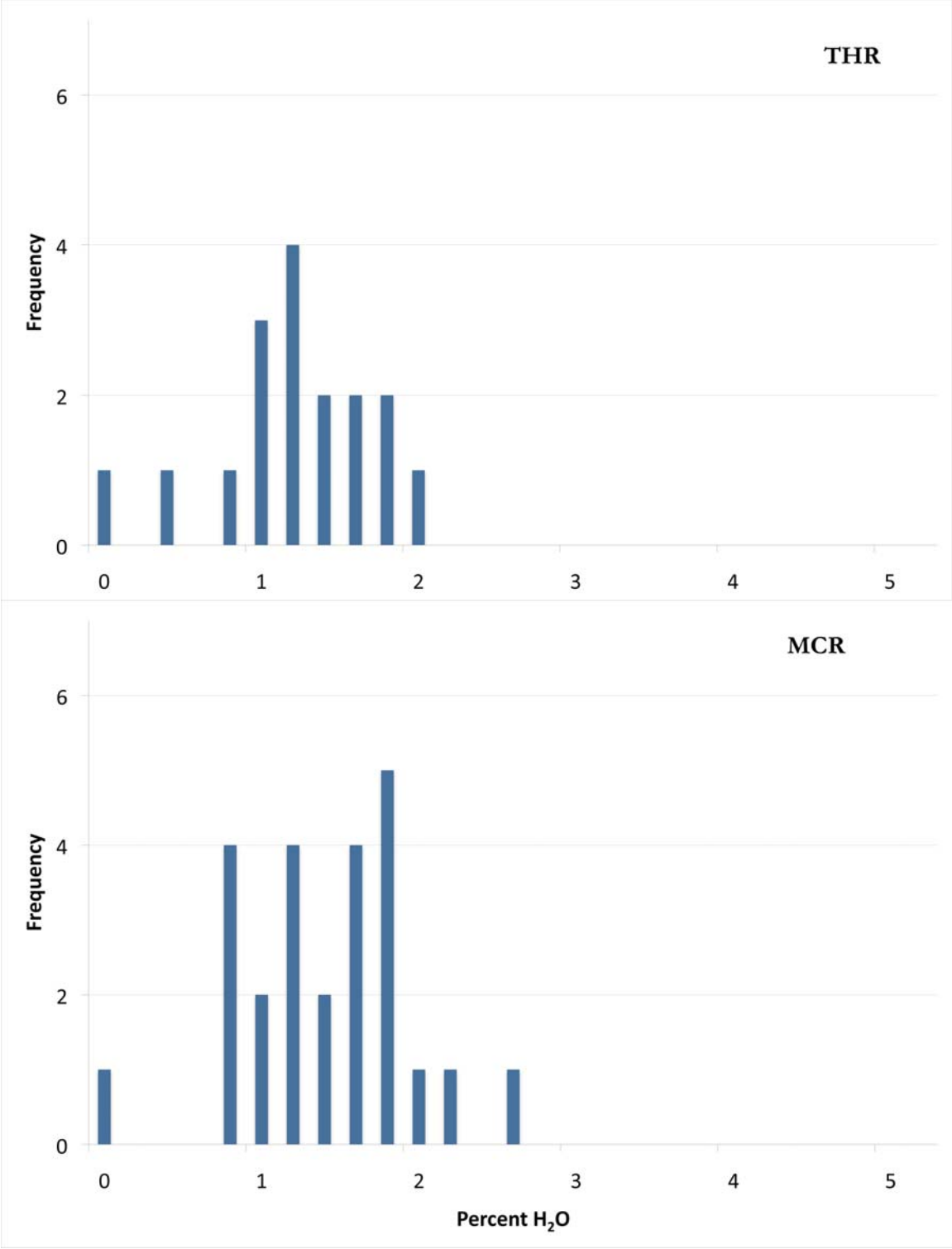

Figure E.10. H_2O in melt inclusions for lava units showing below average H_2O.

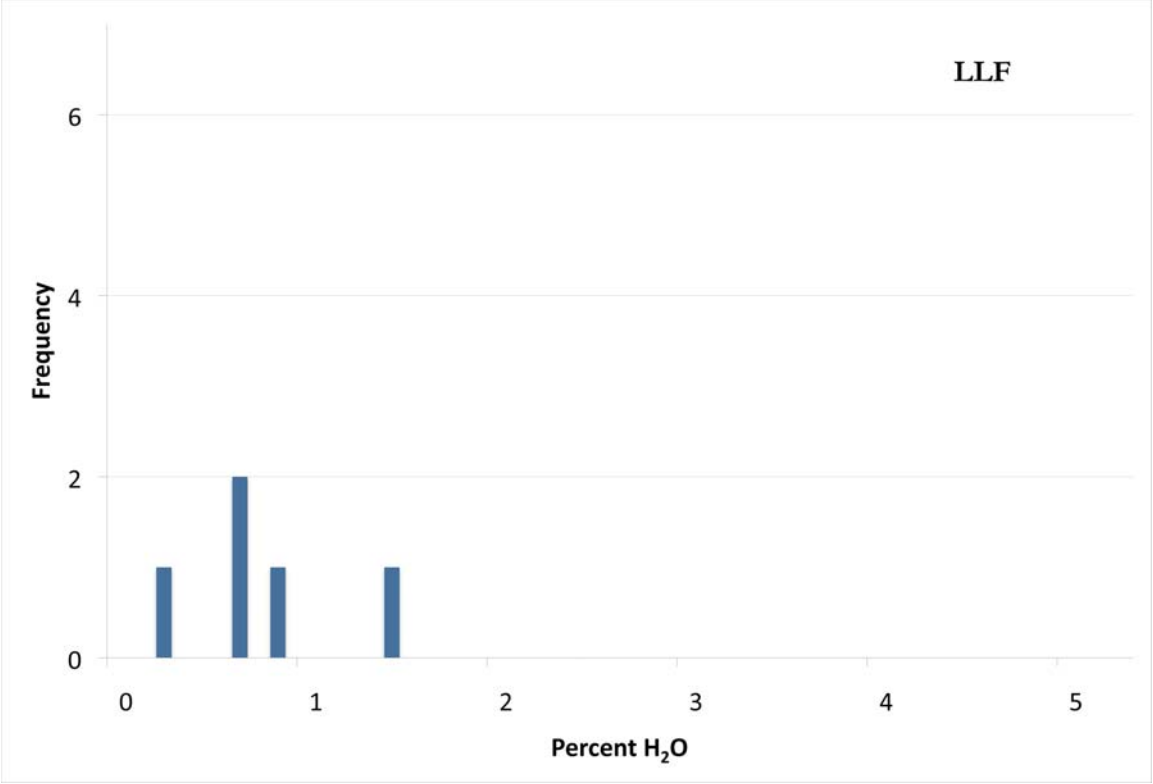

Figure E.10 continued

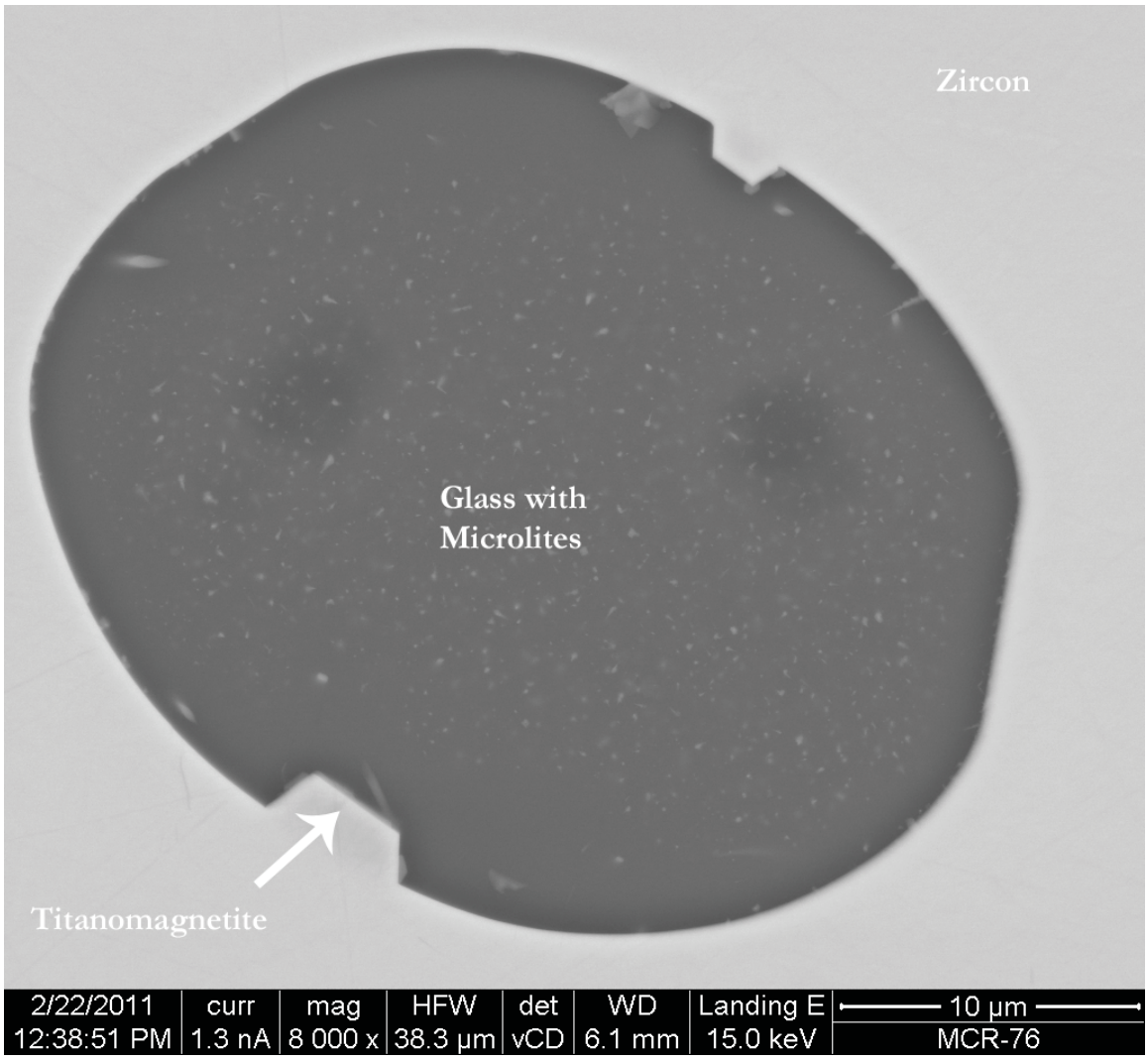

Figure E.11. BSE image of MCR – 76. The image shows post-entrapment growth inside the MI. Titanomagnetite identified by EDS.

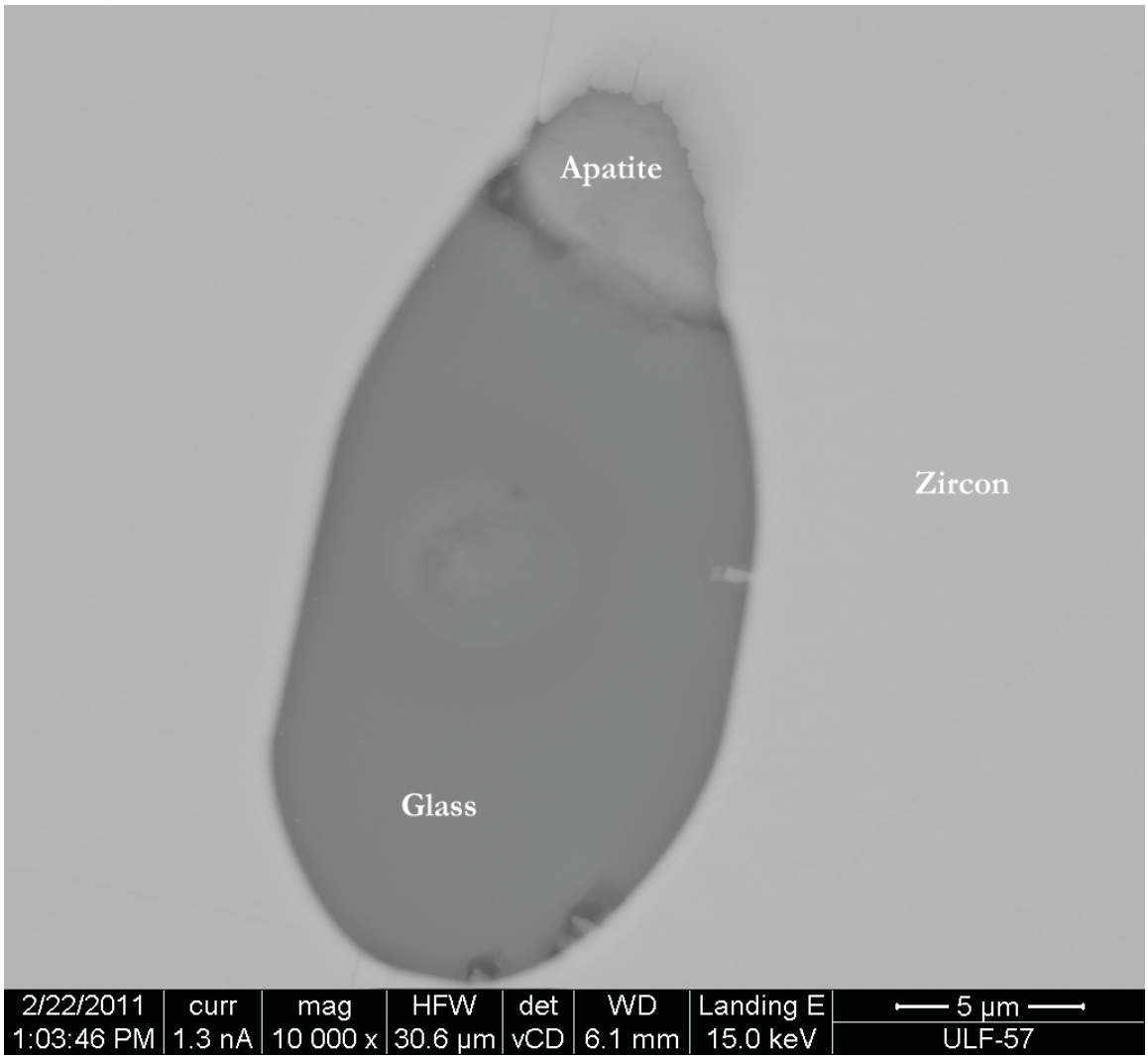

Figure E.12. BSE image of ULF - 57. The image shows post-entrapment growth inside the MI. Apatite identified by EDS.

Table E.3. EPMA analyses of melt inclusions from the rhyolite lavas with evidence of secondary growth or with abnormal elemental concentrations (i.e., high Zr or Fe) that indicate beam overlap on multiple phases

Sample Name	Notes	SiO_2	TiO_2	ZrO_2	Al_2O_3	FeO	MnO	MgO	CaO	BaO	Na_2O	K_2O	F	Cl	Sum
LF1-45-1	plagioclase	57.8	0.08	0.07	24.5	0.46	0.00	0.00	7.37	0.17	6.92	0.59	0.00	0.00	98.0
LF1-45-2	high Fe-Ti	72.9	1.24	0.22	9.88	3.88	0.03	0.02	0.39	0.00	2.22	4.81	0.03	0.03	95.6
LF1-51-1	low Na	74.9	0.25	0.04	11.9	1.91	0.04	0.09	0.59	0.00	1.06	5.42	0.10	0.02	96.3
LF1-52-1	high Si	85.4	0.42	0.06	5.82	1.60	0.00	0.03	0.25	0.00	1.45	2.77	0.02	0.01	97.8
LF1-56-1	high Fe	72.3	0.42	0.00	11.9	3.80	0.11	0.20	0.90	0.00	2.33	5.64	0.08	0.03	97.6
LF1-59-1	low Na	72.0	0.39	0.06	11.5	2.05	0.04	0.20	0.84	0.01	1.68	6.23	0.07	0.02	95.1
LF1-68-2	high Si	78.4	0.35	0.21	10.1	1.66	0.04	0.10	0.61	0.09	2.20	5.00	0.02	0.00	98.7
LF1-75-1	low Na	74.1	0.45	0.02	11.4	1.73	0.02	0.11	1.40	0.94	1.38	6.66	0.00	0.01	98.2
LF1-75-2	high Ca	71.9	0.34	0.00	13.5	1.50	0.05	0.15	2.90	0.00	4.14	2.40	0.05	0.07	97.0
LF1-75-3	alkali feldspar	70.7	0.35	0.00	16.5	1.35	0.04	0.15	0.91	0.00	9.15	0.28	0.09	0.00	99.5
LF1-80-1	high Ca and Mg	72.7	0.43	0.35	11.4	1.97	0.03	0.24	1.12	0.00	2.21	5.66	0.09	0.01	96.2
LLF-12-1	high Fe	73.5	0.29	0.20	11.6	4.35	0.05	0.03	0.85	0.09	2.33	5.55	0.07	0.03	98.9
LLF-46-1	high Fe	73.2	0.25	0.03	11.6	4.36	0.06	0.04	0.73	0.05	2.26	5.68	0.07	0.04	98.4
ULF-49-1	alkali feldspar	61.7	0.04	0.00	23.1	0.36	0.02	0.00	5.74	0.21	7.55	0.90	0.00	0.00	99.7
THR-53-1	ilmenite	0.02	48.8	0.09	0.00	46.5	0.62	0.45	0.02	0.00	0.00	0.00	0.00	0.00	96.5
THR-81-1	high Fe	73.9	0.40	0.08	11.6	3.63	0.05	0.05	0.67	0.07	2.35	5.54	0.07	0.02	98.4
MCR-38-4	alkali feldspar	60.9	0.01	0.06	23.6	0.34	0.02	0.00	8.03	0.06	5.59	3.39	0.00	0.00	102.0
CTR-50-1	pyrrhotite	0.07	0.02	0.25	0.02	77.9	0.00	0.00	0.00	0.00	0.00	0.00	0.00	0.00	78.3
CTR-83-1	pyrrhotite	0.02	0.00	0.00	0.00	77.1	0.05	0.00	0.00	0.02	0.00	0.00	0.00	0.00	77.2
CTR-84-1	low total low Si	71.0	0.29	0.18	10.8	1.15	0.03	0.05	2.06	0.00	1.88	6.07	0.04	0.03	93.6
CTR-91-1	ilmenite	0.07	47.3	0.12	0.01	49.5	0.74	0.93	0.03	0.00	0.00	0.00	0.00	0.00	98.7
CTR-34-1	ilmenite	0.07	50.5	0.14	0.00	46.2	0.66	1.09	0.02	0.00	0.00	0.00	0.00	0.00	98.7
CTR-4-2	plagioclase	58.6	0.01	0.01	23.5	0.33	0.00	0.00	6.43	0.20	7.09	1.23	0.00	0.00	97.4
CTR-47-1	high Zr	53.4	0.11	33.3	5.85	0.34	0.00	0.05	0.26	0.05	2.66	5.40	0.00	0.02	101.5
BJR-1-1	alkali feldspar	65.8	0.52	0.00	15.2	0.12	0.00	0.00	1.36	0.00	2.14	11.18	0.00	0.02	96.3

Table E.3 continued

Sample Name	Notes	SiO_2	TiO_2	ZrO_2	Al_2O_3	FeO	MnO	MgO	CaO	BaO	Na_2O	K_2O	F	Cl	Sum
BJR-24-1	high Si	81.3	0.07	0.01	8.38	0.69	0.02	0.07	0.34	0.05	1.66	3.91	0.00	0.04	96.6
BJR-45-1	low Si	66.0	0.07	0.58	13.5	2.24	0.00	0.02	2.47	0.00	3.04	4.54	0.05	0.05	92.6
BJR-45-2	high Si	88.9	0.02	0.00	5.52	0.50	0.01	0.07	0.61	0.00	2.94	0.28	0.00	0.01	98.9
BJR-64-1	alkali feldspar	68.3	0.01	0.20	18.4	0.75	0.03	0.05	0.51	0.01	10.3	0.32	0.00	0.03	98.9
BJR-69-1	ilmenite	0.24	57.9	0.06	0.00	30.1	1.25	0.53	0.28	0.00	0.00	0.01	0.31	0.01	90.7
BJR-74-1	fracture through MI	75.1	0.21	0.00	11.8	0.64	0.02	0.06	0.56	0.02	3.02	4.07	0.01	0.06	95.5
BJR-74-2	fracture through MI	75.1	0.15	0.21	11.6	0.17	0.00	0.00	0.43	0.00	2.86	4.42	0.08	0.04	95.0
PCR-132-1	alkali feldspar	64.9	0.03	0.00	18.6	0.16	0.00	0.00	0.81	0.20	4.75	9.50	0.00	0.00	99.0
LCR-37-2	plagioclase	59.3	0.01	0.04	23.6	0.40	0.00	0.00	6.33	0.16	6.93	1.37	0.00	0.00	98.1
LCR-37-3	plagioclase	64.7	0.05	0.07	20.6	0.47	0.00	0.00	4.35	0.46	5.40	3.86	0.00	0.01	99.9
LCR-41-1	low Si high Ca	70.1	0.15	0.05	12.2	3.16	0.00	0.27	2.06	0.17	2.91	5.13	0.01	0.03	96.2
SCR-104-2	low Na	74.2	0.40	0.21	11.8	2.05	0.02	0.06	0.38	0.00	0.83	4.72	0.09	0.05	94.8
SCR-104-3	high Fe	71.8	0.22	0.06	11.5	3.97	0.09	0.16	0.76	0.11	2.57	4.91	0.06	0.05	96.3
SCR-109-3	pyrrhotite	0.09	0.00	0.16	0.00	78.4	0.03	0.00	0.00	0.04	0.03	0.03	0.00	0.01	78.8
SCR-38-1	pyrrhotite	0.05	0.04	0.14	0.00	77.5	0.01	0.00	0.01	0.02	0.00	0.01	0.00	0.03	77.8
SCR-42-1	pyrrhotite	0.02	0.00	0.02	0.01	78.9	0.03	0.00	0.00	0.00	0.05	0.00	0.00	0.00	79.1
SCR-71-1	low Si high Ca	69.2	0.09	0.68	11.3	2.25	0.02	0.10	3.44	0.02	2.72	5.48	0.09	0.03	95.4
SCR-86-1	ilmenite	0.05	50.3	0.11	0.00	47.5	0.73	0.94	0.00	0.00	0.00	0.00	0.00	0.00	99.6
SCR-95-1	magnetite	35.1	9.81	0.05	6.38	41.3	0.29	0.44	0.59	0.00	1.41	2.84	0.20	0.03	98.5
DCR-14-1	ilmenite	0.07	49.4	0.19	0.00	46.7	0.77	0.91	0.05	0.00	0.04	0.00	0.00	0.00	98.2
DCR-101-1	pyrrhotite	0.07	0.06	0.07	0.07	78.3	0.03	0.00	0.00	0.01	0.00	0.00	0.00	0.01	78.6
DCR-103-2	pyrrhotite	0.10	0.03	0.10	0.00	74.6	0.06	0.00	0.00	0.00	0.00	0.00	0.00	0.00	74.9
DCR-2-1	high Fe-Ti	72.2	1.54	0.10	11.3	6.19	0.10	0.13	0.53	0.00	2.98	5.13	0.03	0.04	100.3
DCR-21-1	pyrrhotite	0.10	0.07	0.00	0.00	79.2	0.07	0.00	0.01	0.00	0.01	0.00	0.00	0.01	79.5

Table E.4. EPMA analyses of melt inclusions from the CPT with evidence of secondary growth or with abnormal elemental concentrations (i.e., high Zr or Fe) that indicate beam overlap on multiple phases

Sample Number	Notes	SiO_2	TiO_2	ZrO_2	Al_2O_3	FeO	MnO	MgO	CaO	BaO	Na_2O	K_2O	F	Cl	Sum
CPTIII-26-2	high Zr	71.4	0.04	0.83	11.2	6.65	0.00	0.15	0.42	0.00	2.87	5.52	0.35	0.06	99.5
CPTIII-41-2	low total low Si	71.7	0.08	0.37	11.2	3.49	0.02	0.13	1.25	0.00	2.59	5.41	0.19	0.06	96.4
CPTIII-17-1	high Si	78.4	0.04	0.11	12.5	0.31	0.00	0.00	0.24	0.02	2.73	5.87	0.15	0.07	100.5
CPTIII-23-1	low total low Si	73.8	0.08	0.00	12.1	0.32	0.02	0.00	0.32	0.02	1.86	6.96	0.44	0.08	95.9
CPTV-7-1	low Na	77.6	0.17	0.20	11.9	0.16	0.00	0.00	0.20	0.01	1.44	5.70	0.04	0.05	97.5
CPTVII-24-1	high Ti	76.7	0.39	0.12	12.2	0.76	0.00	0.01	0.66	0.00	2.69	5.98	0.10	0.04	99.7
CPTIX-32-2	high Si	79.4	0.03	0.22	11.0	0.10	0.02	0.00	0.08	0.10	2.14	5.56	0.03	0.03	98.8
CPTX-53-1	low total low Si	73.7	0.04	0.11	11.6	0.36	0.00	0.01	0.21	0.07	2.84	5.73	0.09	0.04	94.8
CPTXI-37-1	low Na	74.4	0.20	0.45	12.2	1.02	0.02	0.04	0.80	0.16	1.34	5.55	0.12	0.06	96.3
CPTXII-53-1	high Zr	75.2	0.03	0.97	11.9	0.62	0.00	0.03	0.33	0.12	2.76	6.10	0.16	0.03	98.2
CPTXVb-74-1	high Ca	74.8	0.32	0.08	12.1	0.95	0.00	0.32	1.73	0.01	2.71	5.55	0.07	0.04	98.6
CPTXVj-35-1	high Fe-Ti	74.3	0.34	0.03	11.9	2.30	0.03	0.00	0.33	0.16	2.97	5.84	0.07	0.01	98.3

Table E.5. EPMA analyses of melt inclusions from rhyolite lavas that show no secondary growth (H_2O by

Sample Name	SiO_2	TiO_2	ZrO_2	Al_2O_3	FeO	MnO	MgO	CaO	BaO	Na_2O	K_2O	F	Cl	Sum	H_2O
LF1-72-1	73.8	0.30	0.24	12.4	1.16	0.05	0.17	0.76	0.03	2.41	6.65	0.12	0.03	98.1	1.9
LF1-64-1	73.5	0.32	0.12	11.9	1.89	0.05	0.11	0.98	0.09	2.70	5.70	0.02	0.02	97.5	2.5
LF1-75-4	72.0	0.35	0.10	12.8	1.81	0.06	0.12	1.01	0.05	2.75	6.38	0.07	0.01	97.5	2.5
LF1-61-1	74.5	0.10	0.03	11.7	1.68	0.01	0.08	0.71	0.06	2.19	5.96	0.02	0.03	97.0	3.0
Average LF2	73.5	0.27	0.12	12.2	1.64	0.04	0.12	0.86	0.06	2.51	6.18	0.06	0.02	97.5	2.5
STDEV	1.05	0.11	0.09	0.50	0.33	0.02	0.03	0.15	0.03	0.26	0.42	0.05	0.01	0.44	0.44
LLF-59-1	76.3	0.14	0.07	12.2	1.89	0.02	0.01	0.35	0.01	2.68	5.86	0.06	0.05	99.6	0.4
Average LLF	76.3	0.14	0.07	12.2	1.89	0.02	0.01	0.35	0.01	2.68	5.86	0.06	0.05	99.6	0.4
STDEV	NA	NA	NA	NA	NA	NA	NA	NA	NA	NA	NA	NA	NA	NA	NA
THT-17-2	75.8	0.28	0.03	12.1	1.53	0.02	0.03	0.81	0.08	2.59	5.84	0.07	0.03	99.2	0.8
THR-21-1	75.6	0.17	0.12	11.9	2.55	0.05	0.02	0.93	0.11	2.48	5.32	0.07	0.02	99.3	0.7
THR-25-1	75.2	0.07	0.09	11.8	2.68	0.06	0.02	0.79	0.08	2.41	5.59	0.14	0.03	98.9	1.1
THR-61-2	75.5	0.10	0.15	12.1	2.21	0.00	0.02	0.62	0.05	2.67	5.58	0.12	0.04	99.2	0.8
Average THR	75.5	0.16	0.10	12.0	2.24	0.03	0.02	0.79	0.08	2.54	5.58	0.10	0.03	99.2	0.8
STDEV	0.29	0.09	0.05	0.16	0.52	0.03	0.00	0.13	0.02	0.11	0.21	0.04	0.01	0.18	0.18
MCR-21-1	75.2	0.08	0.00	12.2	2.22	0.00	0.00	0.40	0.11	2.29	5.70	0.11	0.04	98.3	1.7
MCR-28-1	76.1	0.04	0.02	12.0	1.56	0.02	0.00	0.24	0.18	2.64	5.72	0.09	0.04	98.7	1.3

Table E.5 continued

Sample Name	SiO_2	TiO_2	ZrO_2	Al_2O_3	FeO	MnO	MgO	CaO	BaO	Na_2O	K_2O	F	Cl	Sum	H_2O
MCR-30-1	75.5	0.06	0.00	11.7	1.57	0.03	0.00	0.27	0.12	2.88	5.63	0.13	0.05	97.9	2.1
Average MCR	75.6	0.06	0.01	12.0	1.78	0.02	0.00	0.30	0.14	2.60	5.68	0.11	0.04	98.3	1.7
STDEV	0.51	0.02	0.01	0.23	0.38	0.01	0.00	0.08	0.04	0.30	0.05	0.02	0.01	0.37	0.37
CTR-70-1	72.5	0.28	0.12	11.4	1.69	0.03	0.07	0.48	0.00	1.94	6.25	0.00	0.02	94.8	5.2
Average CTR	72.5	0.28	0.12	11.4	1.69	0.03	0.07	0.48	0.00	1.94	6.25	0.00	0.02	94.8	5.2
STDEV	NA	NA	NA	NA	NA	NA	NA	NA	NA	NA	NA	NA	NA	NA	NA
SCR-99-2	75.3	0.33	0.11	12.1	1.74	0.03	0.01	0.24	0.00	3.17	5.61	0.10	0.05	98.8	1.2
SCR-49-1	75.1	0.11	0.10	11.7	2.46	0.03	0.09	0.46	0.10	2.64	5.53	0.10	0.06	98.5	1.5
SCR-17-1	76.2	0.18	0.13	11.9	1.01	0.04	0.02	0.26	0.11	2.39	5.88	0.05	0.05	98.2	1.8
SCR-67-1	75.4	0.37	0.13	11.9	1.48	0.01	0.01	0.32	0.00	2.09	5.69	0.08	0.03	97.5	2.5
SCR-89-2	74.9	0.08	0.13	11.8	1.70	0.02	0.03	0.29	0.07	2.65	5.59	0.10	0.04	97.4	2.6
SCR-104-1	73.4	0.35	0.24	11.8	2.01	0.01	0.03	0.36	0.00	2.78	5.25	0.06	0.06	96.4	3.6
Average SCR	75.0	0.24	0.14	11.9	1.73	0.02	0.03	0.32	0.05	2.62	5.59	0.08	0.05	97.8	2.2
STDEV	0.91	0.13	0.05	0.14	0.49	0.01	0.03	0.08	0.05	0.37	0.21	0.02	0.01	0.90	0.90
IBR-18-1	73.2	0.24	0.34	11.6	2.27	0.04	0.18	0.75	0.02	3.15	5.74	0.09	0.03	97.7	2.3
Average IBR	73.2	0.24	0.34	11.6	2.27	0.04	0.18	0.75	0.02	3.15	5.74	0.09	0.03	97.7	2.3
STDEV	NA	NA	NA	NA	NA	NA	NA	NA	NA	NA	NA	NA	NA	NA	NA

Table E.5 continued

Sample Name	SiO_2	TiO_2	ZrO_2	Al_2O_3	FeO	MnO	MgO	CaO	BaO	Na_2O	K_2O	F	Cl	Sum	H_2O
TCT-50-1	73.9	0.09	0.13	12.2	1.35	0.03	0.02	0.39	0.00	3.17	5.49	0.08	0.11	97.0	3.0
Average TCT	73.9	0.09	0.13	12.2	1.35	0.03	0.02	0.39	0.00	3.17	5.49	0.08	0.11	97.0	3.0
STDEV	NA	NA	NA	NA	NA	NA	NA	NA	NA	NA	NA	NA	NA	NA	NA
Total Average	74.7	0.19	0.11	12.0	1.83	0.03	0.05	0.54	0.06	2.60	5.76	0.08	0.04	98.0	2.0
Total STDEV	1.23	0.11	0.08	0.30	0.44	0.02	0.06	0.26	0.05	0.33	0.33	0.04	0.02	1.14	1.14

Table E.6. EPMA analyses of CPT melt inclusions without secondary phases (H_2O by difference)

Sample Name	SiO_2	TiO_2	ZrO_2	Al_2O_3	FeO	MnO	MgO	CaO	BaO	Na_2O	K_2O	F	Cl	Sum	H_2O
CPTXI-32-1	76.1	0.17	0.11	11.8	1.70	0.01	0.04	0.59	0.00	2.93	5.77	0.08	0.04	99.3	0.7
CPTXI-29-1	75.9	0.22	0.11	11.8	1.66	0.01	0.07	0.65	0.01	2.37	5.80	0.16	0.03	98.7	1.3
CPTXI-26-1	75.7	0.24	0.41	12.1	1.17	0.03	0.02	0.58	0.03	2.44	5.84	0.08	0.07	98.7	1.3
CPTXI-42-1	74.6	0.24	0.14	12.3	1.49	0.01	0.02	0.66	0.07	2.89	5.92	0.01	0.05	98.3	1.7
CPTXI-42-2	75.5	0.19	0.27	11.7	1.15	0.02	0.05	0.63	0.02	2.79	5.73	0.11	0.04	98.1	1.9
CPTXI-17-1	76.0	0.15	0.04	11.7	1.10	0.01	0.04	0.66	0.00	2.47	5.65	0.07	0.04	97.9	2.1
CPTXI-11-1	75.2	0.26	0.09	12.0	1.07	0.04	0.04	0.55	0.07	2.73	5.74	0.03	0.04	97.9	2.1
CPTXI-11-3	75.0	0.22	0.08	11.7	1.16	0.00	0.05	0.62	0.03	2.74	5.77	0.11	0.06	97.6	2.4
CPTXI-11-2	74.5	0.14	0.07	11.9	1.04	0.01	0.05	0.55	0.06	3.11	5.90	0.03	0.04	97.4	2.6
Average	75.4	0.20	0.15	11.9	1.28	0.01	0.04	0.61	0.03	2.72	5.79	0.08	0.04	98.2	1.8
STDEV	0.58	0.04	0.12	0.20	0.26	0.01	0.02	0.04	0.03	0.25	0.08	0.05	0.01	0.60	0.60

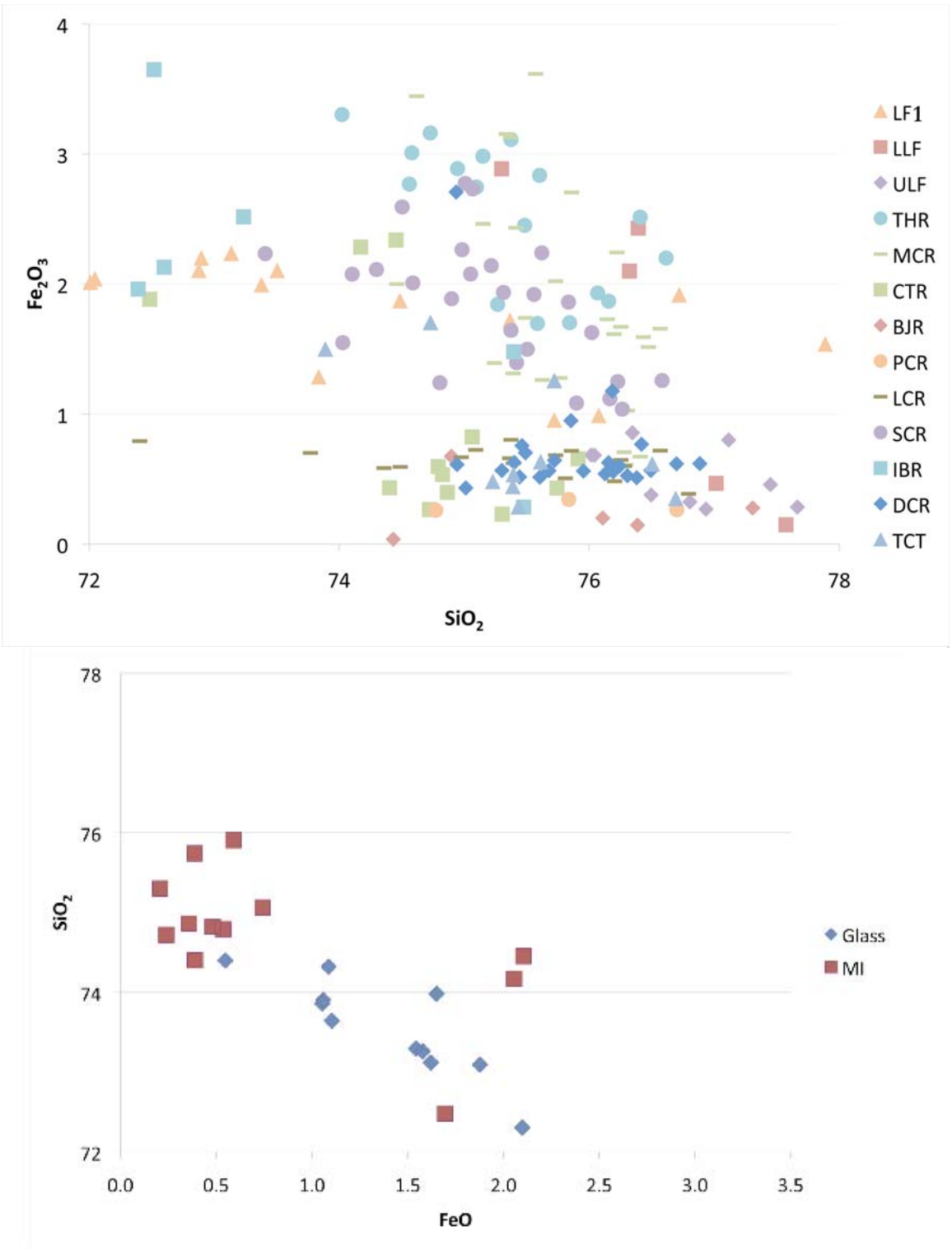

Figure E.13. Compositional variation in lavas from the BJEC. The lower graph includes analyses of glass and the upper graph is from melt inclusion analyses. Data for glass analyses from Nash (unpublished).

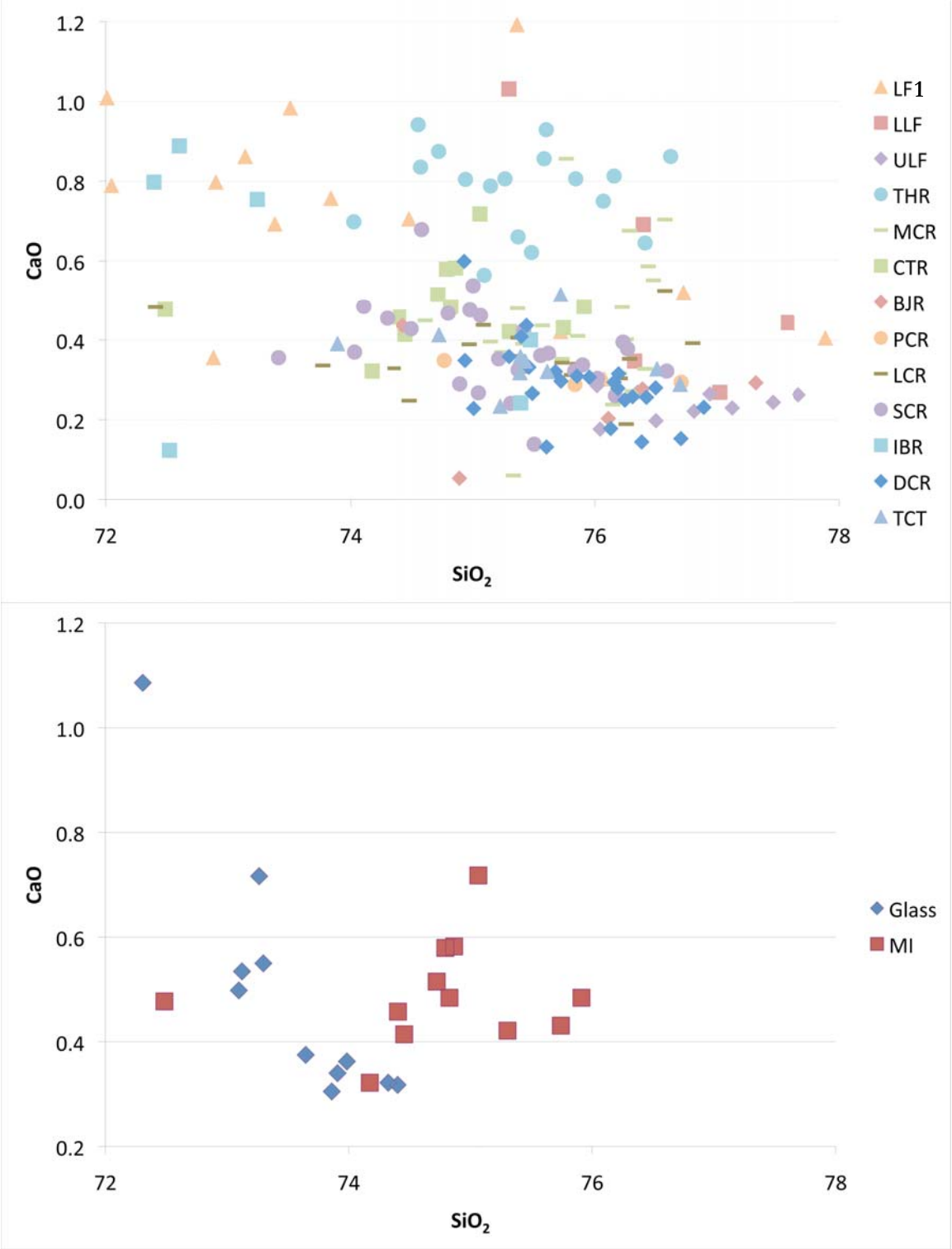

Figure E.14. Compositional variation in lavas from the BJEC. The lower graph includes analyses of glass and the upper graph is from melt inclusion analyses. Data for glass analyses from Nash (unpublished).

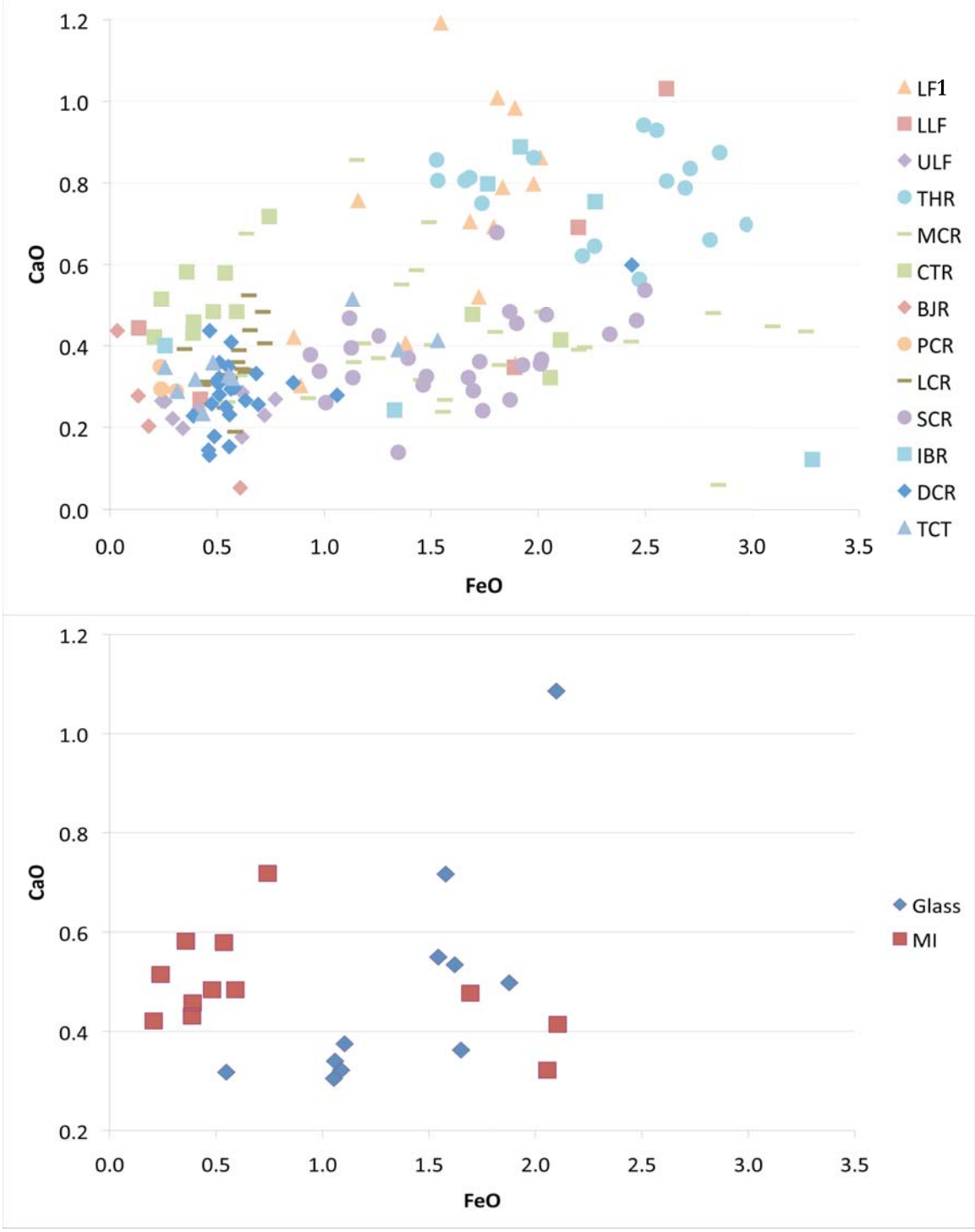

Figure E.14 continued

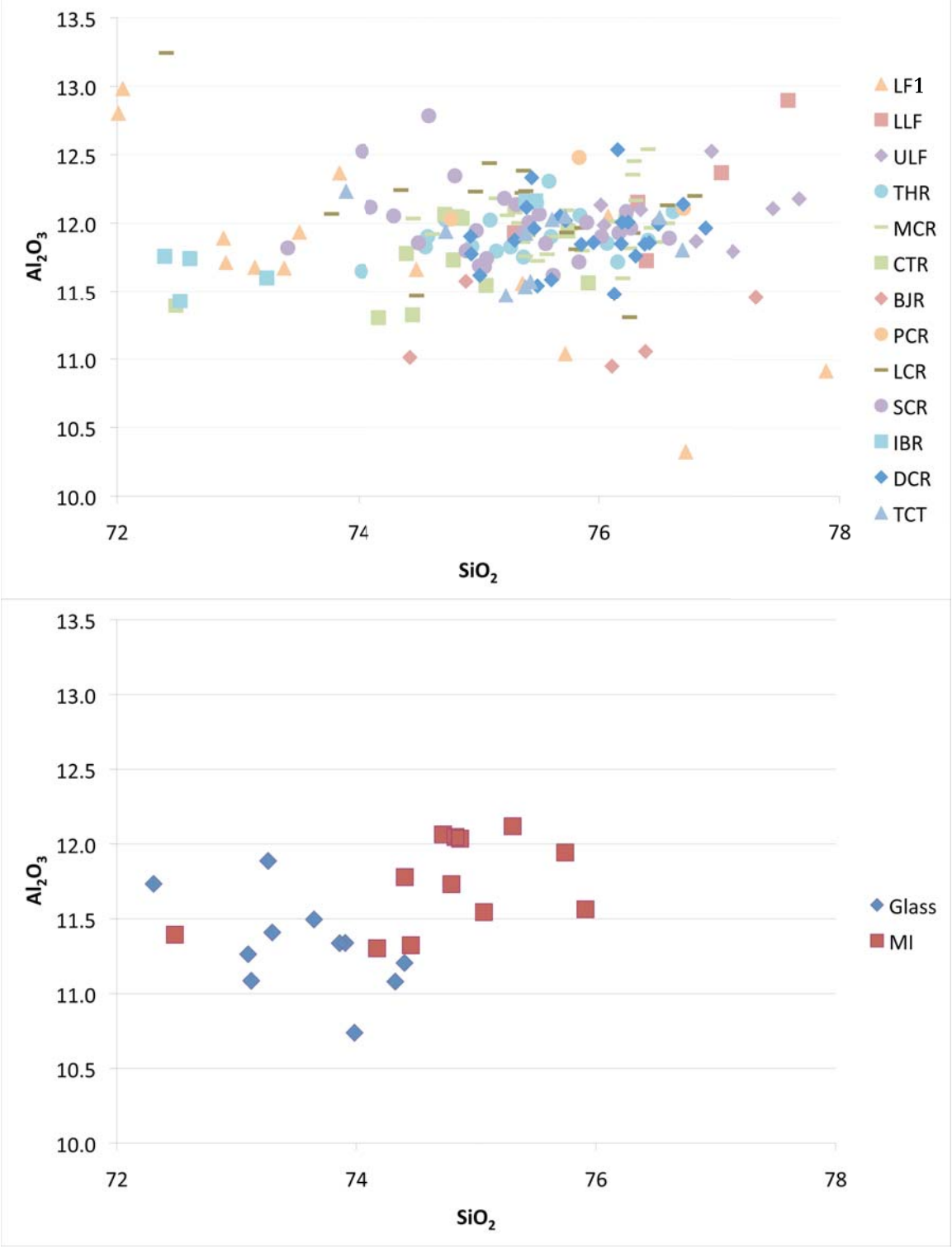

Figure E.15. Compositional variation in lavas from the BJEC. The lower graph includes analyses of glass and the upper graph is from melt inclusion analyses. Data for glass analyses from Nash (unpublished).

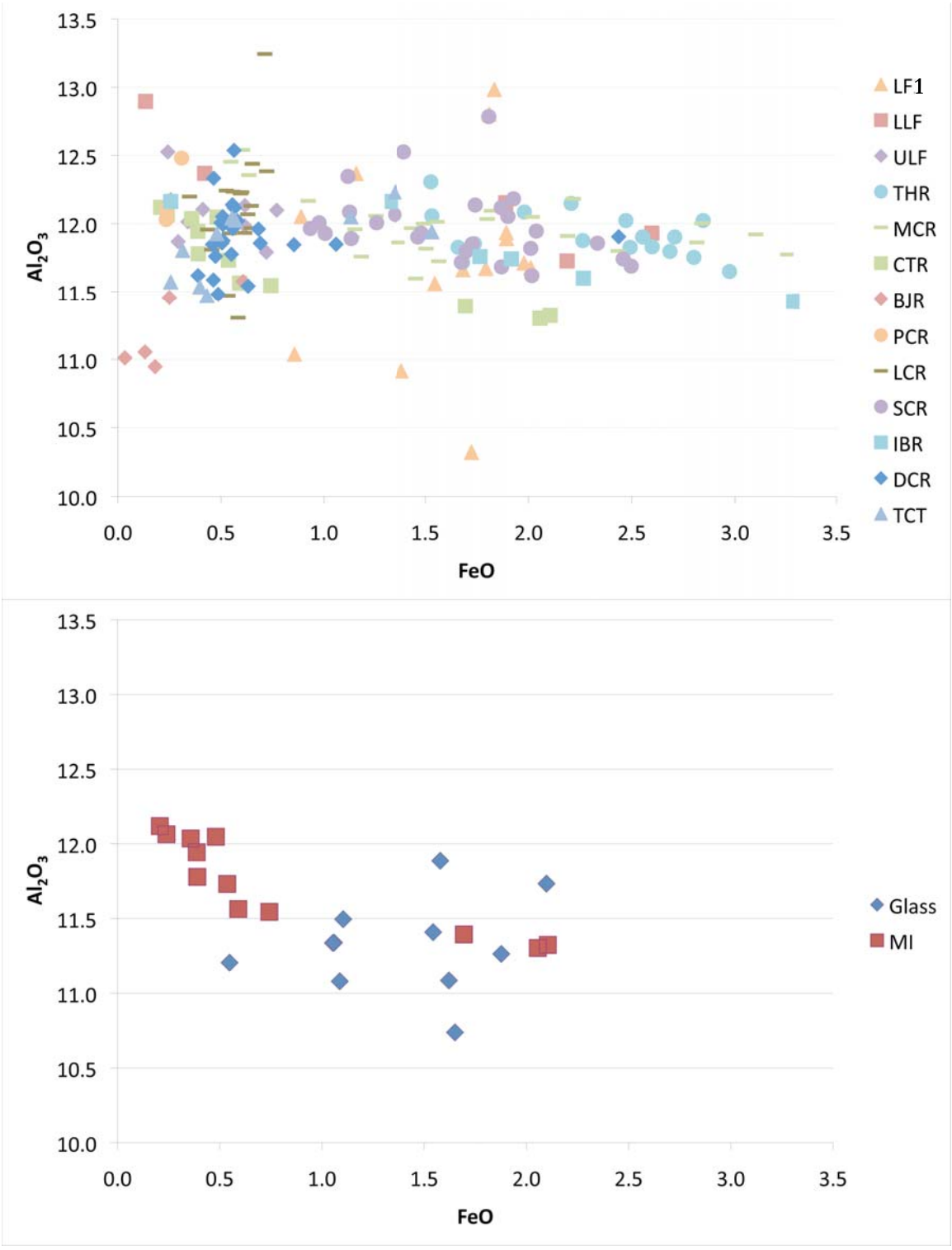

Figure E.15 continued

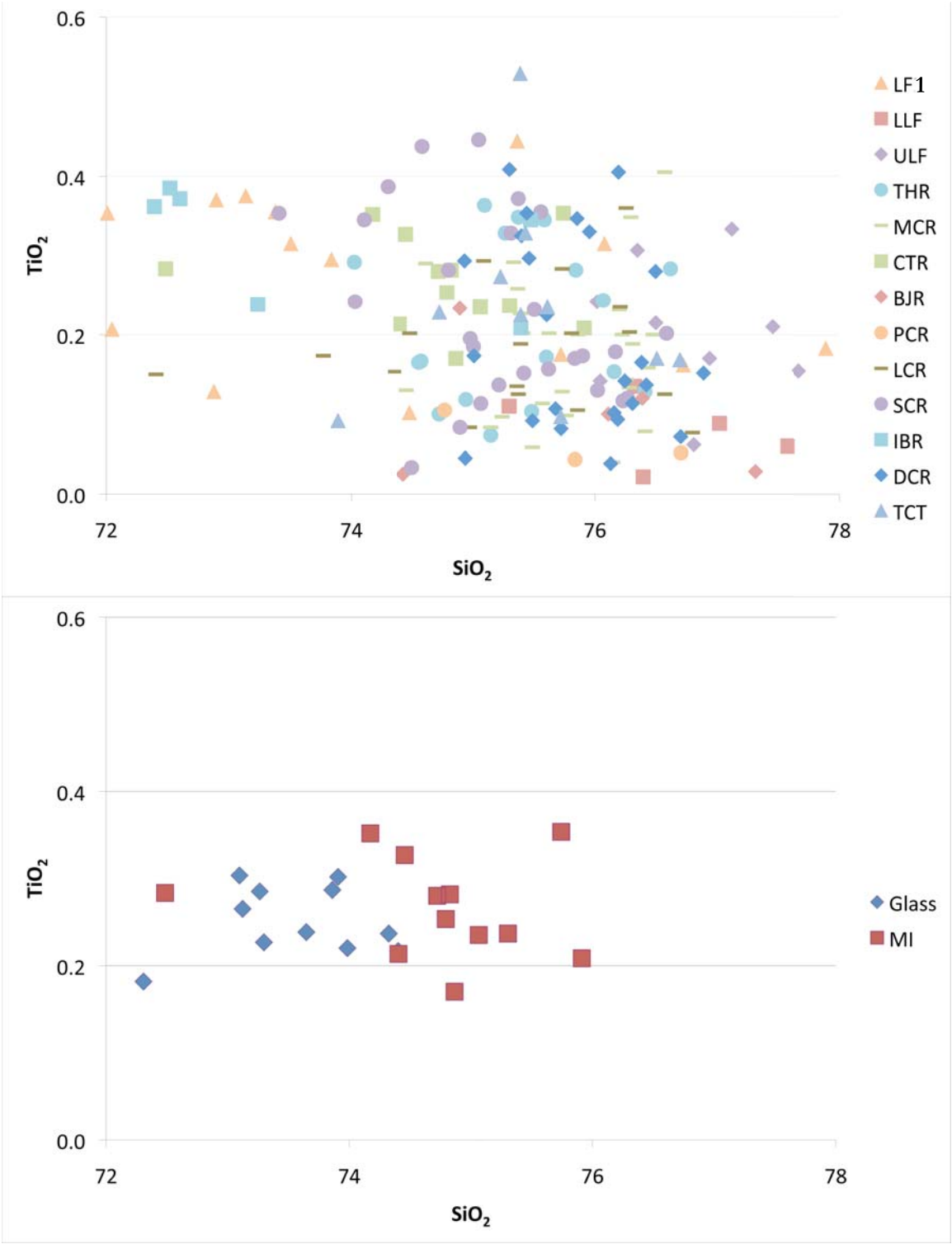

Figure E.16. Compositional variation in lavas from the BJEC. The lower graph includes analyses of glass and the upper graph is from melt inclusion analyses. Data for glass analyses from Nash (unpublished).

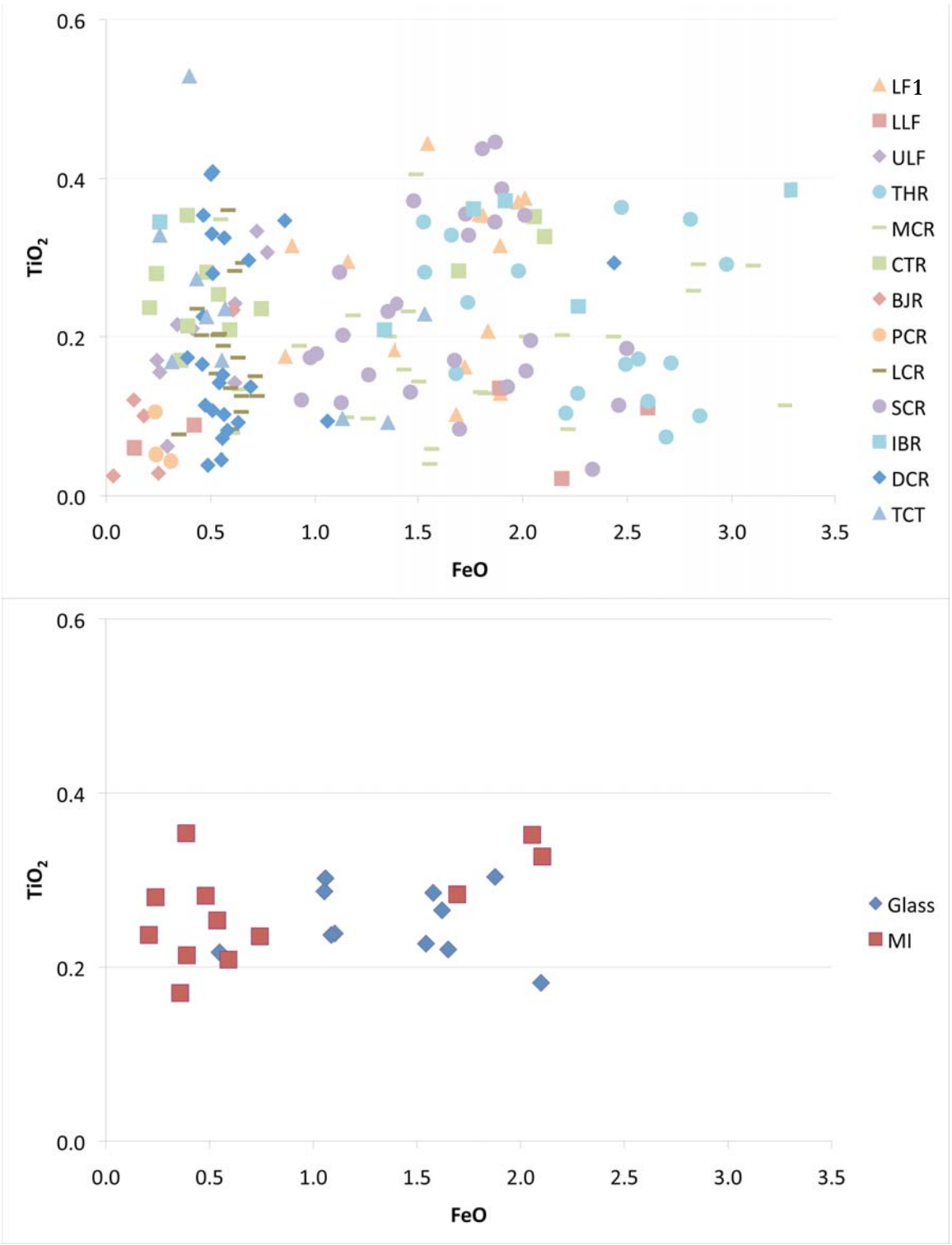

Figure E.16 continued

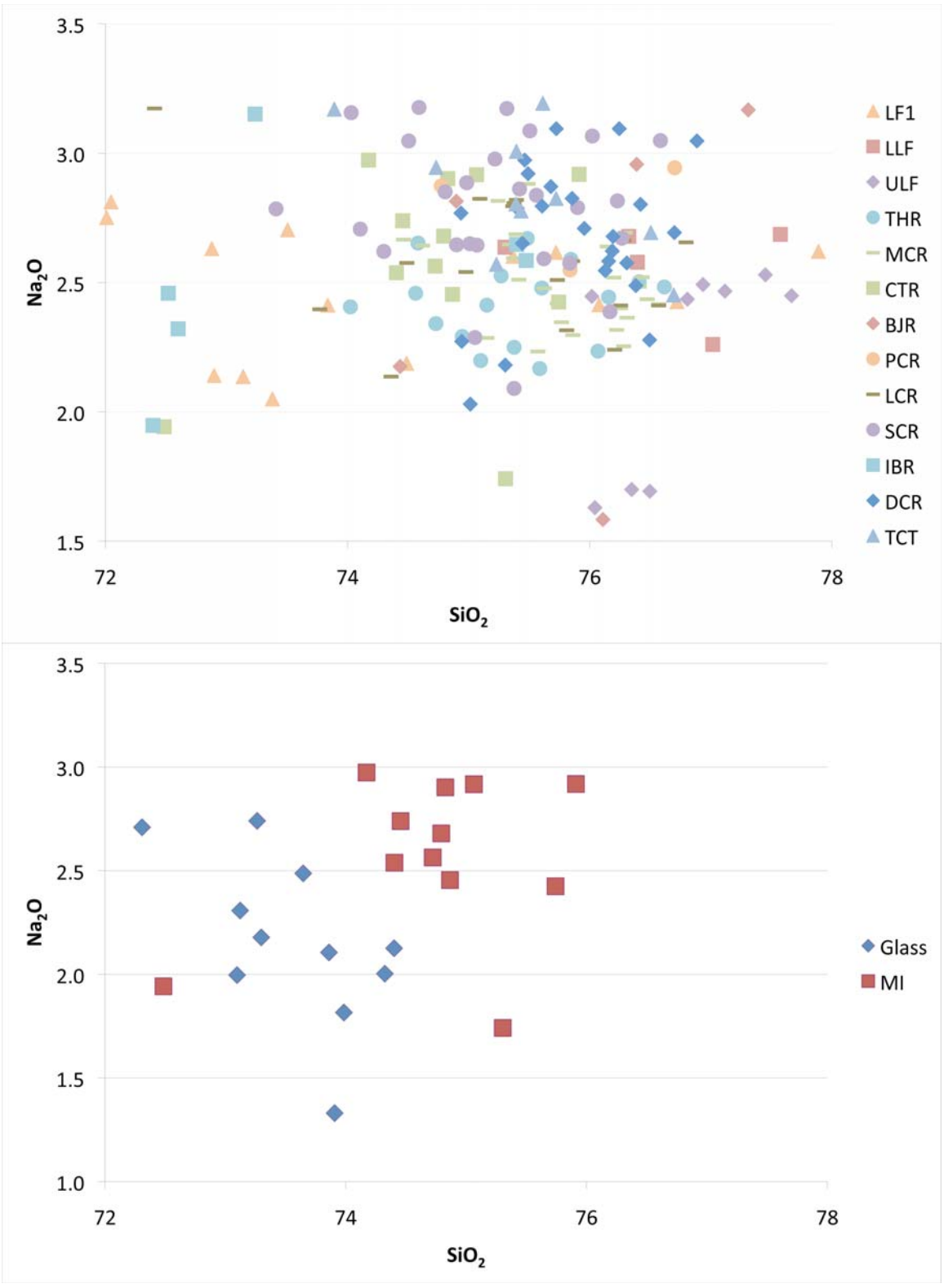

Figure E.17. Compositional variation in lavas from the BJEC. The lower graph includes analyses of glass and the upper graph is from melt inclusion analyses. Data for glass analyses from Nash (unpublished).

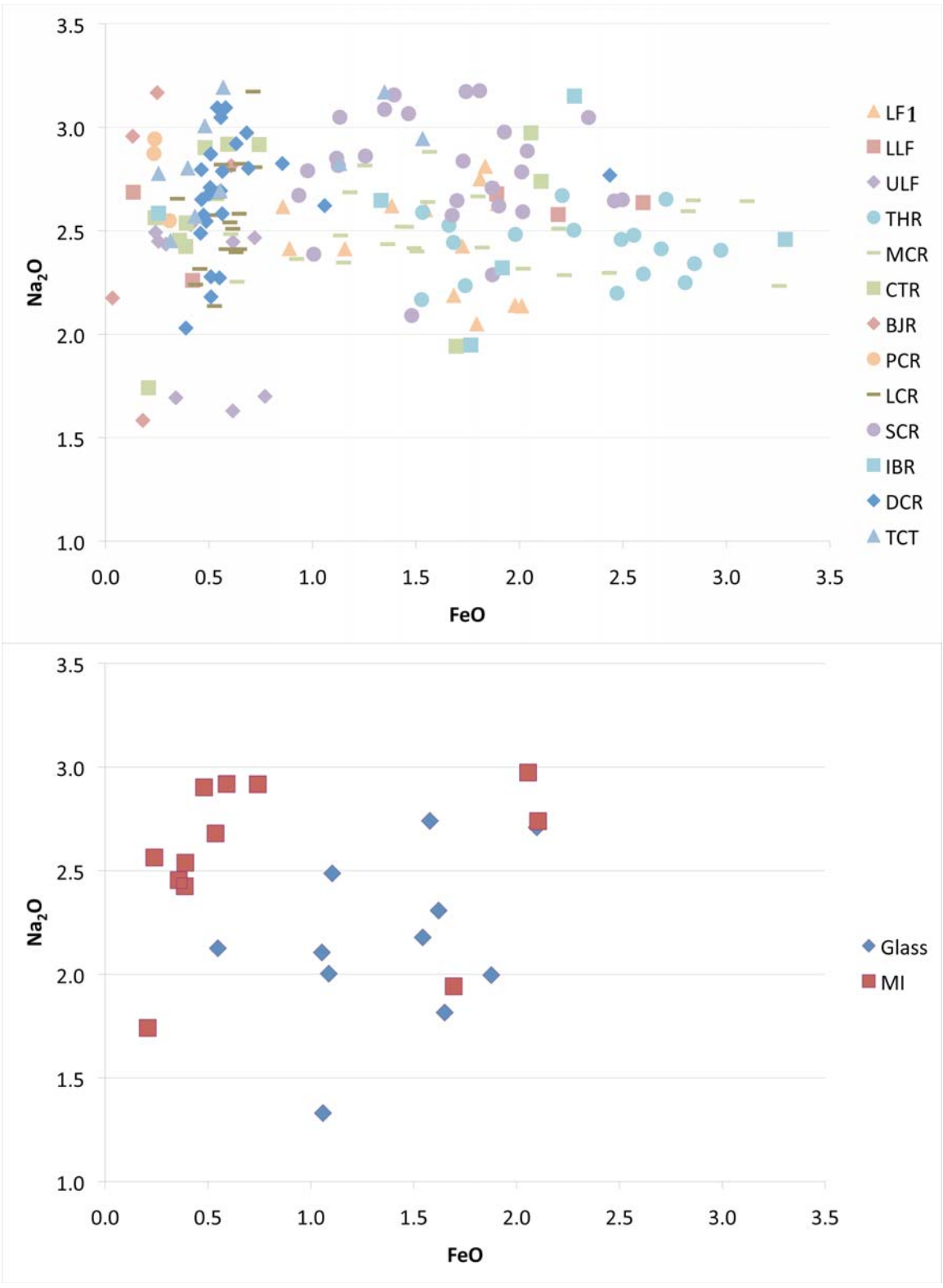

Figure E.17 continued

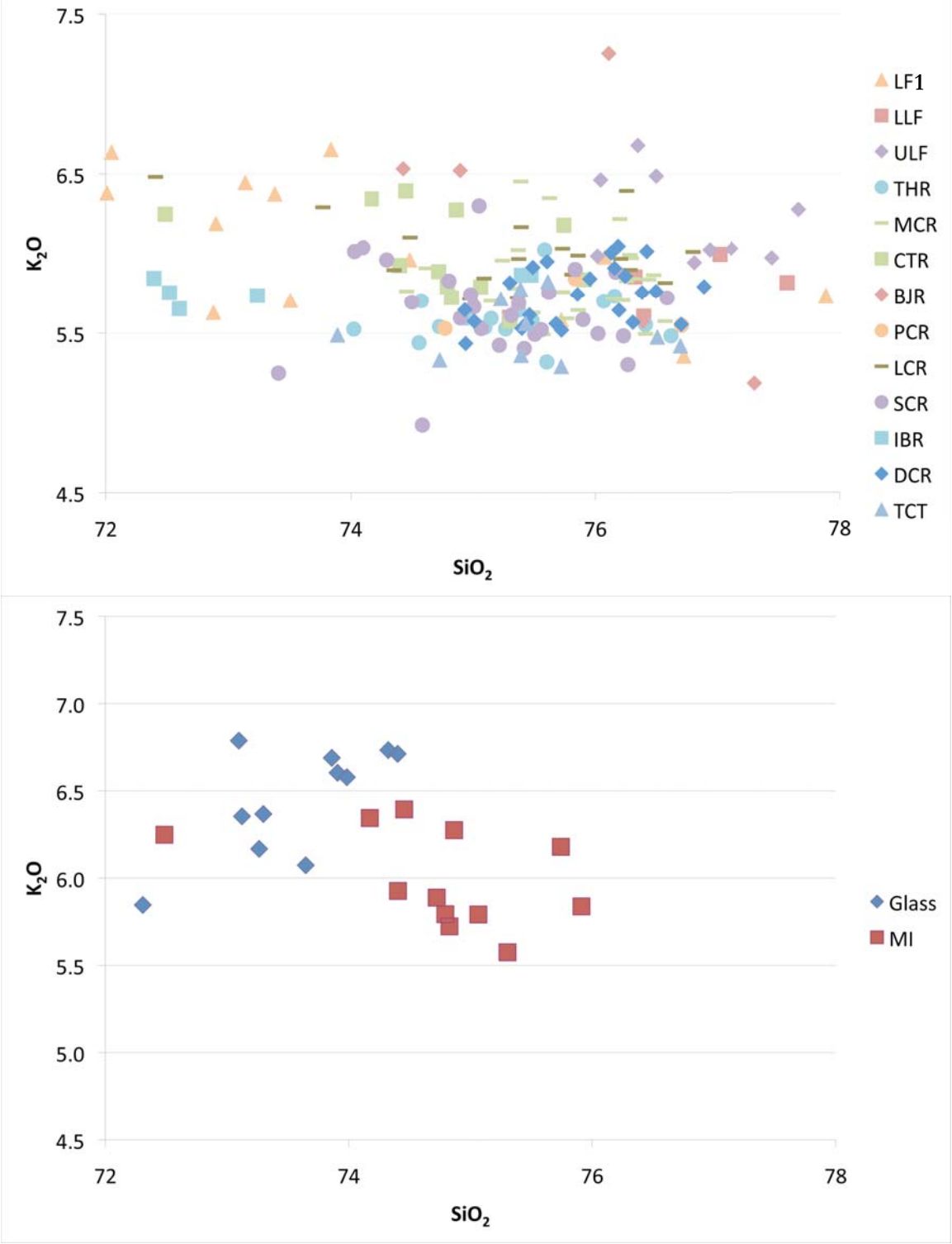

Figure E.18. Compositional variation in lavas from the BJEC. The lower graph includes analyses of glass and the upper graph is from melt inclusion analyses. Data for glass analyses from Nash (unpublished).

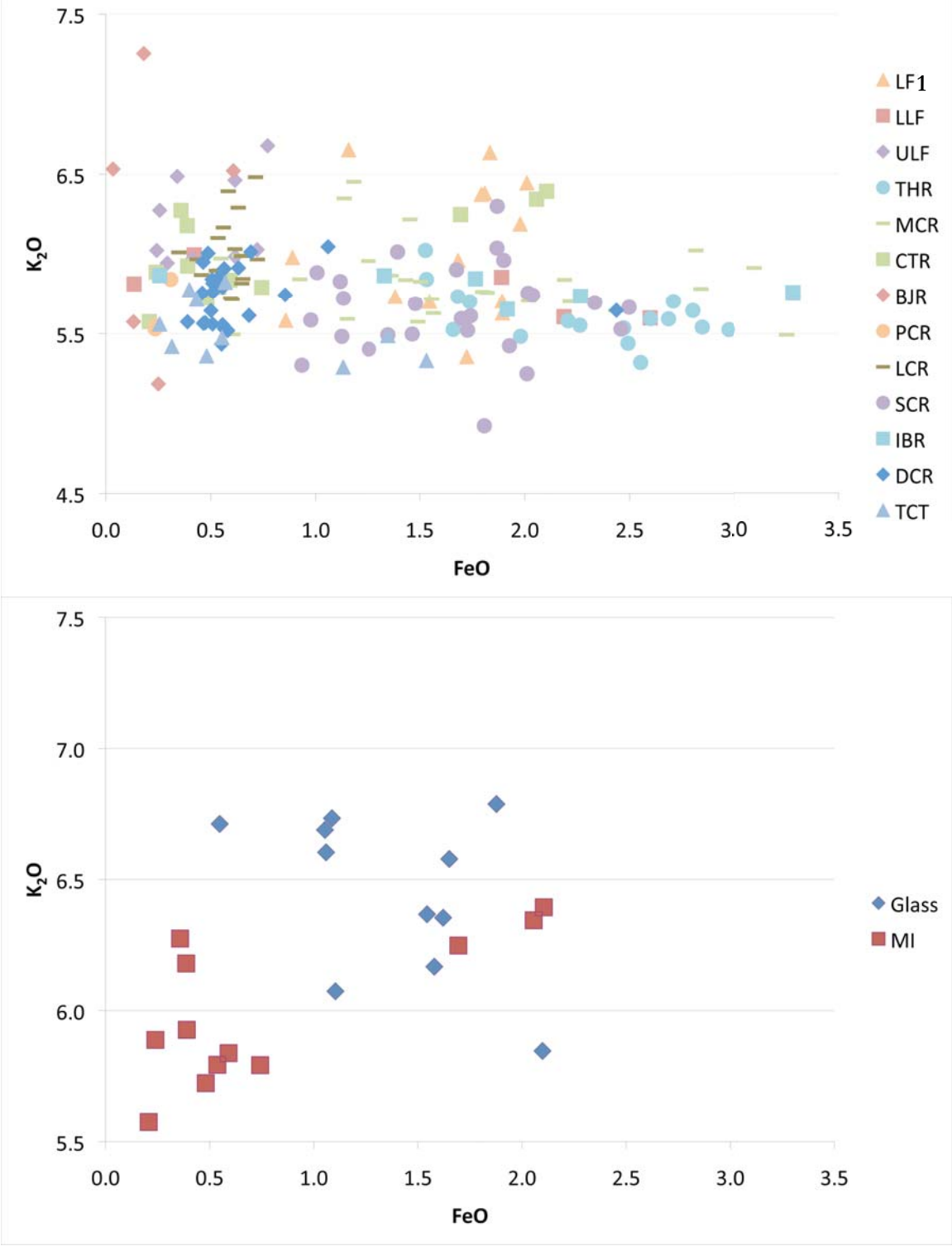

Figure E.18 continued

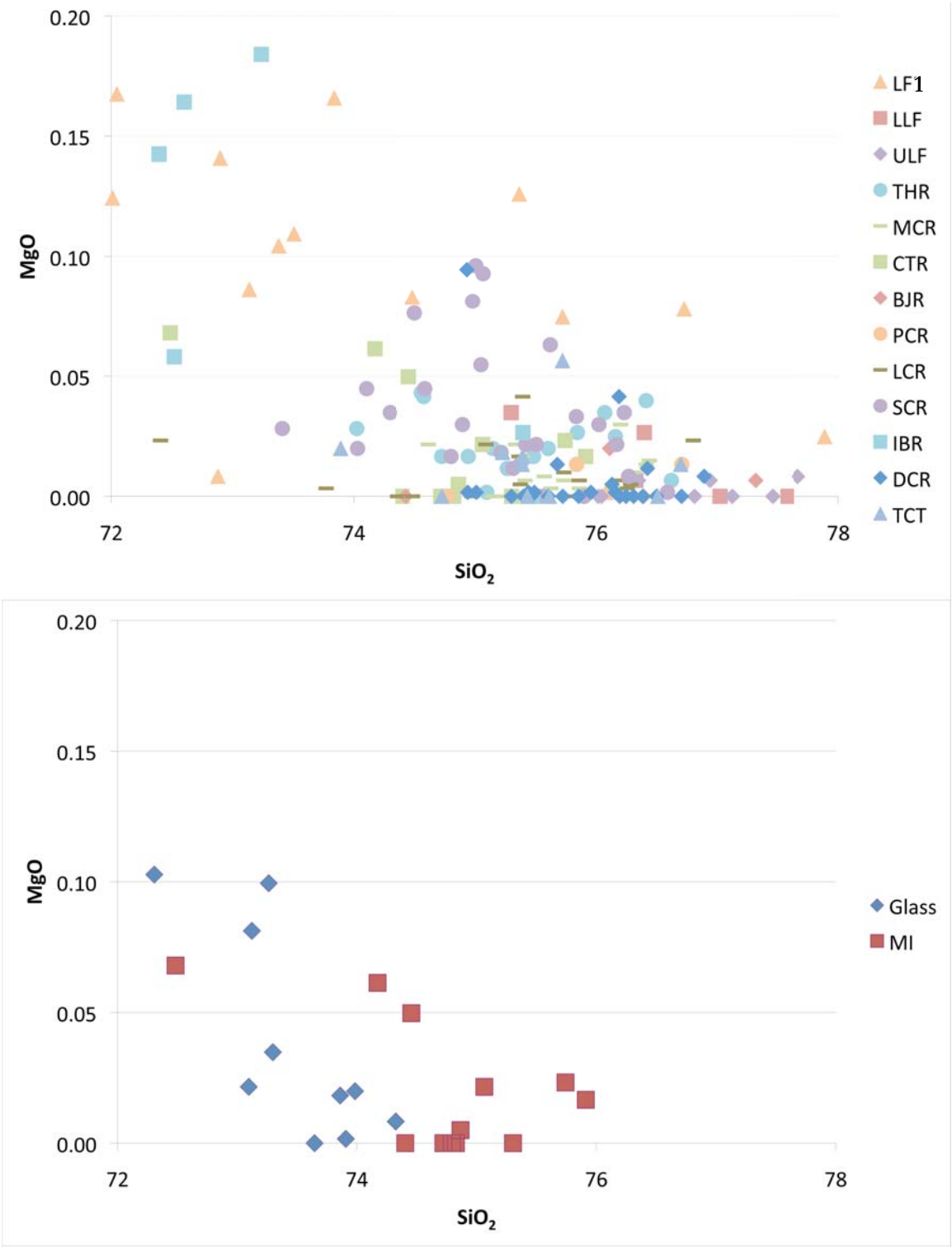

Figure E.19. Compositional variation in lavas from the BJEC. The lower graph includes analyses of glass and the upper graph is from melt inclusion analyses. Data for glass analyses from Nash (unpublished).

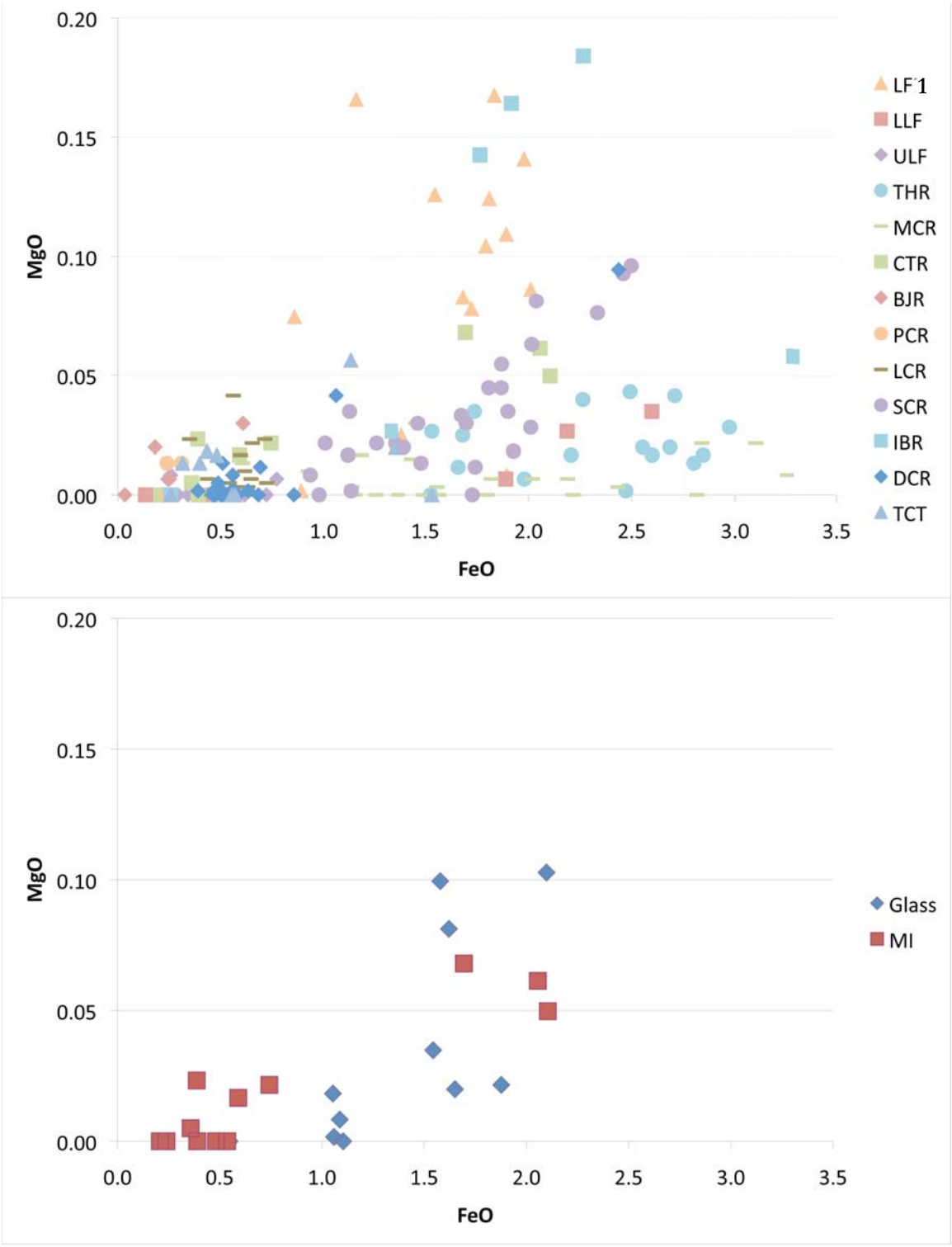

Figure E.19 continued

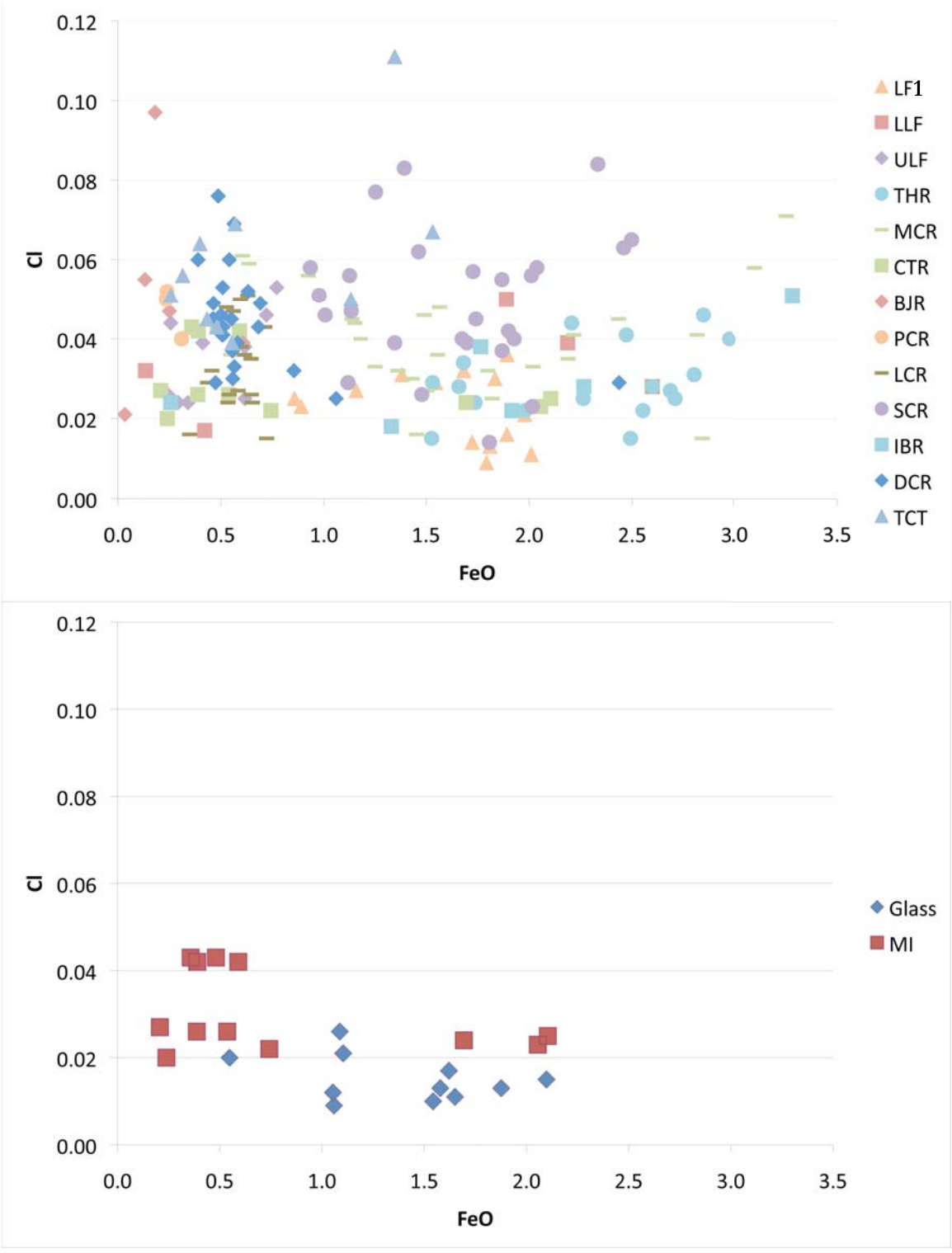

Figure E.20. Compositional variation in glass from lavas of the BJEC. The lower graph includes analyses of glass and the upper graph is from melt inclusion analyses. Data for glass analyses from Nash (unpublished).

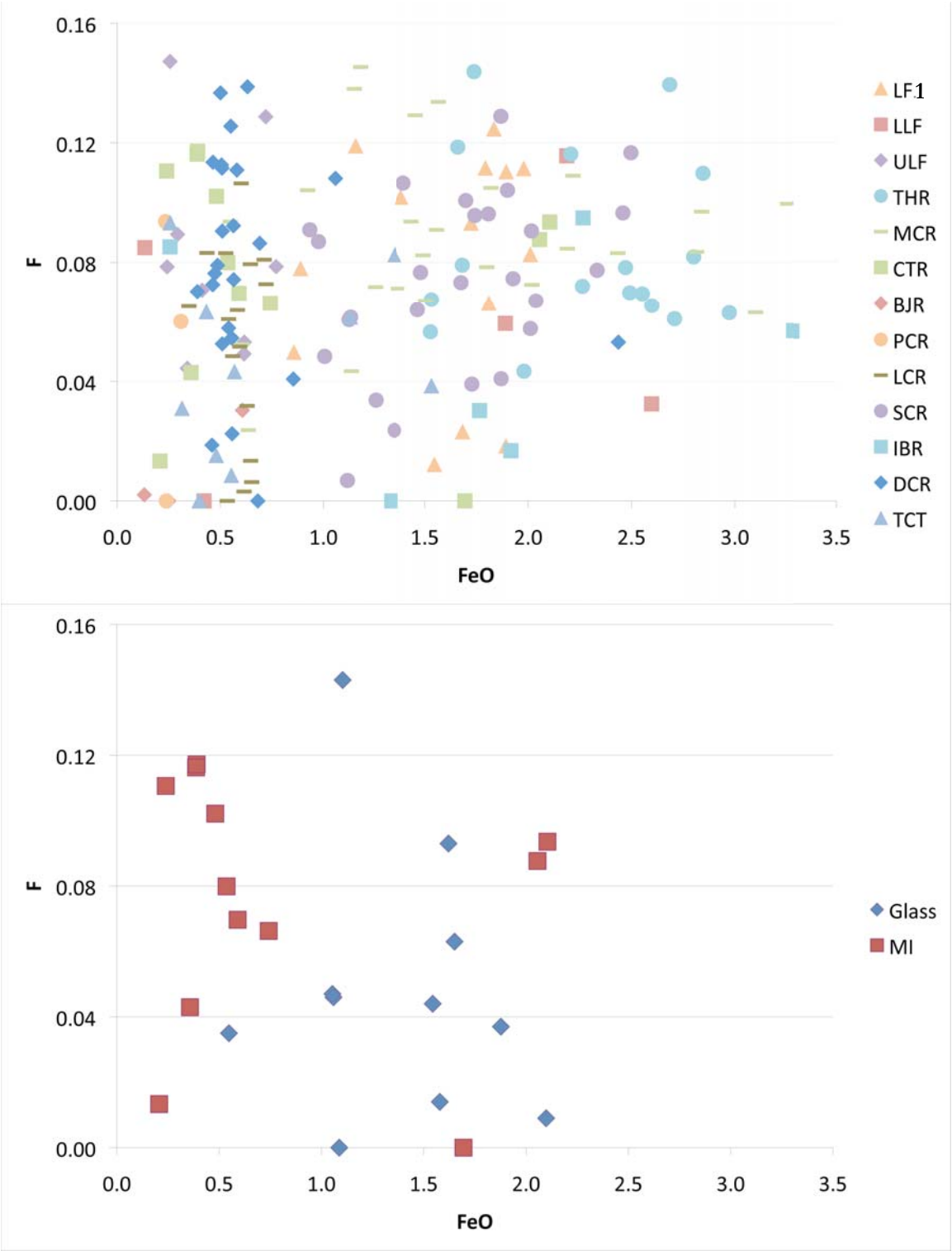

Figure E.21. Compositional variation in glass from lavas of the BJEC. The lower graph includes analyses of glass and the upper graph is from melt inclusion analyses. Data for glass analyses from Nash (unpublished).

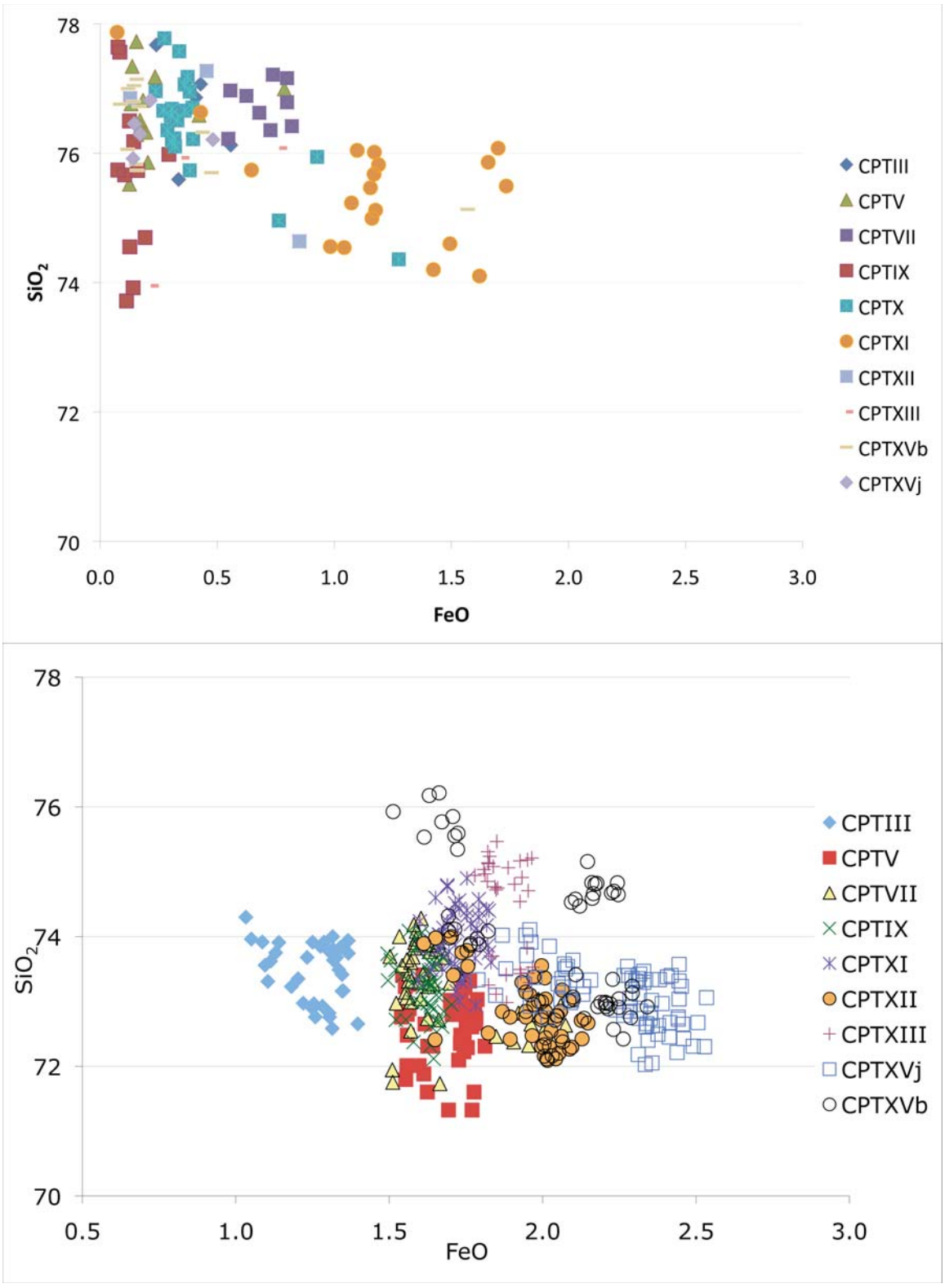

Figure E.22. Compositional variation in glasses for the CPT from the BJEC. The lower graph is airfall glass and the upper graph is from melt inclusion analyses. Data for glass analyses from Nash (unpublished).

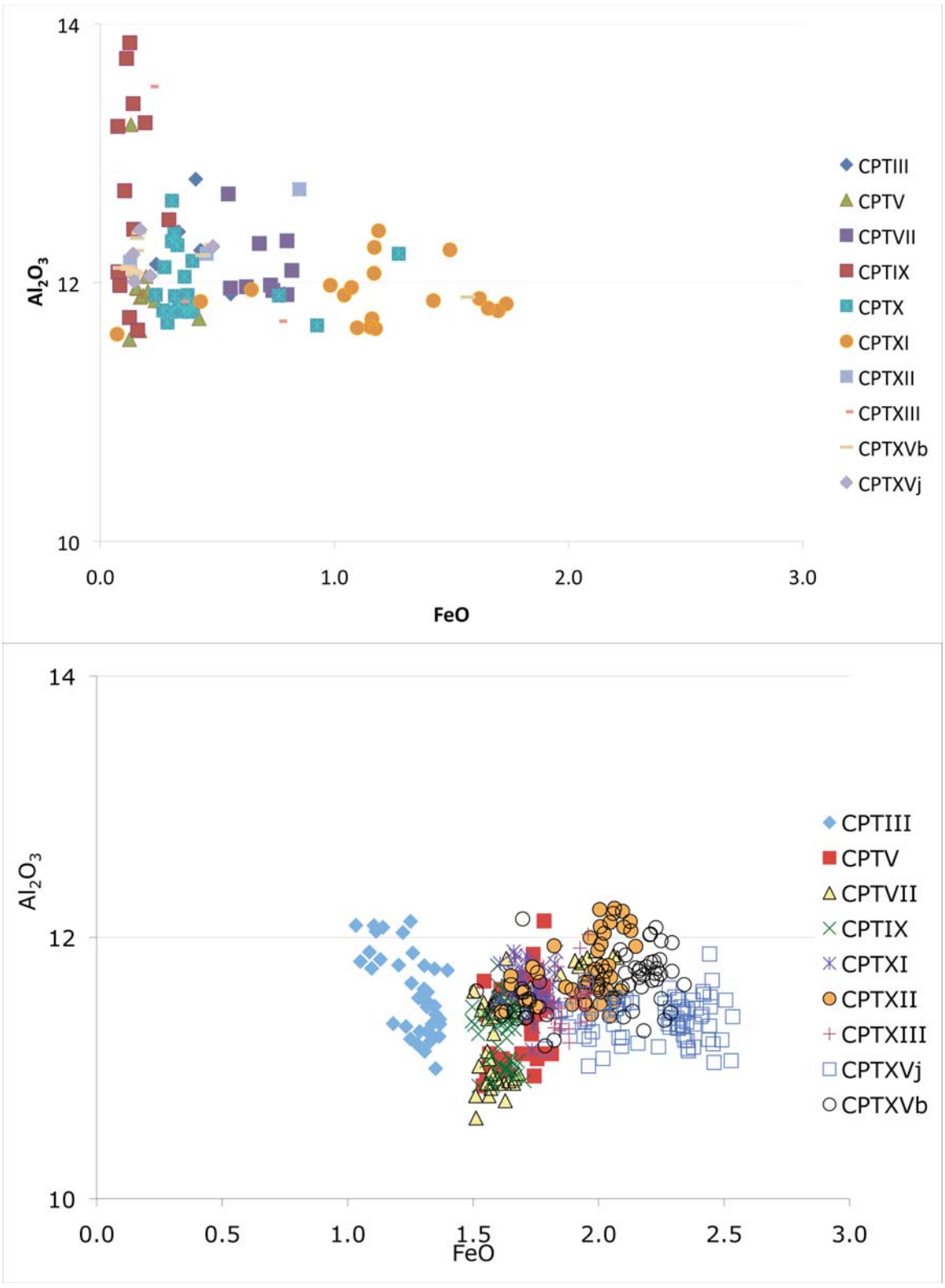

Figure E.23. Compositional variation in glasses for the CPT from the BJEC. The lower graph is airfall glass and the upper graph is from melt inclusion analyses. Data for glass analyses from Nash (unpublished).

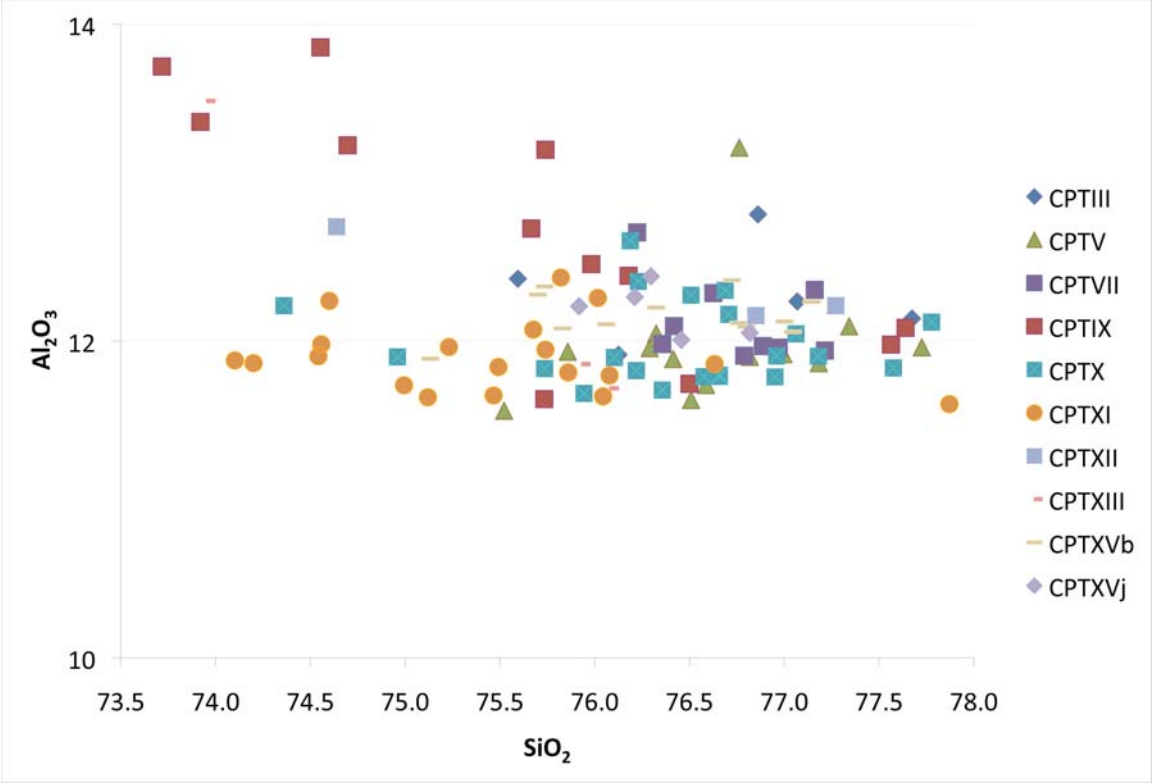

Figure E.23 continued

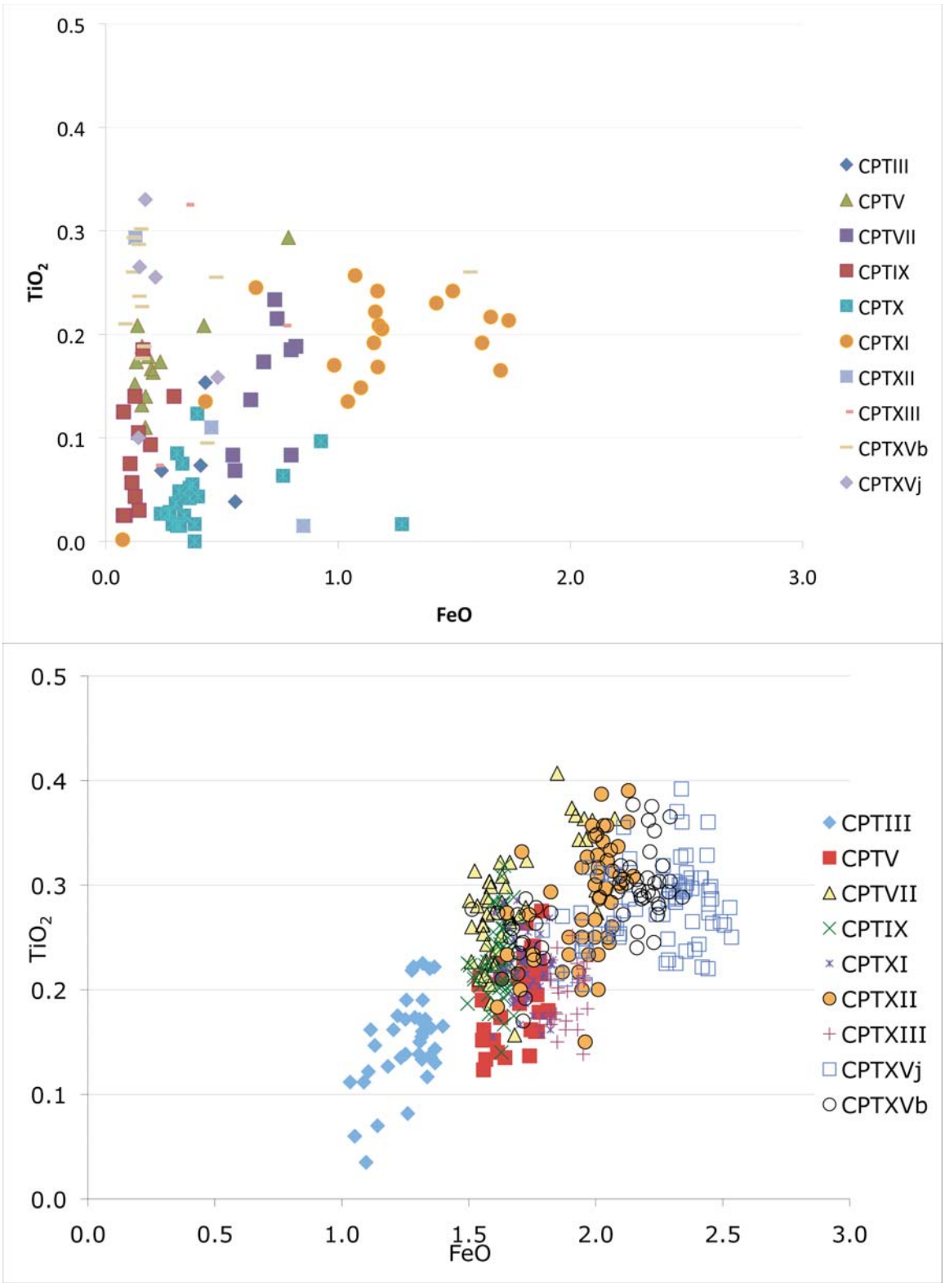

Figure E.24. Compositional variation in glasses for the CPT from the BJEC. The lower graph is airfall glass and the upper graph is from melt inclusion analyses. Data for glass analyses from Nash (unpublished).

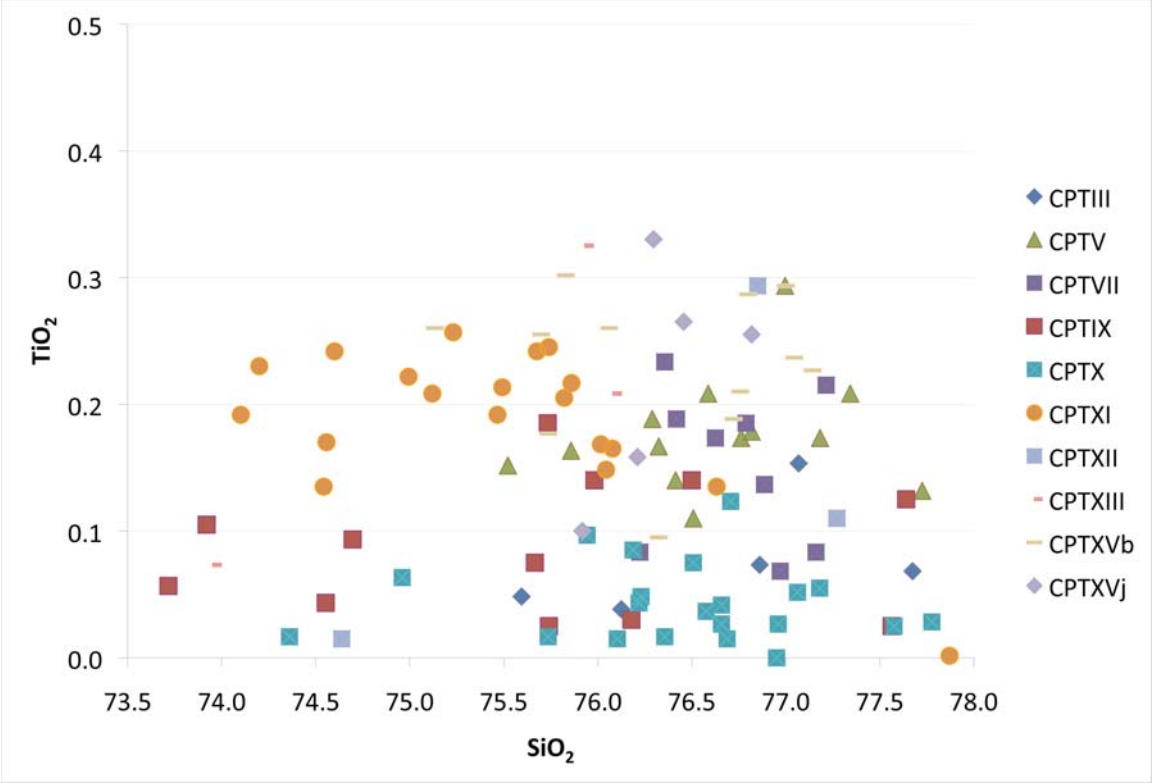

Figure E.24 continued

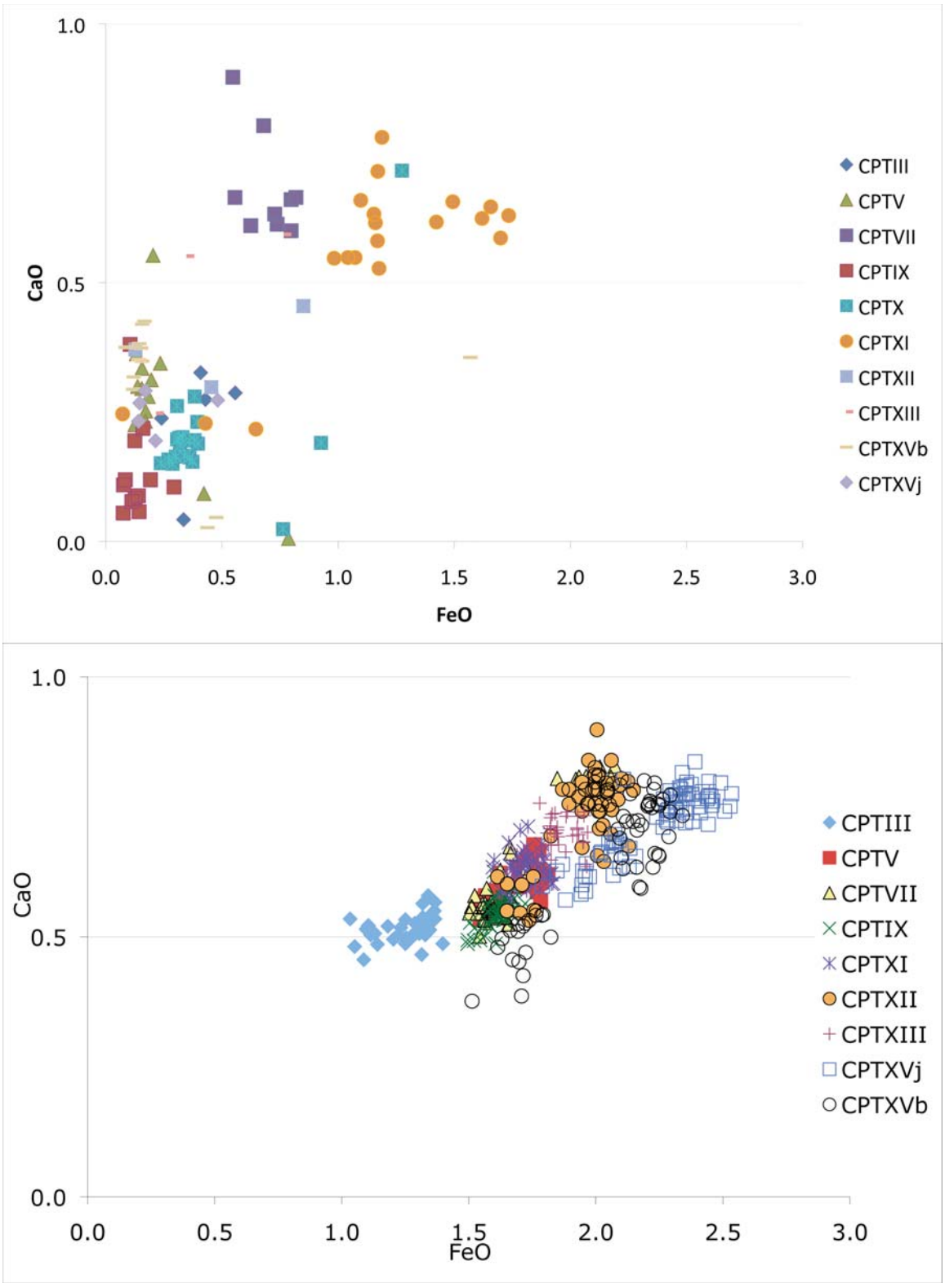

Figure E.25. Compositional variation in glasses for the CPT from the BJEC. The lower graph is airfall glass and the upper graph is from melt inclusion analyses. Data for glass analyses from Nash (unpublished).

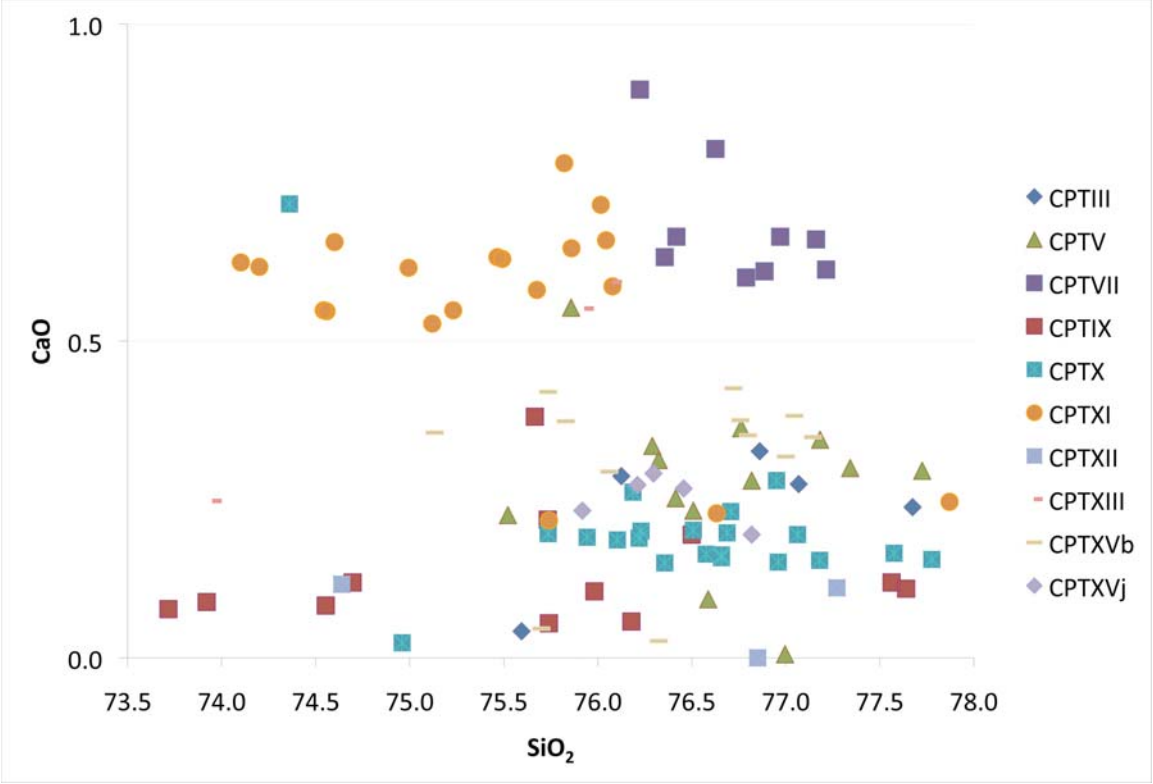

Figure E.25 continued

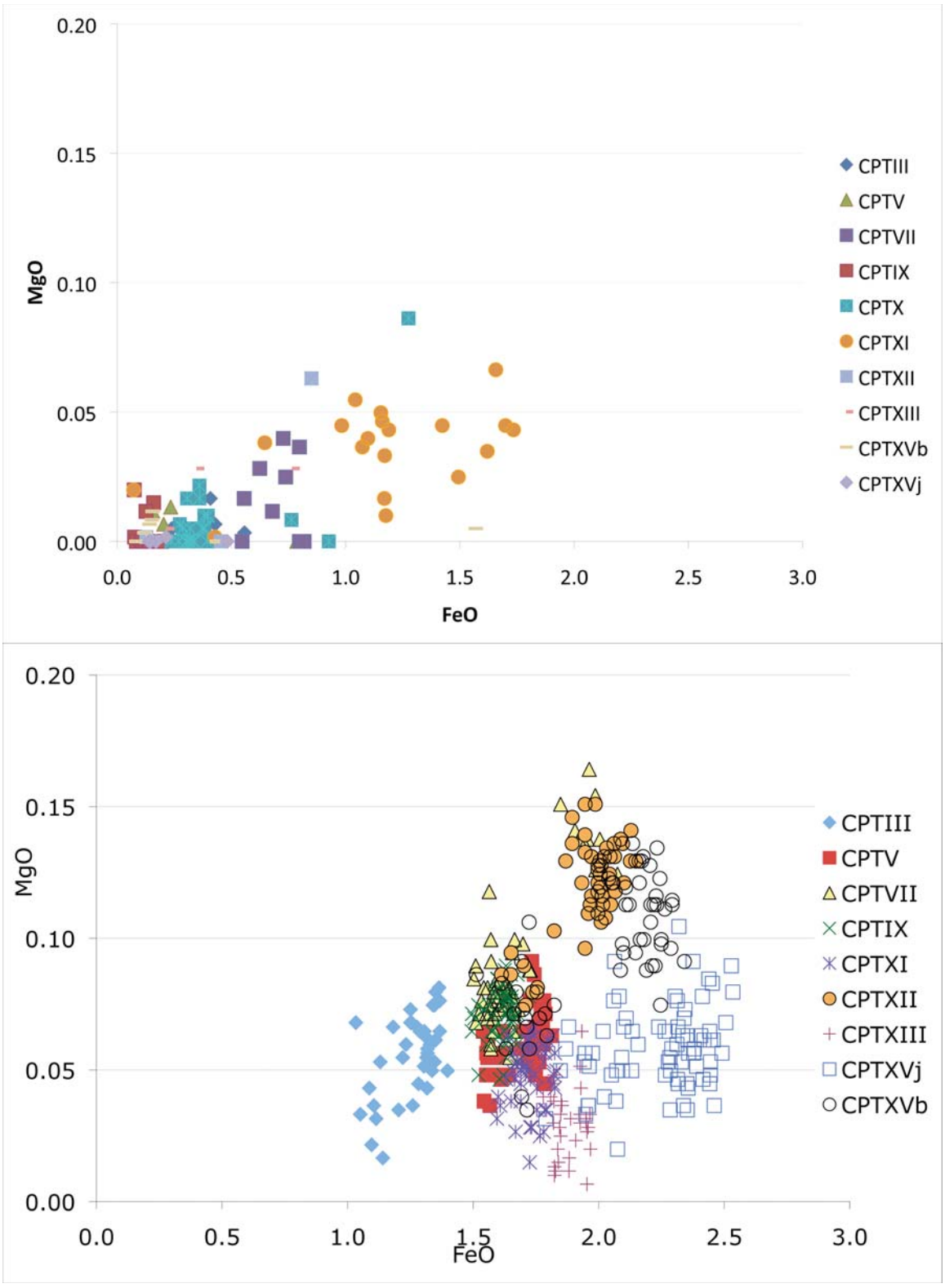

Figure E.26. Compositional variation in glasses for the CPT from the BJEC. The lower graph is airfall glass and the upper graph is from melt inclusion analyses. Data for glass analyses from Nash (unpublished).

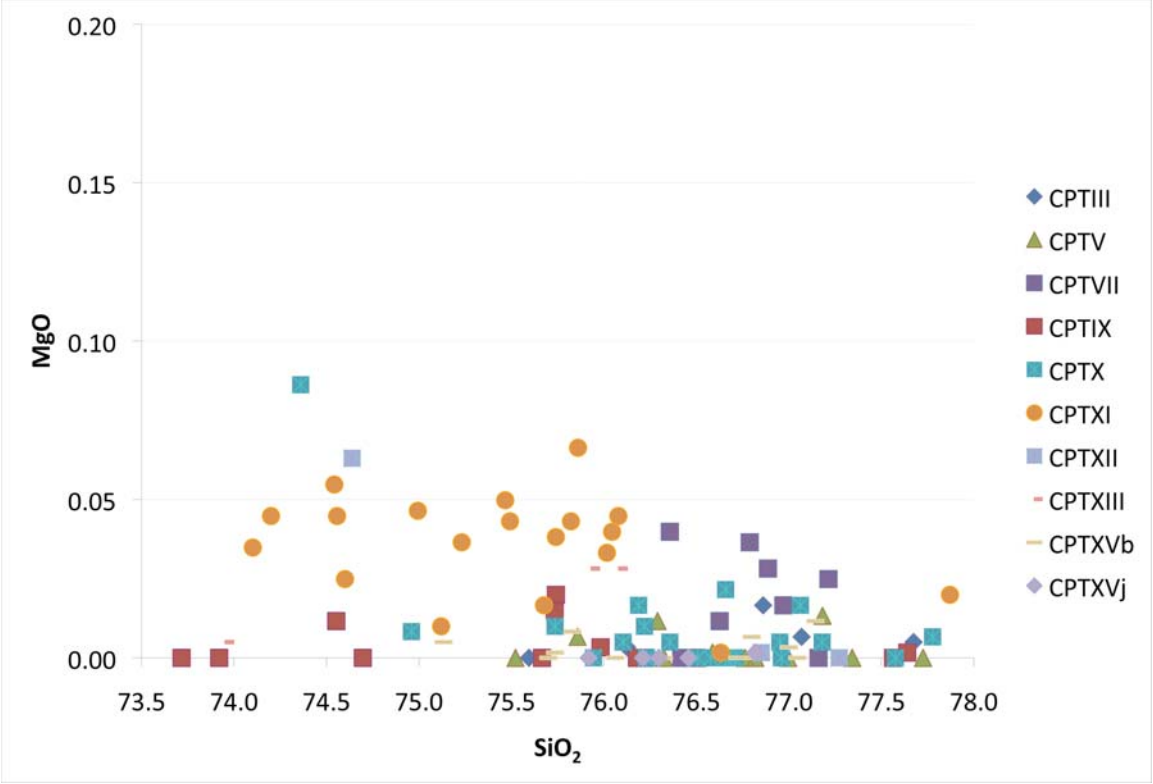

Figure E.26 continued

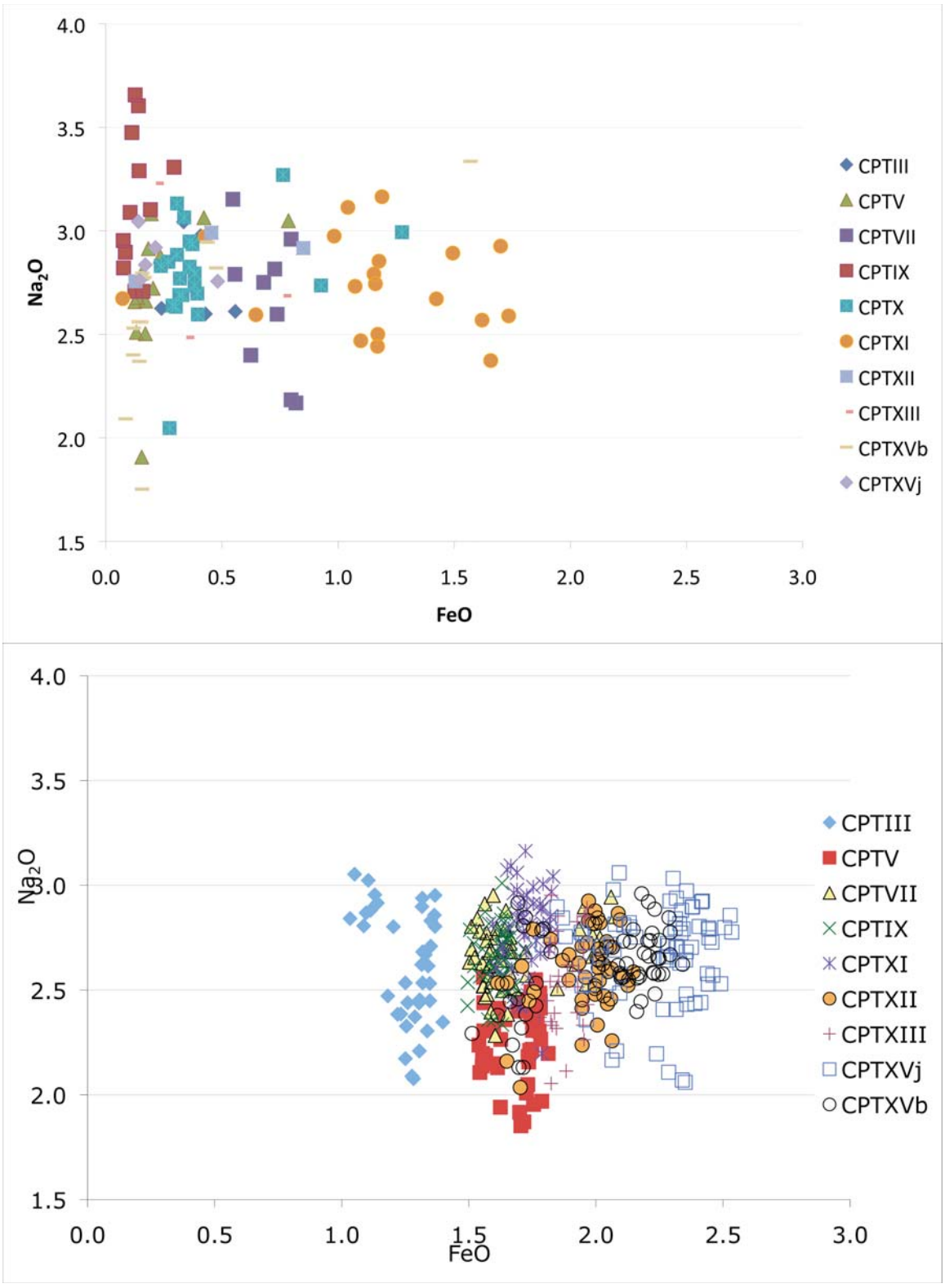

Figure E.27. Compositional variation in glasses for the CPT from the BJEC. The lower graph is airfall glass and the upper graph is from melt inclusion analyses. Data for glass analyses from Nash (unpublished).

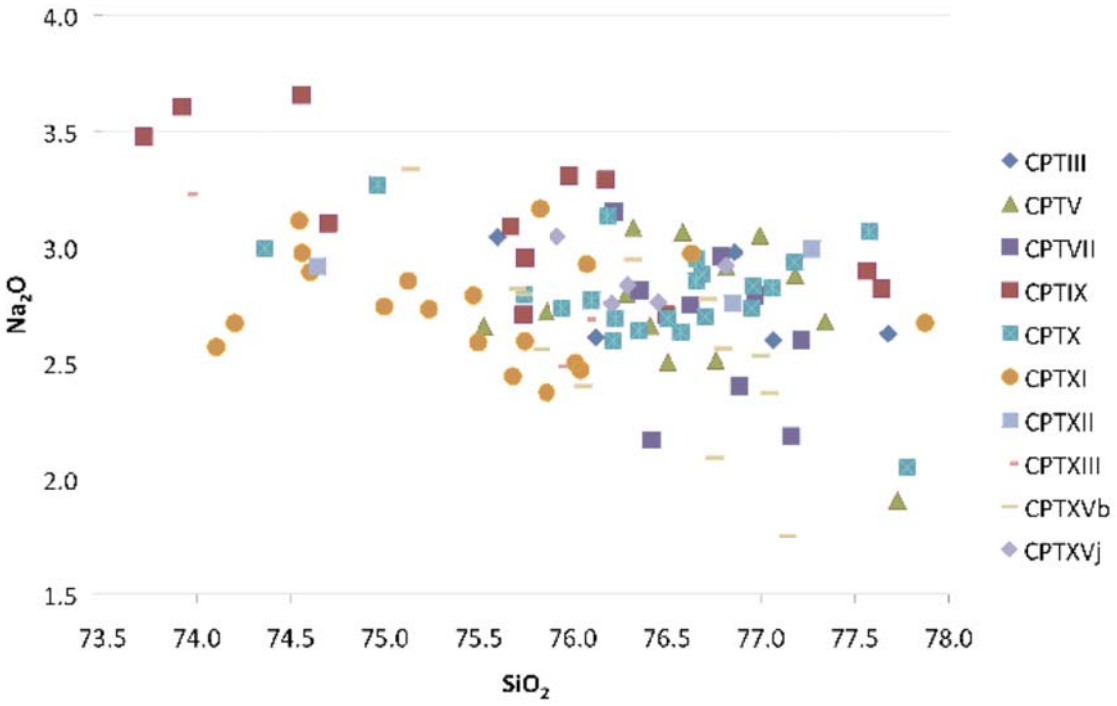

Figure E.27 continued

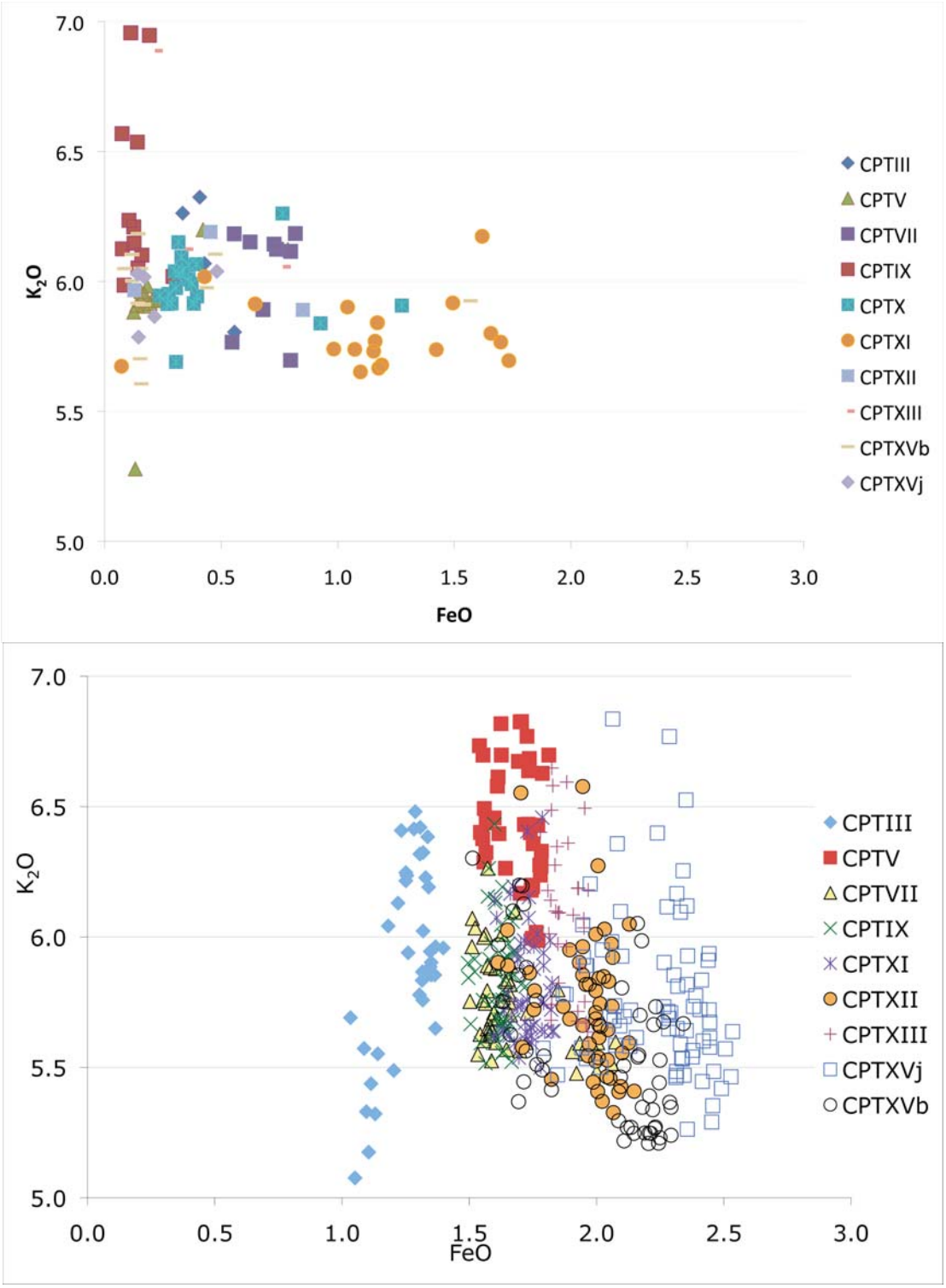

Figure E.28. Compositional variation in glasses for the CPT from the BJEC. The lower graph is airfall glass and the upper graph is from melt inclusion analyses. Data for glass analyses from Nash (unpublished).

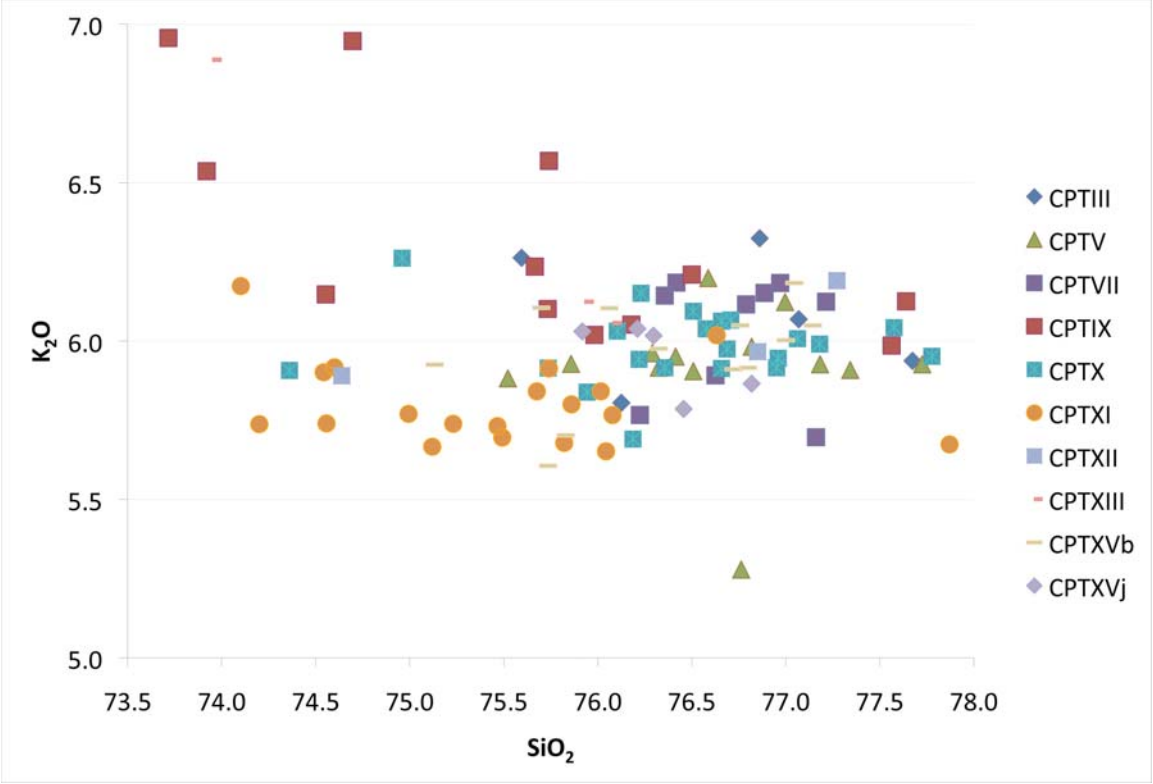

Figure E.28 continued

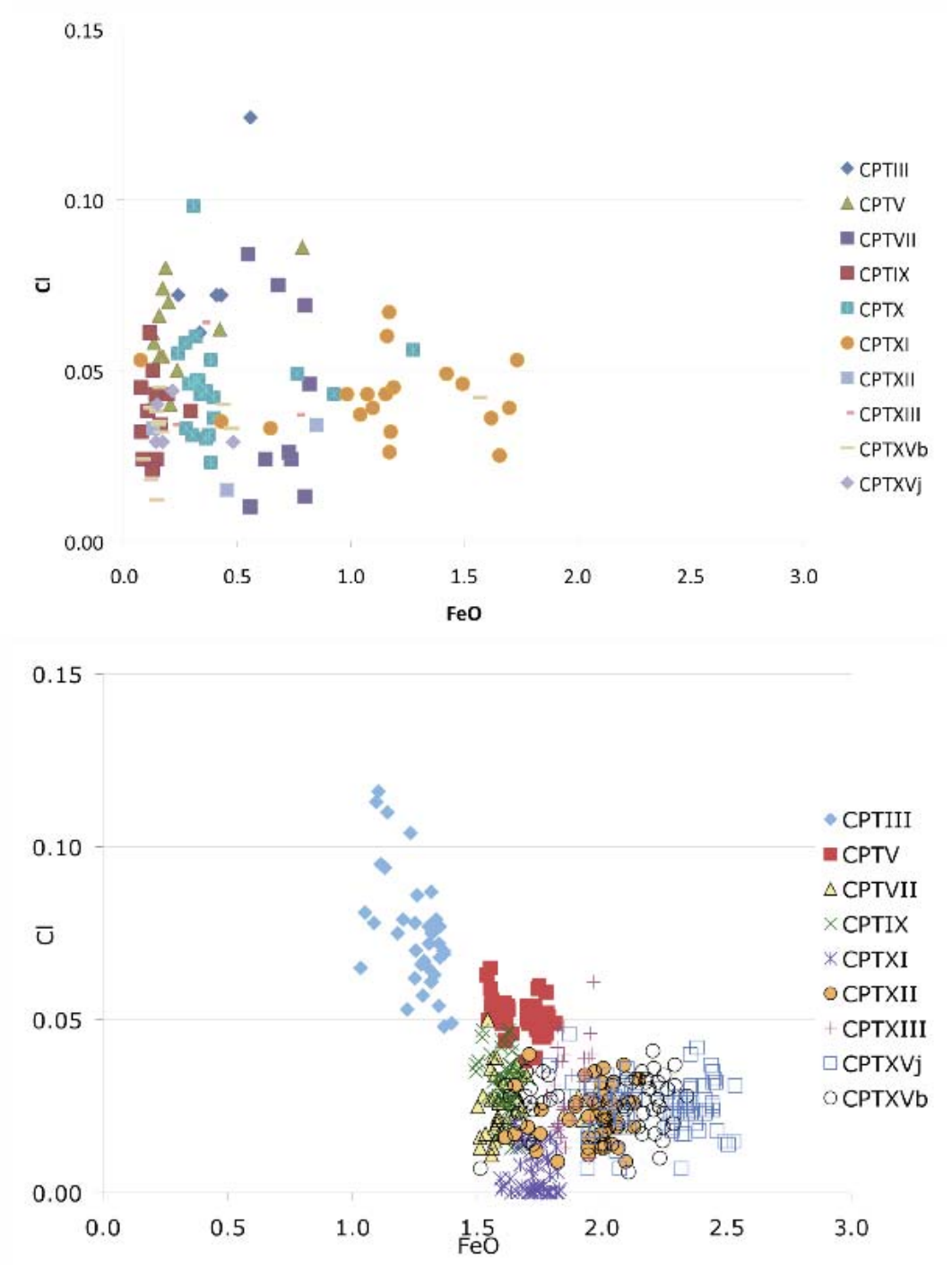

Figure E.29. Compositional variation in glasses for the CPT from the BJEC. The lower graph is airfall glass and the upper graph is from melt inclusion analyses. Data for glass analyses from Nash (unpublished).

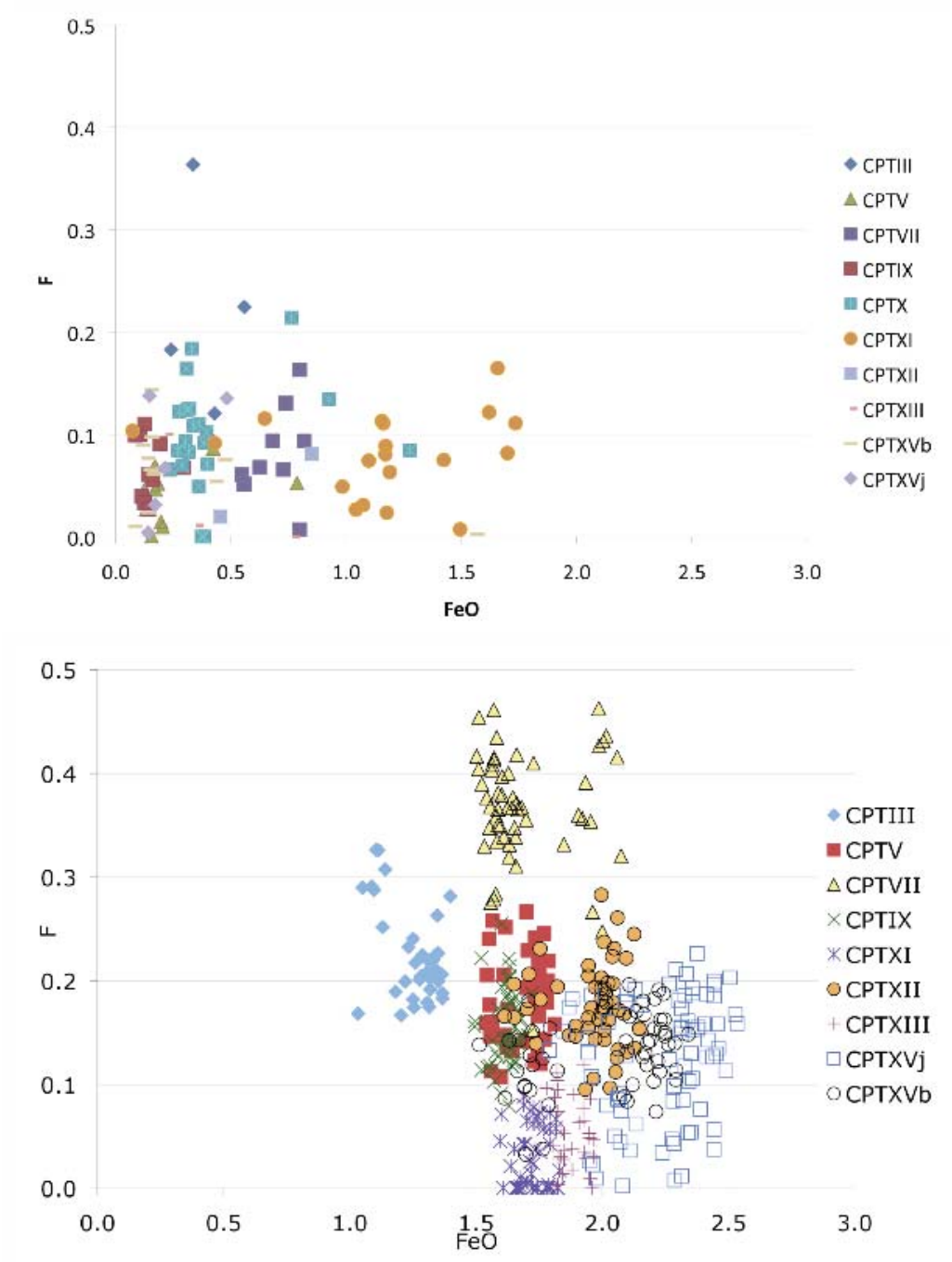

Figure E.30. Compositional variation in glasses for the CPT from the BJEC. The lower graph is airfall glass and the upper graph is from melt inclusion analyses. Data for glass analyses from Nash (unpublished).

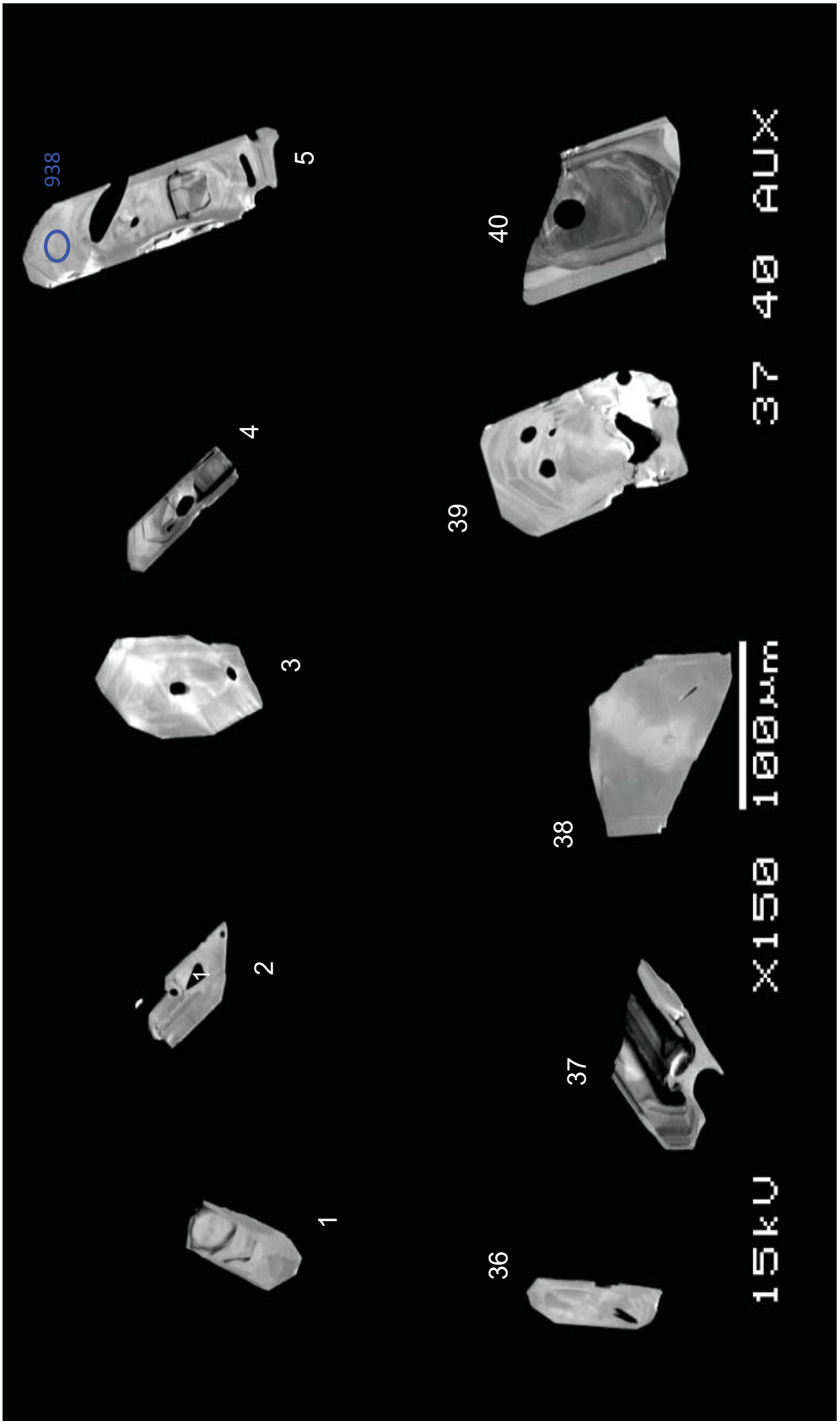

DCR

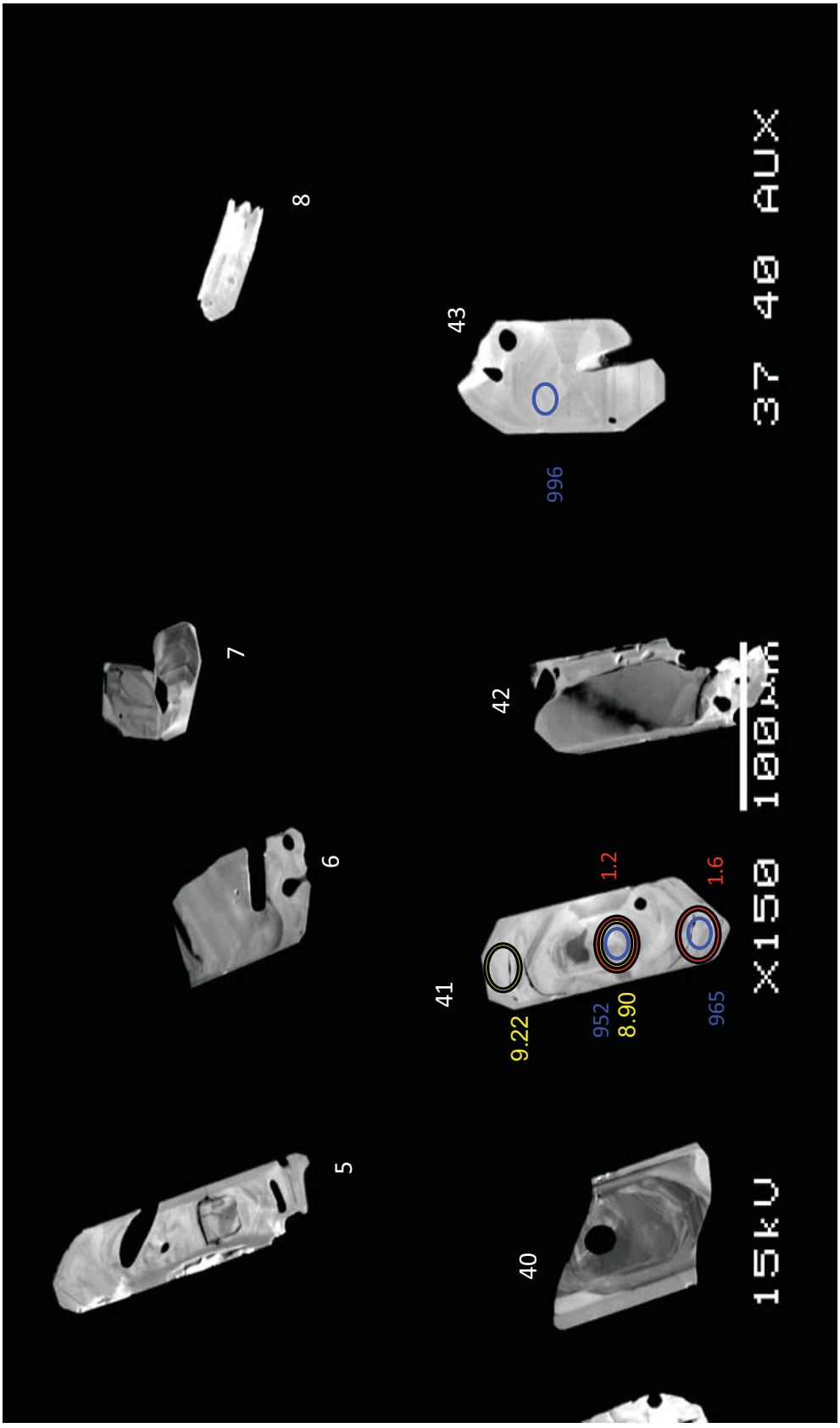
15kV X150 100µm 37 40 AUX
DCR
40
41
42
43
5
6
7
8
9.22
8.90
952
1.2
1.6
965
996

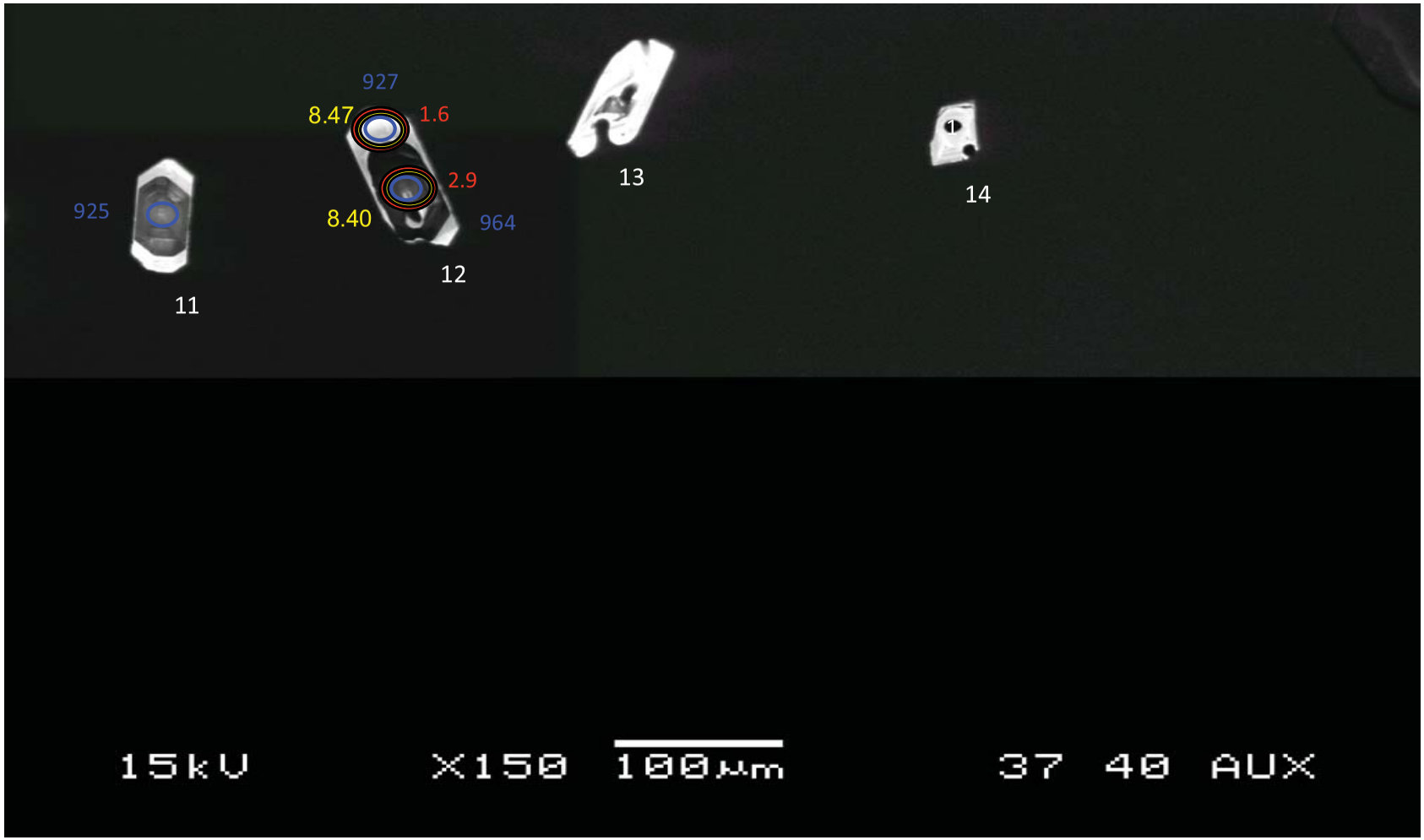

DCR

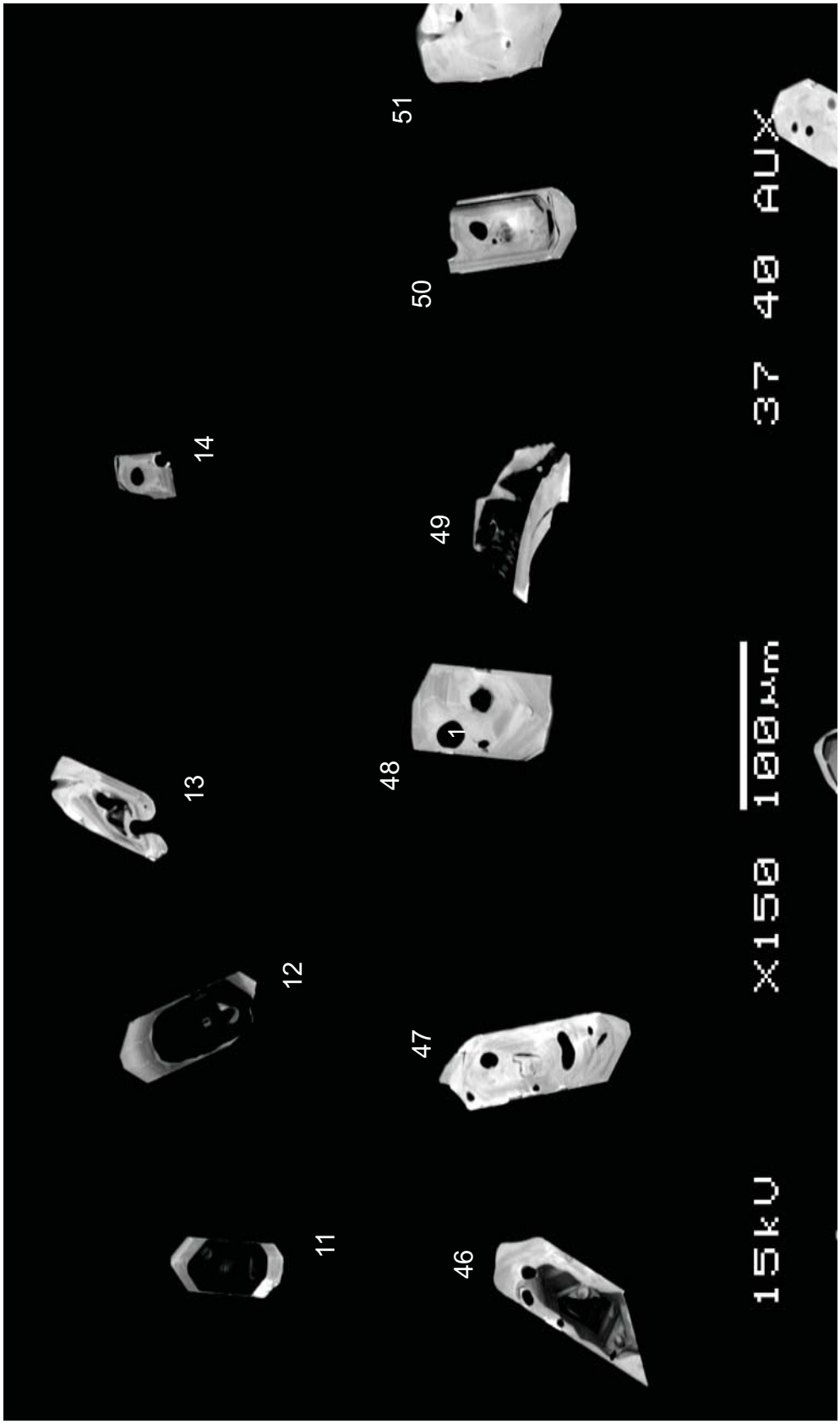
15kU X150 100µm 37 40 AUX
11
46
12
47
13
48
14
1
49
50
51
DCR

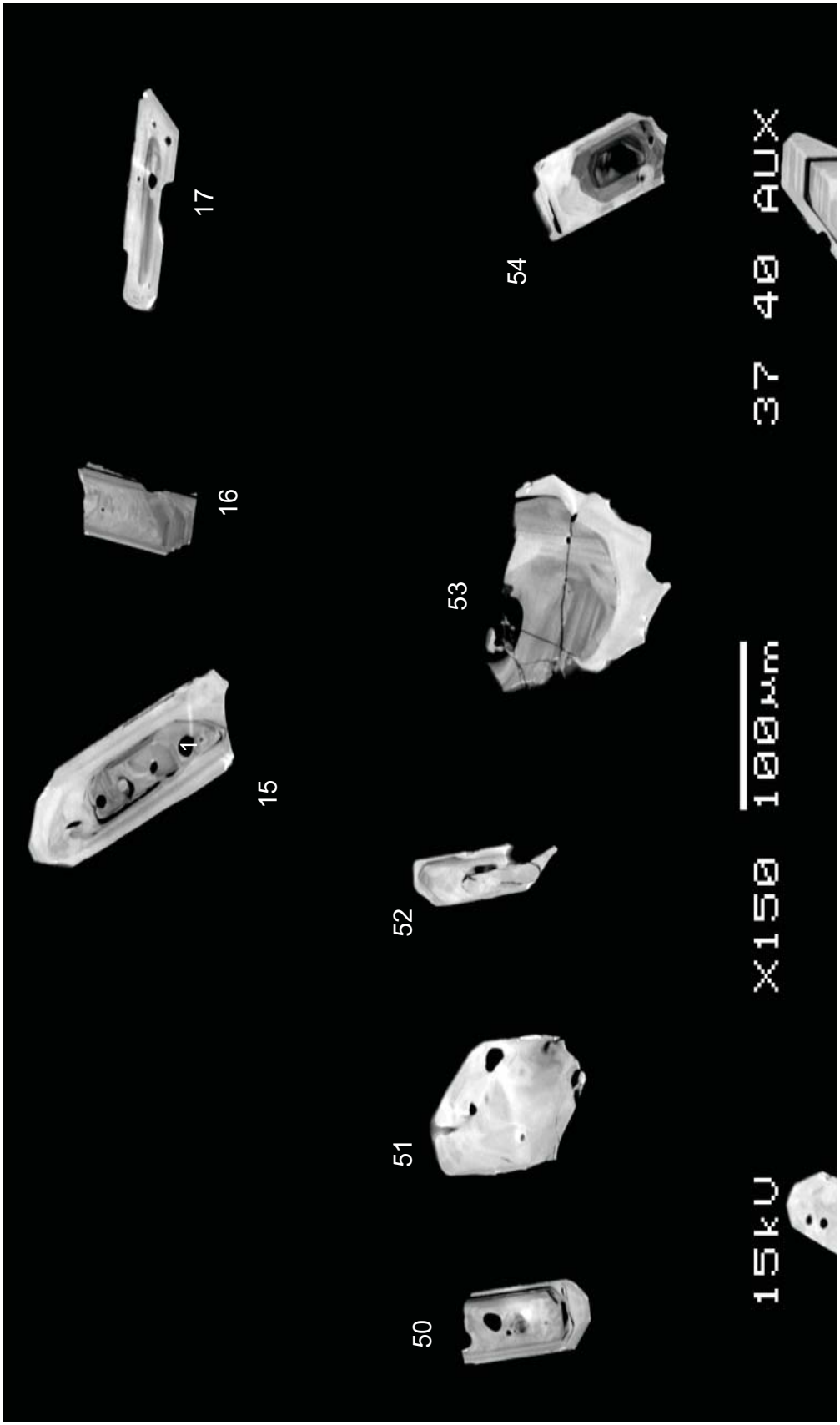

DCR

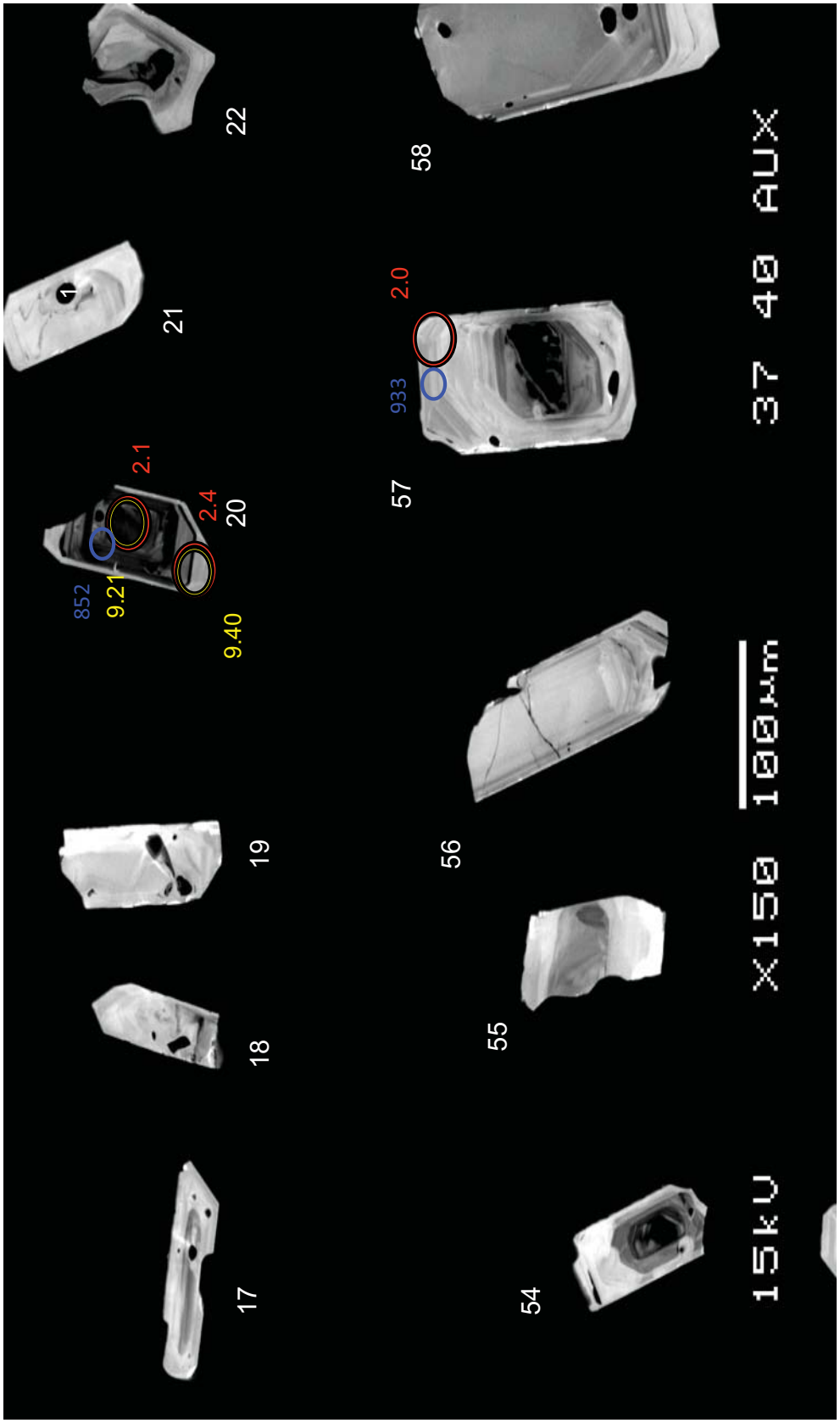
15kU X150 100µm 37 40 AUX
DCR
1
17
18
19
20
21
22
54
55
56
57
58
852
9.21
9.40
2.1
2.4
933
2.0

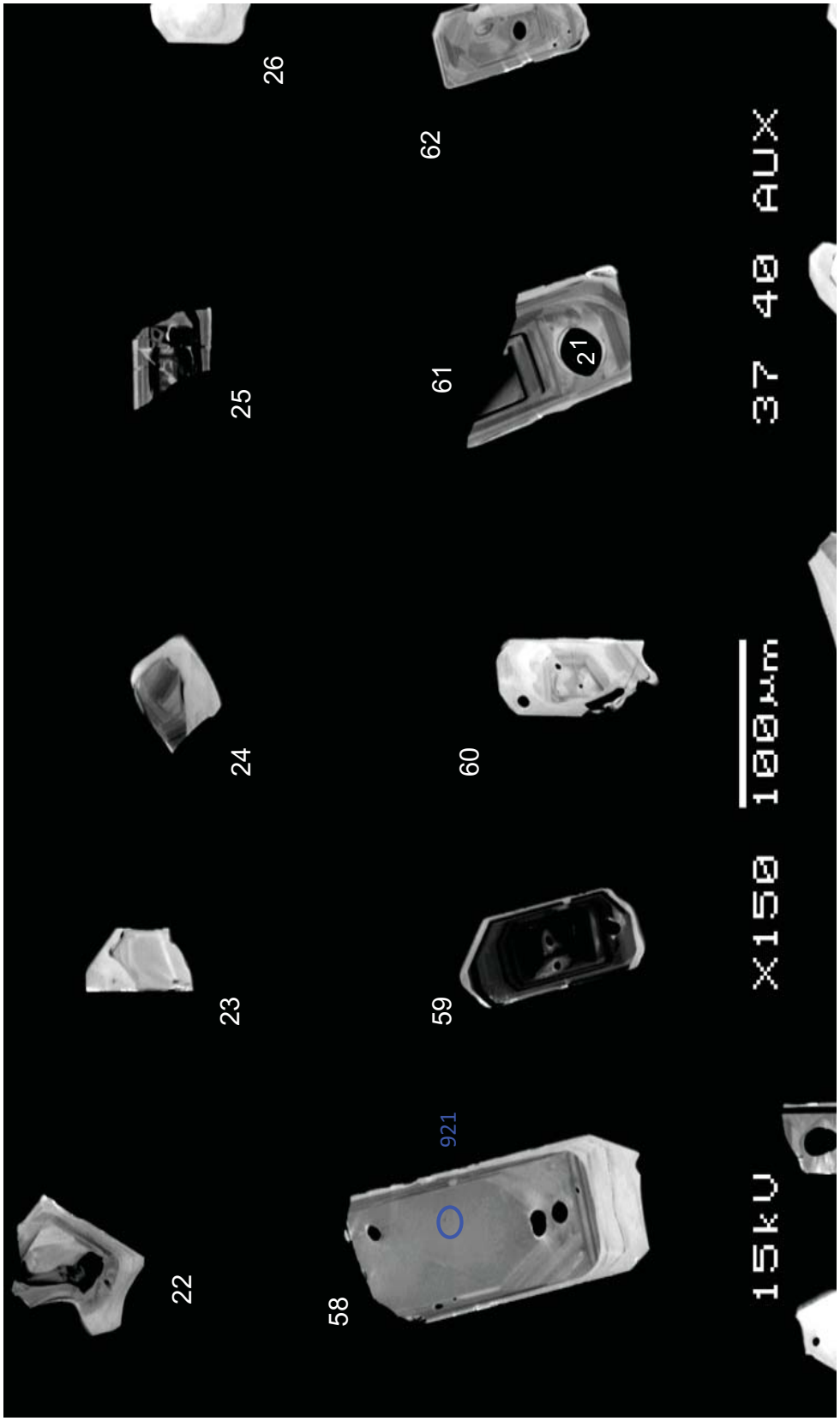
15kV X150 100µm 37 40 AUX
22
58
921
23
59
24
60
25
61
21
26
62
DCR

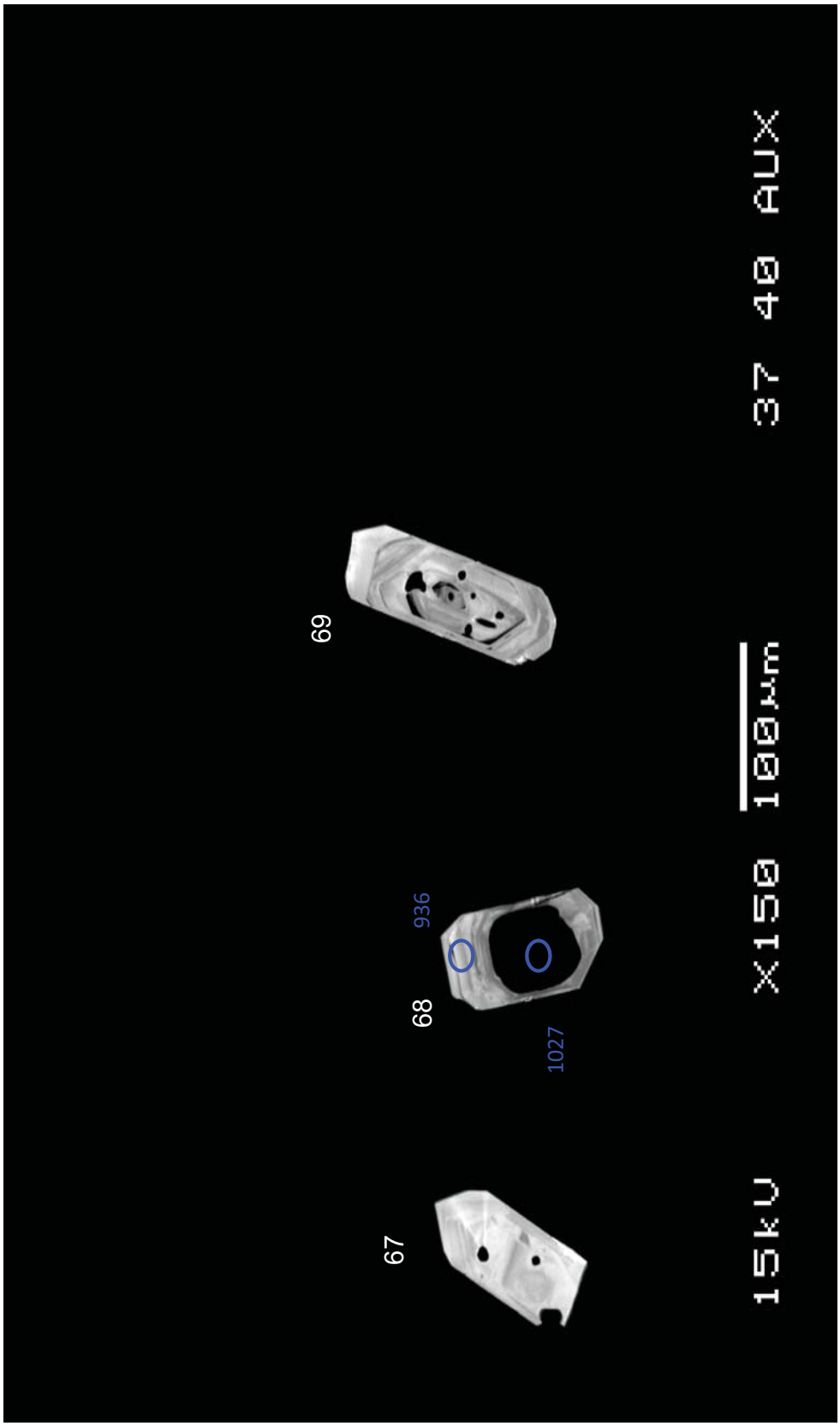

DCR

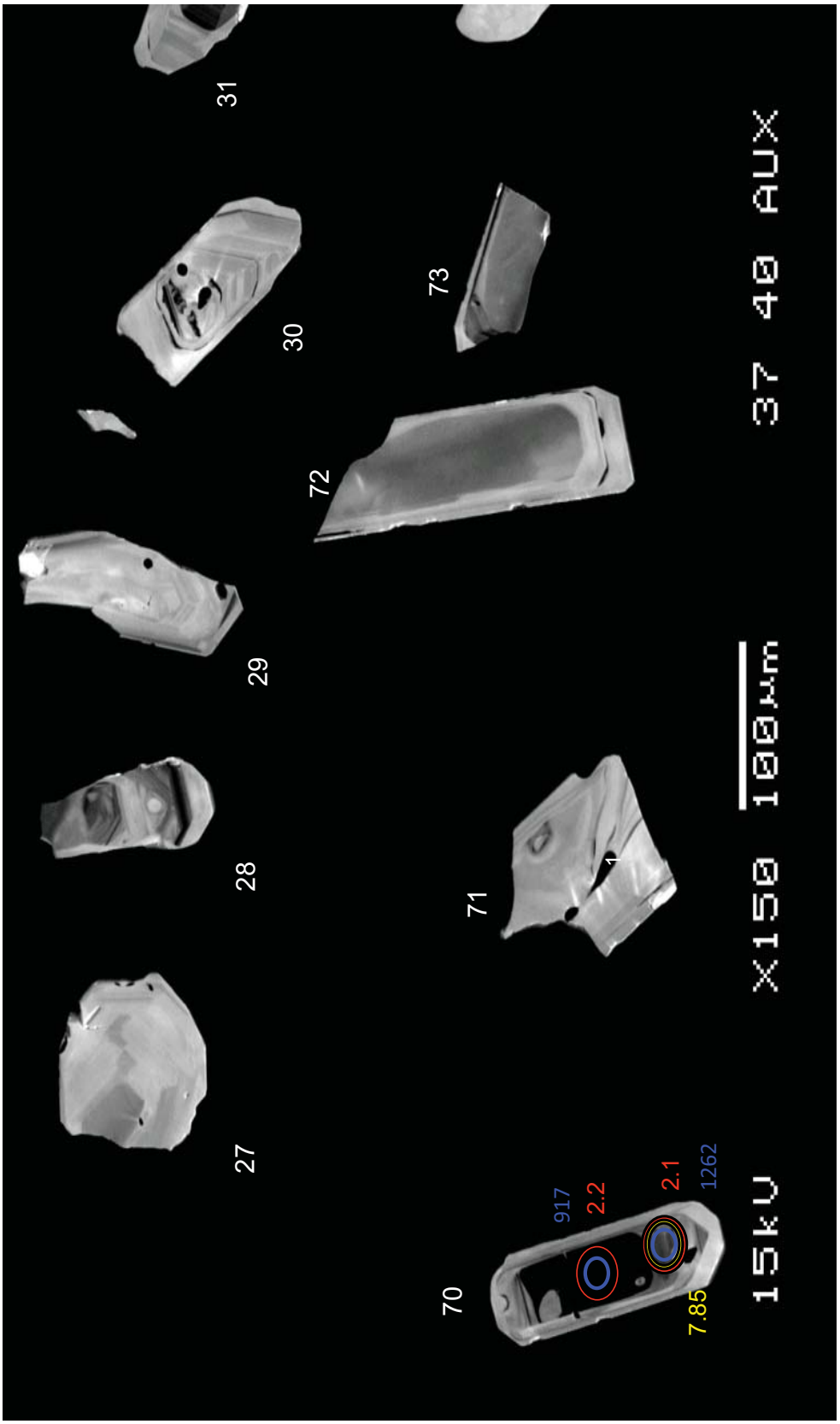
15kV X150 100µm 37 40 AUX
70
27
28
29
30
31
71
72
73
917
2.2
2.1
1262
7.85
1

DCR

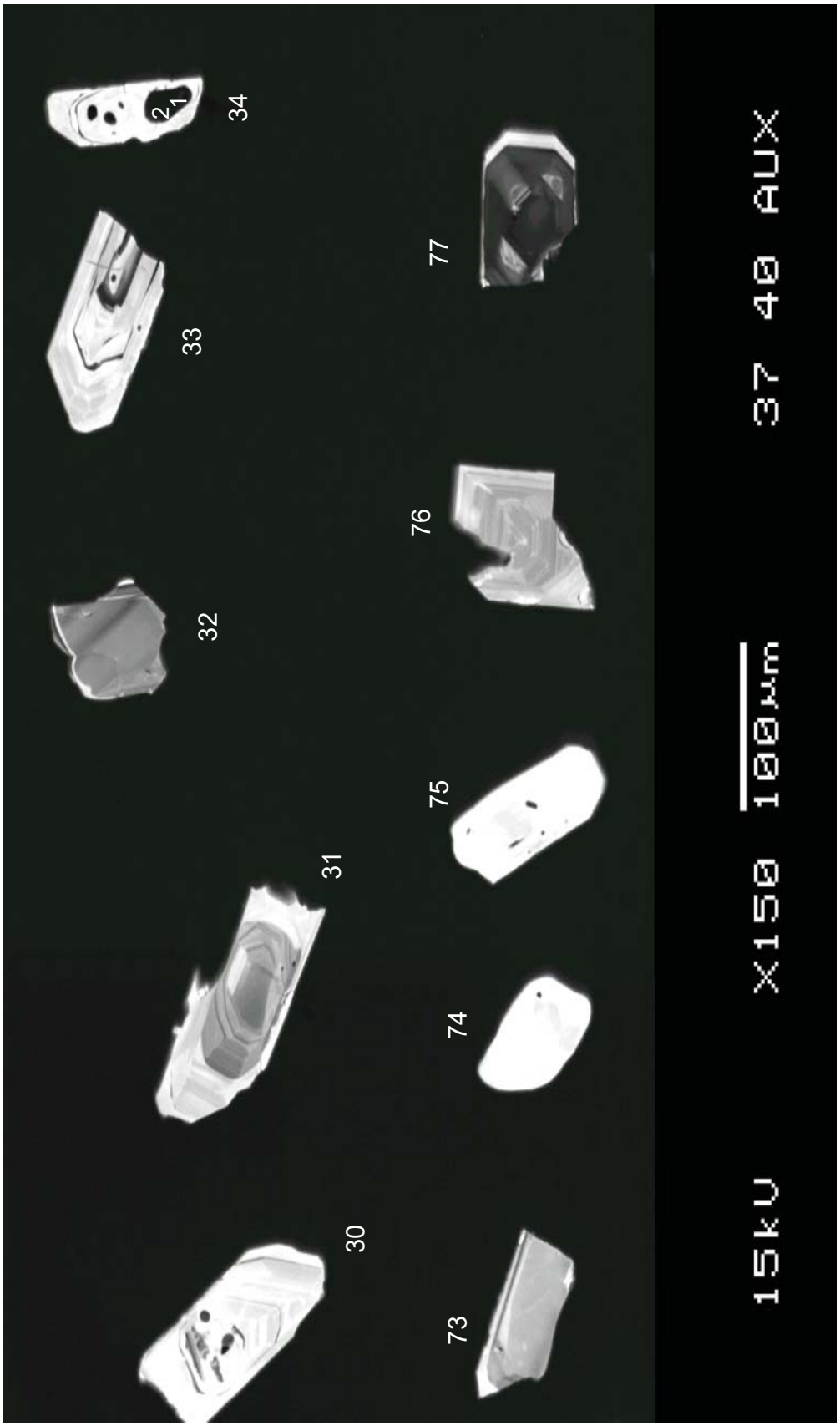
15kU X150 100µm 37 40 AUX
DCR
21
34
33
32
31
30
73
74
75
76
77

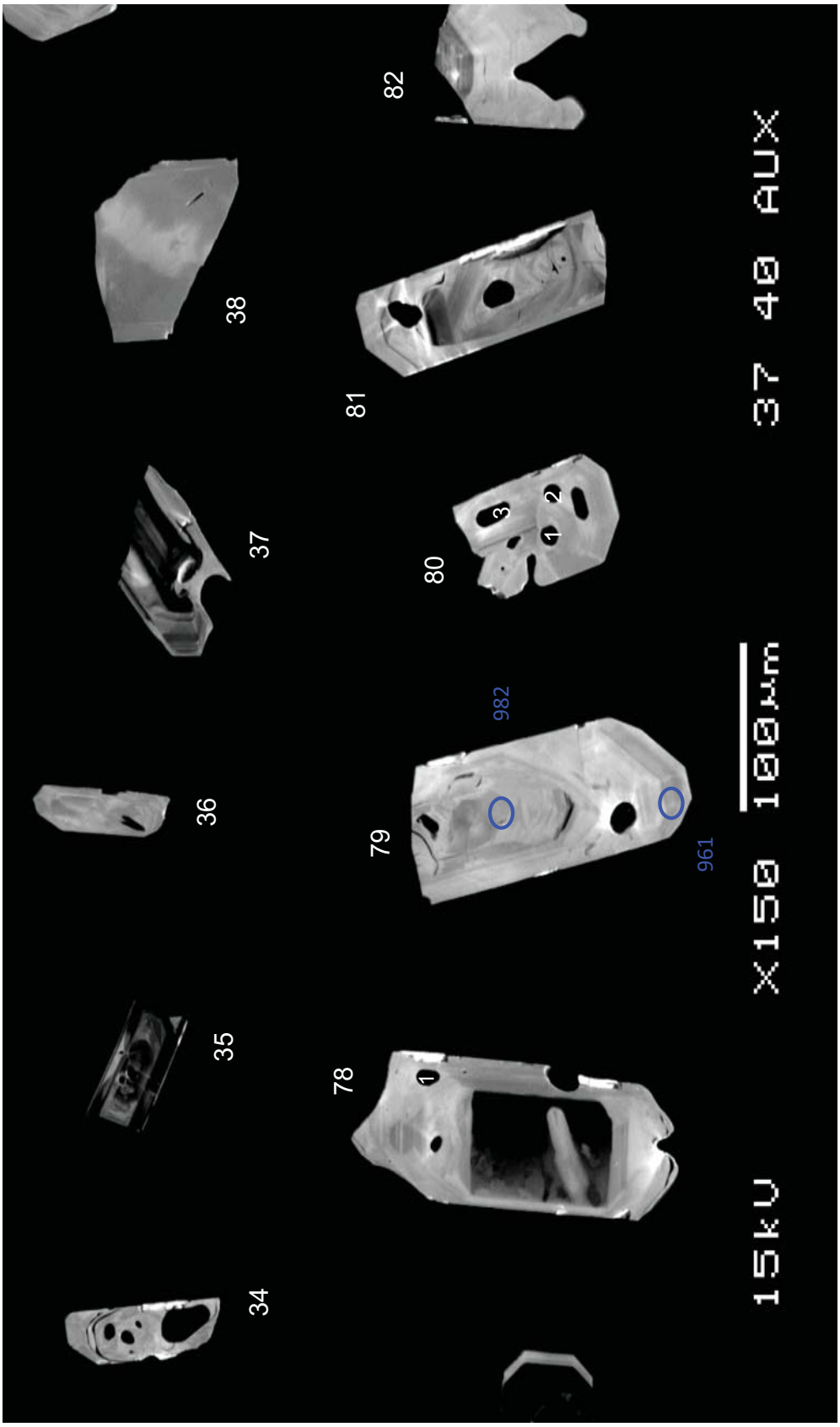
34
35
36
78
1
79
982
961
37
38
80
3
1
2
81
82
15kV X150 100µm 37 40 AUX

DCR

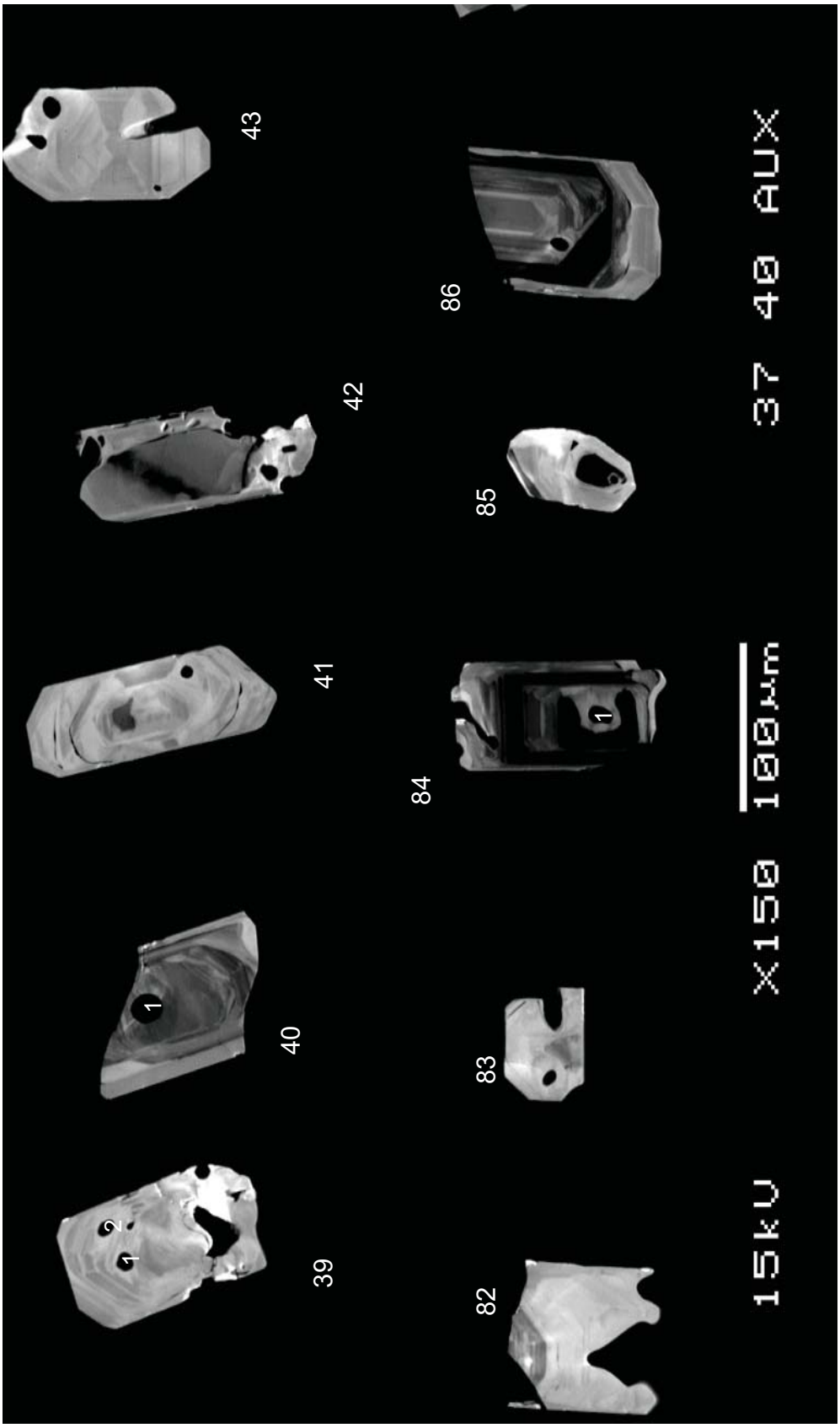

DCR

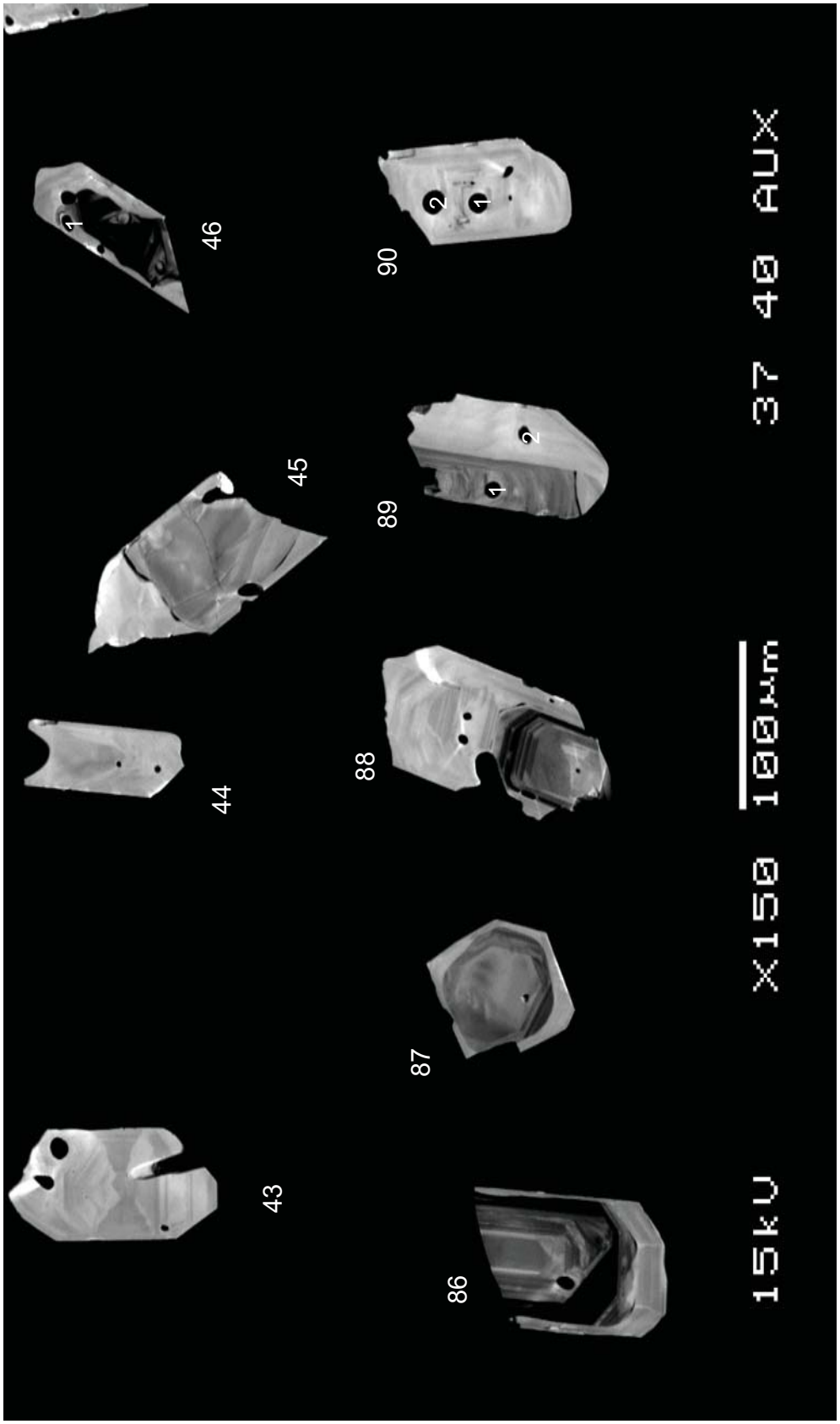

DCR

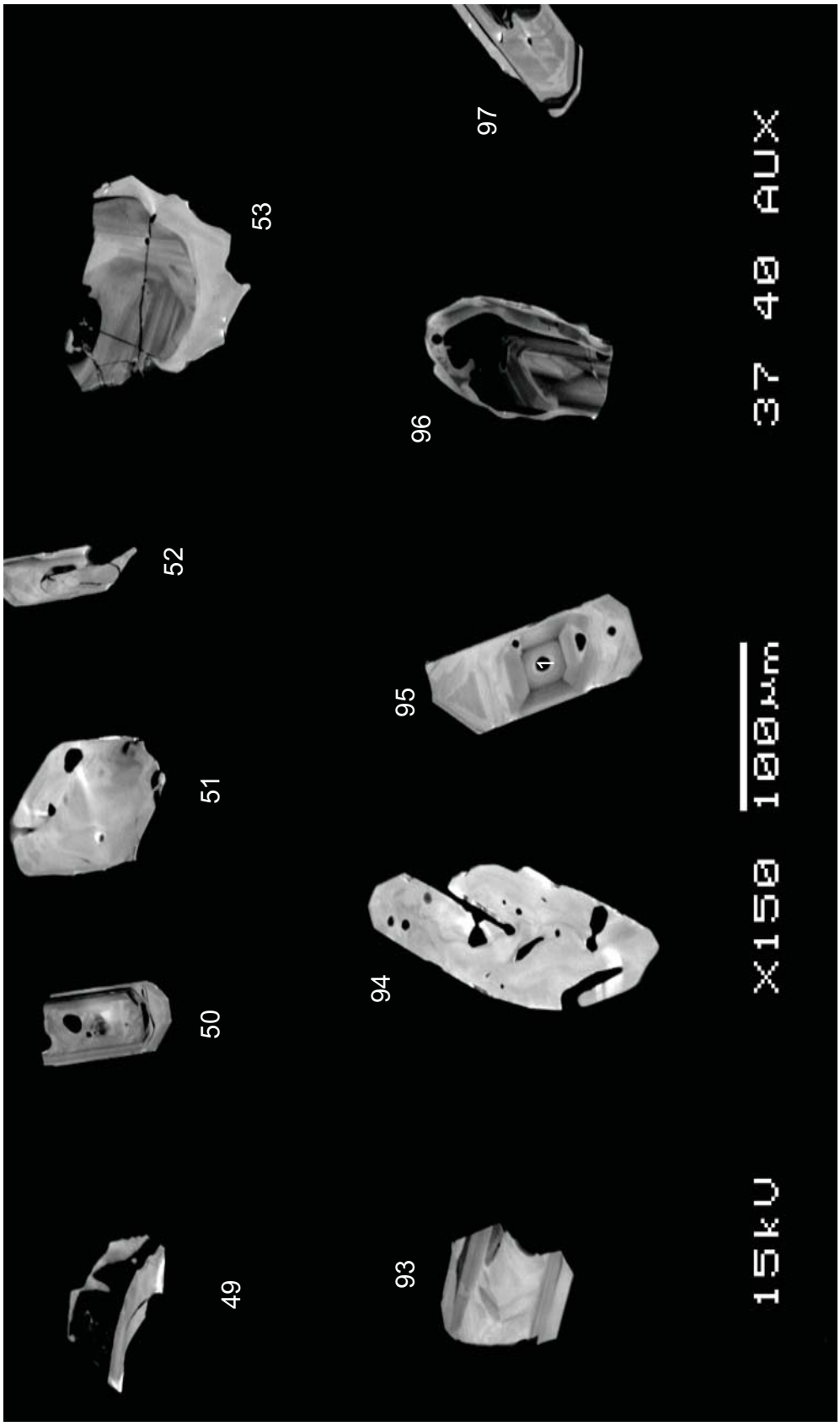

DCR

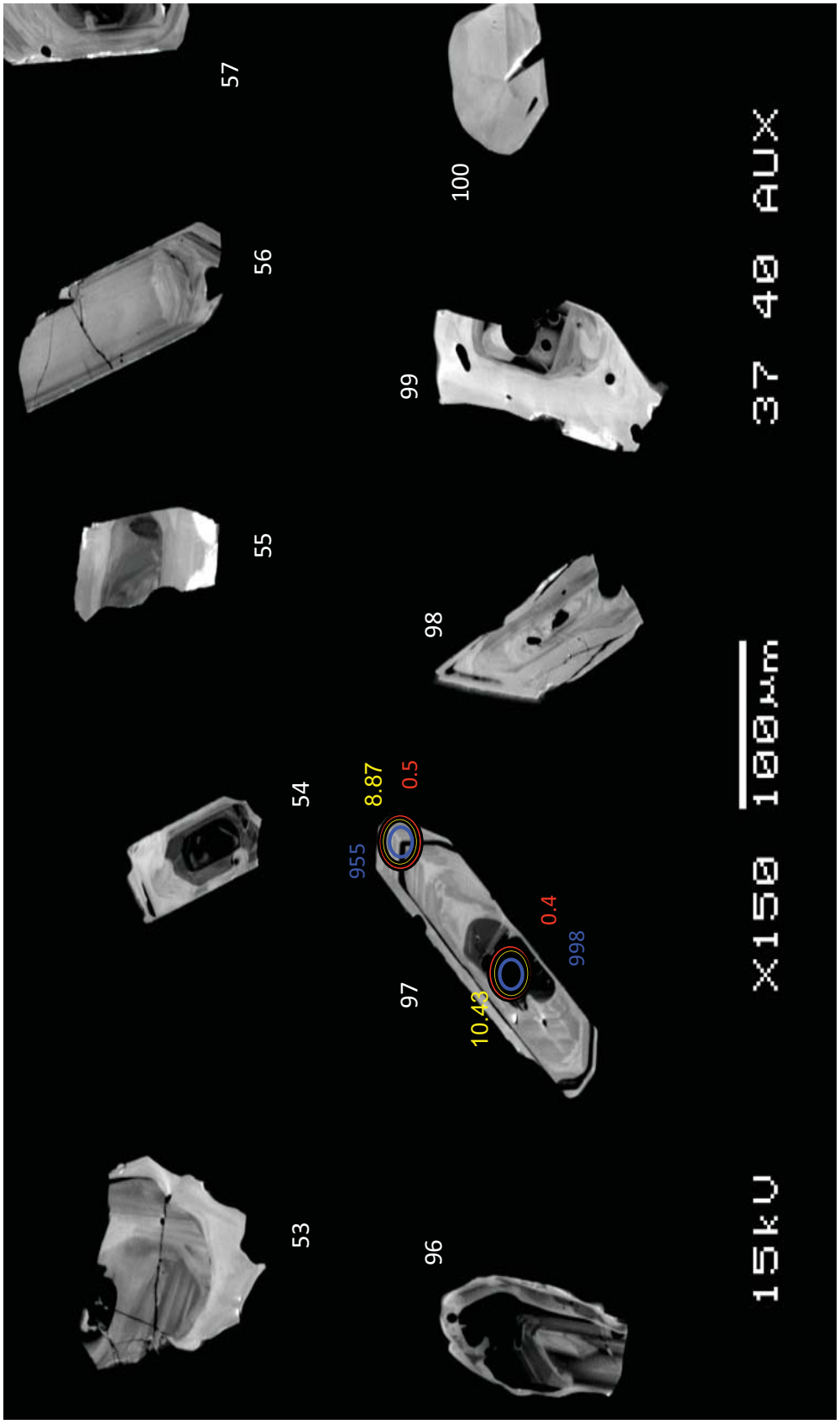
15kV X150 100µm 37 40 AUX
DCR
53
54
55
56
57
96
97
98
99
100
955
8.87
0.5
10.43
998
0.4

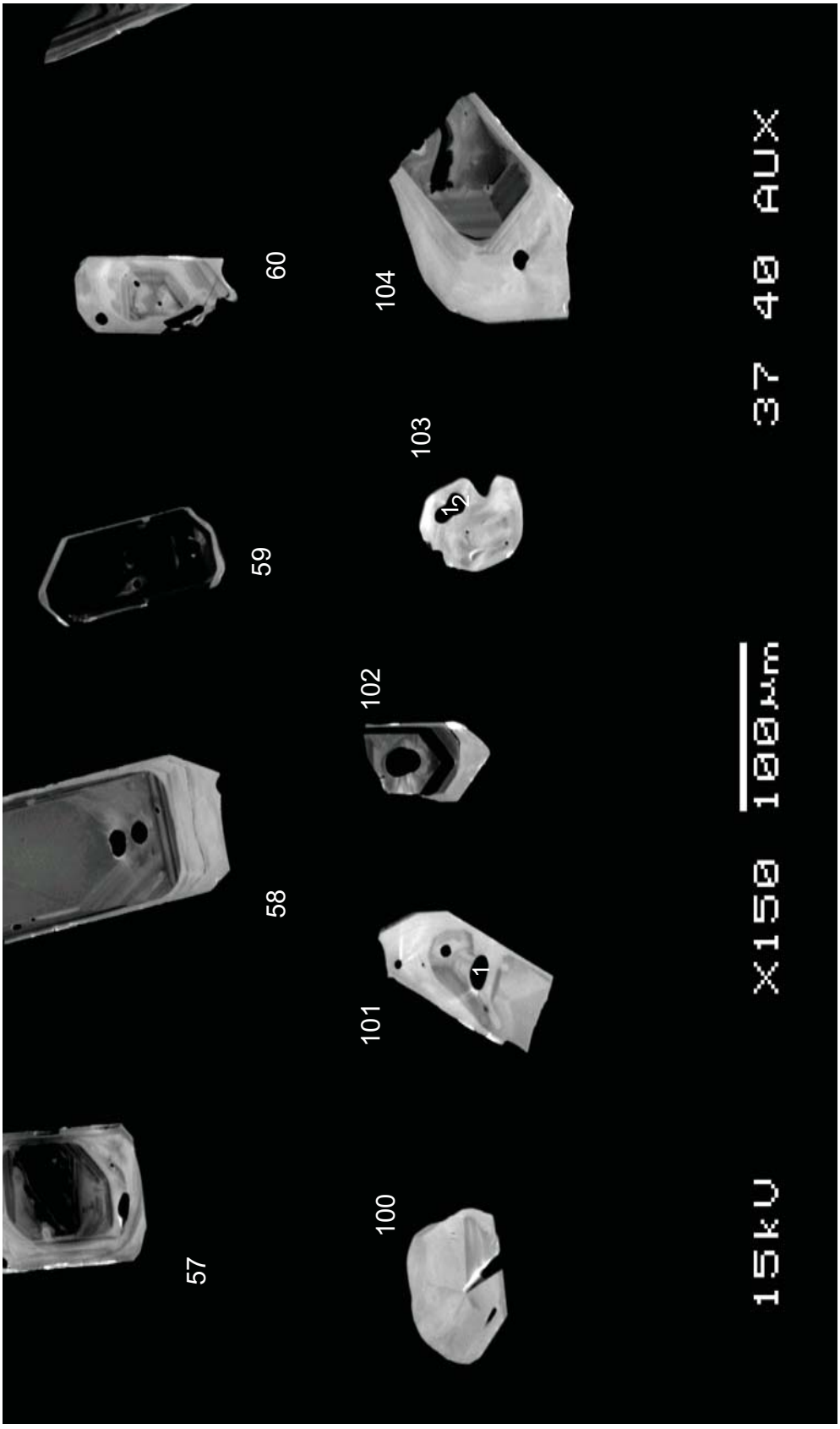

DCR

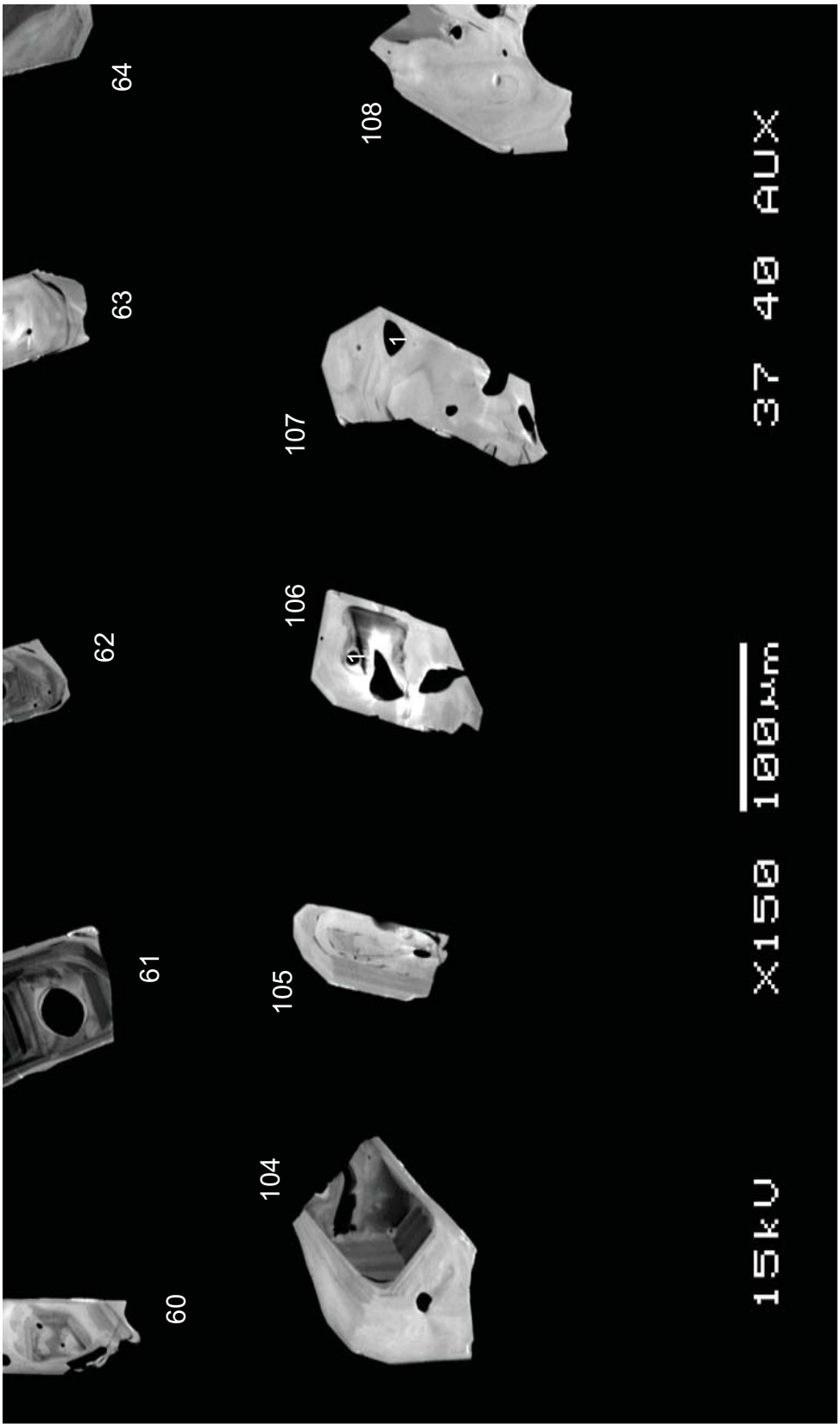

DCR

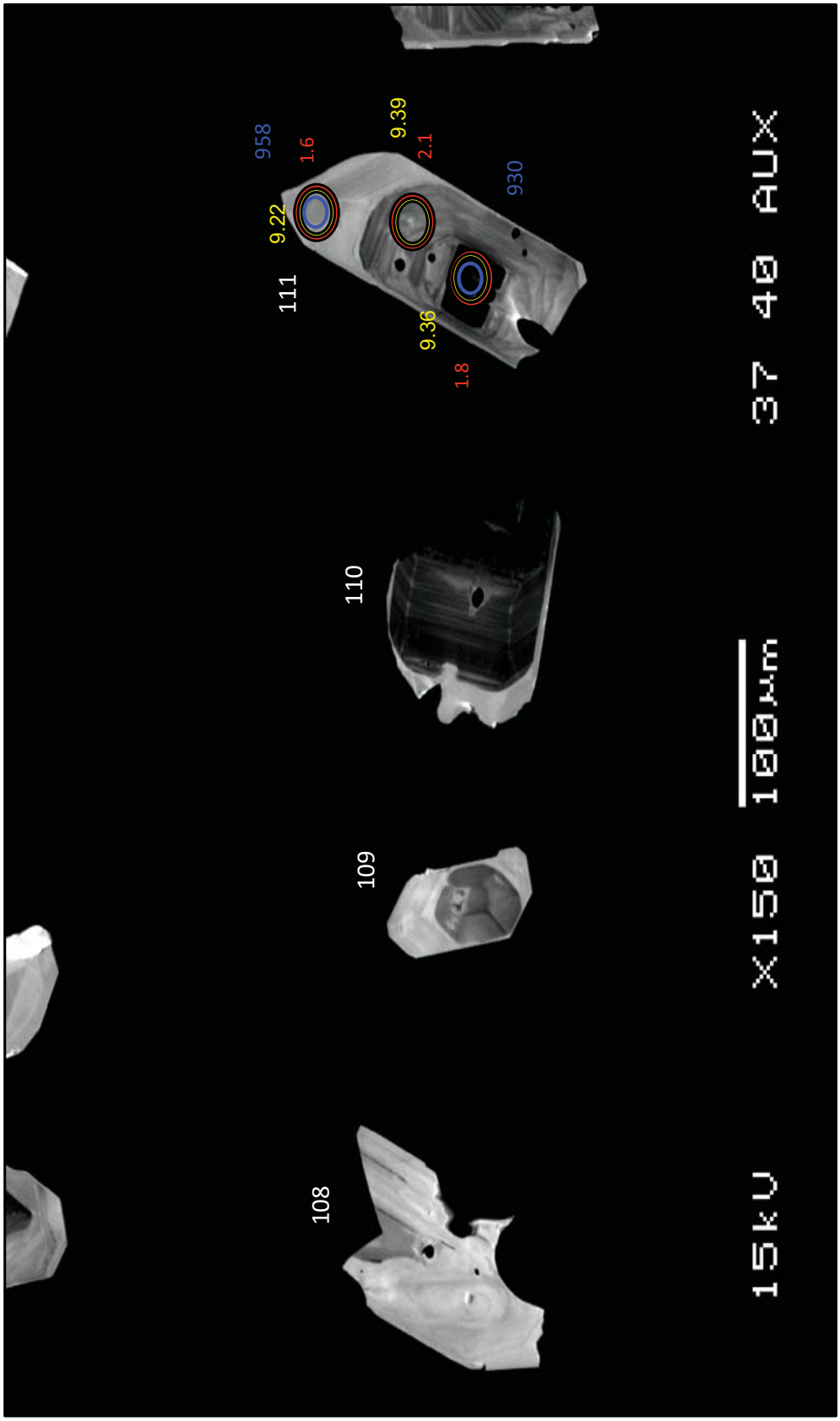
15kV X150 100µm 37 40 AUX
DCR
108
109
110
111
9.22
1.6
958
9.39
2.1
930
9.36
1.8

LF2-02

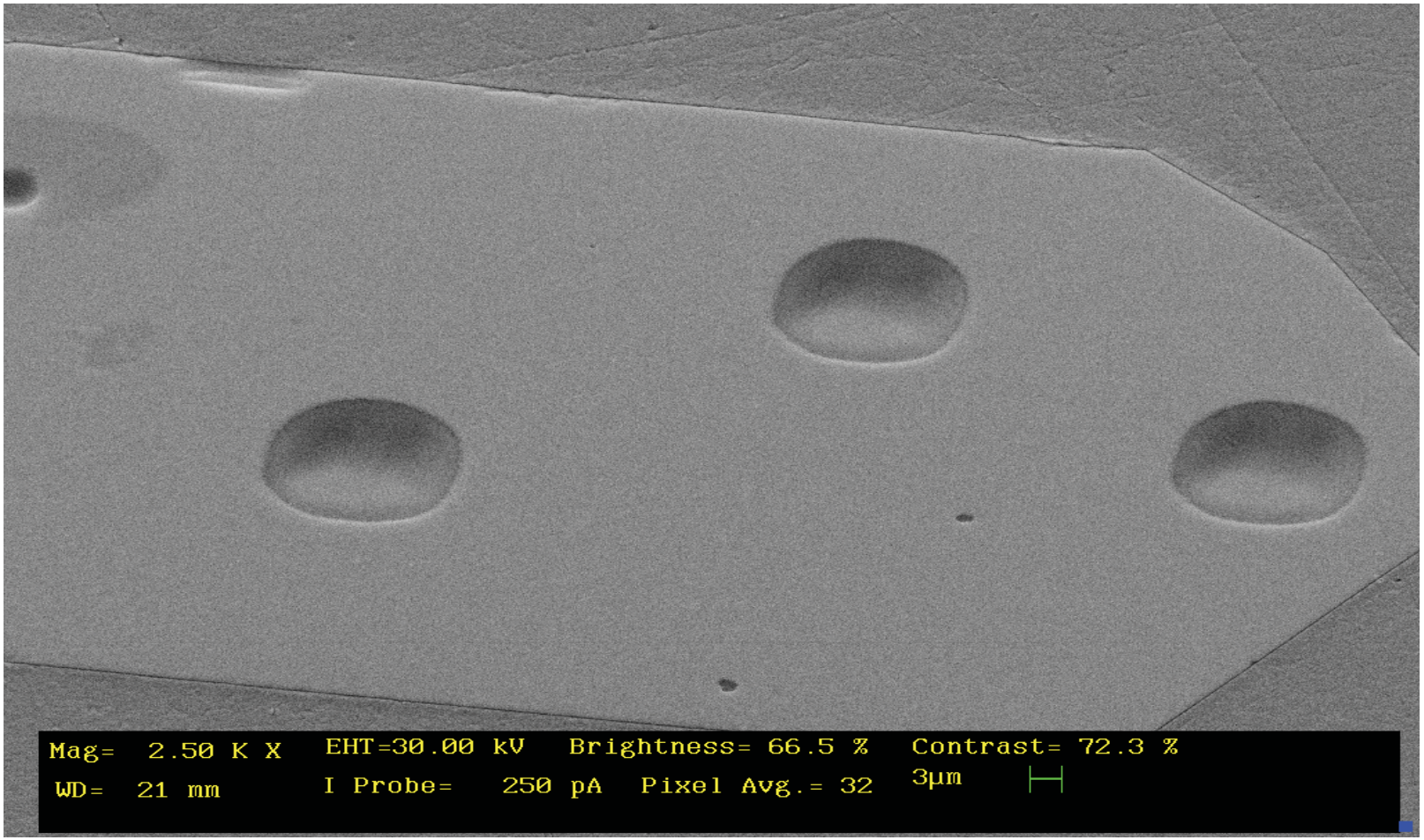
Mag= 2.50 K X
EHT=30.00 kV
Brightness= 66.5 %
Contrast= 72.3 %
WD= 21 mm
I Probe= 250 pA
Pixel Avg.= 32
3µm

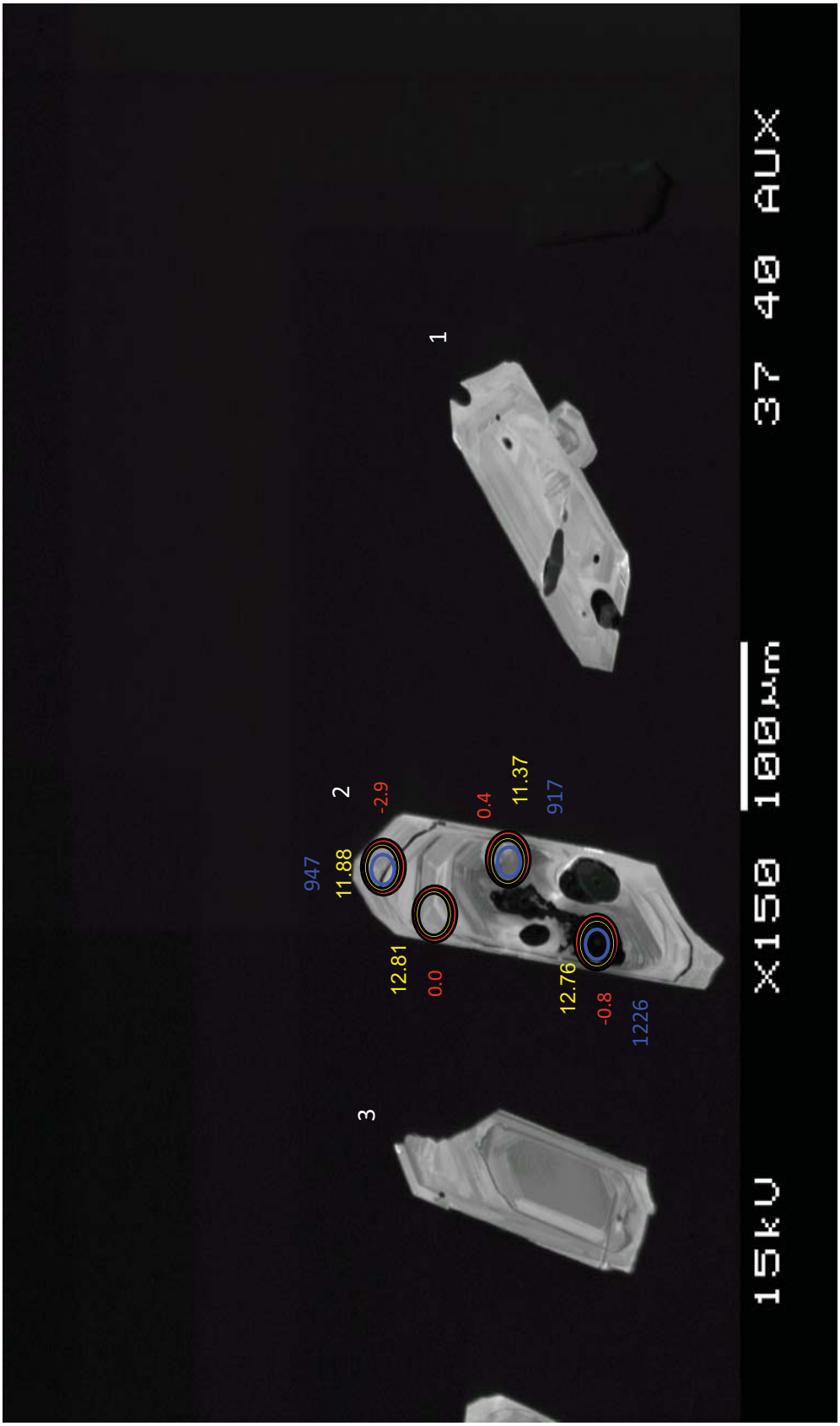
15kU X150 100µm 37 40 AUX
1
2
3
947
11.88
-2.9
12.81
0.0
0.4
11.37
917
12.76
-0.8
1226

LF2

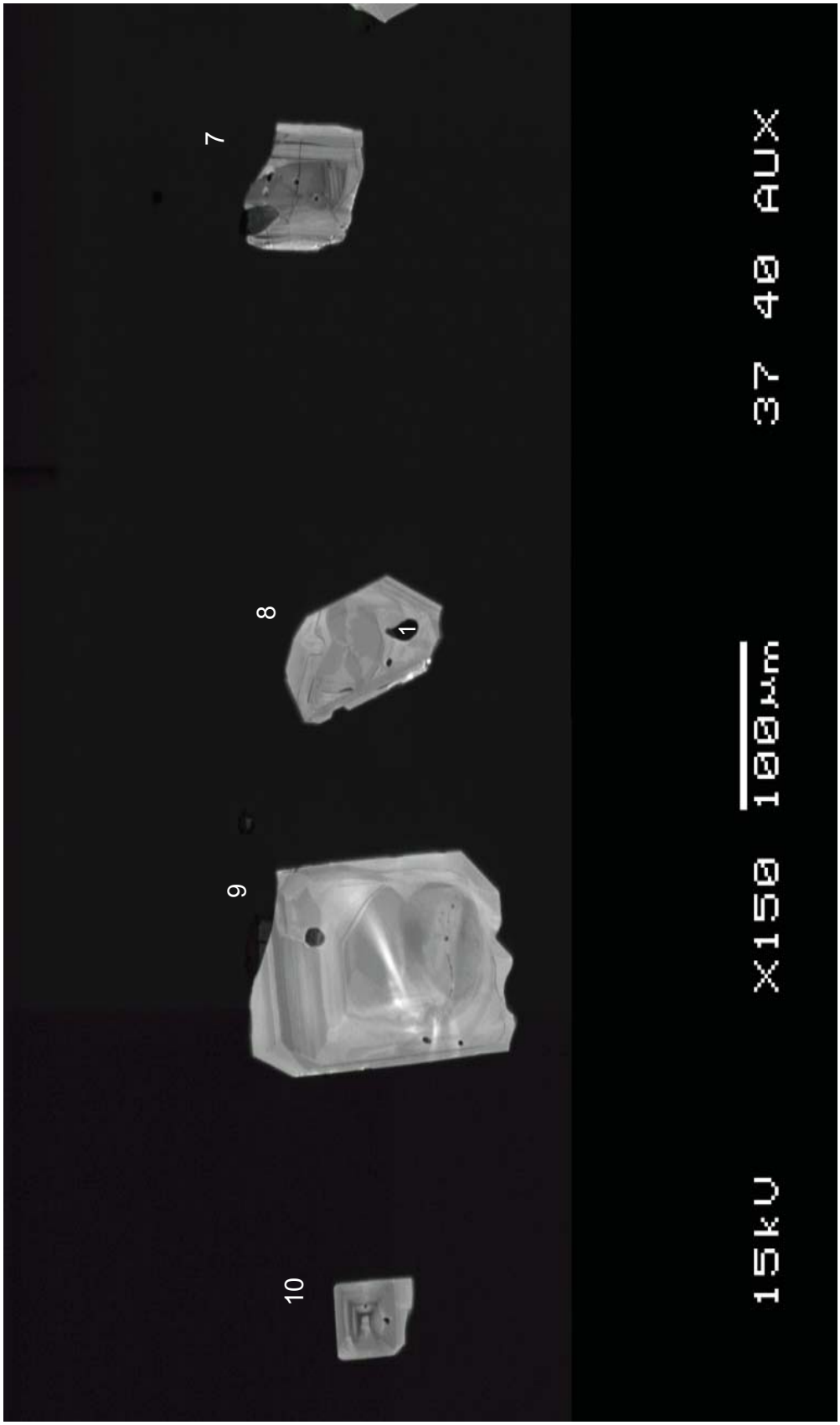

LF2

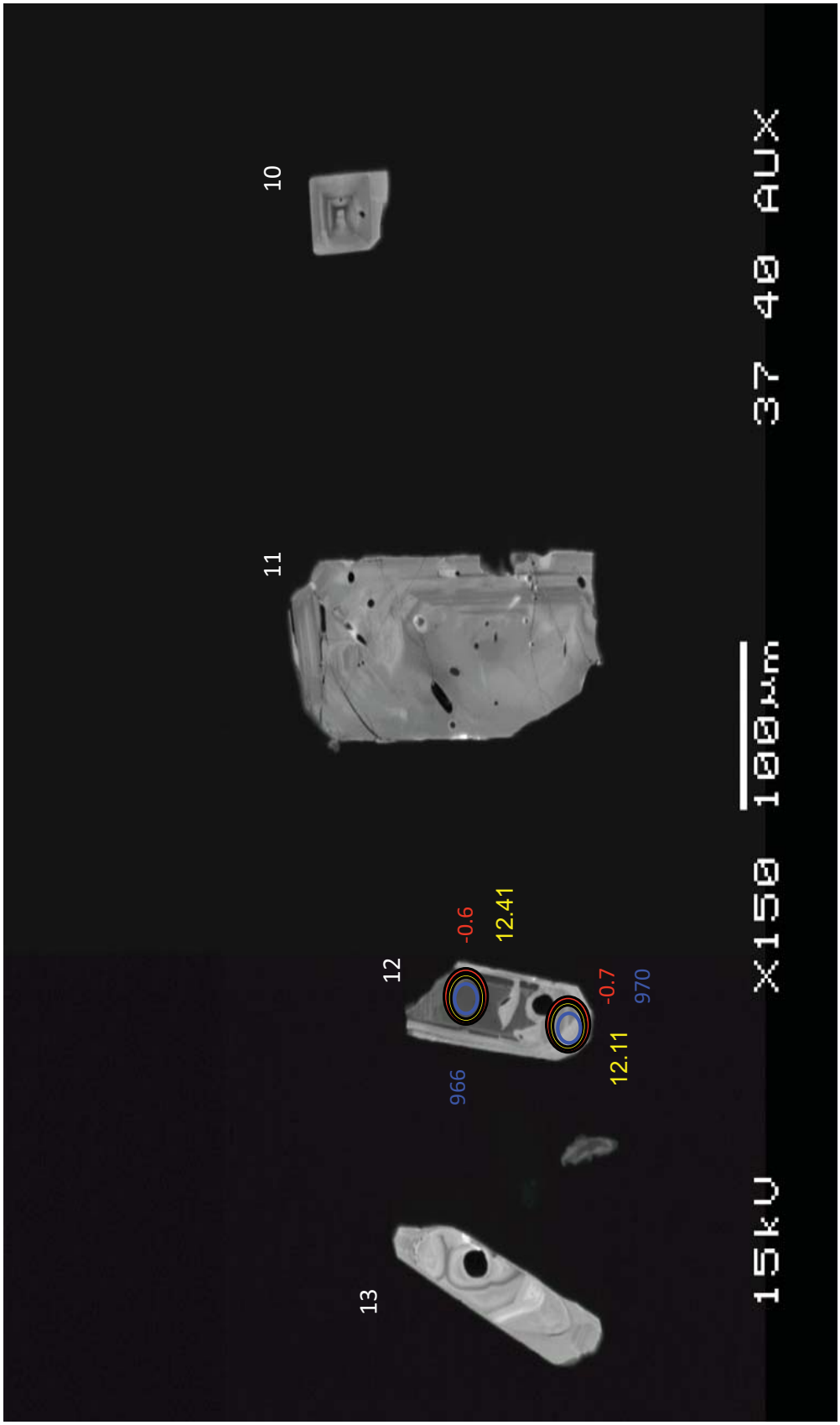

LF2

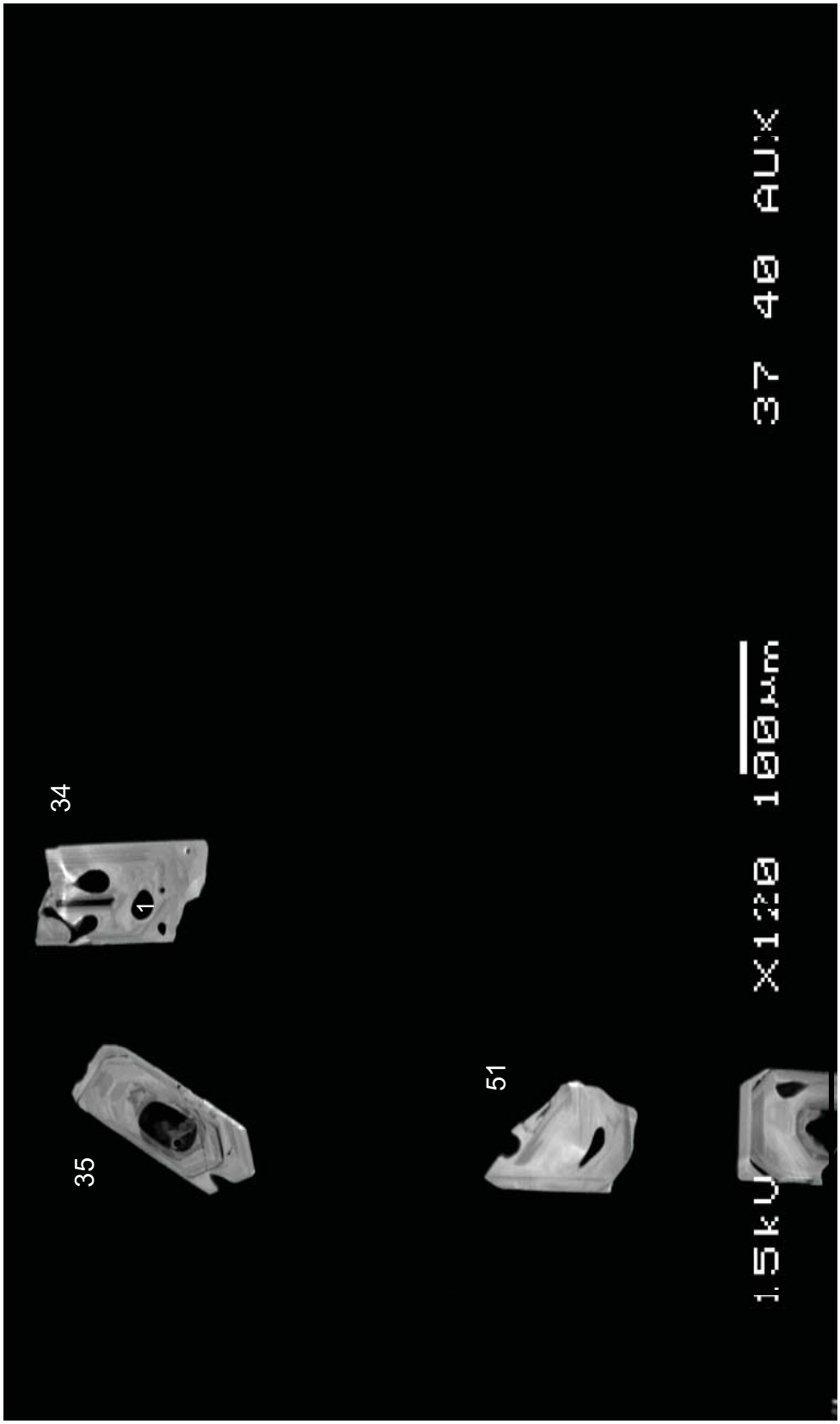

LF2

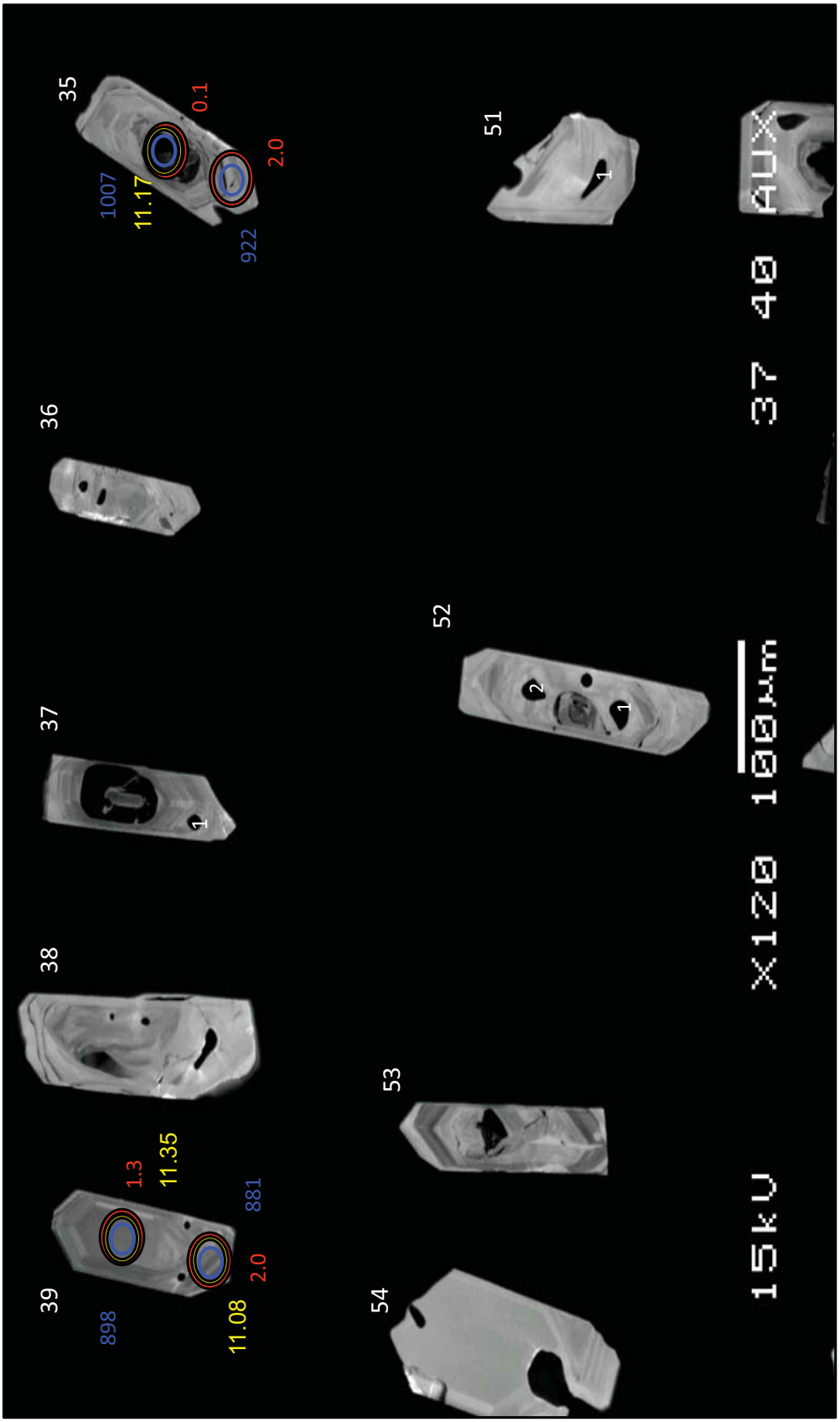
35
1007
11.17
0.1
2.0
922
36
37
1
38
39
898
1.3
11.35
881
11.08
2.0
53
54
52
2
1
51
1
15kU X120 100µm
37 40 AUX

LF1

LF1-35

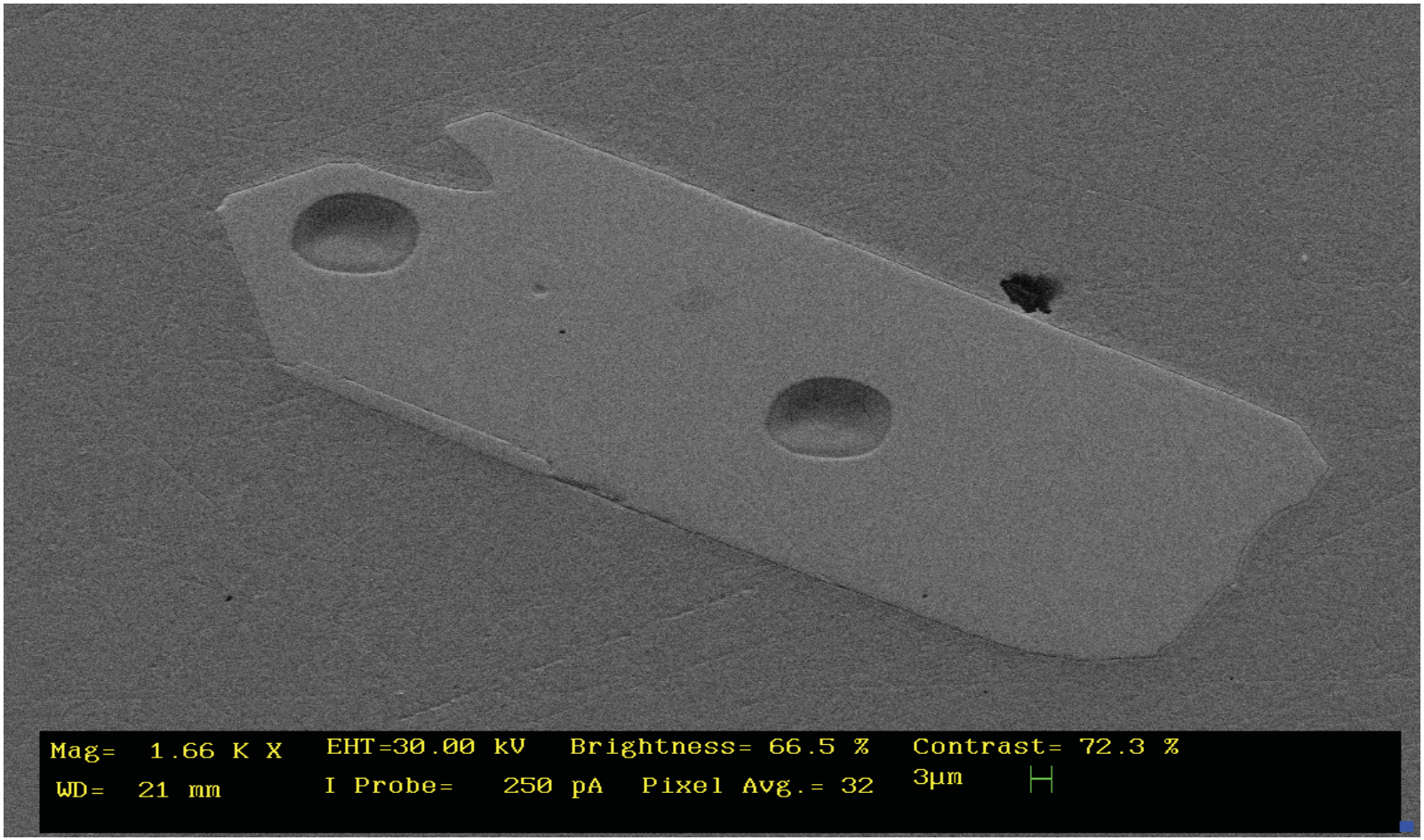
Mag= 1.66 K X
EHT=30.00 kV
Brightness= 66.5 %
Contrast= 72.3 %
WD= 21 mm
I Probe= 250 pA
Pixel Avg.= 32
3µm

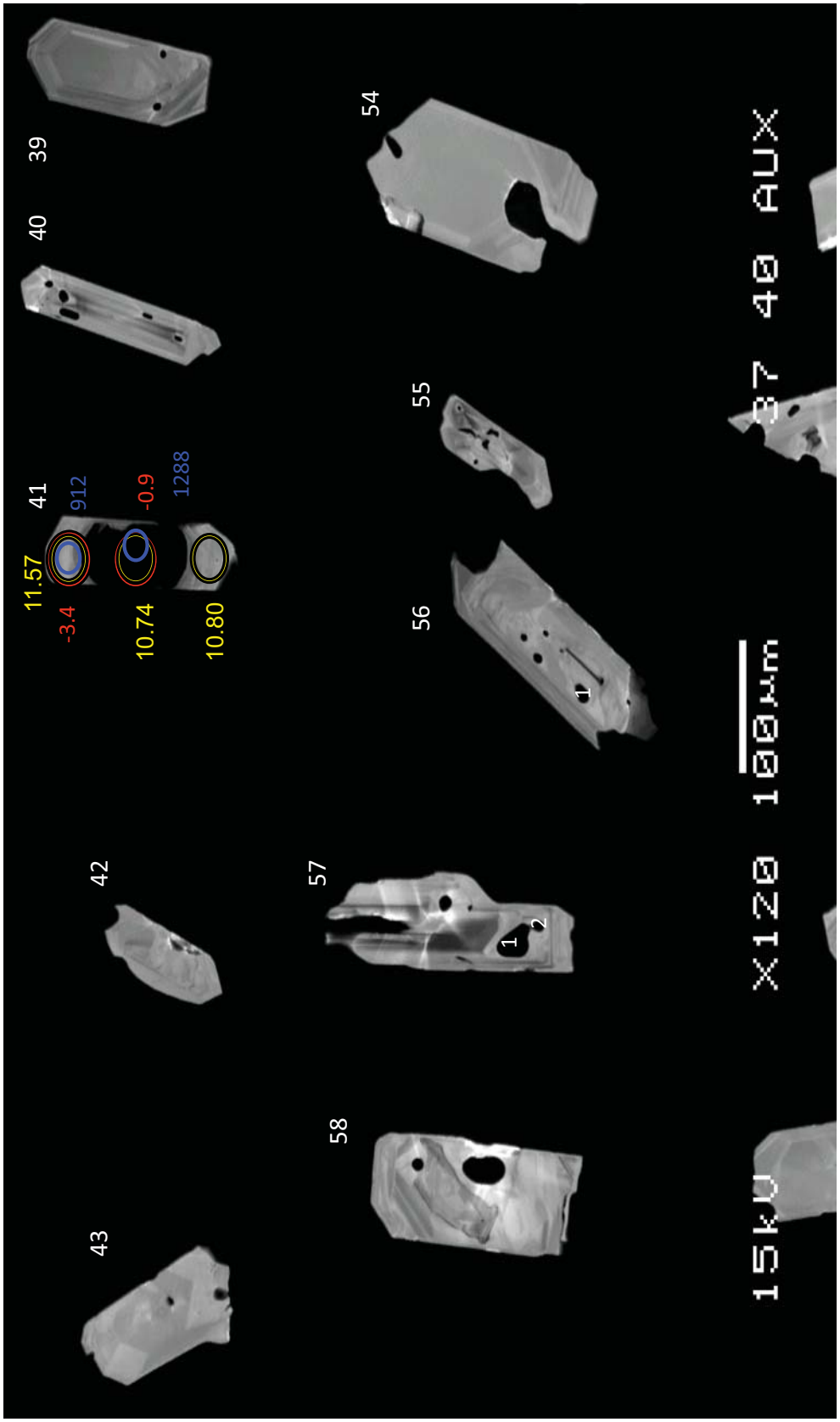
39
40
41
912
-0.9
1288
11.57
-3.4
10.74
10.80
54
55
56
42
57
58
43
1
2
1
X120 100µm
15kV
87 40 AUX

LF1

LF1-41

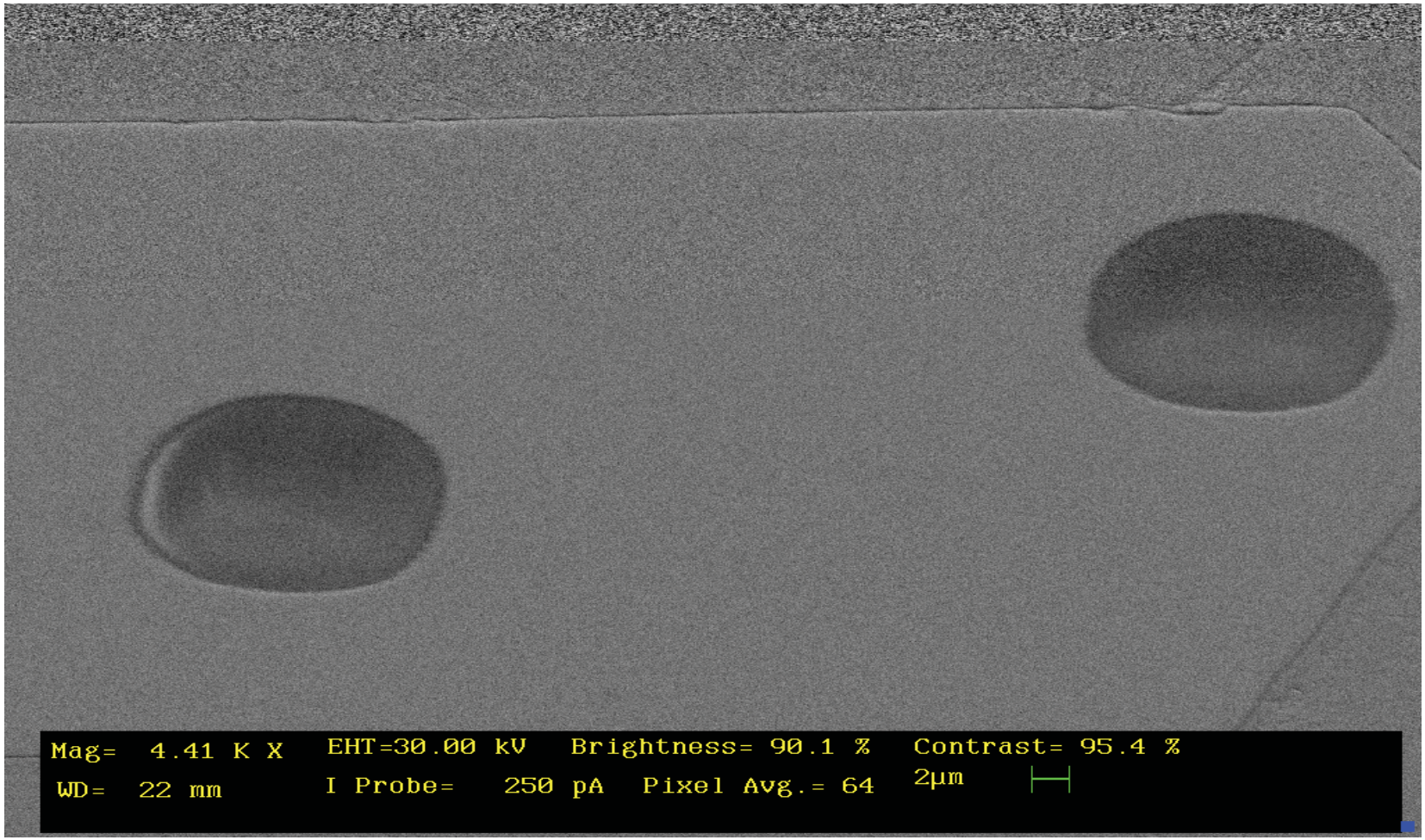
Mag= 4.41 K X
EHT=30.00 kV
Brightness= 90.1 %
Contrast= 95.4 %
WD= 22 mm
I Probe= 250 pA
Pixel Avg.= 64
2µm

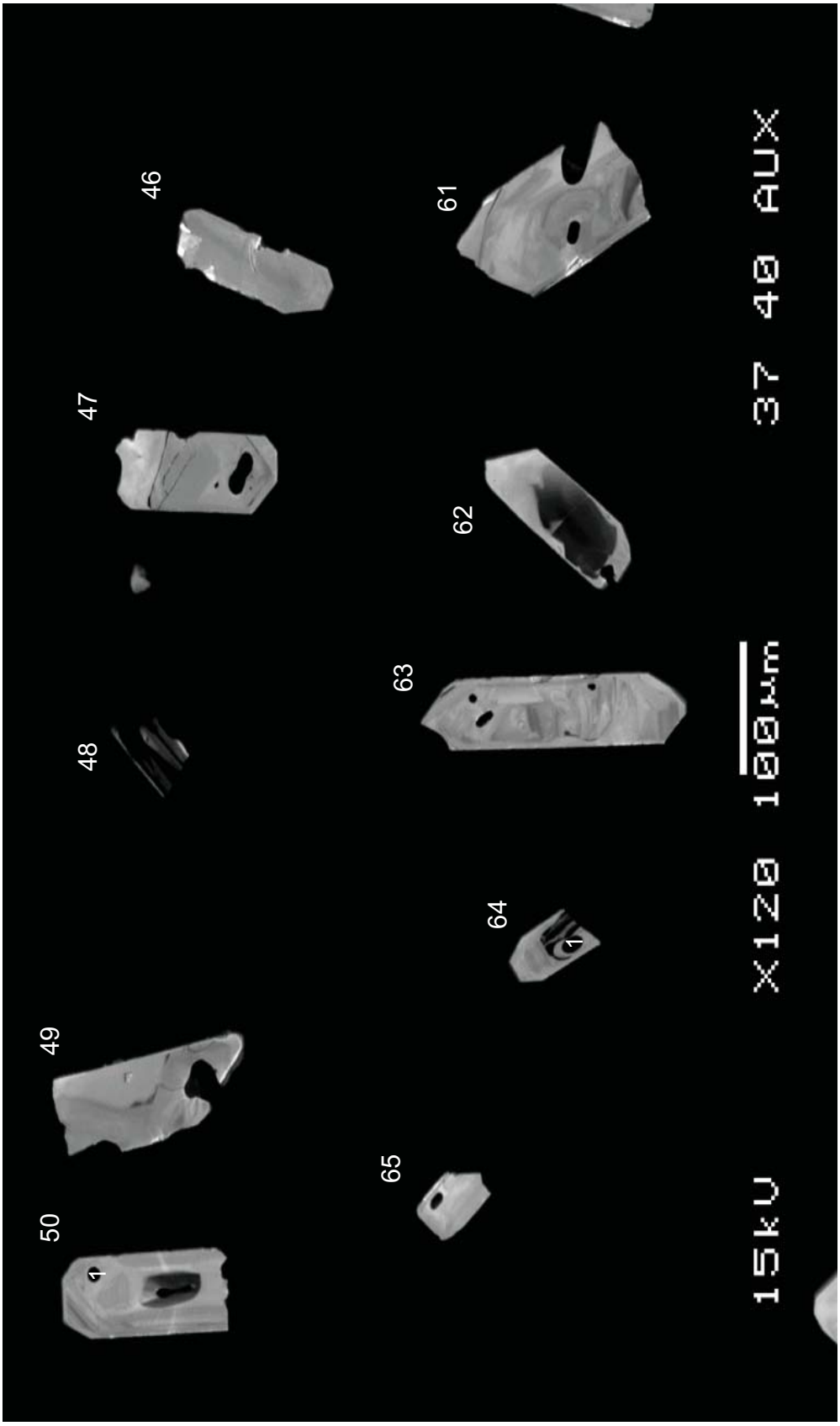

LF1

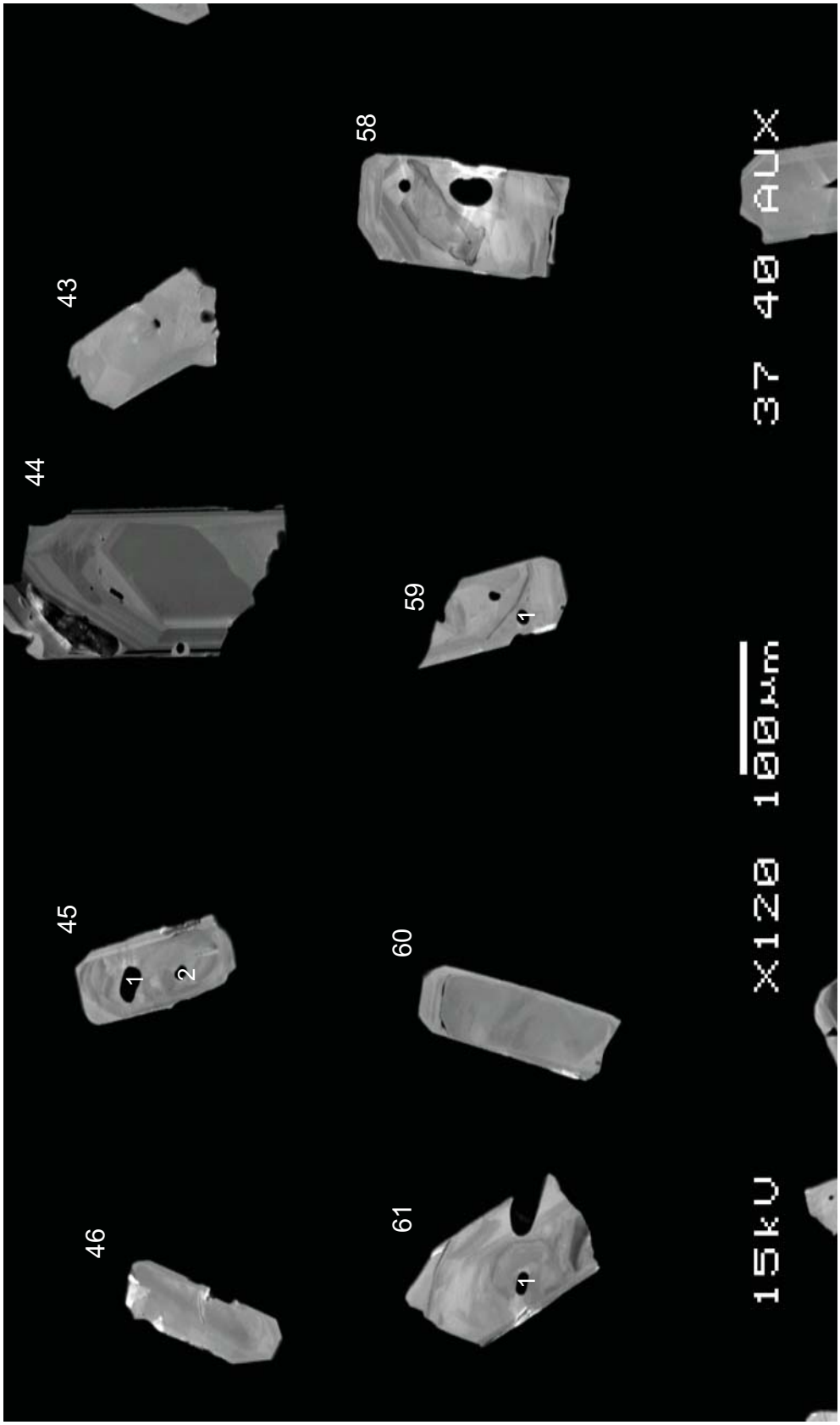

LF1

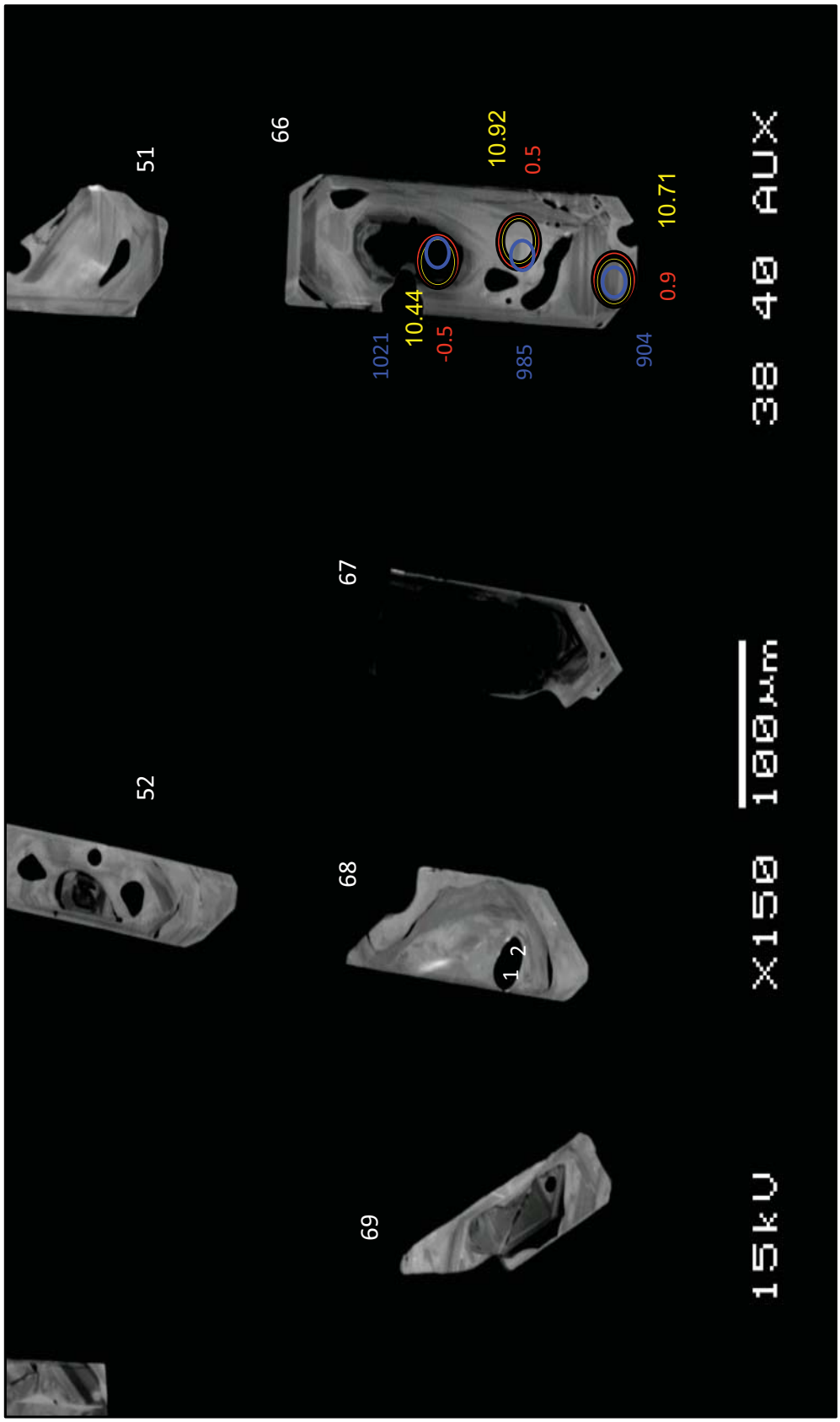
15kV X150 100µm 38 40 AUX
51
52
66
67
68
69
1 2
1021
10.44
-0.5
985
10.92
0.5
904
0.9
10.71

LF1

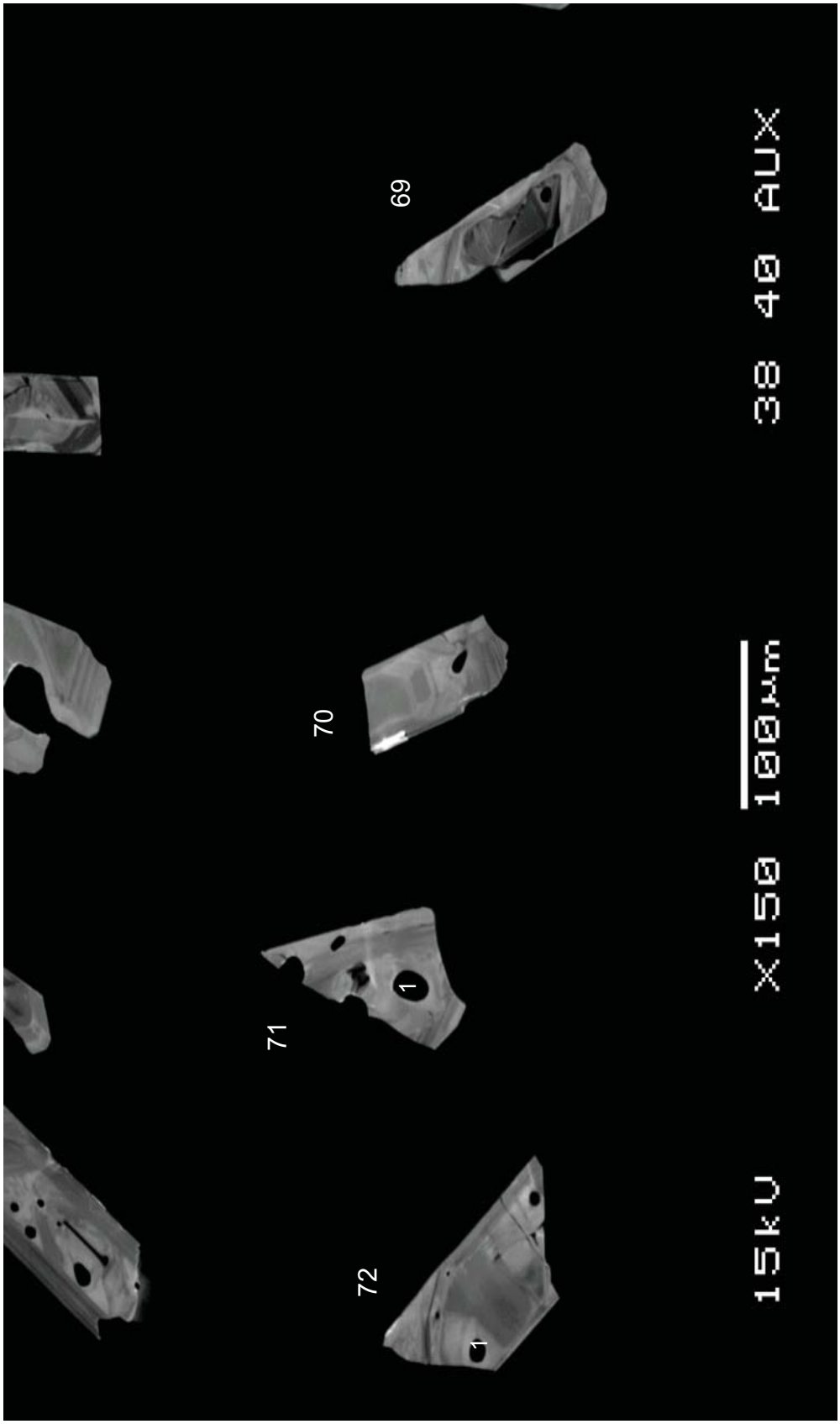

LF1

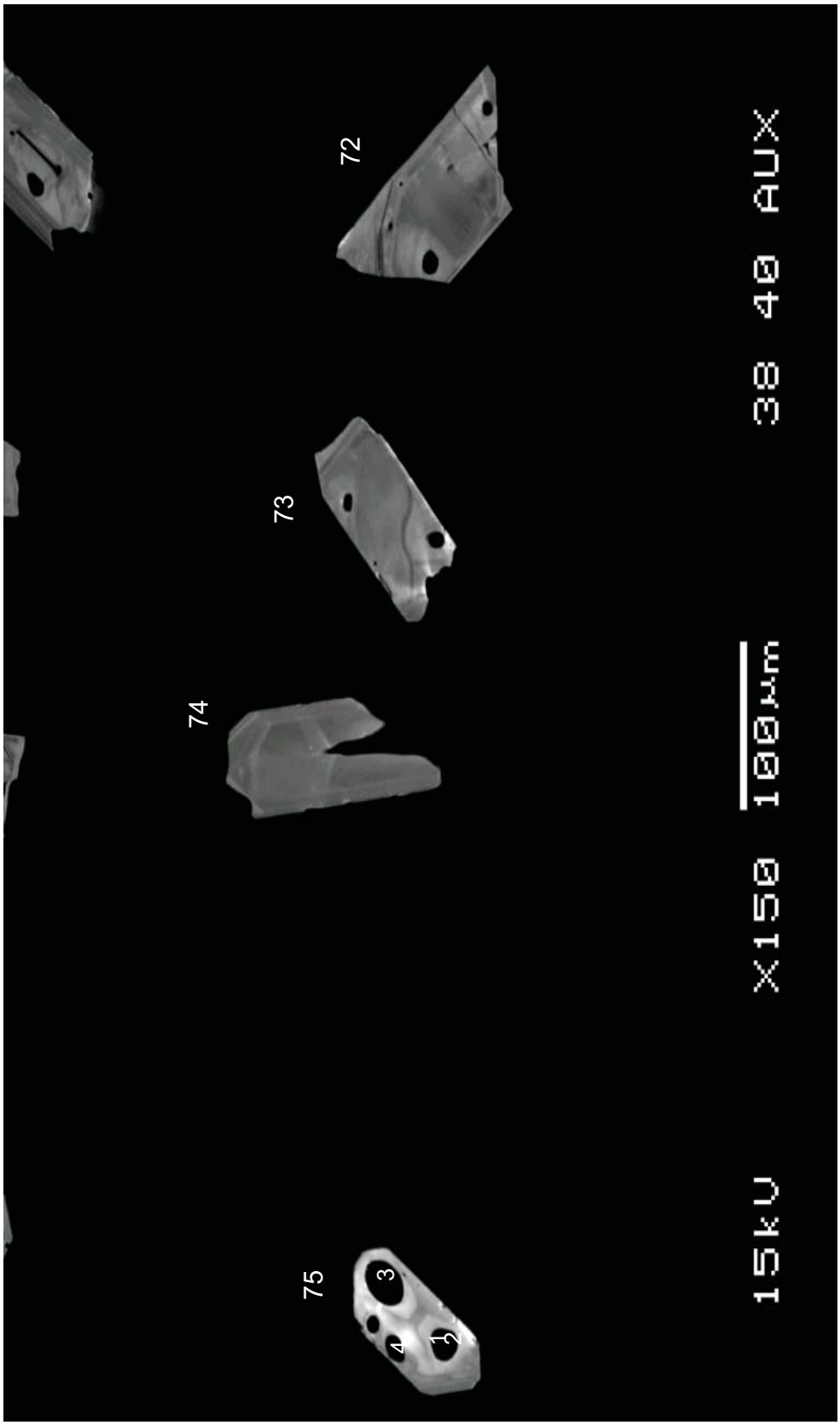

LF1

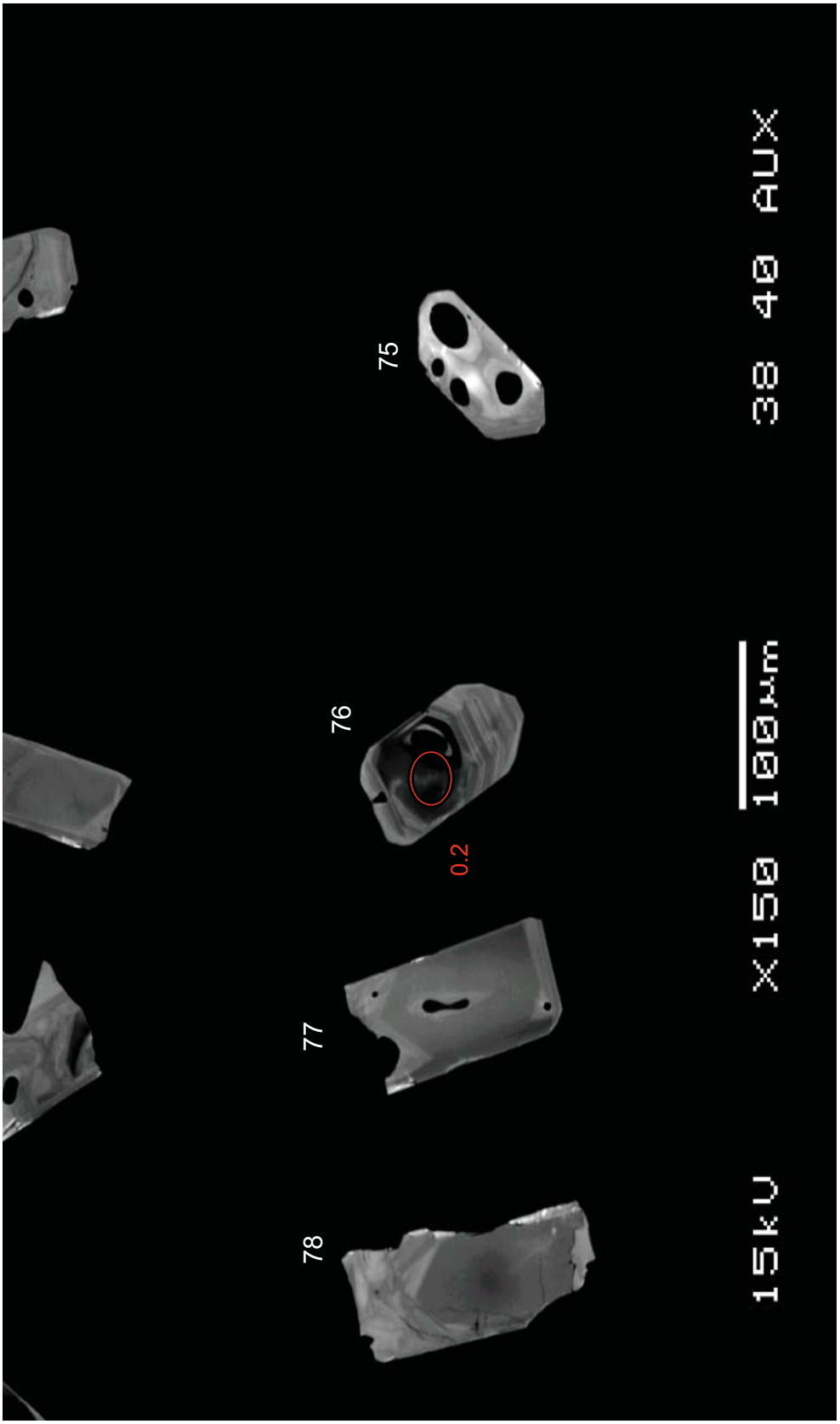

LF1

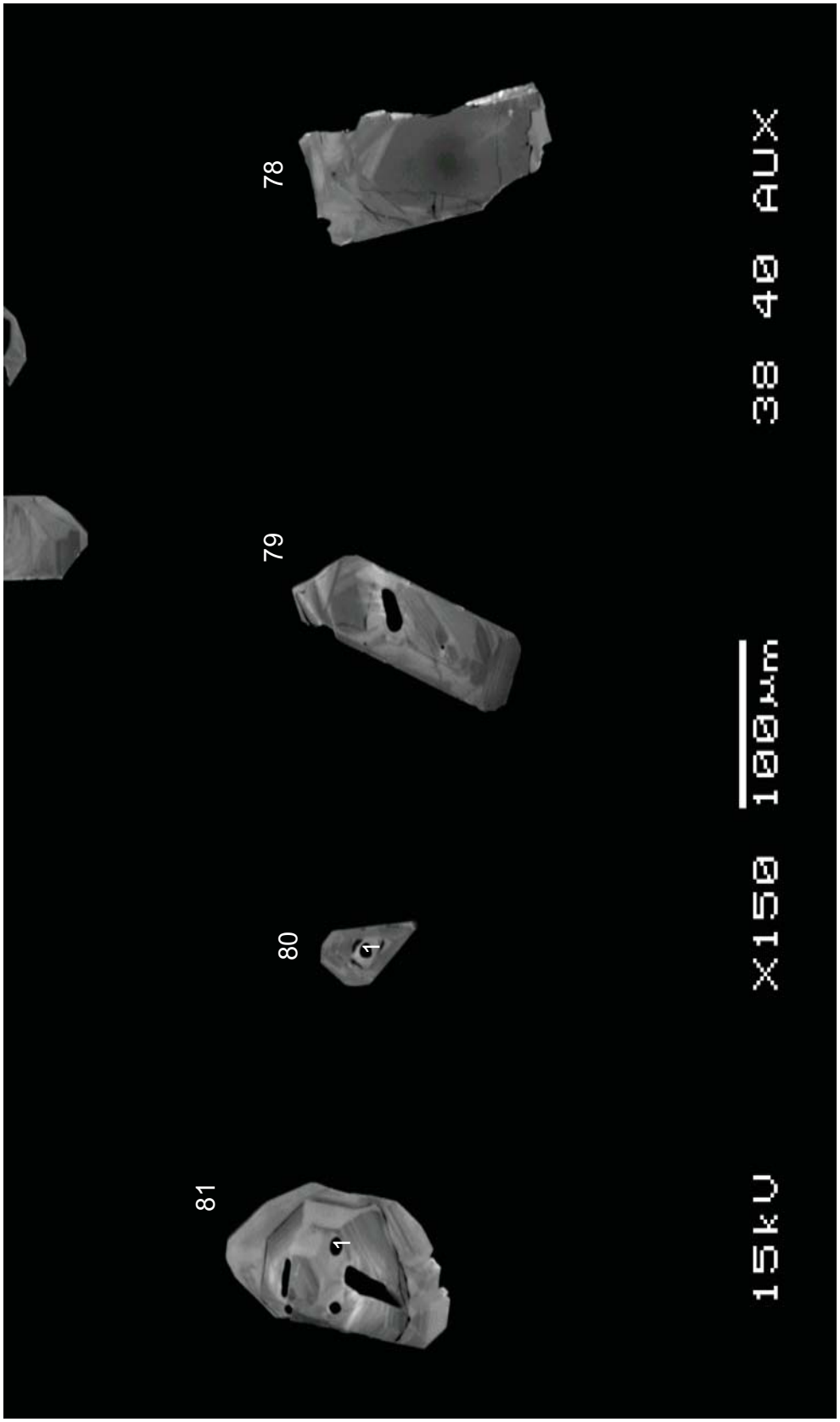

LF1

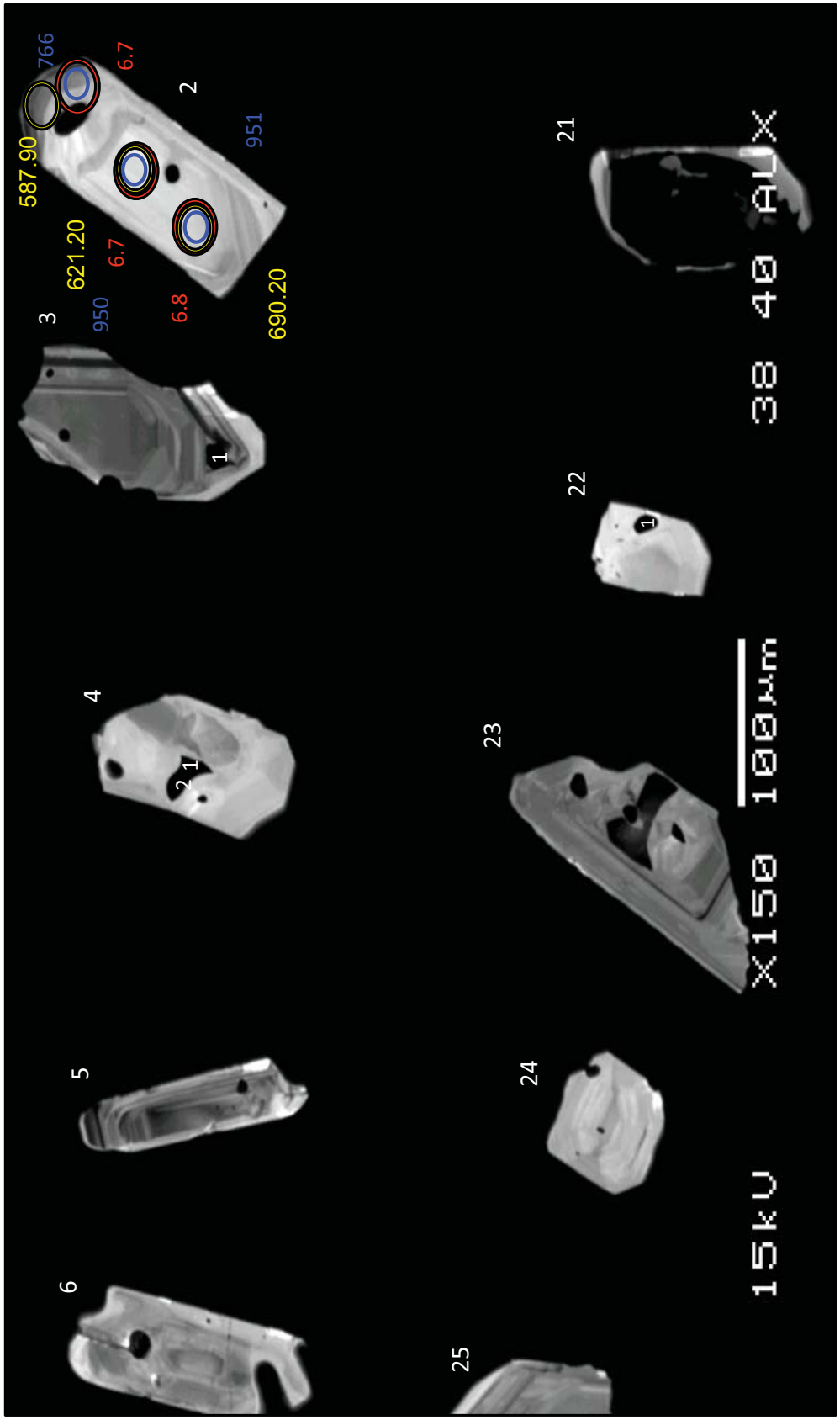
587.90
766
6.7
2
951
621.20
6.7
950
6.8
690.20
3
1
4
2
1
5
6
25
24
23
22
1
21
15kV X150 100μm 38 40 ALX
SCR

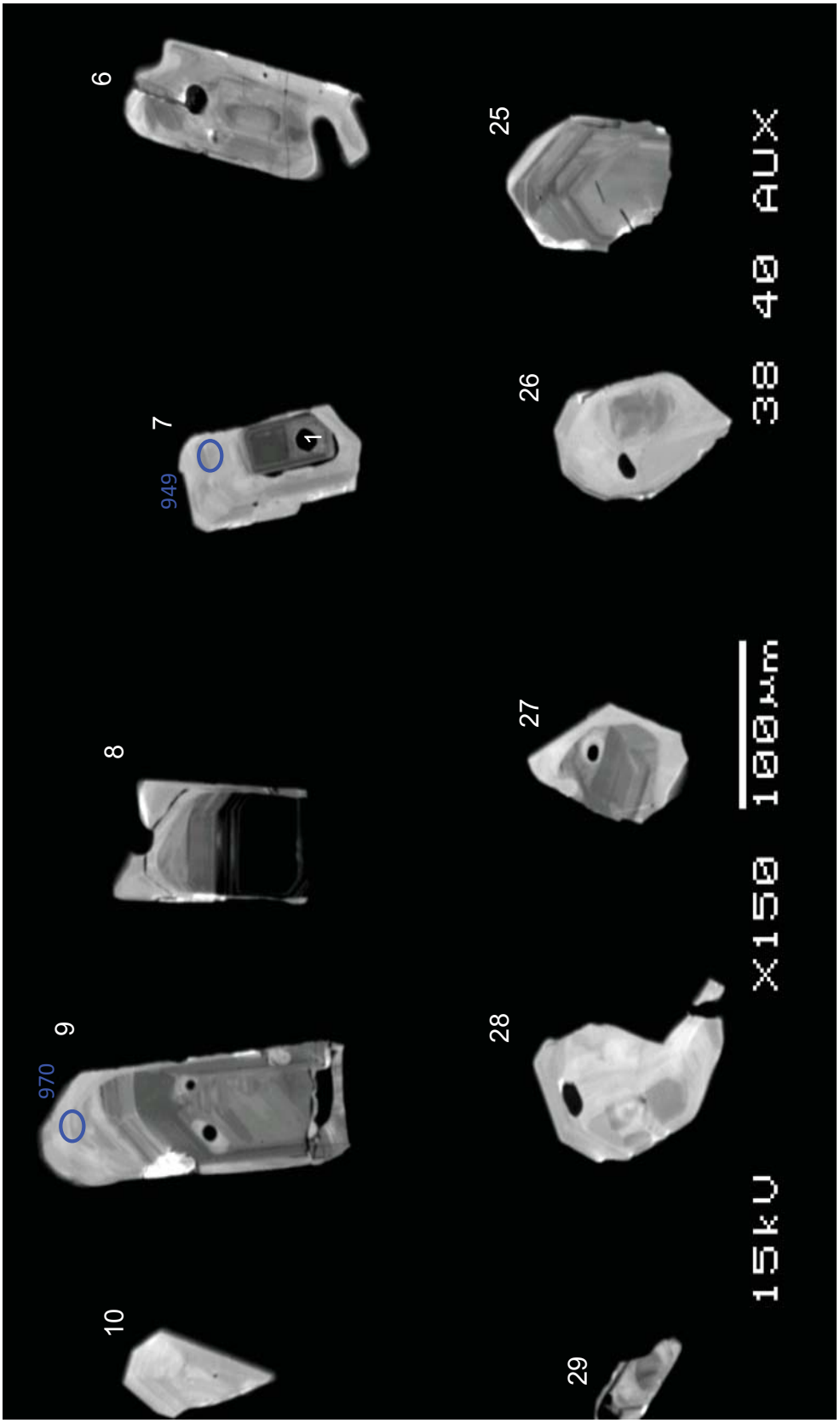

SCR

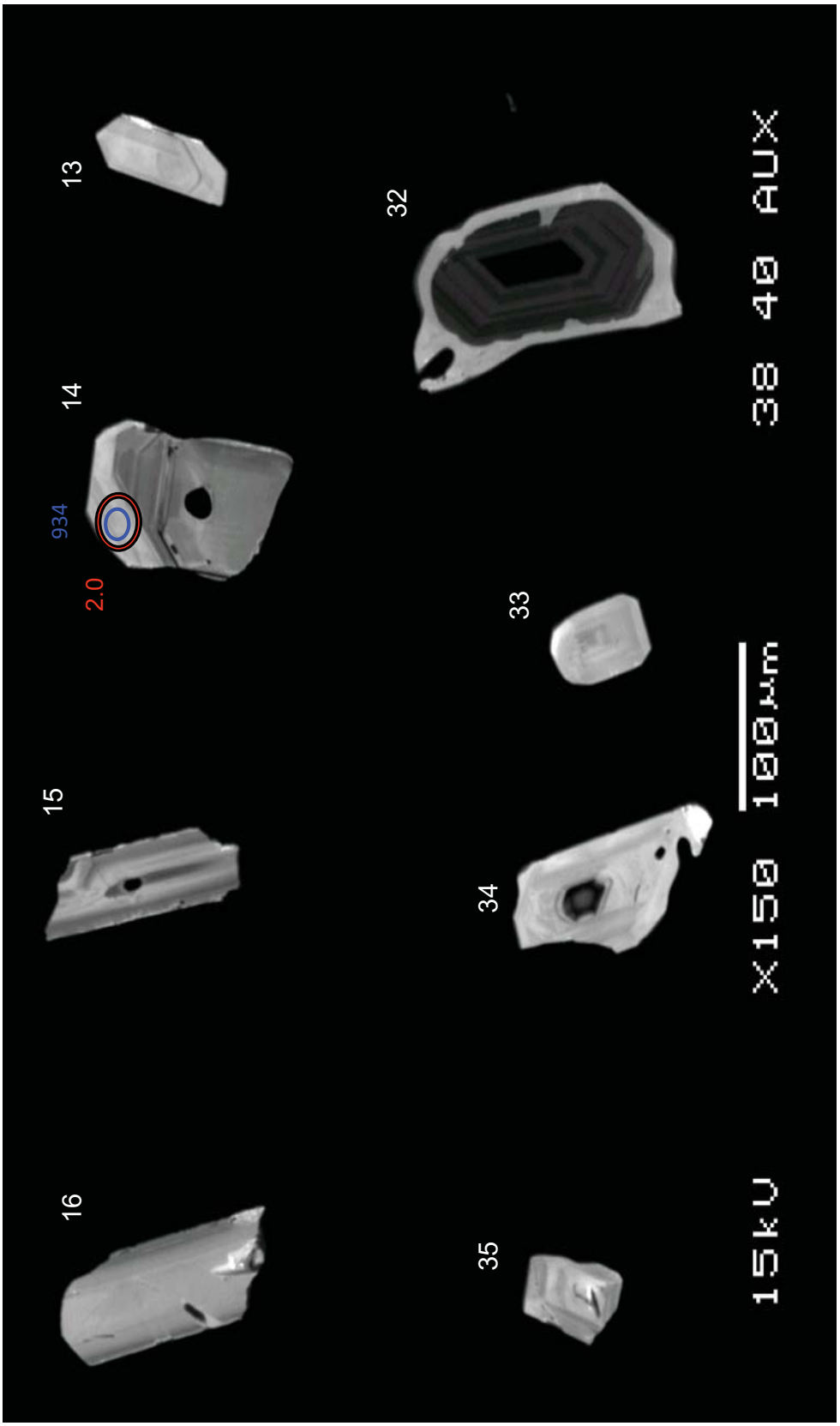

SCR

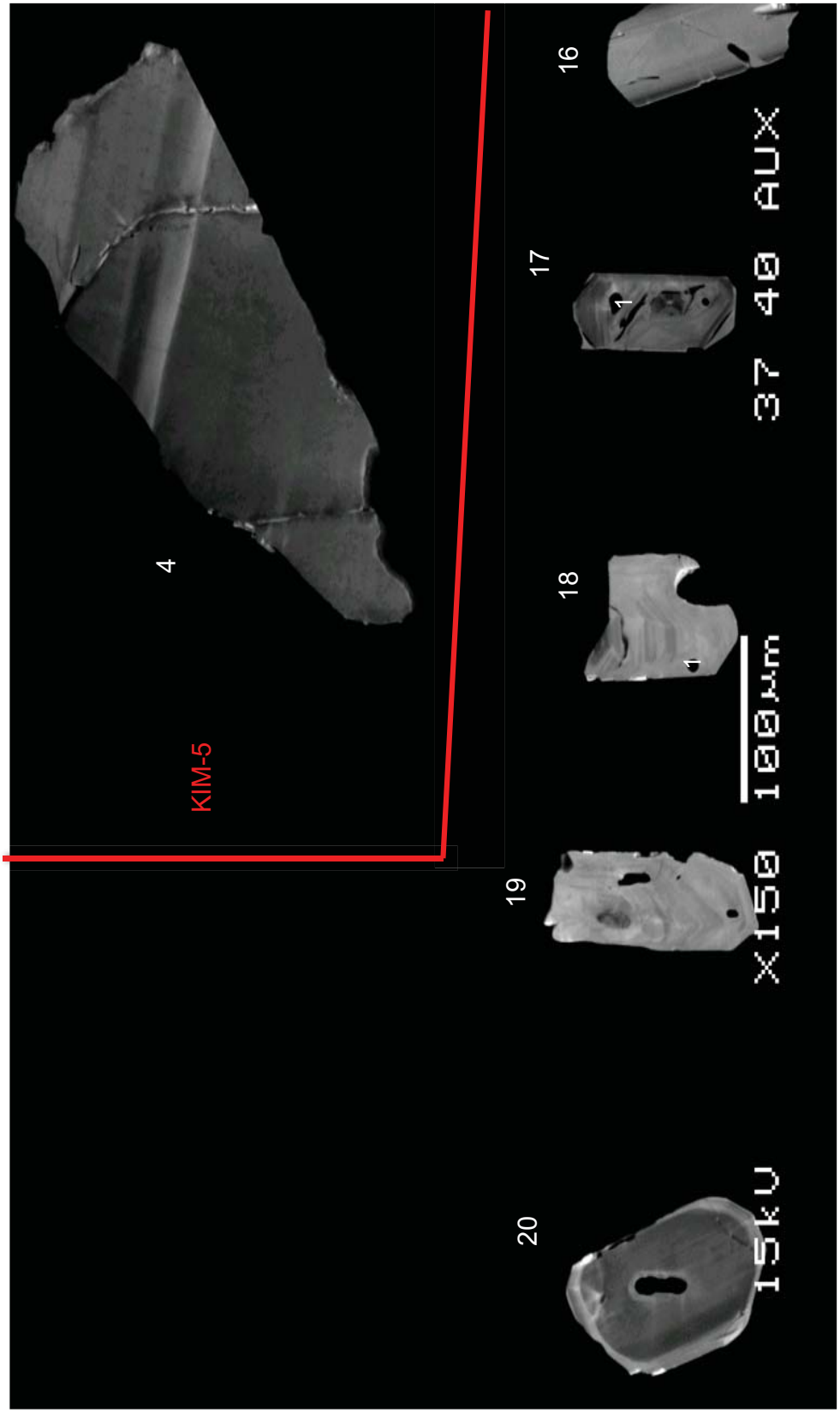

SCR

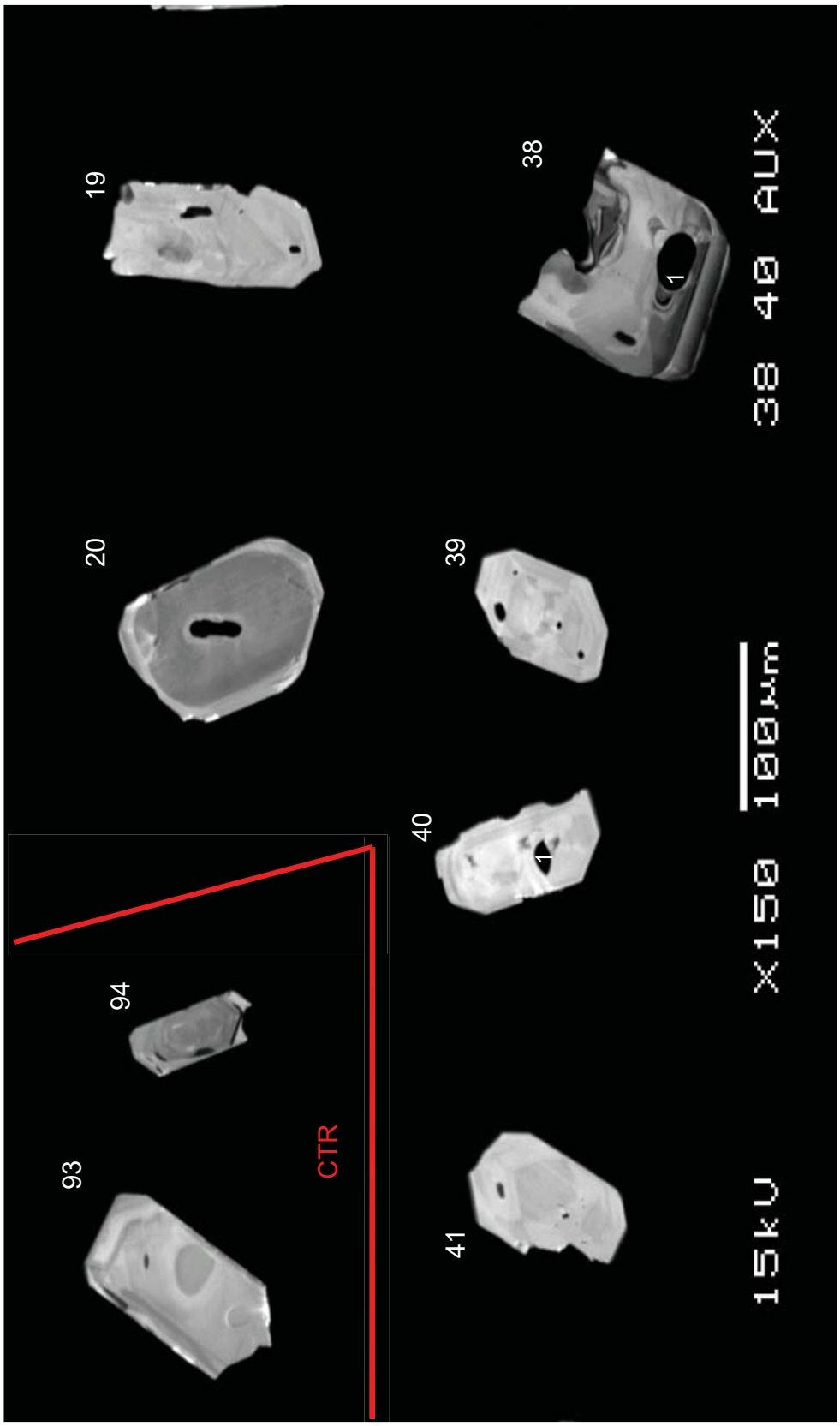

SCR

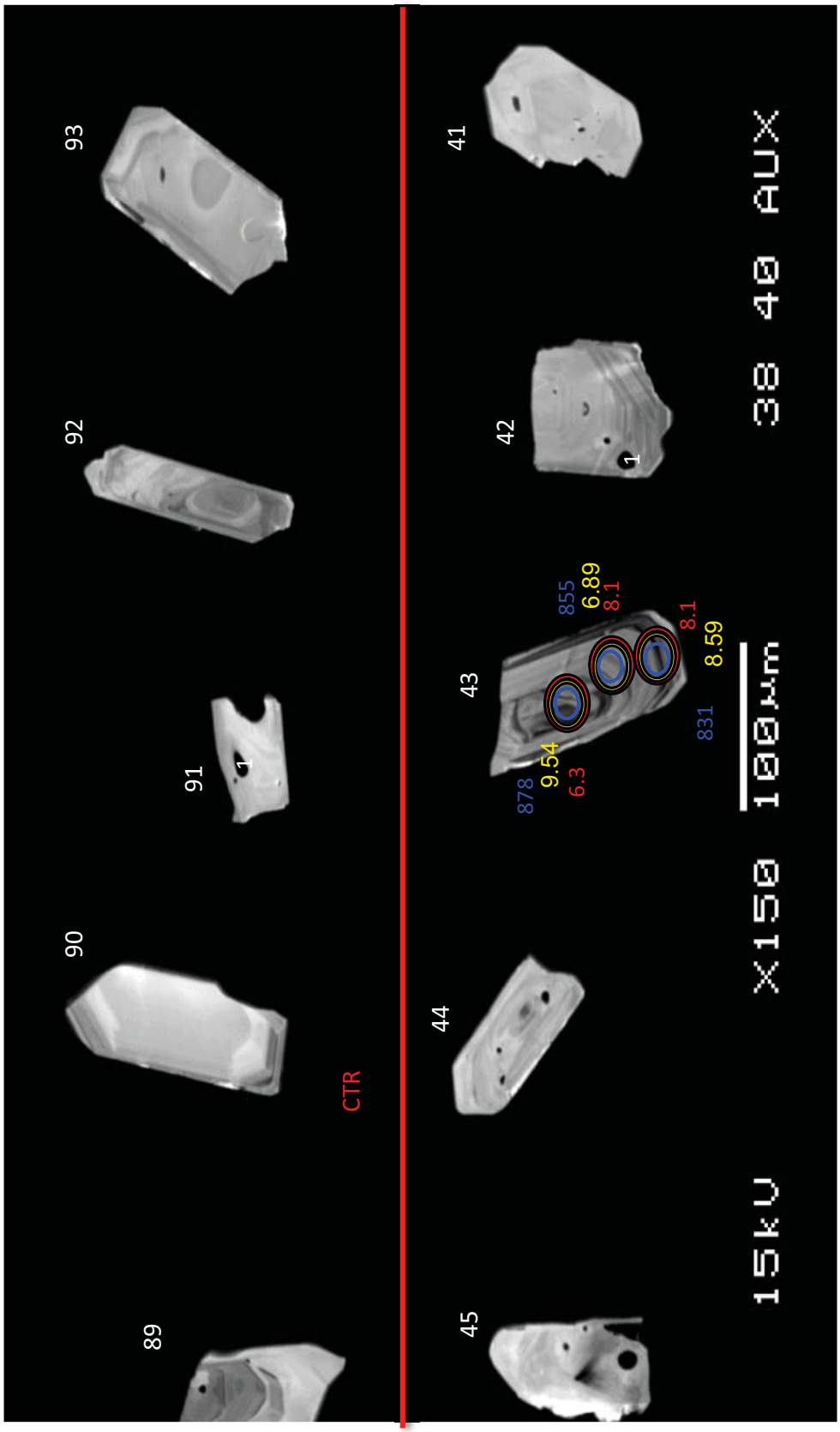
15kV X150 100µm 38 40 AUX
SCR
CTR
89
90
91
92
93
45
44
43
42
41
1
1
878
9.54
6.3
831
855
6.89
8.1
8.1
8.59

SCR-43

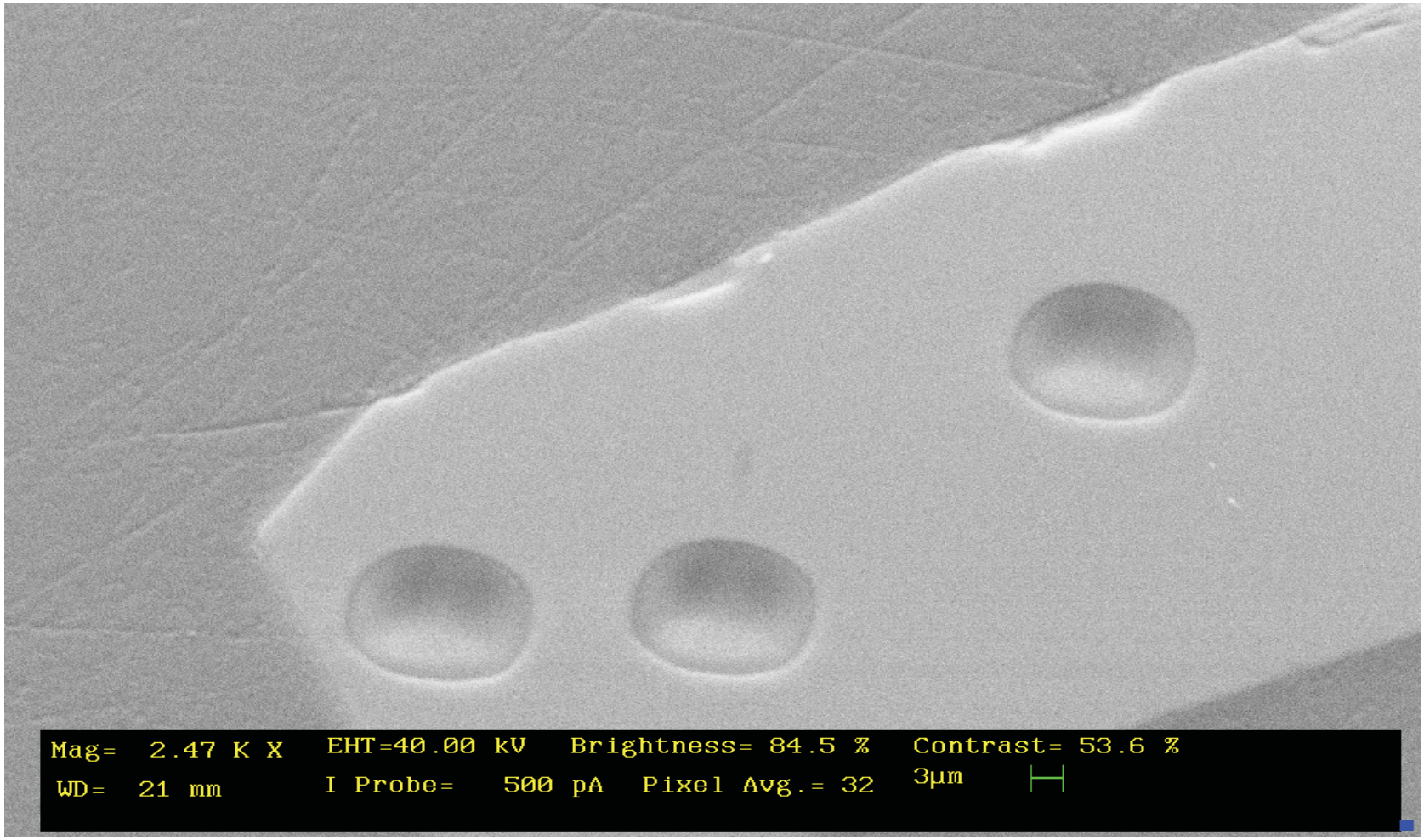
Mag= 2.47 K X
EHT=40.00 kV
Brightness= 84.5 %
Contrast= 53.6 %
WD= 21 mm
I Probe= 500 pA
Pixel Avg.= 32
3µm

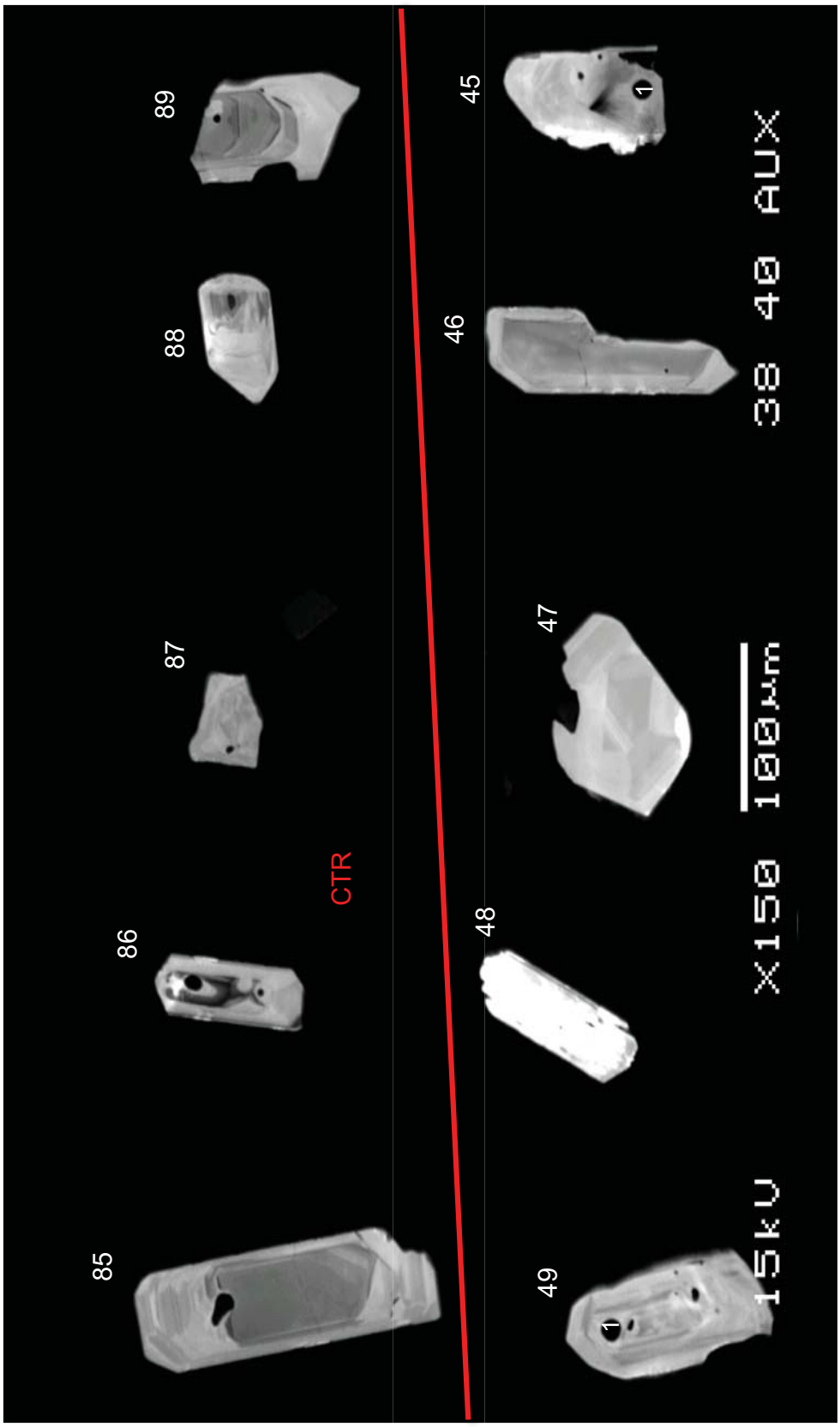

SCR

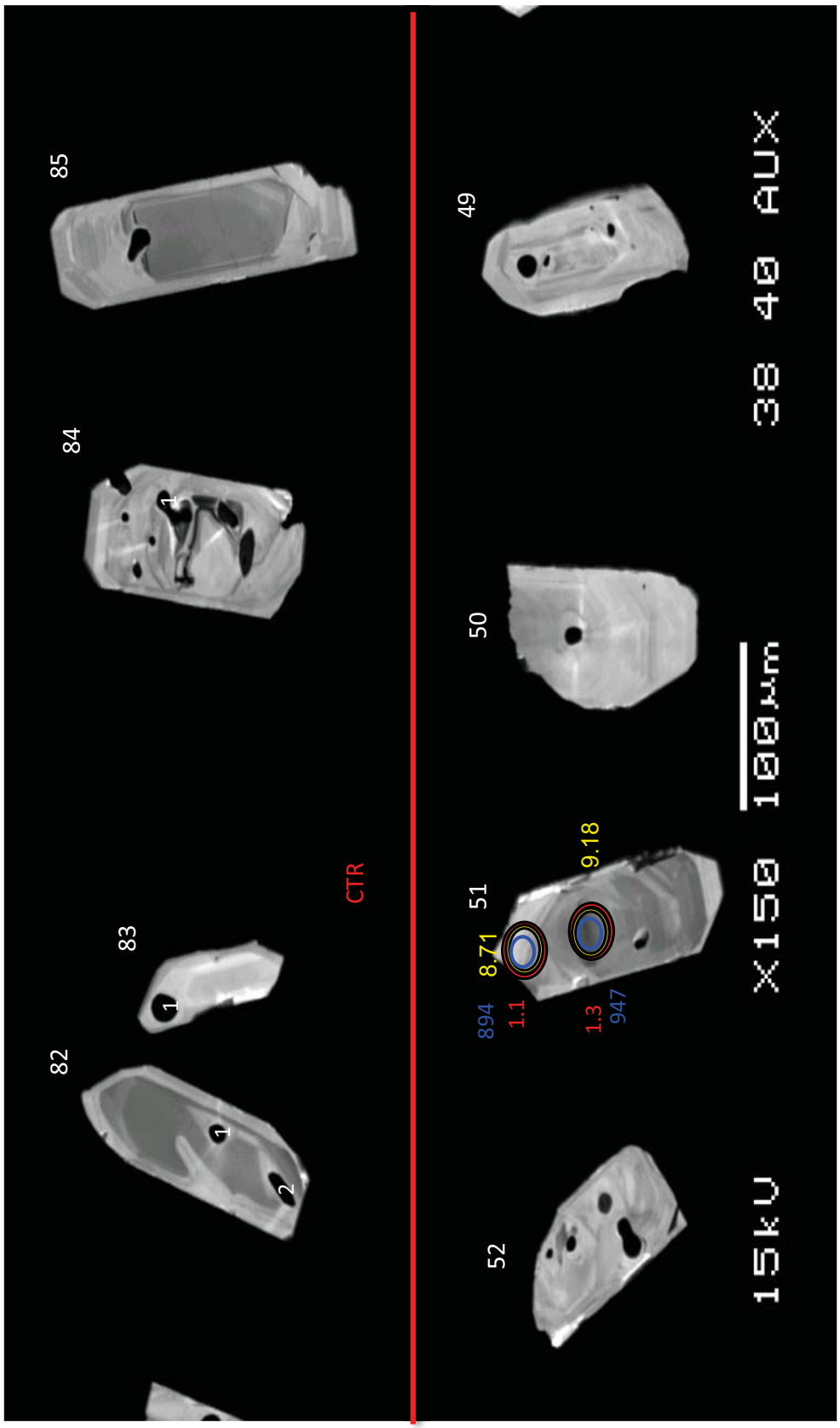
85
84
83
82
1
1
1
2
CTR
49
50
51
52
8.71
9.18
894
1.1
1.3
947
15kV X150 100µm SE 40 4UX

SCR

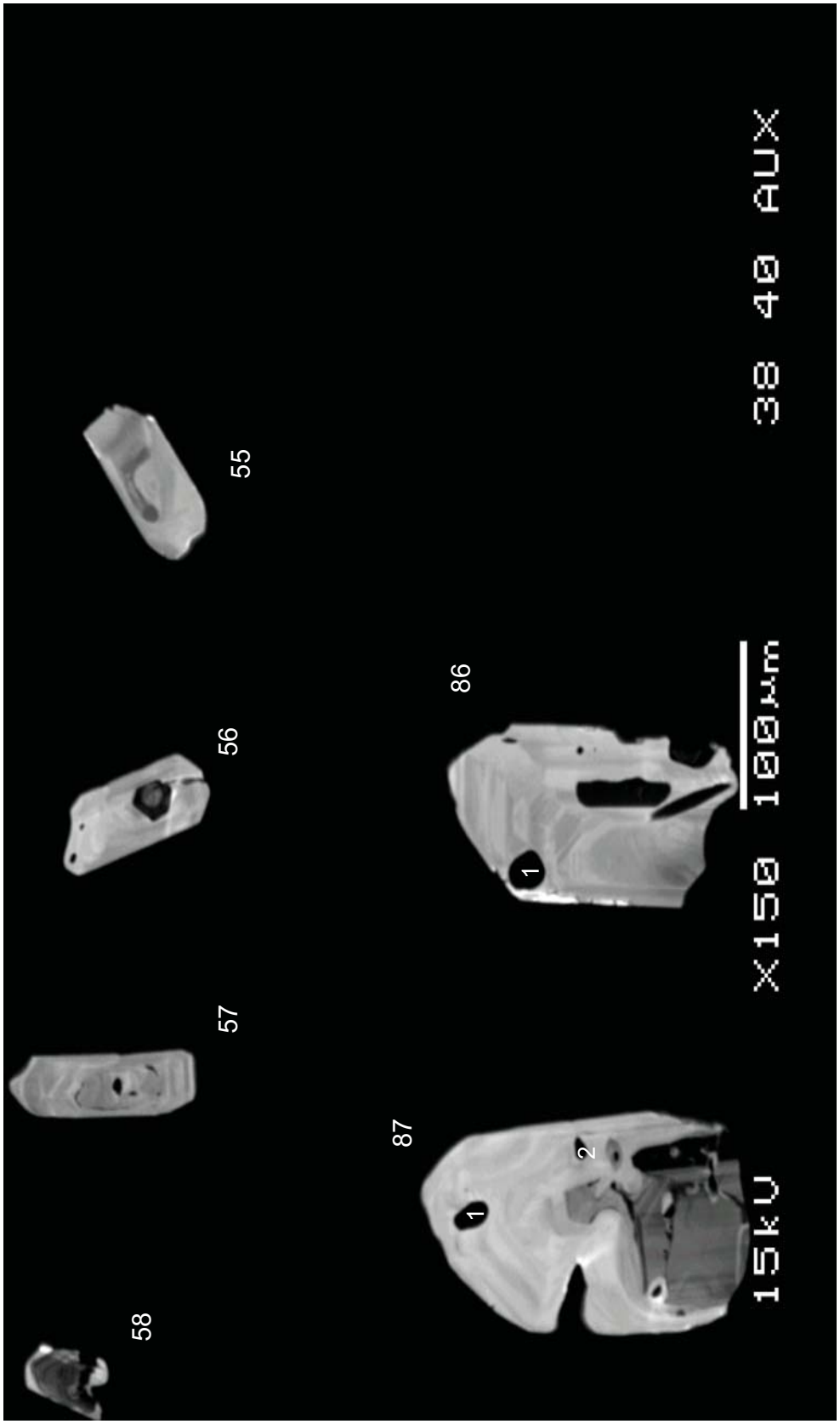

SCR

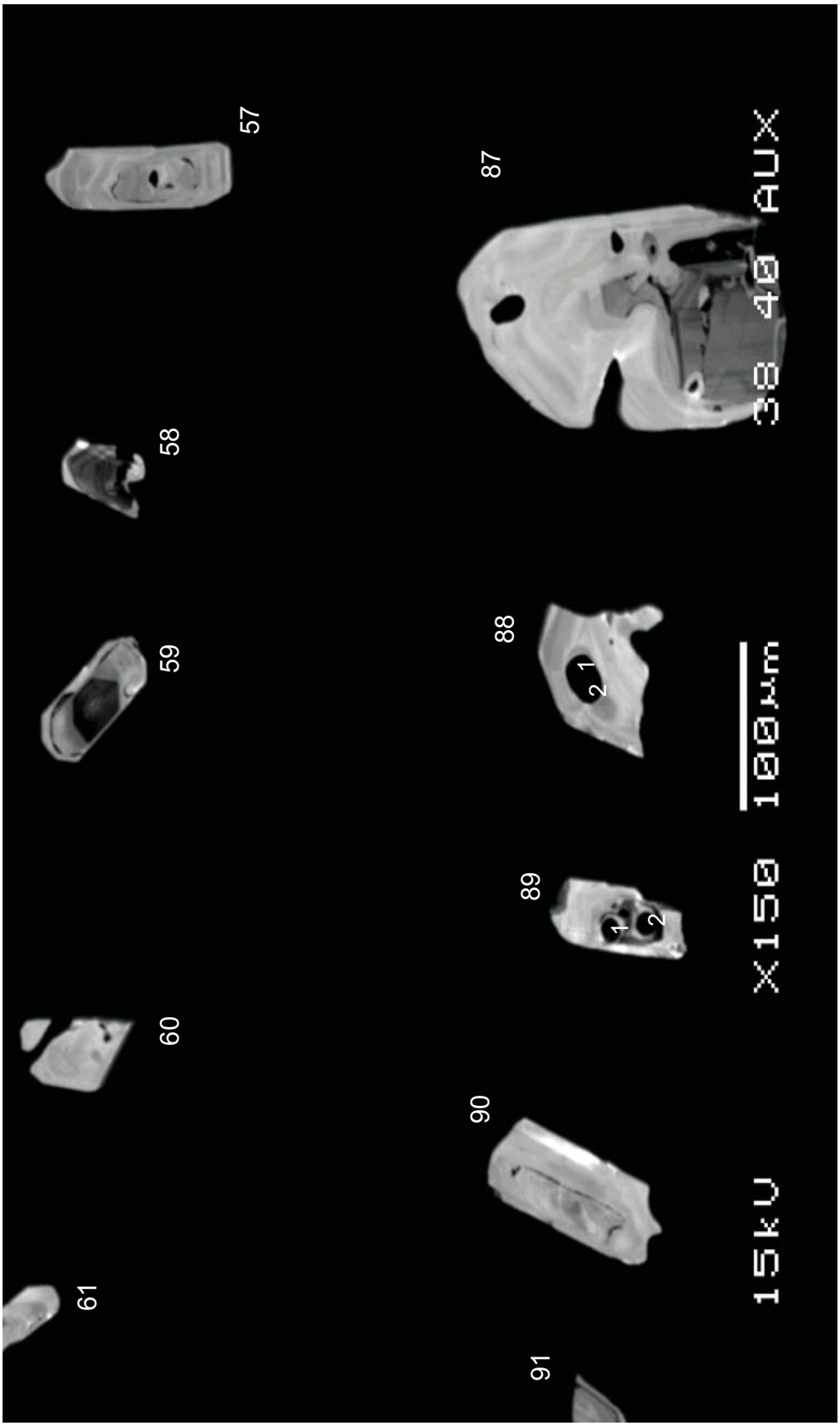

SCR

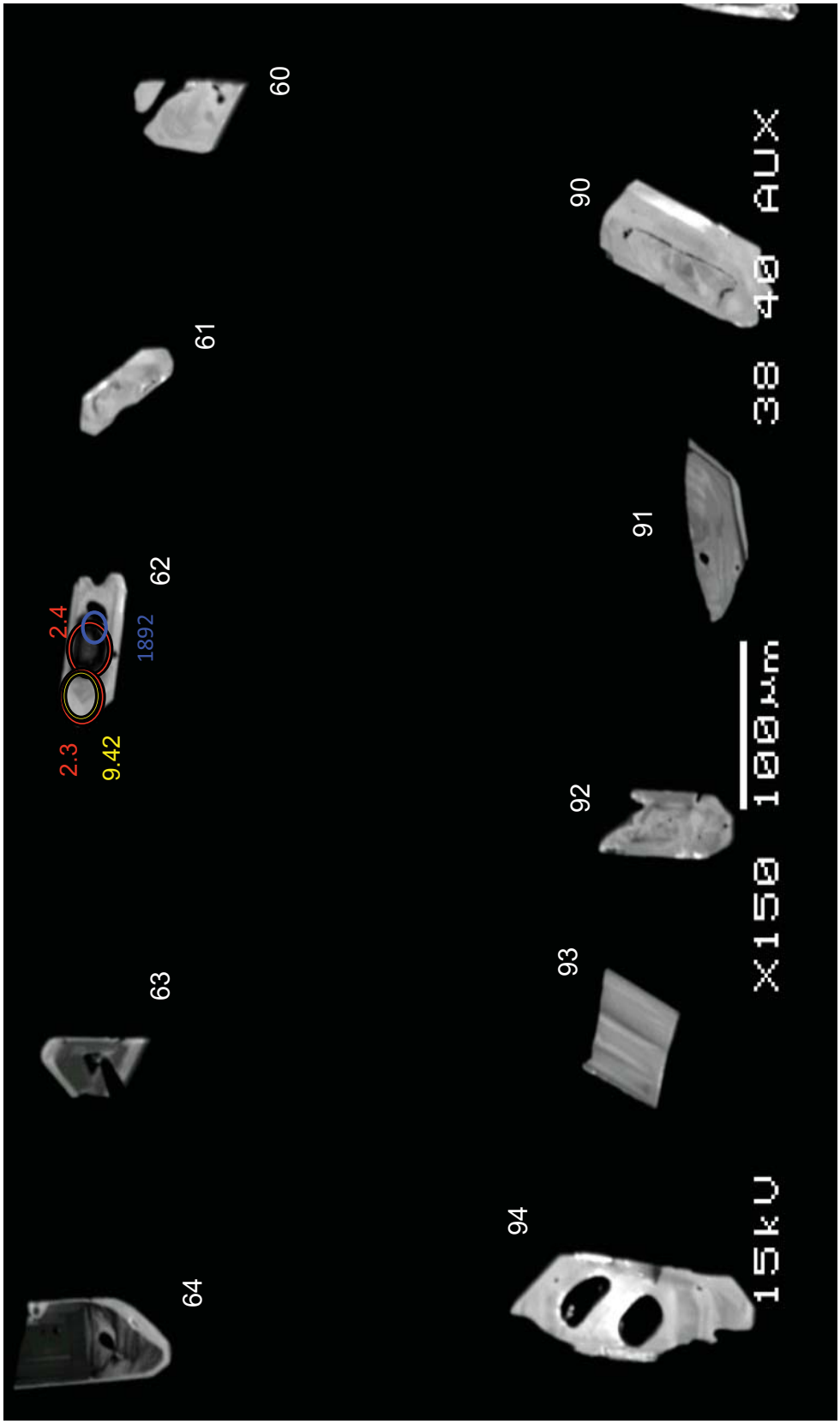
60
61
62
63
64
90
91
92
93
94
2.4
1892
2.3
9.42
15kV X150 100µm 38 40 AUX

SCR

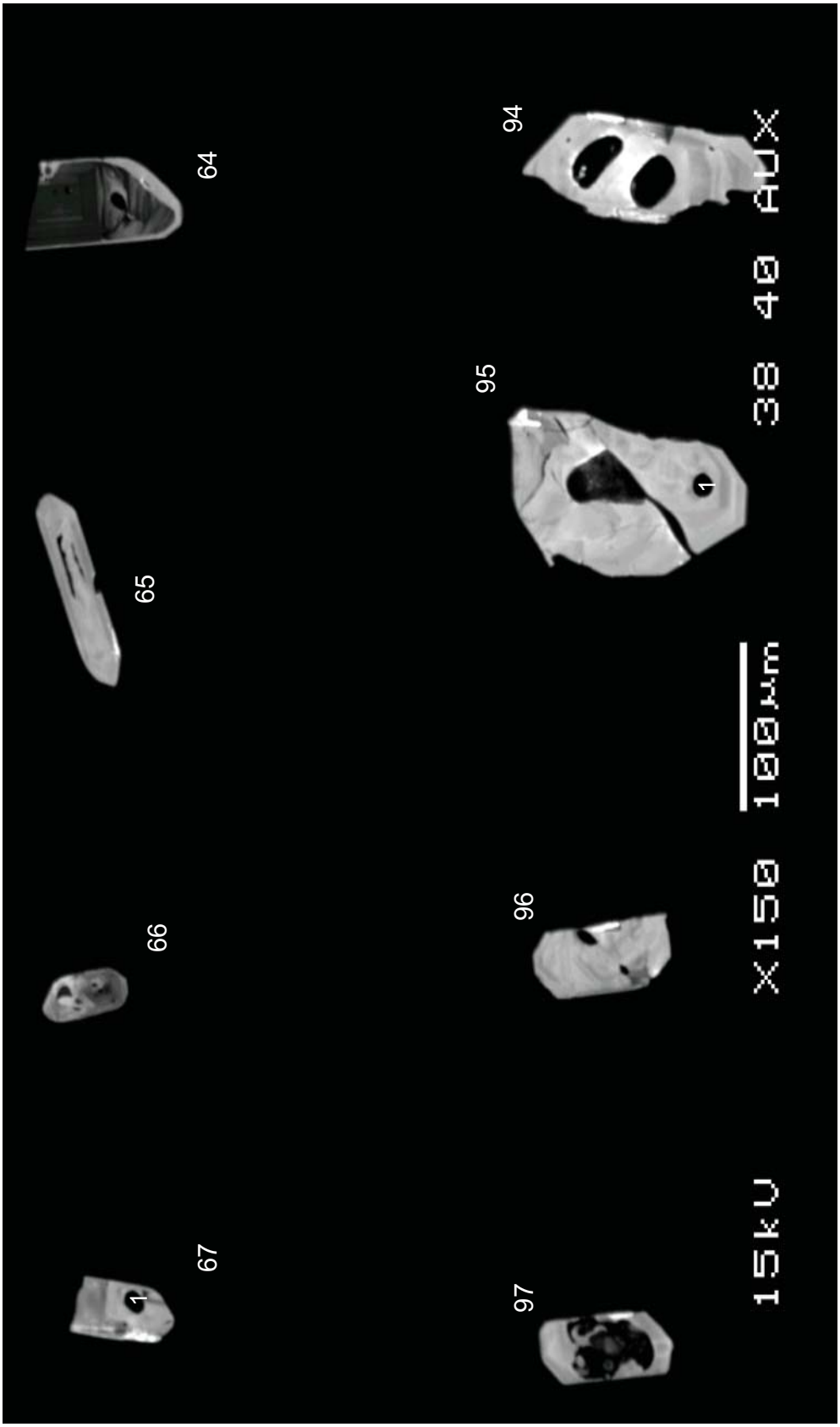
15kU X150 100µm
38 40 40µX
SCR
1
64
65
66
67
94
95
96
97

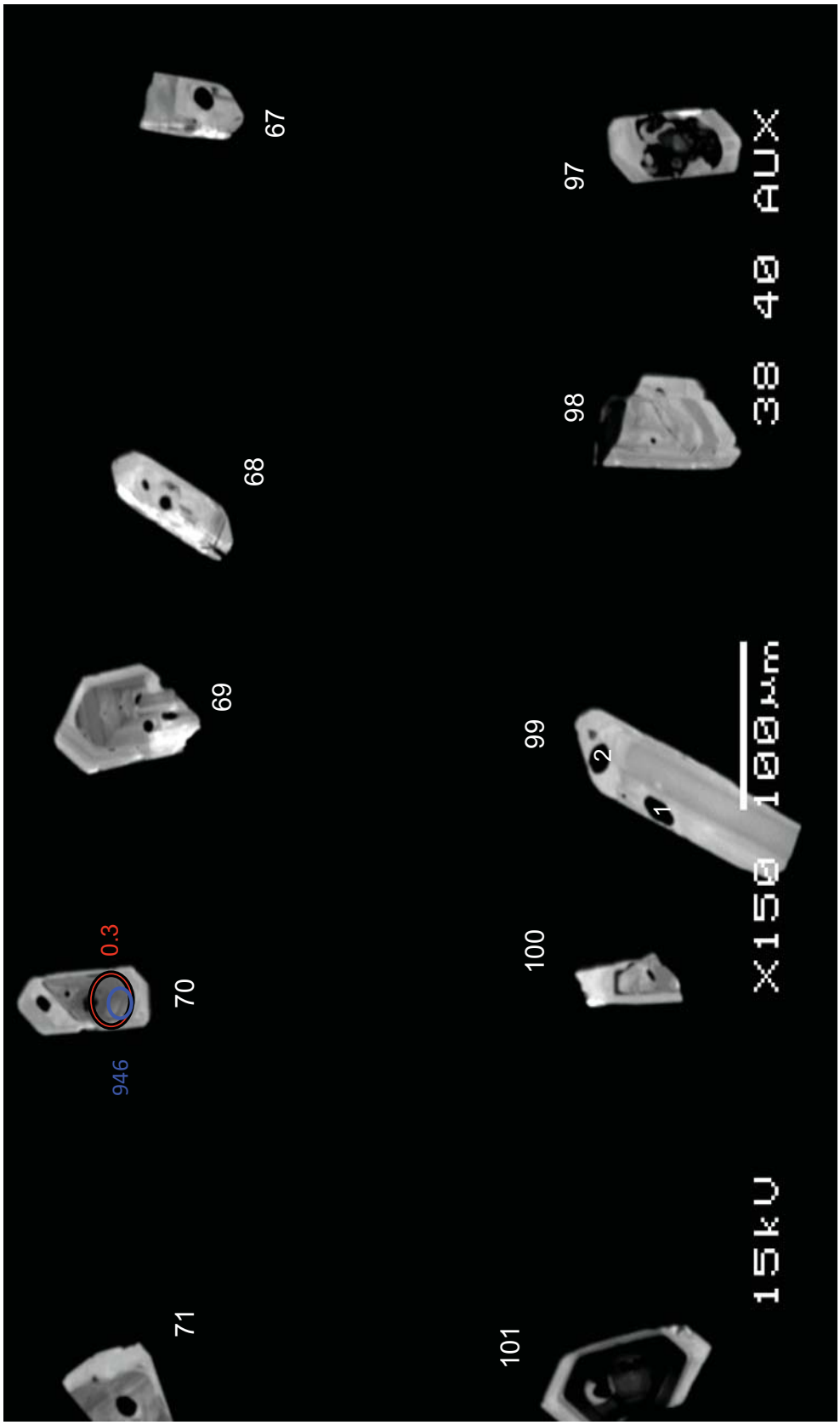
15kU X150 100µm 38 40 AUX
0.3
946
71
70
69
68
67
101
100
99
2
1
98
97
SCR

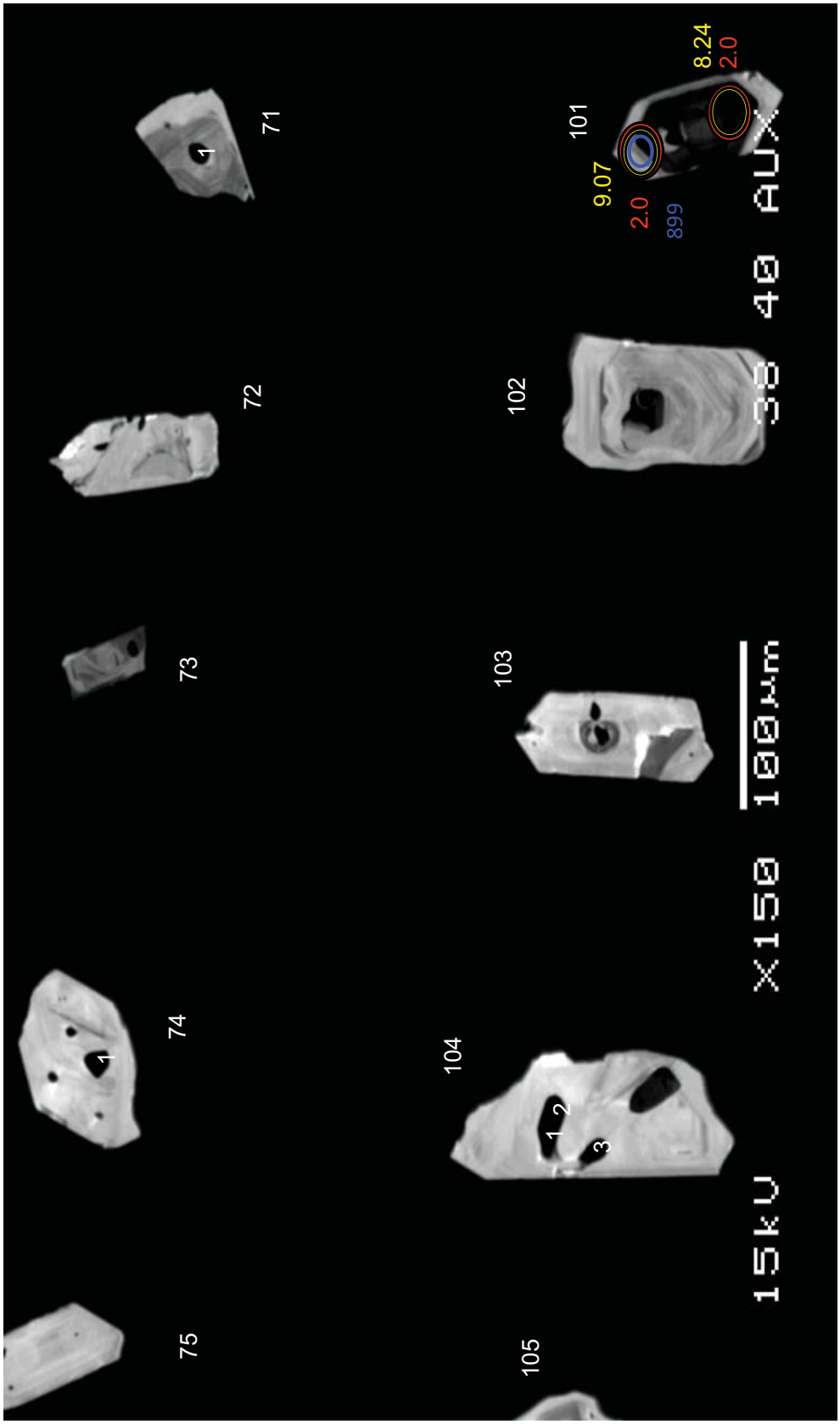
15kU X150 100µm
71
72
73
74
75
101
102
103
104
105
8.24
2.0
9.07
2.0
899
SCR

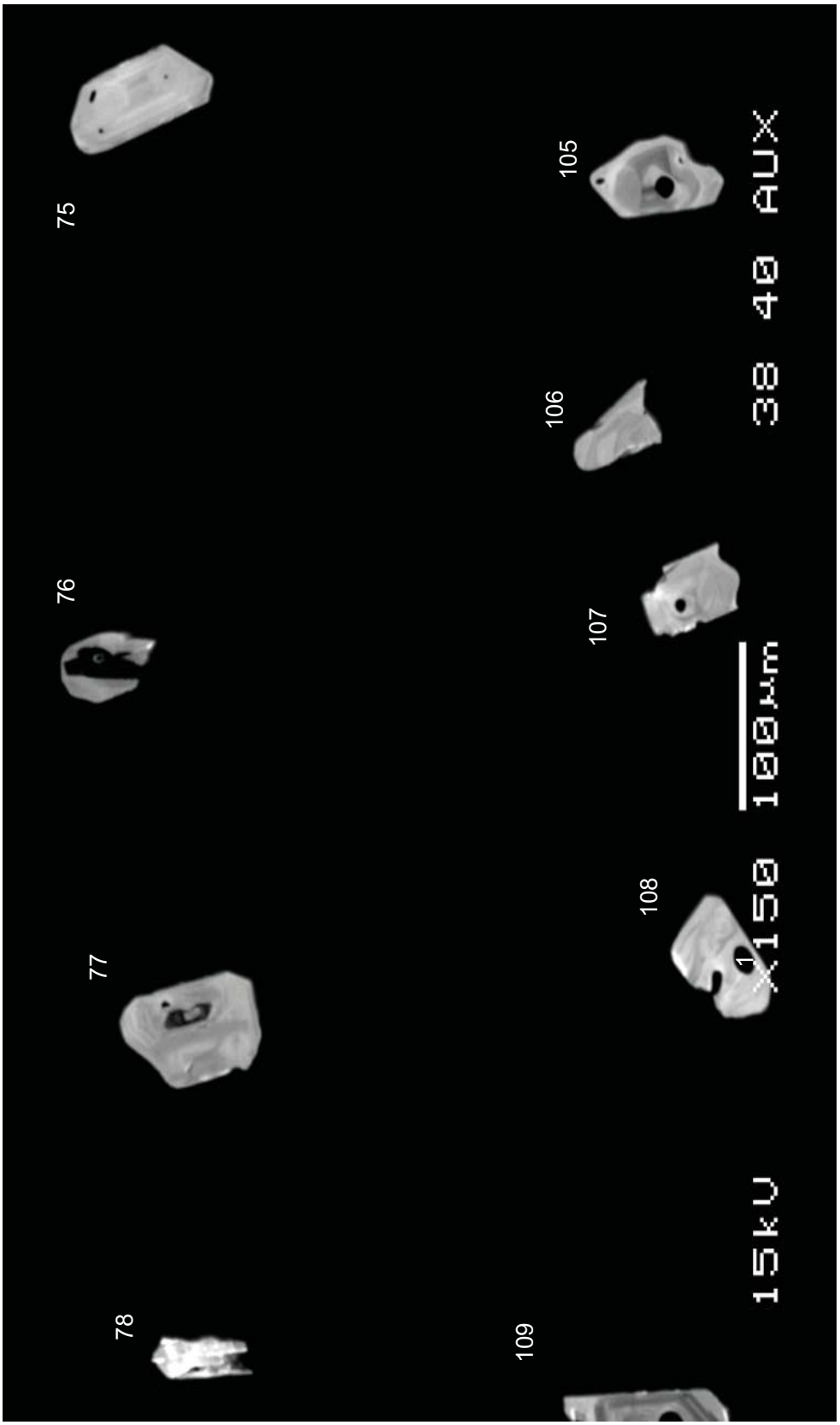

SCR

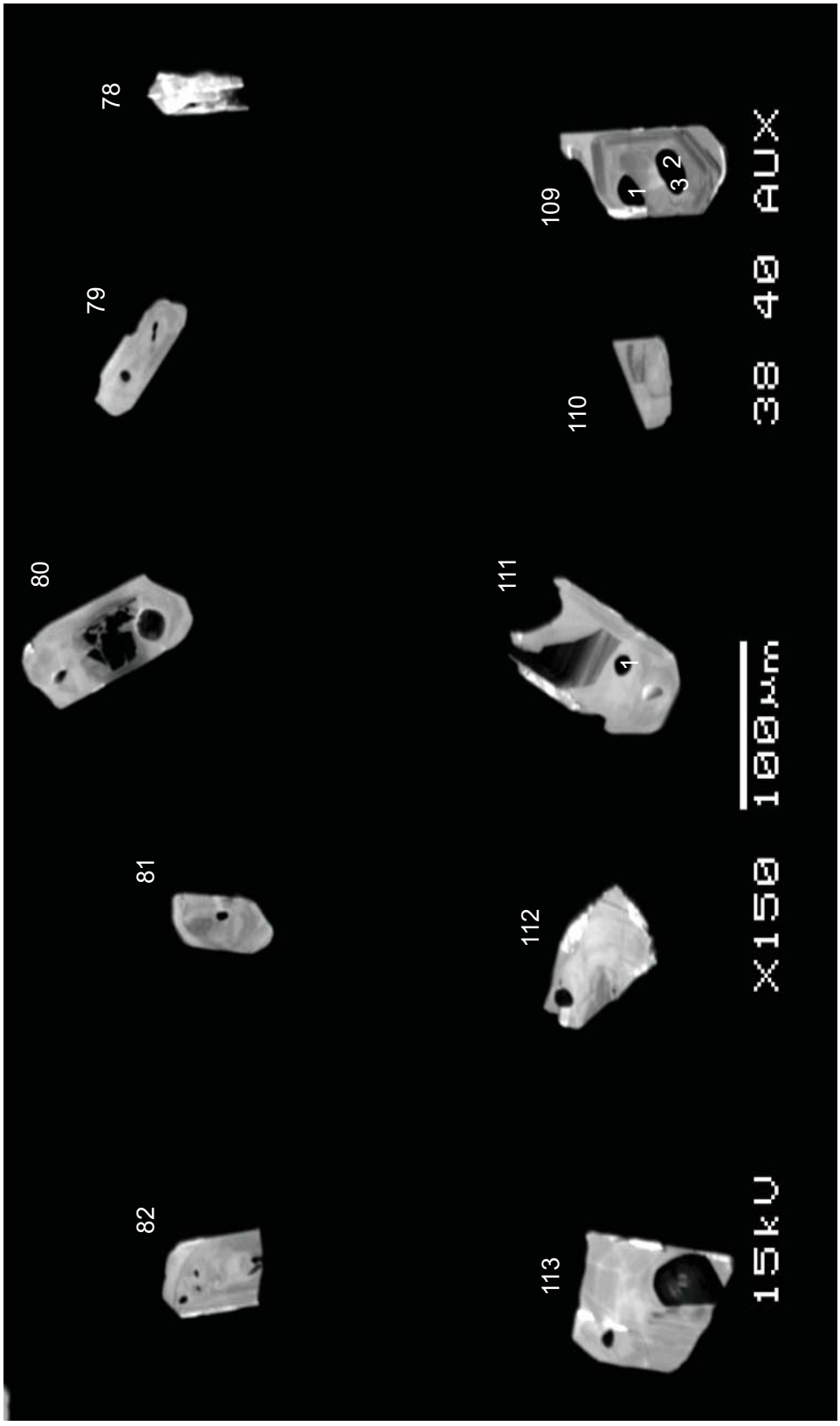

SCR

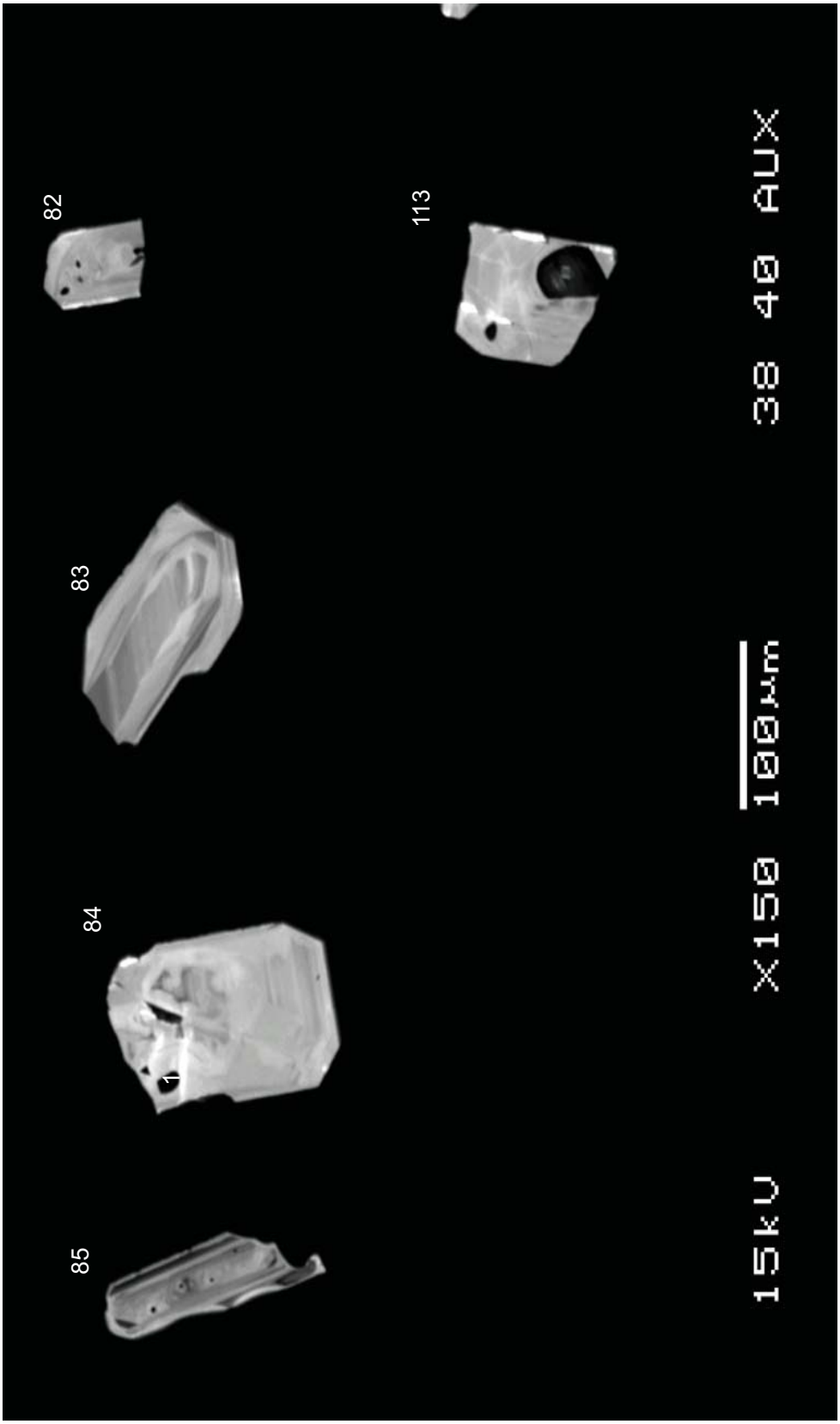

SCR

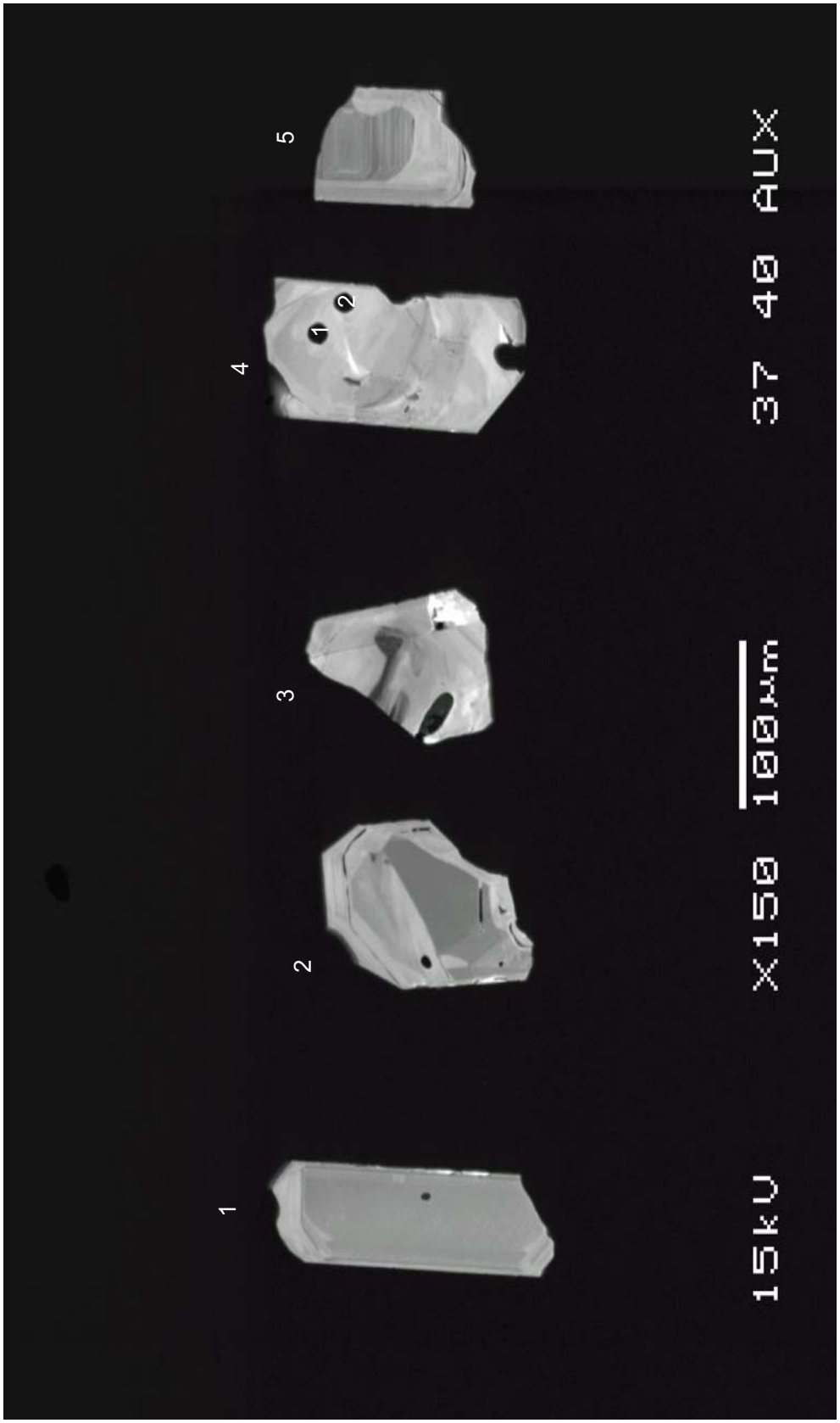

CTR

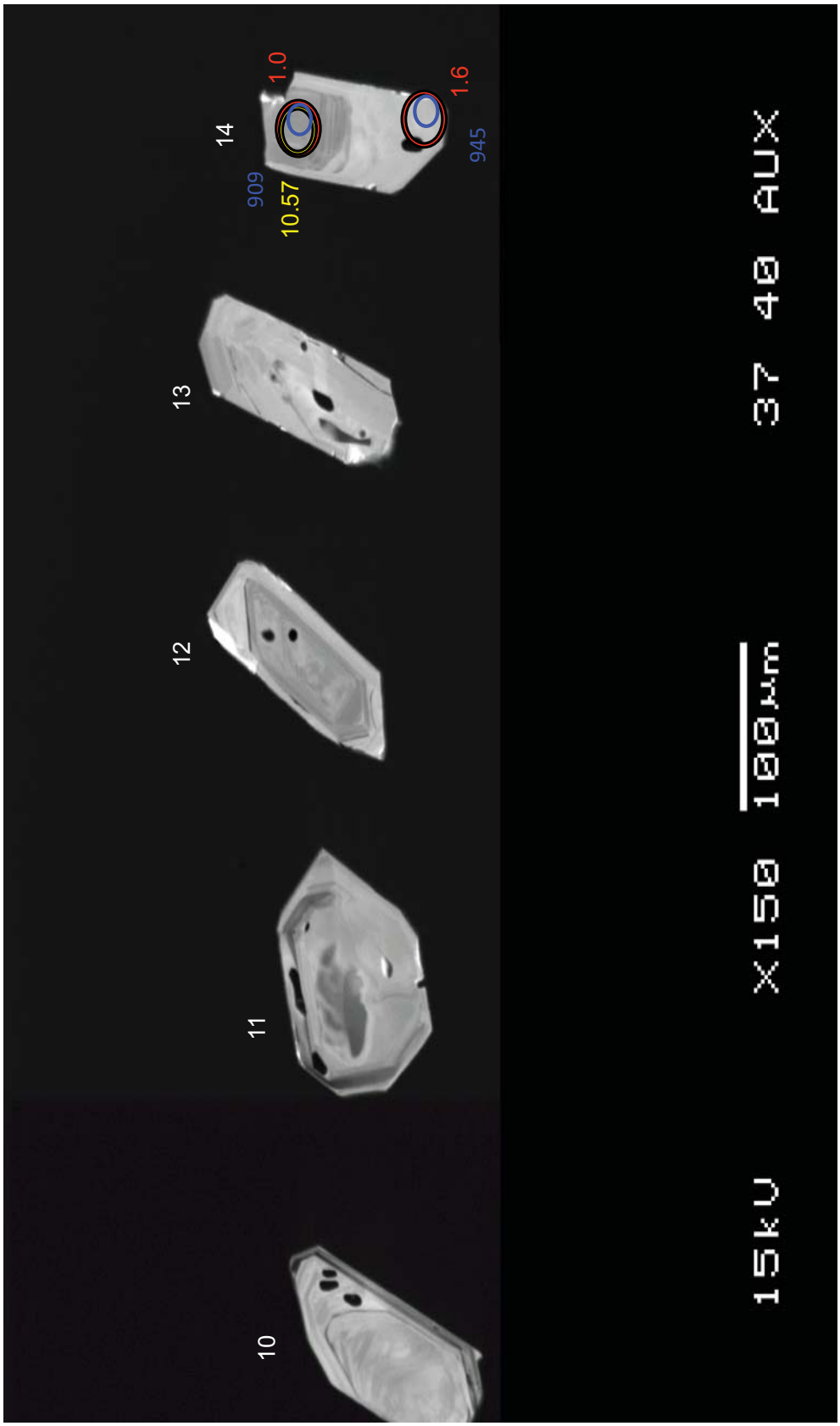

CTR

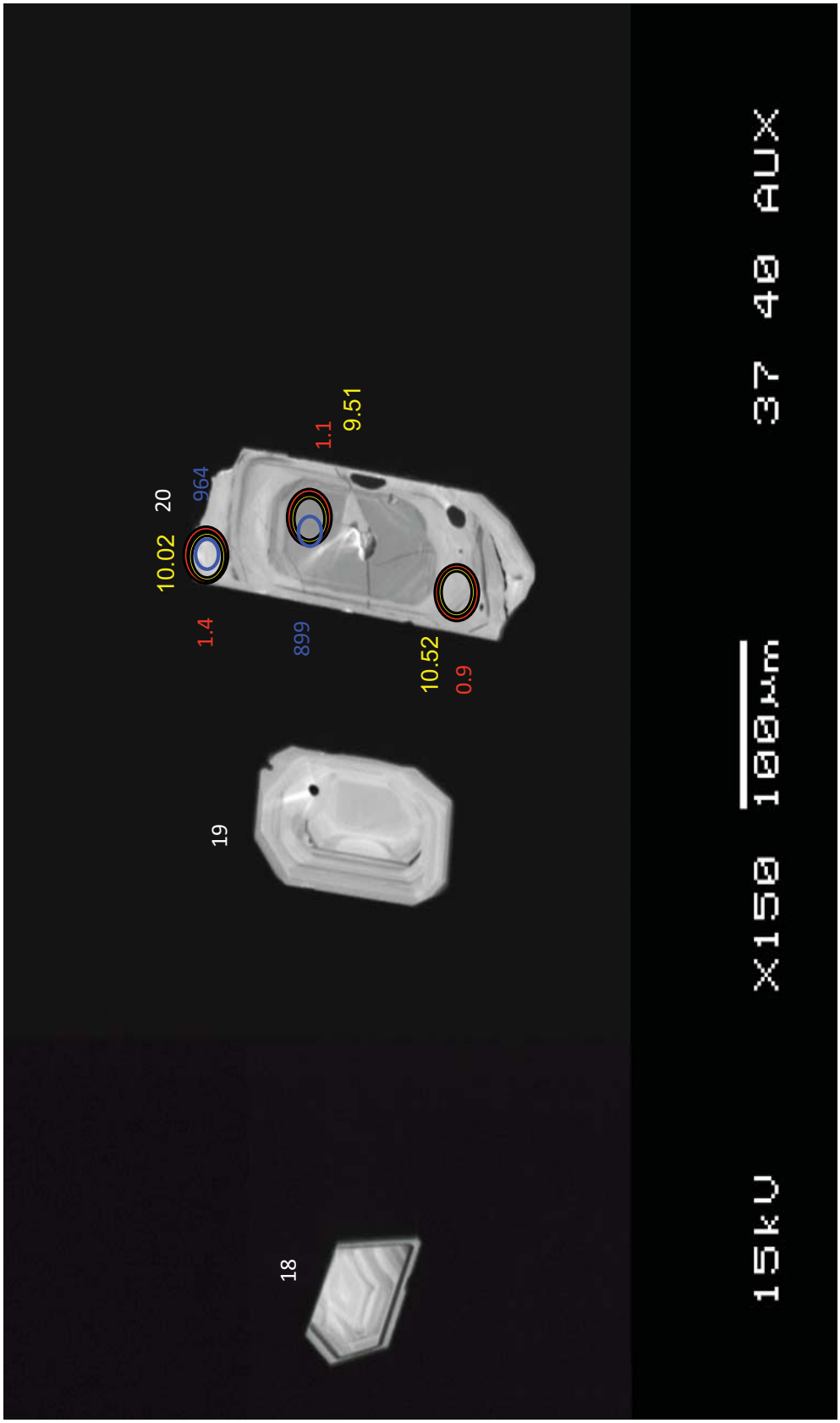

CTR

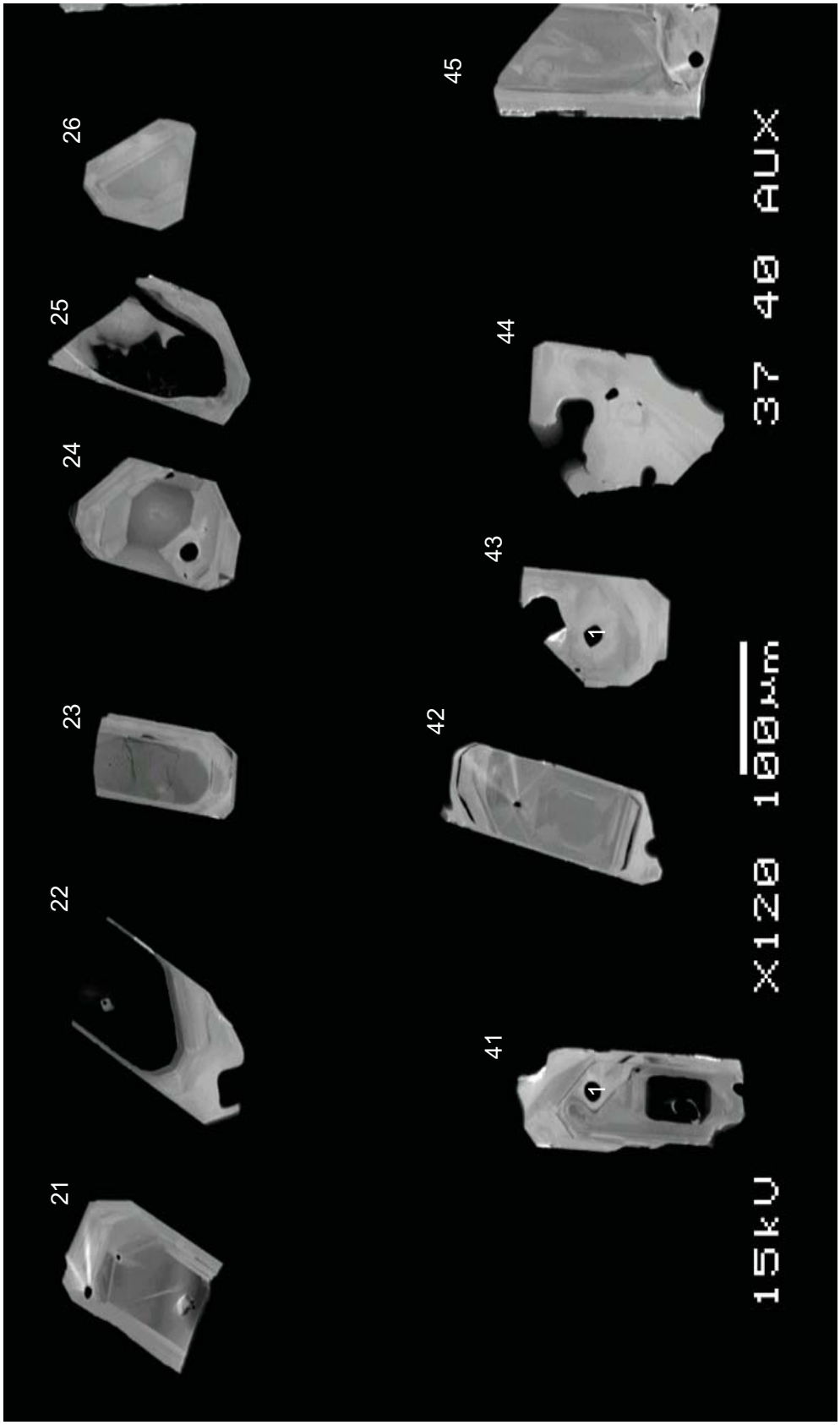

CTR

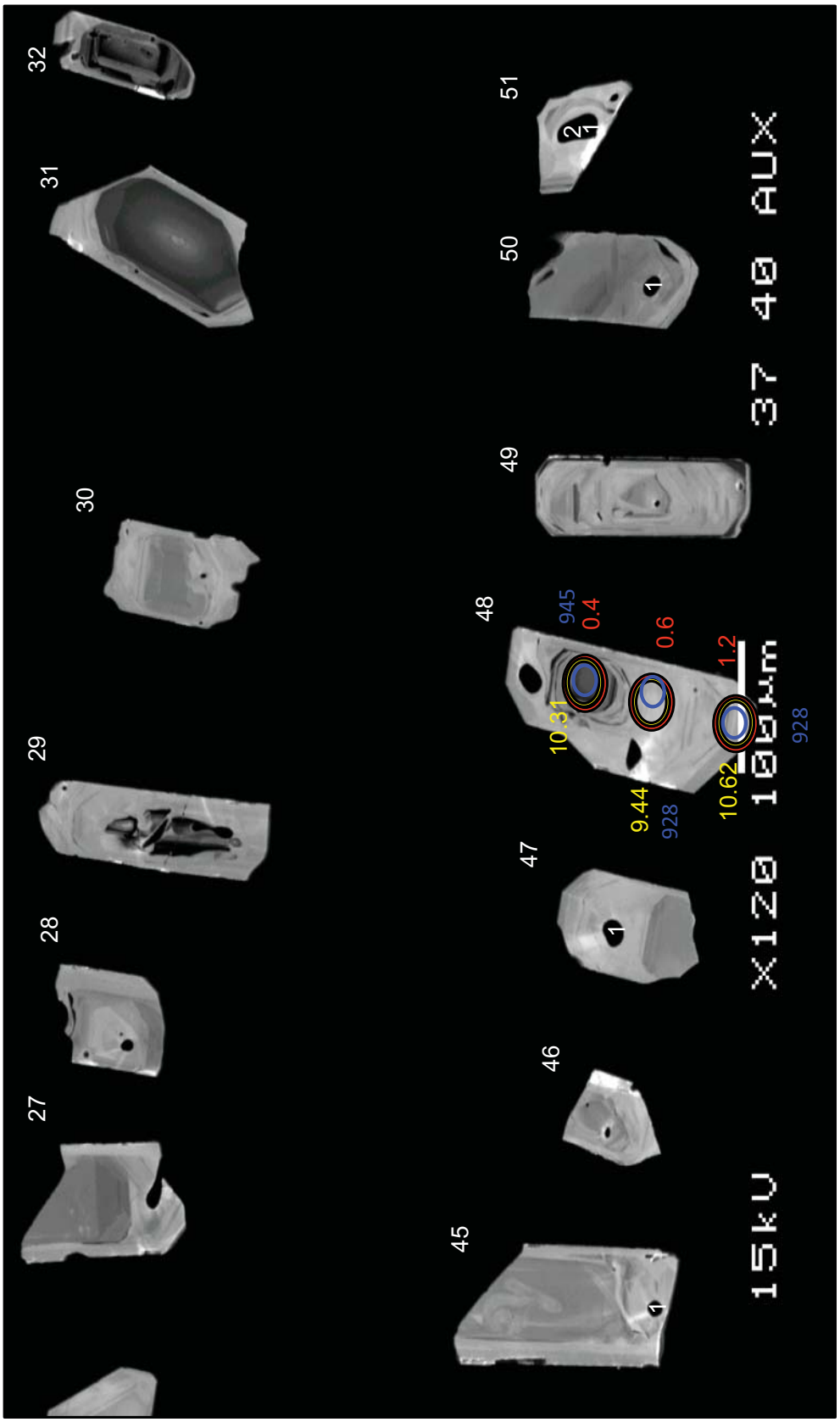
15kU X1120 100um
37 40 AUX
CTR
32
31
30
29
28
27
45
46
47
48
49
50
51
1
2
945
0.4
0.6
1.2
10.31
9.44
10.62
928
928

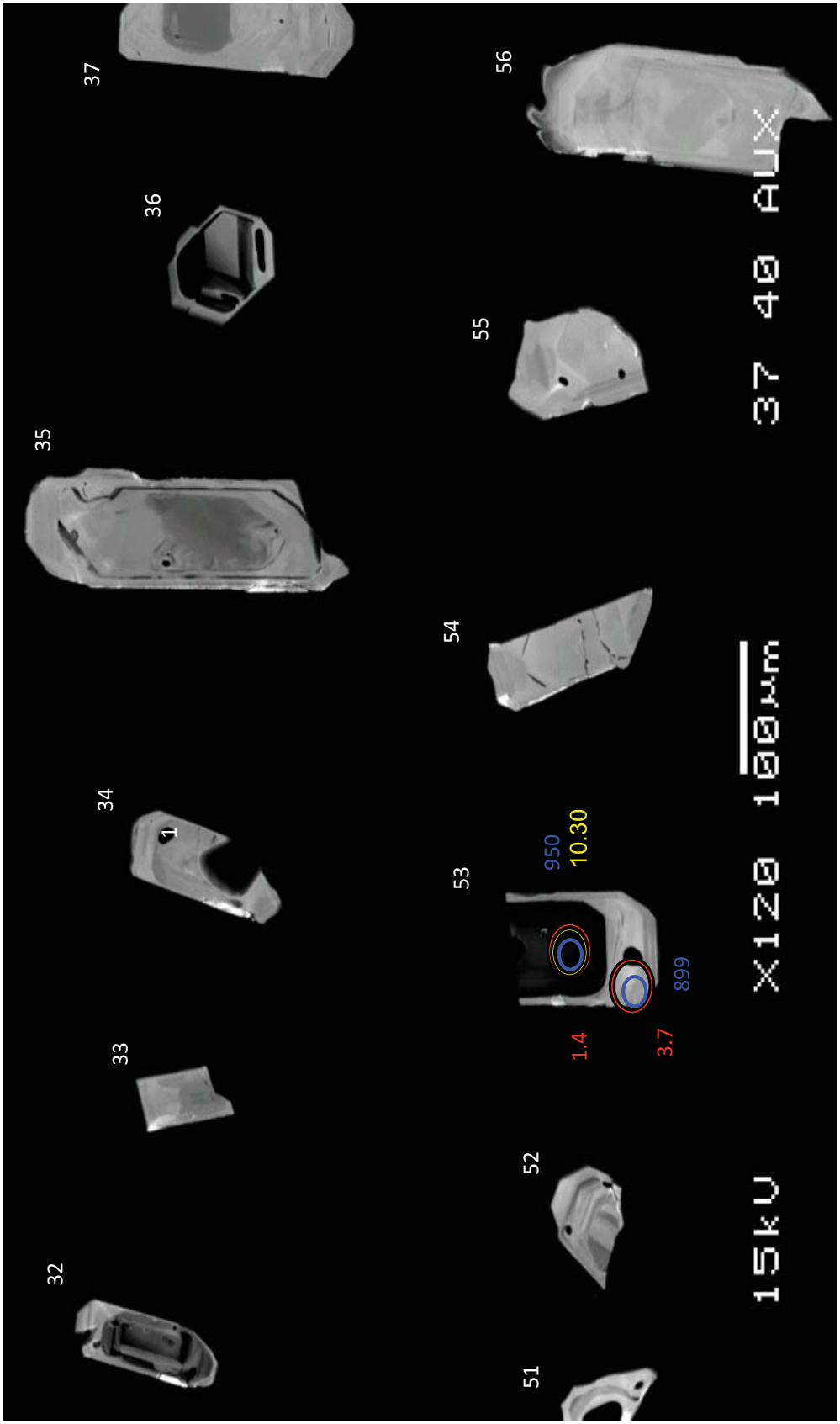
15kV X1120 100µm 37 40 AUX
32
51
33
52
34
1
53
950
10.30
1.4
3.7
899
54
35
55
36
56
37

CTR

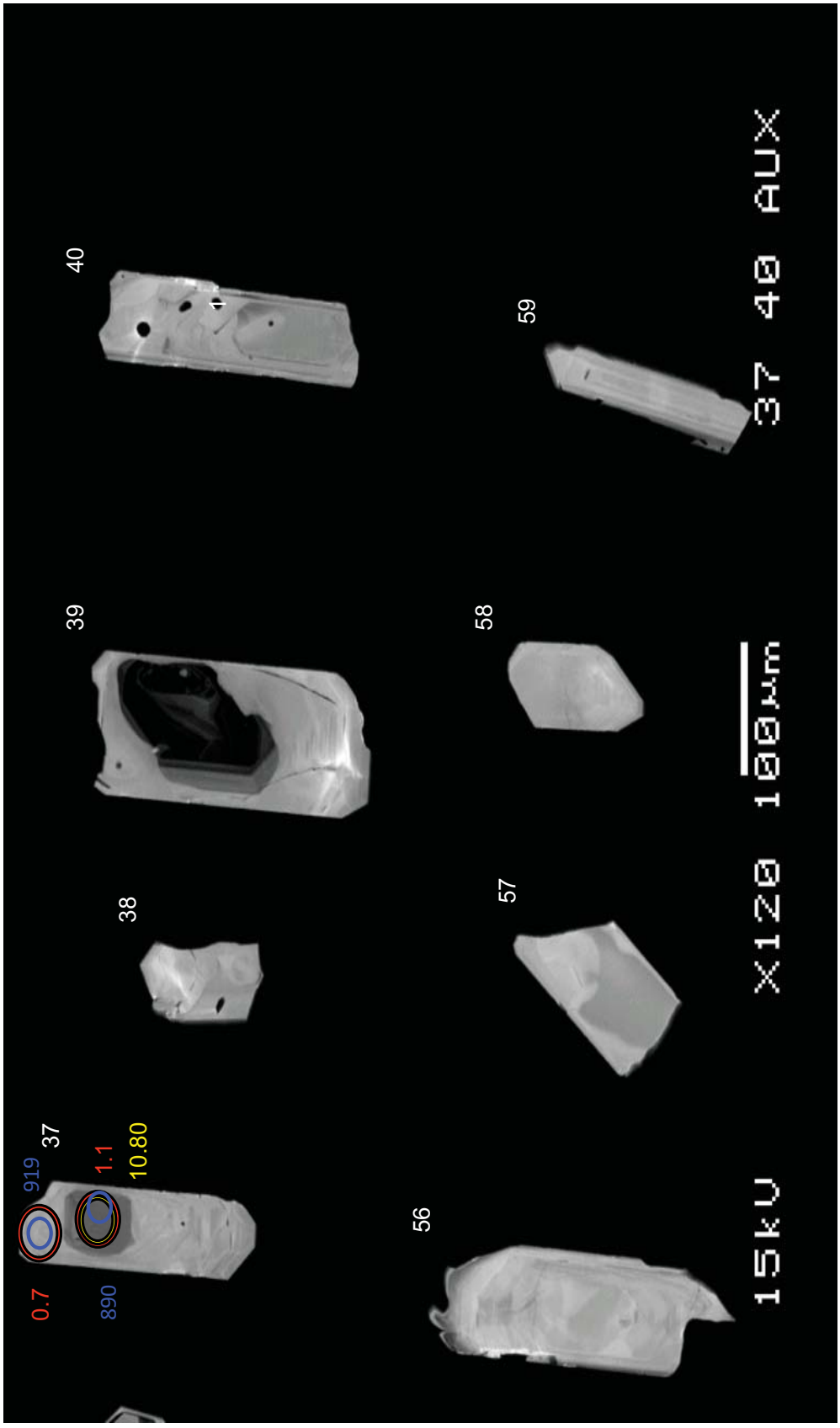
15kV X120 100µm 37 40 AUX
37
38
39
40
56
57
58
59
0.7
890
919
1.1
10.80

CTR

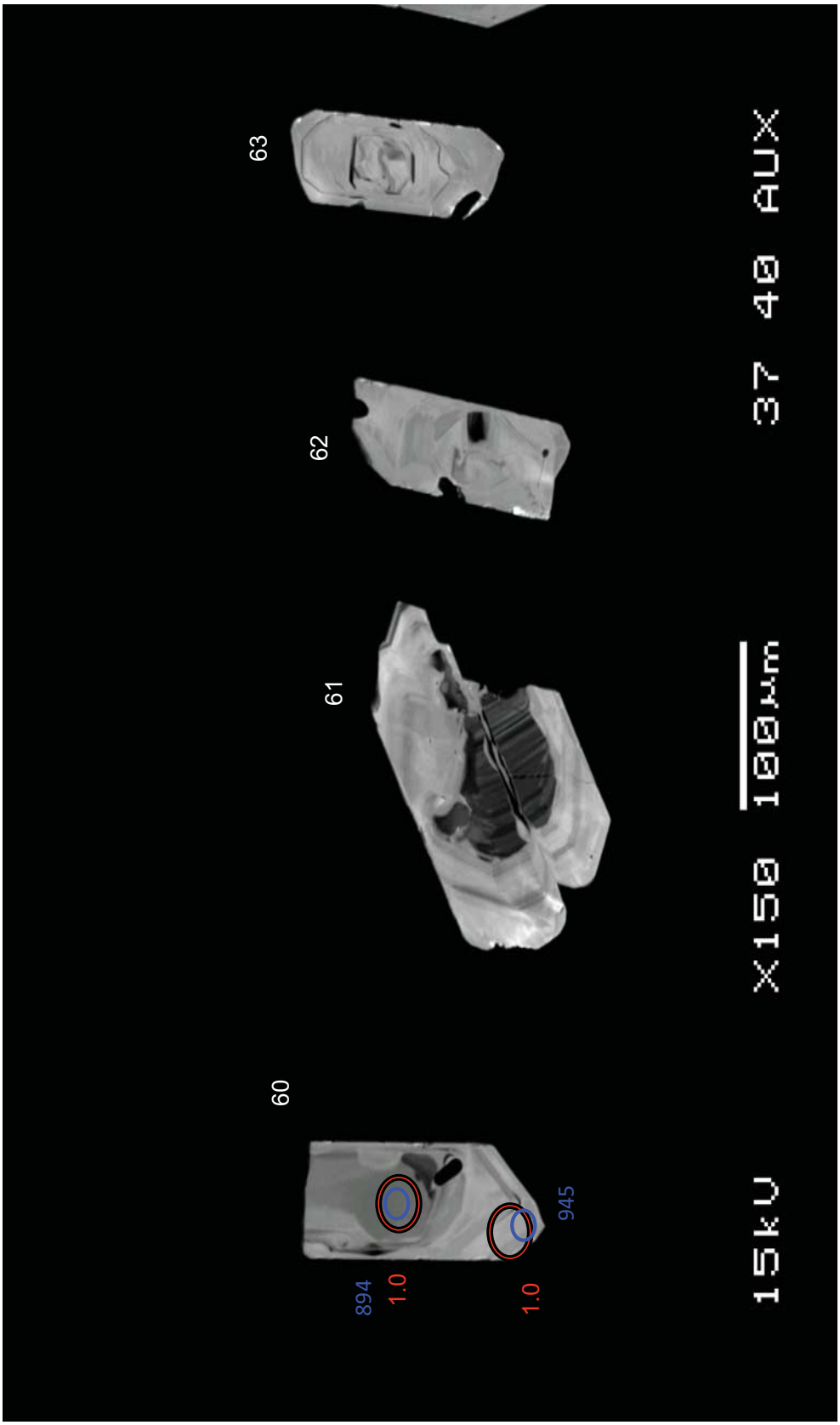

CTR

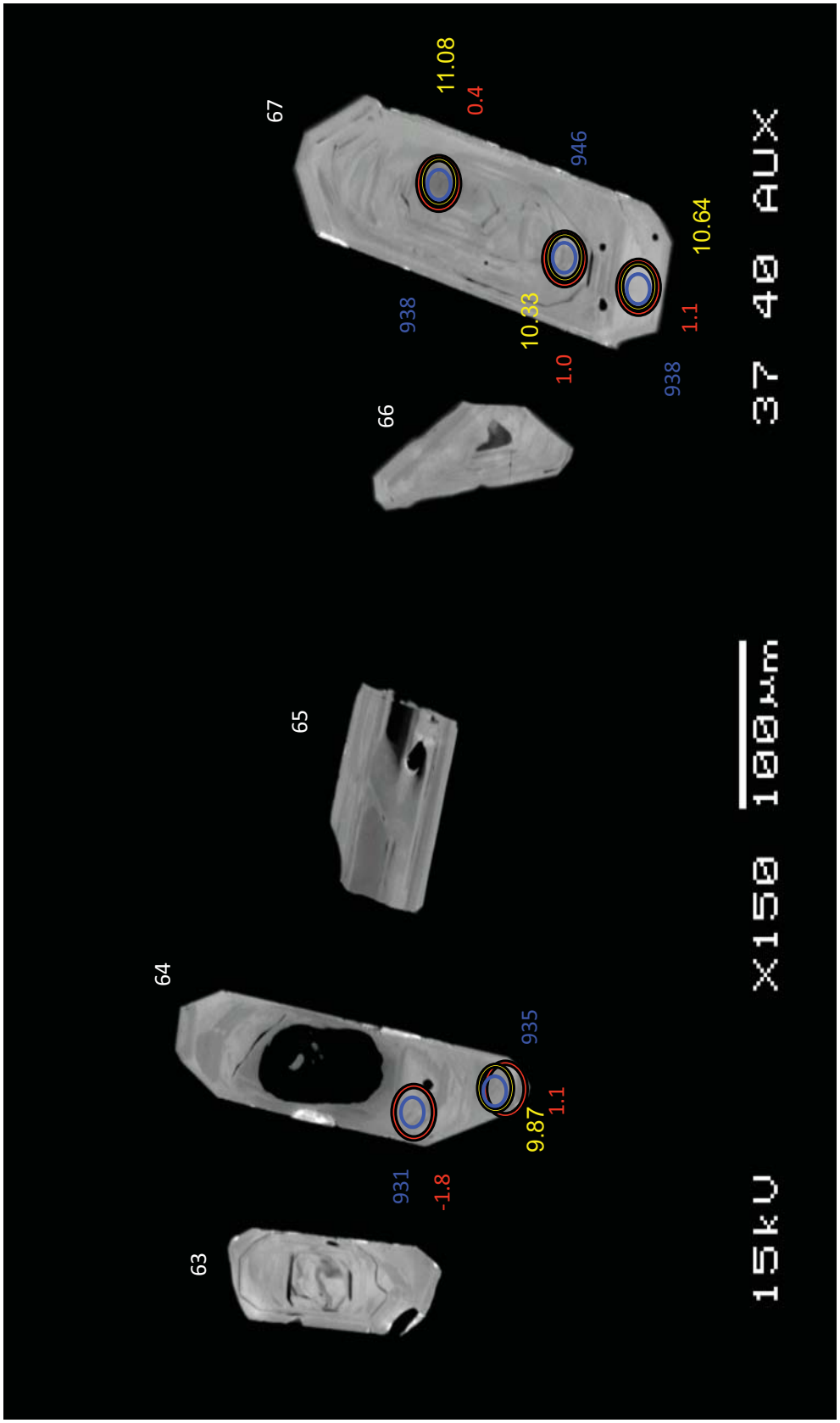
15kV X150 100µm 37 40 AUX
63
64
65
66
67
931
-1.8
935
9.87
1.1
938
10.33
1.0
946
11.08
0.4
938
1.1
10.64

CTR

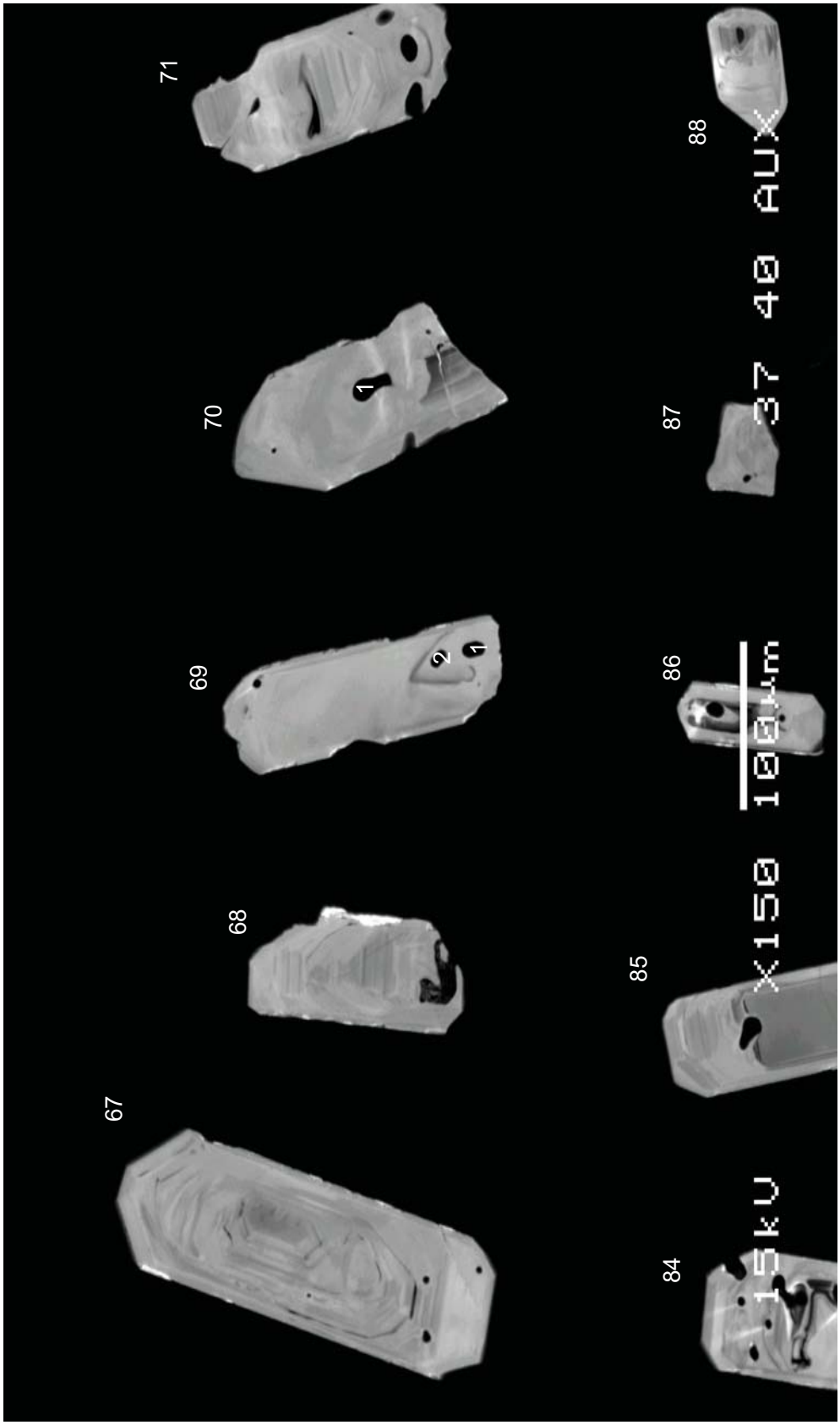

CTR

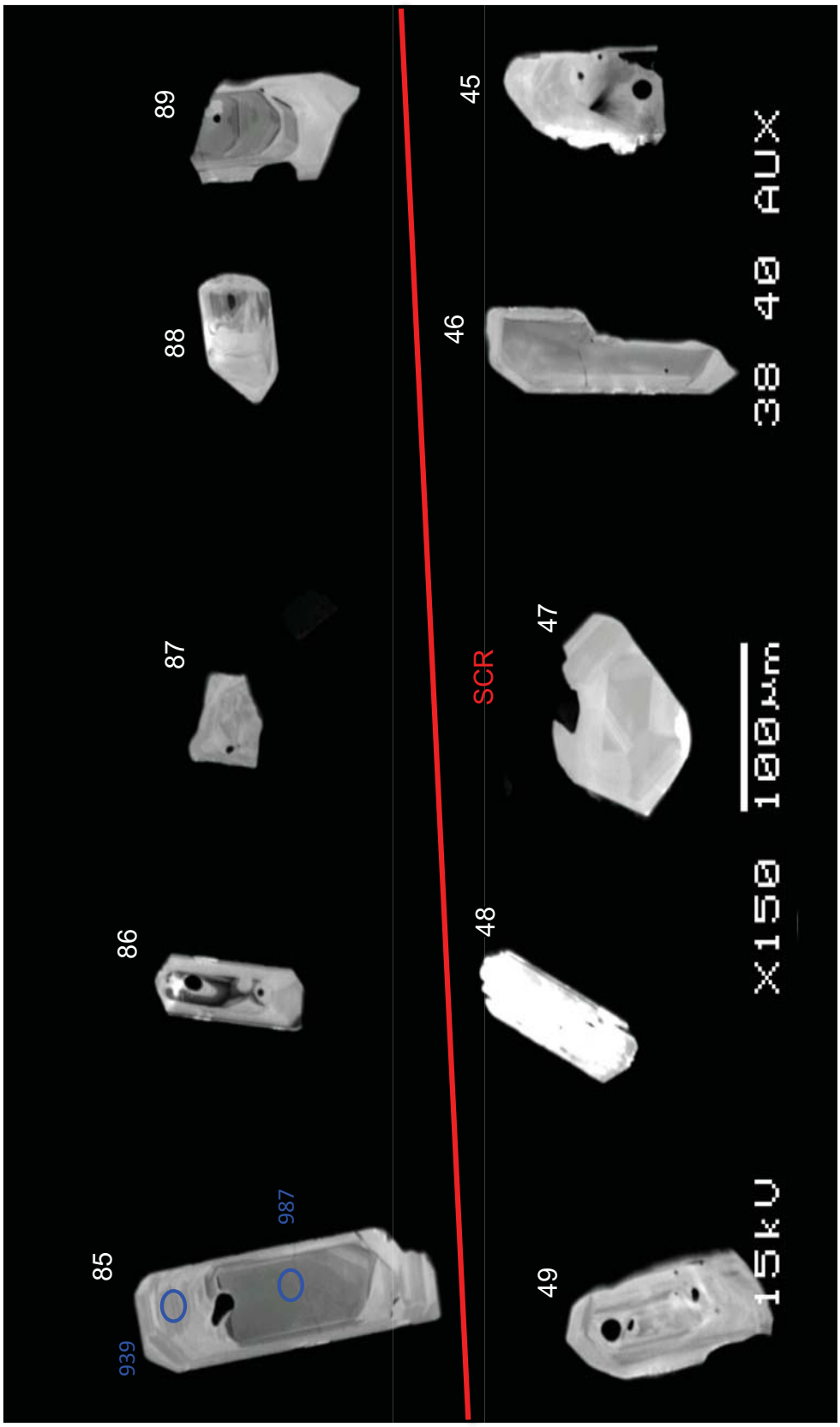

CTR

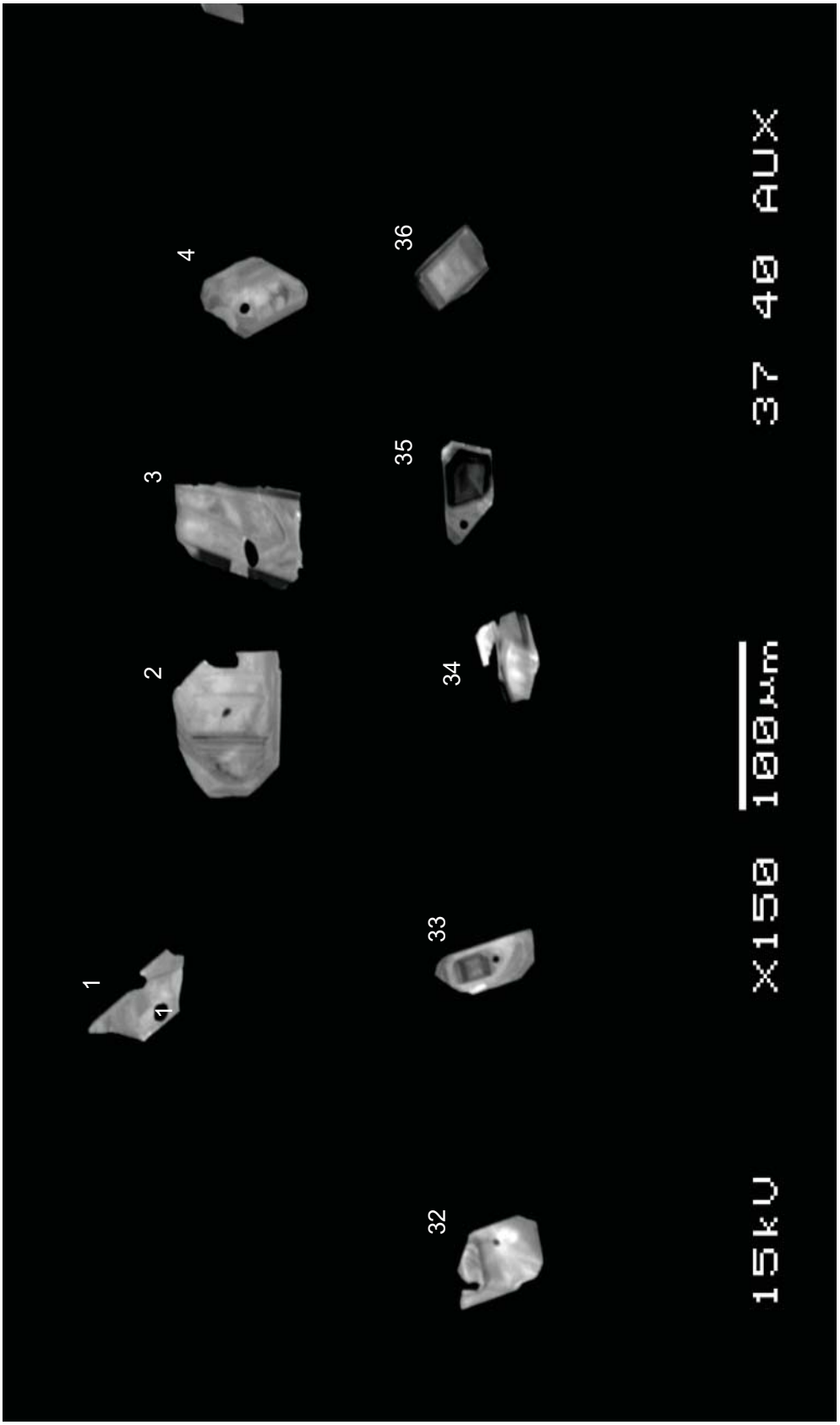
15kU X150 100µm 37 40 AUX
BJR
1
1
2
3
4
32
33
34
35
36

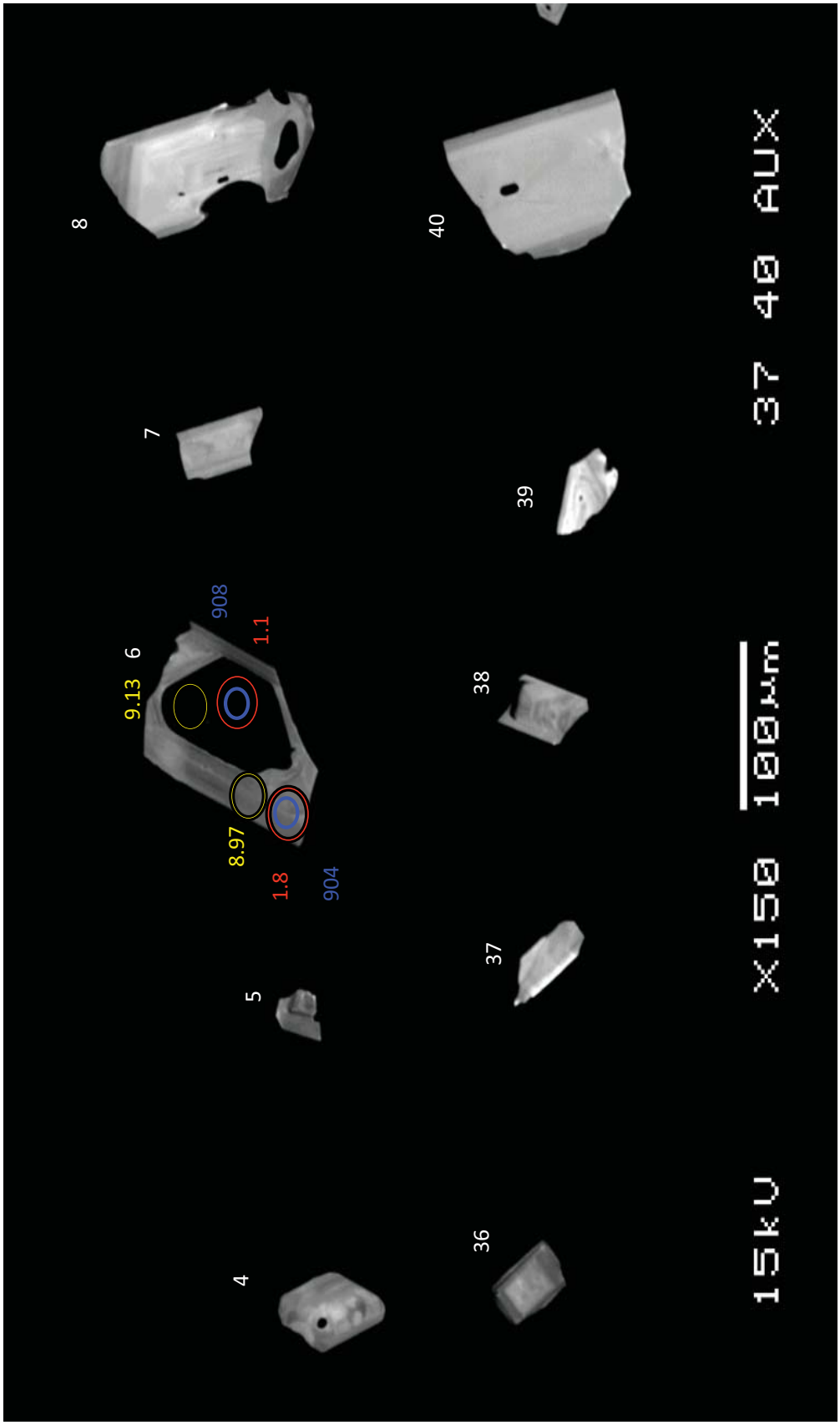
15kV X150 100µm 37 40 AUX
BJR
4
5
6
7
8
9.13
8.97
1.8
1.1
908
904
36
37
38
39
40

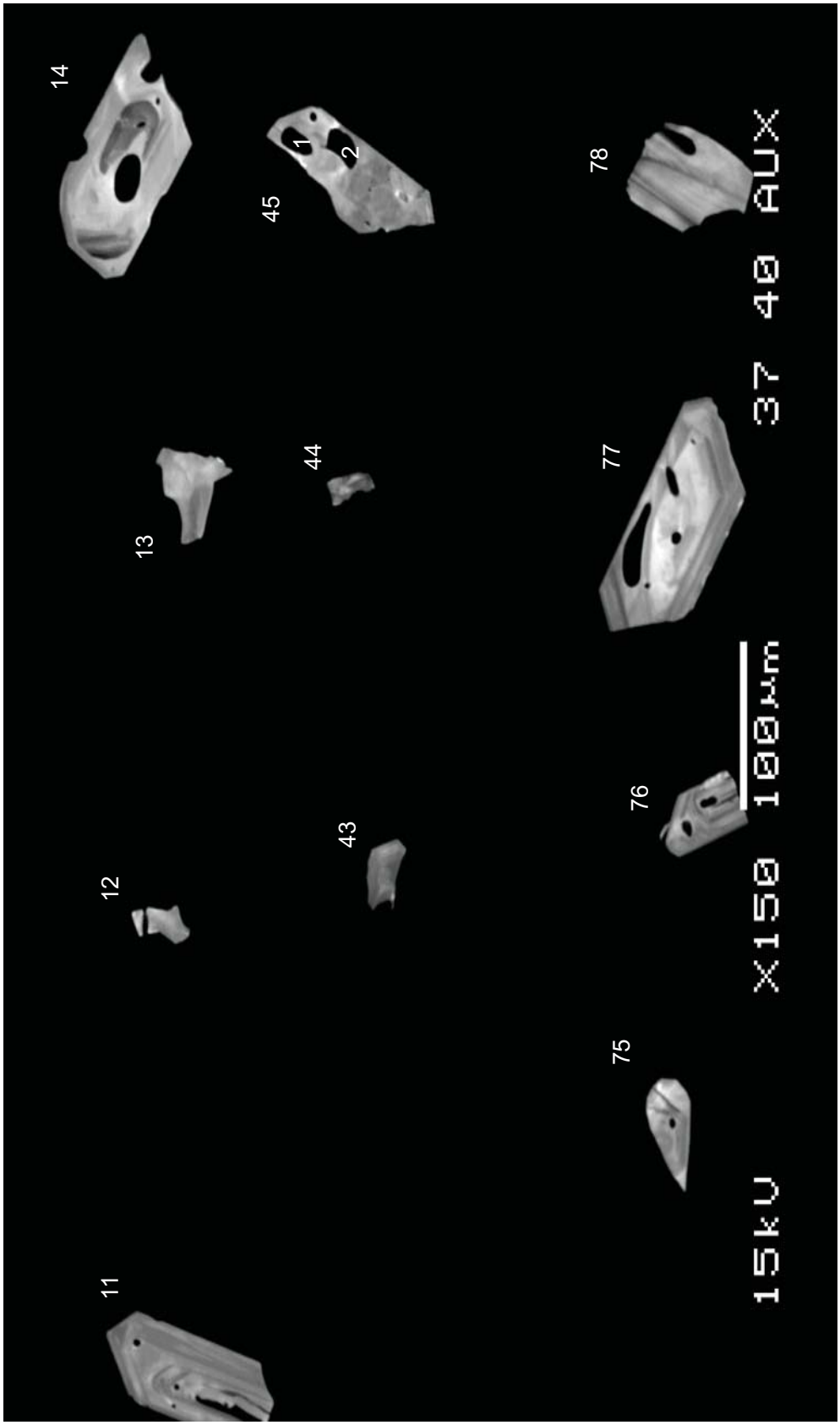
14
45
1
2
78
13
44
77
12
43
76
75
11
15kU X150 100µm 37 40 AUX
BJR

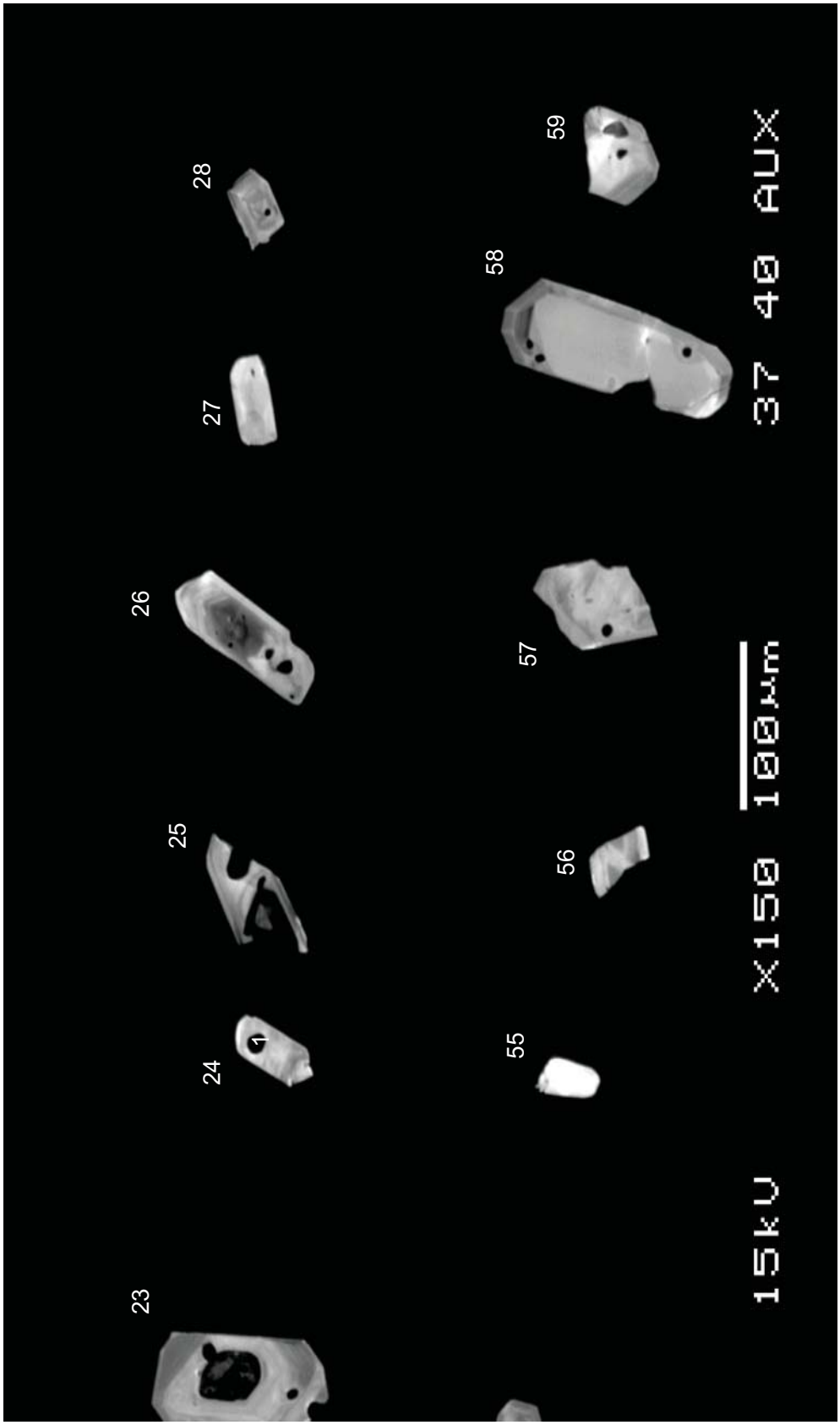
23
24
25
26
27
28
55
56
57
58
59
15kU X150 100µm 37 40 AUX
BJR

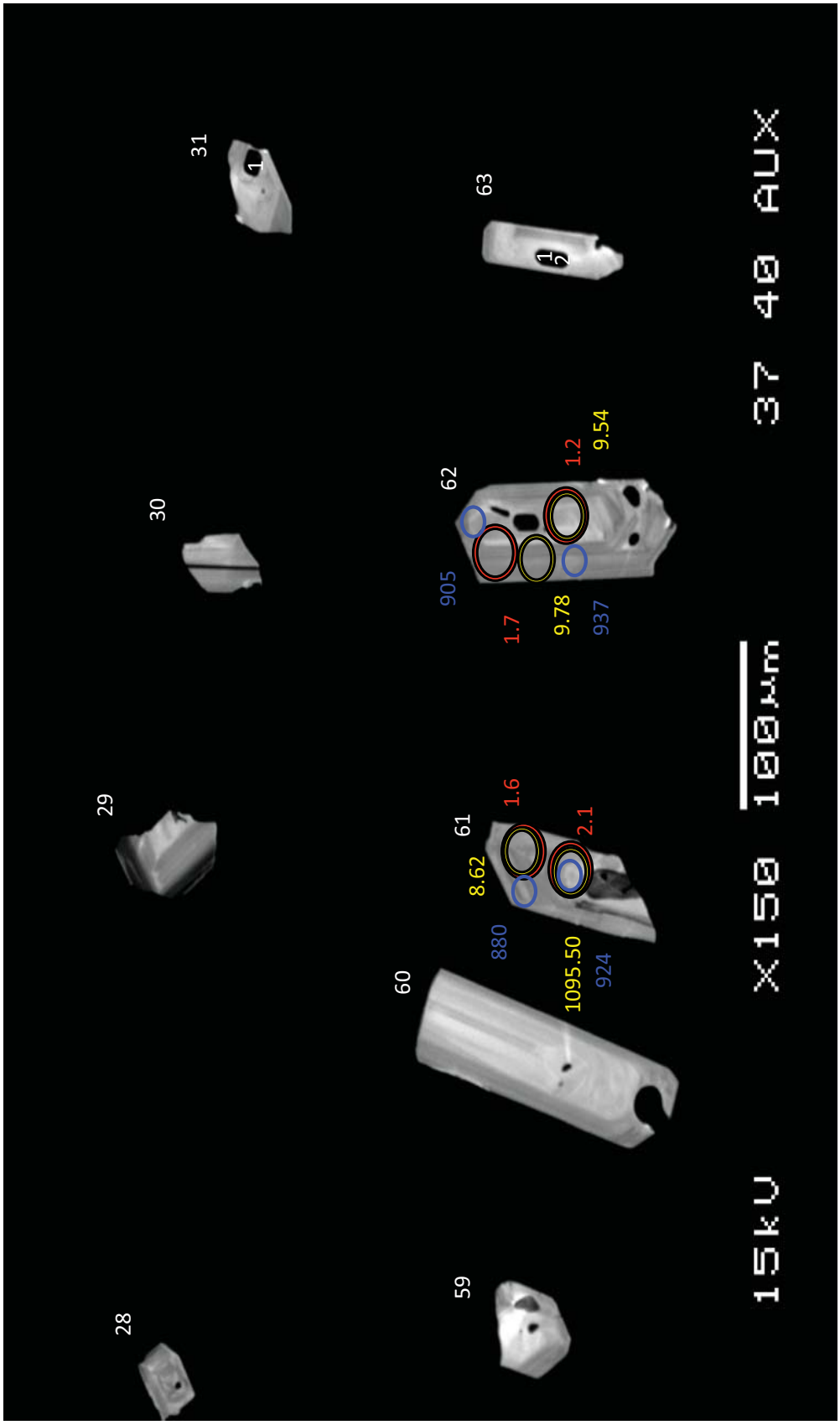
15kV X150 100µm 37 40 AUX
28
59
60
29
61
8.62
1.6
2.1
880
1095.50
924
30
62
905
1.7
9.78
1.2
9.54
937
31
1
63
1
2

BJR

BJR-61

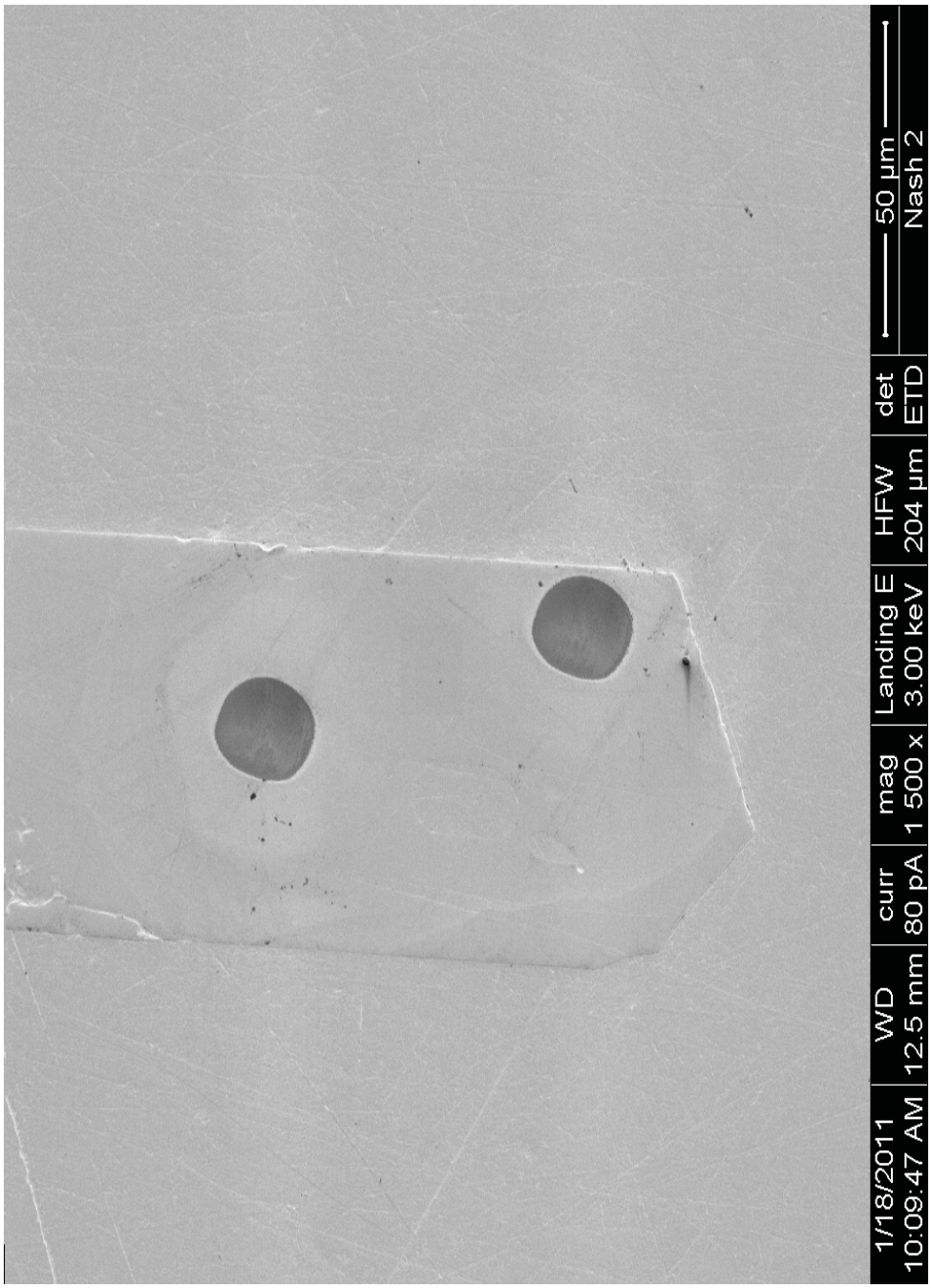
1/18/2011
10:09:47 AM
WD
12.5 mm
curr
80 pA
mag
1 500 x
Landing E
3.00 keV
HFW
204 µm
det
ETD
50 µm
Nash 2

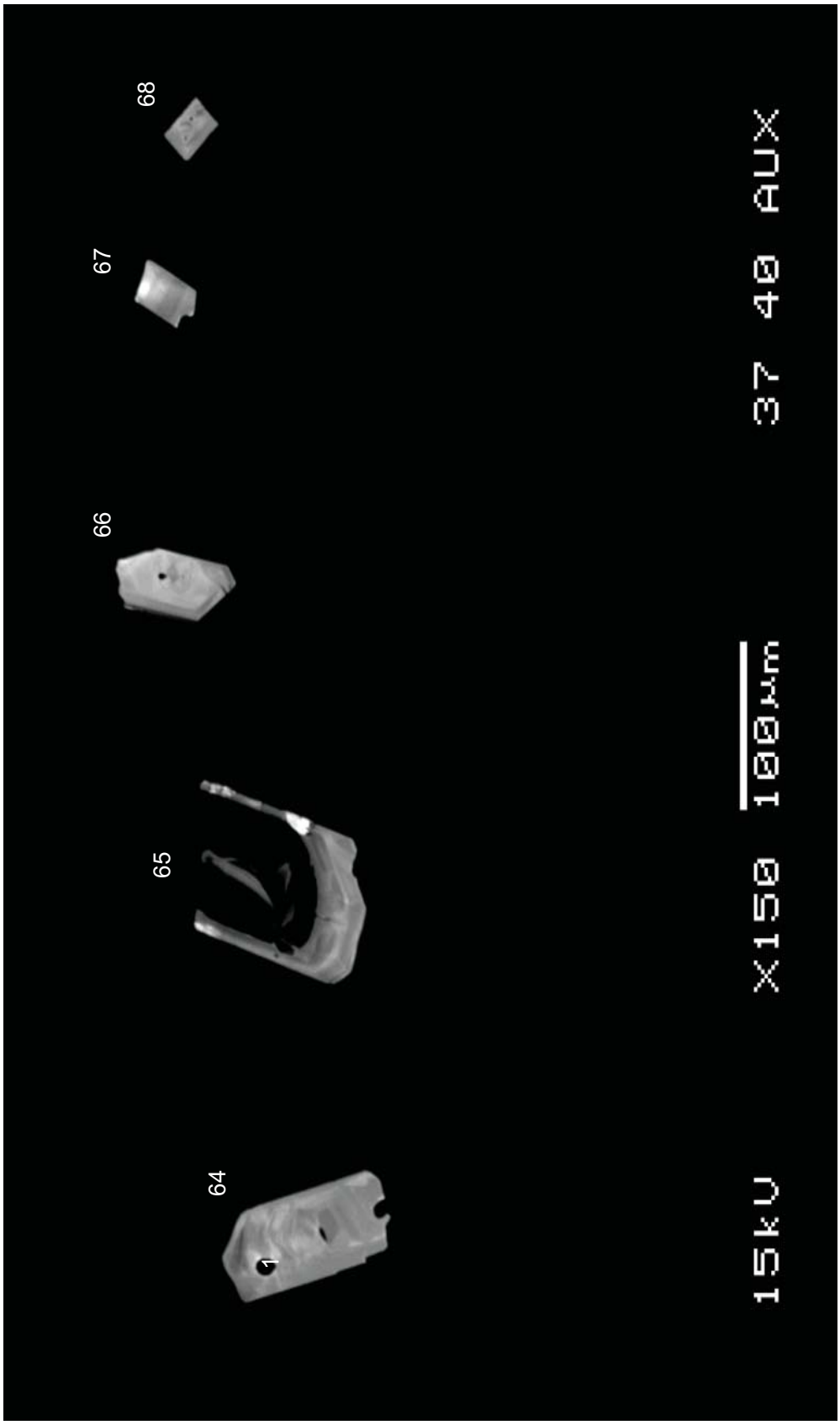
68
67
66
65
64
1
15kU X150 100µm 37 40 AUX
BJR

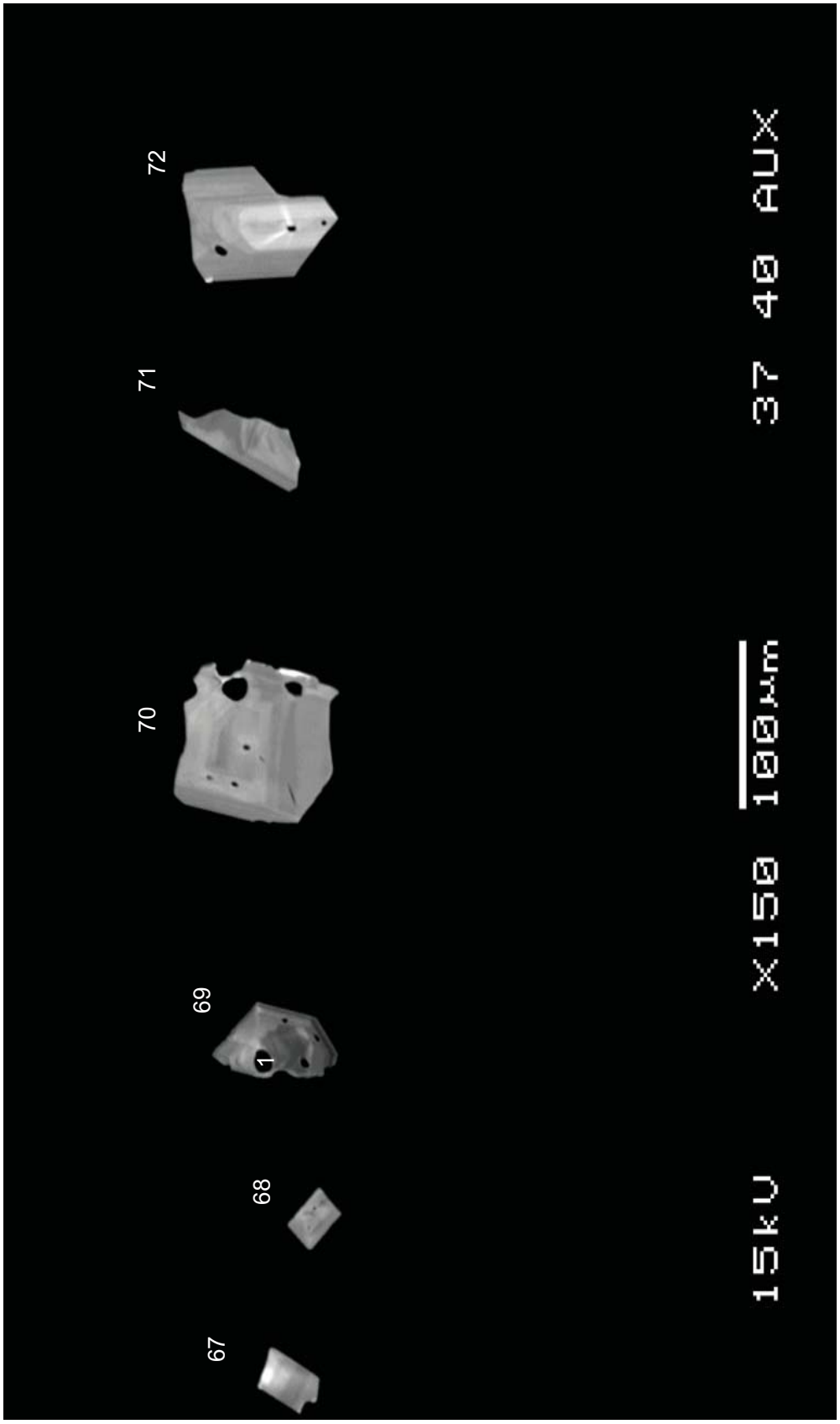
72
71
70
69
1
68
67
15kV X150 100µm 37 40 AUX
BJR

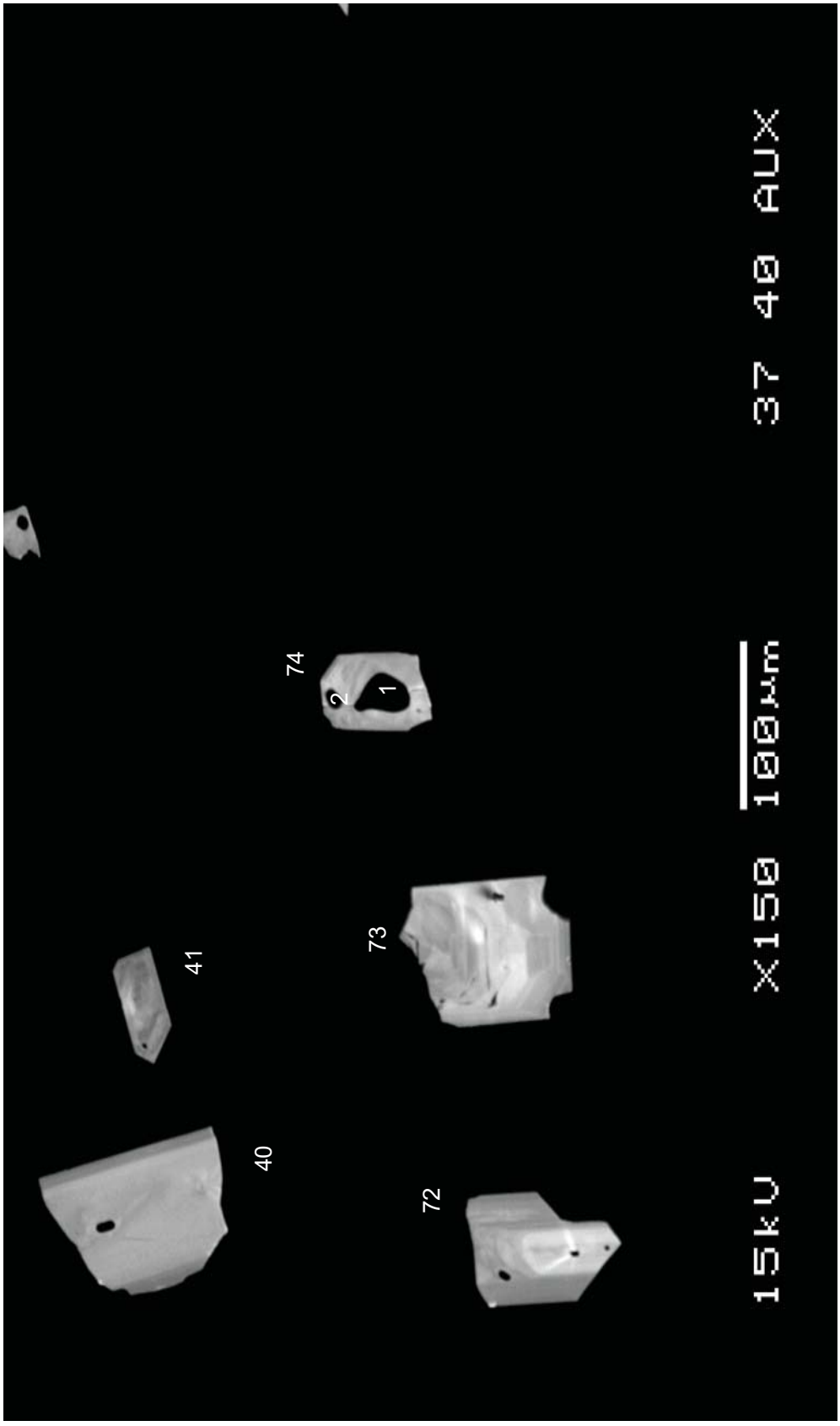
15kU X150 100µm 37 40 AUX
BJR
74
2
1
41
73
40
72

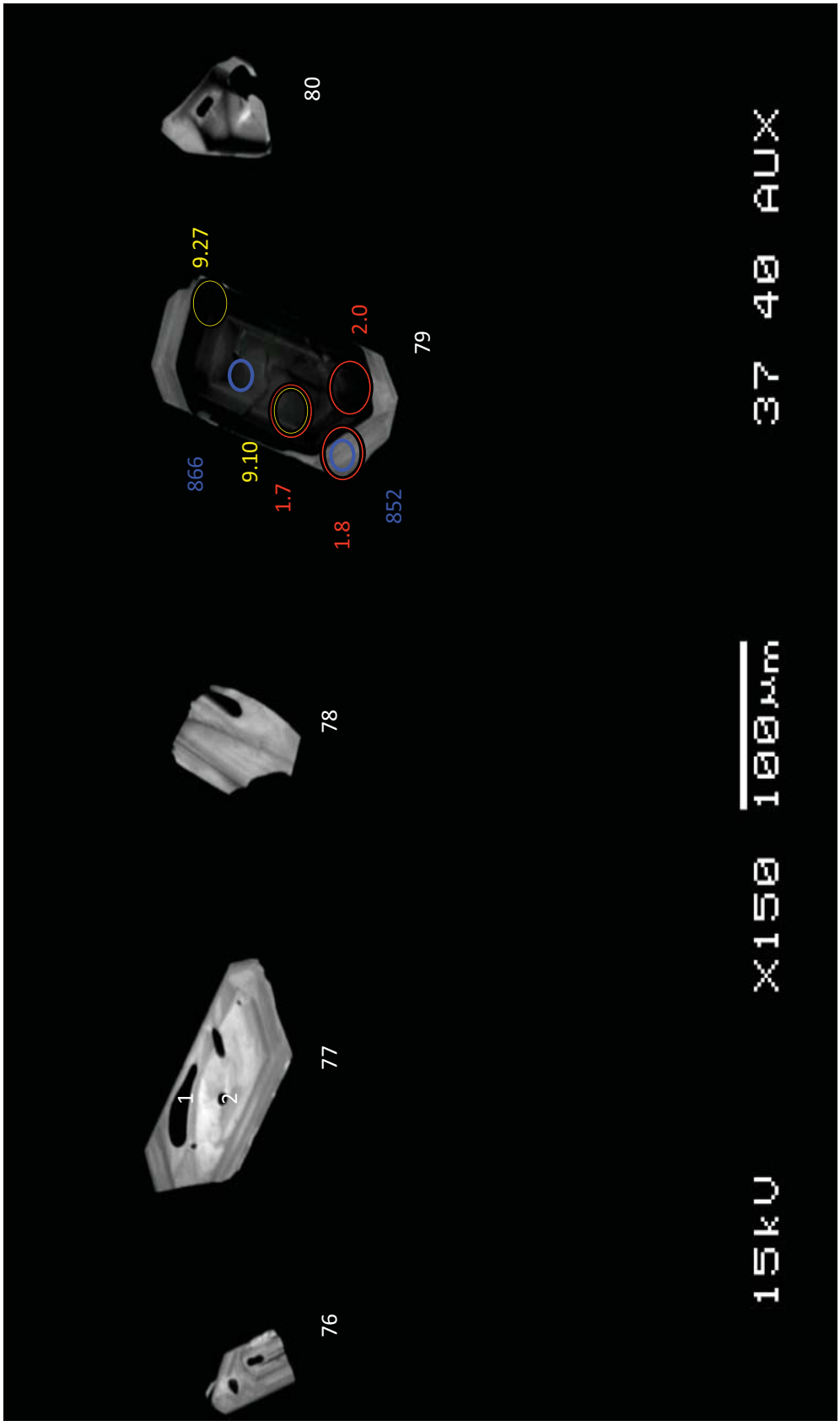
15kU X150 100µm 37 40 AUX
BJR
76
77
78
79
80
1
2
866
9.10
1.7
1.8
852
9.27
2.0

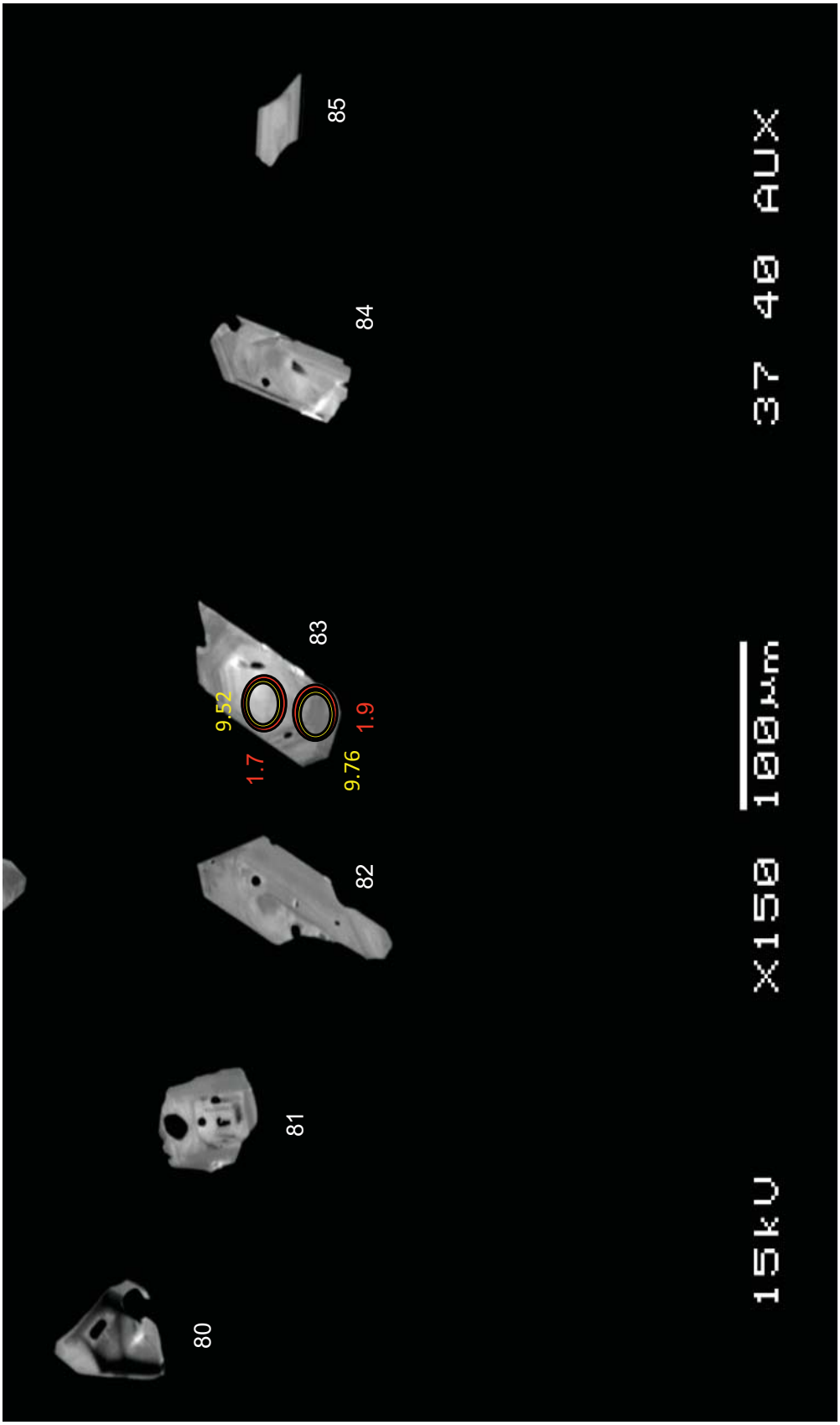
80
81
82
83
84
85
9.52
1.7
9.76
1.9
15kU X150 100µm 37 40 AUX
BJR

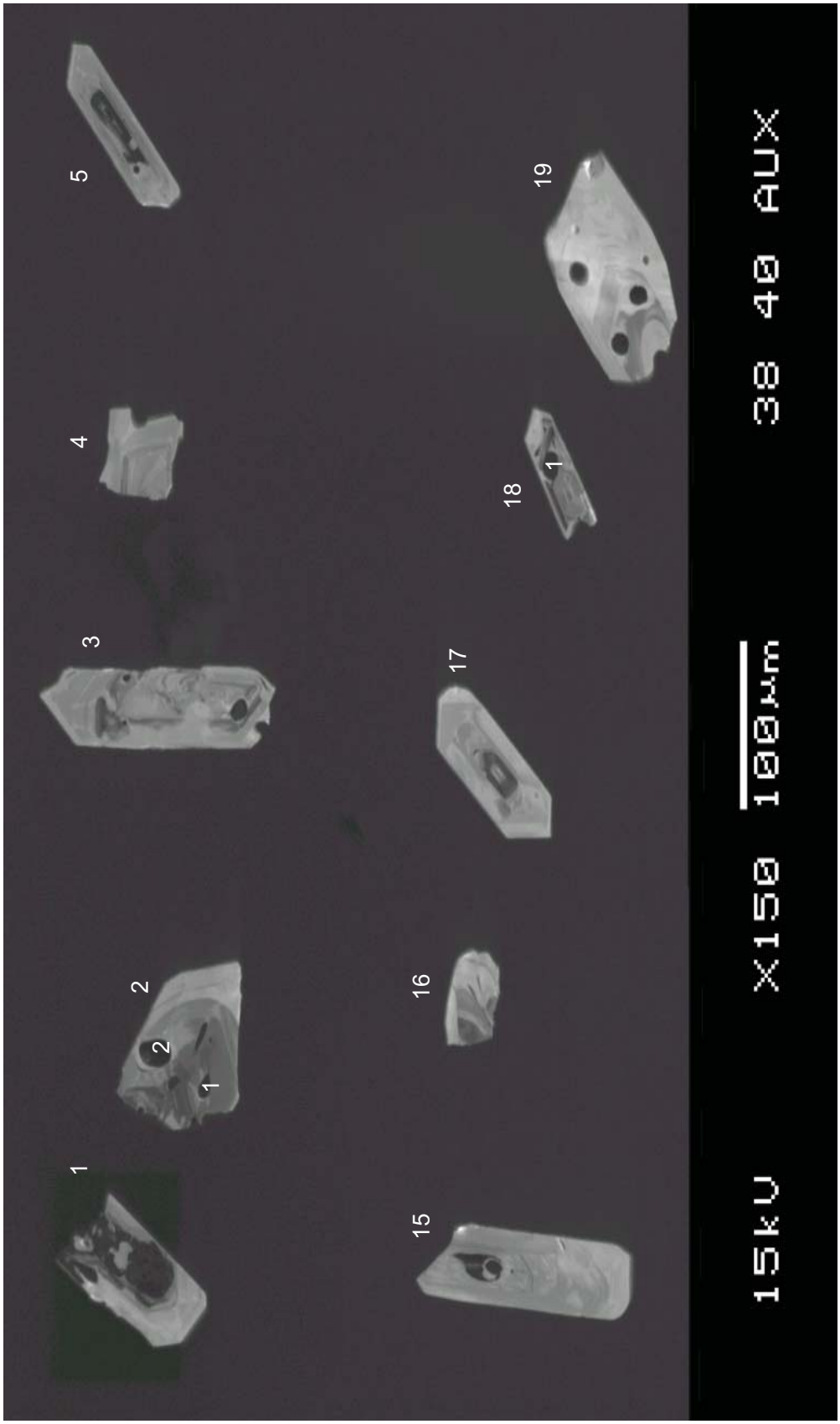

IBR

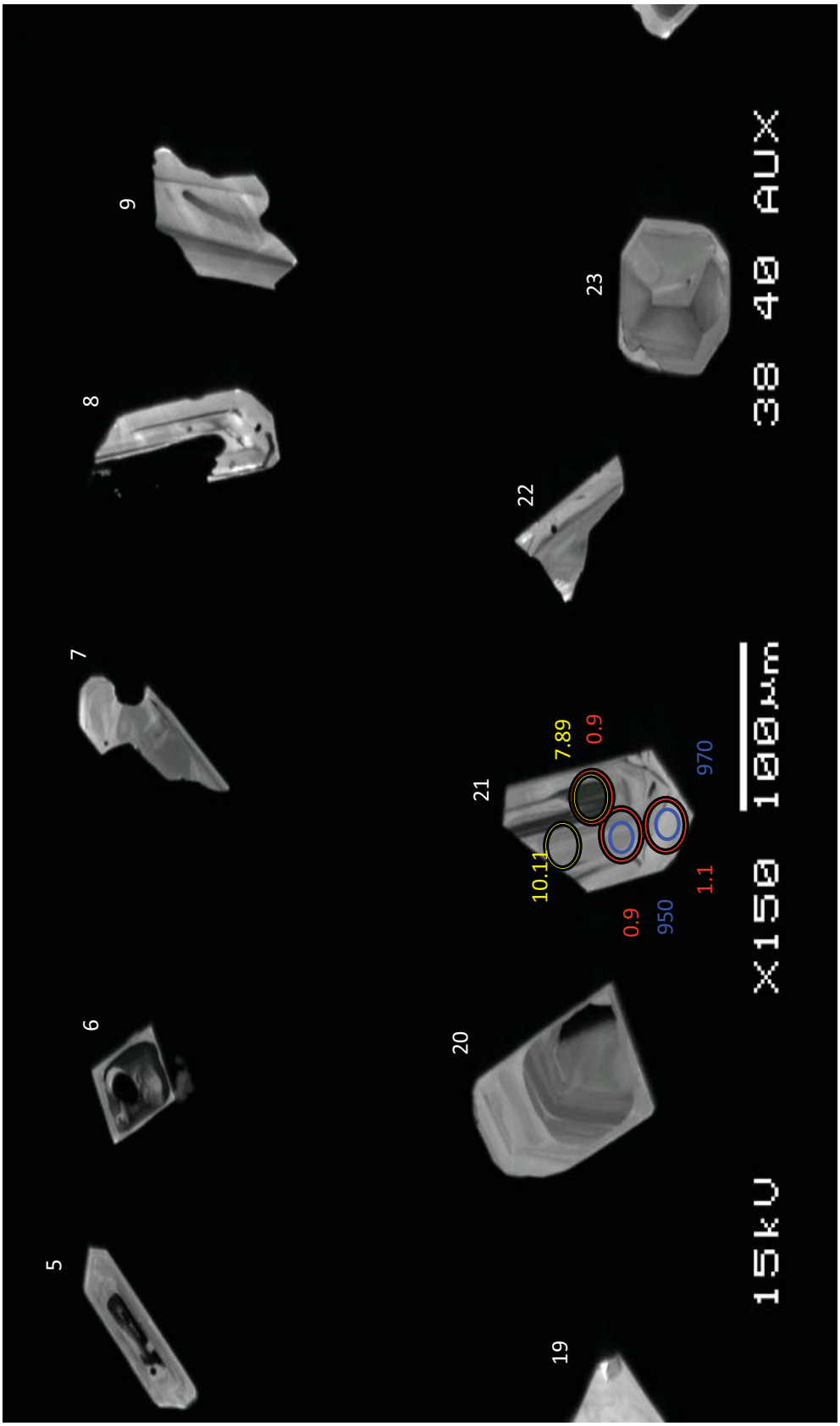
15kV X150 100µm 38 40 AUX
5
6
7
8
9
19
20
21
22
23
10.11
7.89
0.9
0.9
950
1.1
970

IBR

IBR-21

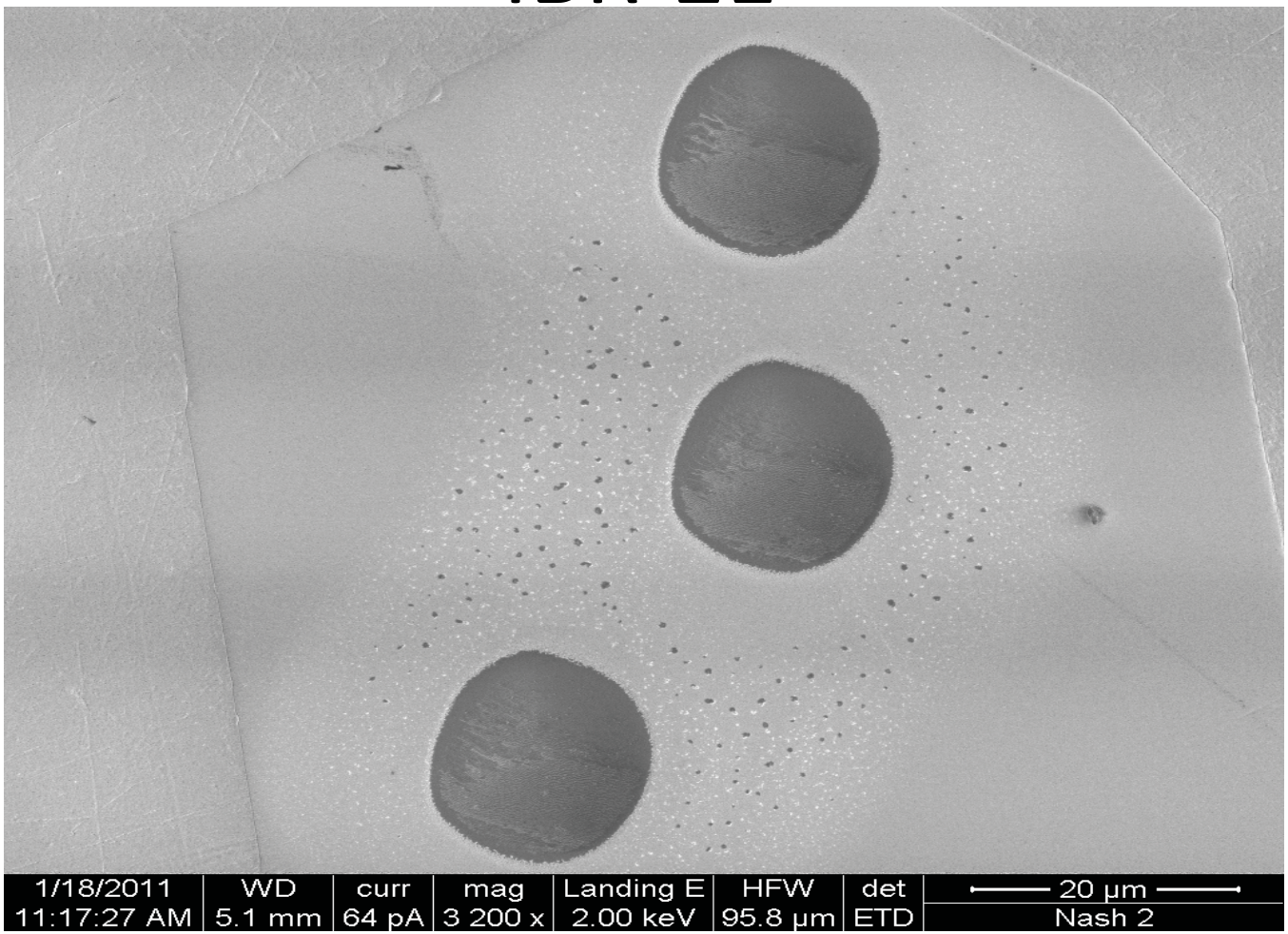
1/18/2011
11:17:27 AM
WD
5.1 mm
curr
64 pA
mag
3 200 x
Landing E
2.00 keV
HFW
95.8 µm
det
ETD
20 µm
Nash 2

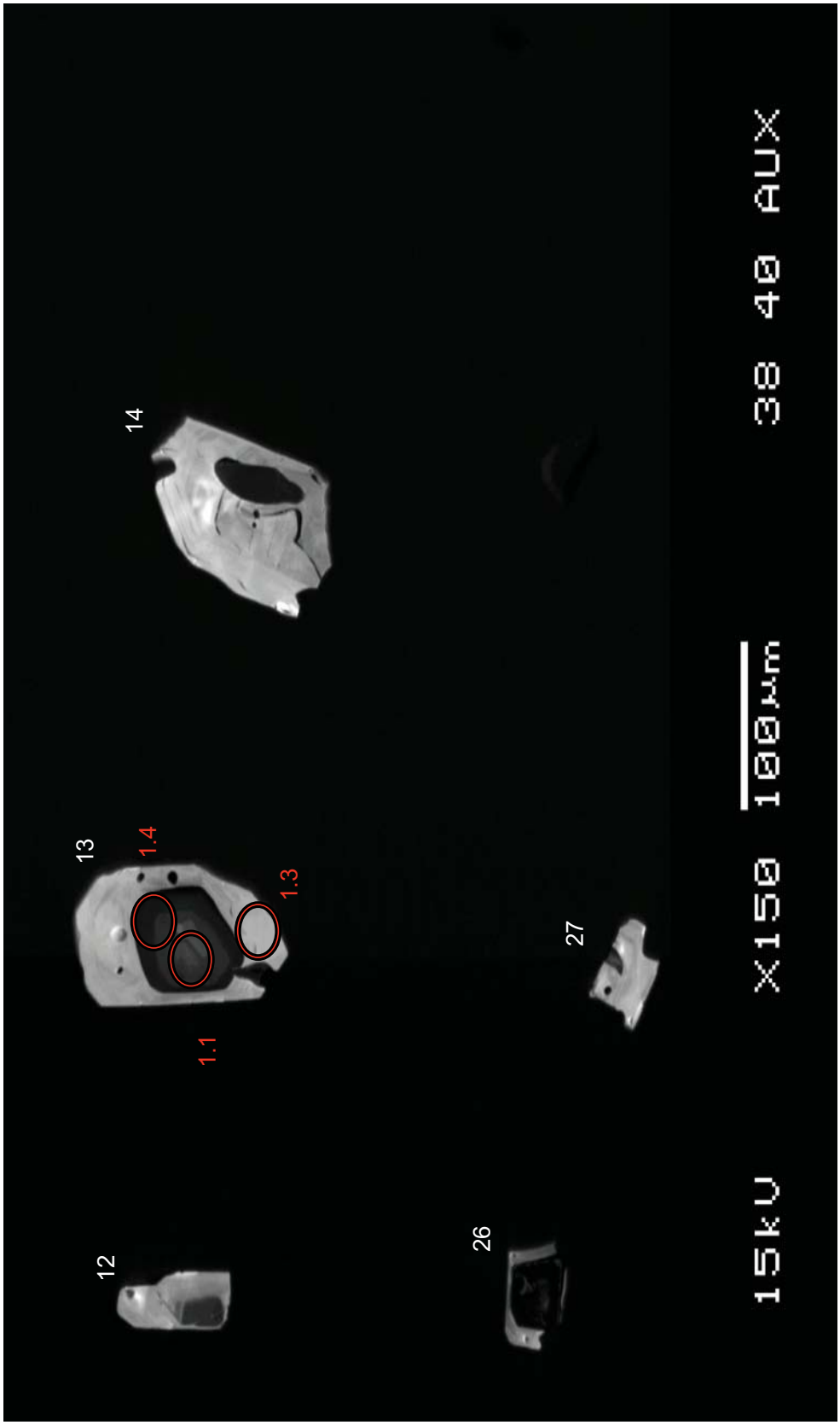

IBR

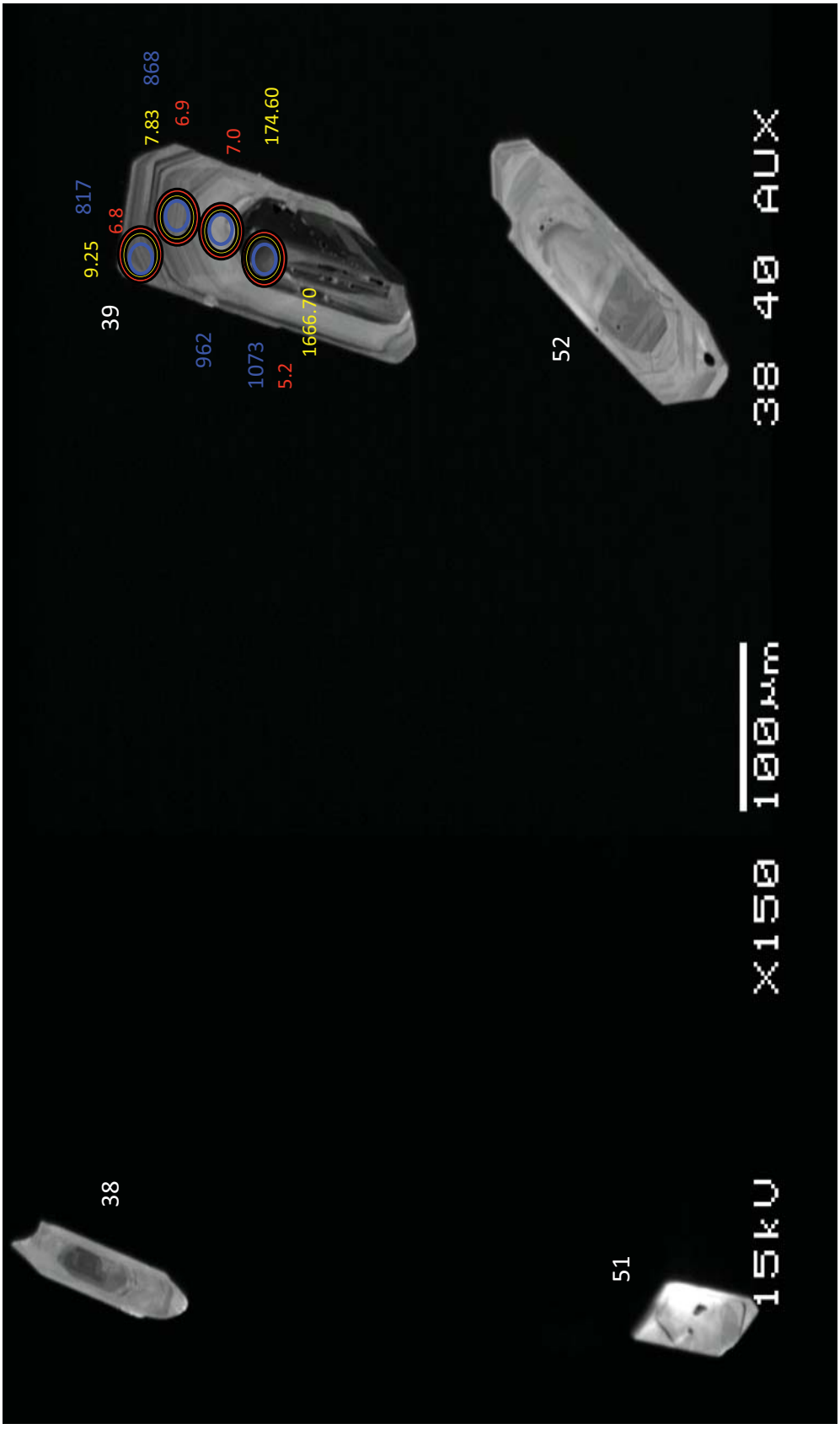
15kV X150 100µm 38 40 AUX
38
51
39
52
962
1073
5.2
1666.70
9.25
817
6.8
7.83
868
6.9
7.0
174.60

IBR

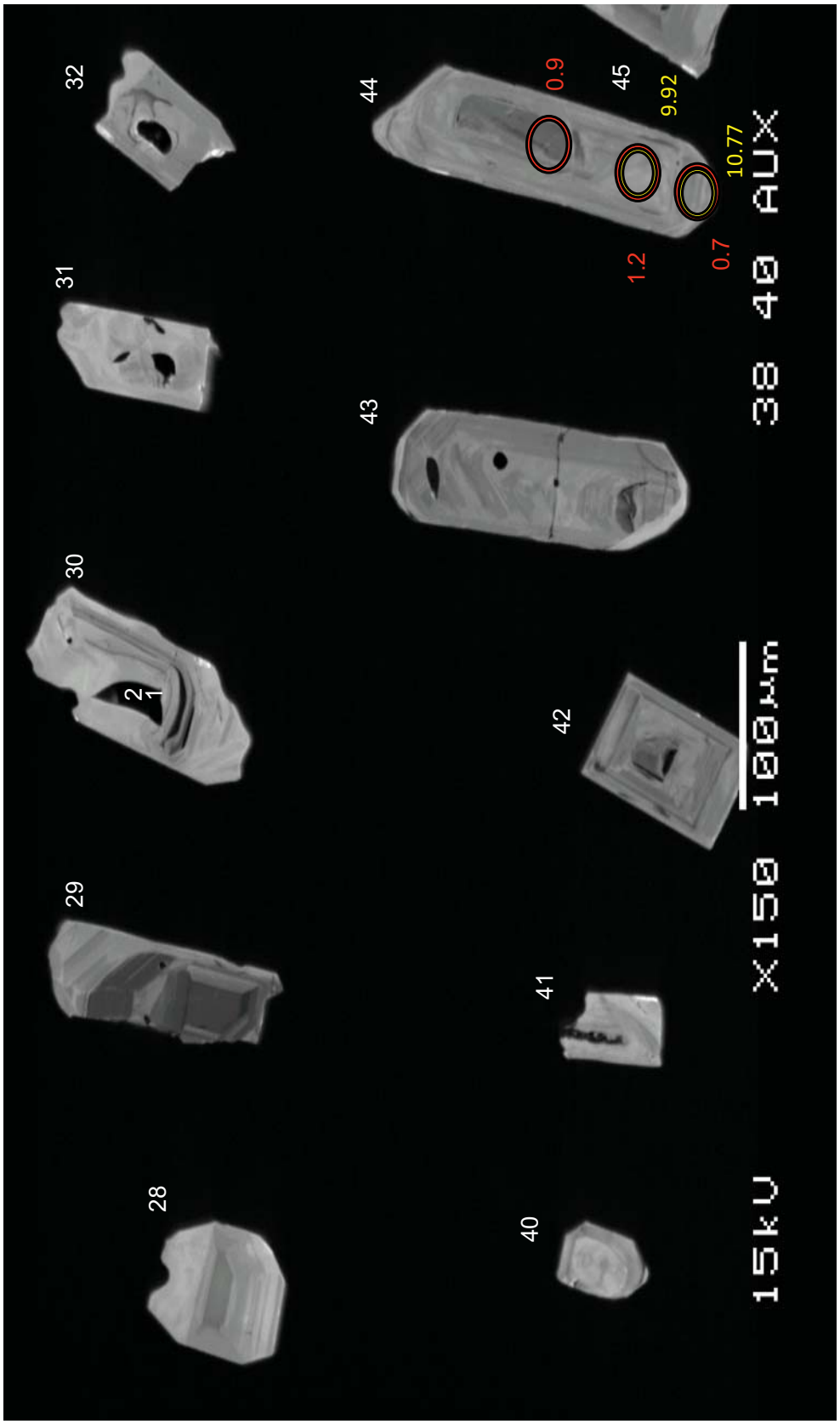
15kV X150 100µm
38 40 AUX
28
40
29
41
30
2
1
42
31
43
32
44
0.9
45
9.92
1.2
0.7
10.77

IBR

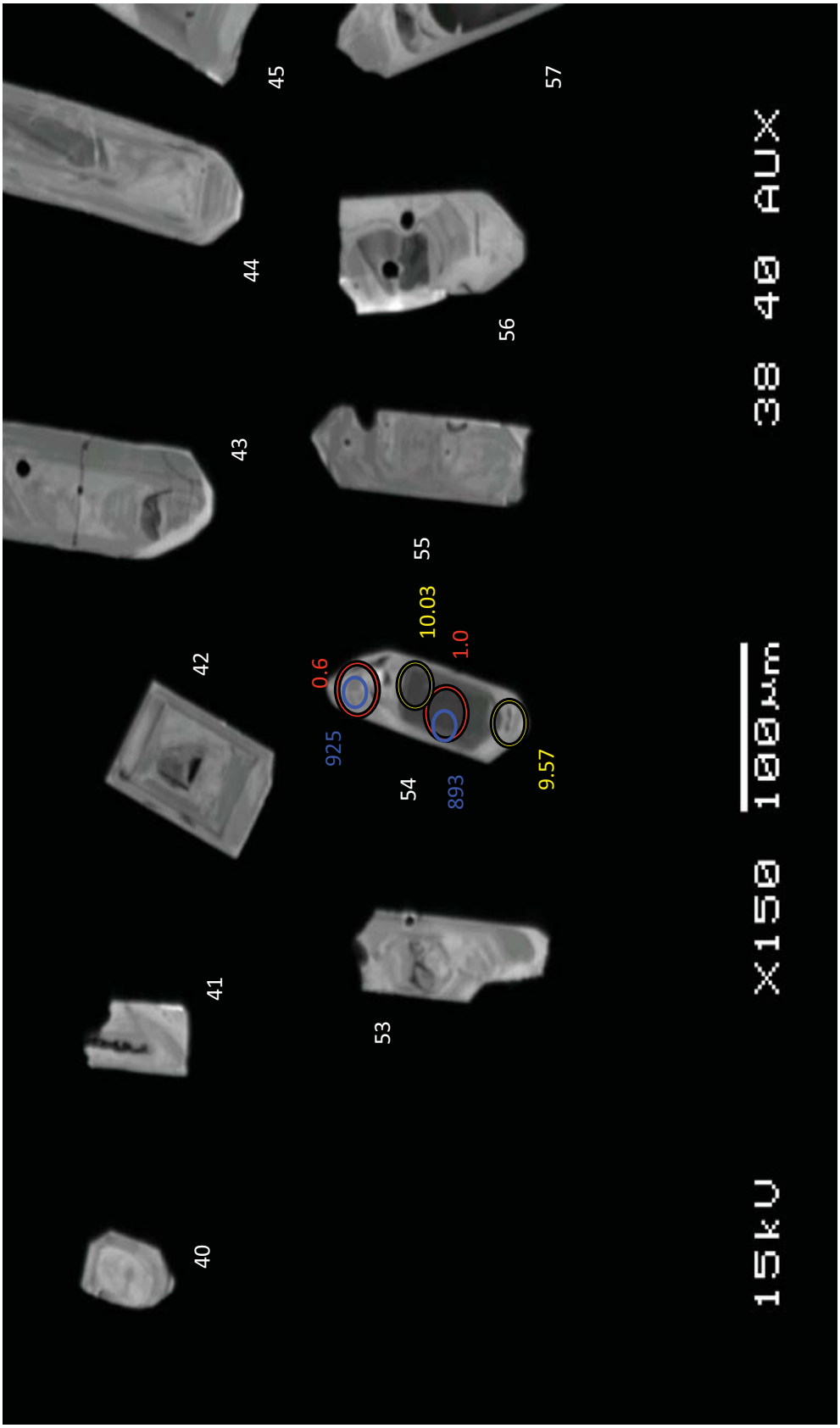
15kU X150 100µm 38 40 AUX
40
41
42
43
44
45
53
54
55
56
57
925
0.6
893
10.03
1.0
9.57

IBR

IBR-54

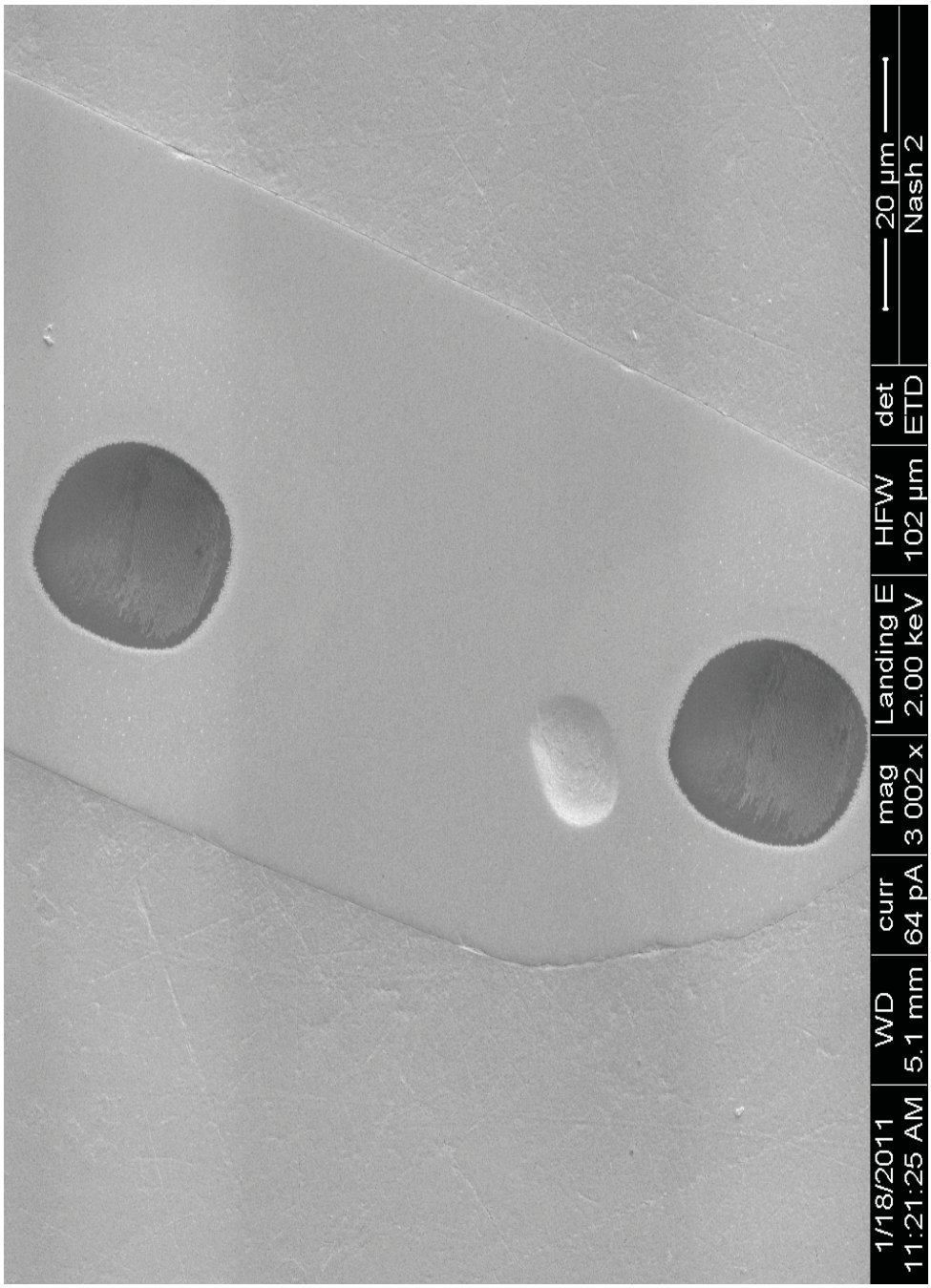
1/18/2011
11:21:25 AM
WD
5.1 mm
curr
64 pA
mag
3 002 x
Landing E
2.00 keV
HFW
102 µm
det
ETD
20 µm
Nash 2

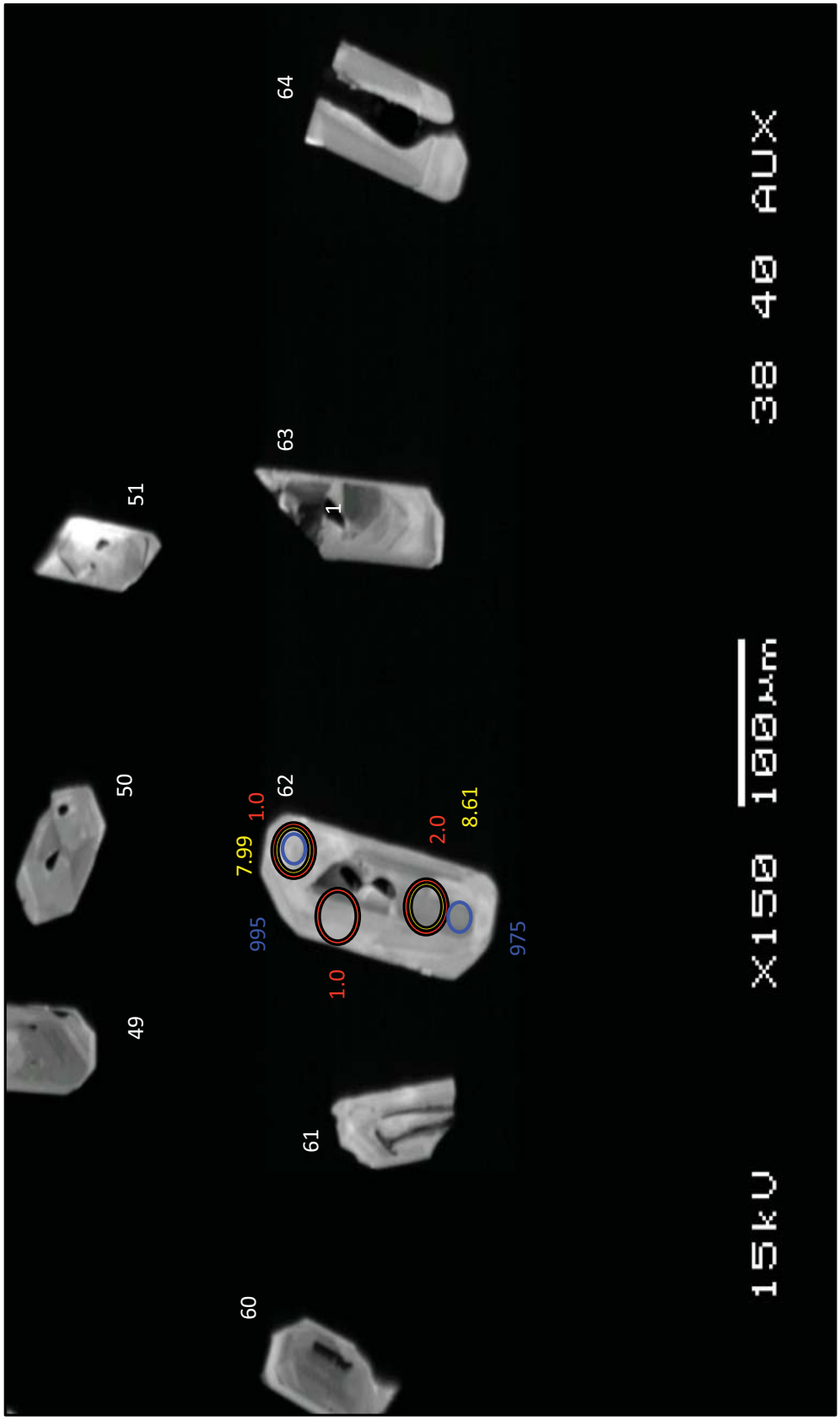
15kU X150 100µm 38 40 AUX
60
49
50
51
61
62
63
64
1
995
7.99
1.0
1.0
2.0
8.61
975

IBR

IBR-62

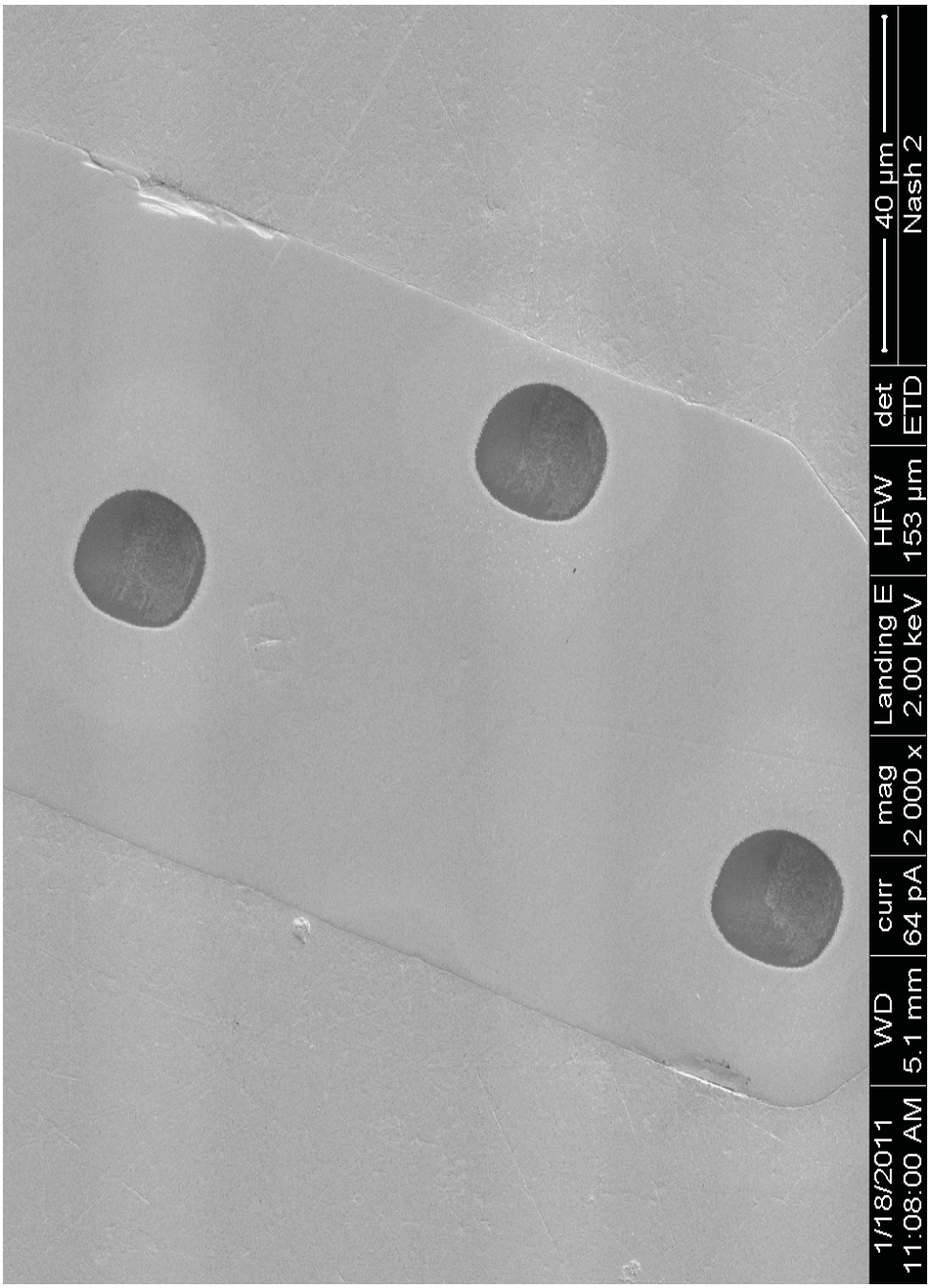
1/18/2011
11:08:00 AM
WD
5.1 mm
curr
64 pA
mag
2 000 x
Landing E
2.00 keV
HFW
153 µm
det
ETD
40 µm
Nash 2

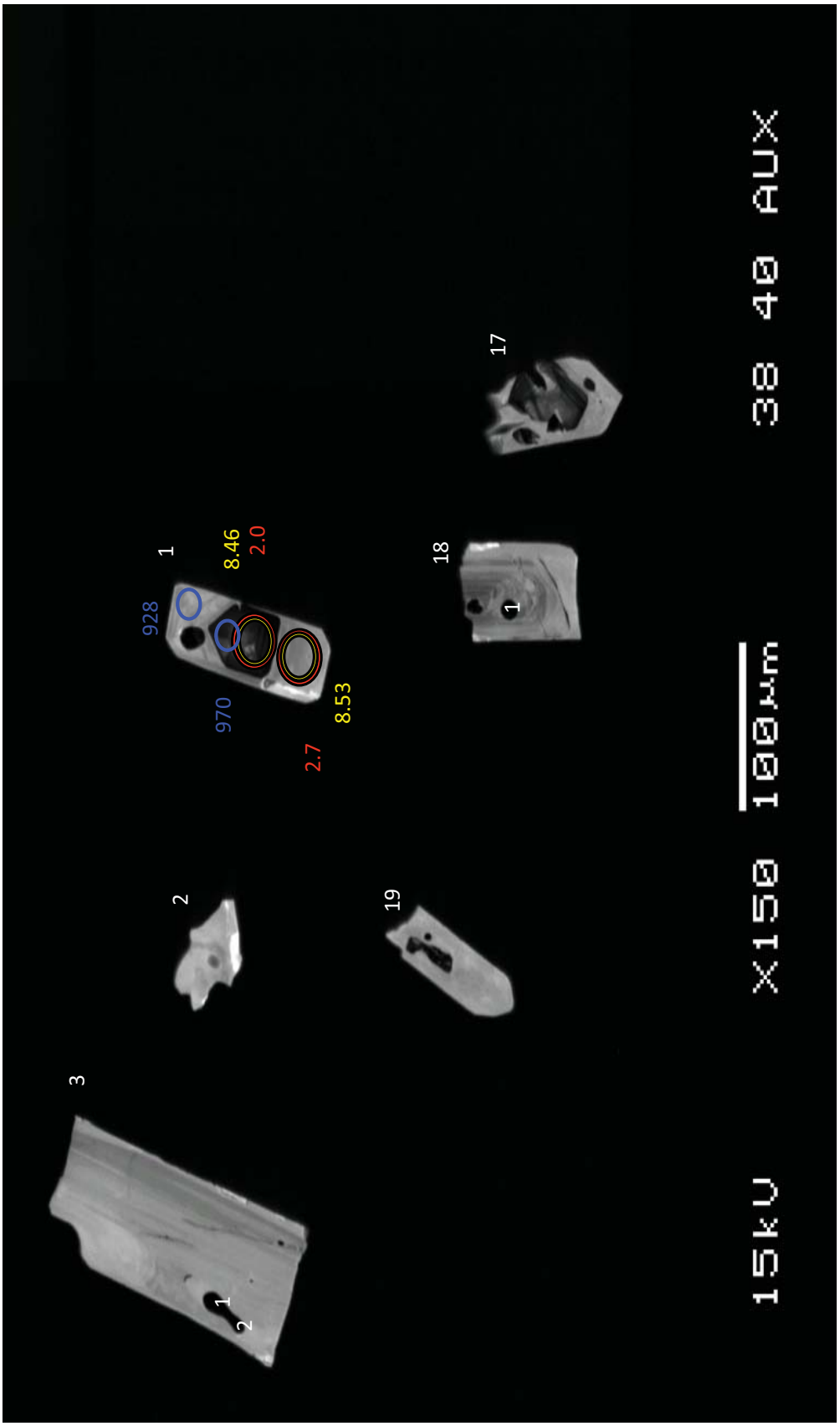
15kV X150 100µm 38 40 AUX
TCT
3
2
1
2
19
928
970
1
8.46
2.0
2.7
8.53
18
1
17

TCT-1


1/18/2011
10:29:32 AM
WD
5.0 mm
curr
64 pA
mag
4 000 x
Landing E
2.00 keV
HFW
76.6 µm
det
ETD
20 µm
Nash 2

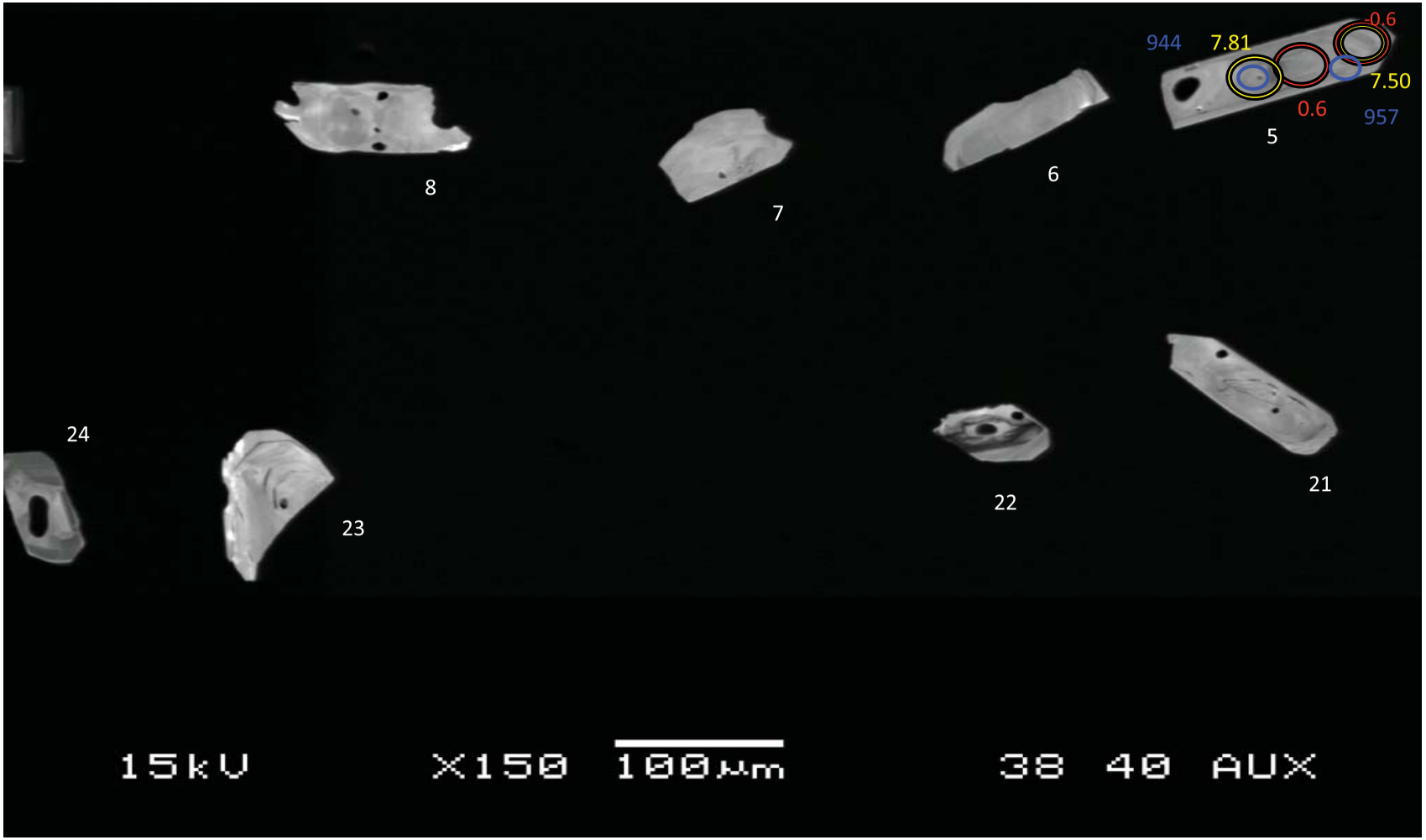

TCT

TCT-5

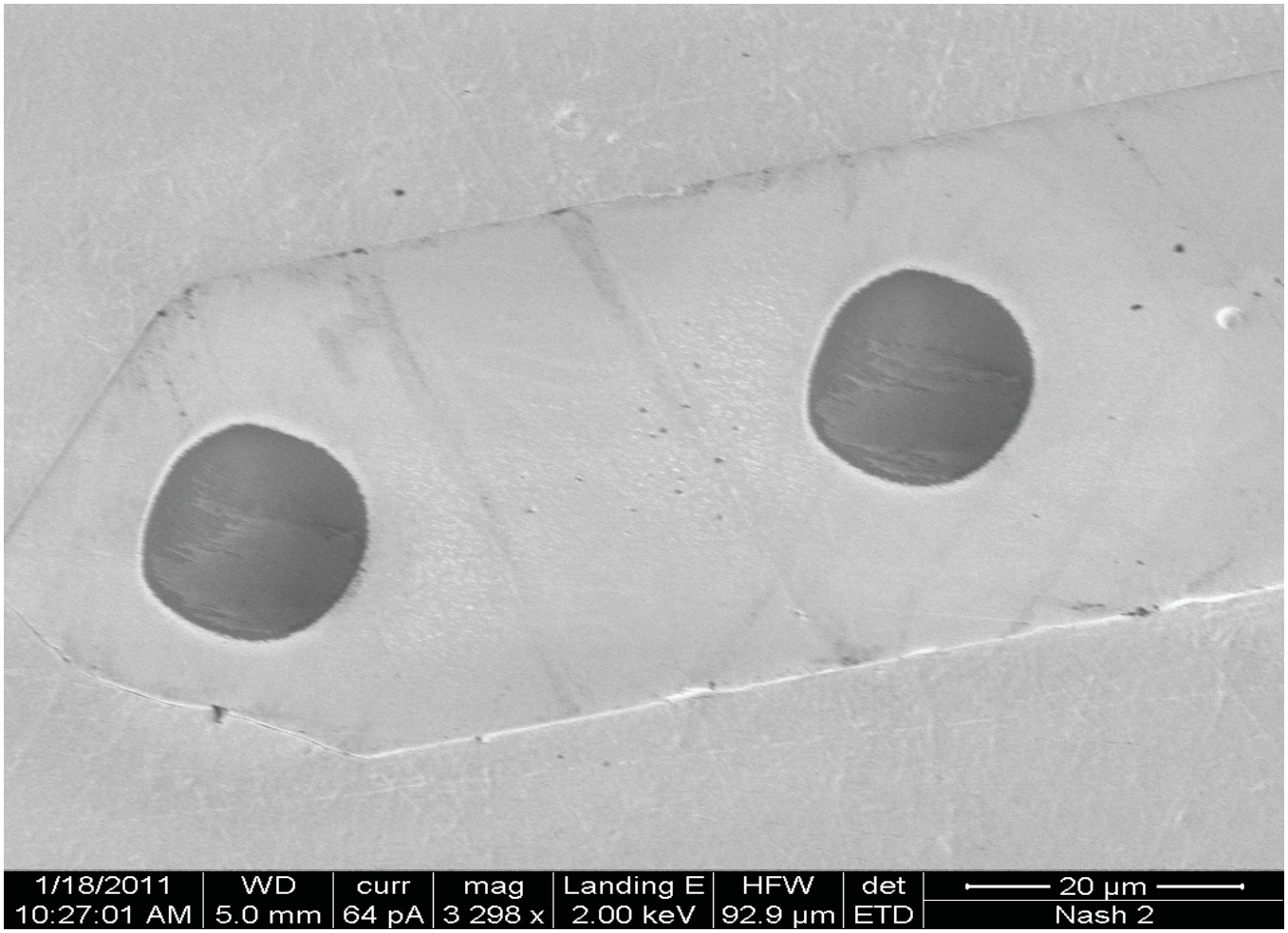
1/18/2011
10:27:01 AM
WD
5.0 mm
curr
64 pA
mag
3 298 x
Landing E
2.00 keV
HFW
92.9 µm
det
ETD
20 µm
Nash 2

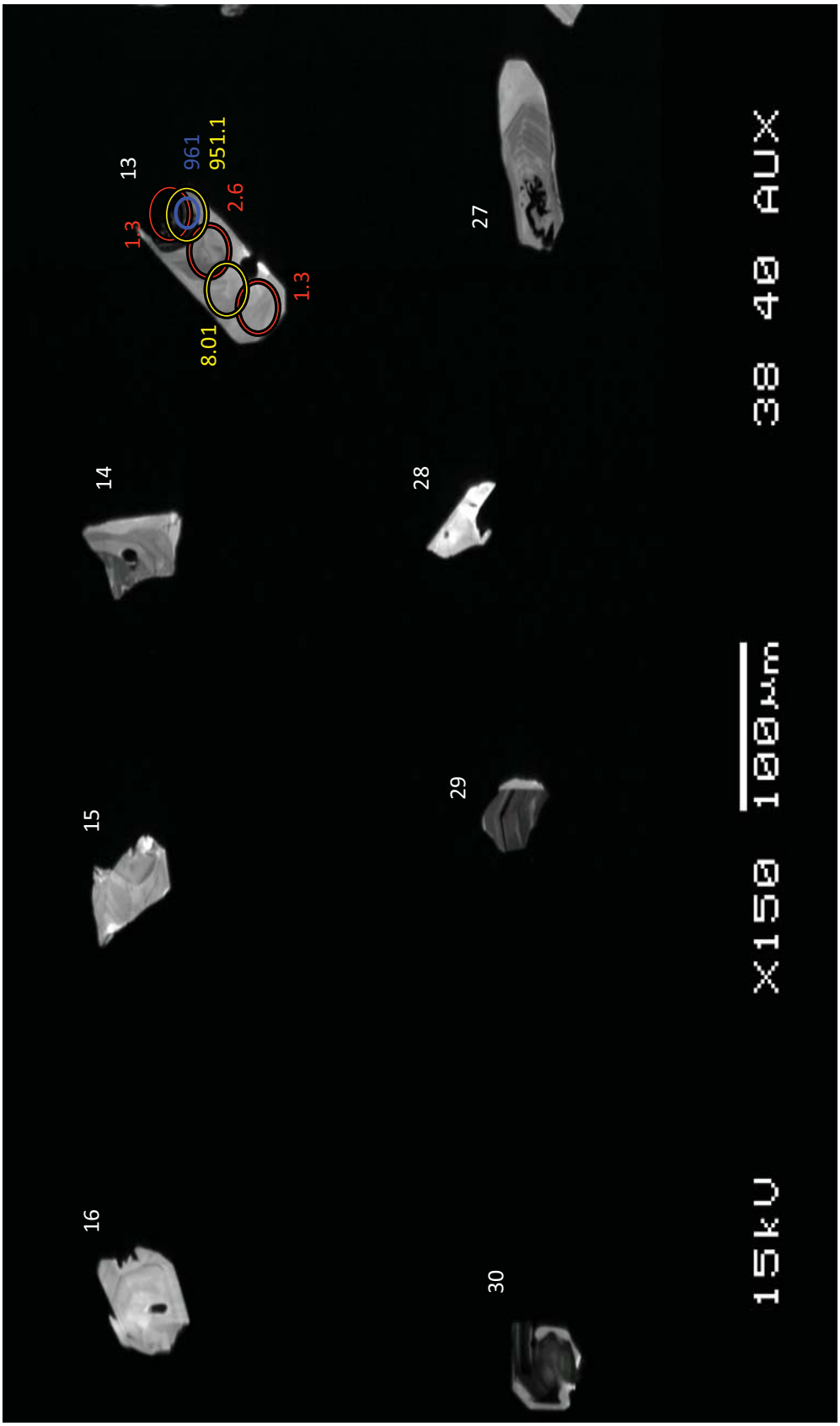
15kV X150 100µm 38 40 AUX
TCT
13
14
15
16
27
28
29
30
961
951.1
2.6
1.3
1.3
8.01

TCT-13

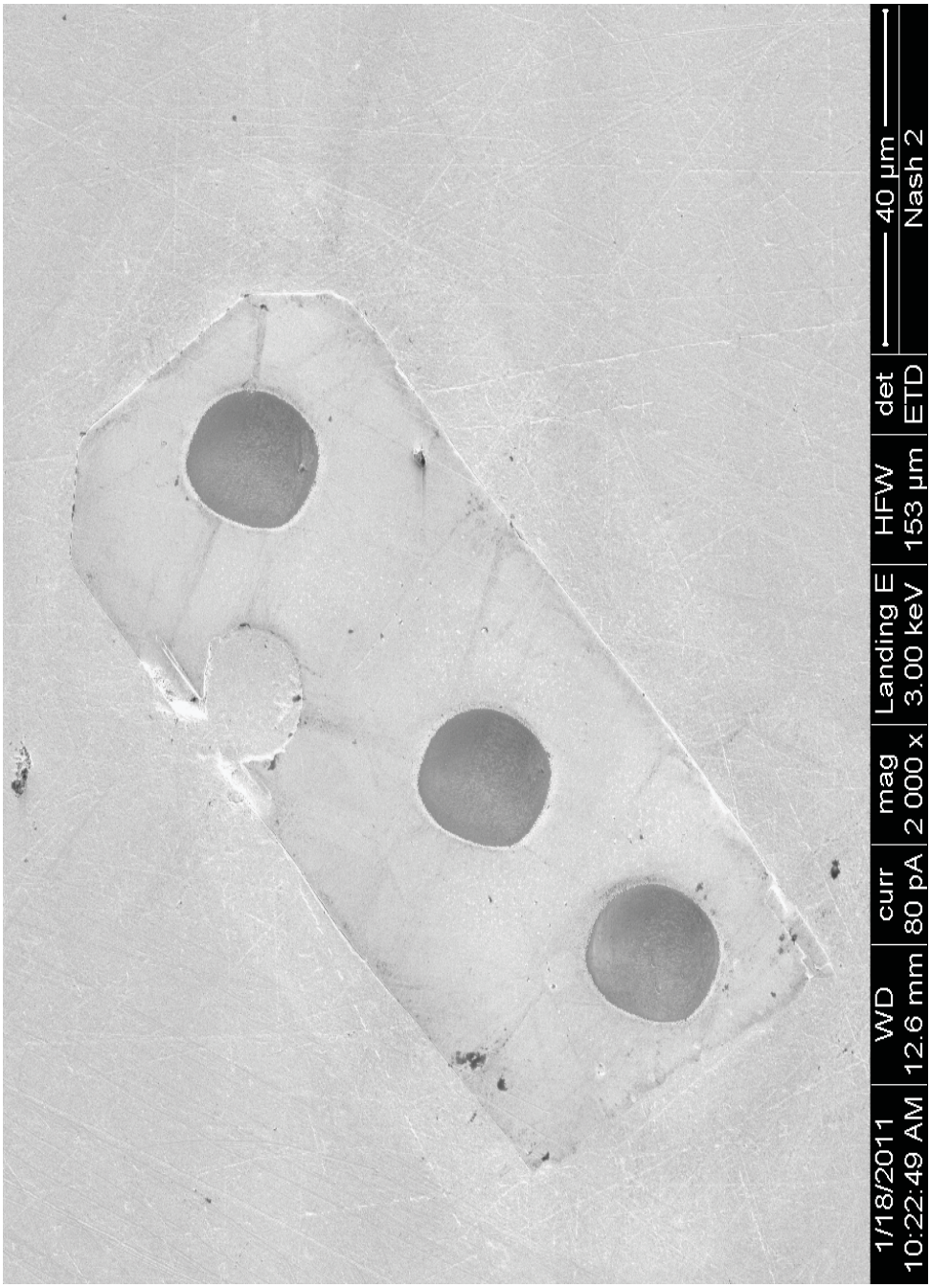
1/18/2011
10:22:49 AM
WD
12.6 mm
curr
80 pA
mag
2 000 x
Landing E
3.00 keV
HFW
153 µm
det
ETD
40 µm
Nash 2

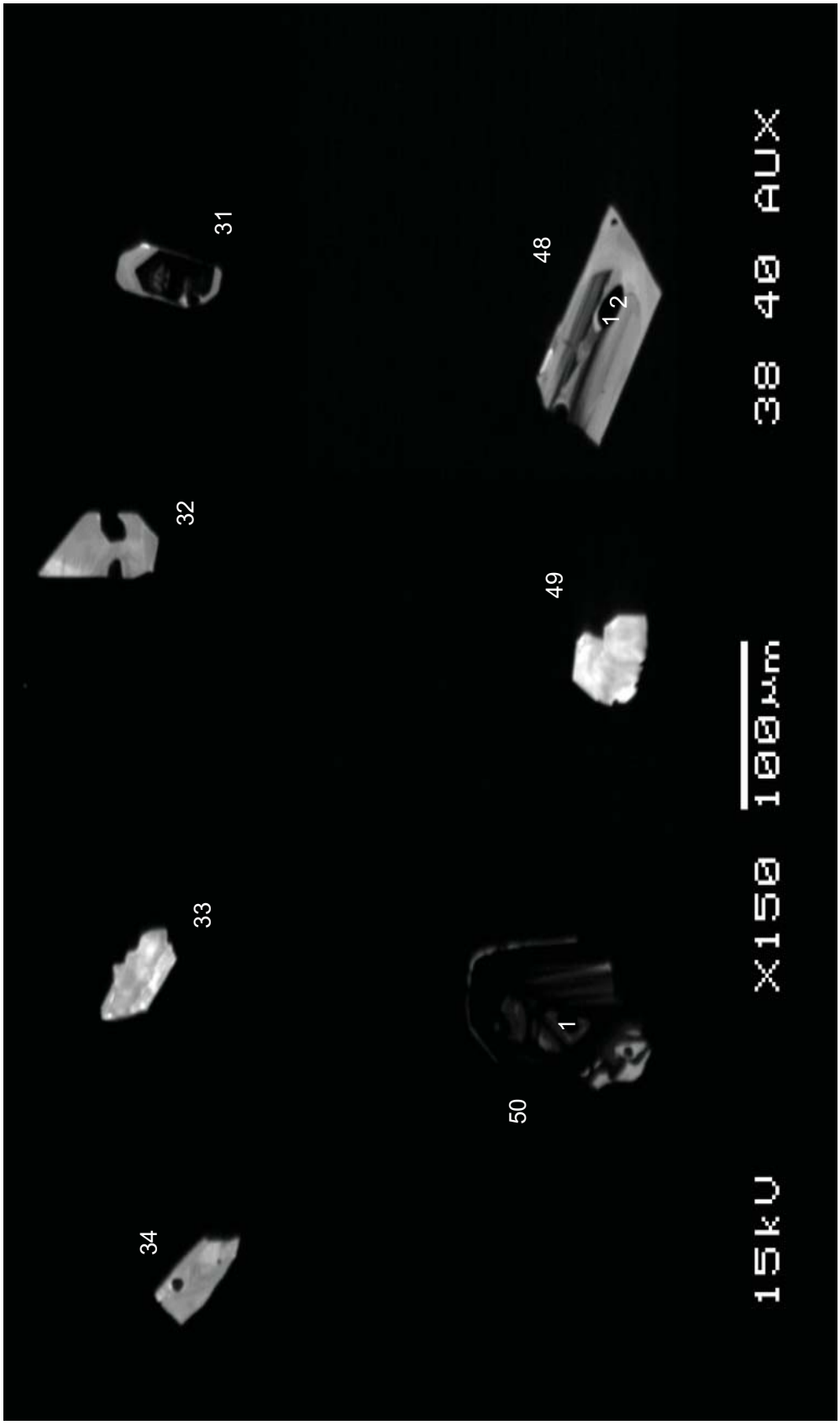

TCT

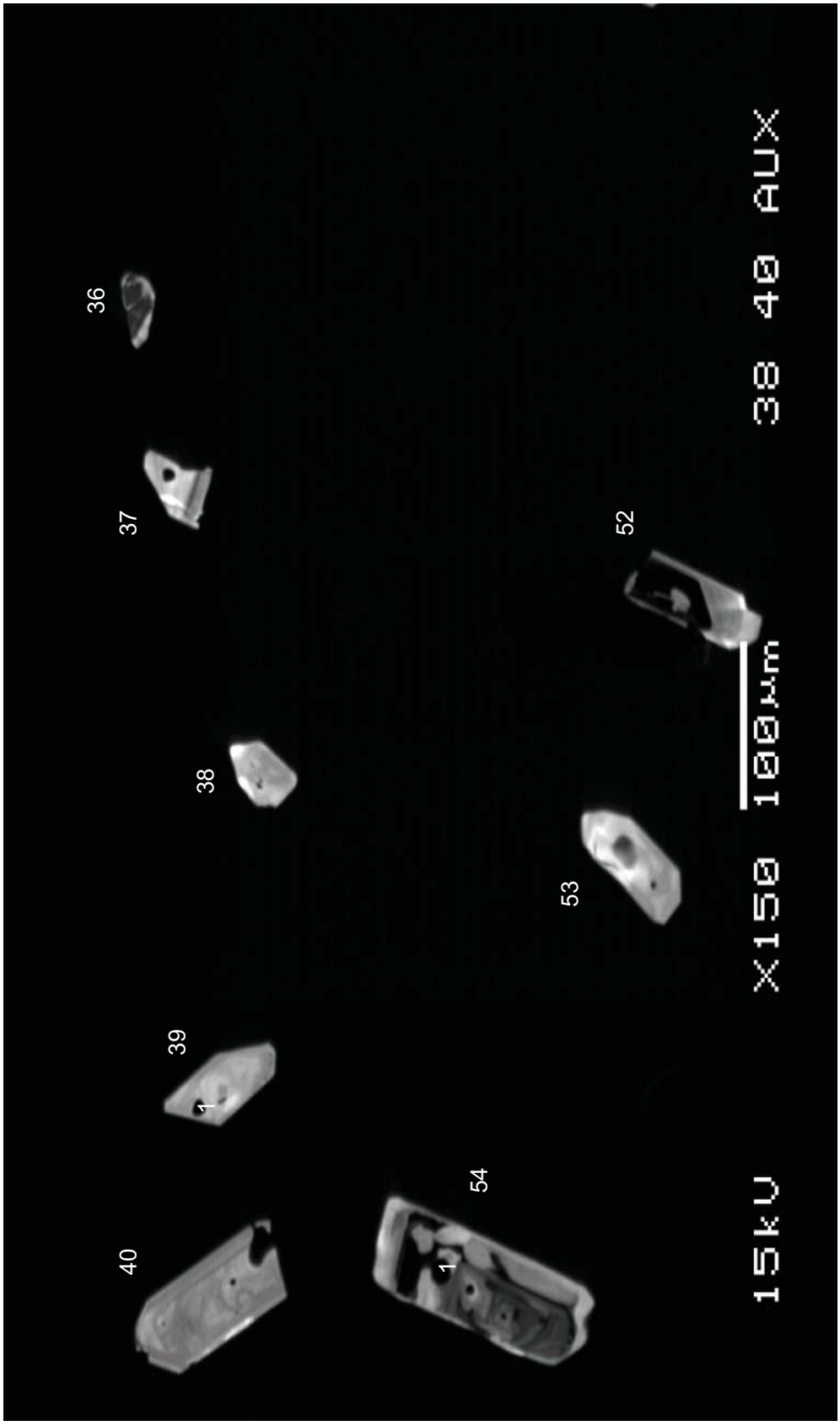

TCT

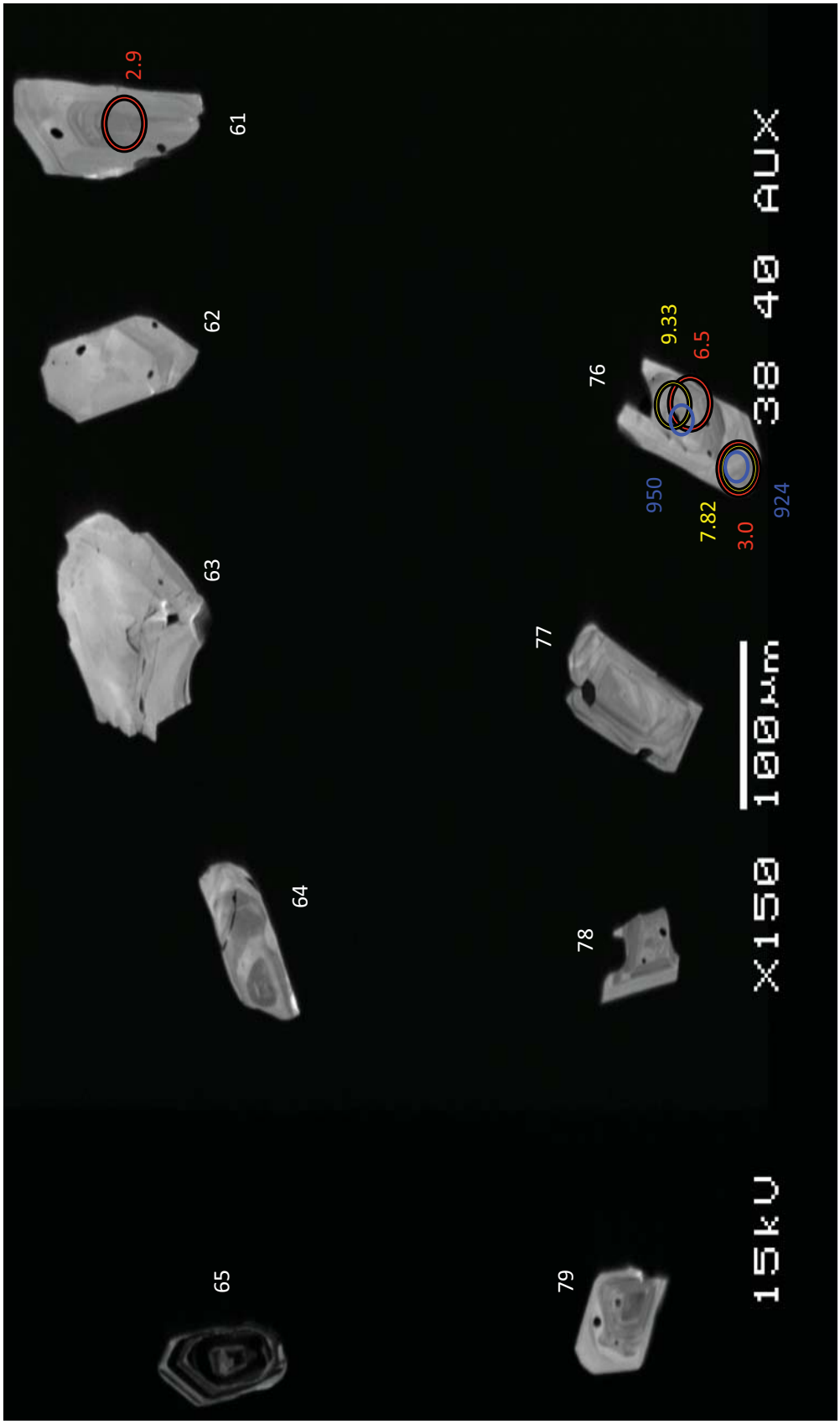
15kV X150 100µm 38 40 AUX
61
62
63
64
65
76
77
78
79
2.9
9.33
6.5
950
7.82
3.0
924

TCT

TCT-76

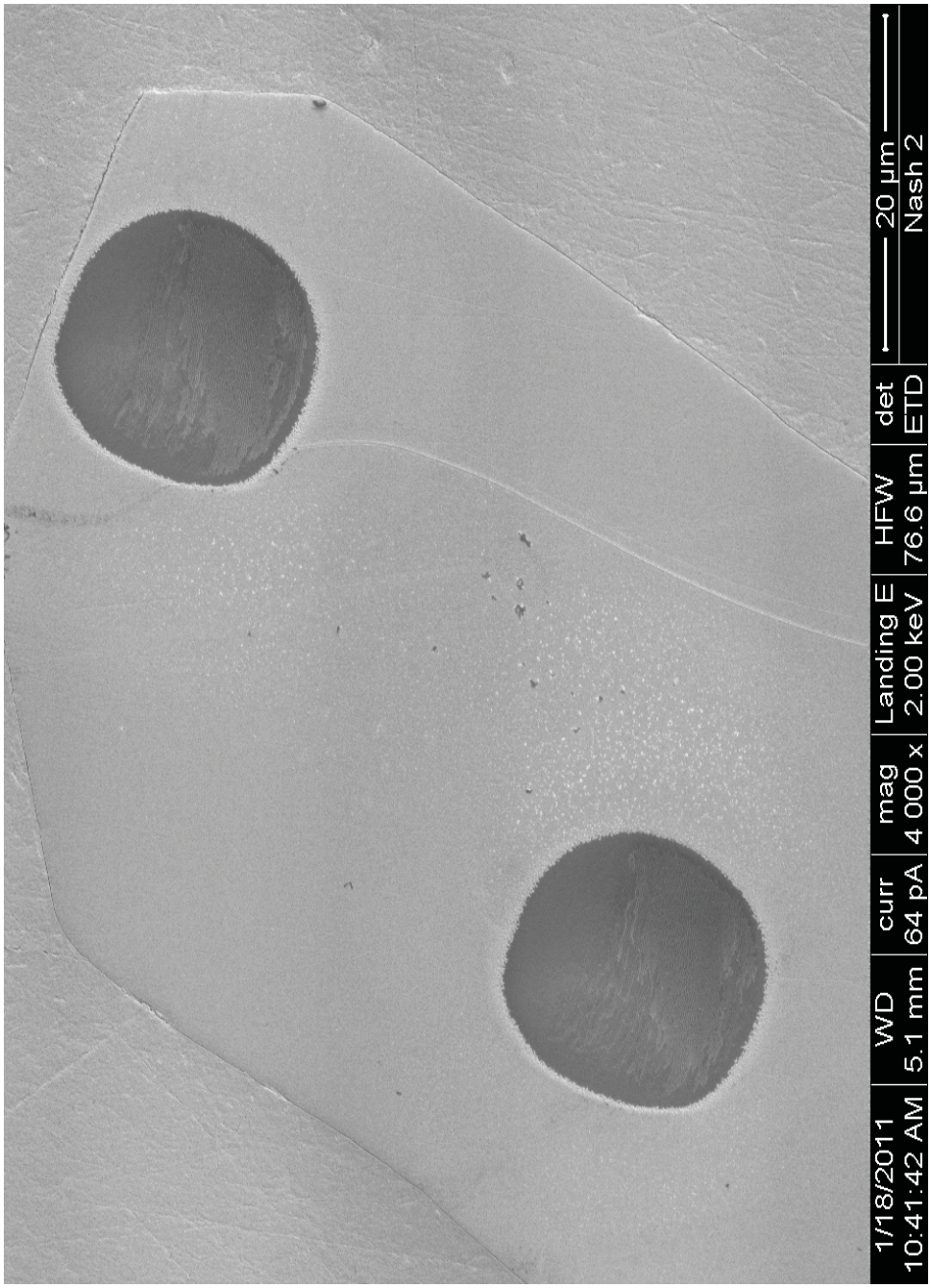
1/18/2011
10:41:42 AM
WD
5.1 mm
curr
64 pA
mag
4 000 x
Landing E
2.00 keV
HFW
76.6 µm
det
ETD
20 µm
Nash 2

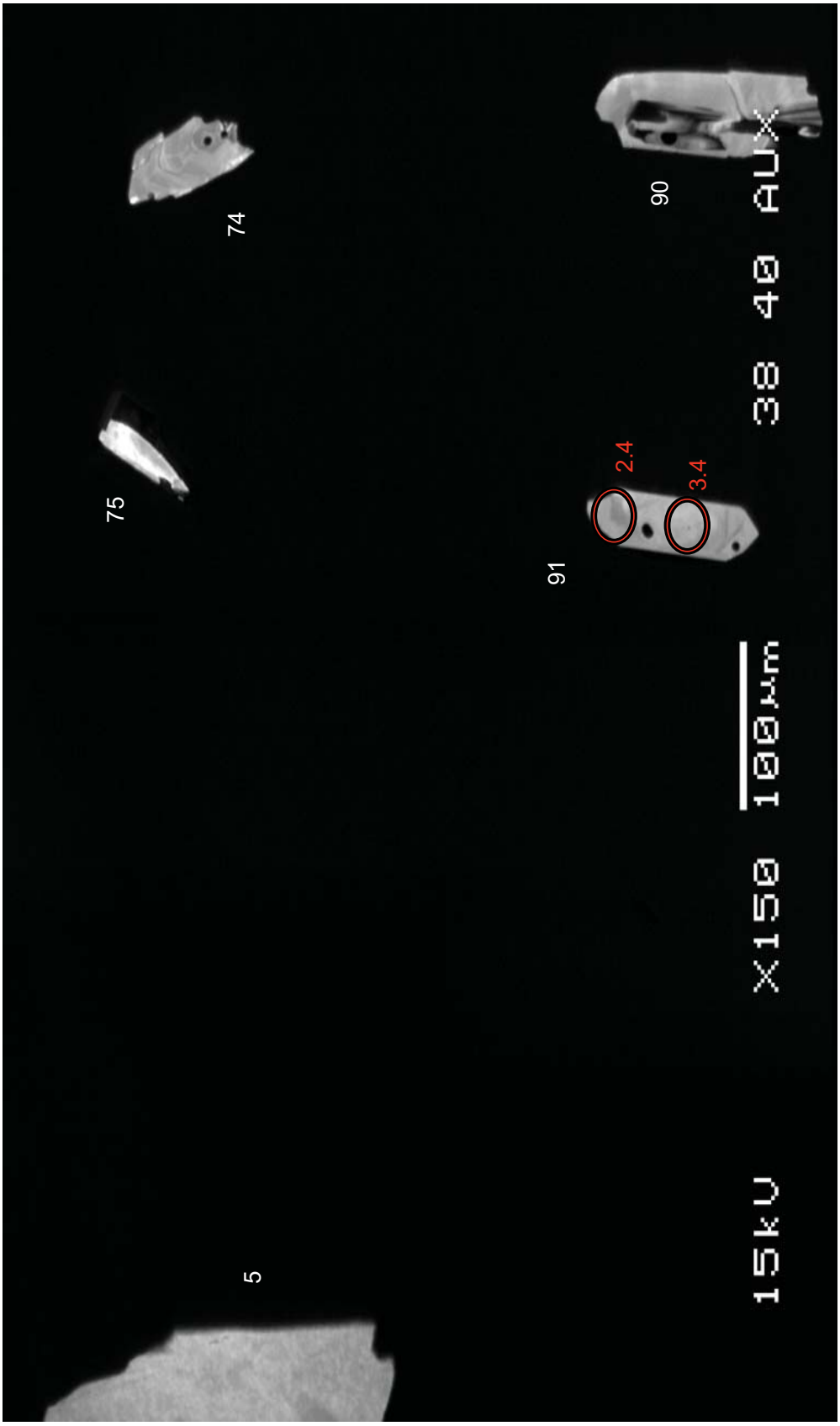

TCT

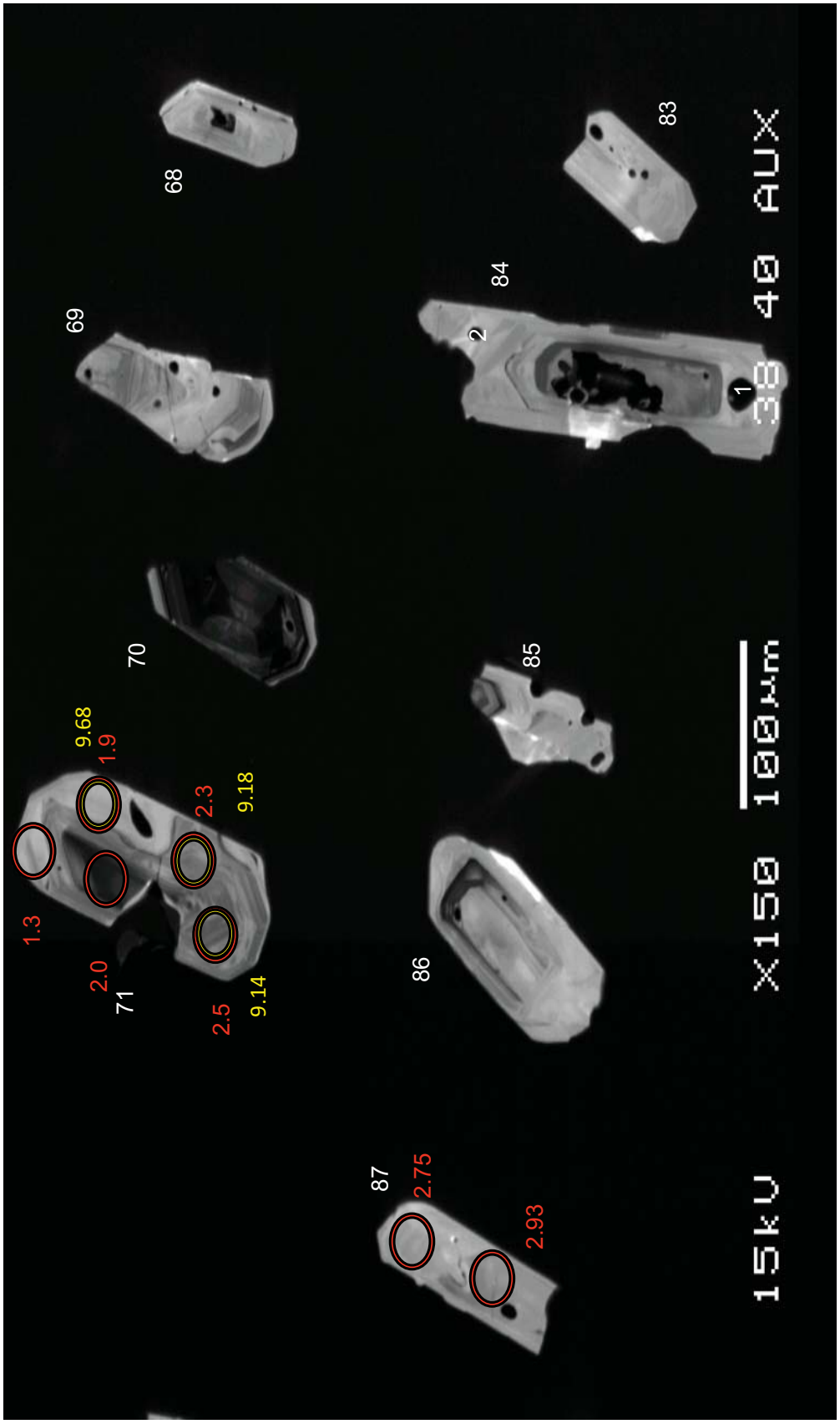
15kU X150 100µm
TCT
1
2
38 40 AUX
68
69
70
71
83
84
85
86
87
1.3
2.0
2.5
9.14
9.68
1.9
2.3
9.18
2.75
2.93

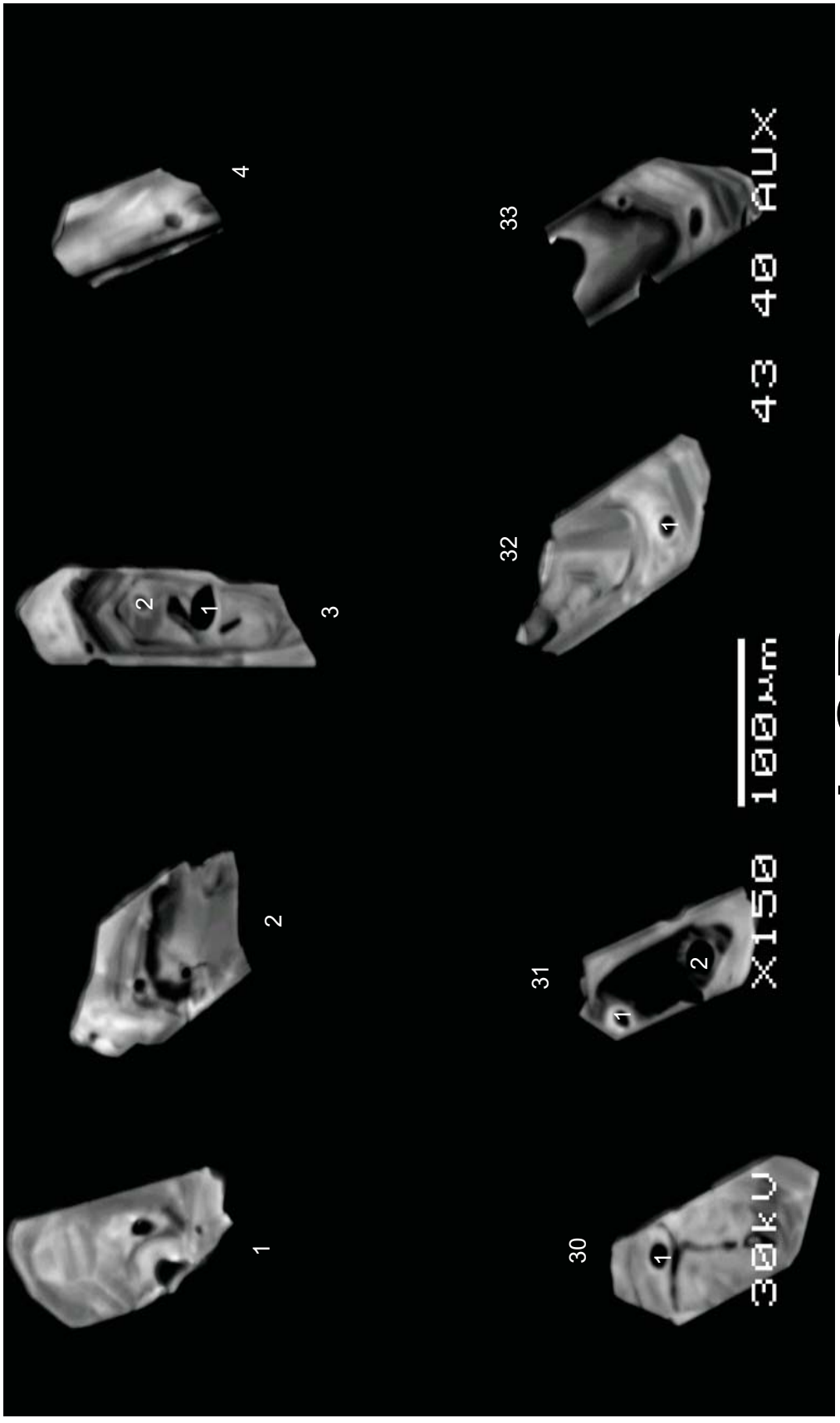
LCR
30kV X150 100µm 43 40 AUX
1
2
3
4
30
31
32
33

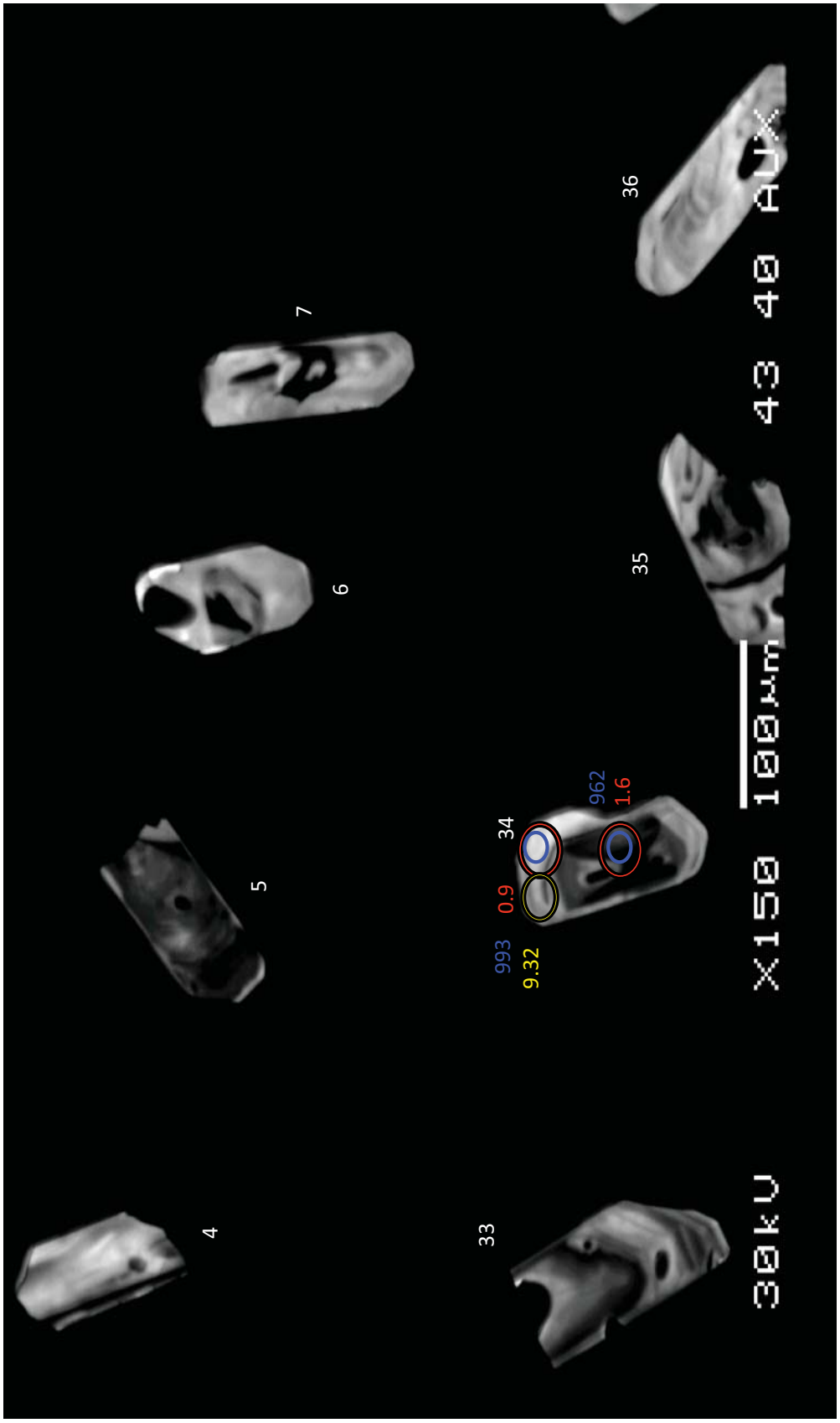

LCR

LCR-34

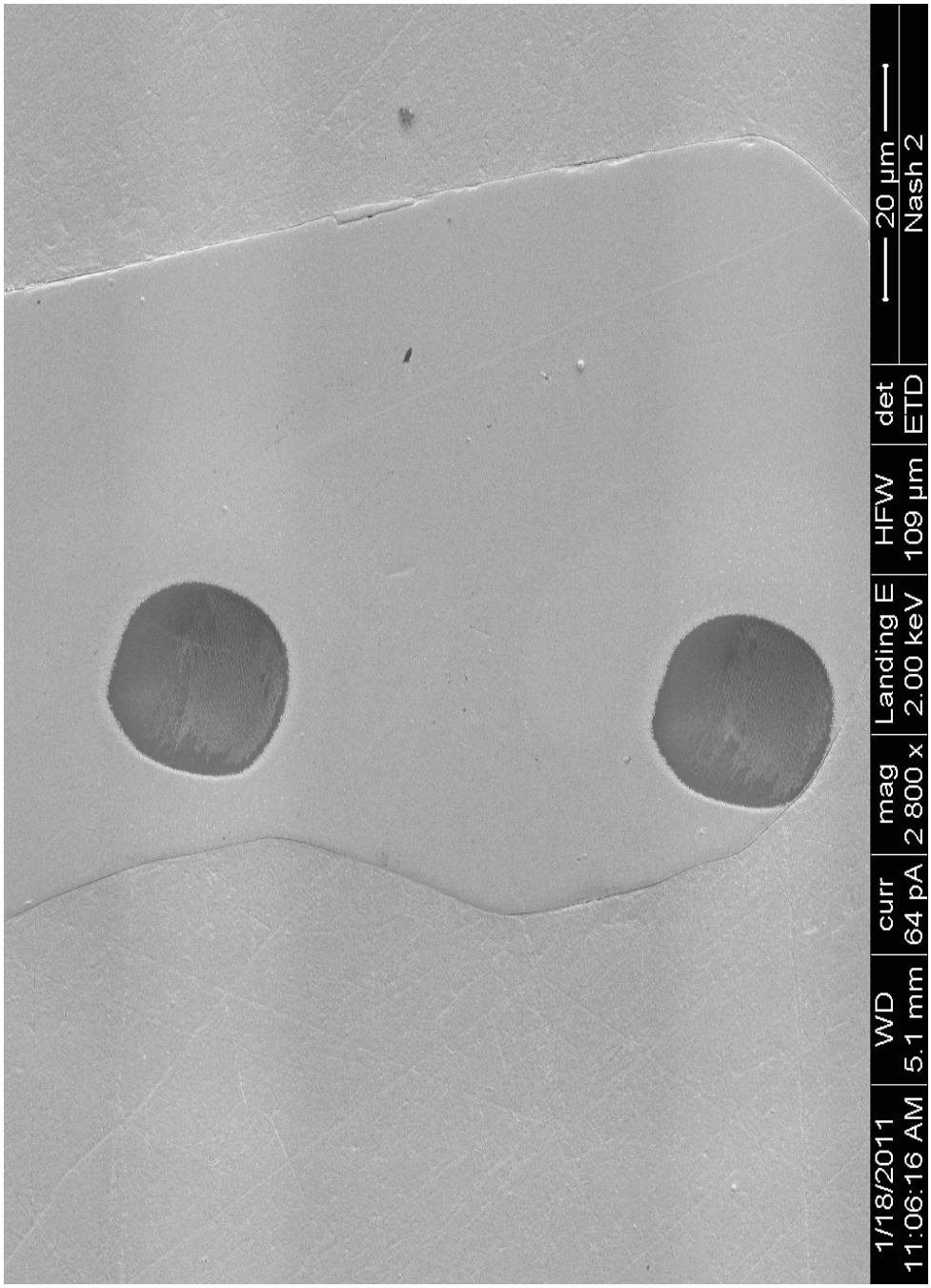
1/18/2011
11:06:16 AM
WD
5.1 mm
curr
64 pA
mag
2 800 x
Landing E
2.00 keV
HFW
109 µm
det
ETD
20 µm
Nash 2

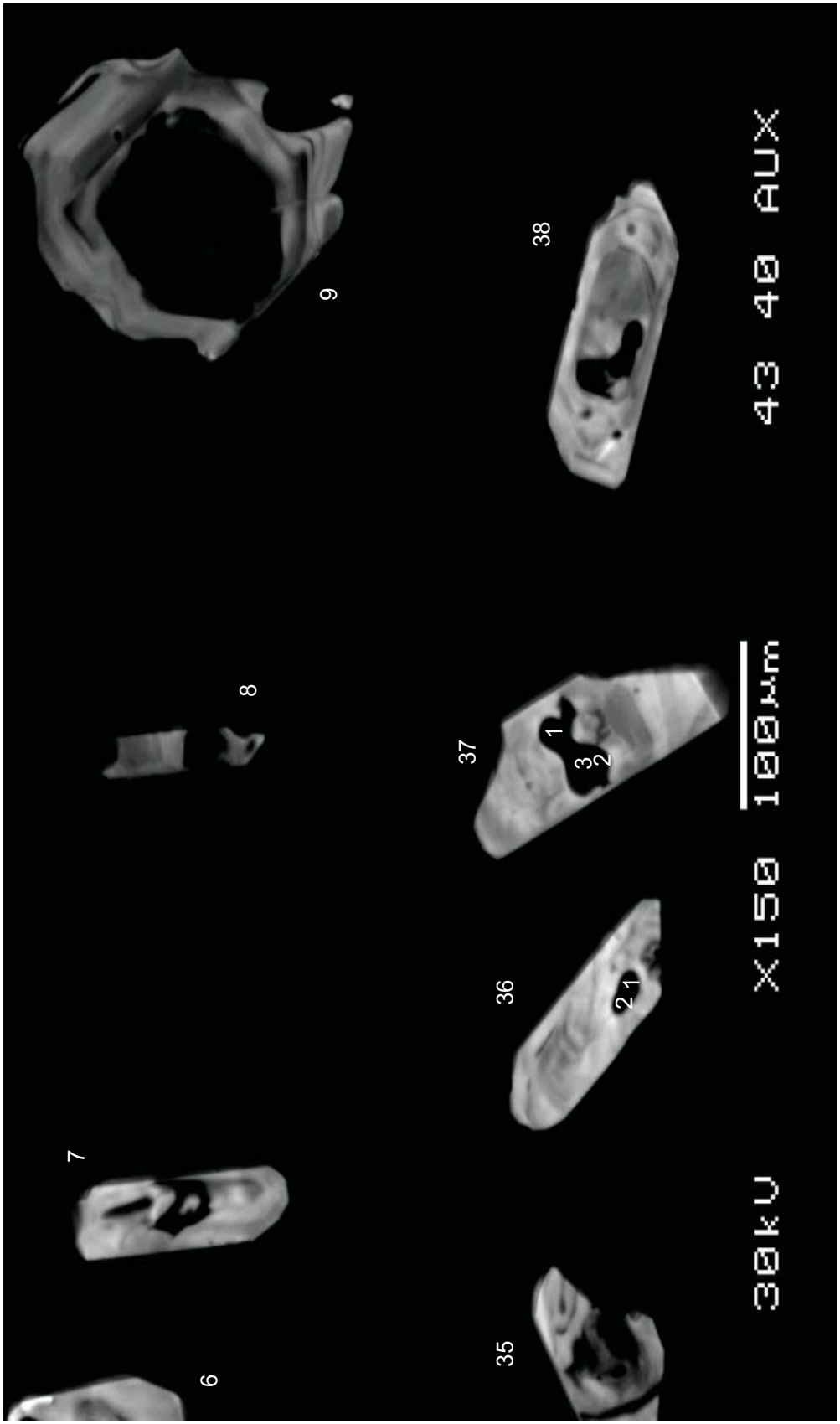
30kV X150 100µm 43 40 AUX
LCR
6
7
8
9
35
36
37
38
1
2
3
21

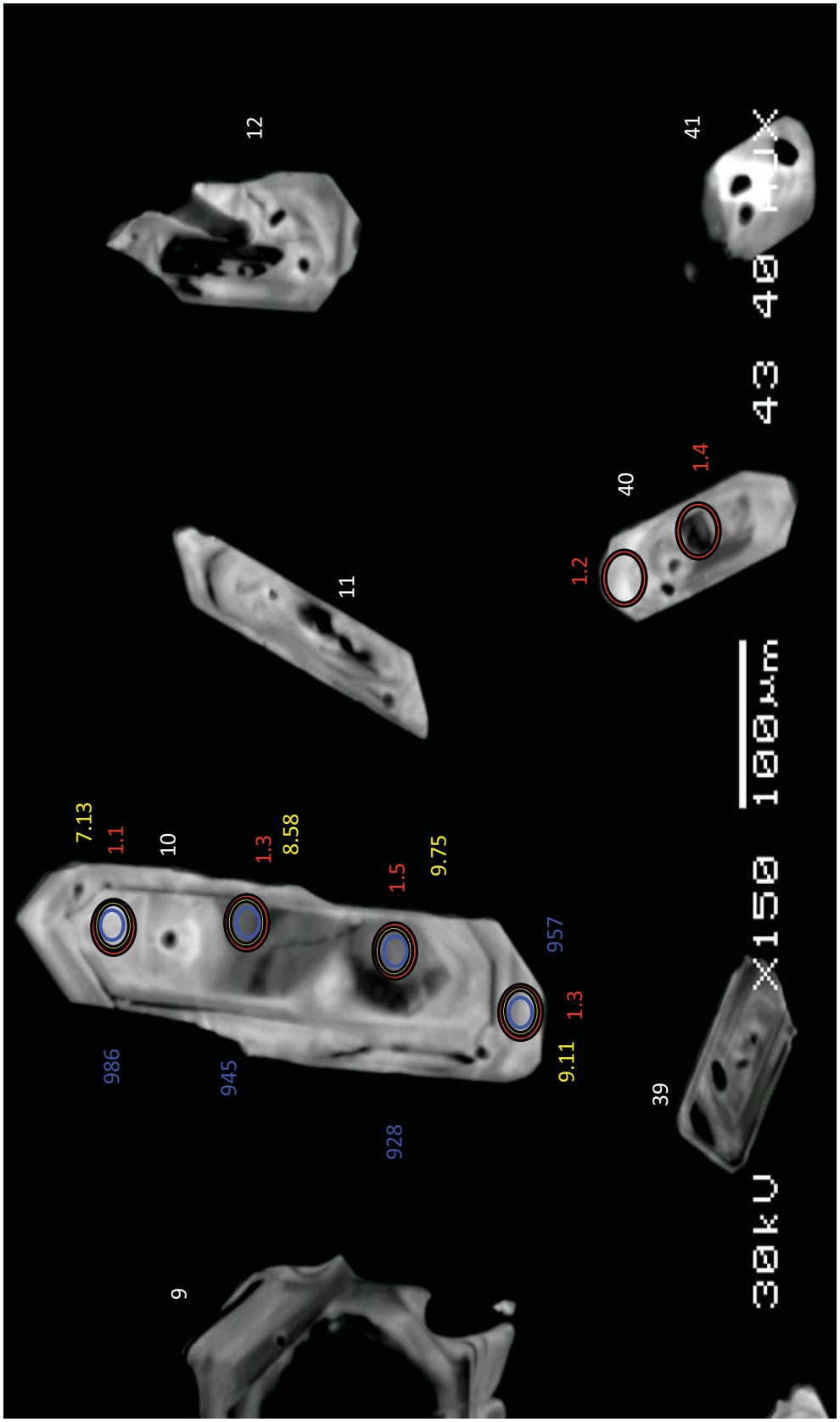
30kV X150 100µm
9
10
11
12
39
40
41
7.13
1.1
8.58
1.3
9.75
1.5
9.11
1.3
957
986
945
928
1.2
1.4

LCR

LCR-10

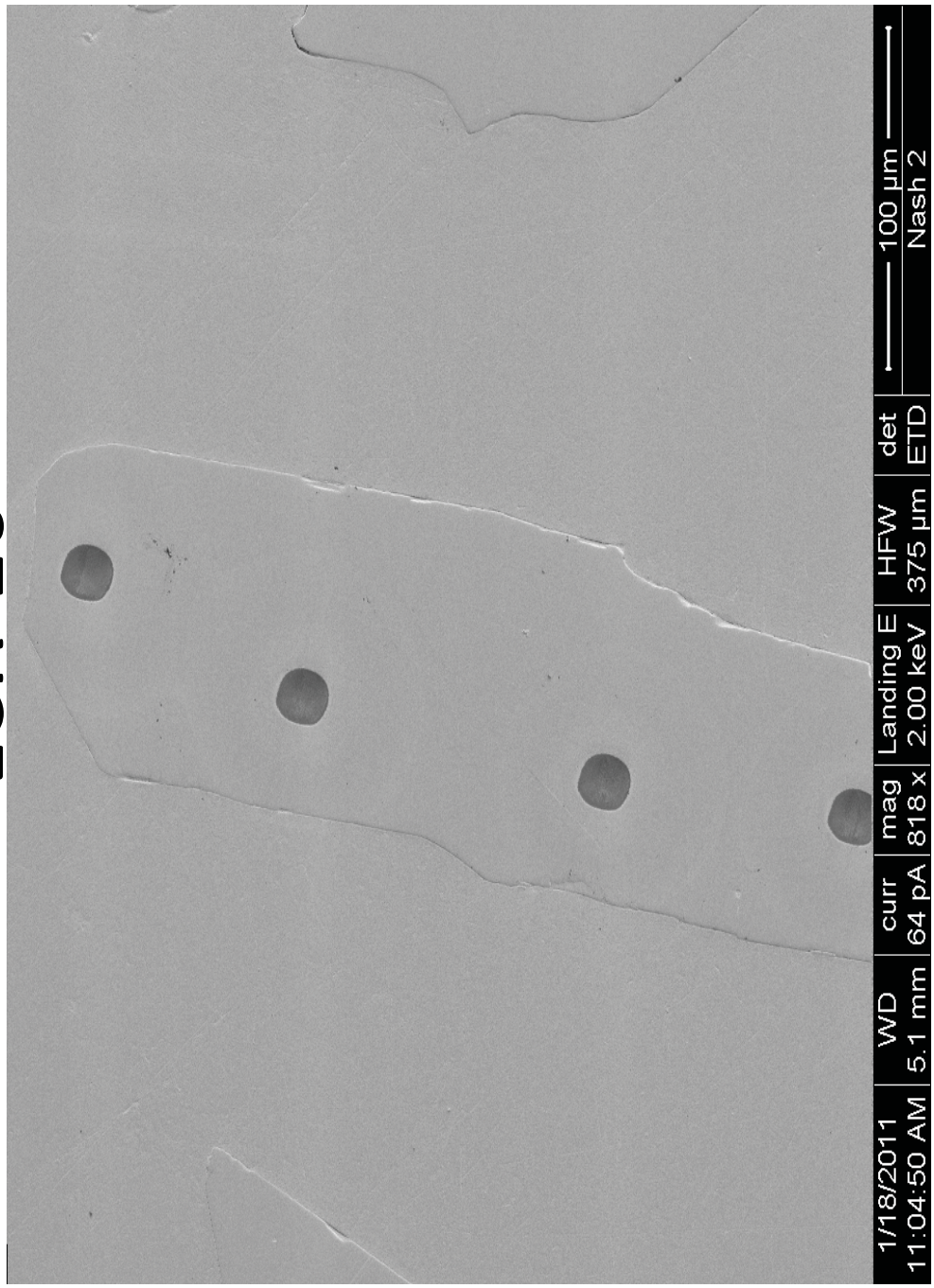
1/18/2011
11:04:50 AM
WD
5.1 mm
curr
64 pA
mag
818 x
Landing E
2.00 keV
HFW
375 µm
det
ETD
100 µm
Nash 2

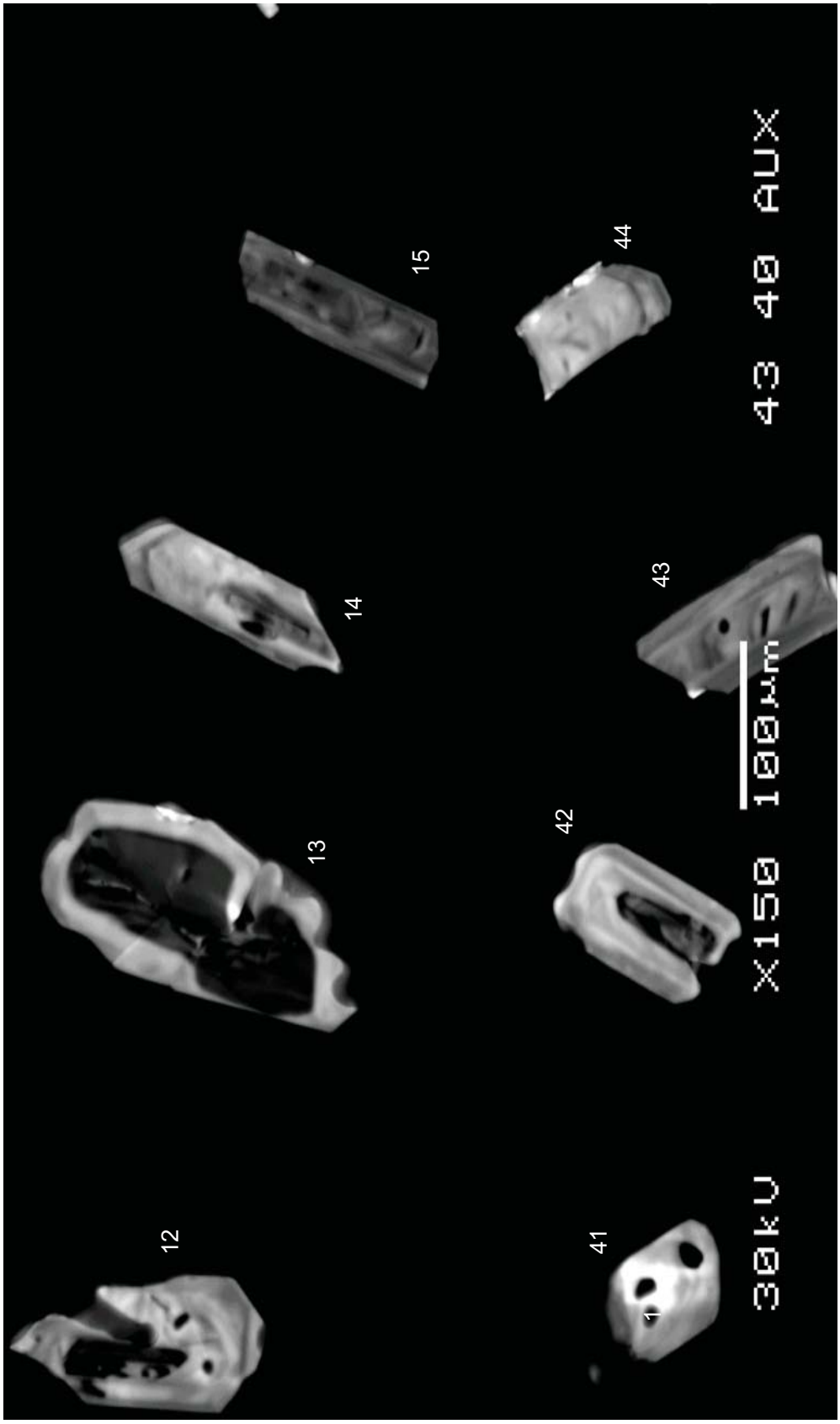
12
41
1
13
42
14
43
15
44
30kV X150 100µm 43 40 AUX
LCR

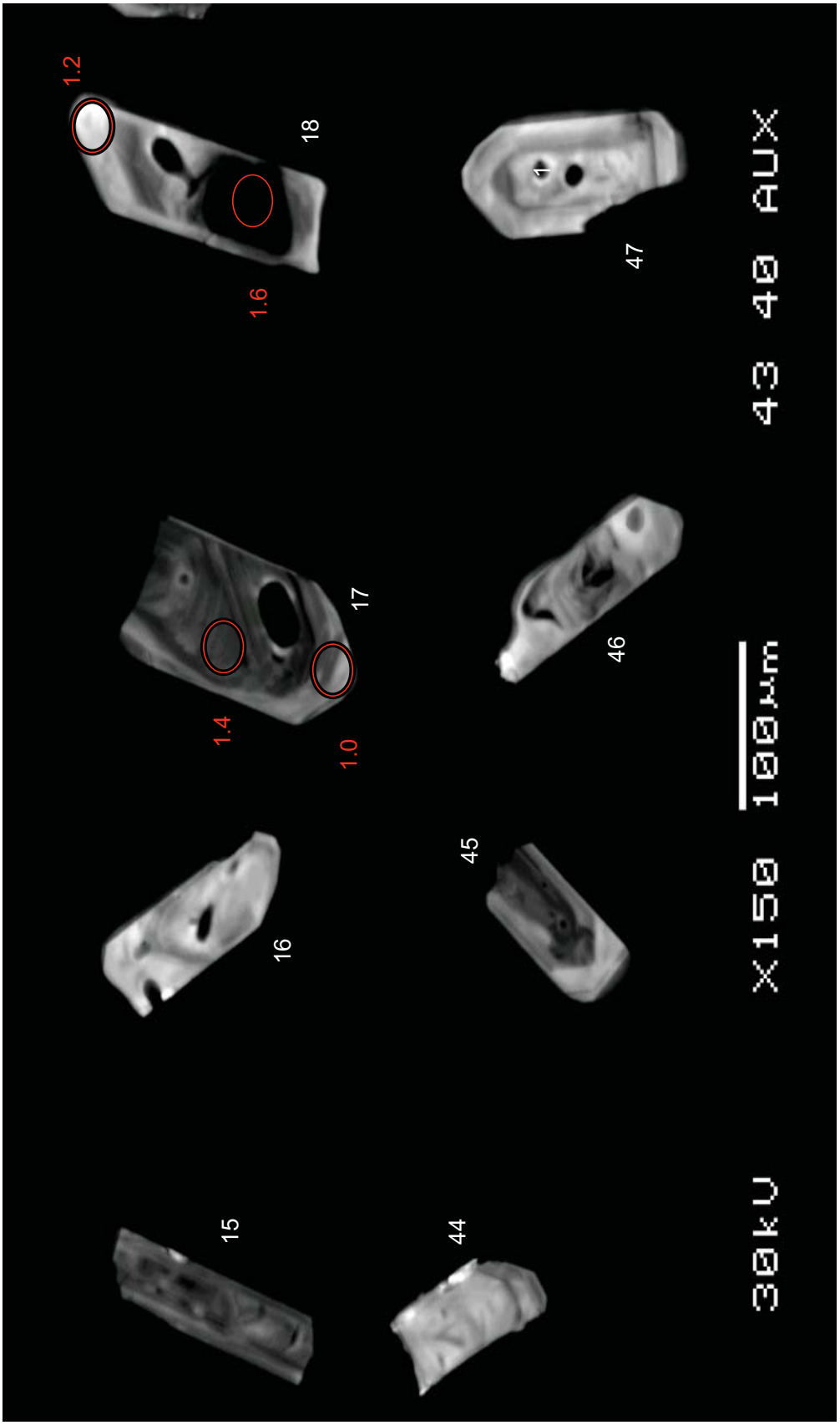
30kV X150 100µm 43 40 AUX
LCR
1.2
1.6
1.4
1.0
18
17
16
15
45
44
46
47
1

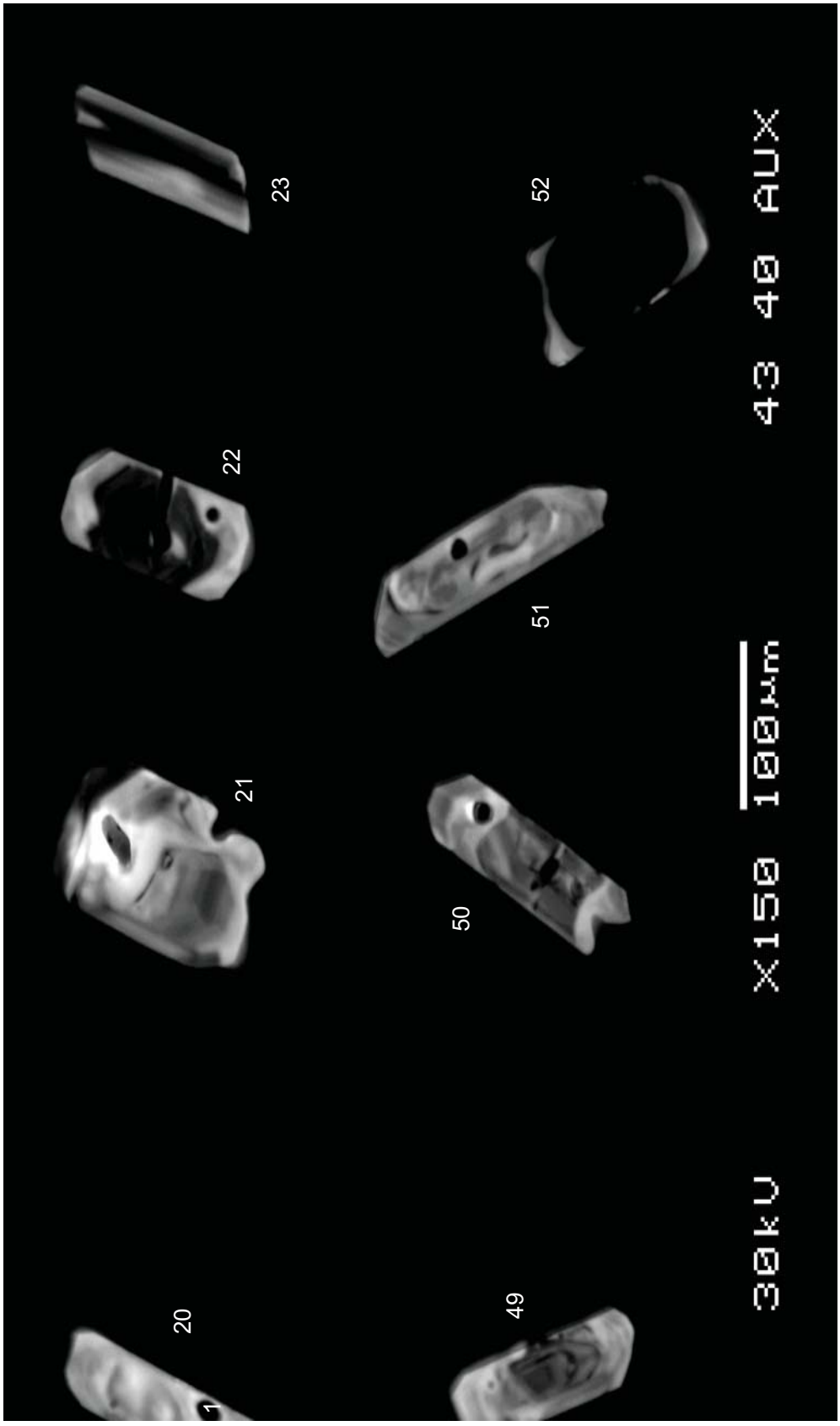

LCR


1
2
good
62
61
60
59
88
9.07
1.1
10.27
1.2
89
90
91
92
30kU X120 100µm
43 40 AUX

LCR

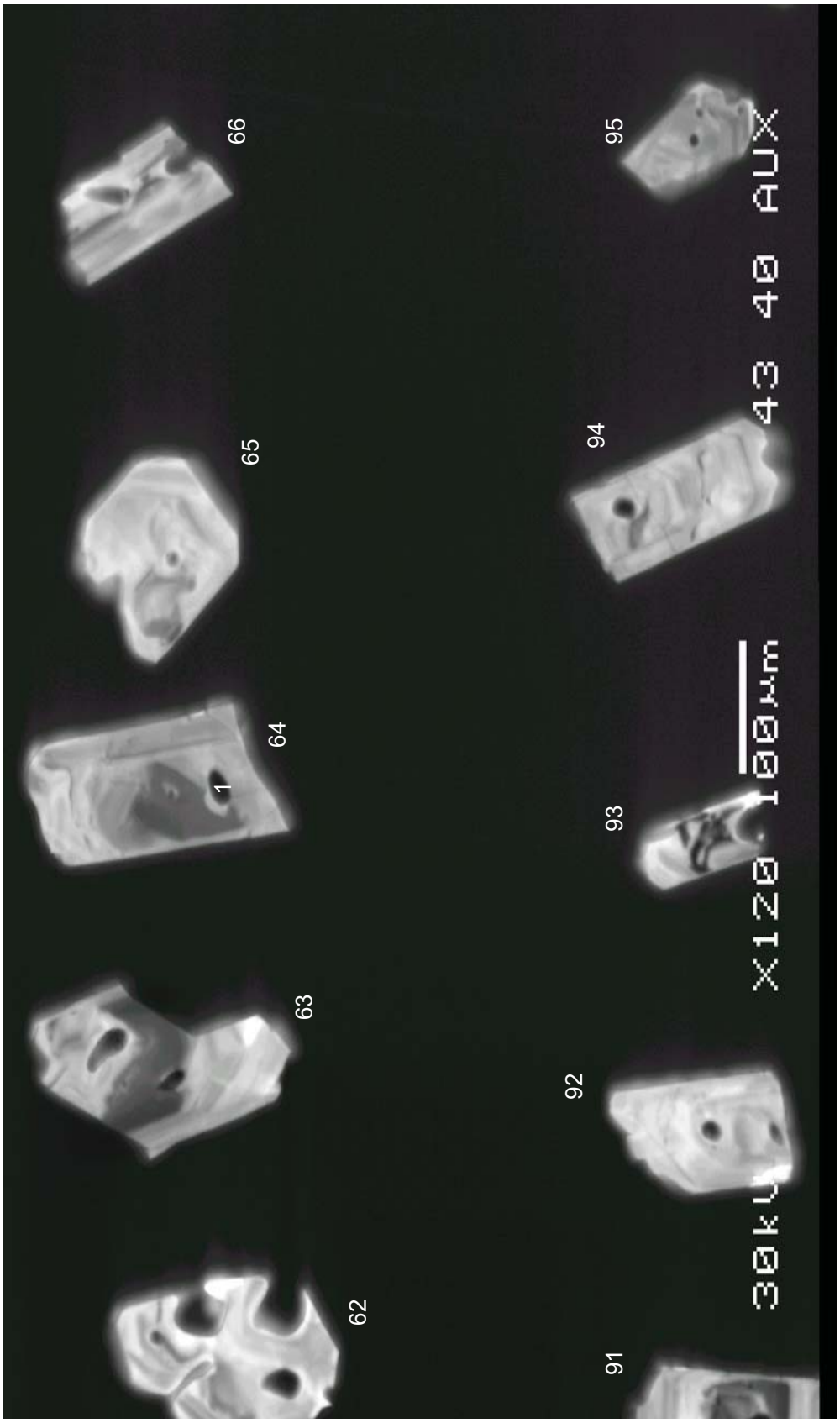
LCR
30kV X1,200 100µm
AUX 04 34 03
1
62
63
64
65
66
91
92
93
94
95

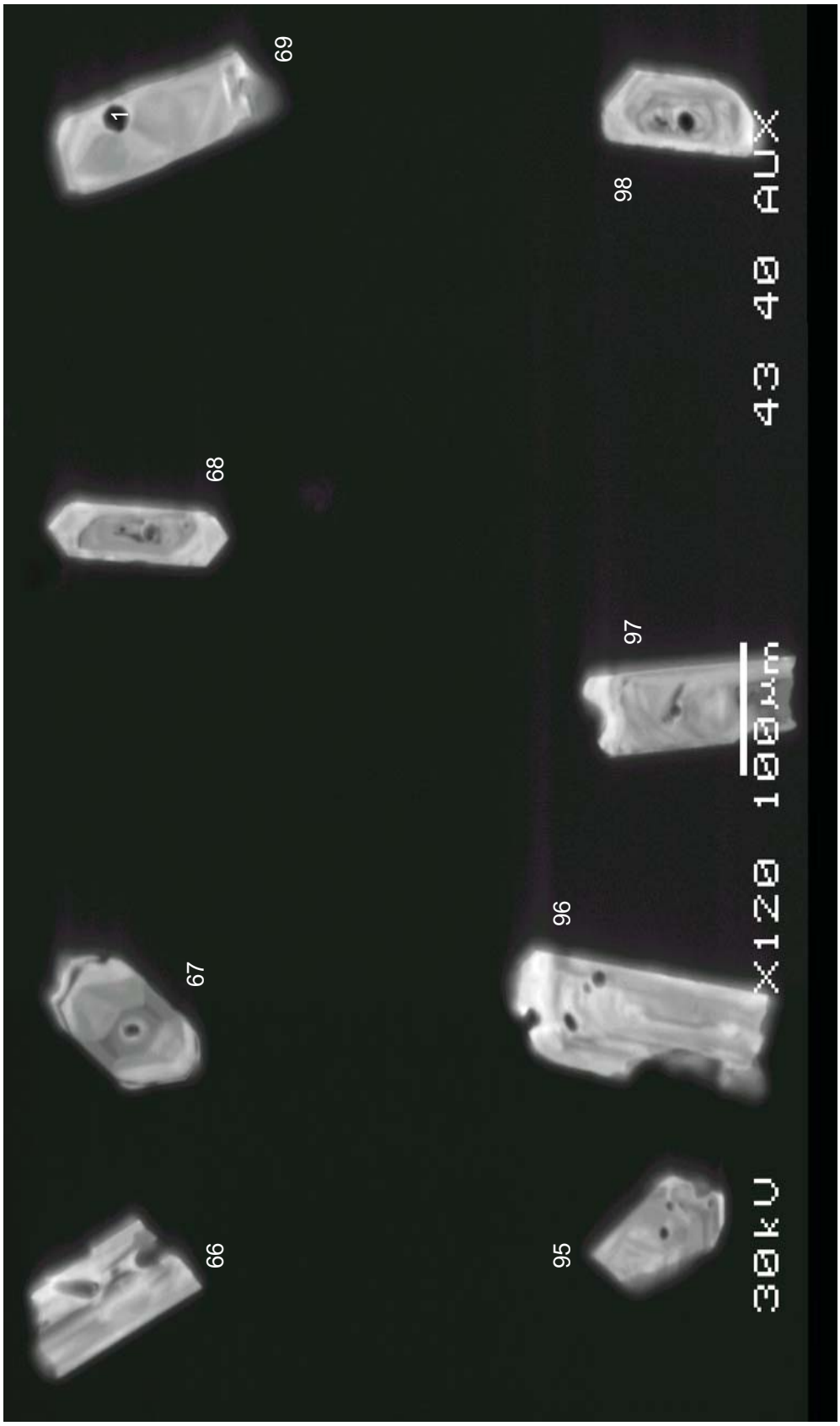

LCR

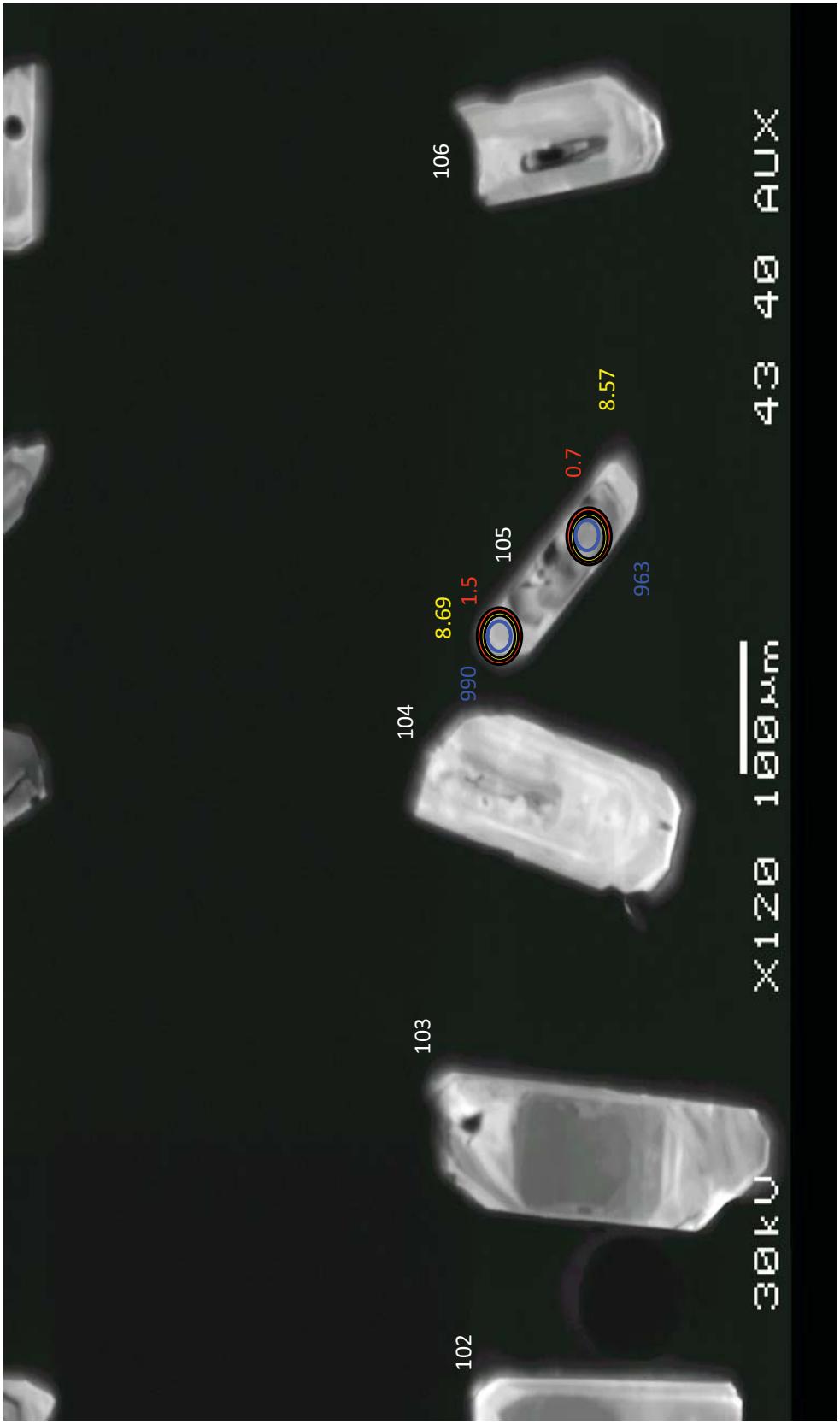
30kV X120 100µm 43 40 AUX
102
103
104
105
106
990
8.69
1.5
0.7
8.57
963

LCR

LCR-105

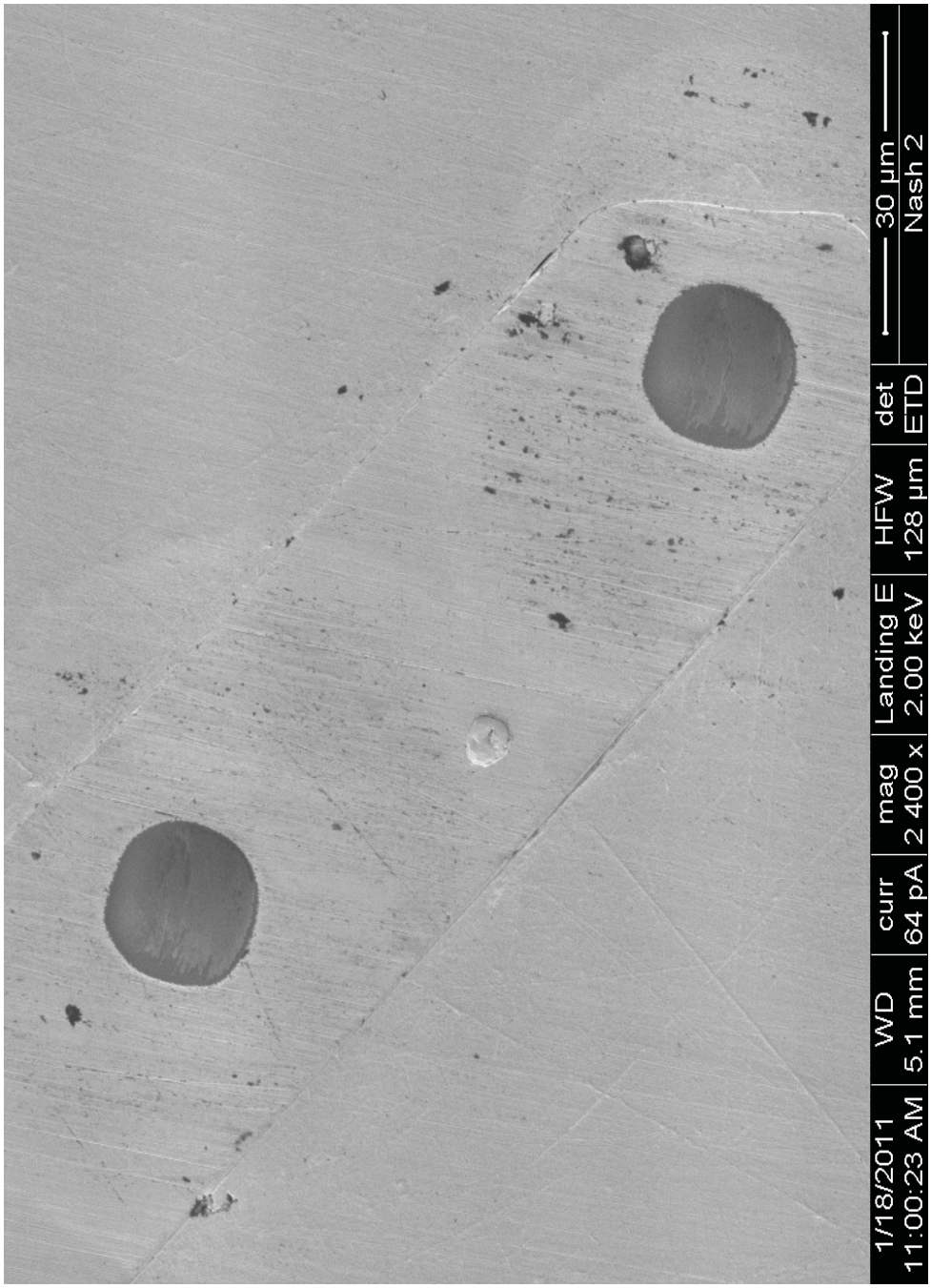
1/18/2011
11:00:23 AM
WD
5.1 mm
curr
64 pA
mag
2 400 x
Landing E
2.00 keV
HFW
128 µm
det
ETD
30 µm
Nash 2

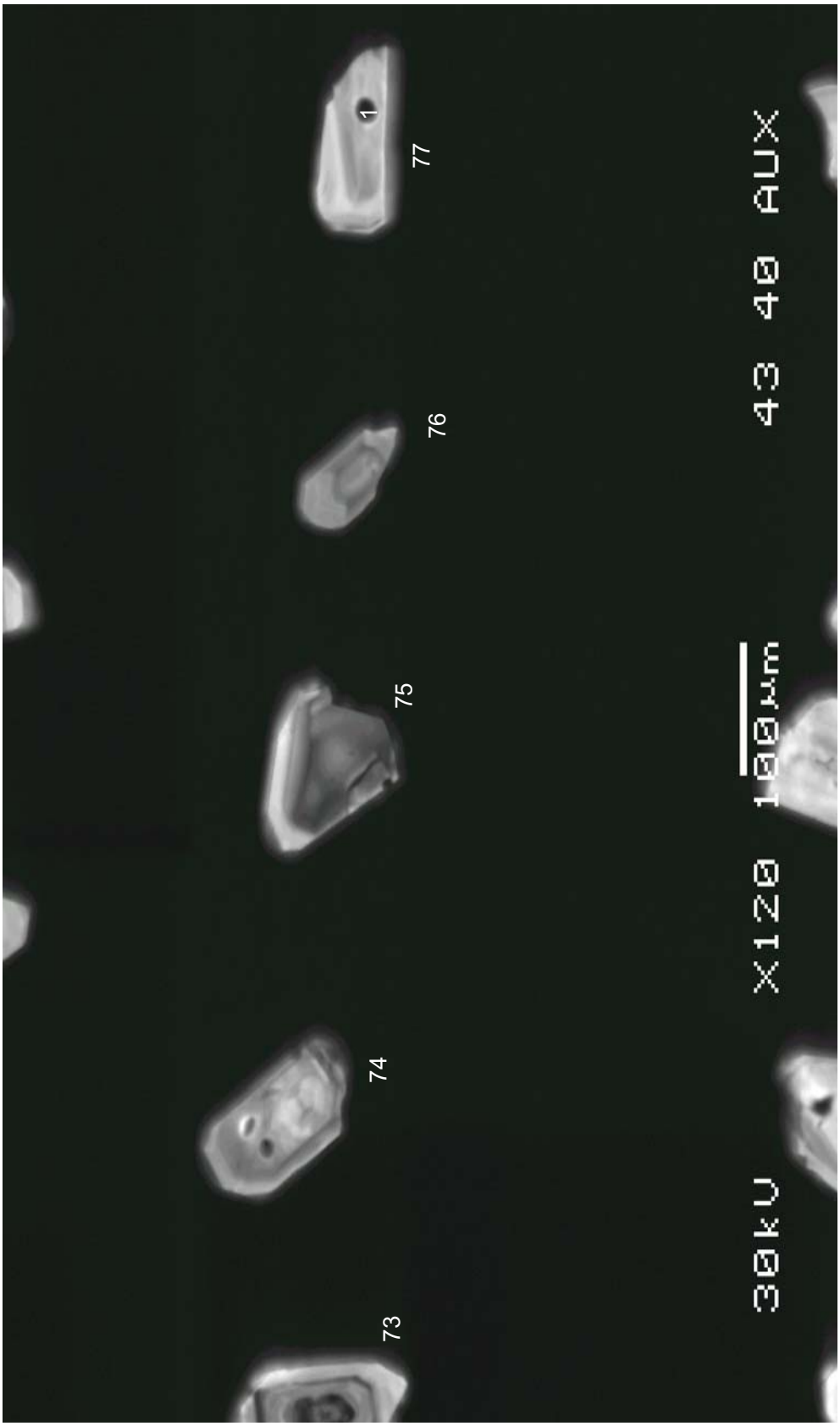

LCR

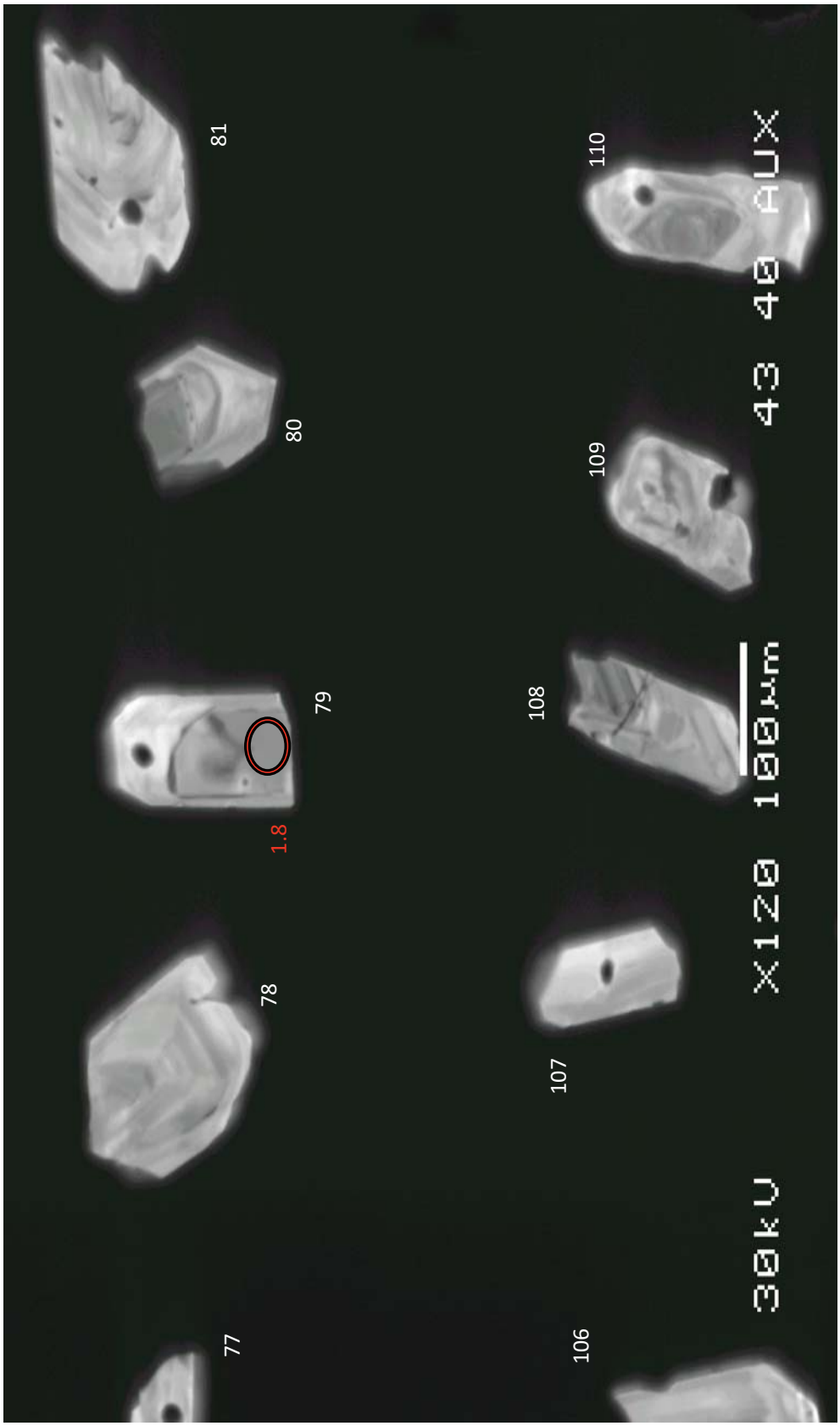

LCR

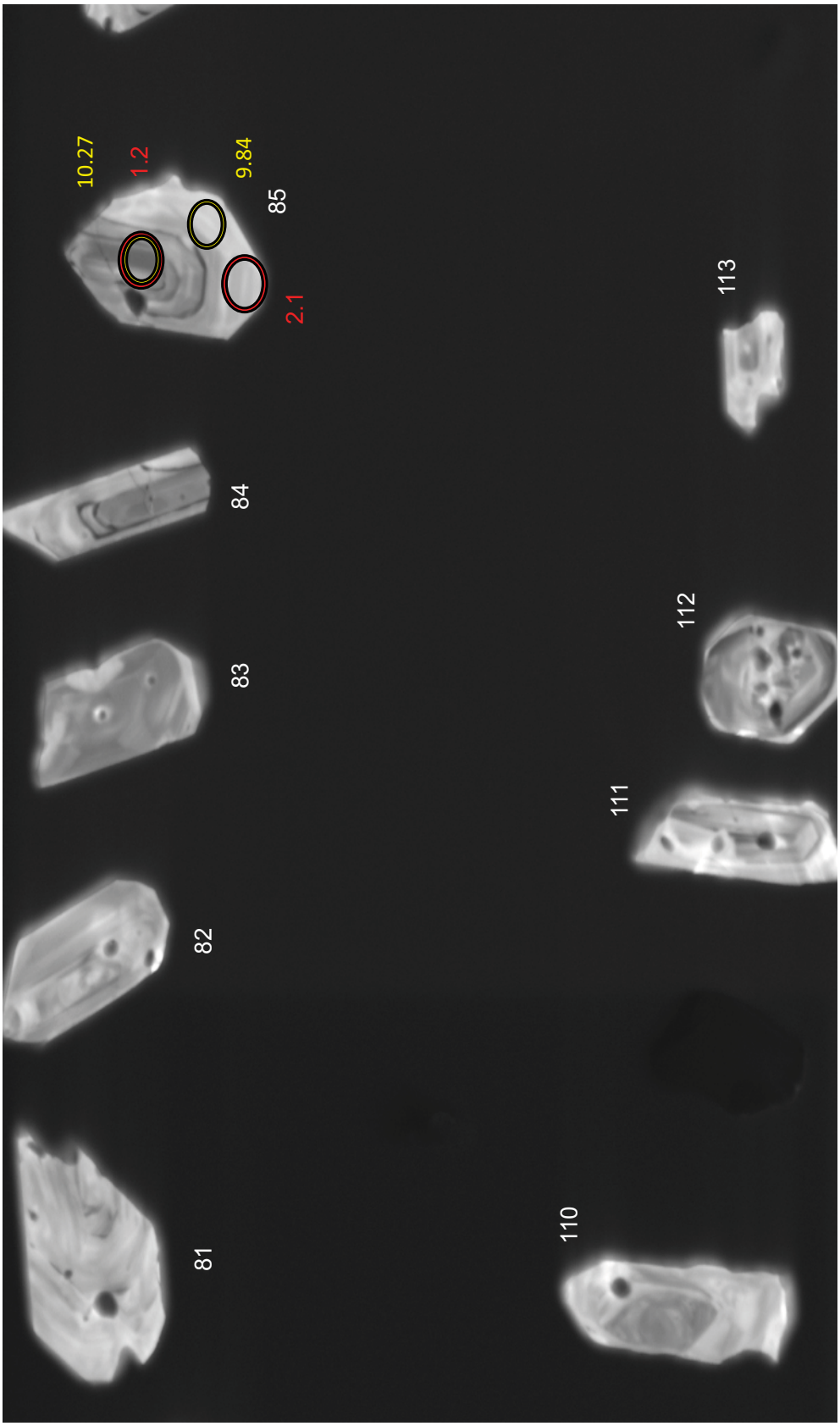
10.27
1.2
9.84
85
2.1
84
83
82
81
110
111
112
113
LCR

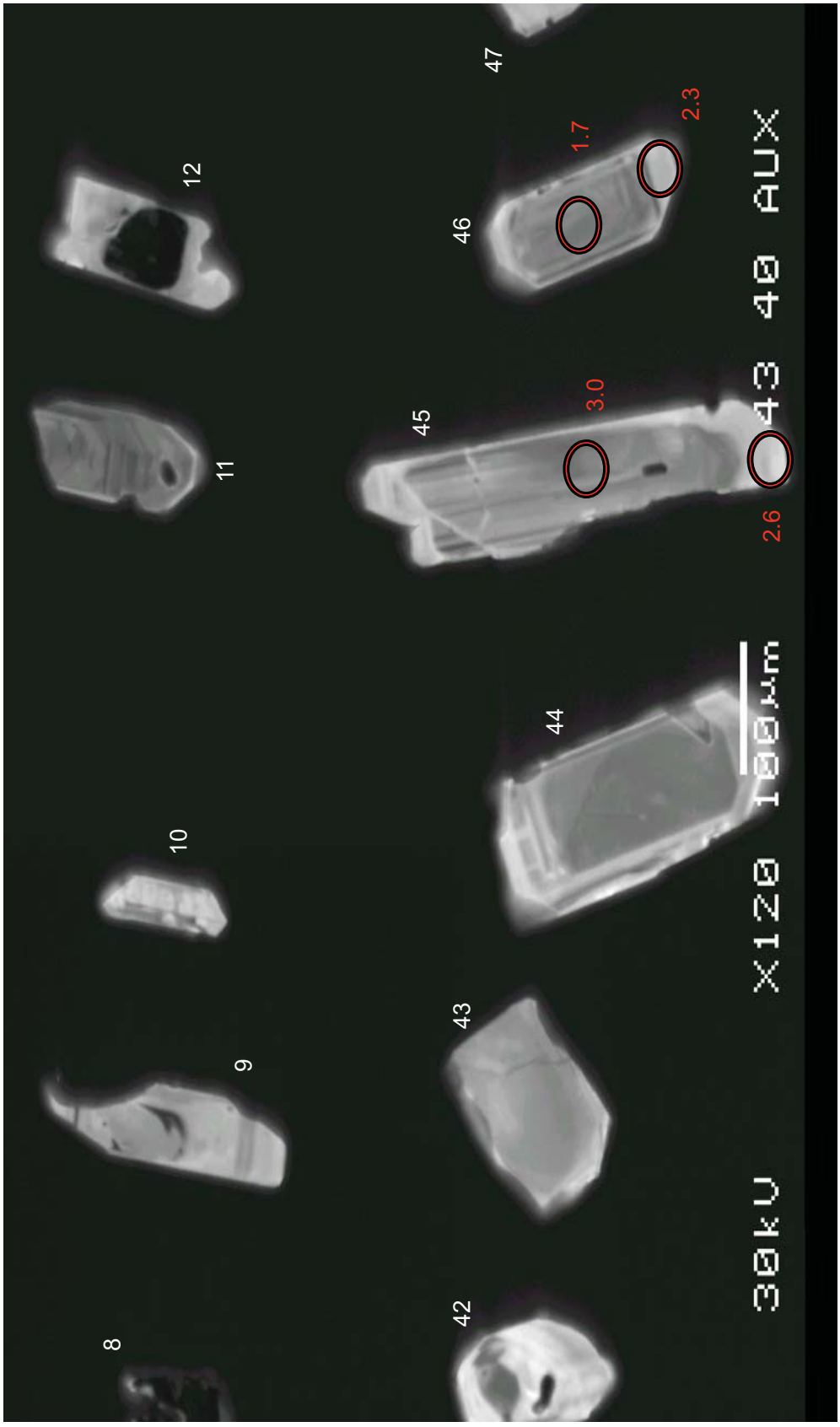

PCR

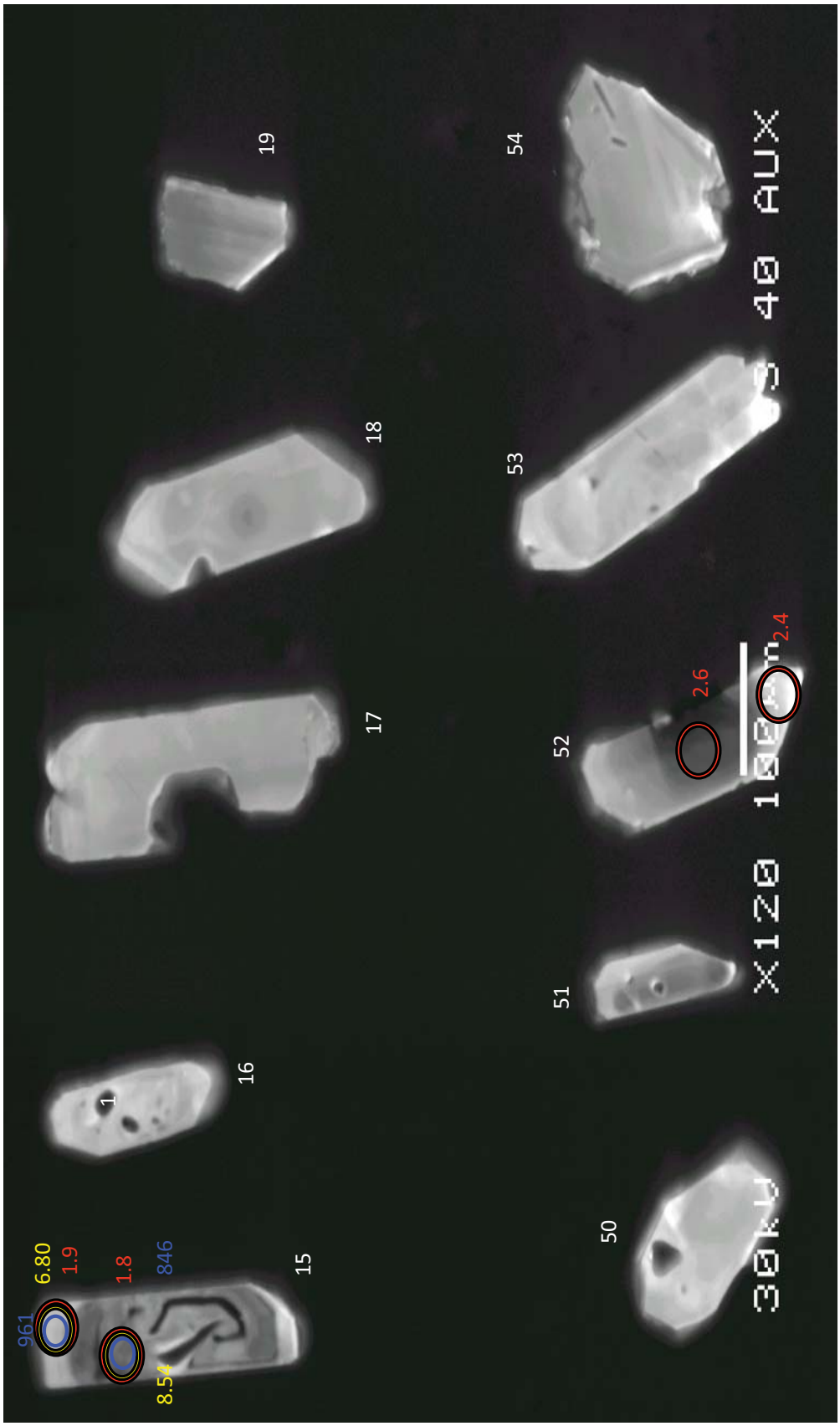
961
6.80
1.9
1.8
846
8.54
15
16
1
50
51
52
17
18
53
54
19
2.6
2.4
30kV X1200 10μm
40 AUX

PCR

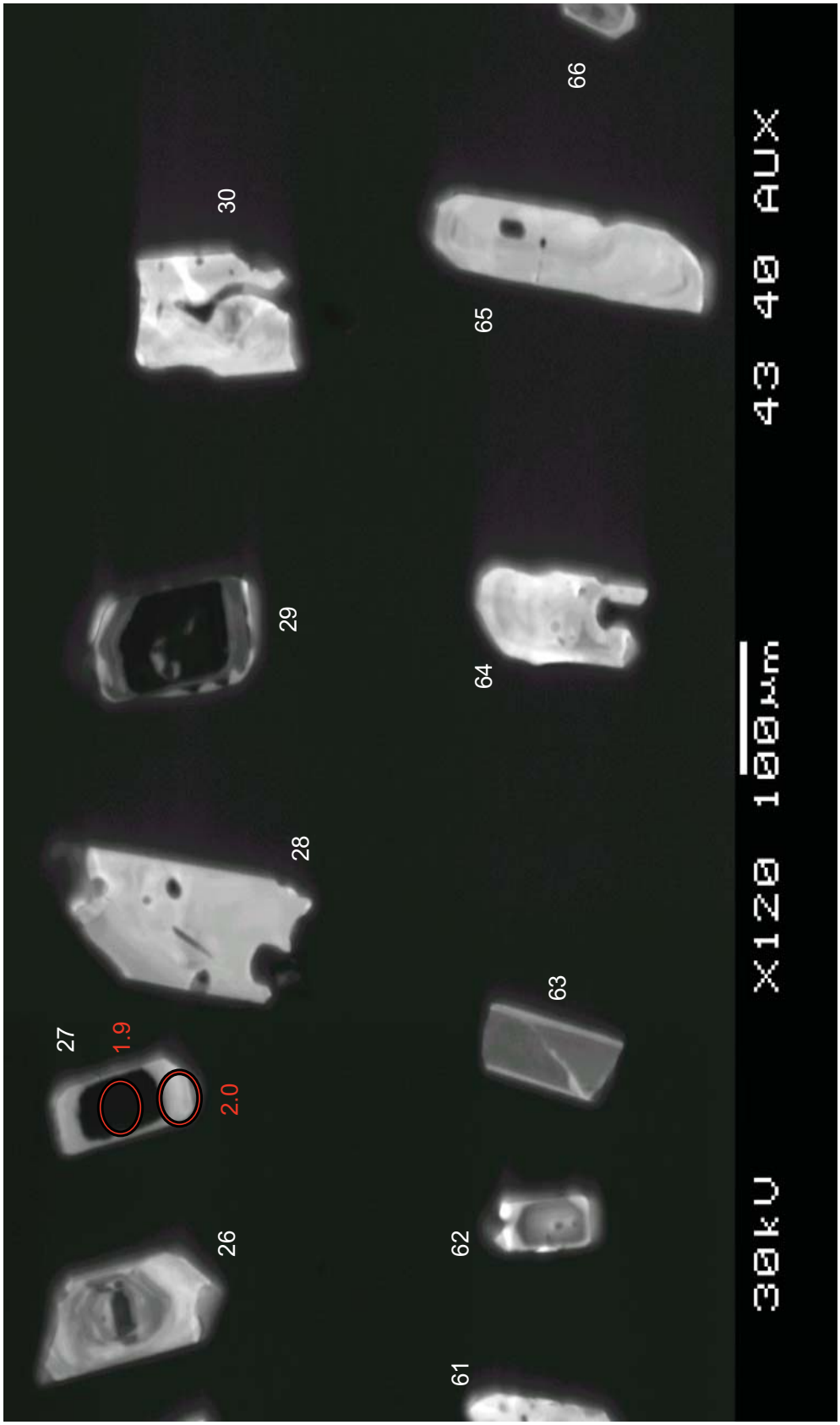

PCR

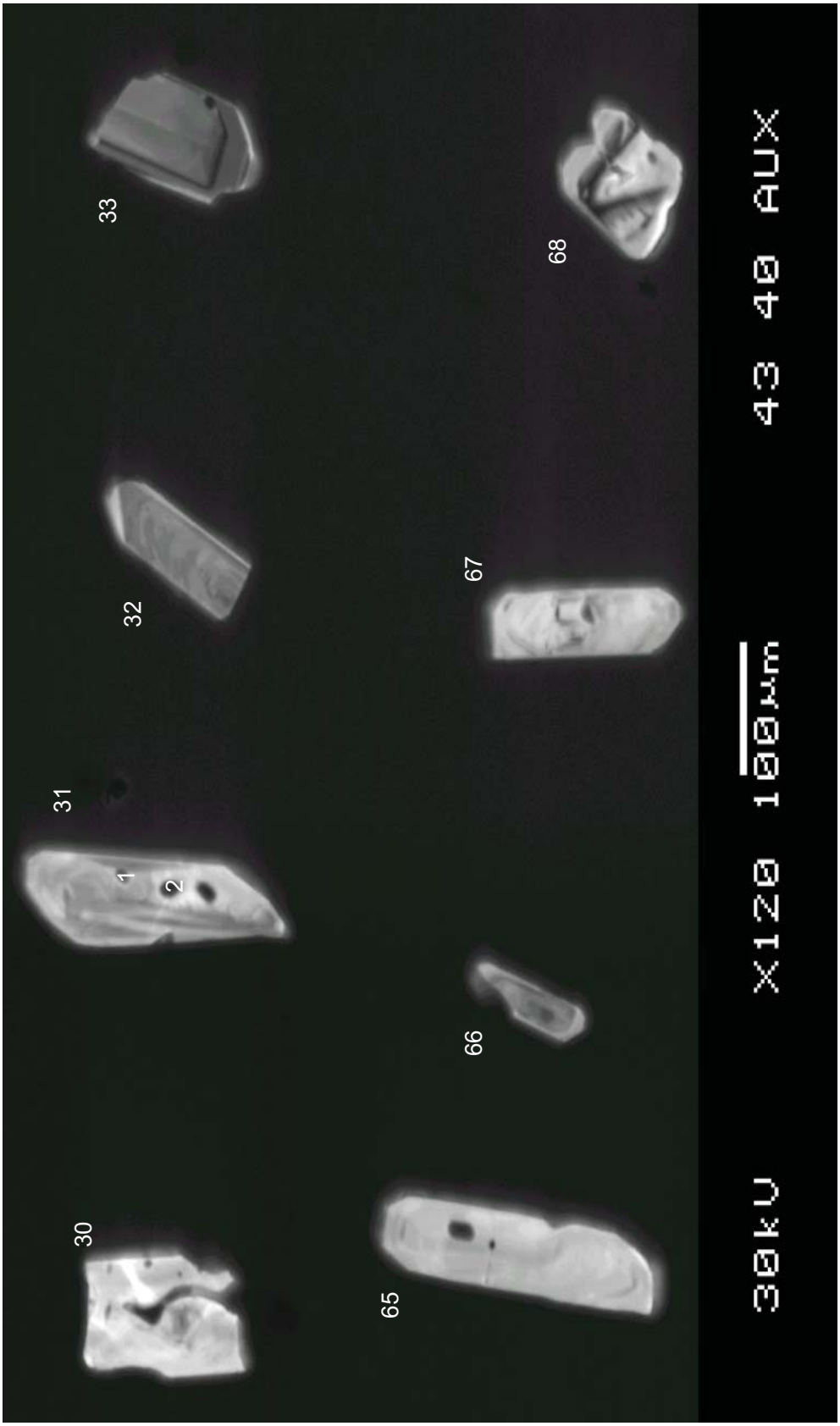

PCR

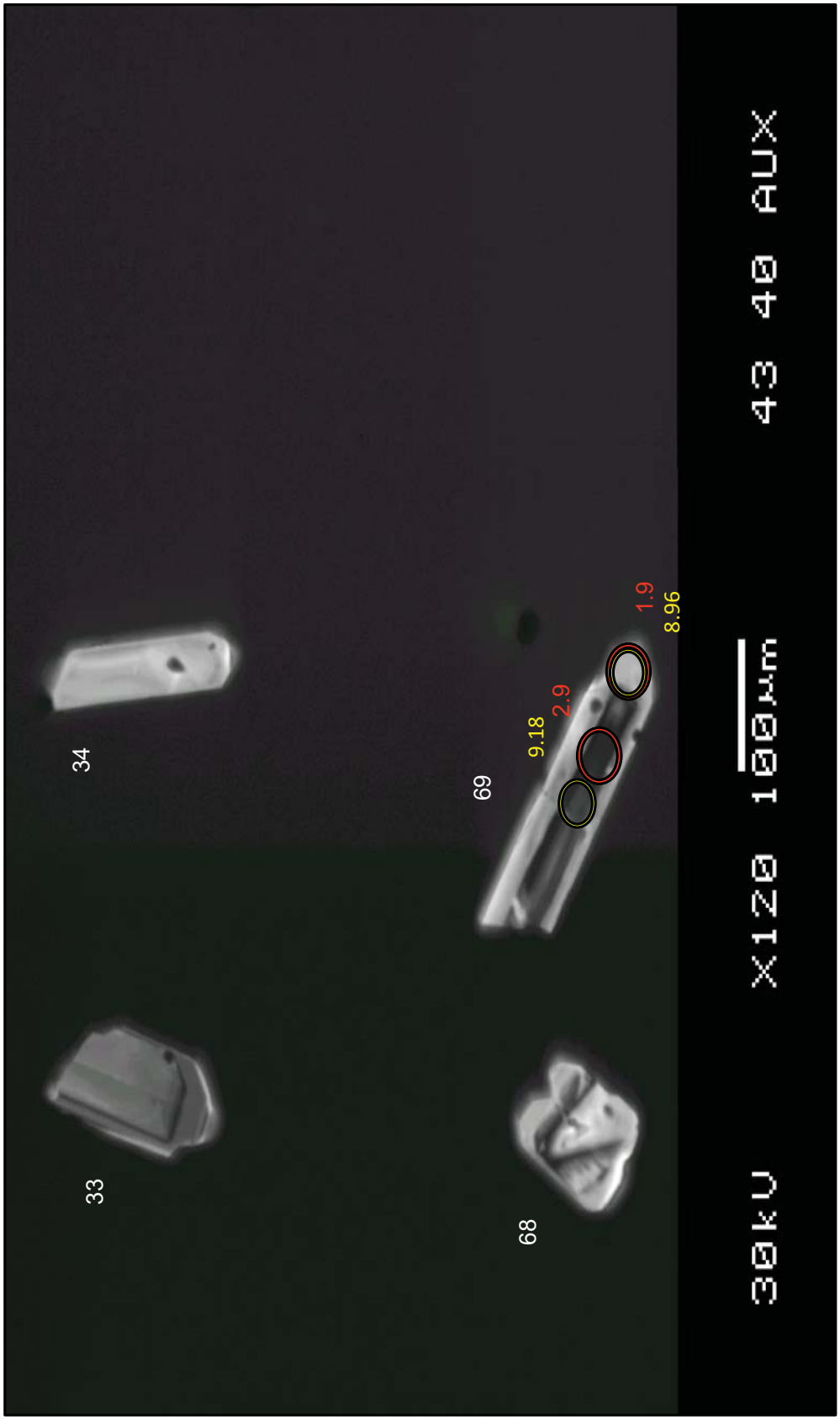

PCR

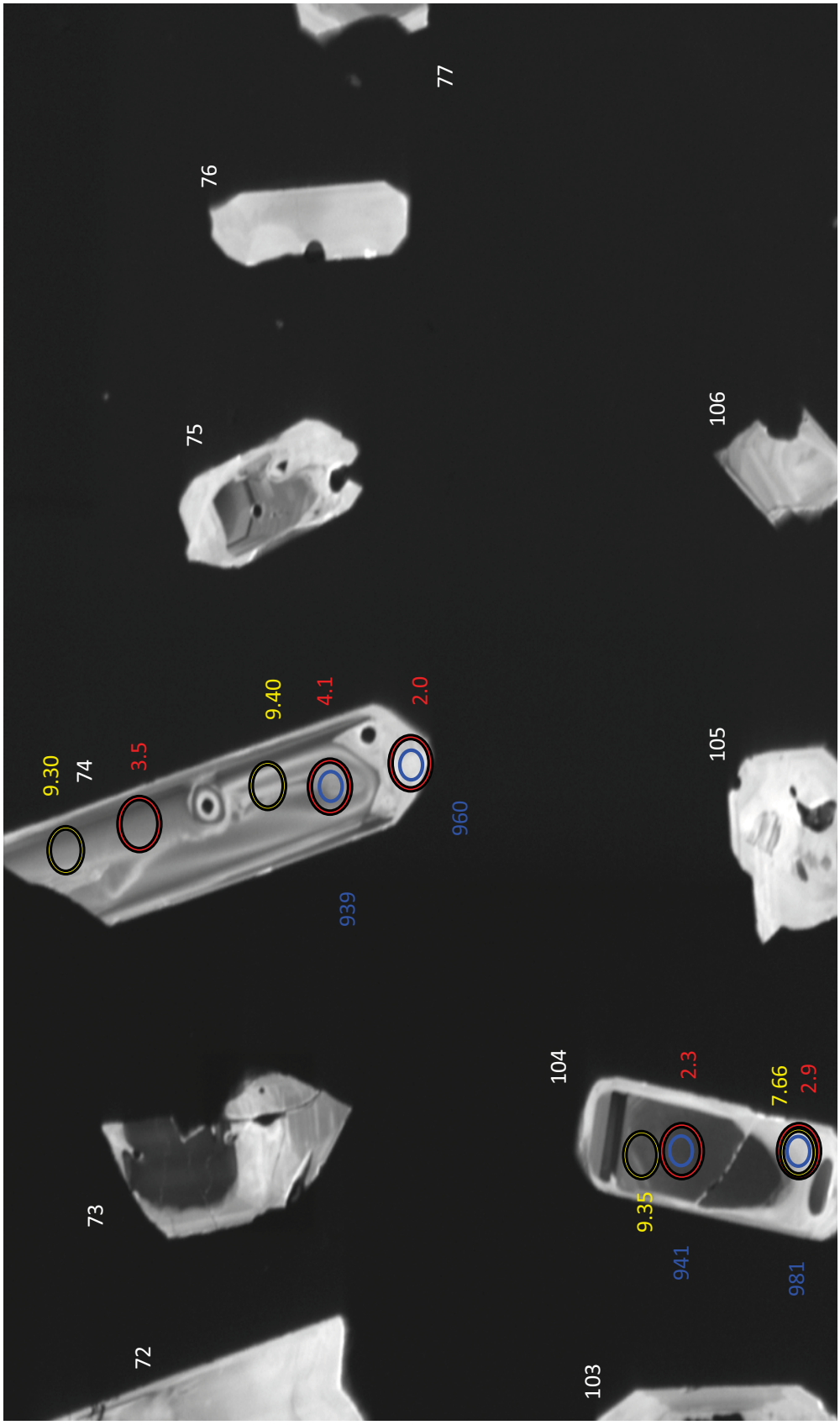
72
73
74
75
76
77
103
104
105
106
9.30
3.5
9.40
4.1
2.0
939
960
9.35
2.3
7.66
2.9
941
981

PCR

PCR-74

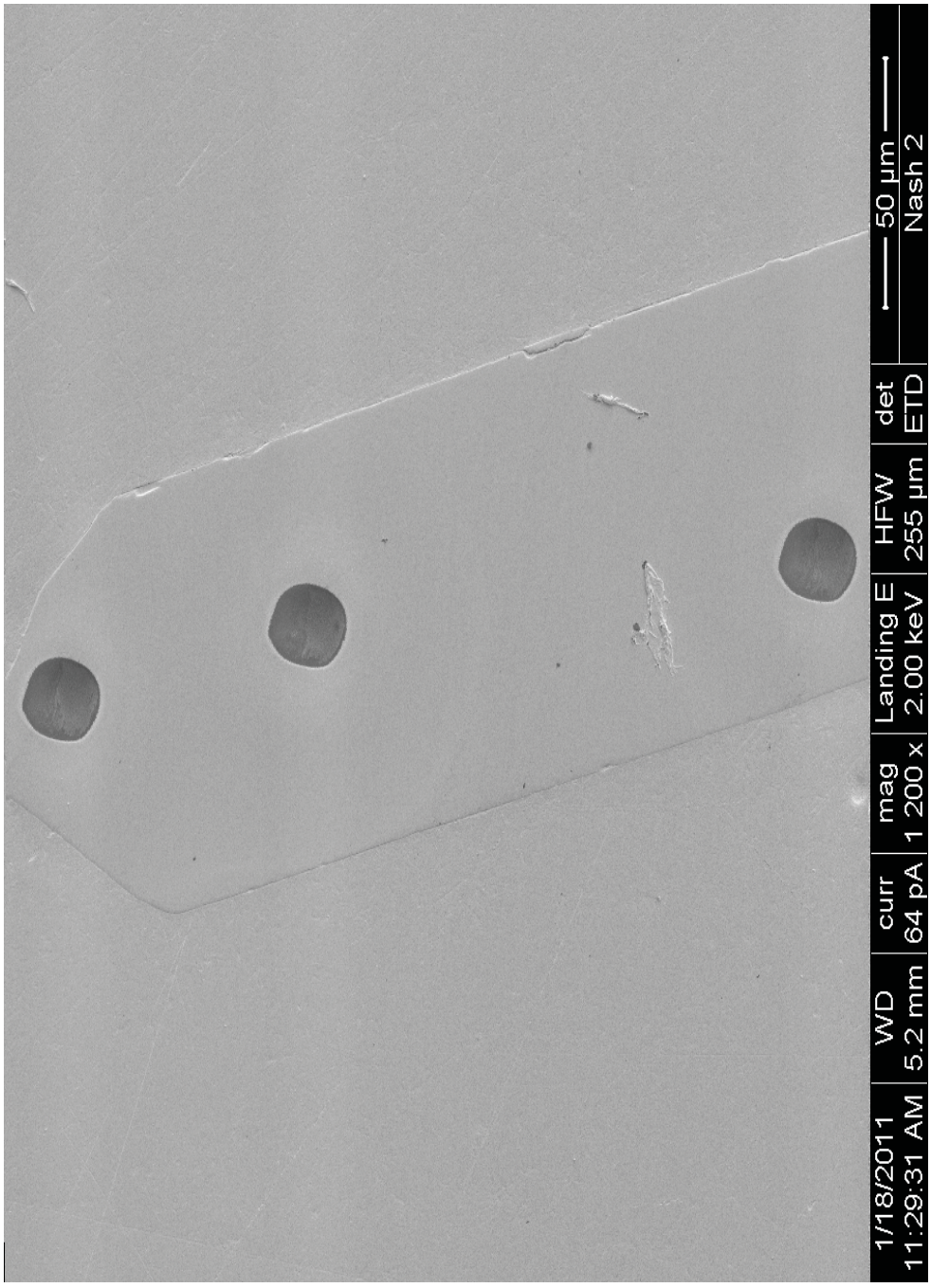
1/18/2011
11:29:31 AM
WD
5.2 mm
curr
64 pA
mag
1 200 x
Landing E
2.00 keV
HFW
255 µm
det
ETD
50 µm
Nash 2

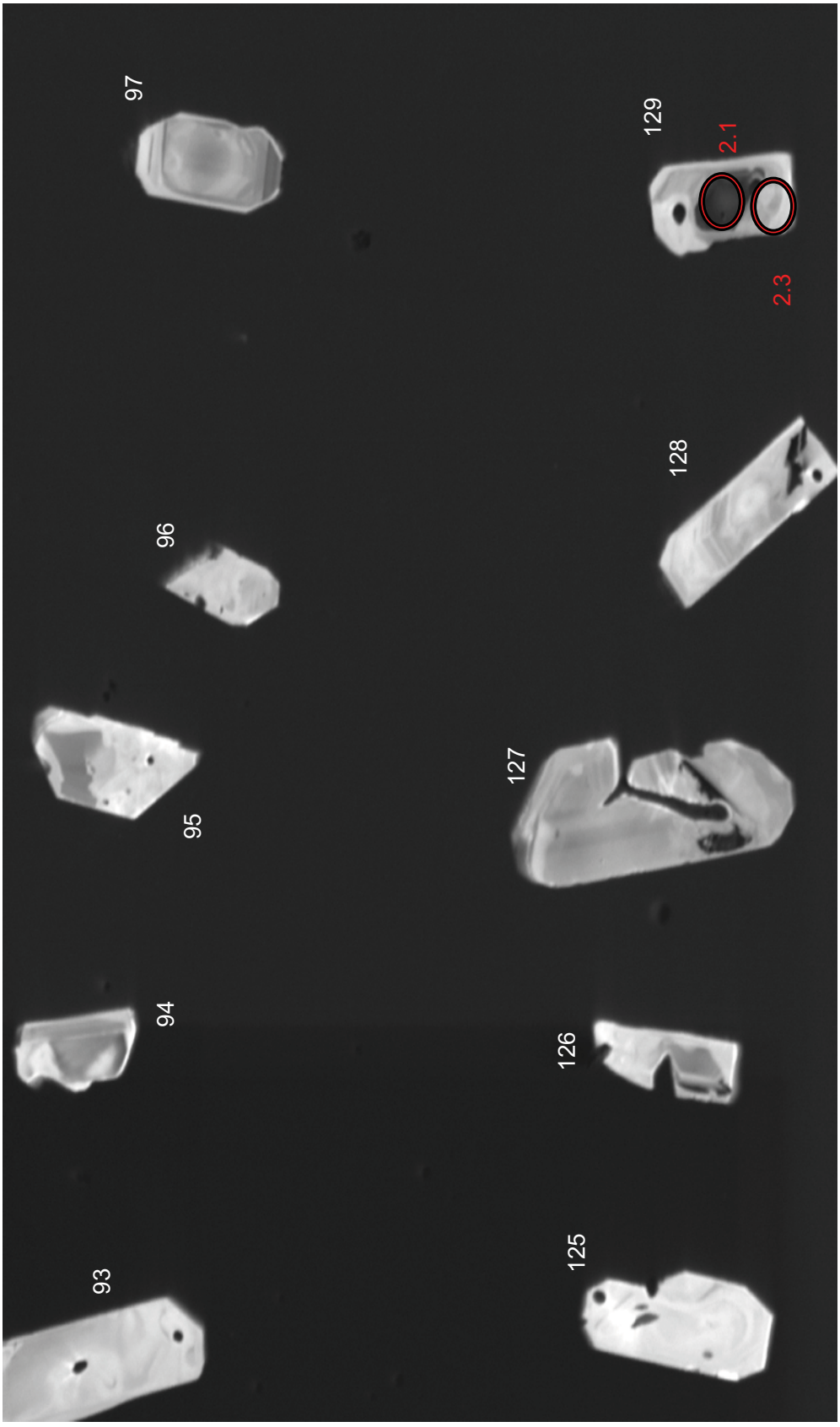

PCR

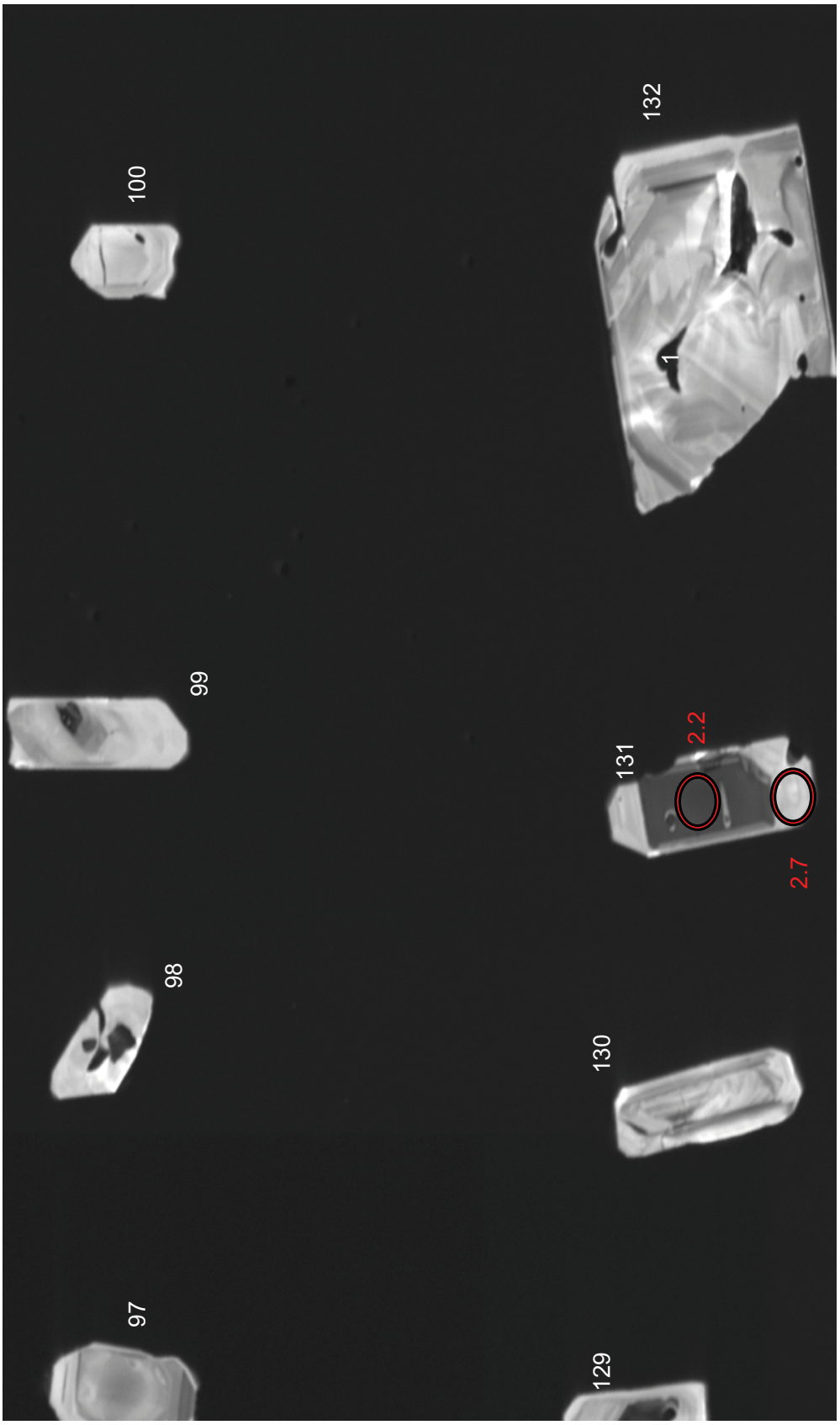
97
98
99
100
129
130
131
132
1
2.2
2.7
PCR

PCR-104

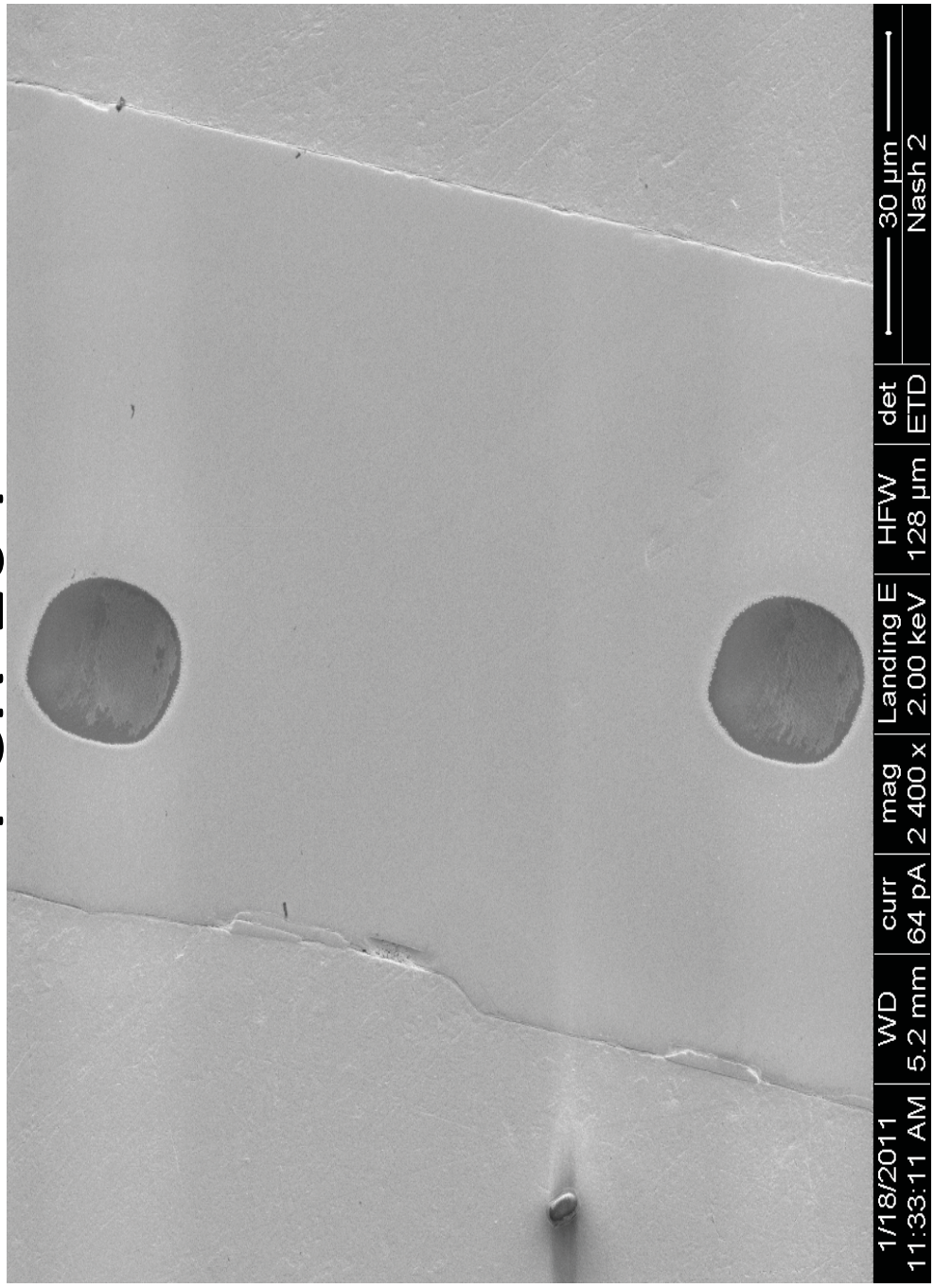
1/18/2011
11:33:11 AM
WD
5.2 mm
curr
64 pA
mag
2 400 x
Landing E
2.00 keV
HFW
128 µm
det
ETD
30 µm
Nash 2

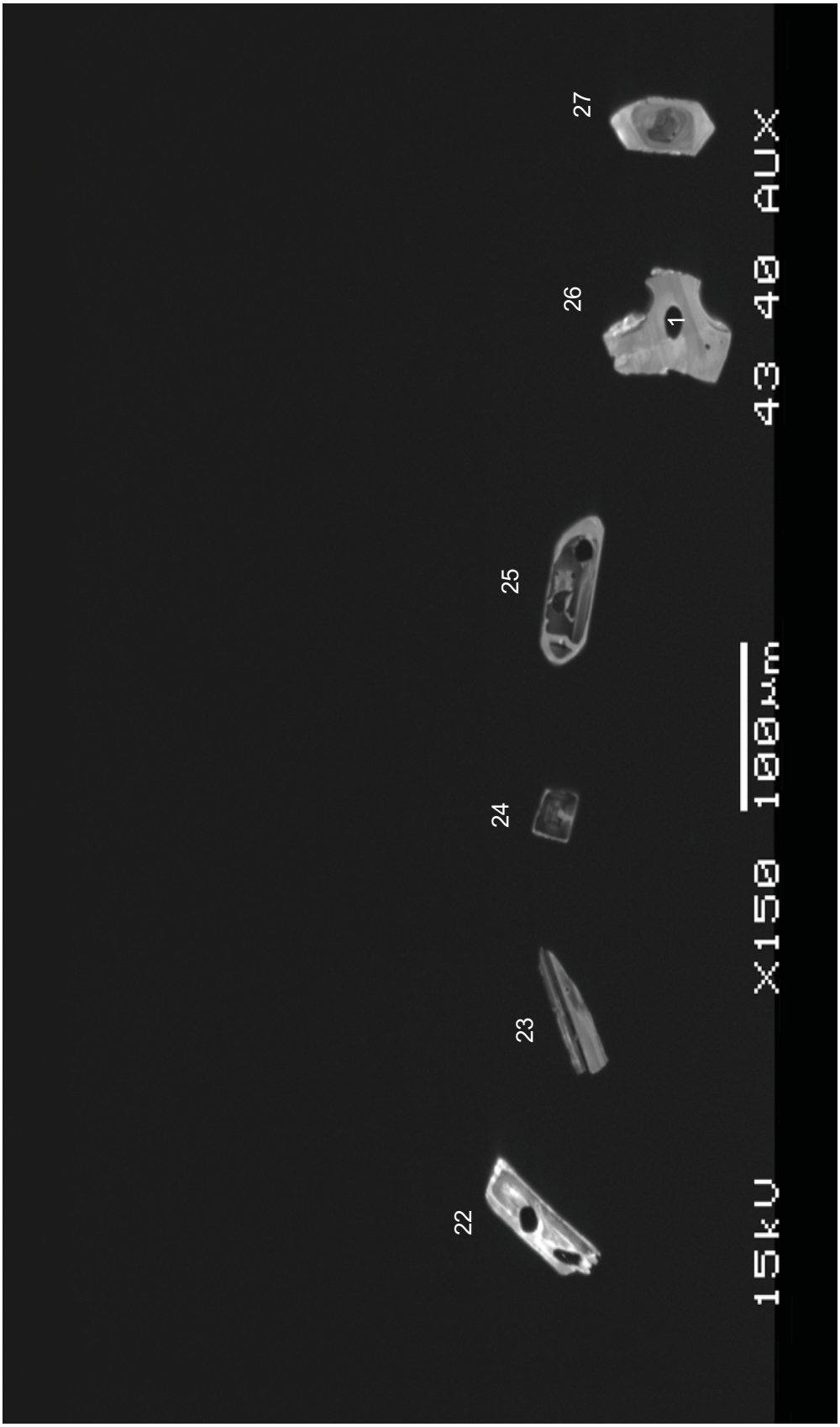

MCR

MCR-26-1

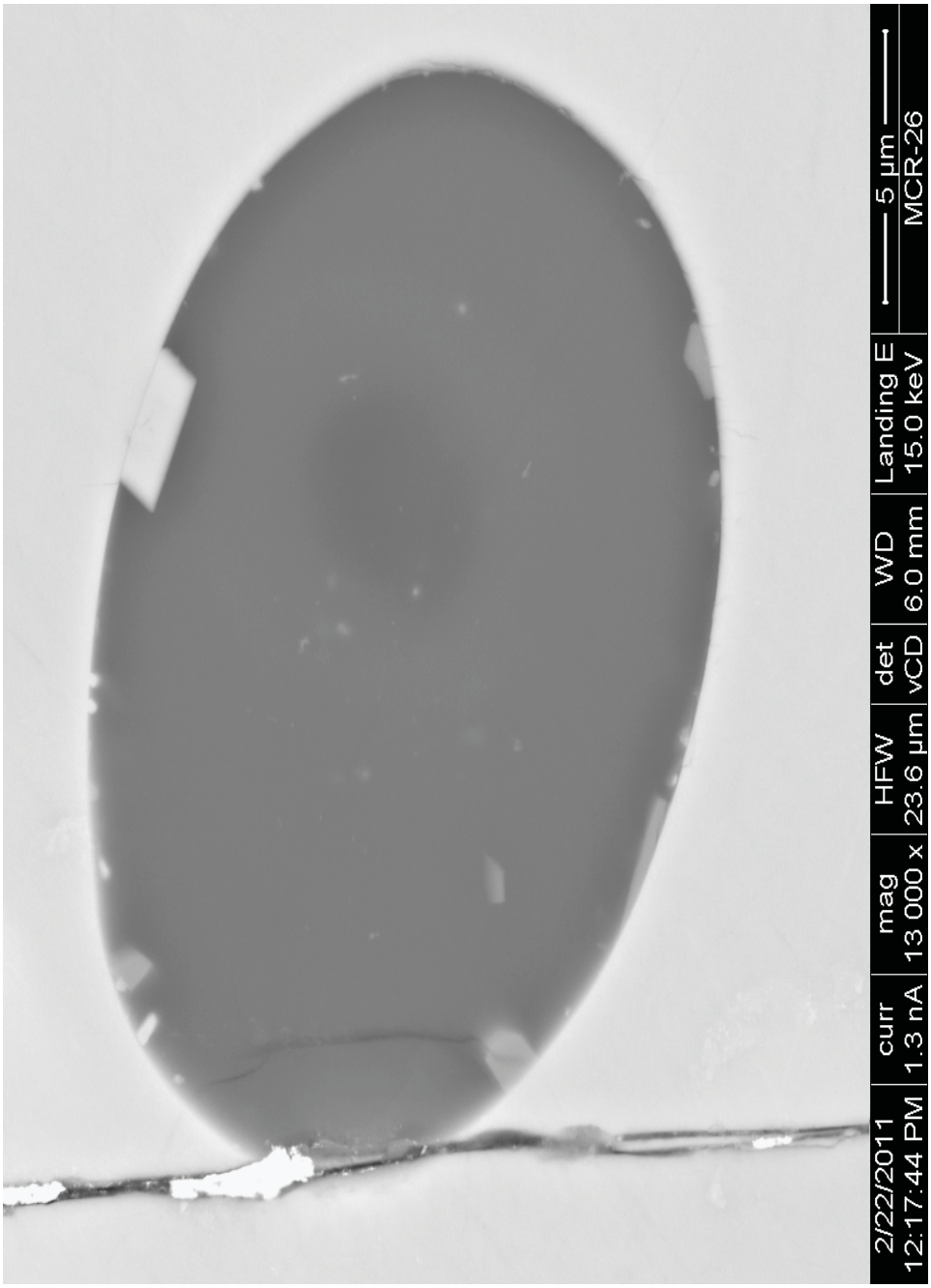
2/22/2011
12:17:44 PM
curr
1.3 nA
mag
13 000 x
HFW
23.6 µm
det
vCD
WD
6.0 mm
Landing E
15.0 keV
5 µm
MCR-26

MCR-26-1
EDS Reading

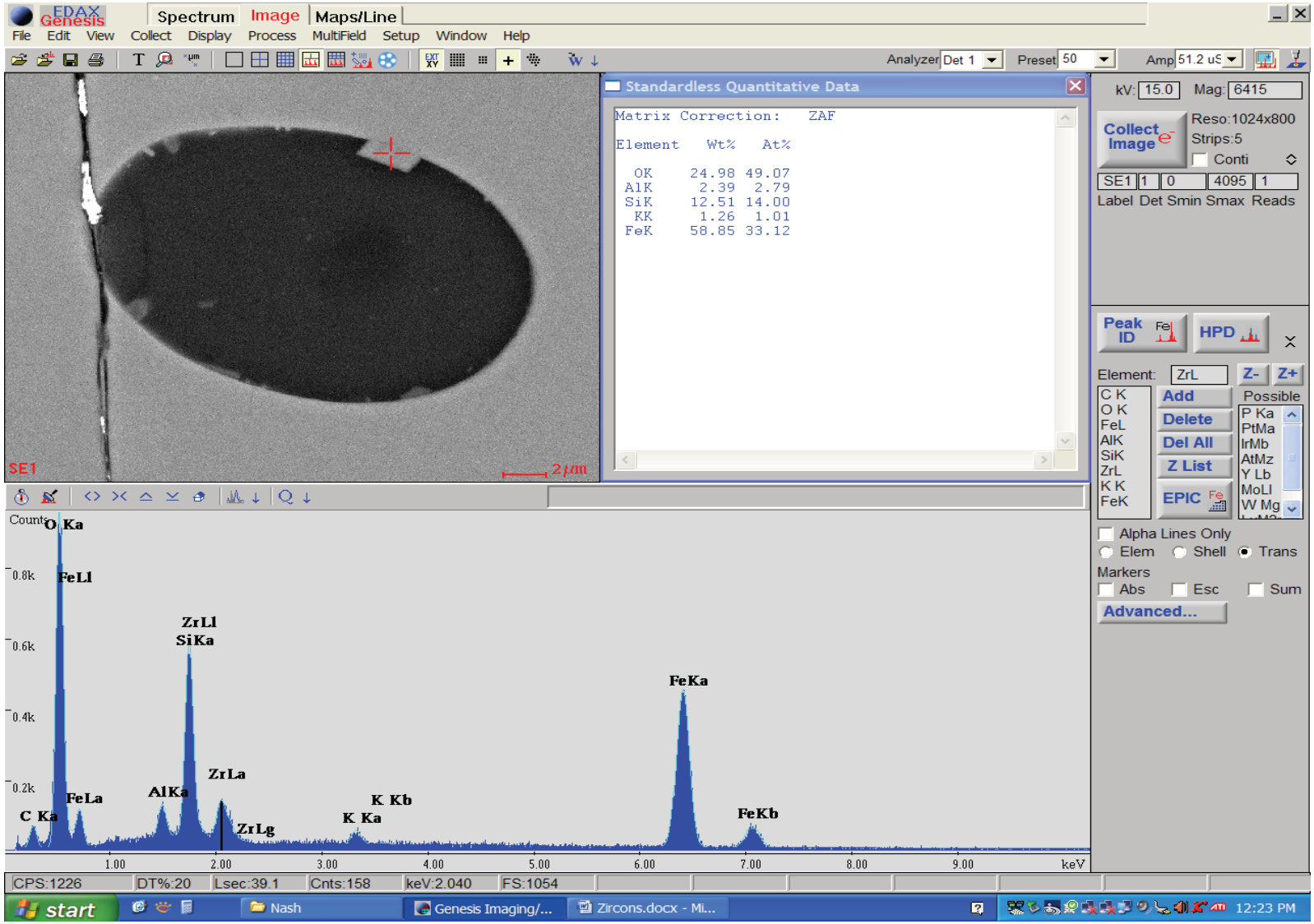

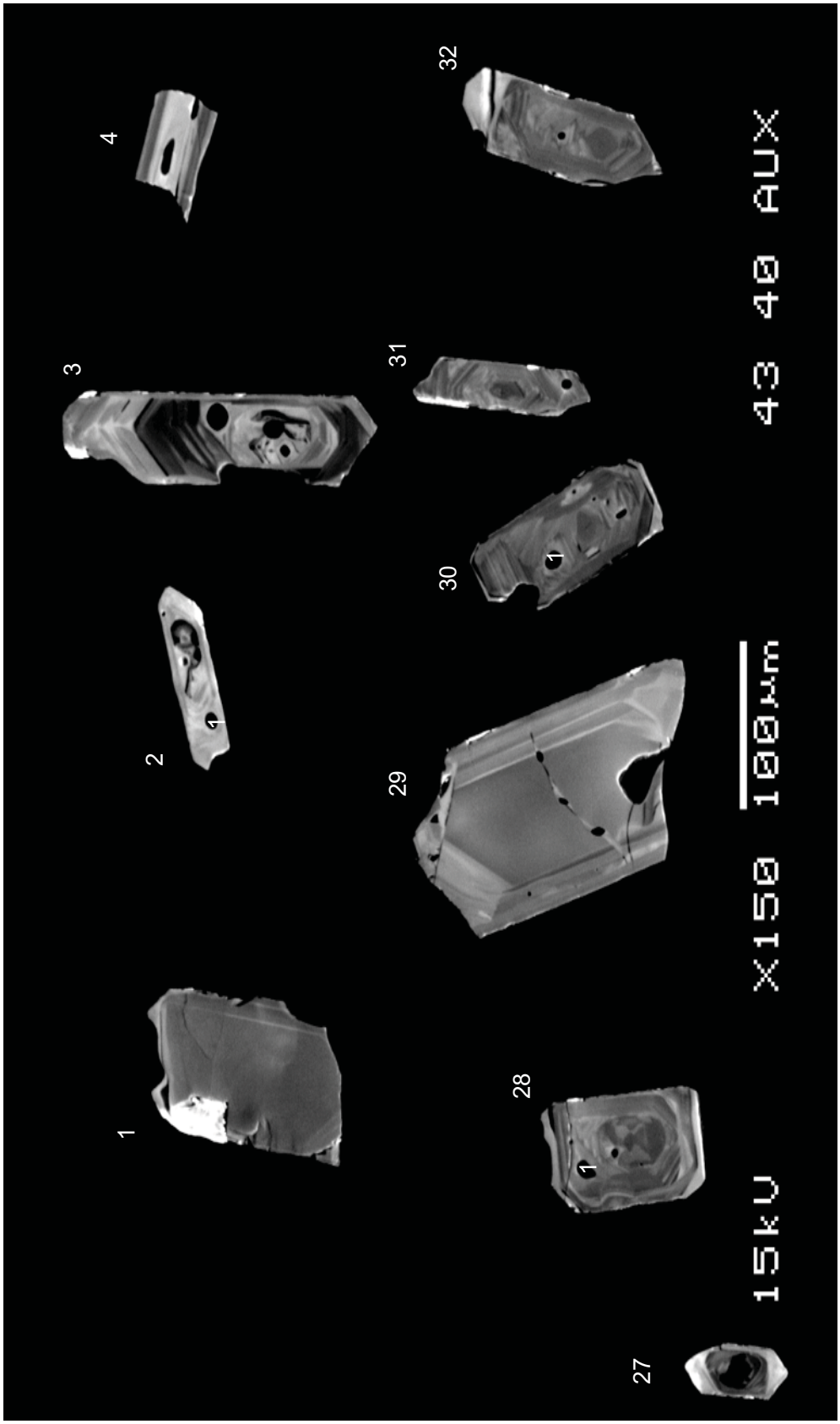

MCR

MCR-28-1

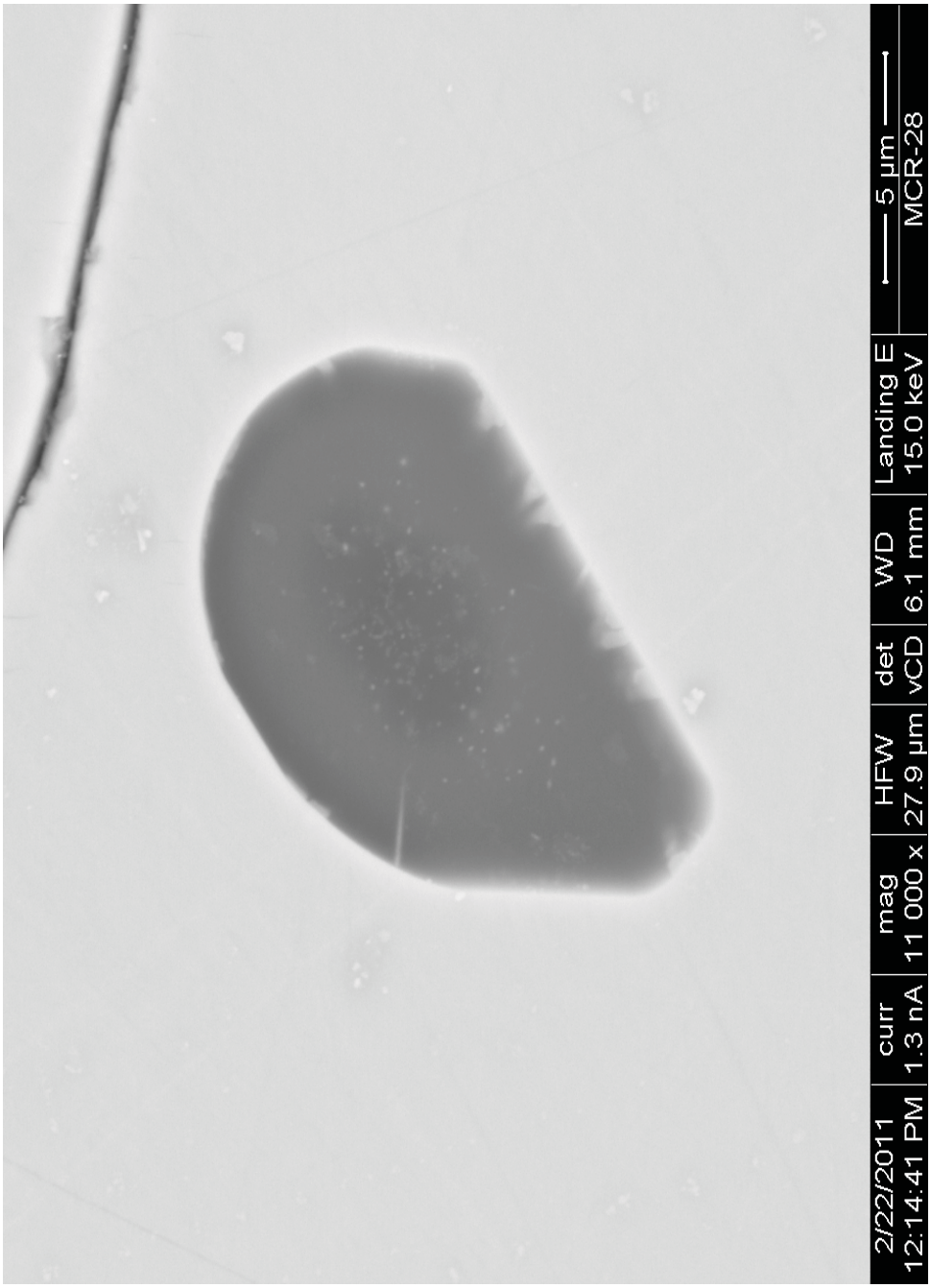
2/22/2011
12:14:41 PM
curr
1.3 nA
mag
11 000 x
HFW
27.9 µm
det
vCD
WD
6.1 mm
Landing E
15.0 keV
5 µm
MCR-28

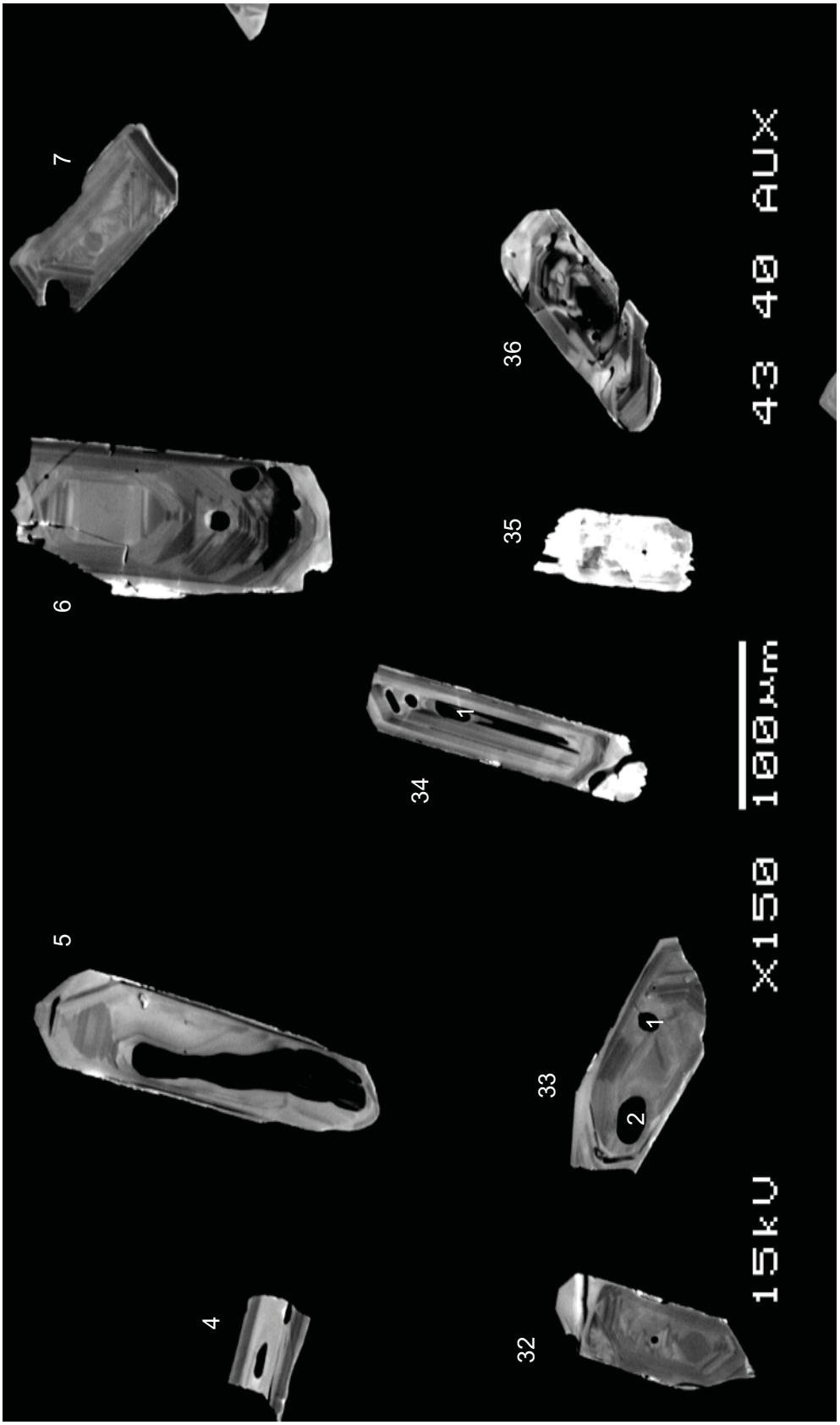
15kU X150 100µm 43 40 AUX
MCR
4
5
6
7
32
33
34
35
36
1
2

MCR-33-1

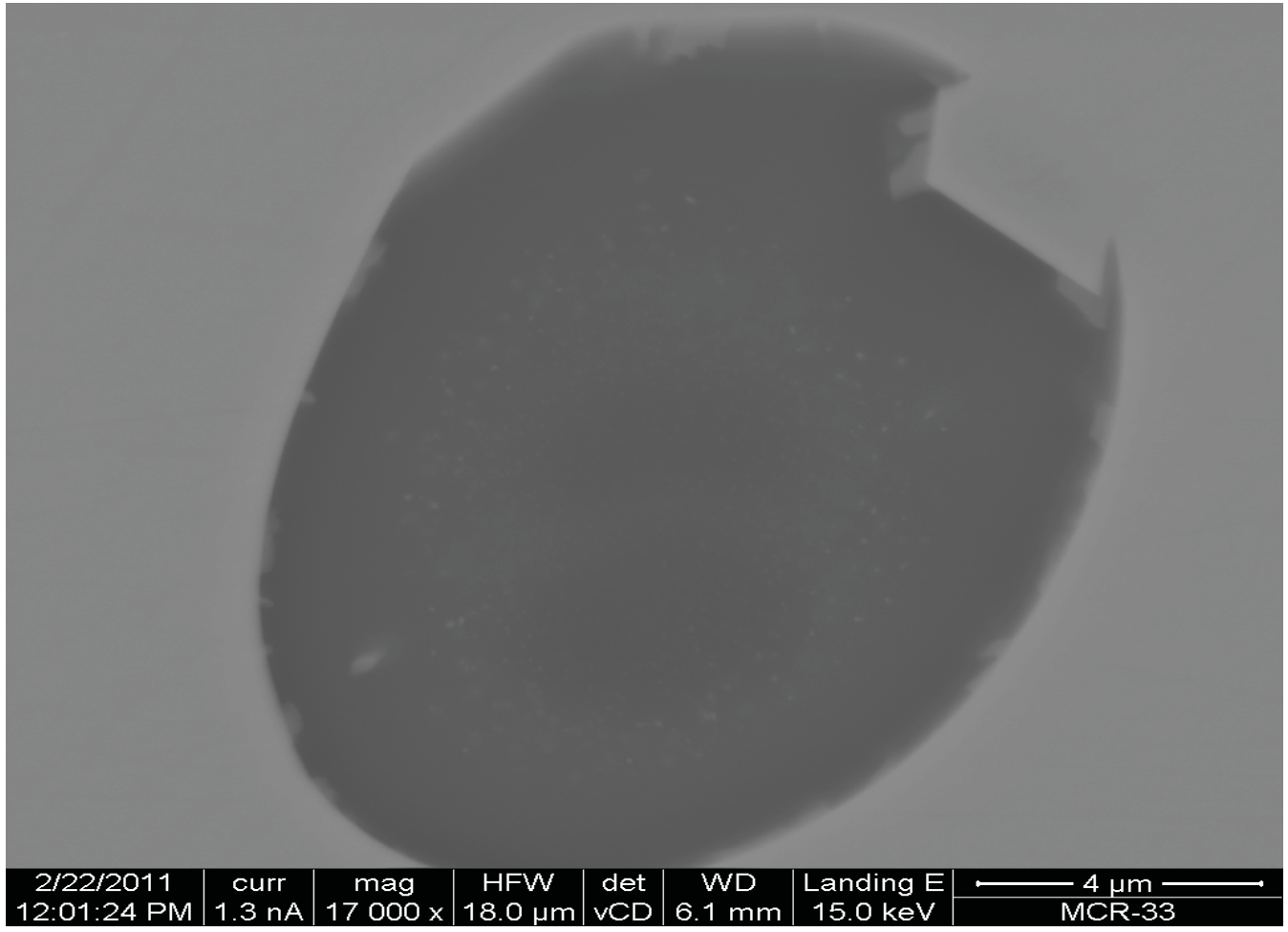
2/22/2011
12:01:24 PM
curr
1.3 nA
mag
17 000 x
HFW
18.0 µm
det
vCD
WD
6.1 mm
Landing E
15.0 keV
4 µm
MCR-33

MCR-33-1 EDS Reading

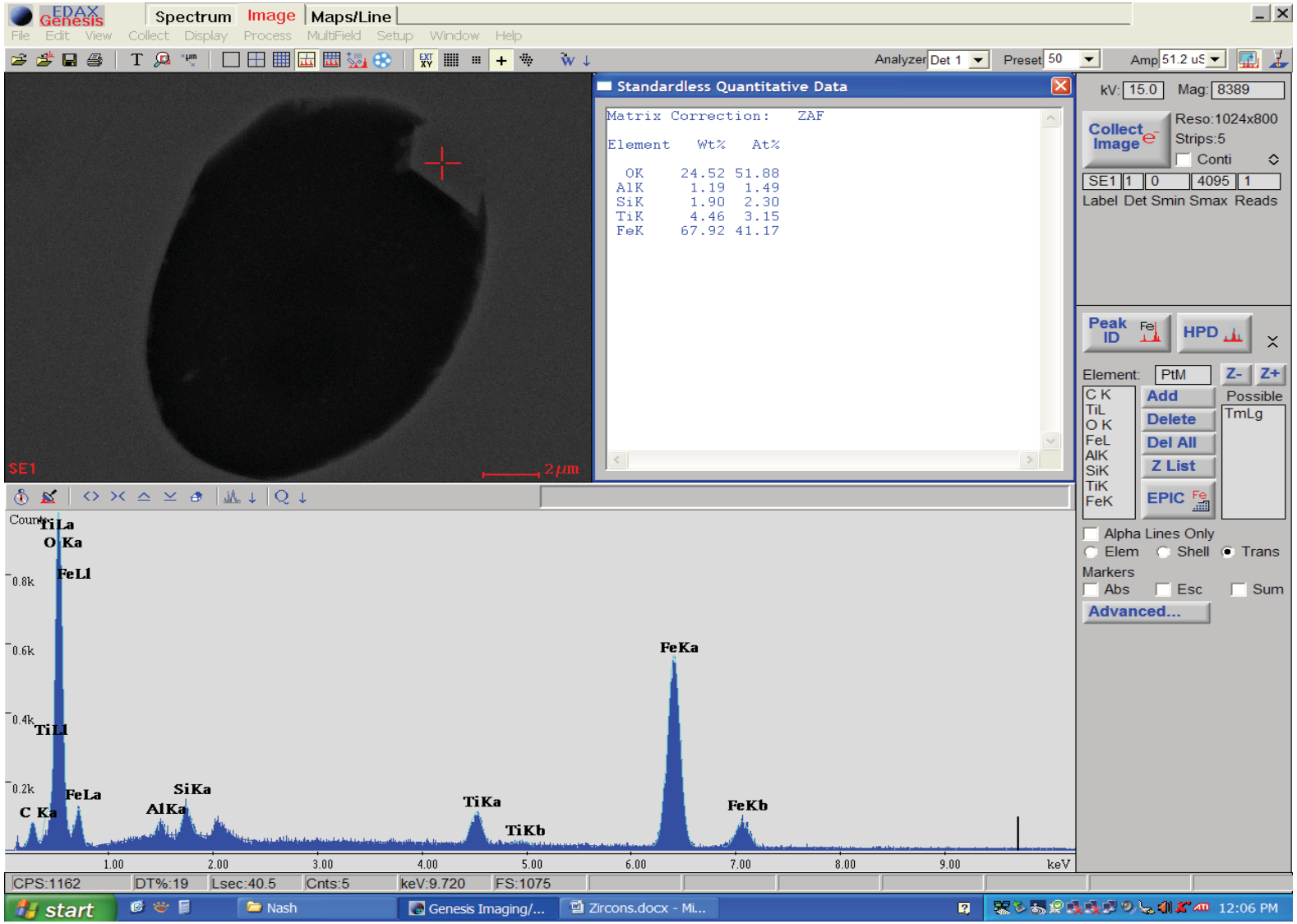

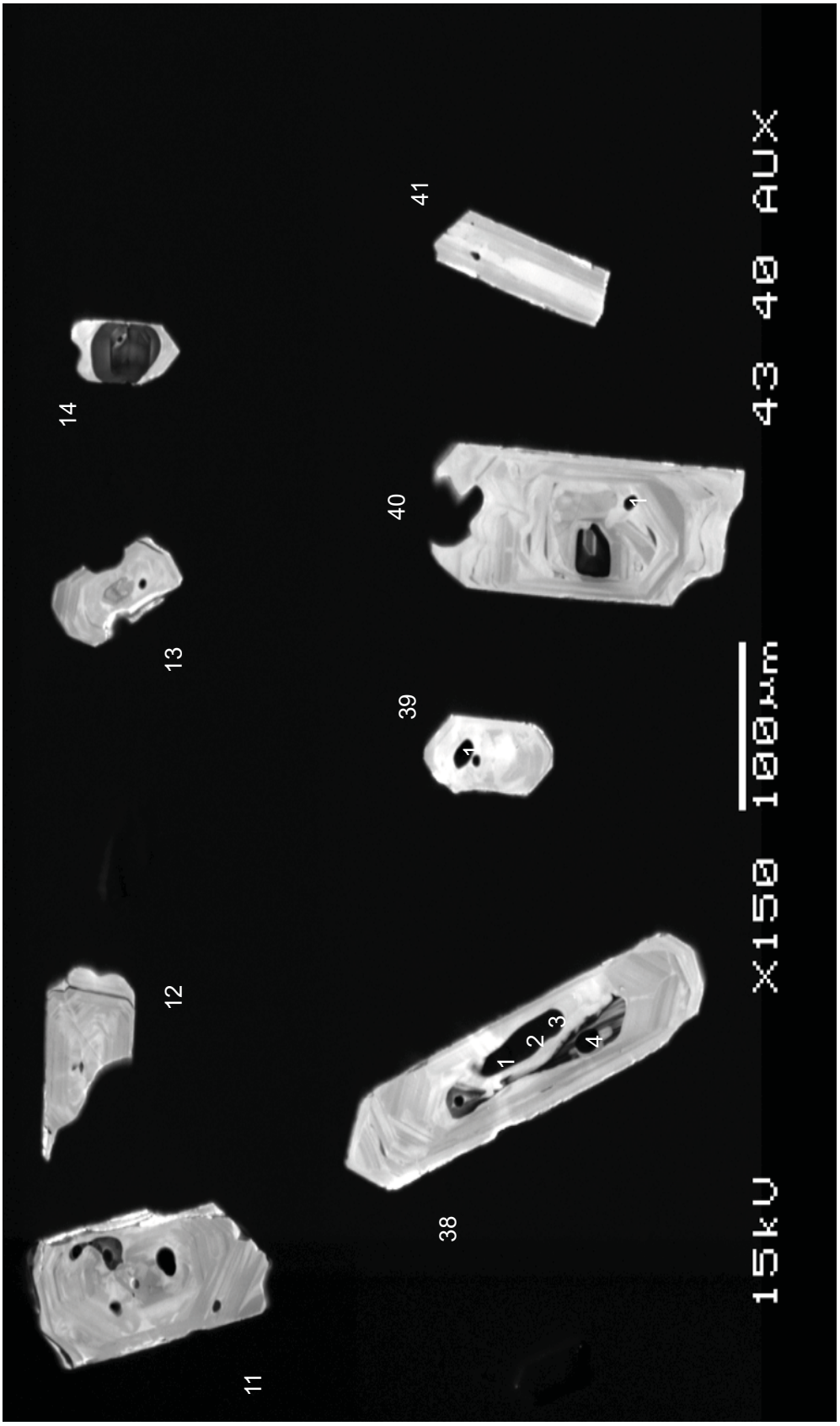

MCR

MCR-40-1

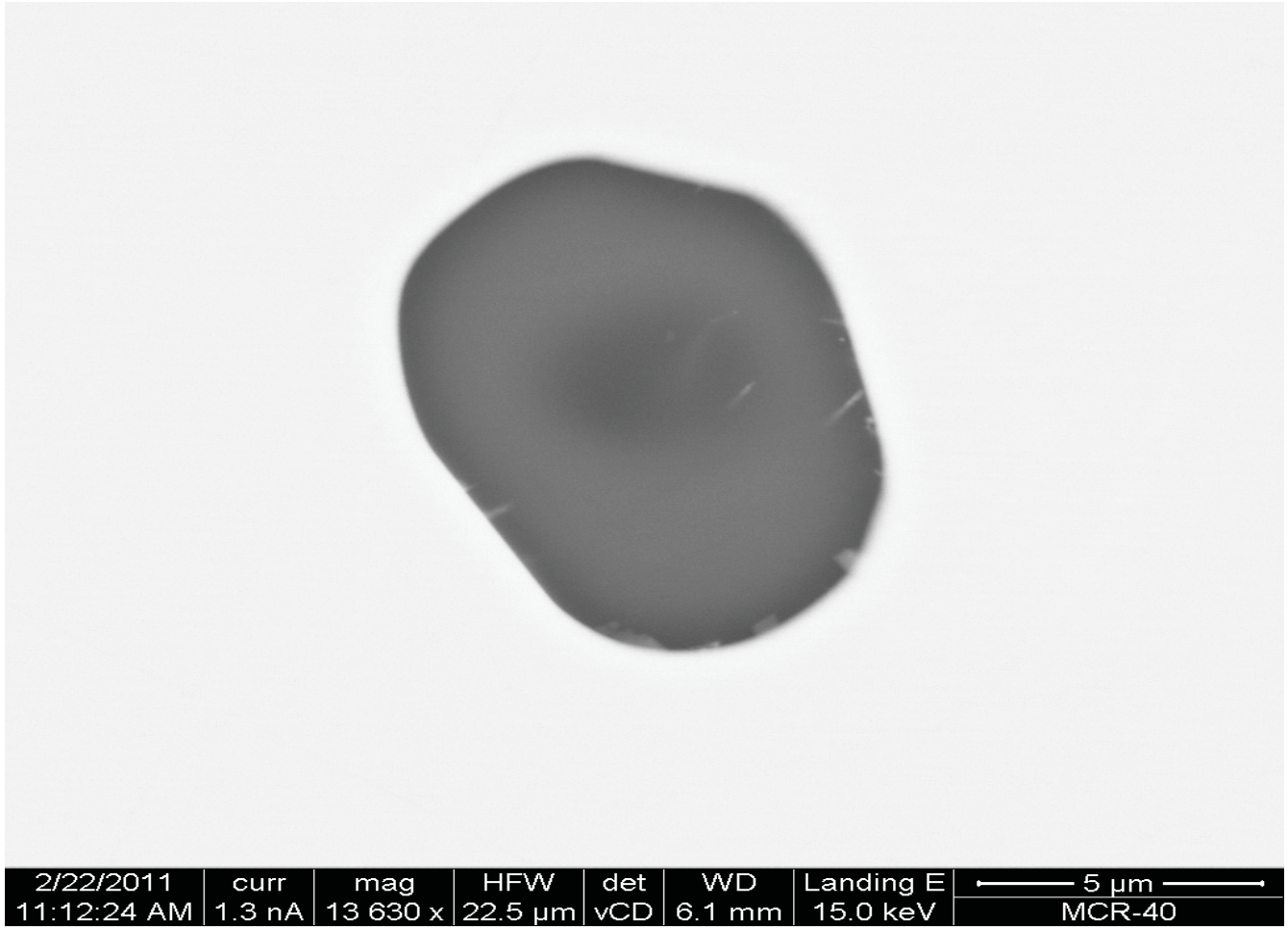
2/22/2011
11:12:24 AM
curr
1.3 nA
mag
13 630 x
HFW
22.5 µm
det
vCD
WD
6.1 mm
Landing E
15.0 keV
5 µm
MCR-40

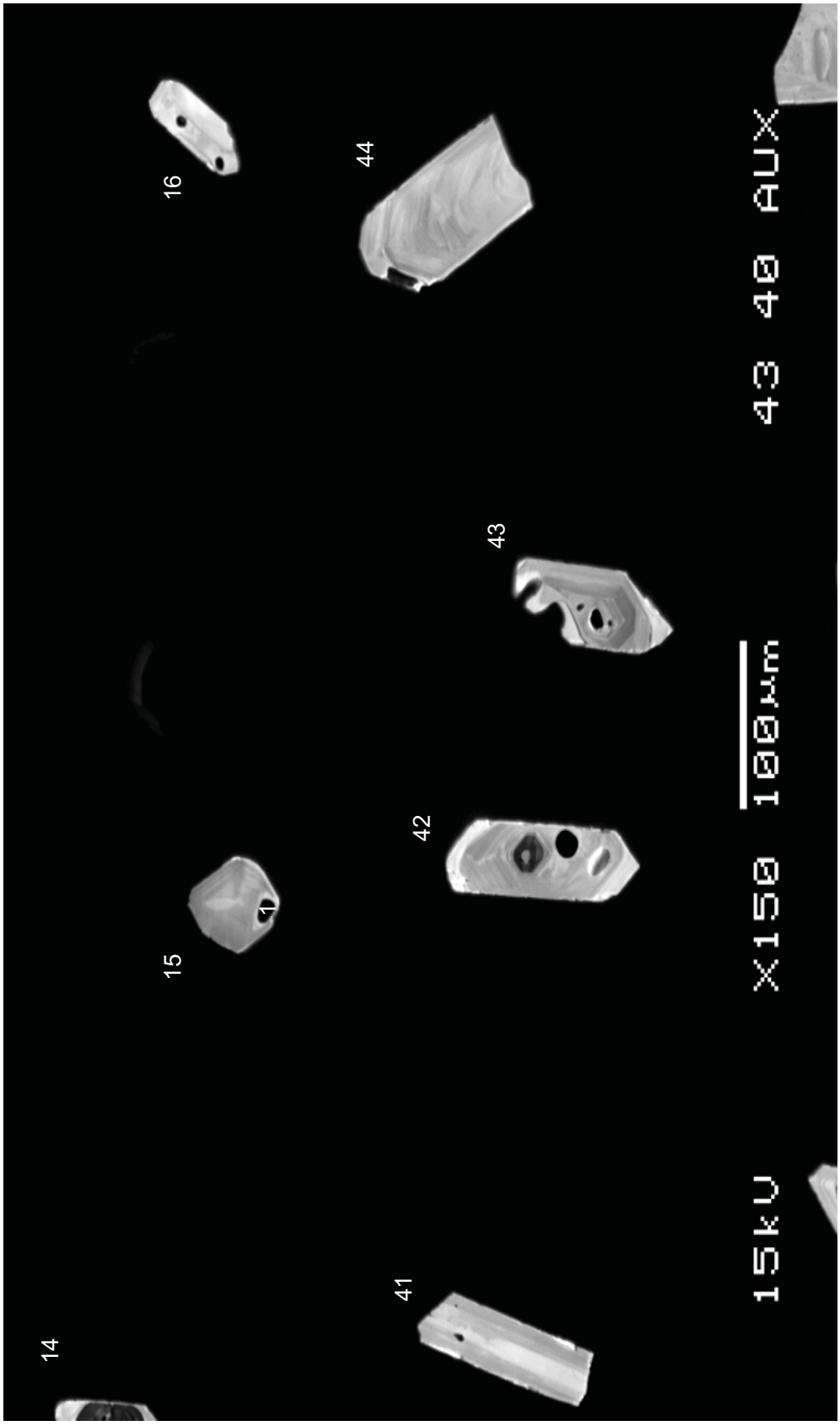

MCR

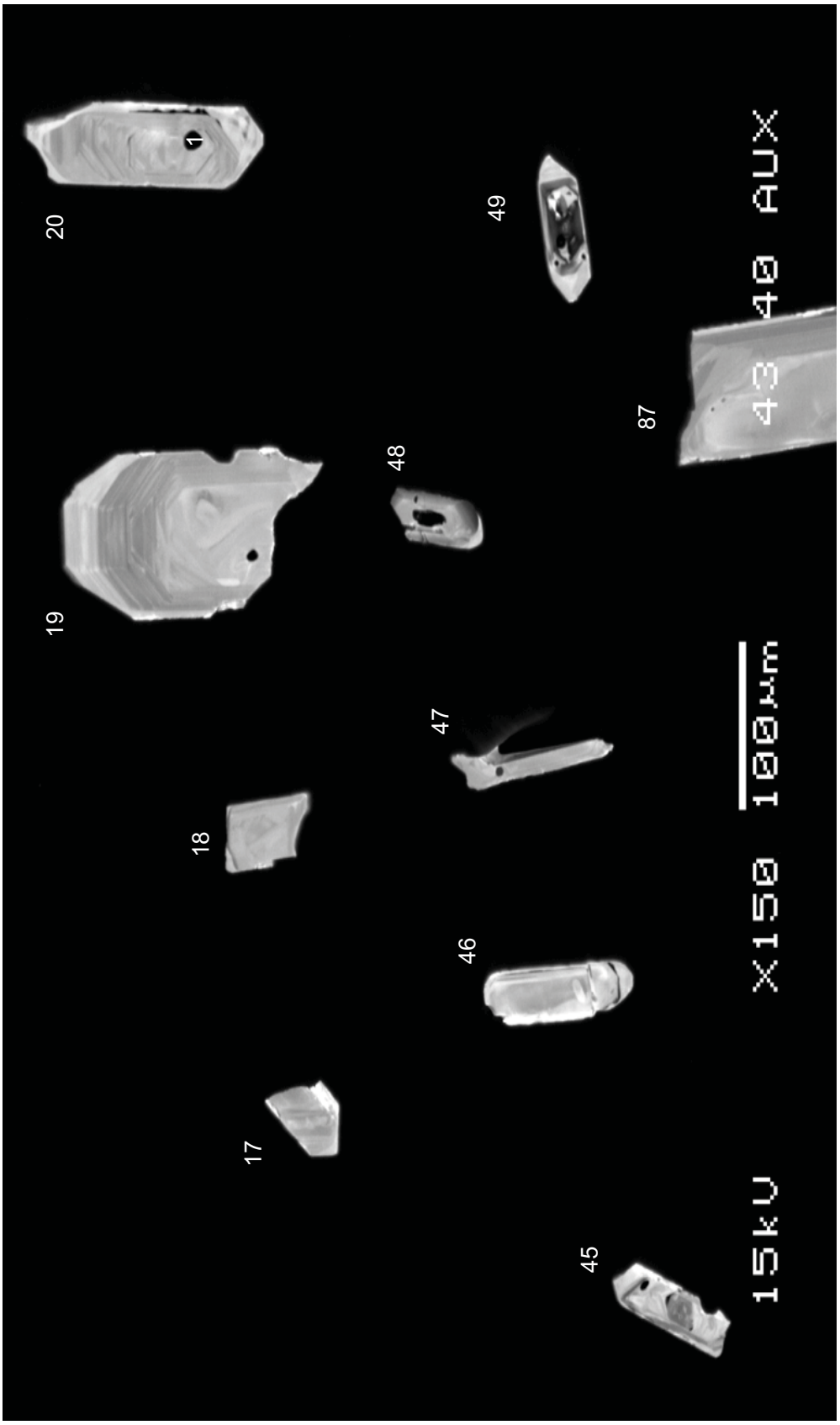
15kU X150 100µm
MCR
1
20
19
18
17
45
46
47
48
49
87
43 40 AUX

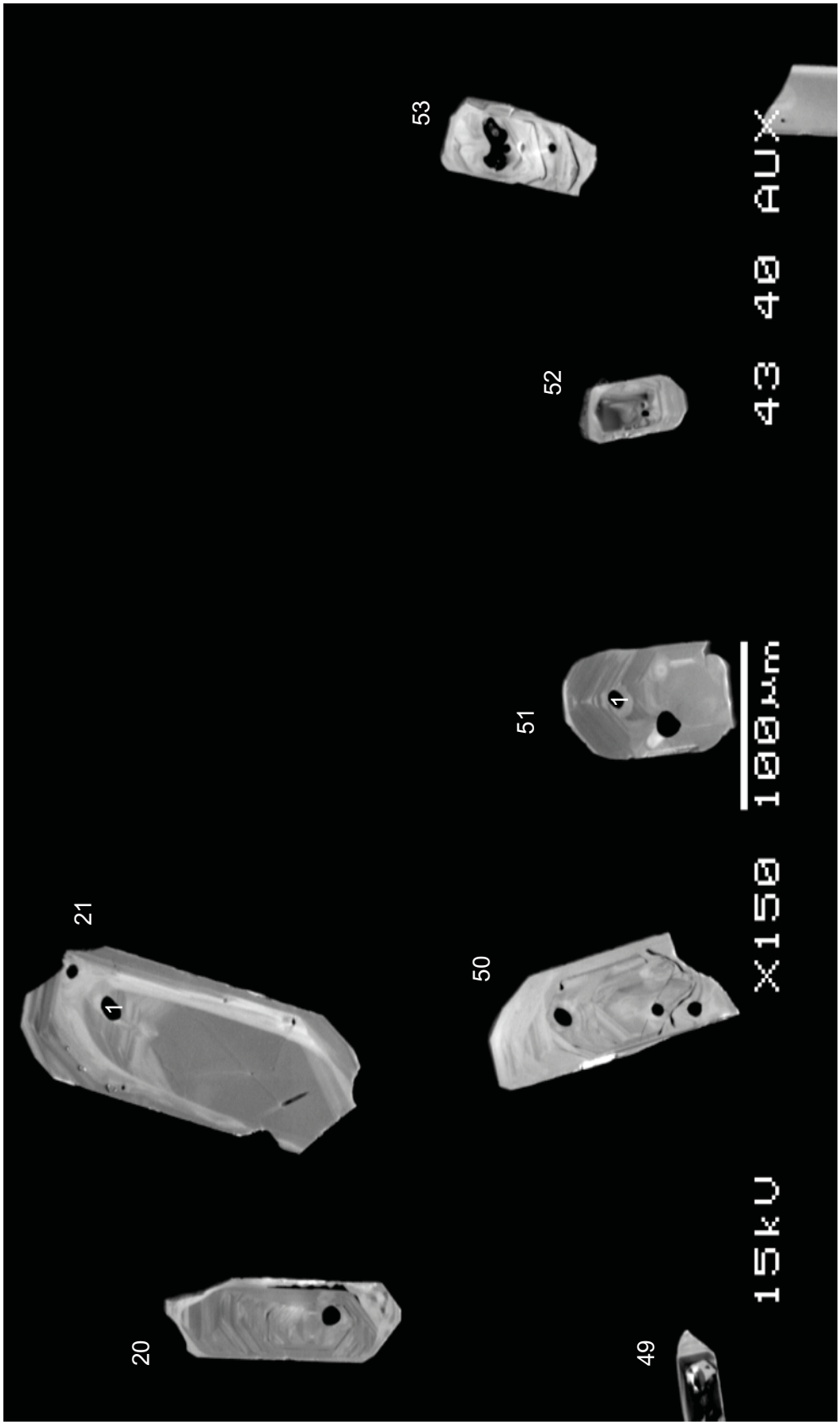
15kU X150 100µm 43 40 AUX
MCR
20
49
21
1
50
51
1
52
53

MCR-51-1

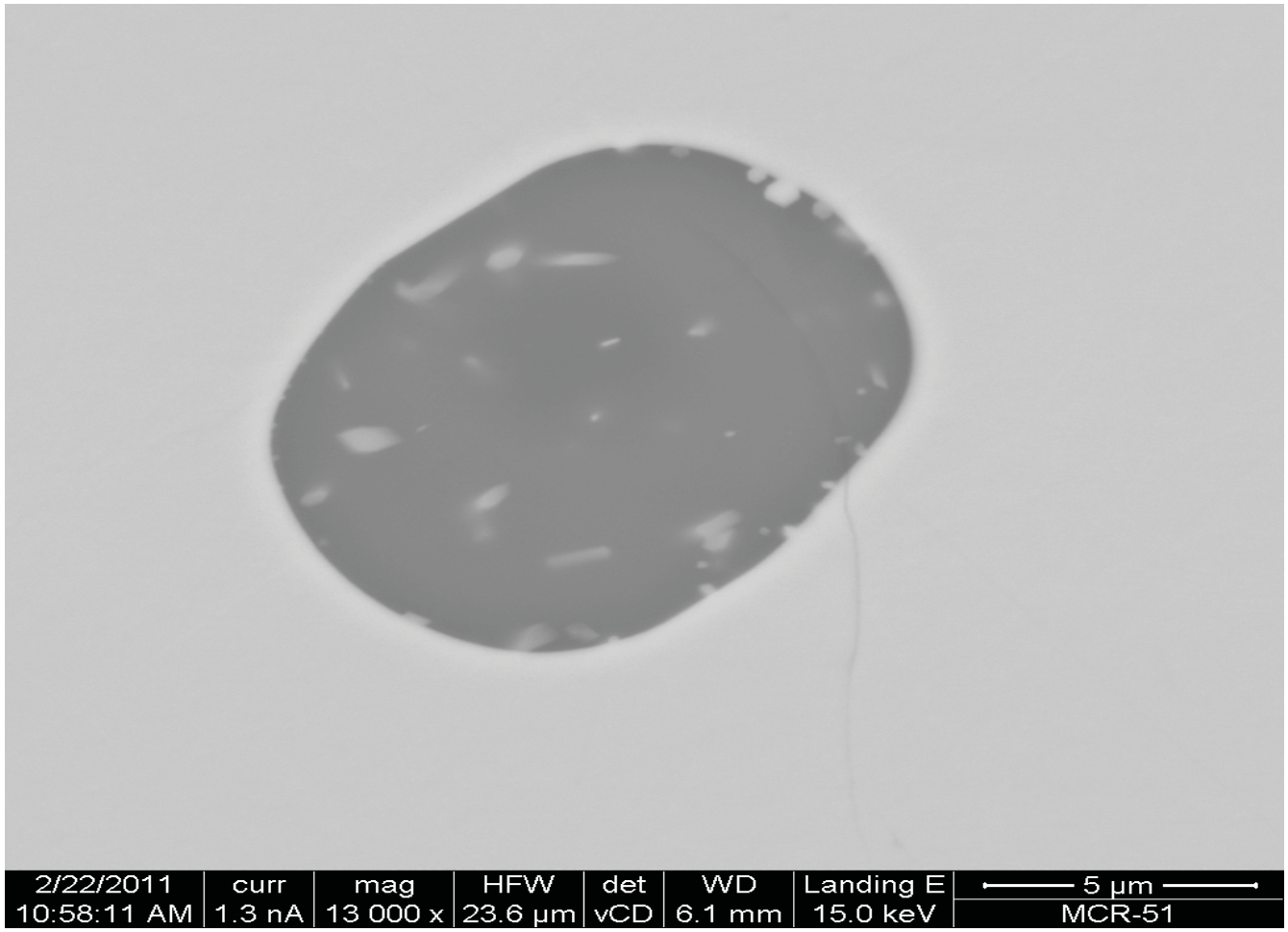
2/22/2011
10:58:11 AM
curr
1.3 nA
mag
13 000 x
HFW
23.6 µm
det
vCD
WD
6.1 mm
Landing E
15.0 keV
5 µm
MCR-51

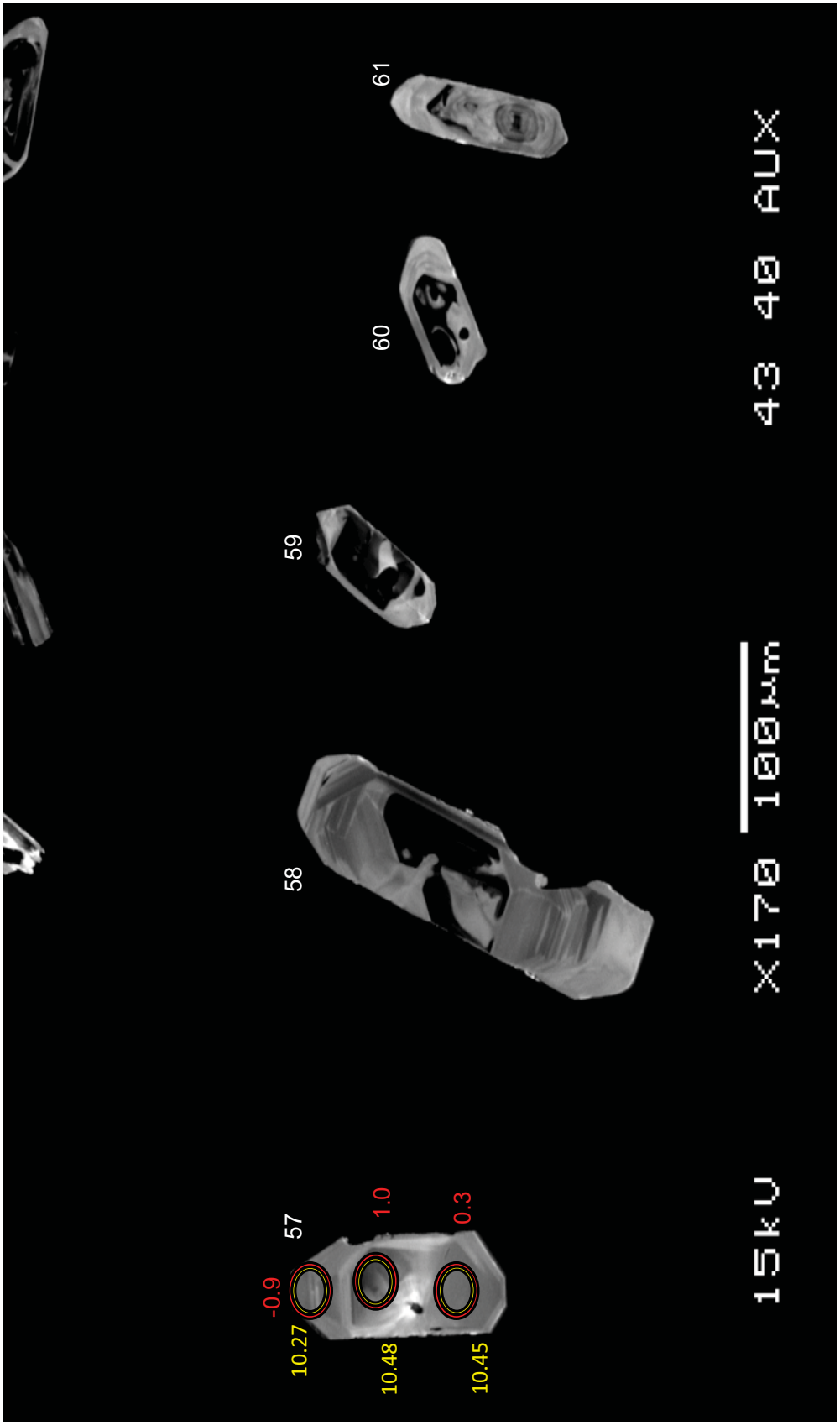
15kU X170 100µm 43 40 AUX
MCR
57
58
59
60
61
-0.9
10.27
1.0
10.48
0.3
10.45

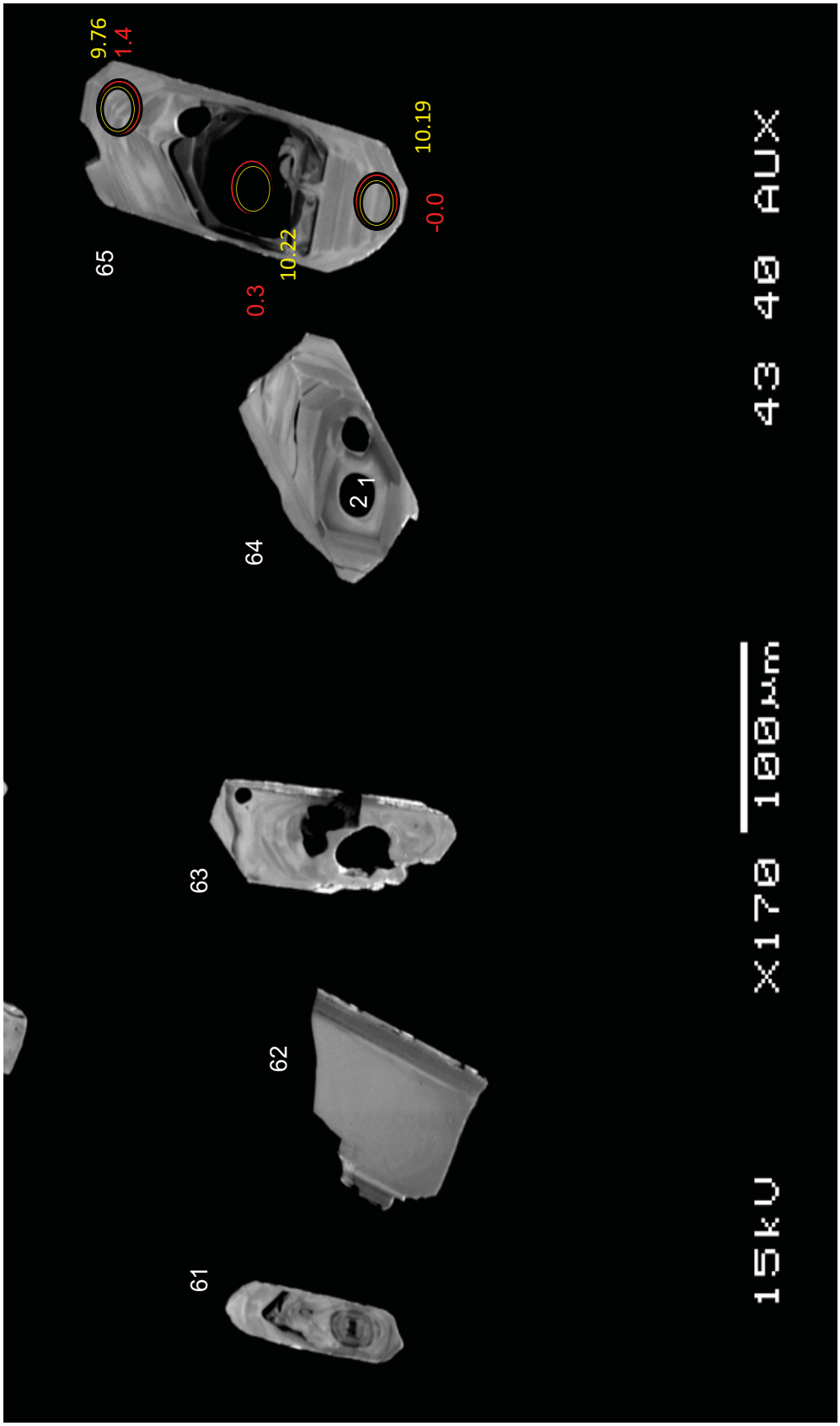
15kU X170 100µm 43 40 AUX
MCR
61
62
63
64
65
2 1
9.76
1.4
10.19
-0.0
10.22
0.3

MCR-64-1 and MCR-64-2

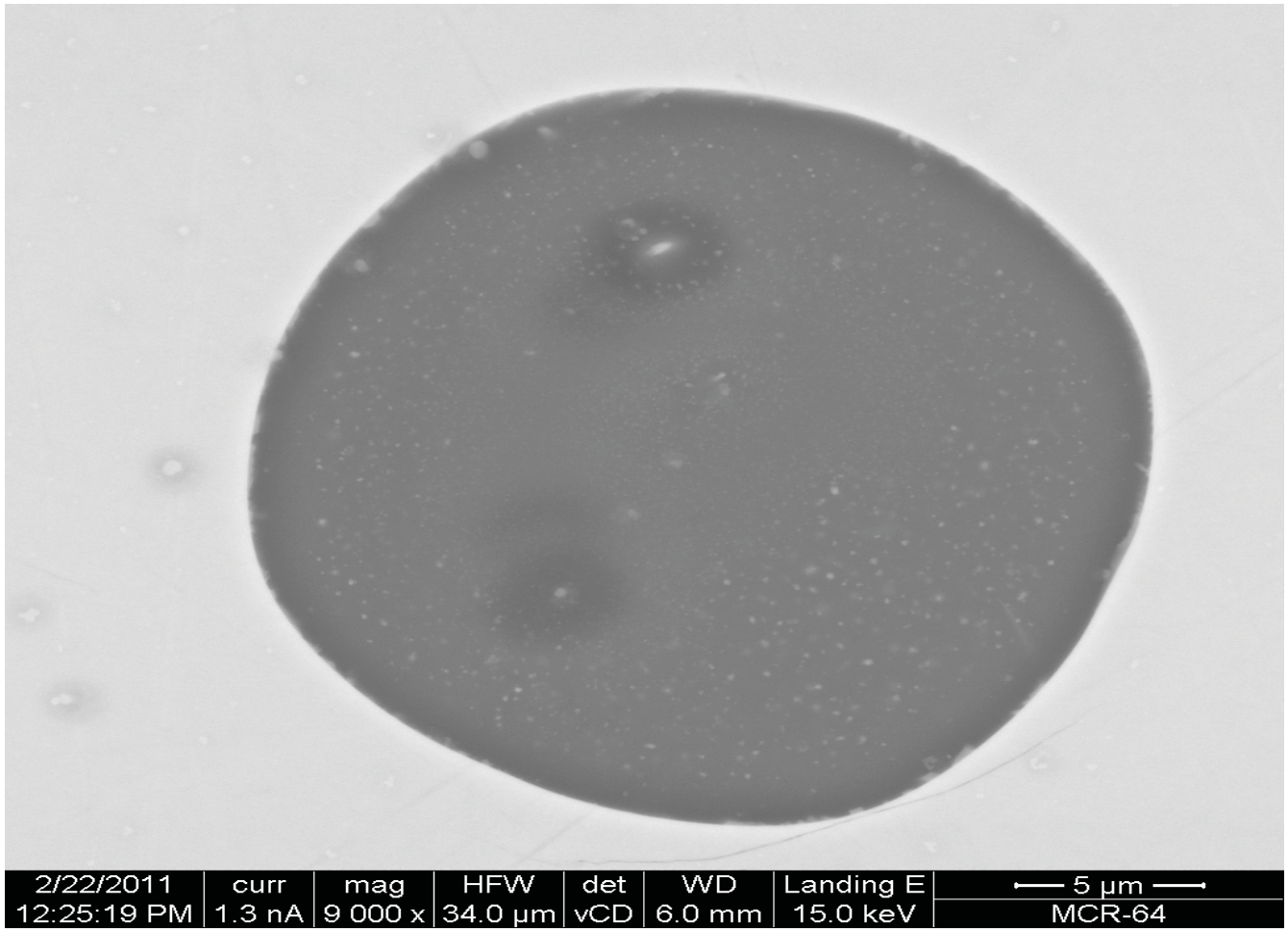

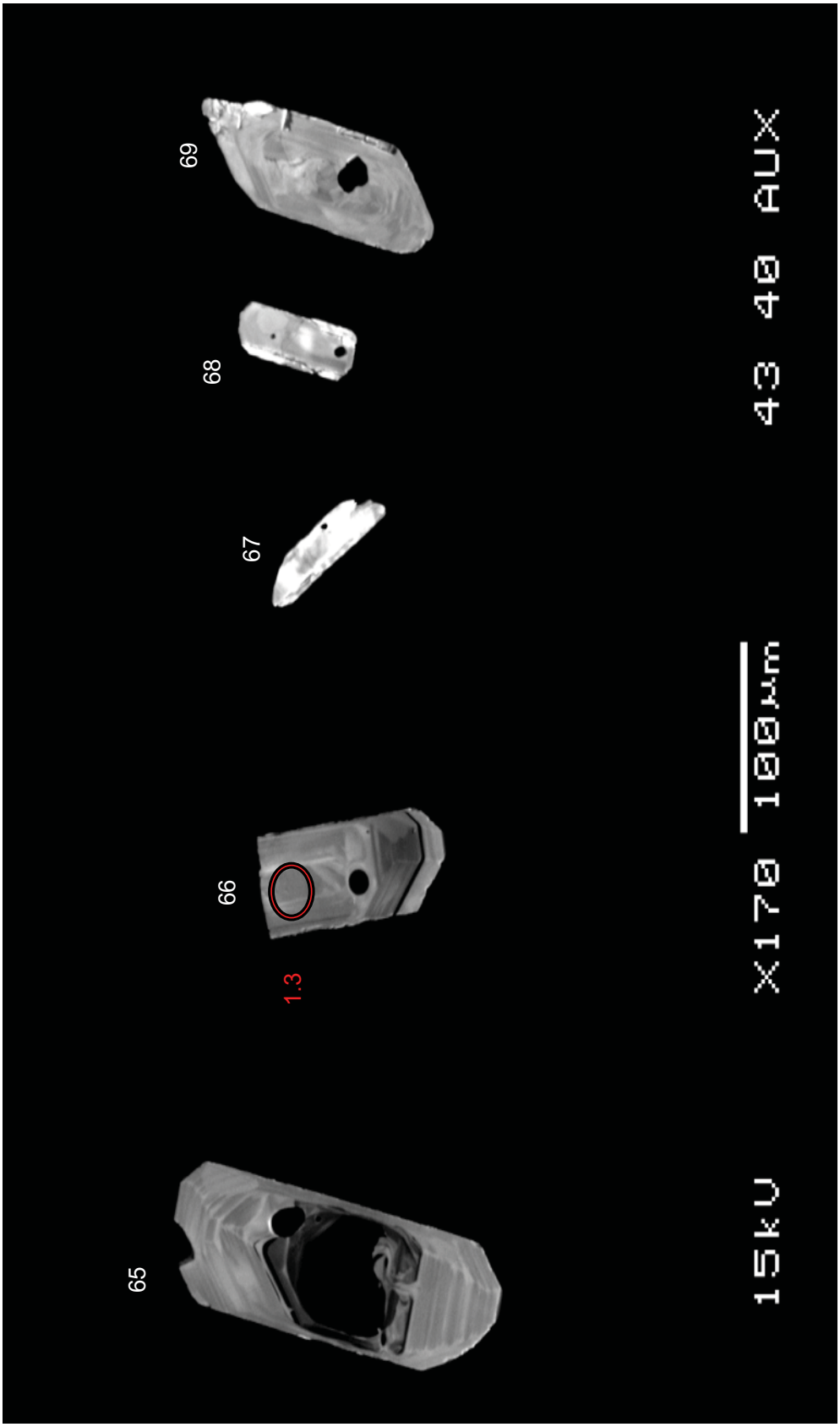
15kU X170 100µm 43 40 AUX
65
66
1.3
67
68
69
MCR

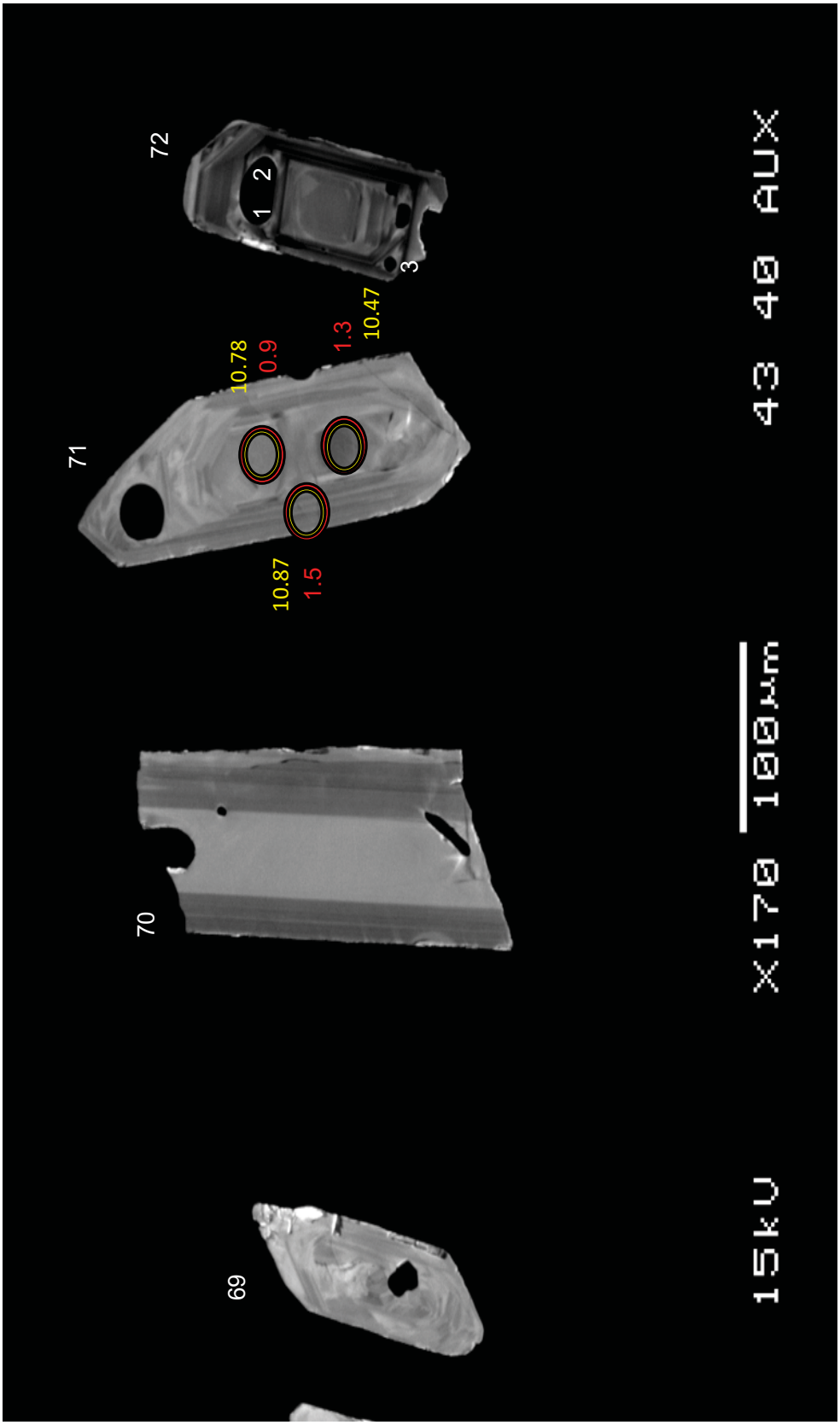
15kV X170 100µm 43 40 AUX
MCR
69
70
71
72
1 2
3
10.78
0.9
1.3
10.47
10.87
1.5

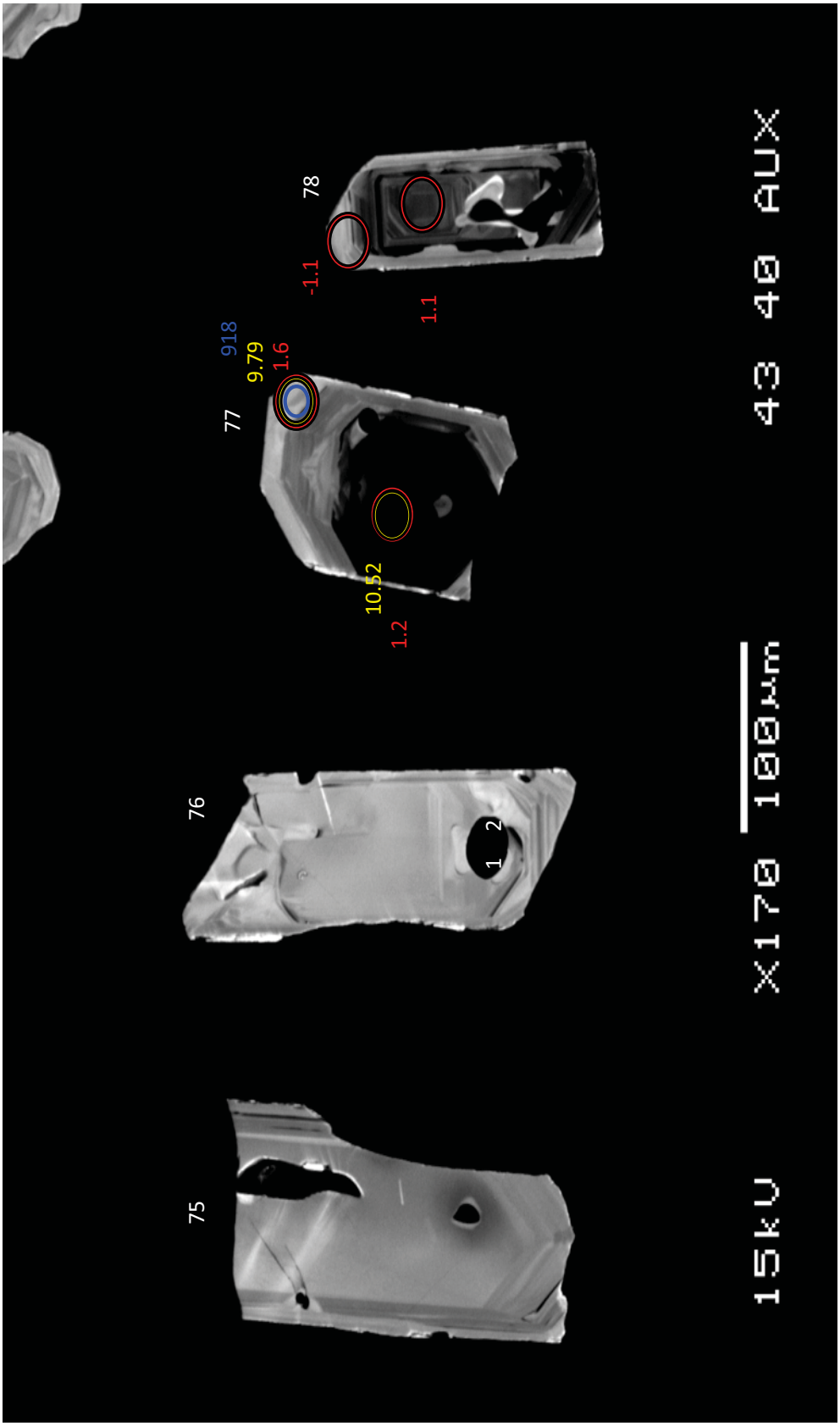

MCR

MCR-77

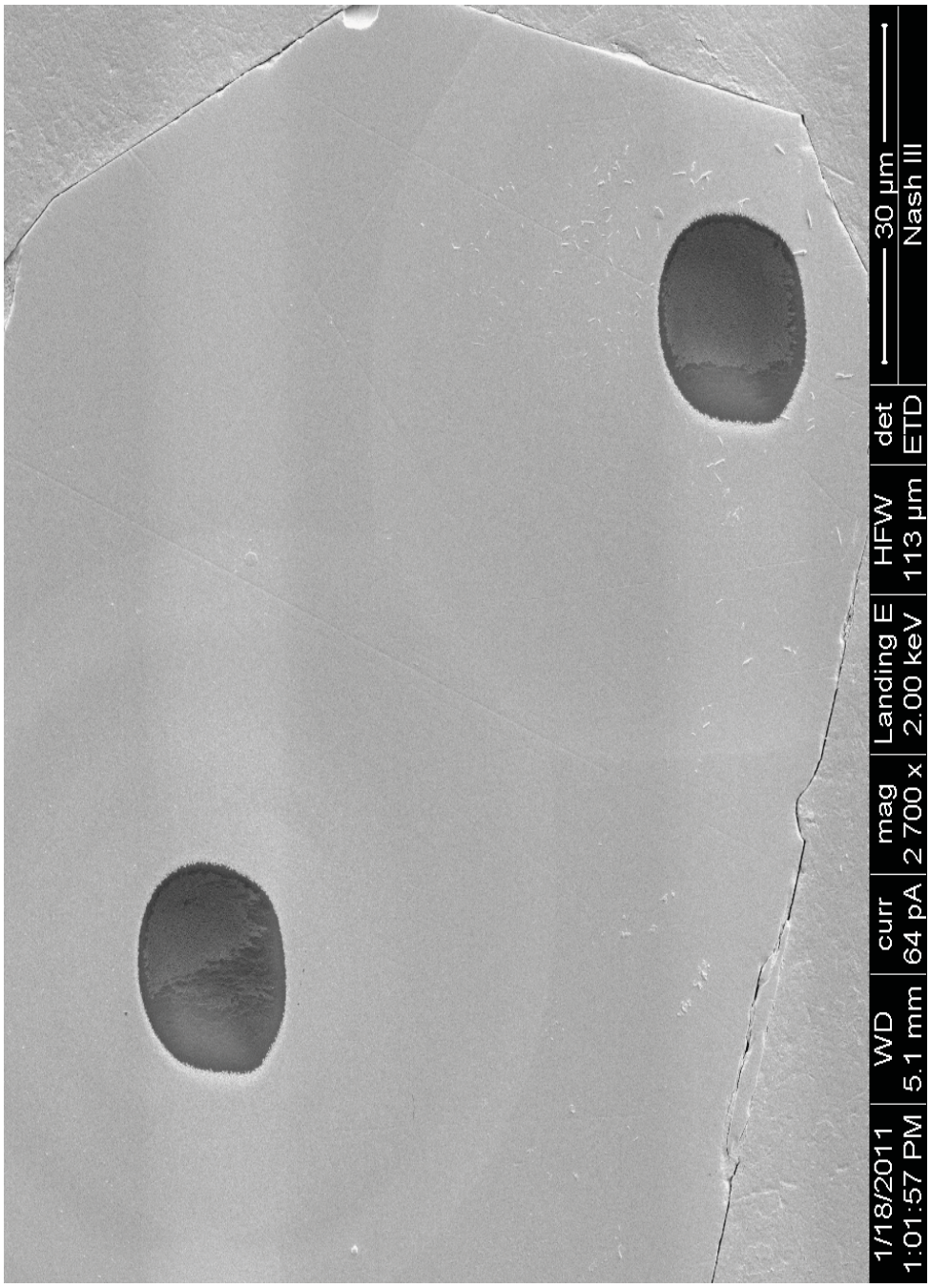
1/18/2011
1:01:57 PM
WD
5.1 mm
curr
64 pA
mag
2 700 x
Landing E
2.00 keV
HFW
113 µm
det
ETD
30 µm
Nash III

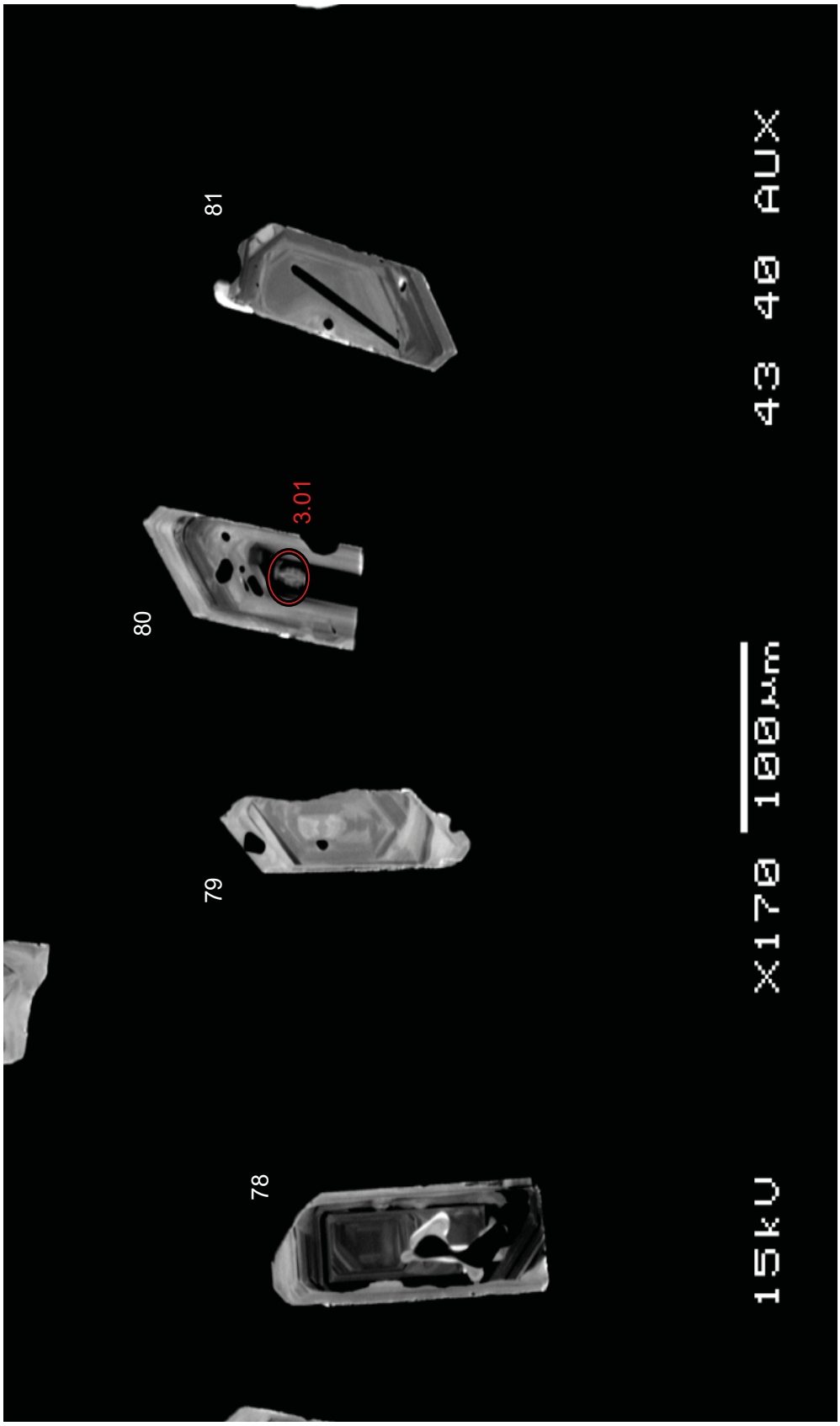
15kV X170 100µm
81
80
79
78
3.01
MCR

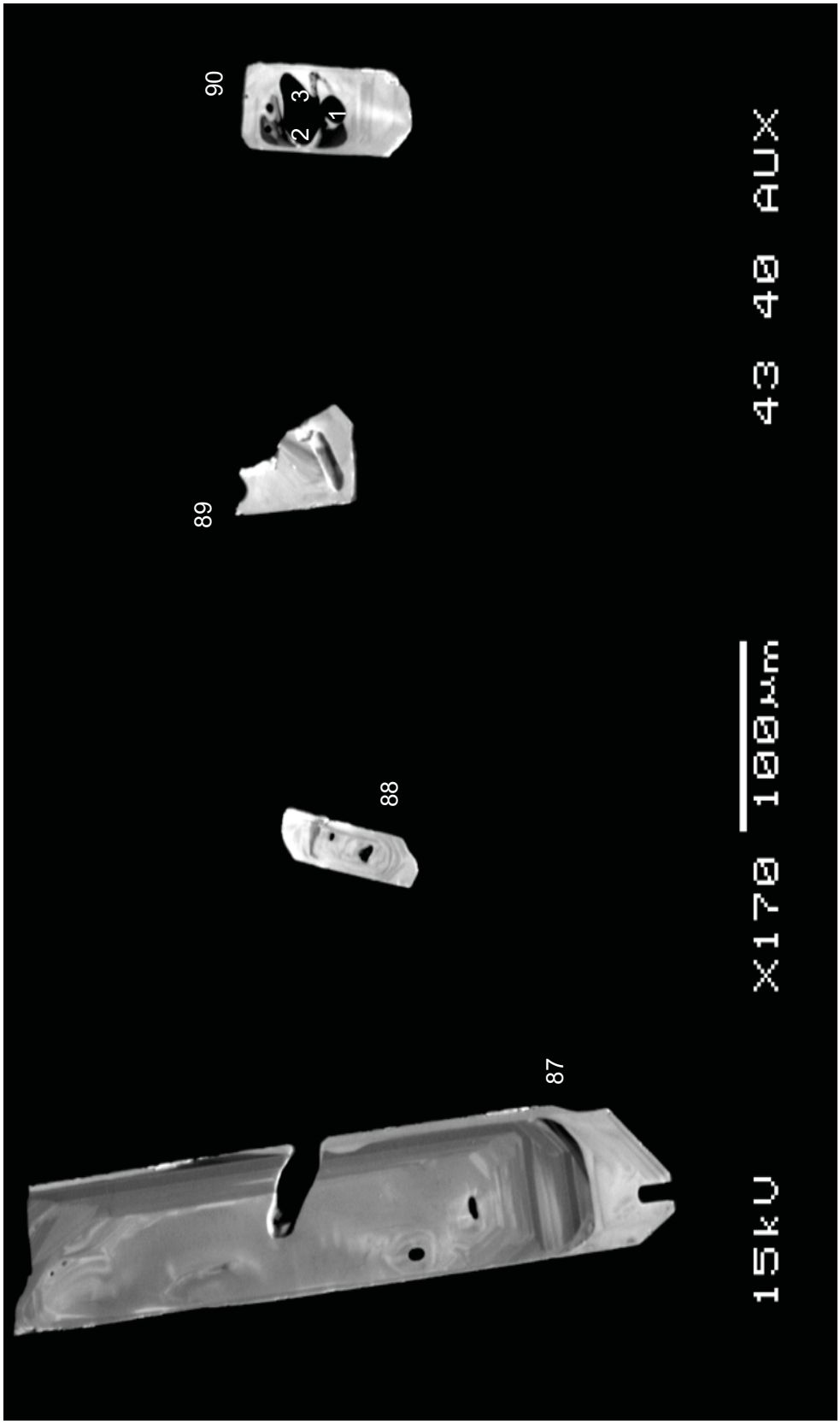

MCR

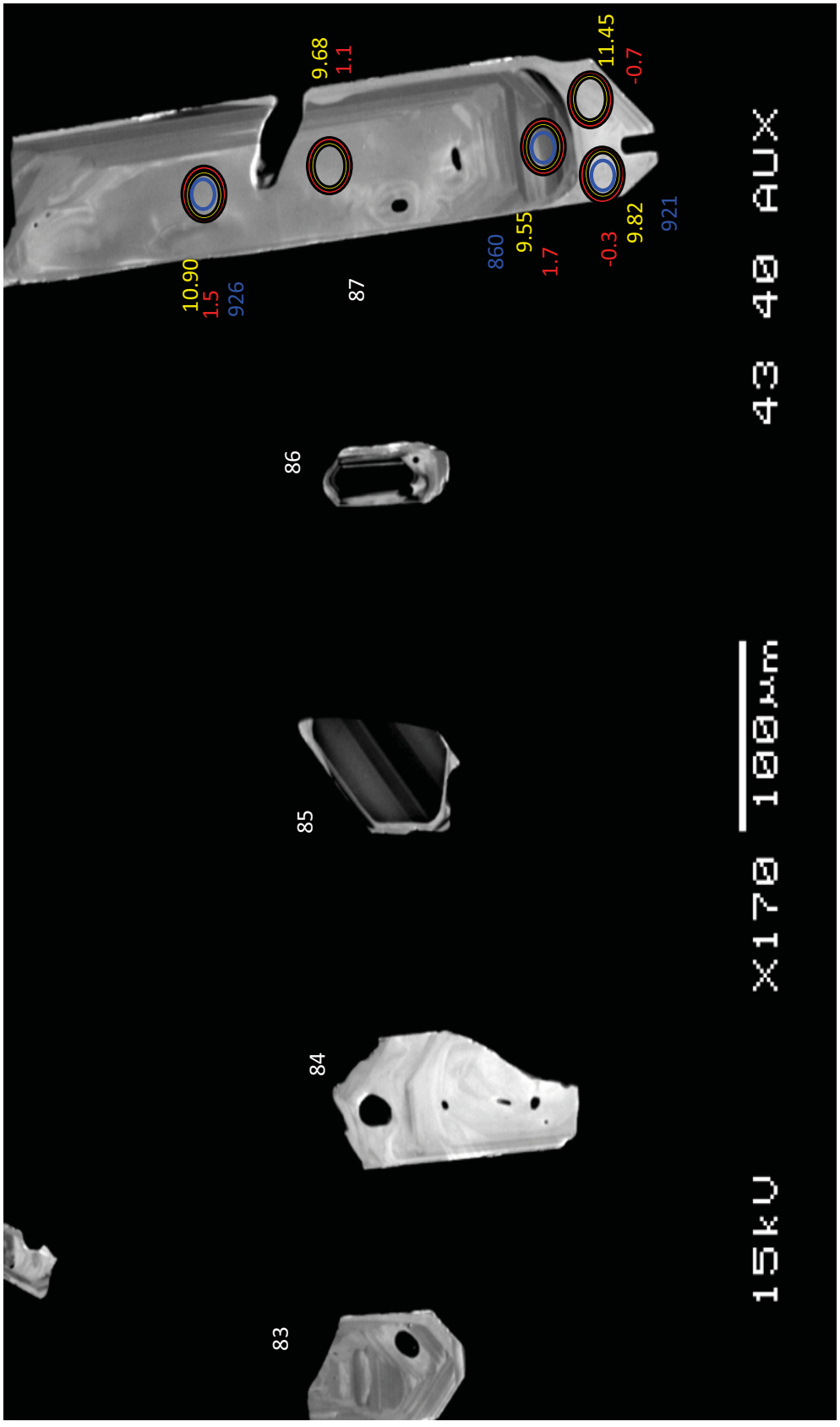
15kU X170 100µm 43 40 AUX
83
84
85
86
87
10.90
1.5
926
9.68
1.1
860
9.55
1.7
-0.3
9.82
921
11.45
-0.7

MCR

MCR-87

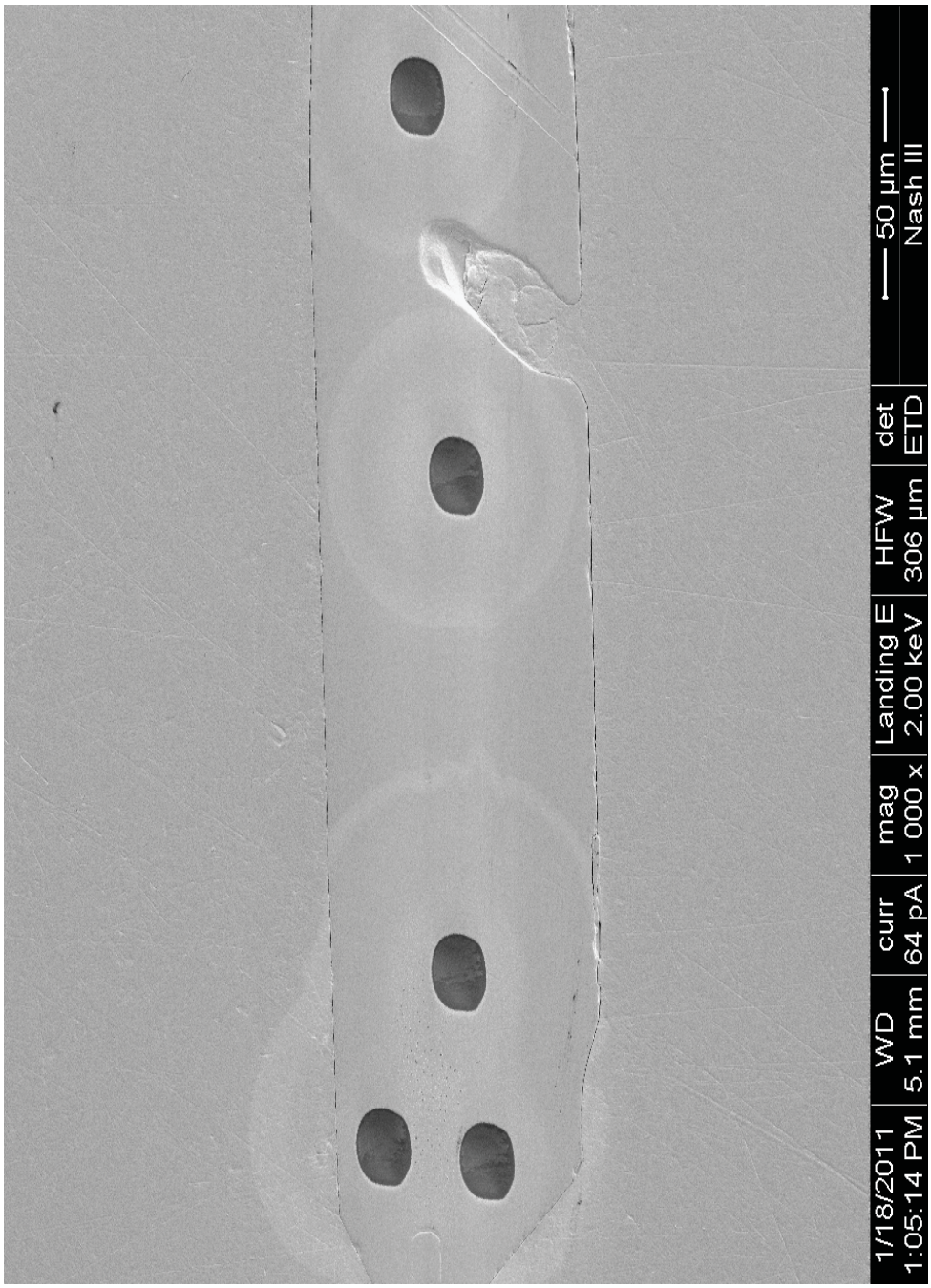
1/18/2011
1:05:14 PM
WD
5.1 mm
curr
64 pA
mag
1 000 x
Landing E
2.00 keV
HFW
306 µm
det
ETD
50 µm
Nash III

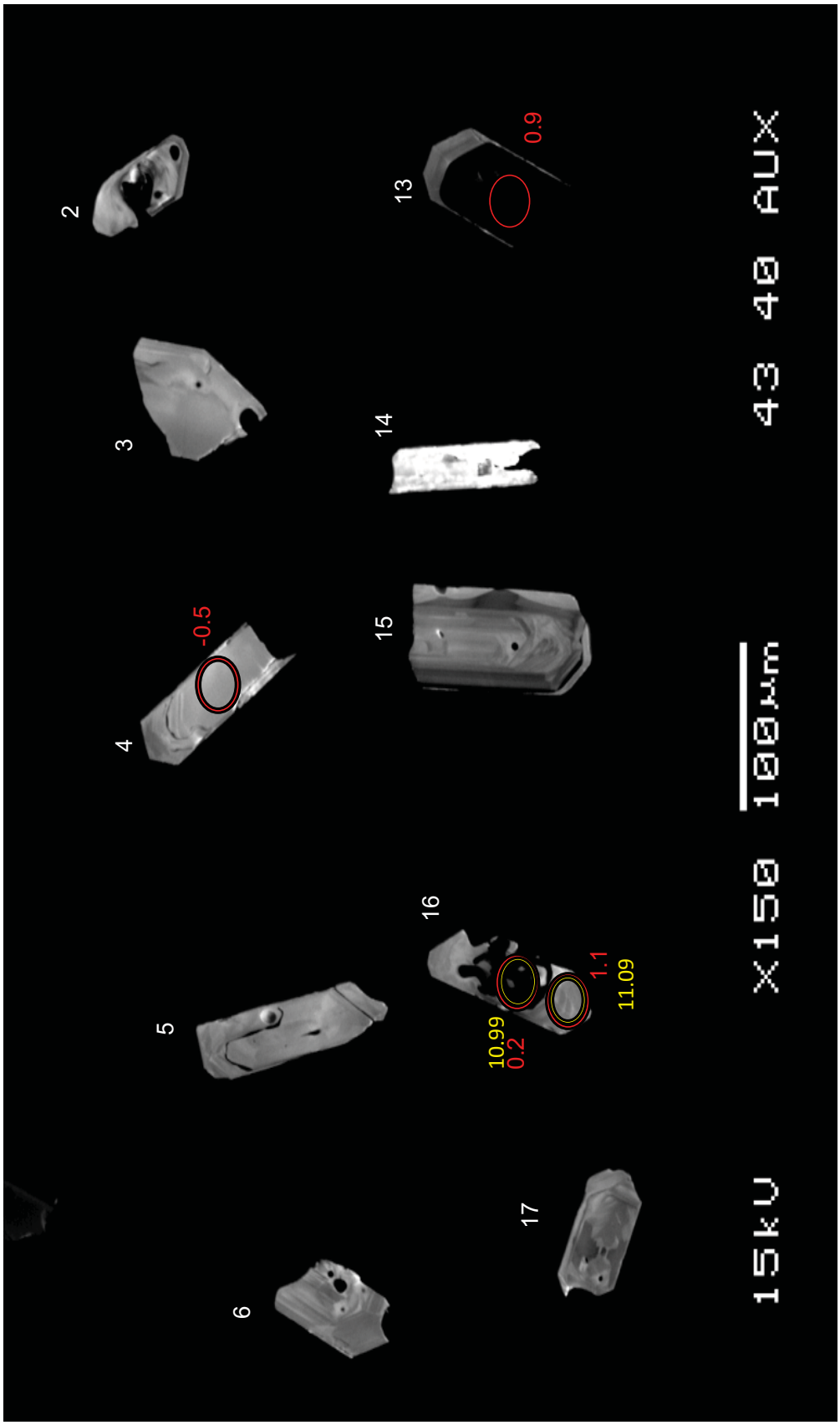
15kV X150 100µm 43 40 AUX
ULF
2
3
4
-0.5
5
6
16
10.99
0.2
1.1
11.09
17
15
14
13
0.9

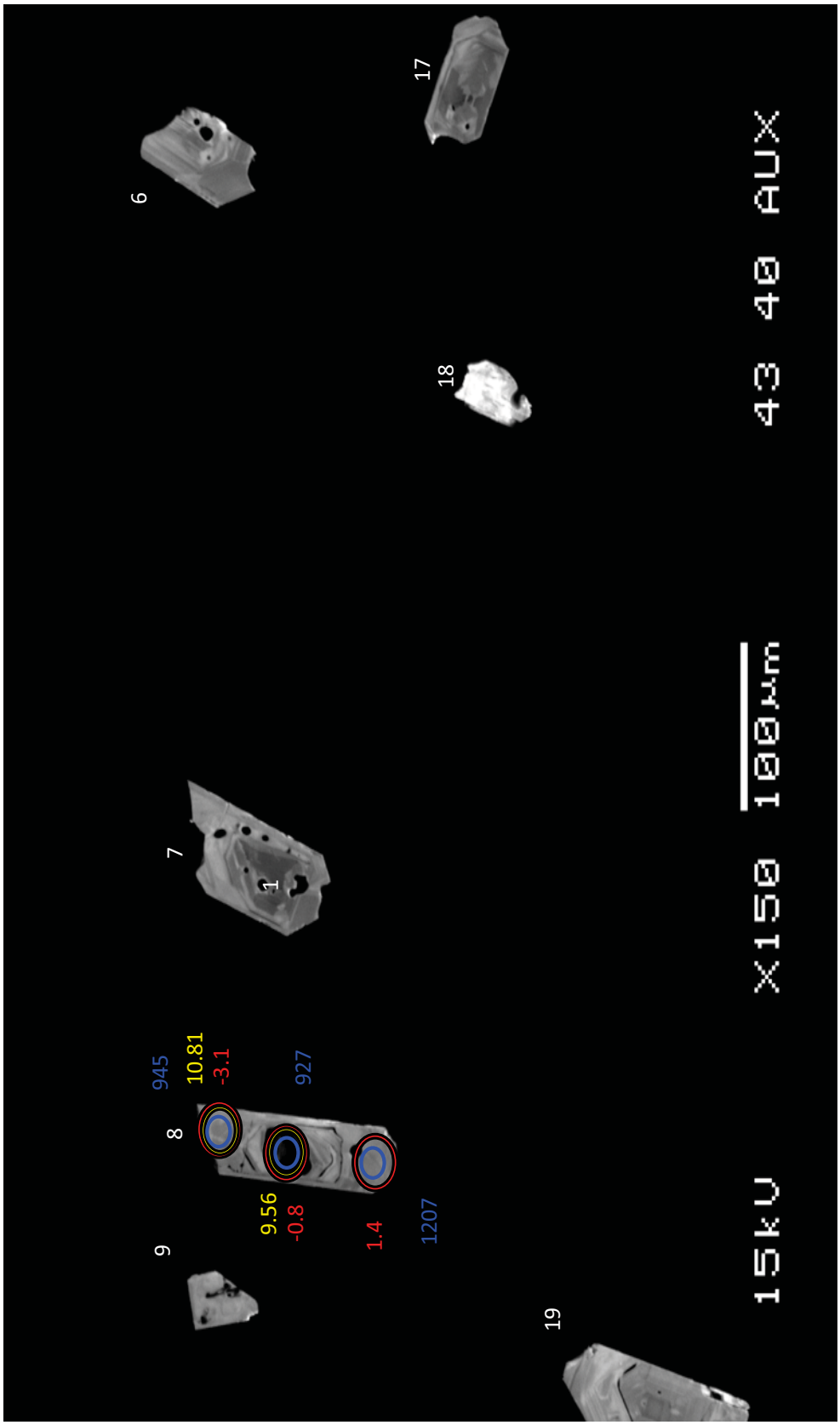
15kV X150 100µm 43 40 AUX
ULF
6
17
18
7
1
8
945
10.81
-3.1
927
9.56
-0.8
1.4
1207
9
19

ULF-8

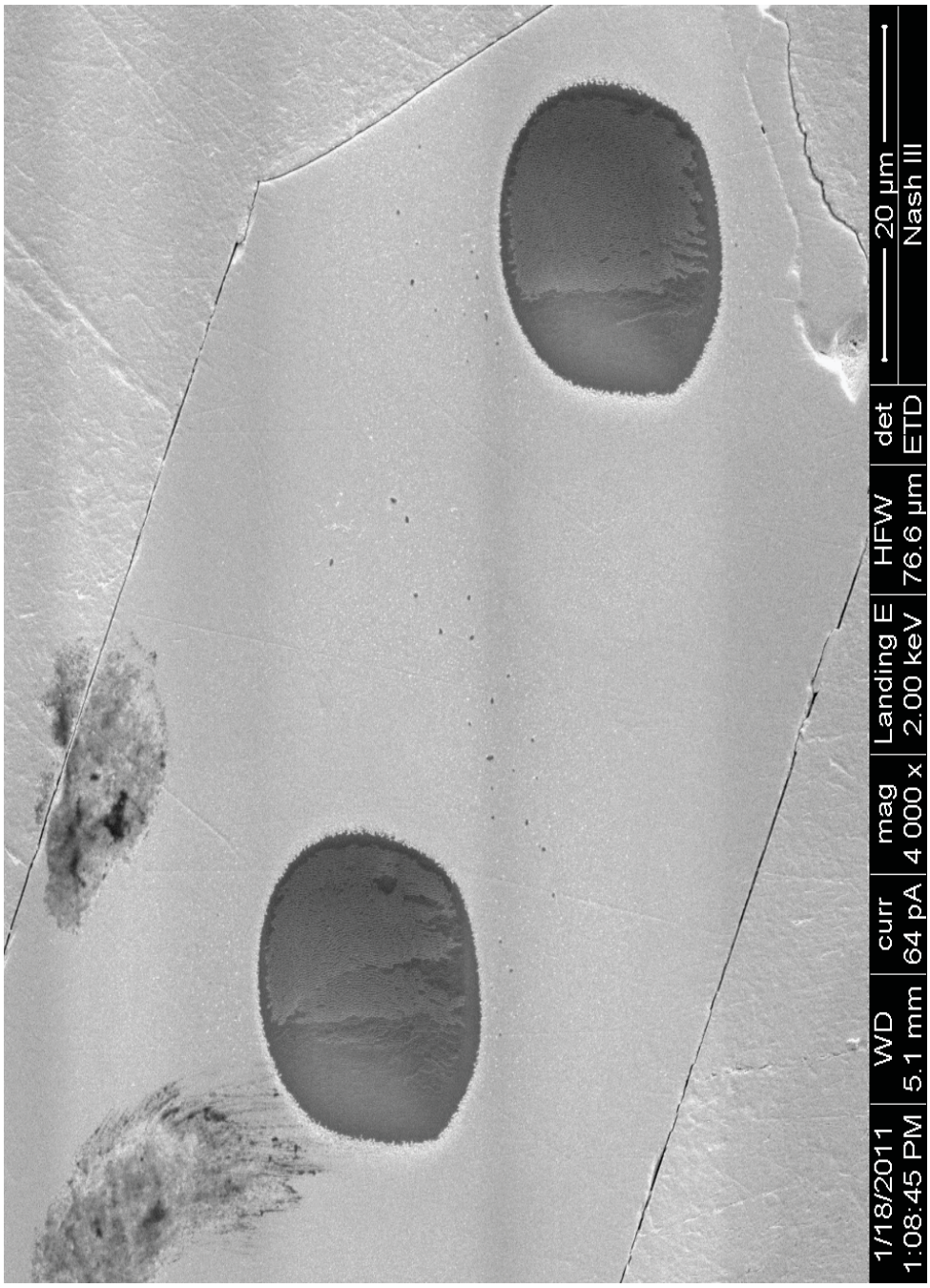
1/18/2011
1:08:45 PM
WD
5.1 mm
curr
64 pA
mag
4 000 x
Landing E
2.00 keV
HFW
76.6 µm
det
ETD
20 µm
Nash III

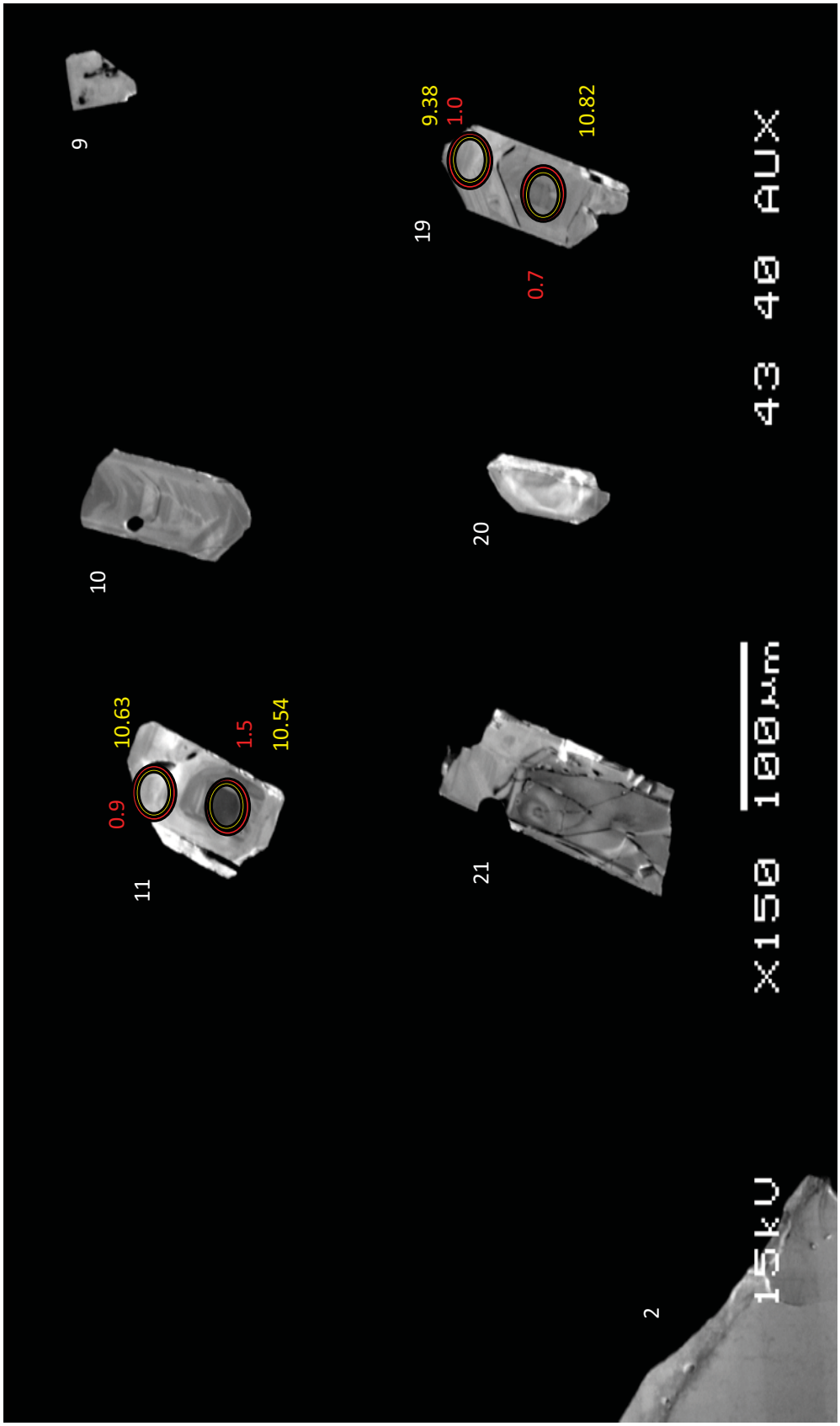
15kU X150 100µm 43 40 AUX
ULF
9
10
11
0.9
10.63
1.5
10.54
19
9.38
1.0
0.7
10.82
20
21
2

ULF-11

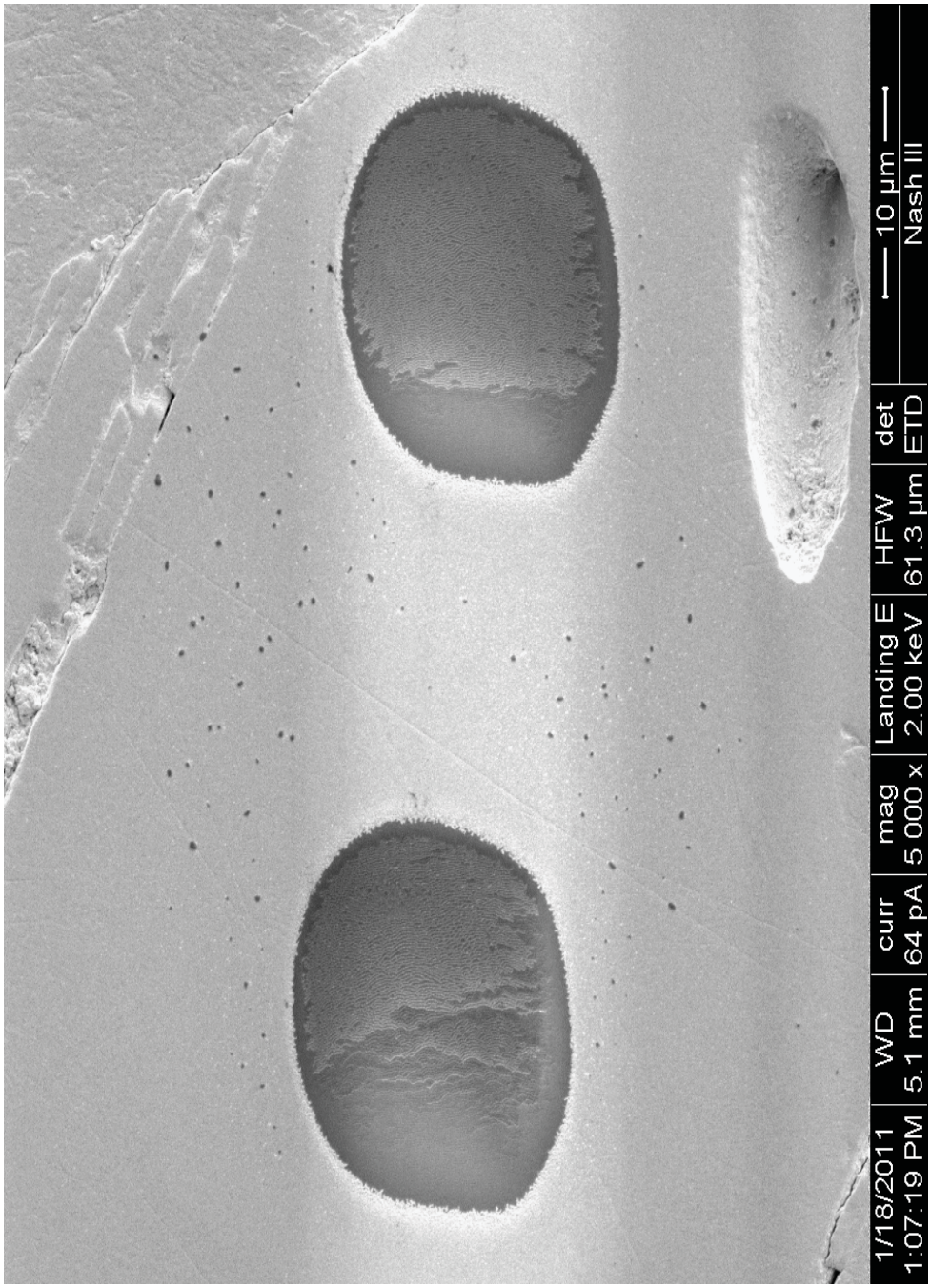
1/18/2011
1:07:19 PM
WD
5.1 mm
curr
64 pA
mag
5 000 x
Landing E
2.00 keV
HFW
61.3 µm
det
ETD
10 µm
Nash III

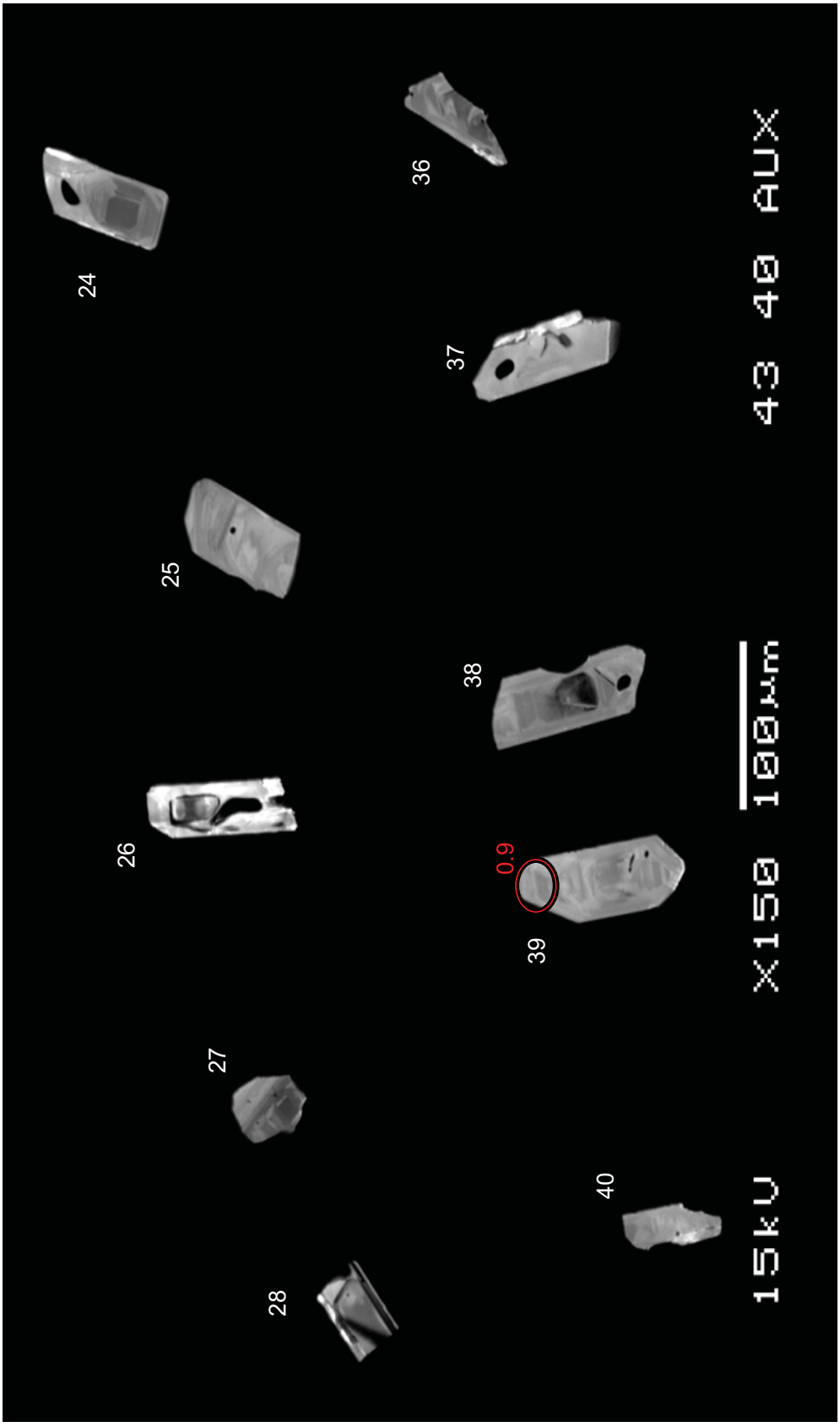
15kV X150 100µm 43 40 AUX
ULF
24
25
26
27
28
36
37
38
39
40
0.9

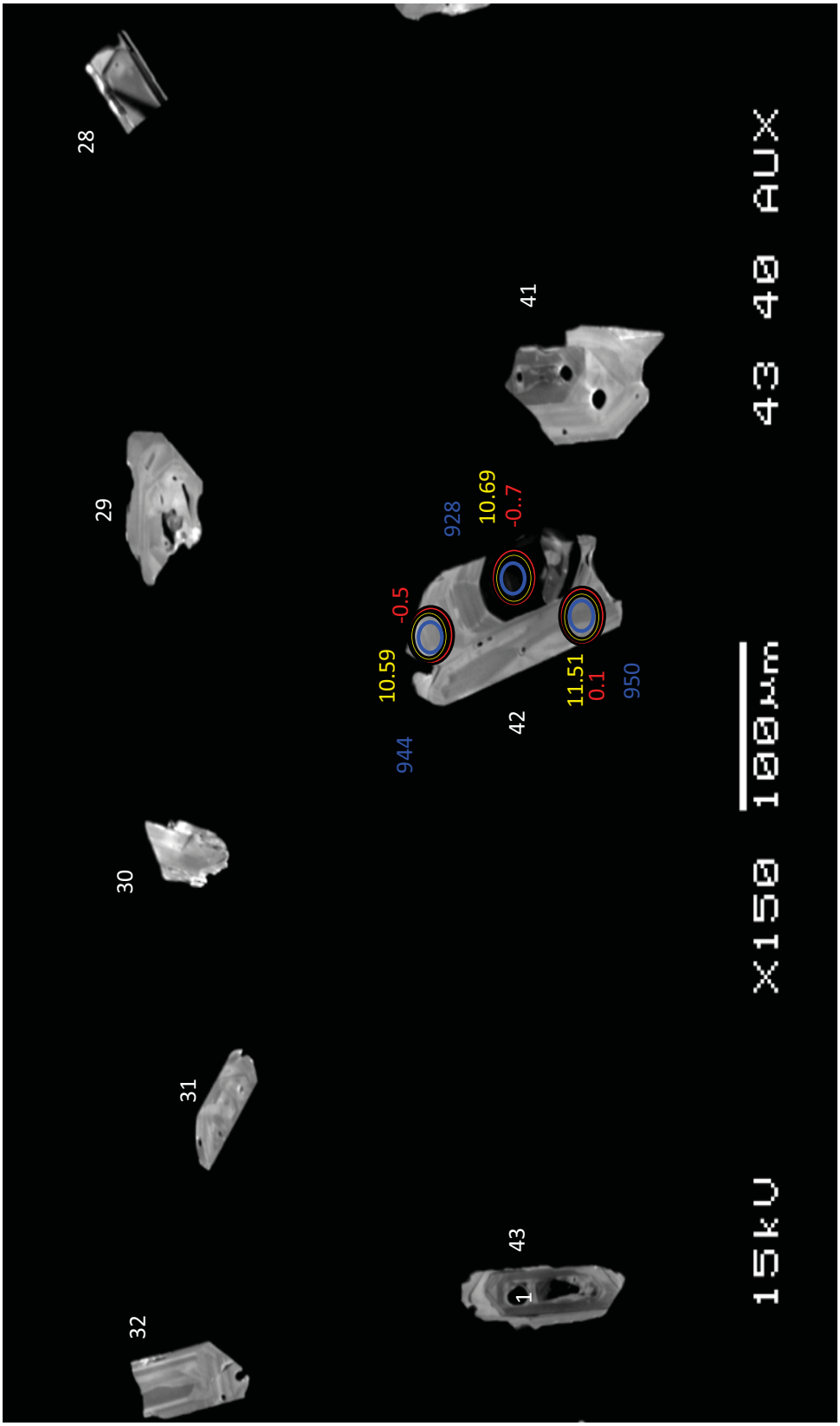
15kU X150 100µm 43 40 AUX
ULF
28
29
30
31
32
1
43
42
41
944
10.59
-0.5
928
10.69
-0.7
11.51
0.1
950

ULF-42

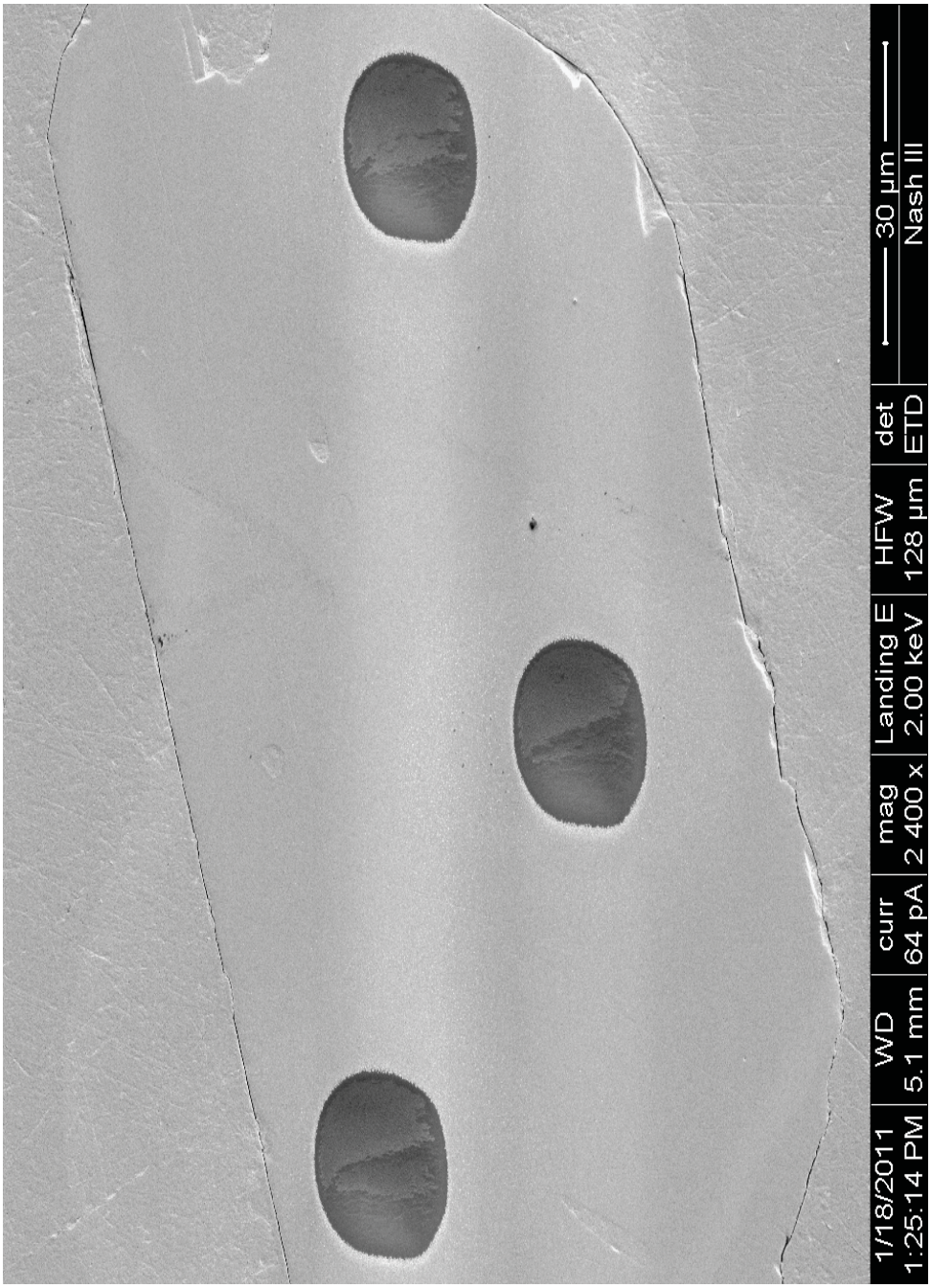
1/18/2011
1:25:14 PM
WD
5.1 mm
curr
64 pA
mag
2 400 x
Landing E
2.00 keV
HFW
128 µm
det
ETD
30 µm
Nash III

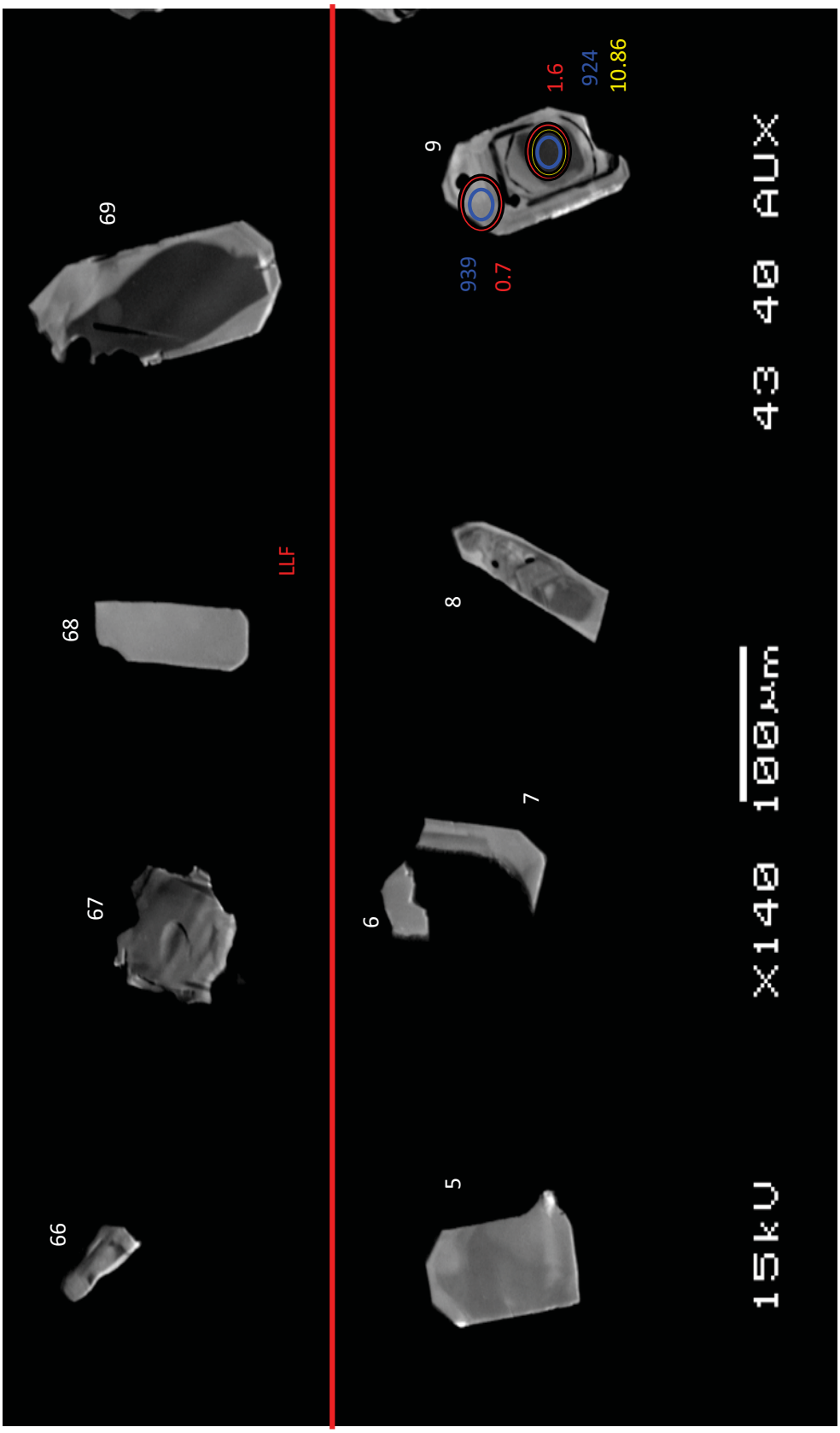
15kV X140 100µm 43 40 AUX
THR
LLF
66
67
68
69
5
6
7
8
9
939
0.7
1.6
924
10.86

THR-9

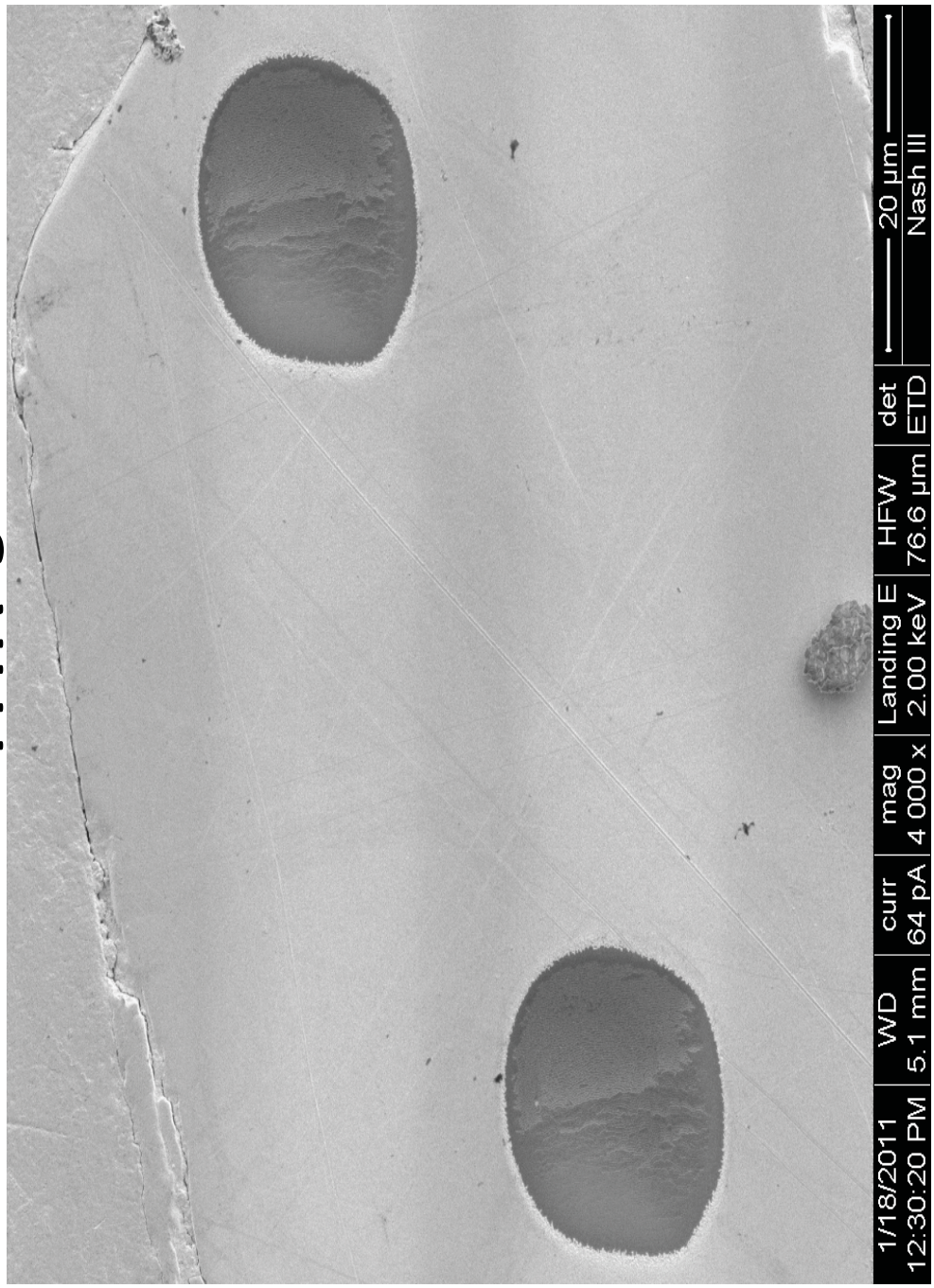
1/18/2011
12:30:20 PM
WD
5.1 mm
curr
64 pA
mag
4 000 x
Landing E
2.00 keV
HFW
76.6 µm
det
ETD
20 µm
Nash III

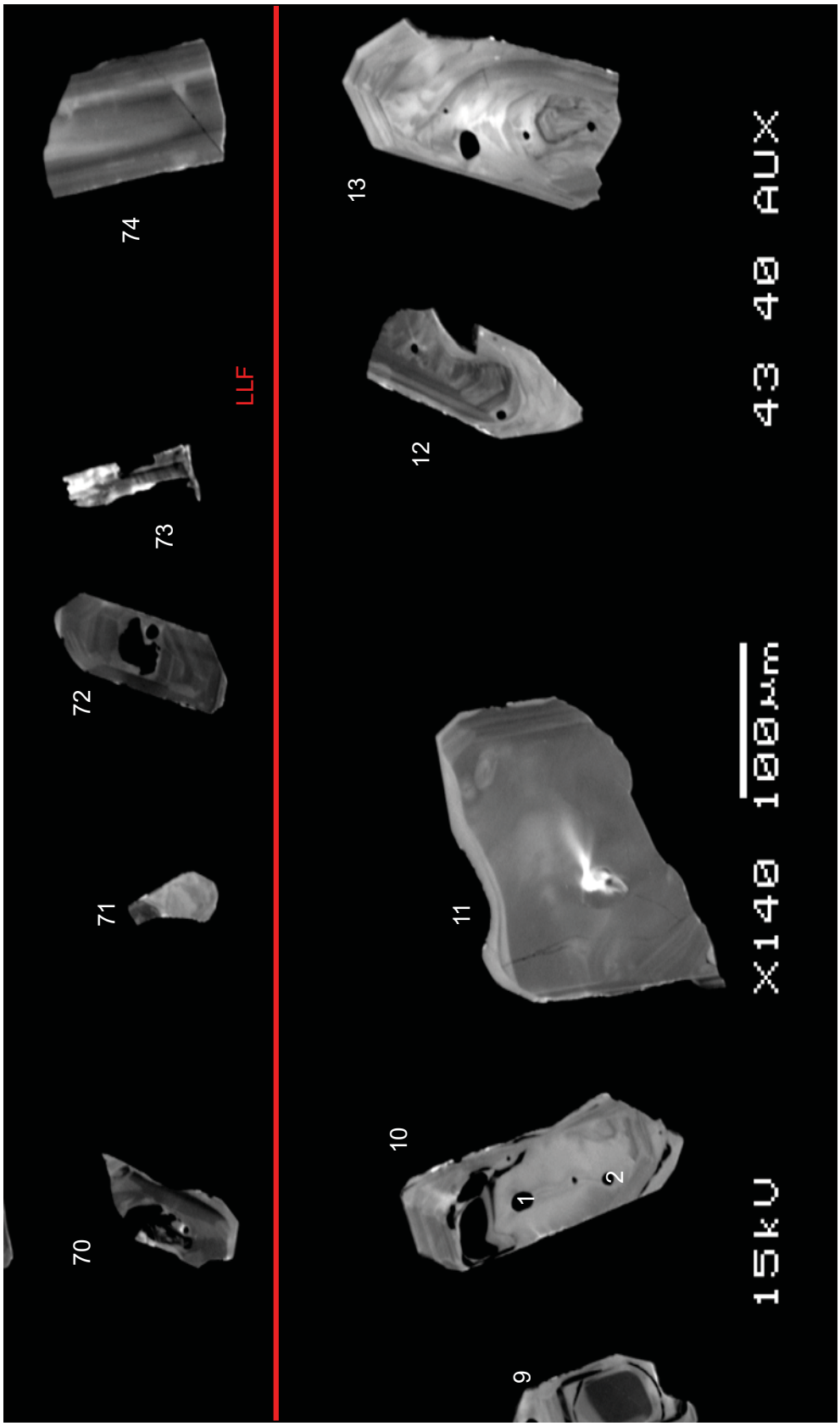

THR

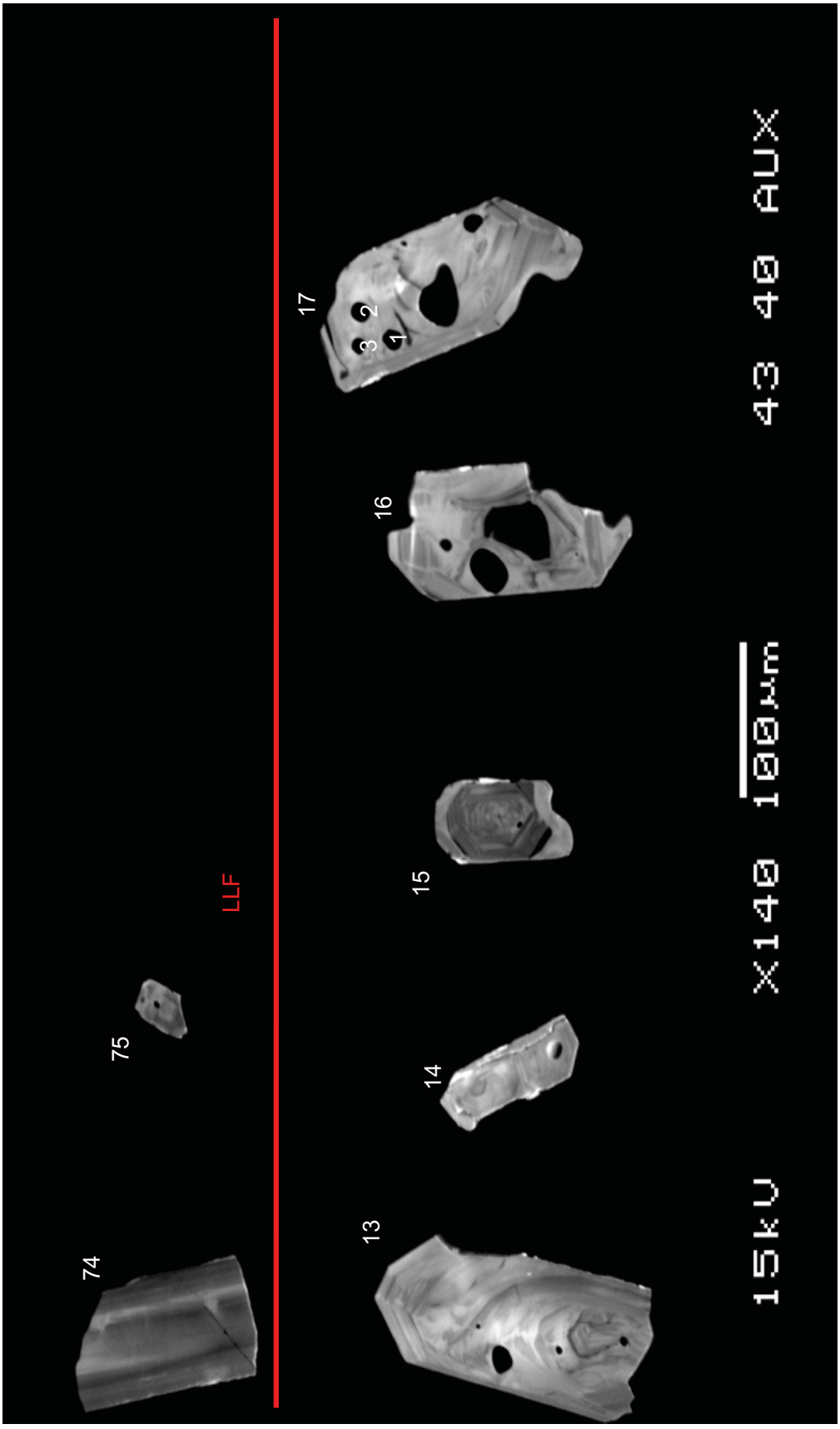
15kU X140 100µm 43 40 AUX
74
75
LLF
13
14
15
16
17
3 2 1
THR

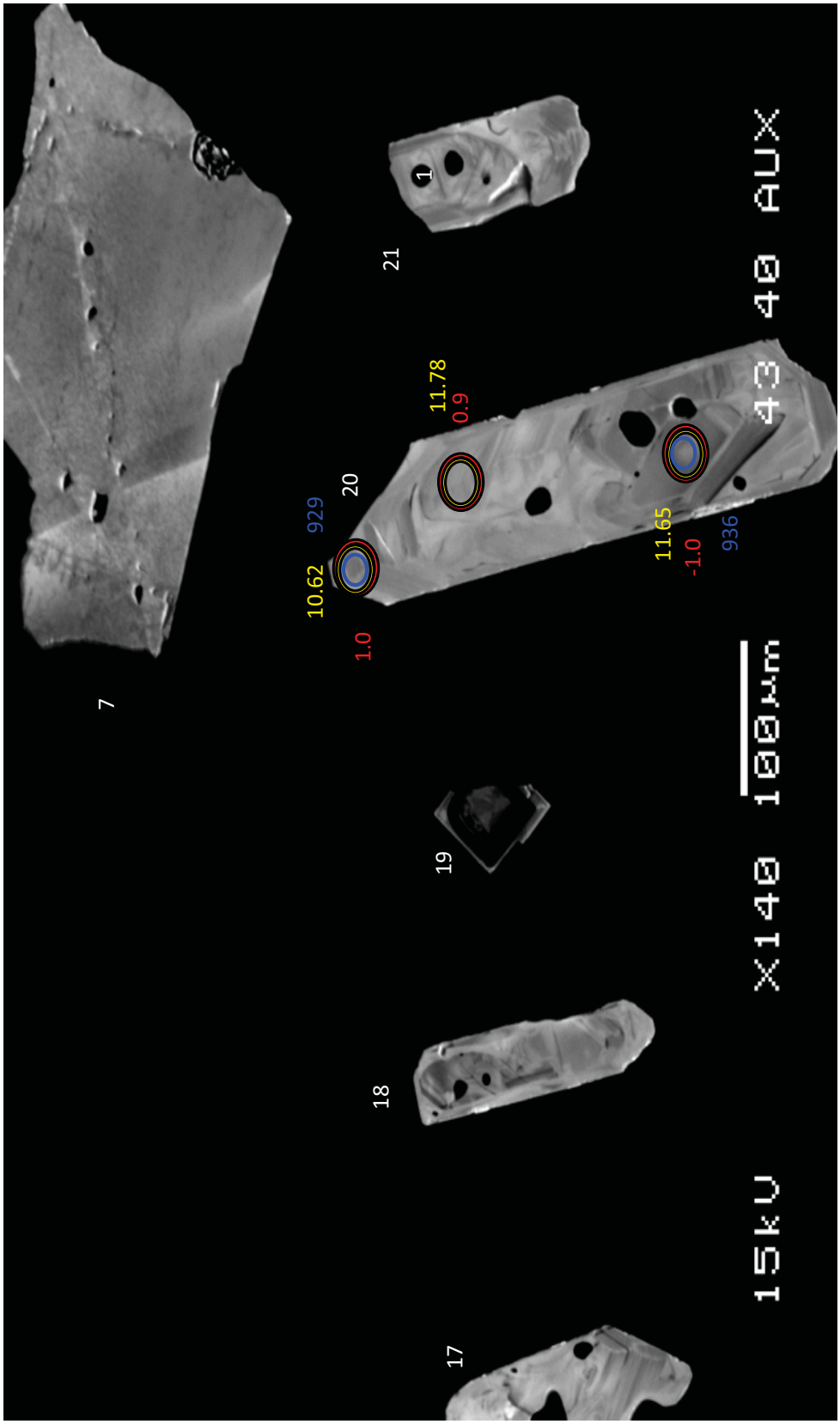
15kV X140 100µm 43 40 AUX
THR
7
17
18
19
20
21
1
10.62
929
1.0
11.78
0.9
11.65
-1.0
936

THR-20

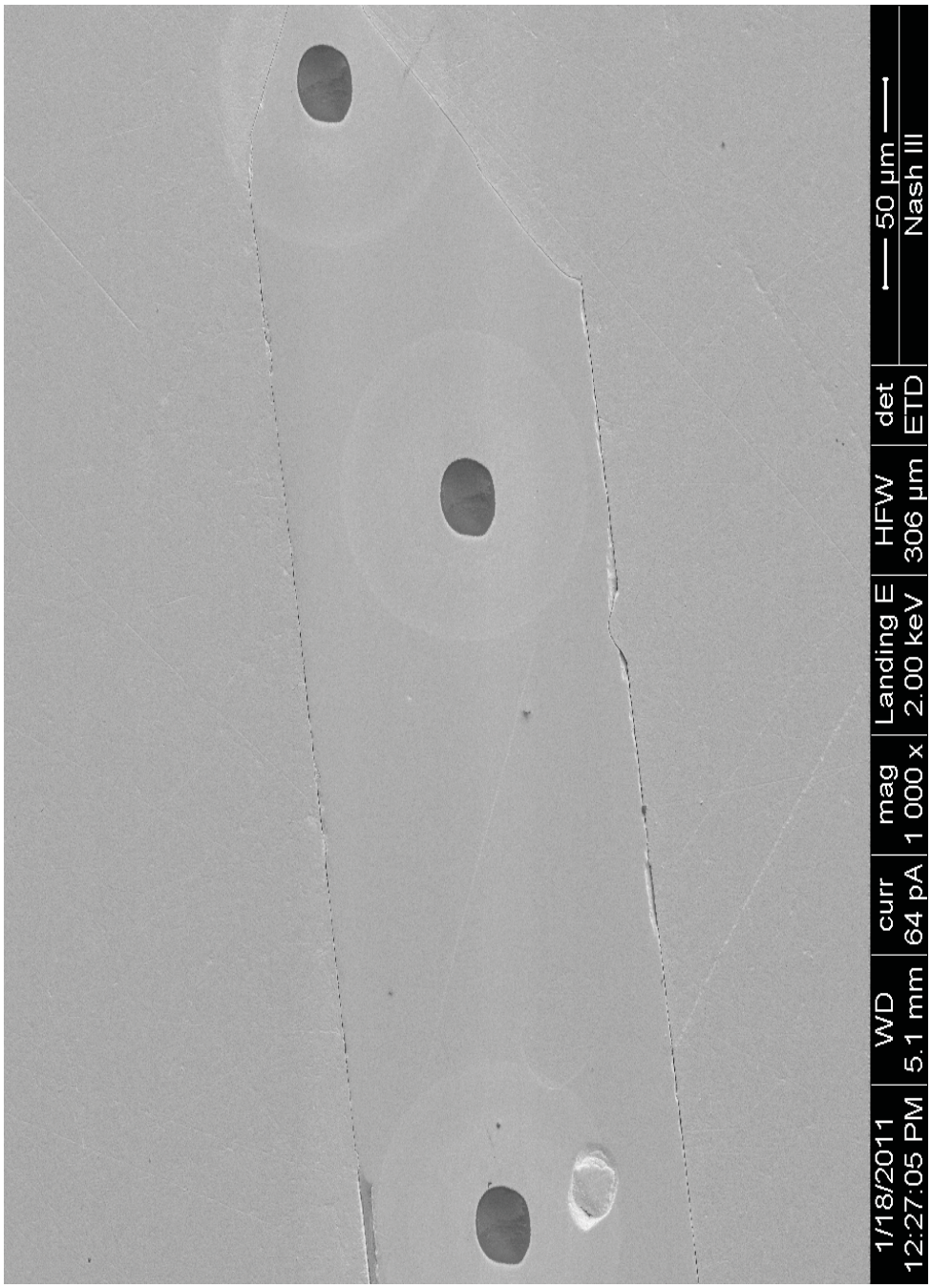
1/18/2011
12:27:05 PM
WD
5.1 mm
curr
64 pA
mag
1 000 x
Landing E
2.00 keV
HFW
306 µm
det
ETD
50 µm
Nash III

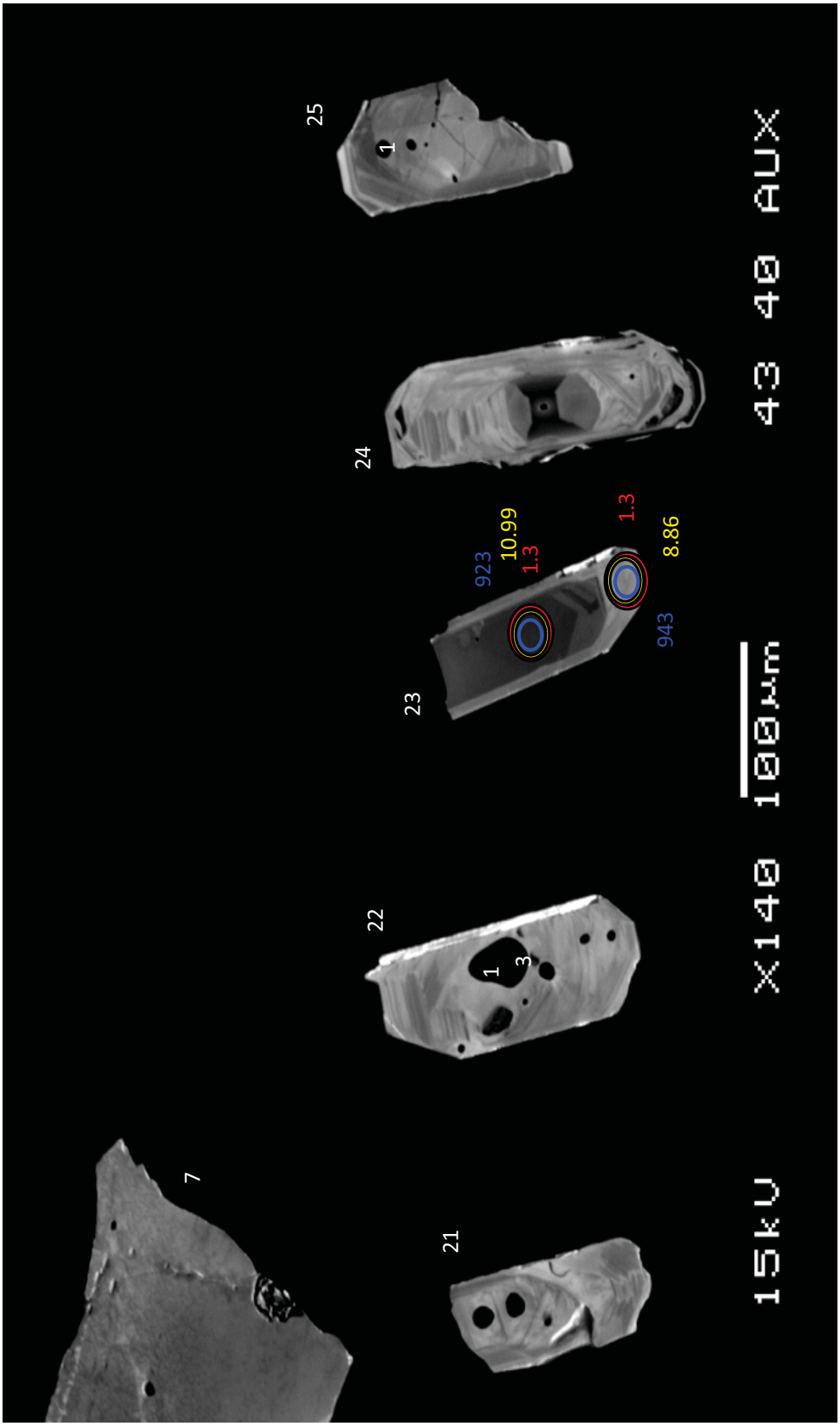
15kV X140 100µm 43 40 AUX
THR
25
1
24
23
923
10.99
1.3
943
1.3
8.86
22
1
3
21
7

THR-23

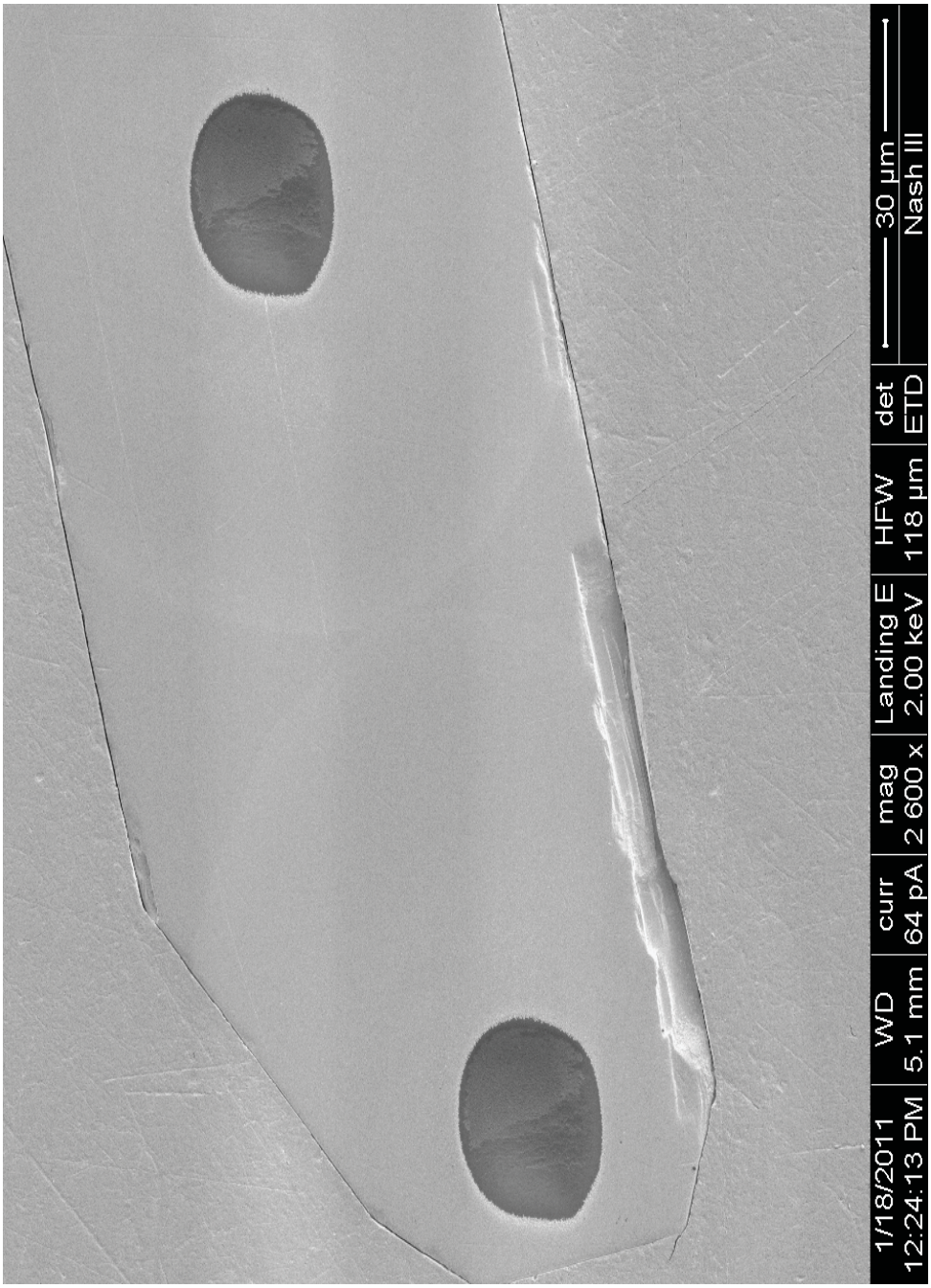
1/18/2011
12:24:13 PM
WD
5.1 mm
curr
64 pA
mag
2 600 x
Landing E
2.00 keV
HFW
118 µm
det
ETD
30 µm
Nash III

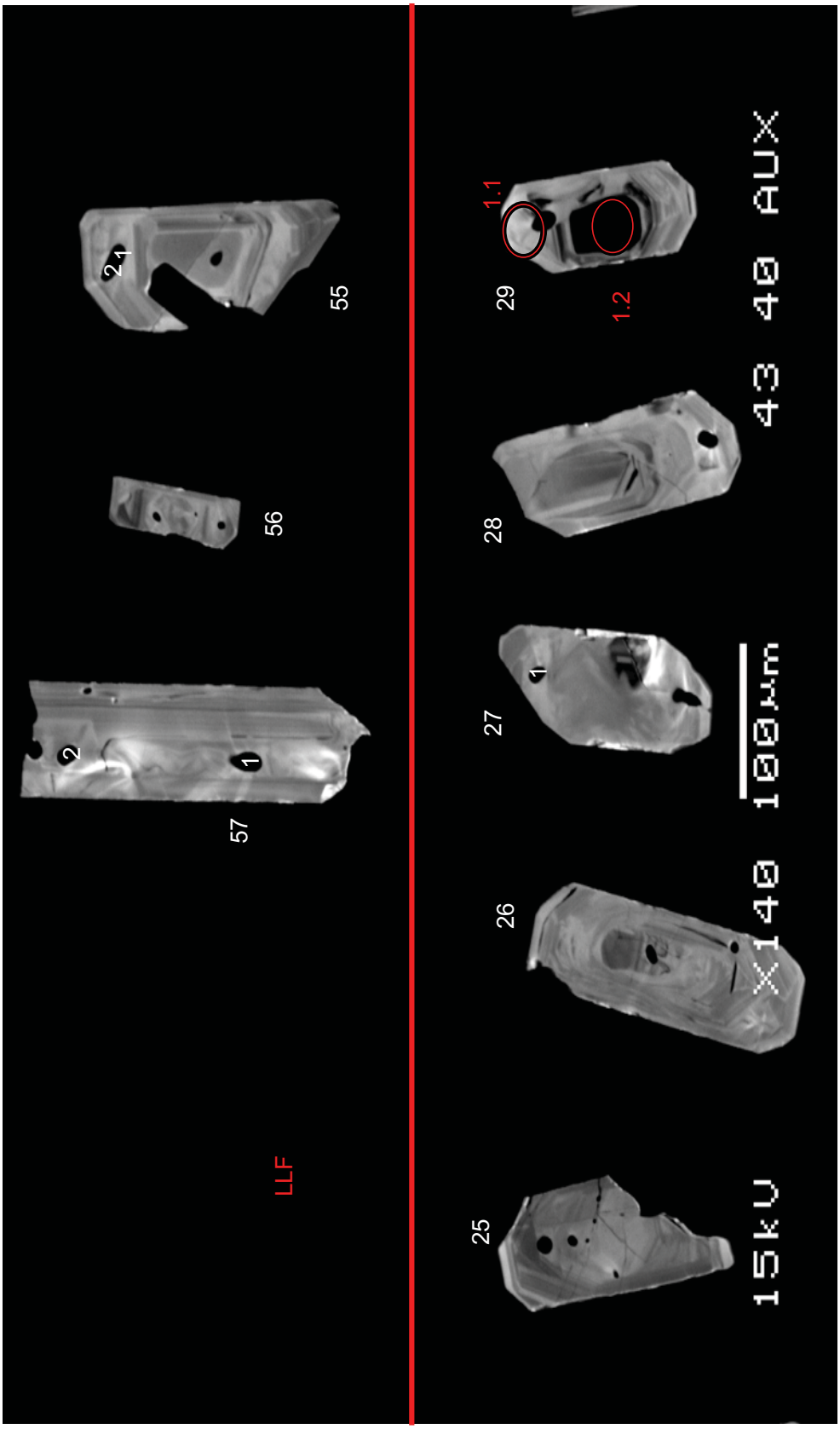
LLF
THR
15kU X140 100µm
43 40 AUX
2.1
55
56
2
1
57
25
26
27
1
28
29
1.1
1.2

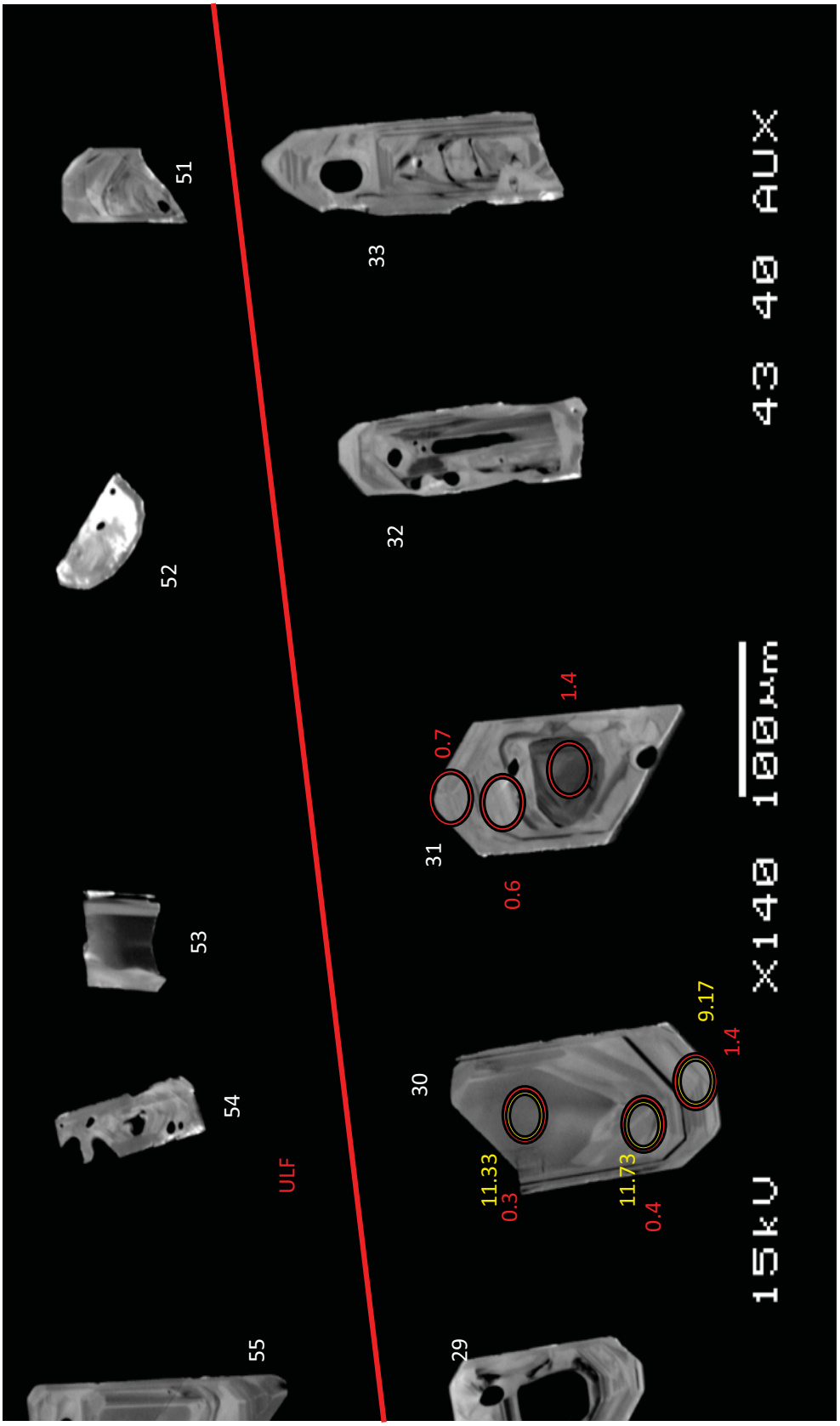
15kV X140 100µm 43 40 AUX
ULF
55
54
53
52
51
29
30
31
32
33
11.33
0.3
11.73
0.4
9.17
1.4
0.6
0.7
1.4

THR

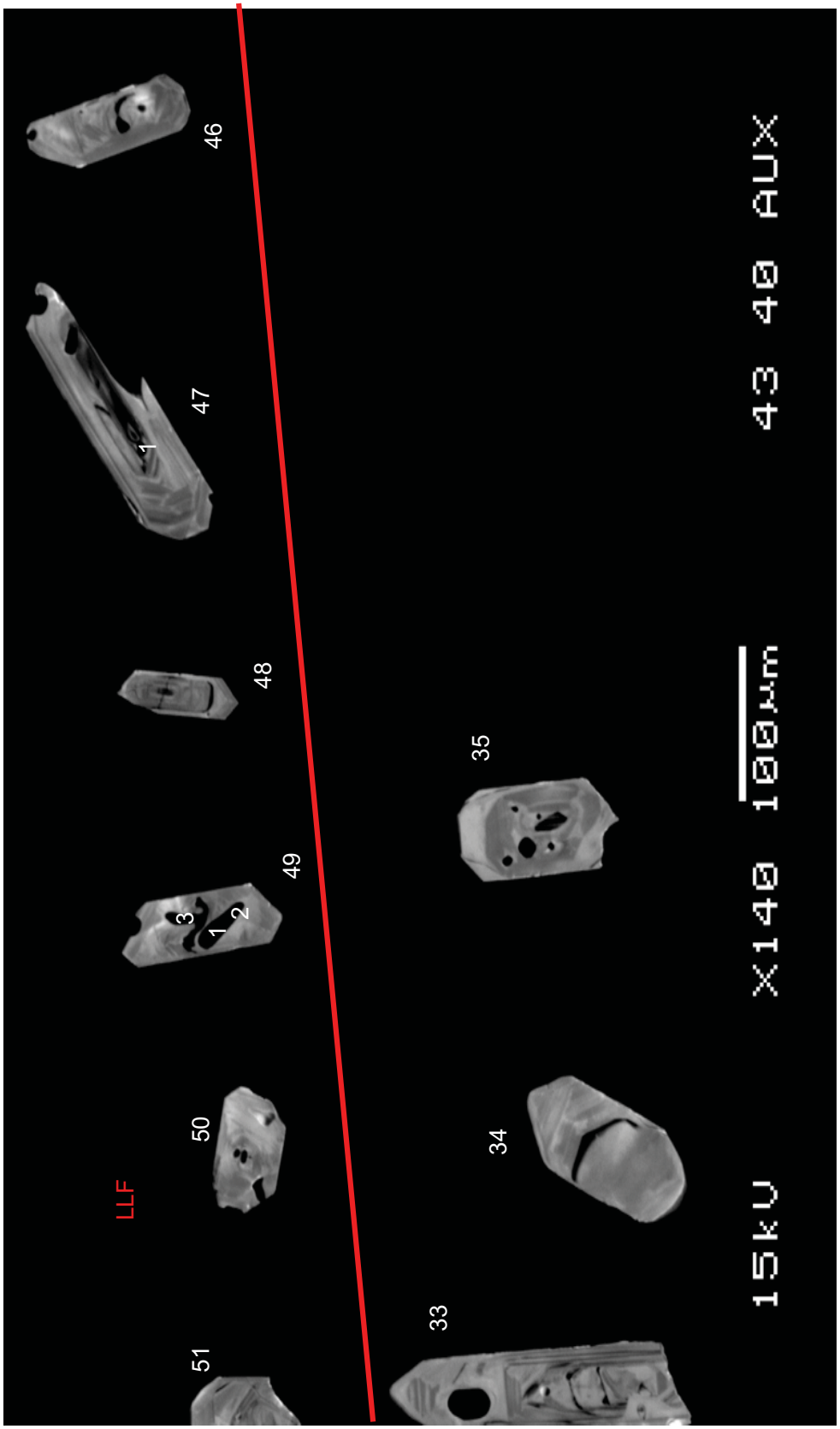

THR

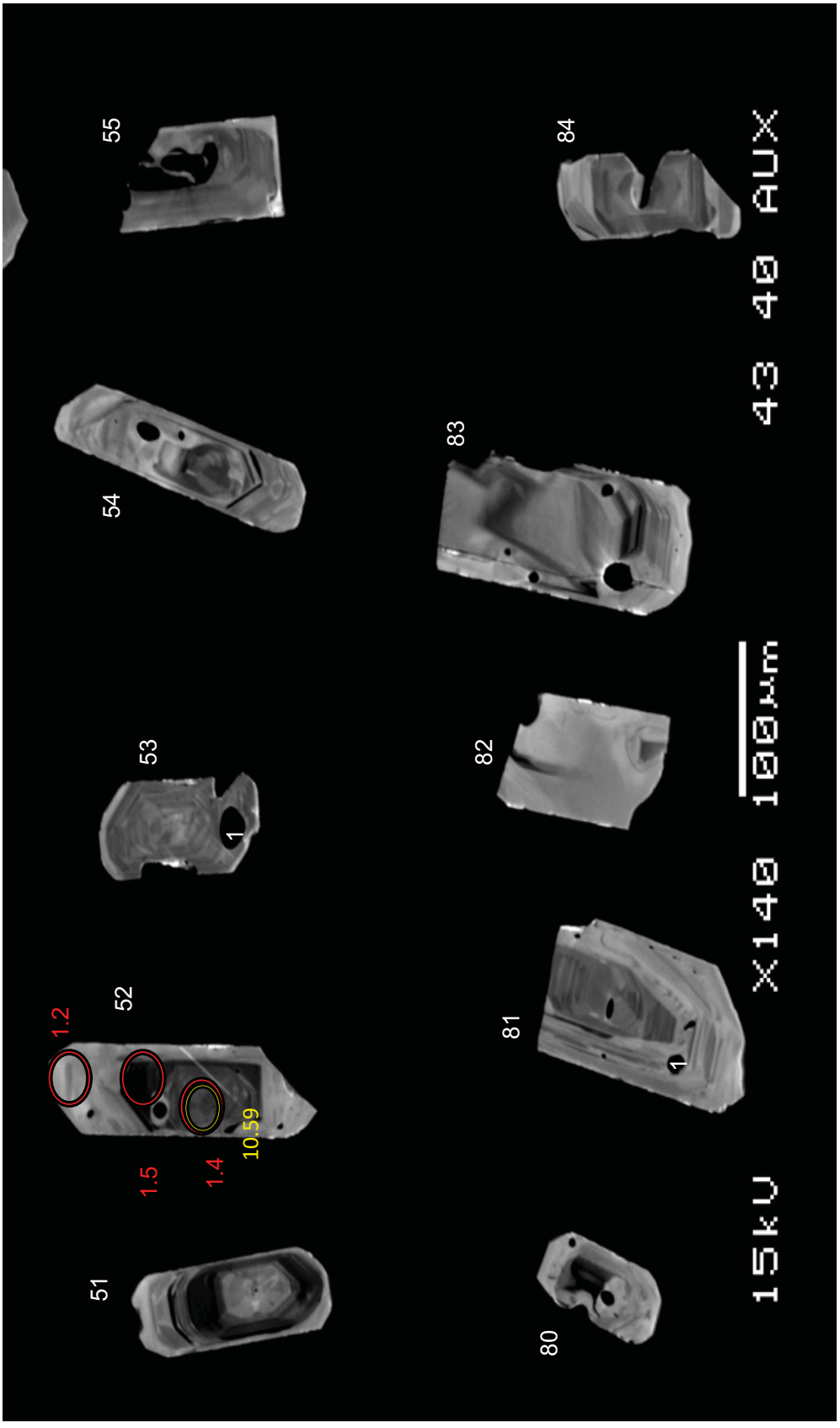
15kU X1400 100µm 43 40 AUX
THR
51
52
53
54
55
80
81
82
83
84
1.2
1.5
1.4
1059
1
1

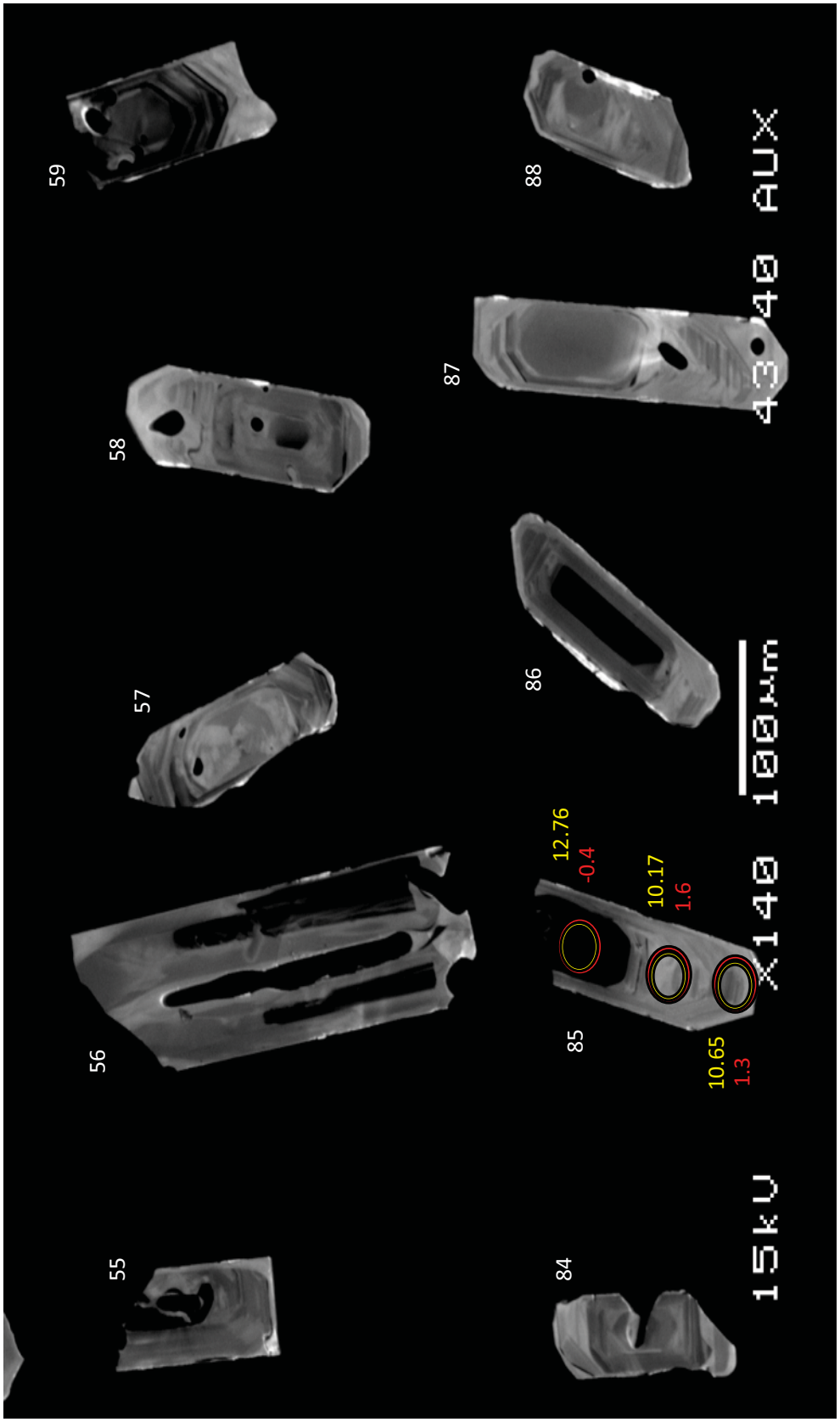
15kU X140 100µm
43 40 AUX
55
56
57
58
59
84
85
86
87
88
12.76
-0.4
10.17
1.6
10.65
1.3

THR

THR-85

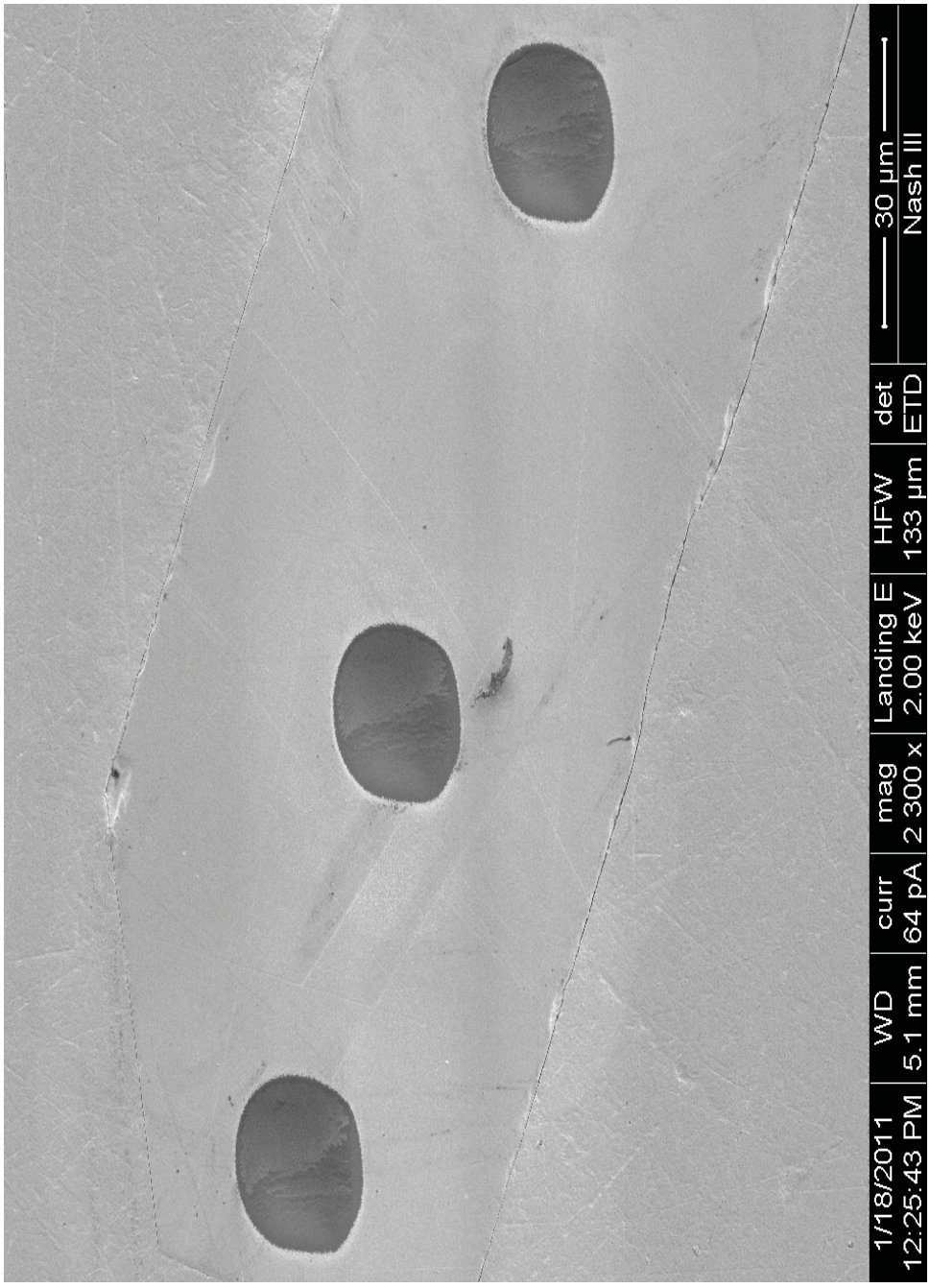
1/18/2011
12:25:43 PM
WD
5.1 mm
curr
64 pA
mag
2 300 x
Landing E
2.00 keV
HFW
133 µm
det
ETD
30 µm
Nash III

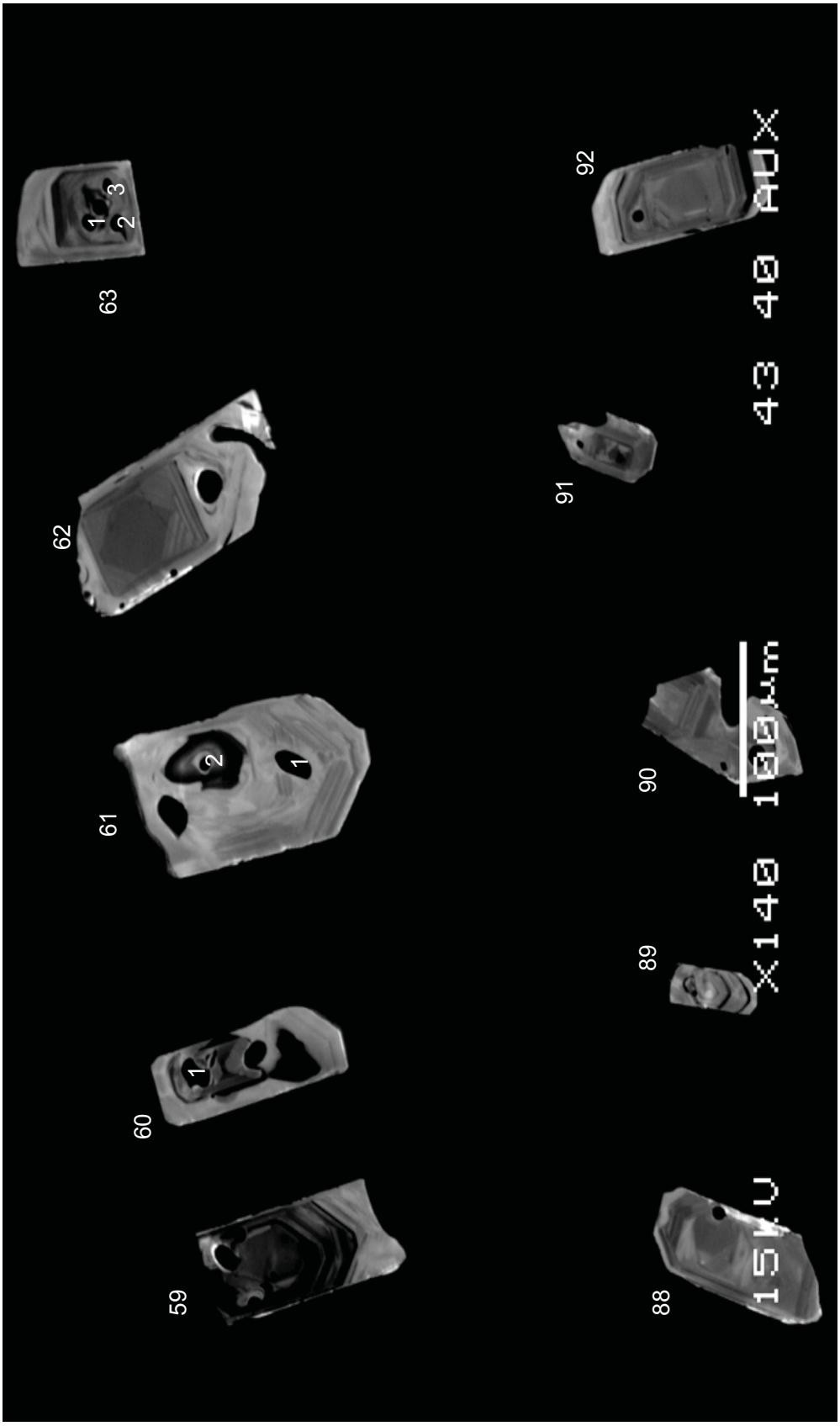

THR

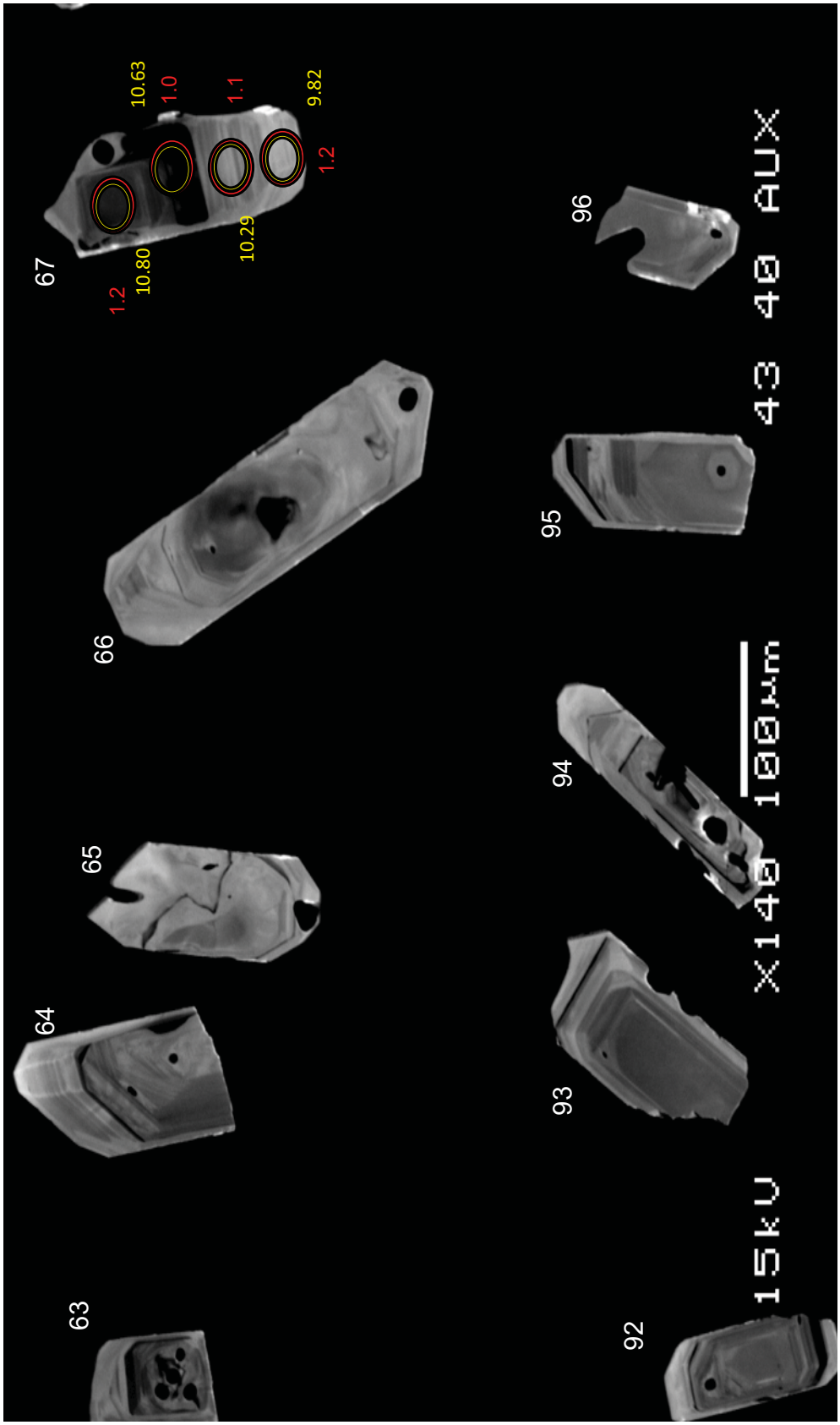
63
64
65
66
67
92
93
94
95
96
10.63
1.0
1.1
9.82
1.2
10.80
1.2
10.29
15kU X1400 100μm
43 40 AUX

THR

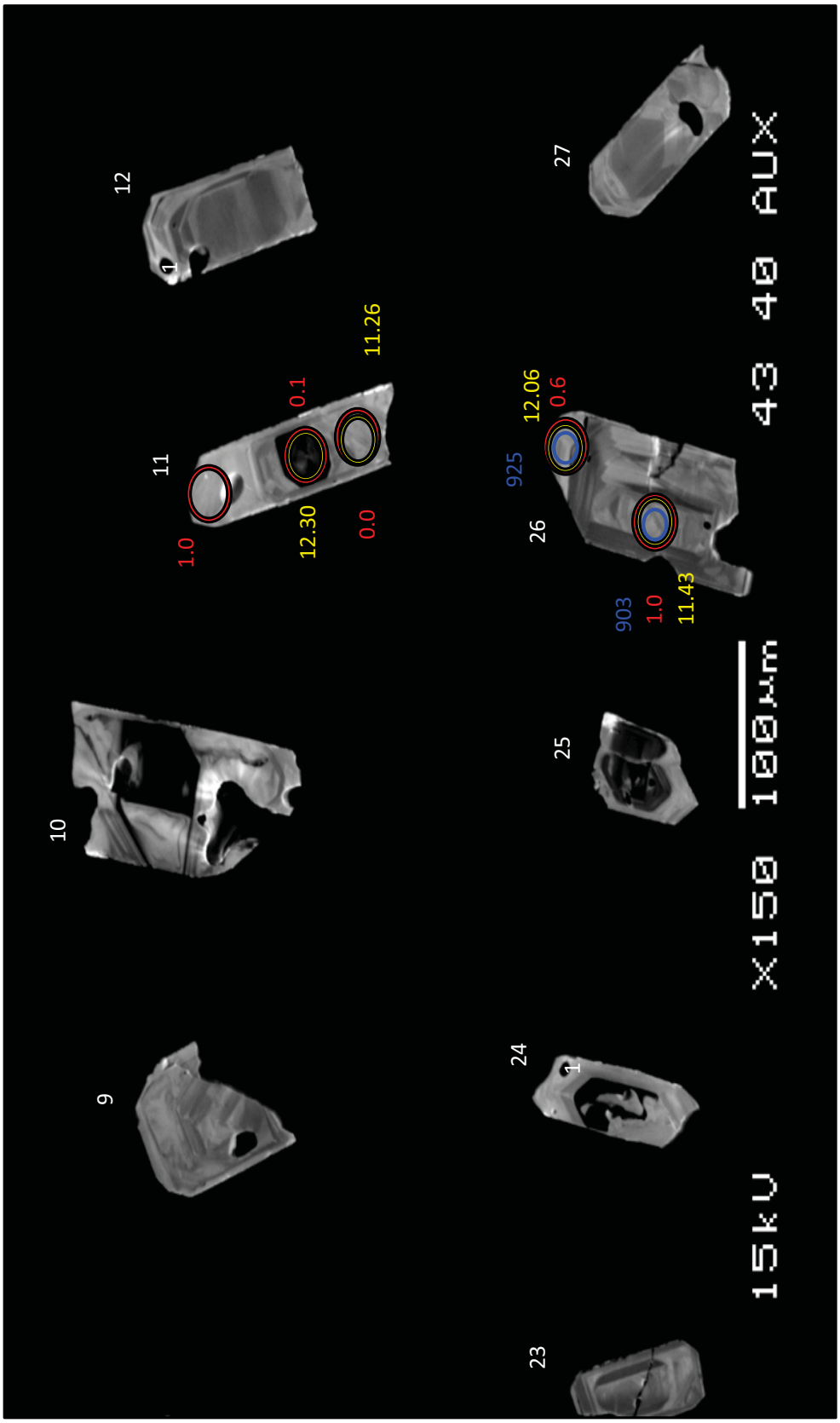
15kV X150 100µm 43 40 AUX
LLF
12
1
11
1.0
12.30
0.0
0.1
11.26
10
9
24
1
23
25
26
925
903
1.0
11.43
12.06
0.6
27

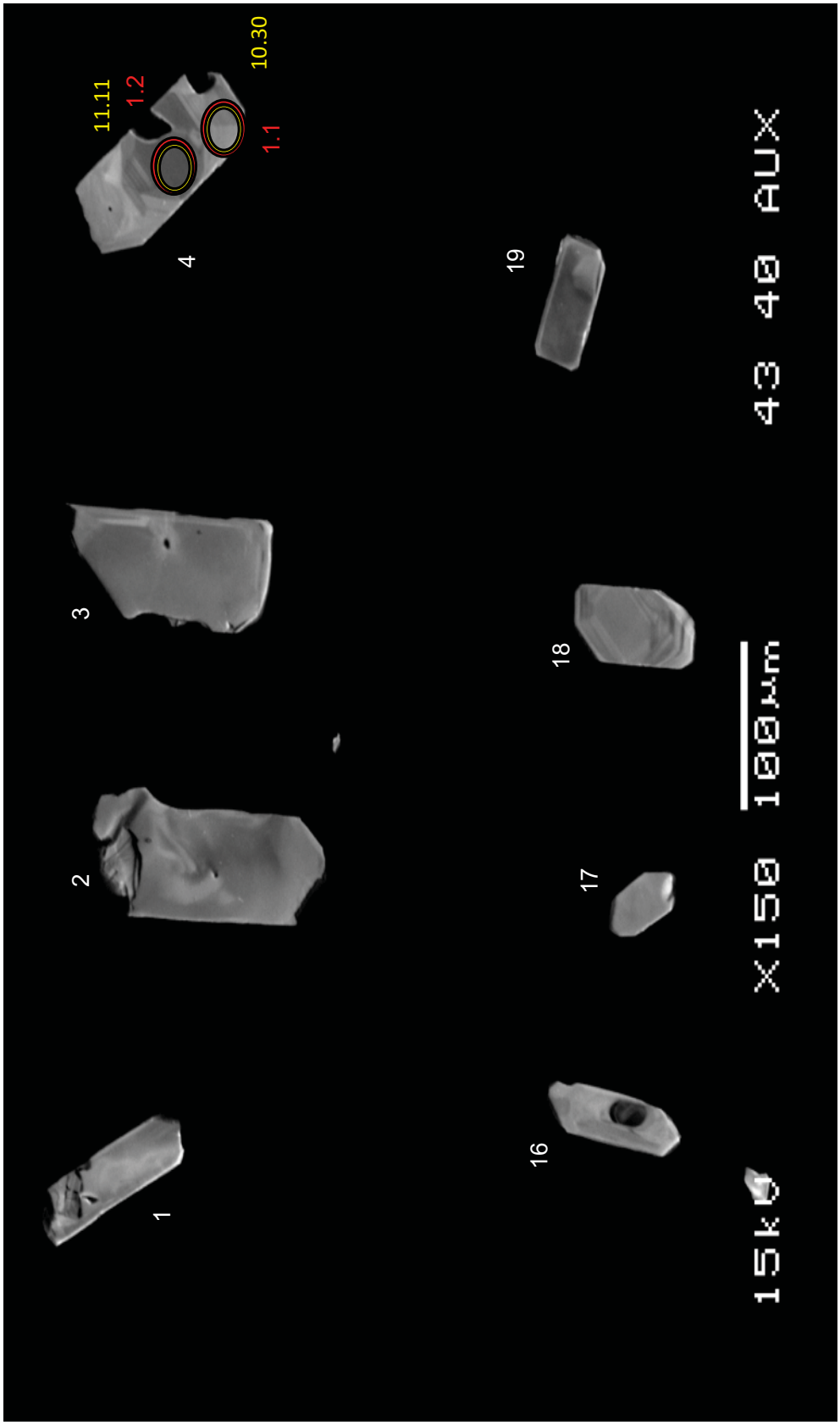
11.11
1.2
10.30
1.1
4
19
3
18
2
17
16
1
15kV X150 100µm 43 40 AUX
LLF

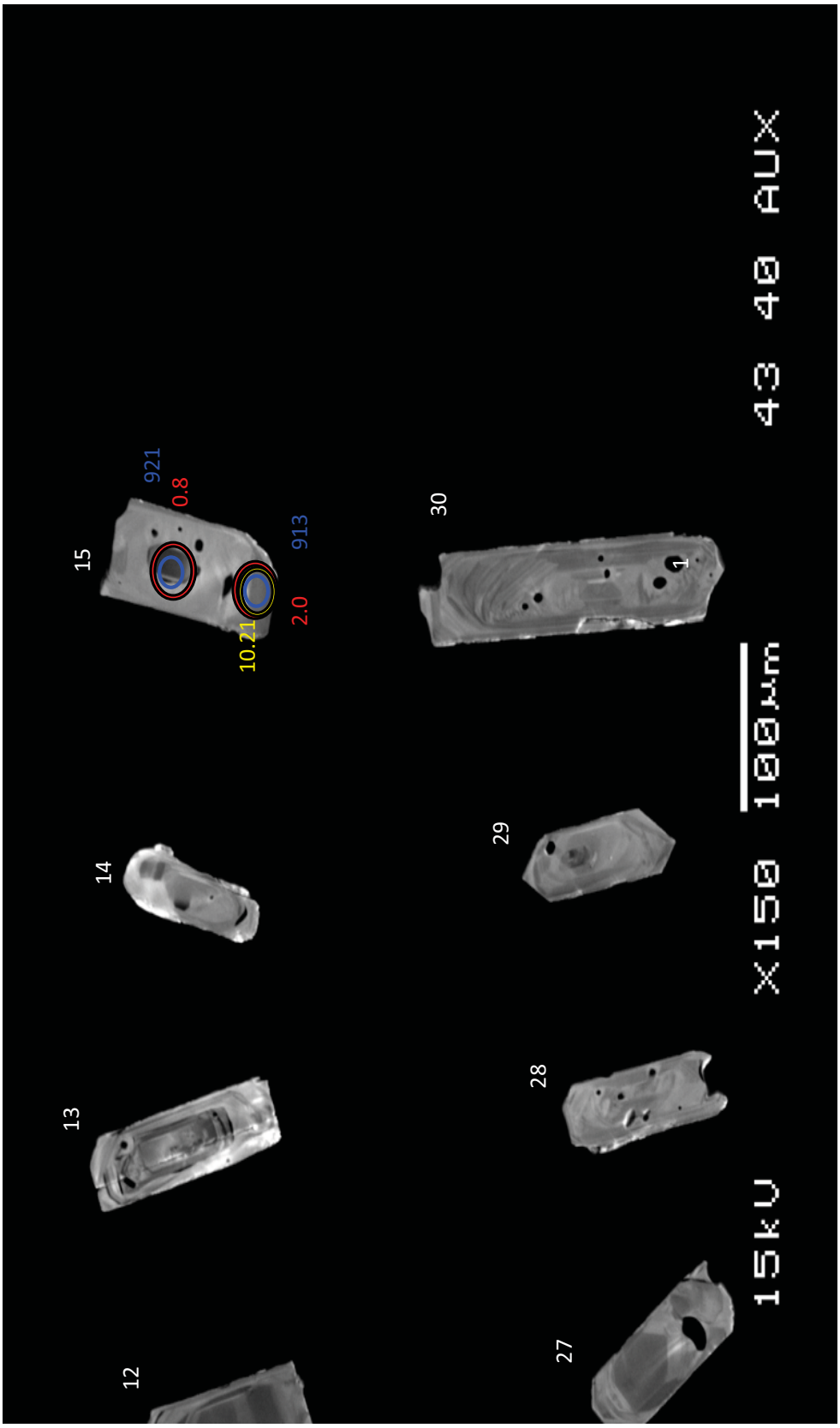
15kV X150 100µm 43 40 AUX
LLF
12
13
14
15
27
28
29
30
1
921
0.8
913
2.0
10.21

LLF-15

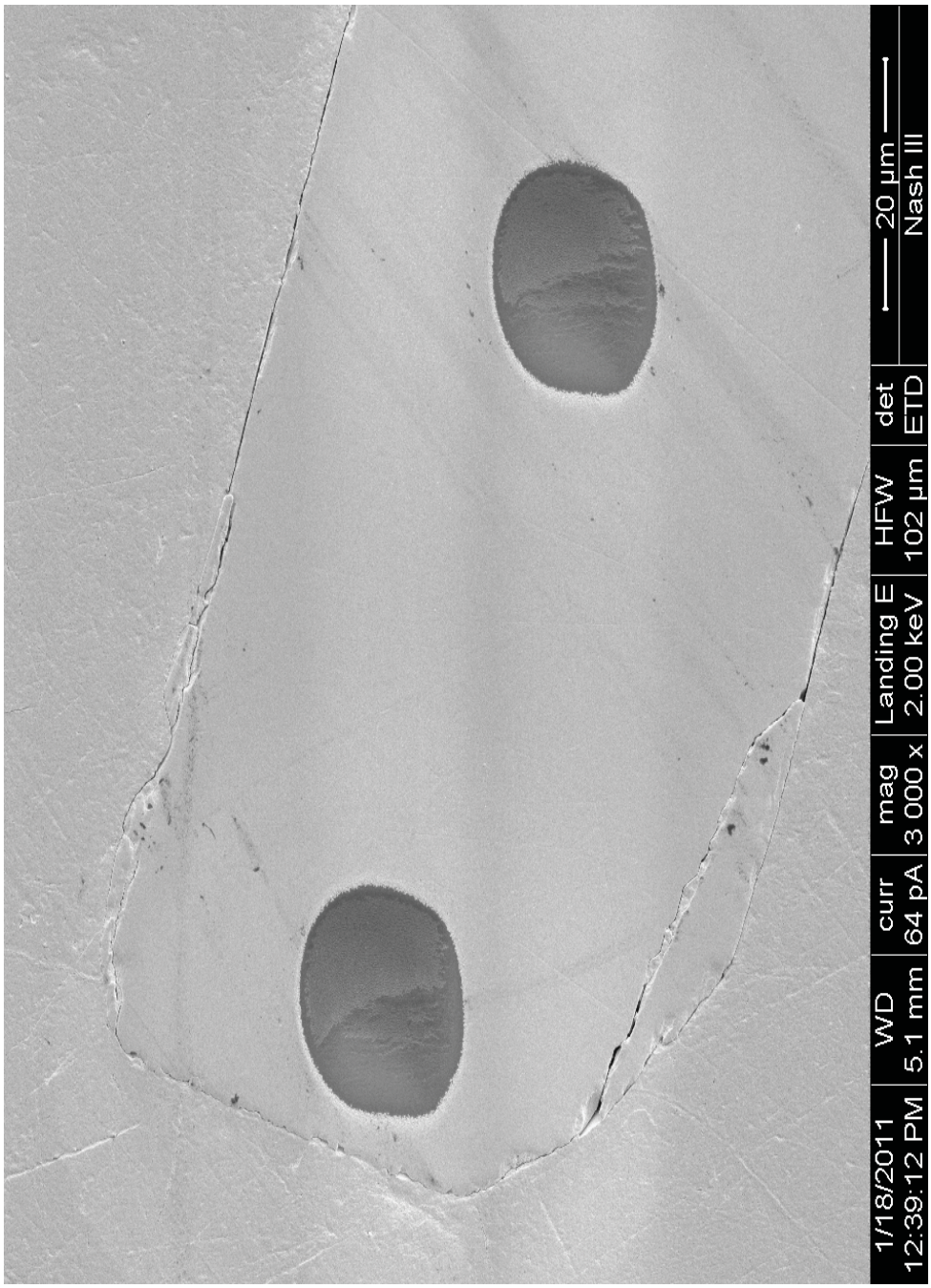
1/18/2011
12:39:12 PM
WD
5.1 mm
curr
64 pA
mag
3 000 x
Landing E
2.00 keV
HFW
102 µm
det
ETD
20 µm
Nash III

LLF-26

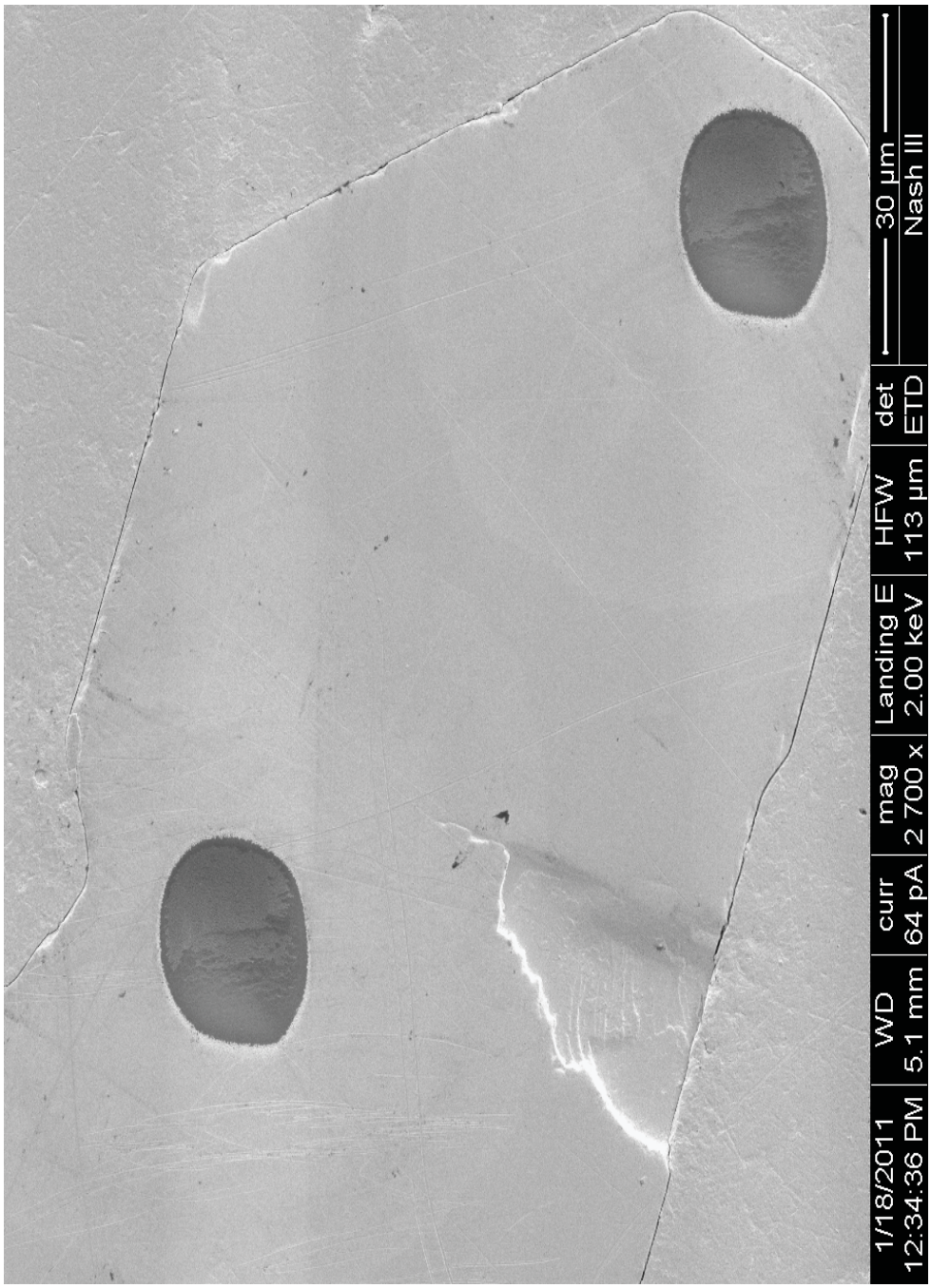
1/18/2011
12:34:36 PM
WD
5.1 mm
curr
64 pA
mag
2 700 x
Landing E
2.00 keV
HFW
113 µm
det
ETD
30 µm
Nash III

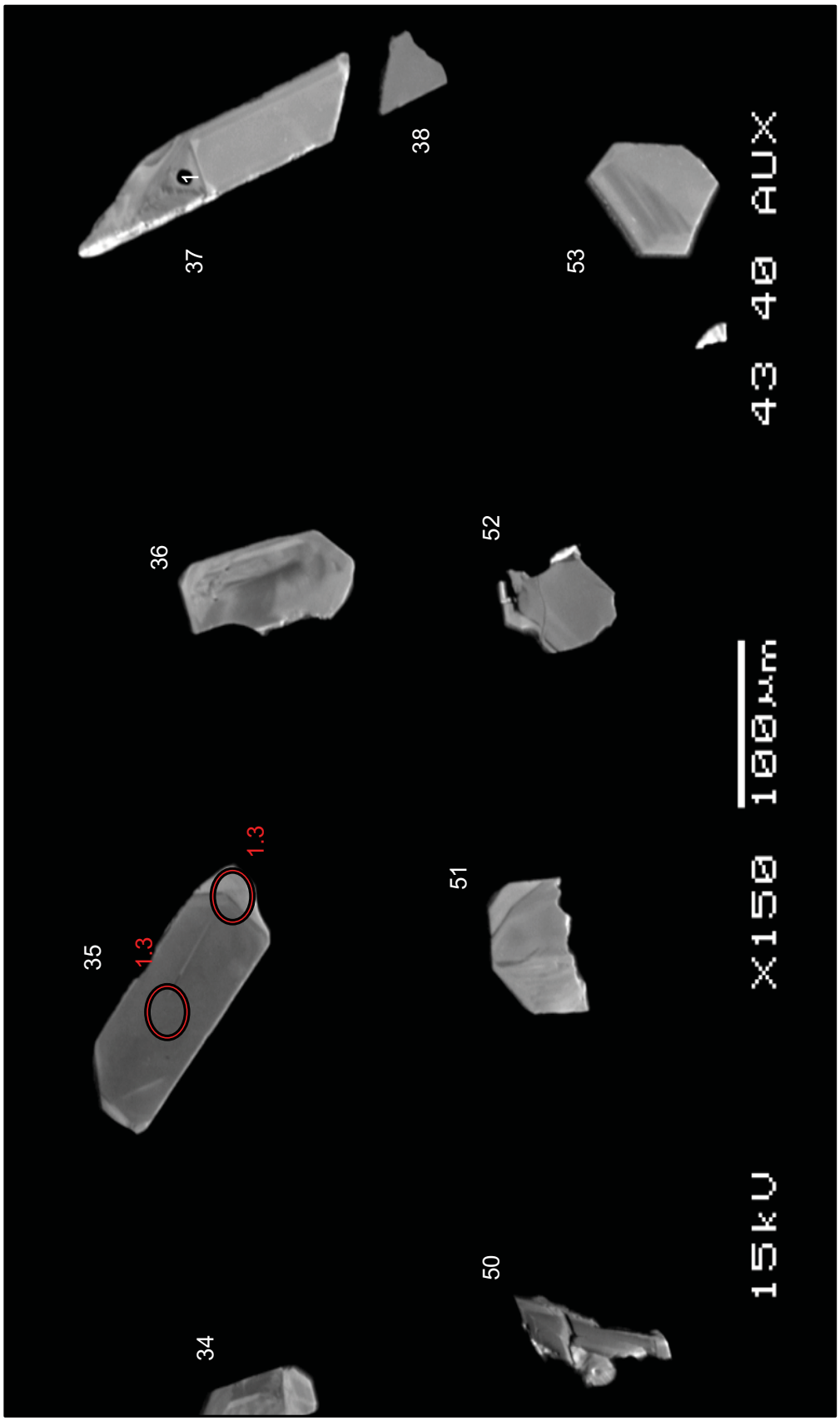
15kV X150 100µm 43 40 AUX
LLF
1
37
38
53
36
52
35
1.3
1.3
51
50
34

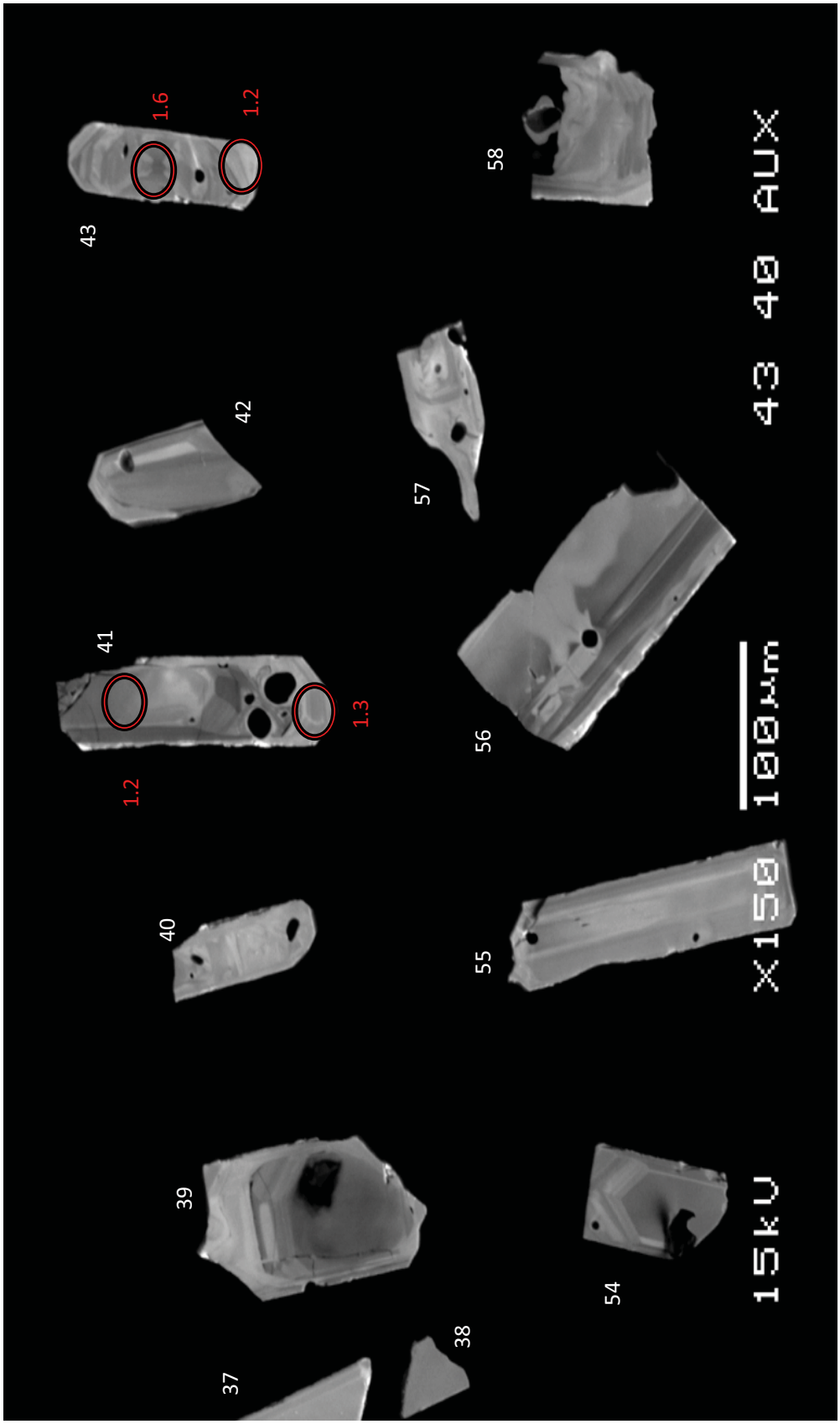
15kV X150 100µm 43 40 AUX
43
1.6
1.2
42
41
1.2
1.3
40
39
38
37
57
58
56
55
54

LLF

LLF-43

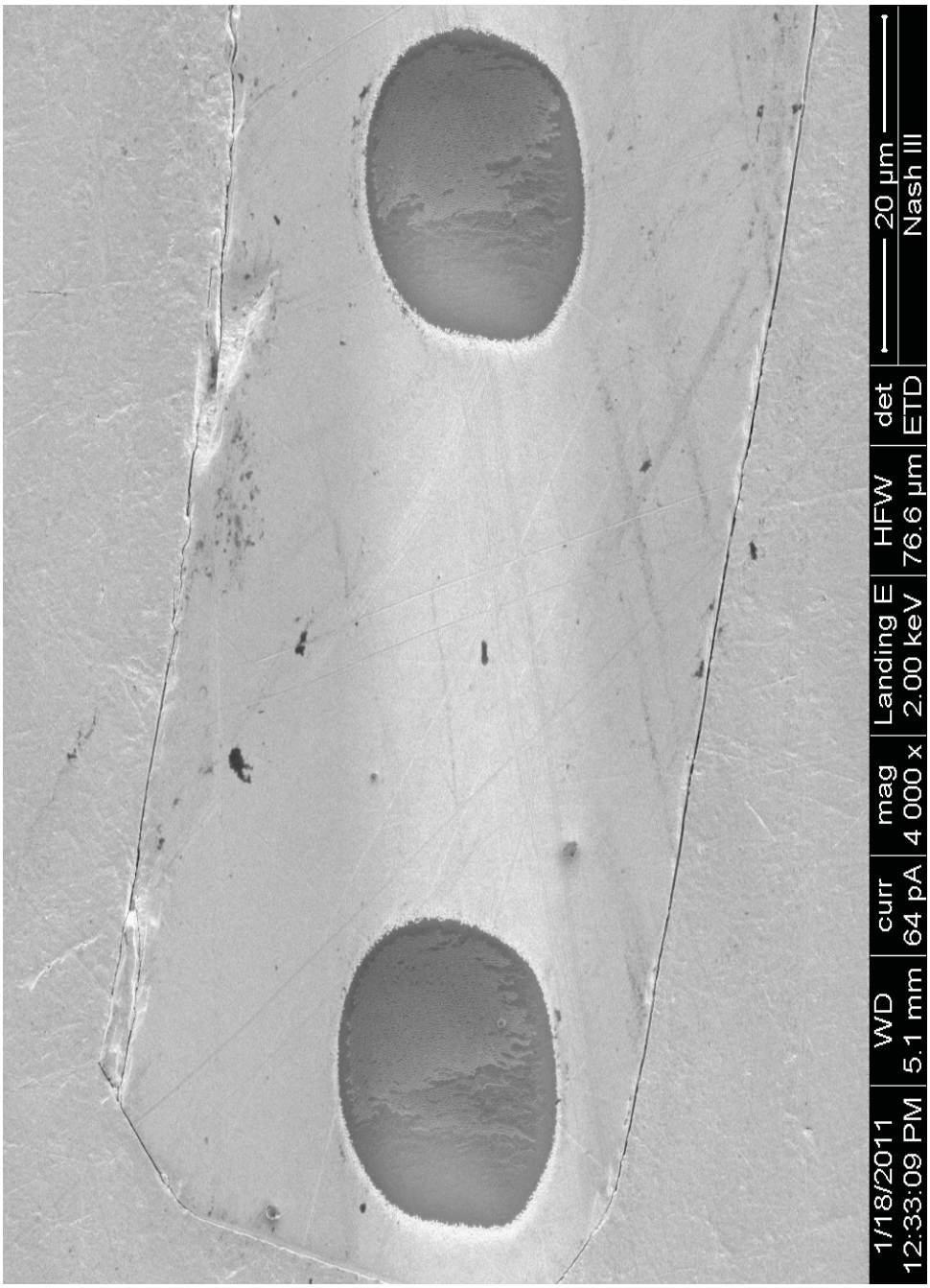
1/18/2011
12:33:09 PM
WD
5.1 mm
curr
64 pA
mag
4 000 x
Landing E
2.00 keV
HFW
76.6 µm
det
ETD
20 µm
Nash III

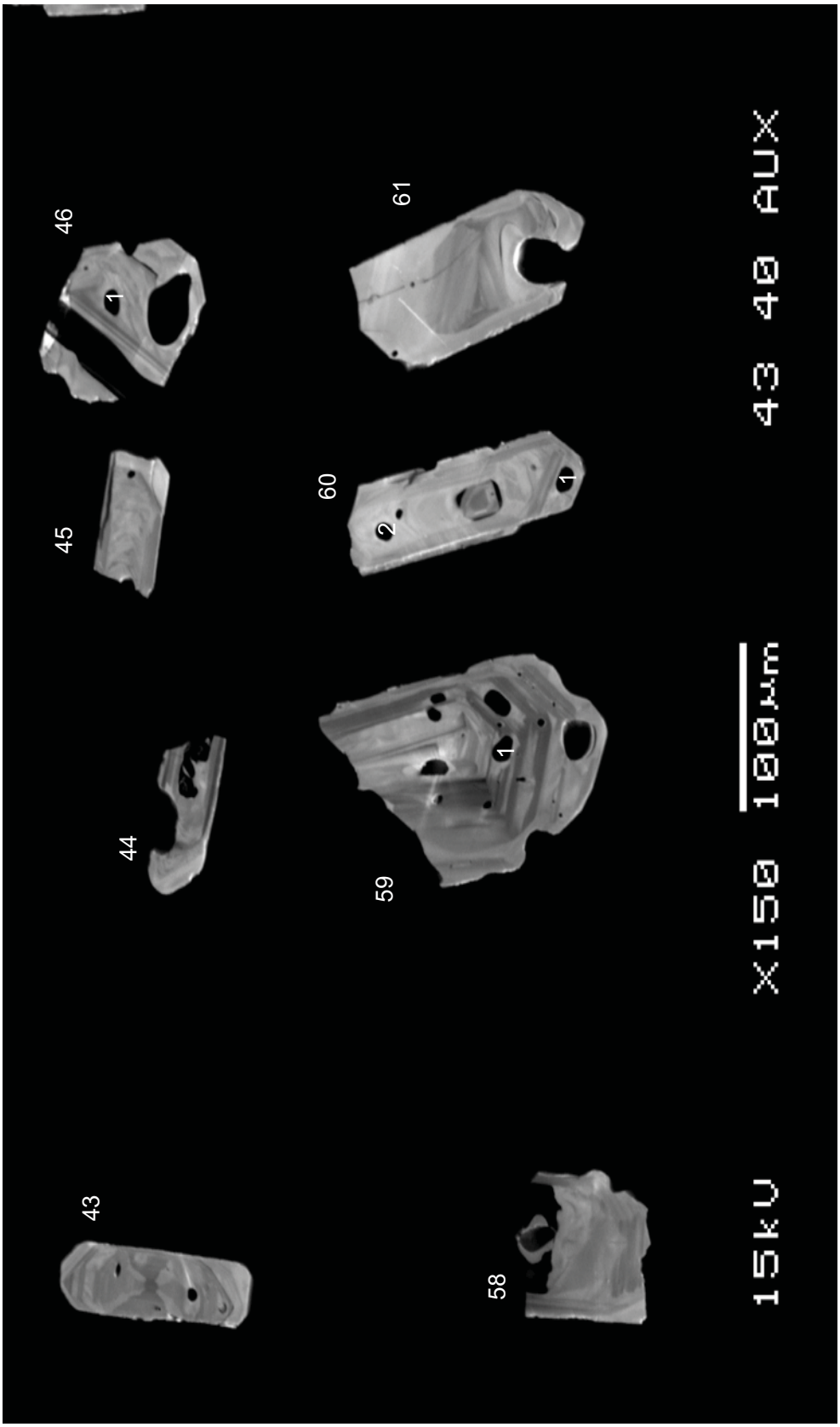
15kV X150 100µm 43 40 AUX
LLF
43
58
44
59
45
60
1
2
1
46
1
61

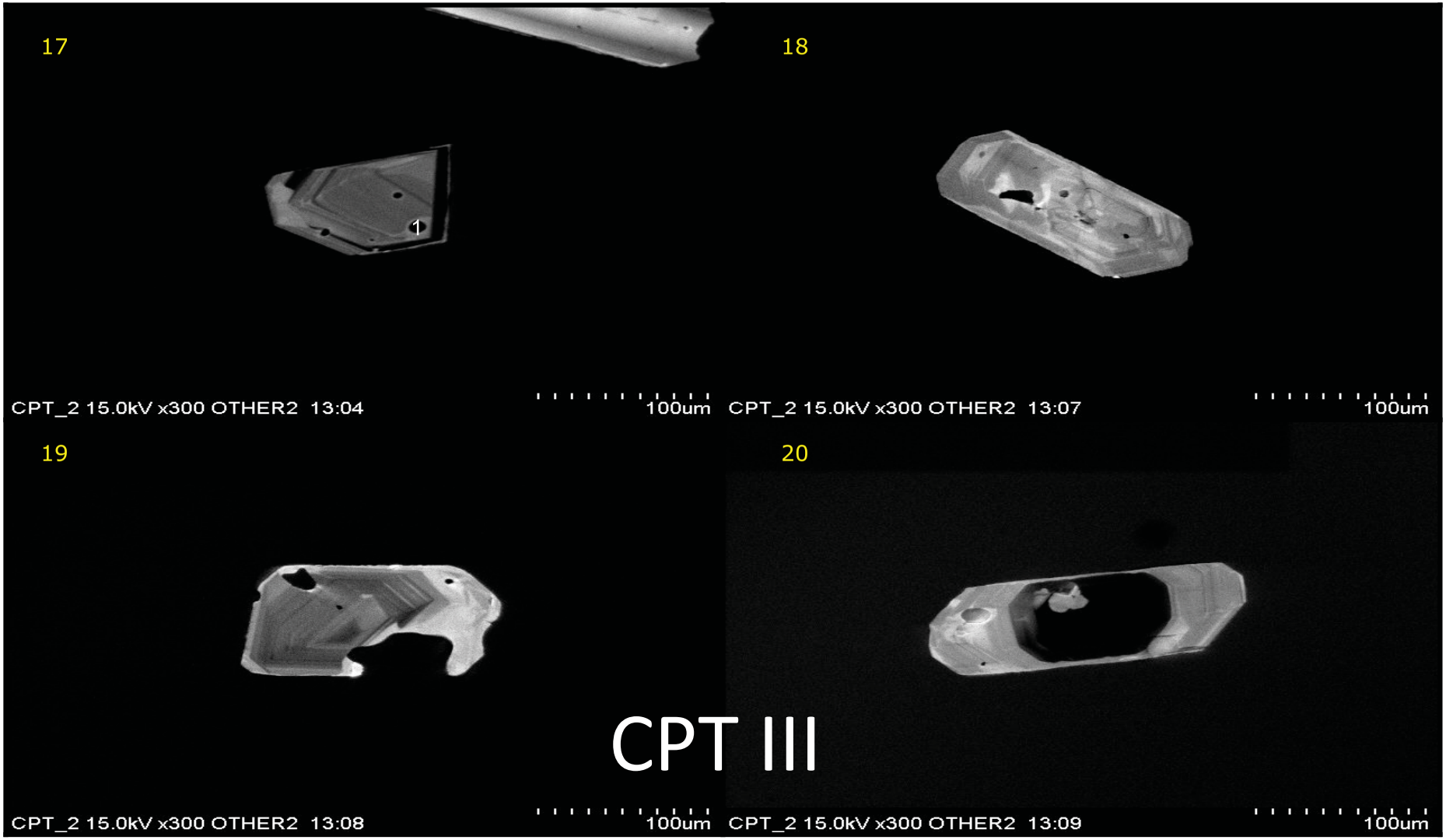
17
1
CPT_2 15.0kV x300 OTHER2 13:04
100um
18
CPT_2 15.0kV x300 OTHER2 13:07
100um
19
CPT_2 15.0kV x300 OTHER2 13:08
100um
20
CPT_2 15.0kV x300 OTHER2 13:09
100um

CPT III

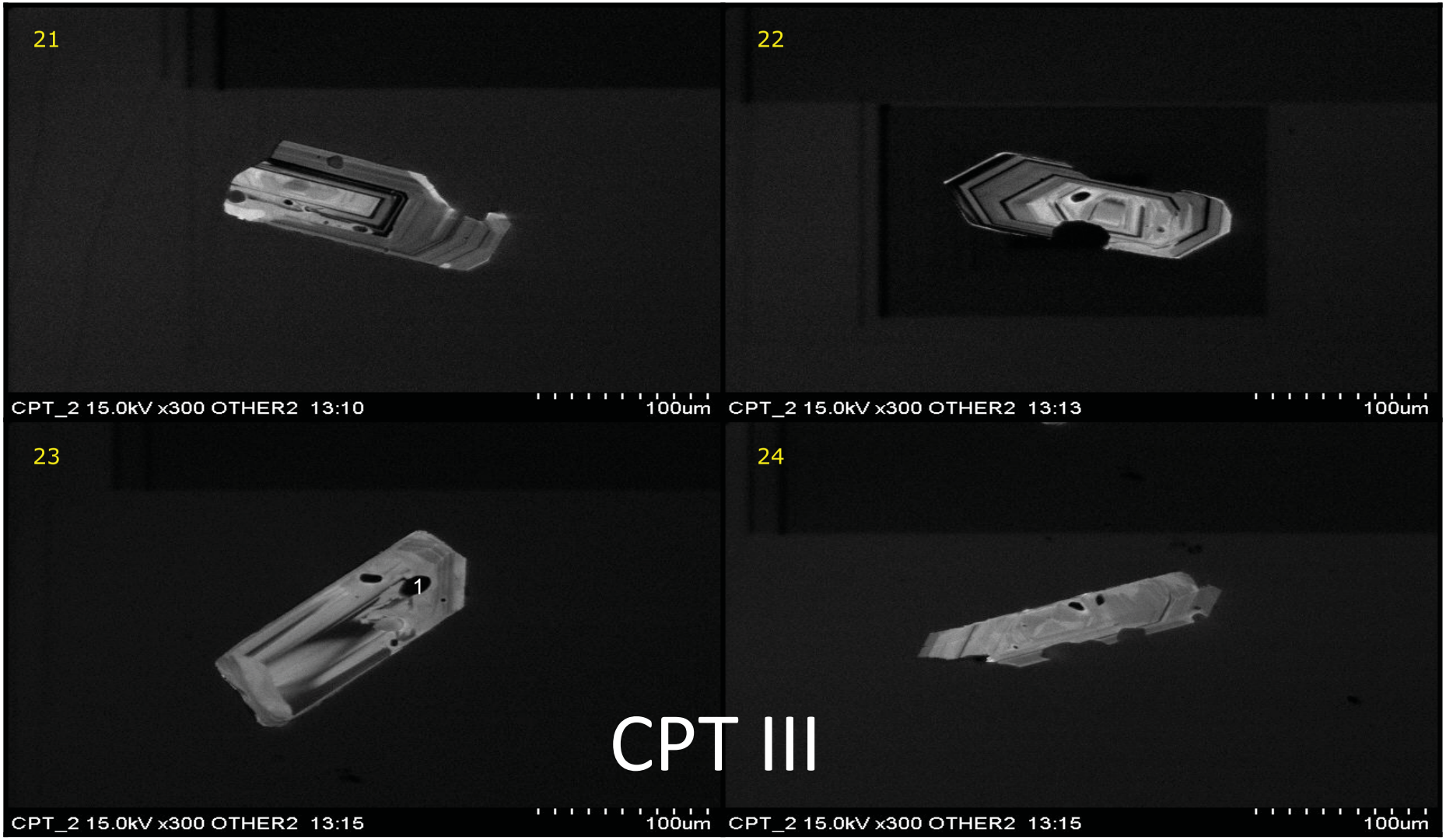
21
CPT_2 15.0kV x300 OTHER2 13:10
100um
22
CPT_2 15.0kV x300 OTHER2 13:13
100um
23
1
CPT_2 15.0kV x300 OTHER2 13:15
100um
24
CPT_2 15.0kV x300 OTHER2 13:15
100um

CPT III

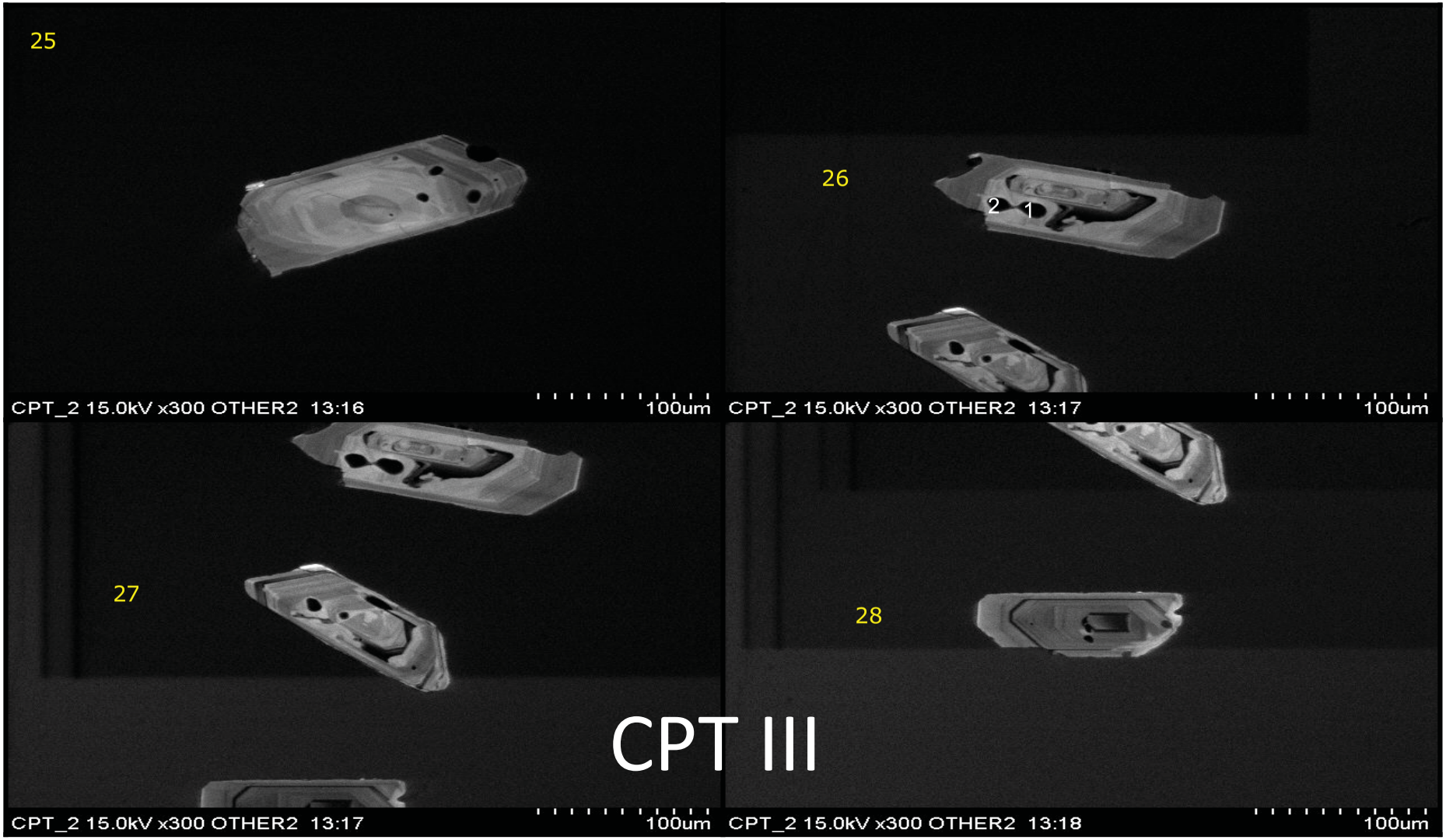
25
CPT_2 15.0kV x300 OTHER2 13:16
100um
26
2
1
CPT_2 15.0kV x300 OTHER2 13:17
100um
27
CPT_2 15.0kV x300 OTHER2 13:17
100um
28
CPT_2 15.0kV x300 OTHER2 13:18
100um
CPT III

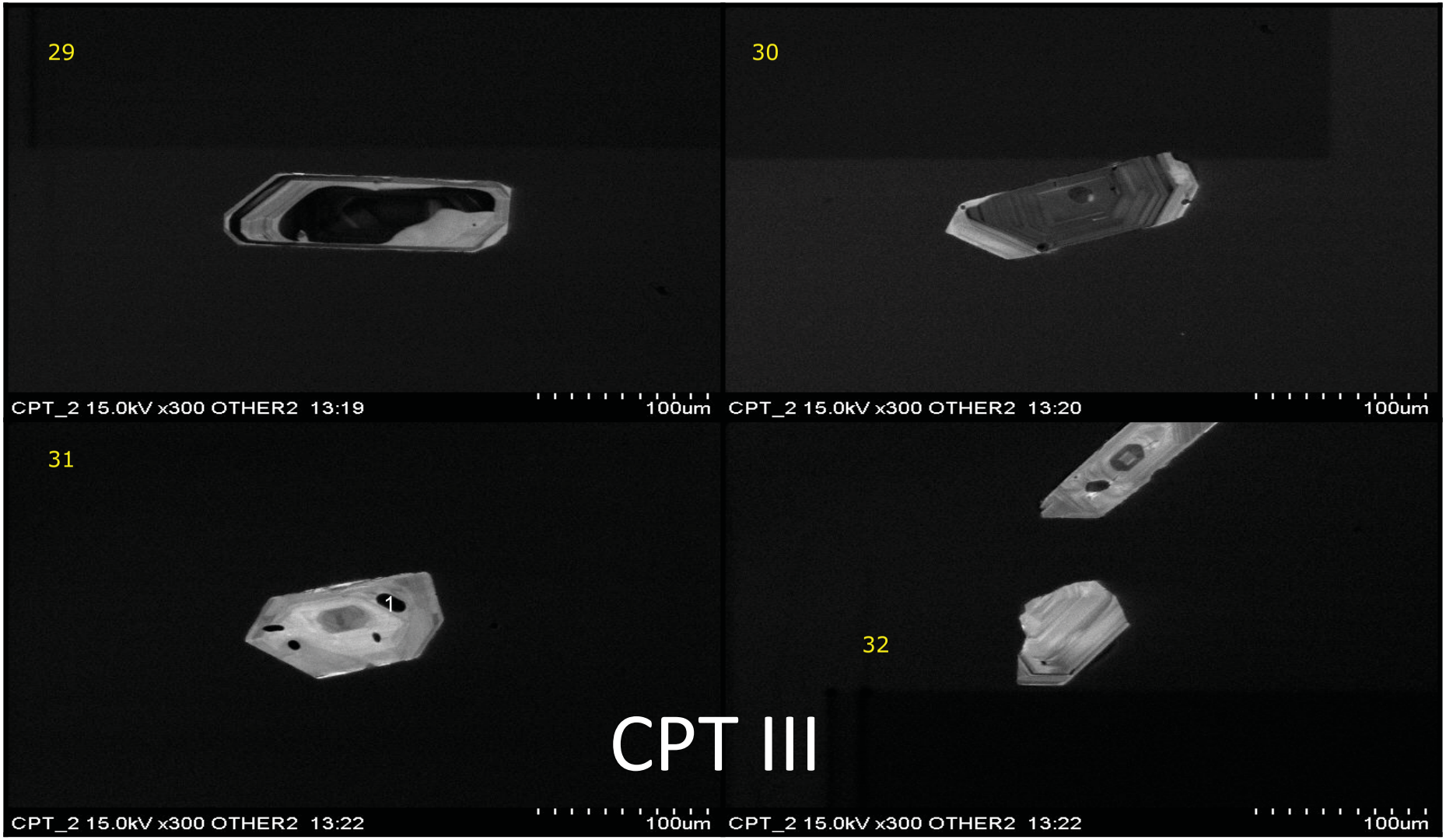
29
CPT_2 15.0kV x300 OTHER2 13:19
100um
30
CPT_2 15.0kV x300 OTHER2 13:20
100um
31
1
CPT_2 15.0kV x300 OTHER2 13:22
100um
32
CPT_2 15.0kV x300 OTHER2 13:22
100um

CPT III

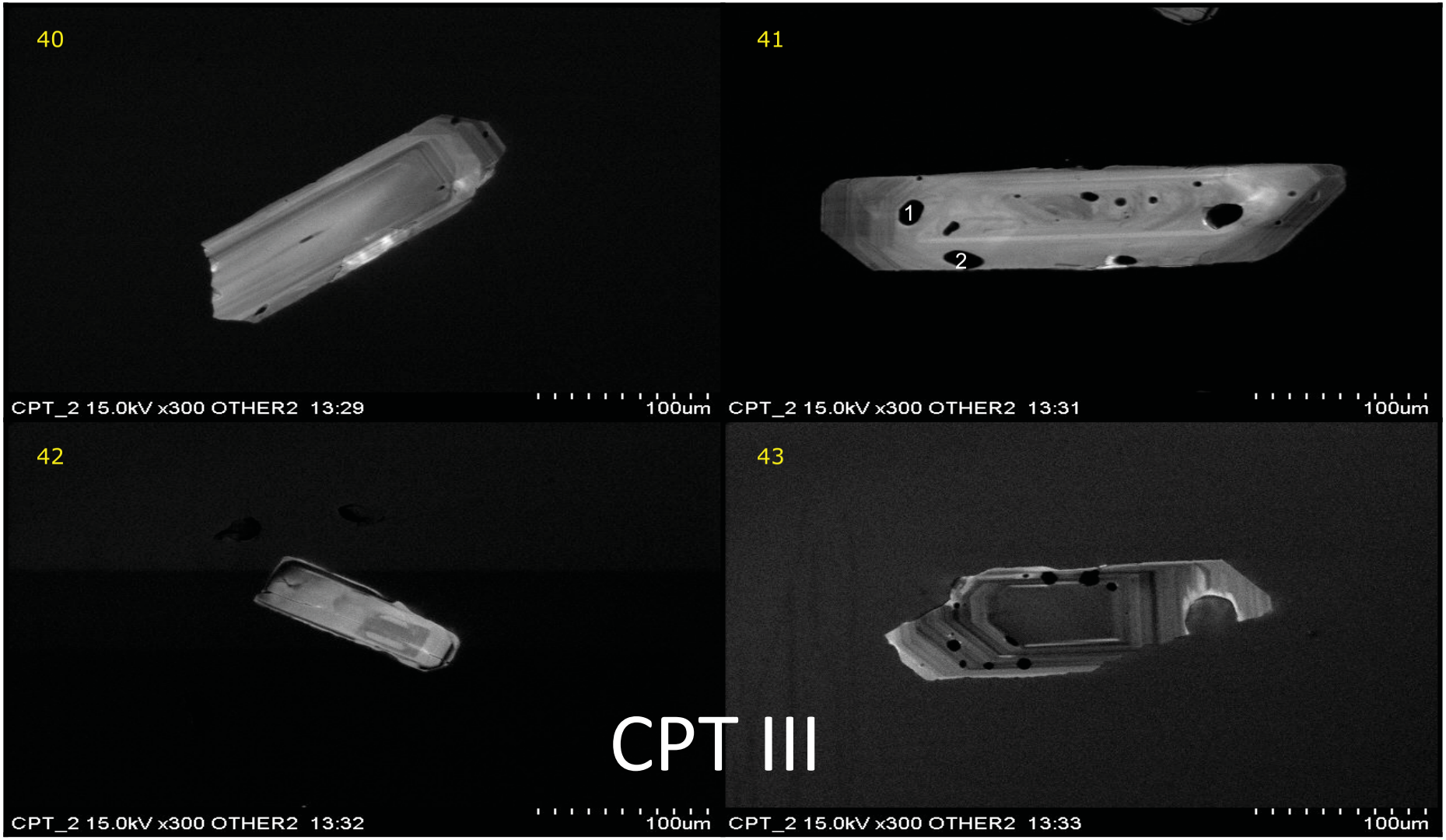
40
CPT_2 15.0kV x300 OTHER2 13:29
100um
41
1
2
CPT_2 15.0kV x300 OTHER2 13:31
100um
42
CPT_2 15.0kV x300 OTHER2 13:32
100um
43
CPT_2 15.0kV x300 OTHER2 13:33
100um

CPT III

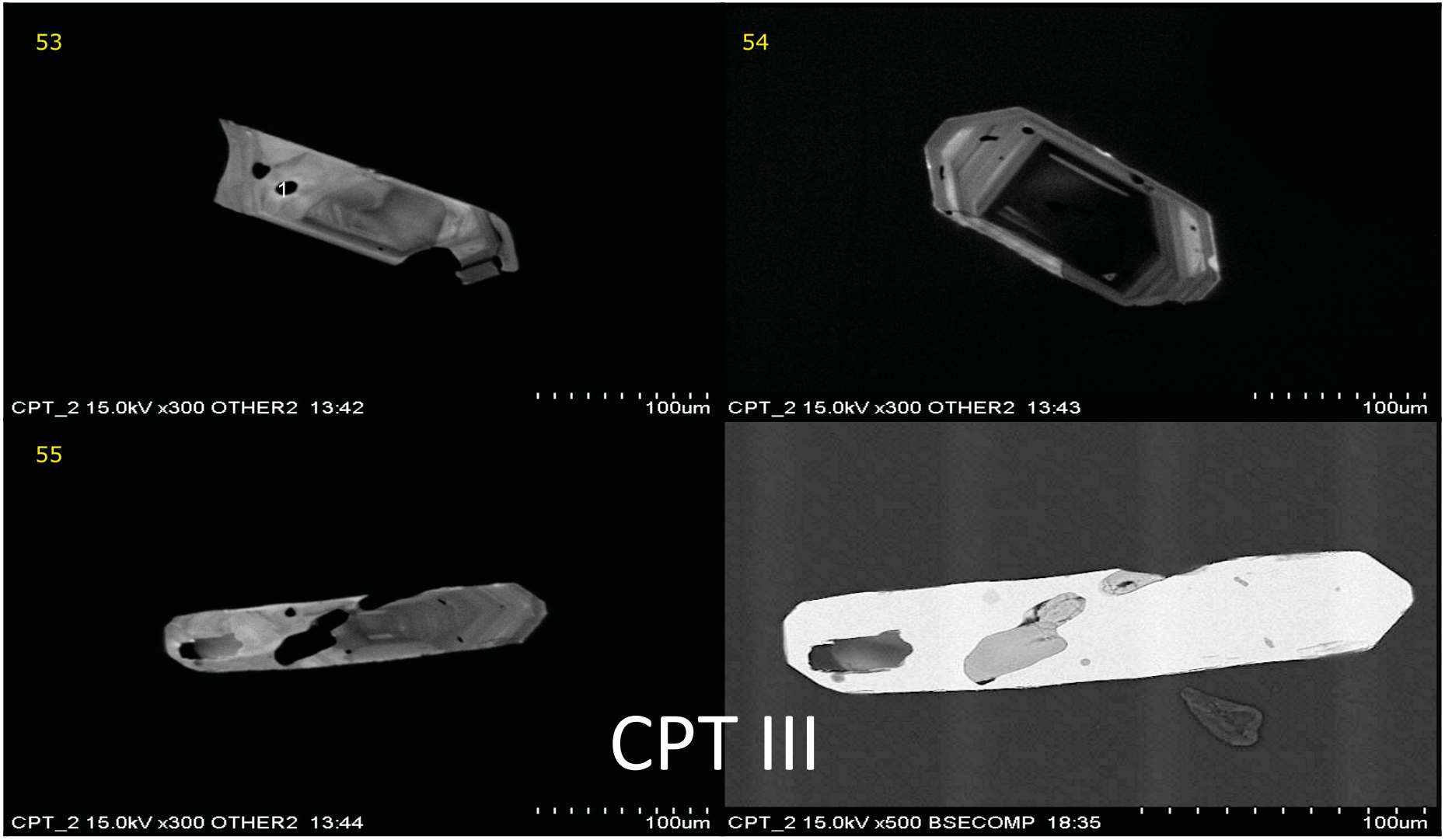
53
1
CPT_2 15.0kV x300 OTHER2 13:42
100um
54
CPT_2 15.0kV x300 OTHER2 13:43
100um
55
CPT_2 15.0kV x300 OTHER2 13:44
100um
CPT_2 15.0kV x500 BSECOMP 18:35
100um

CPT III

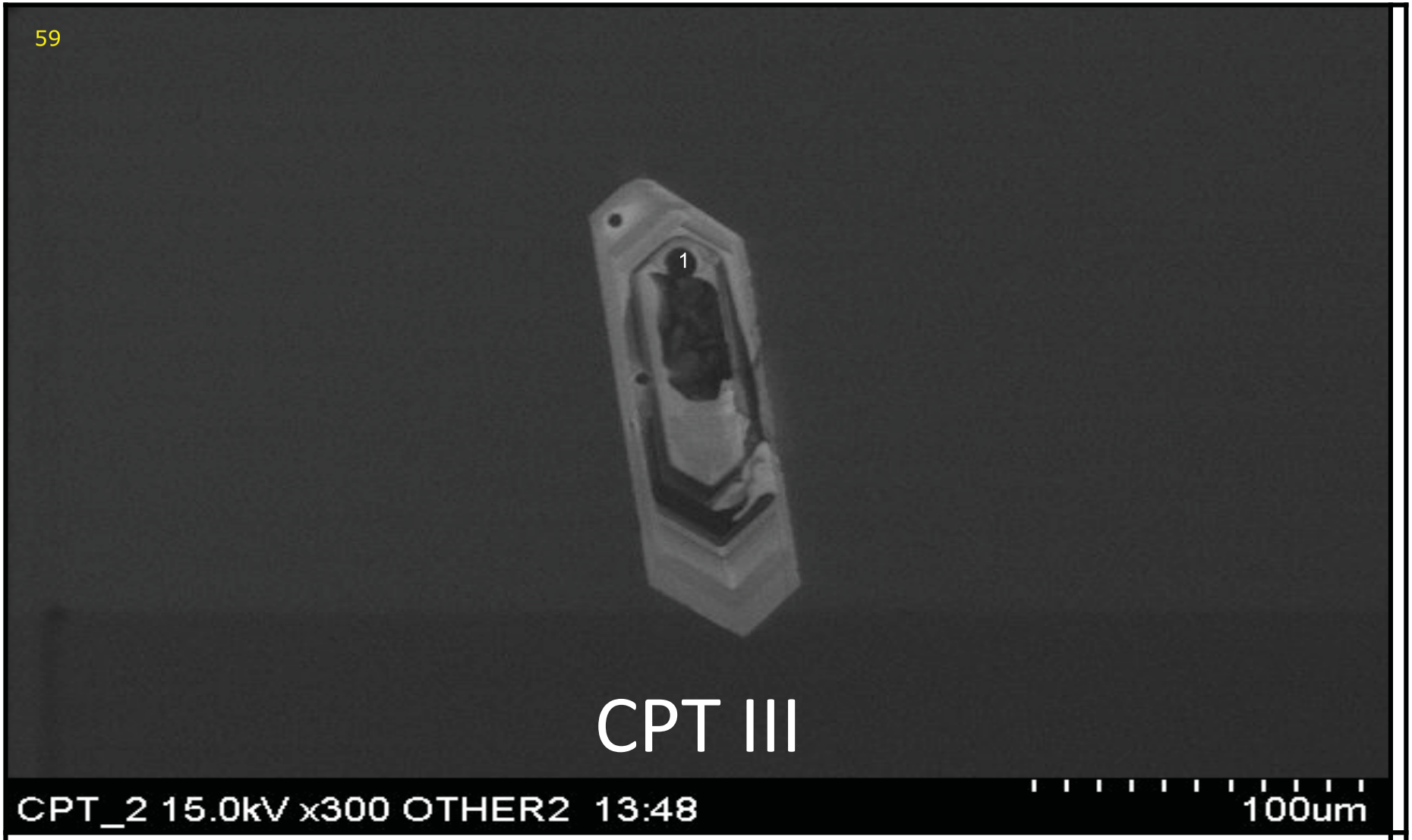
59
1
CPT III
CPT_2 15.0kV x300 OTHER2 13:48
100um

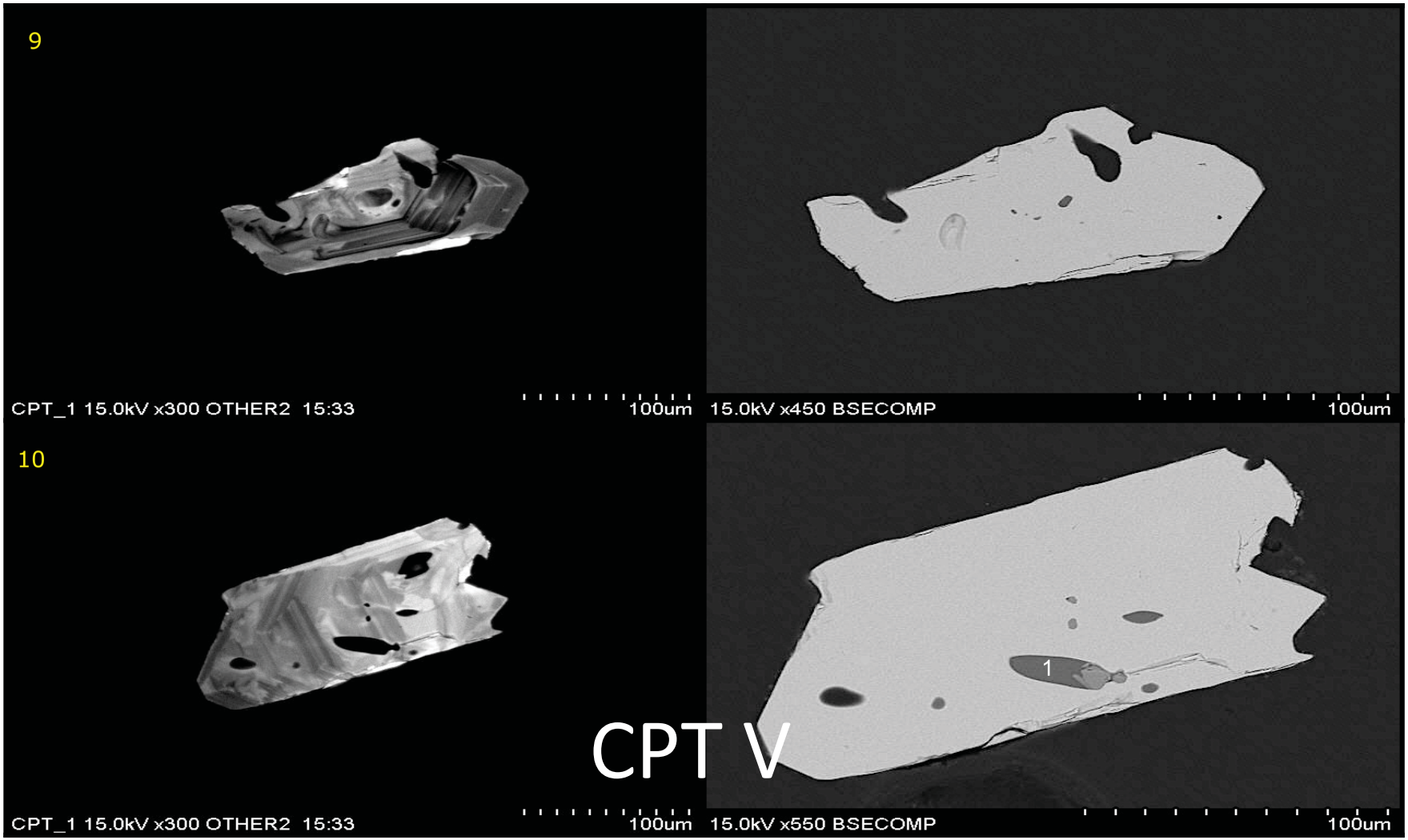
9
CPT_1 15.0kV x300 OTHER2 15:33
100um
15.0kV x450 BSECOMP
100um
10
CPT_1 15.0kV x300 OTHER2 15:33
100um
1
15.0kV x550 BSECOMP
100um
CPT V

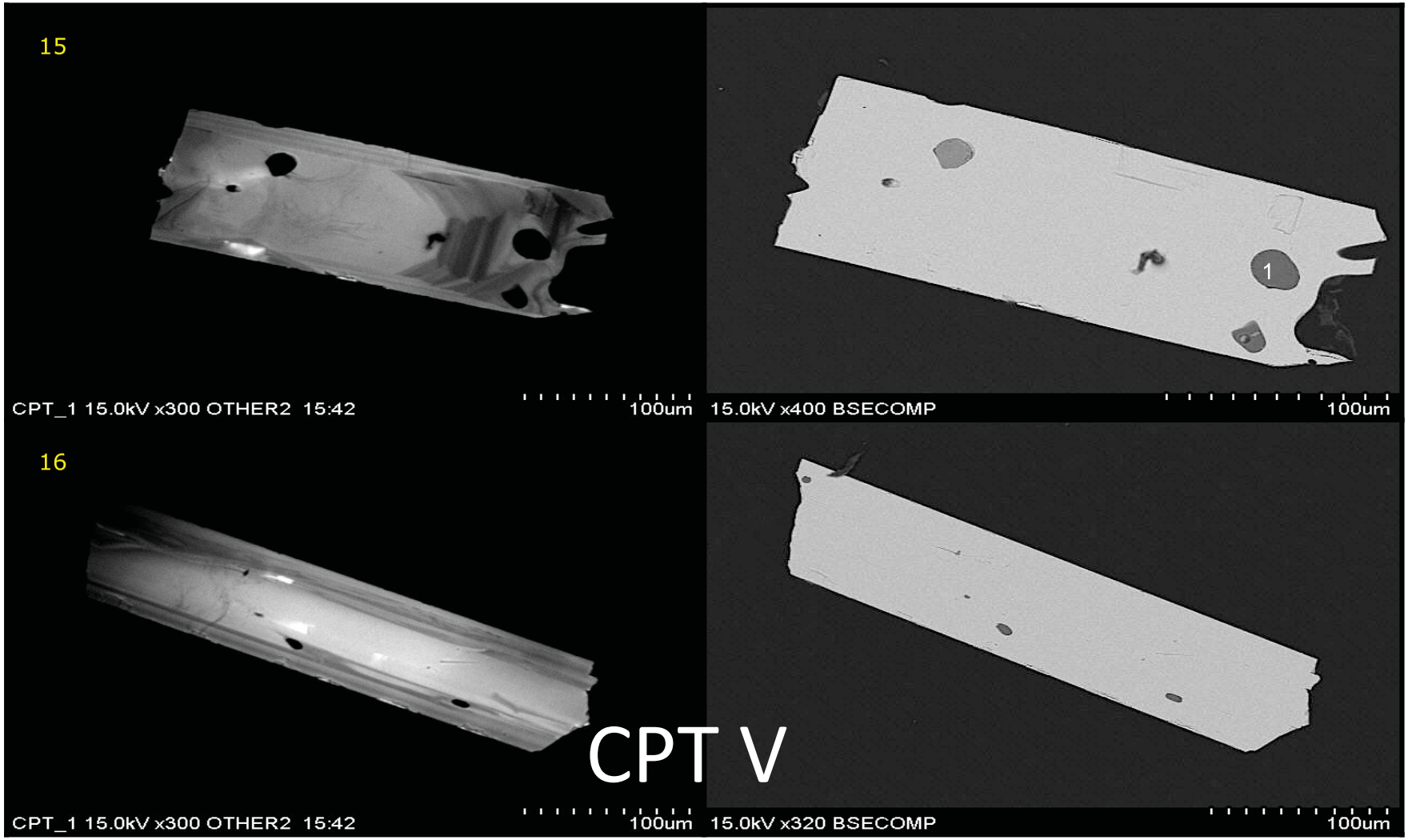
15
CPT_1 15.0kV x300 OTHER2 15:42
100um
1
15.0kV x400 BSECOMP
100um
16
CPT_1 15.0kV x300 OTHER2 15:42
100um
15.0kV x320 BSECOMP
100um

CPT V

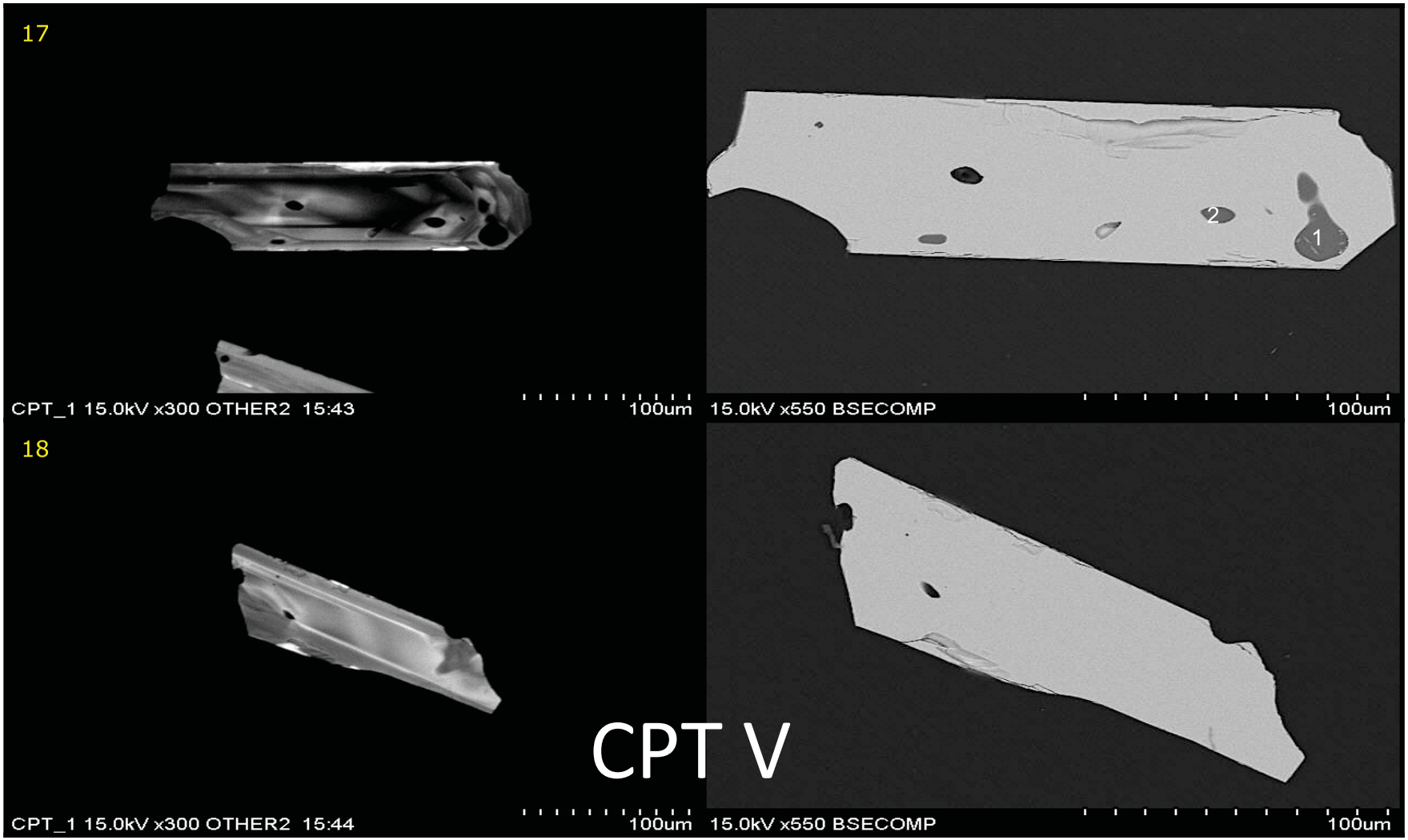
17
CPT_1 15.0kV x300 OTHER2 15:43
100um
2
1
15.0kV x550 BSECOMP
100um
18
CPT_1 15.0kV x300 OTHER2 15:44
100um
15.0kV x550 BSECOMP
100um
CPT V

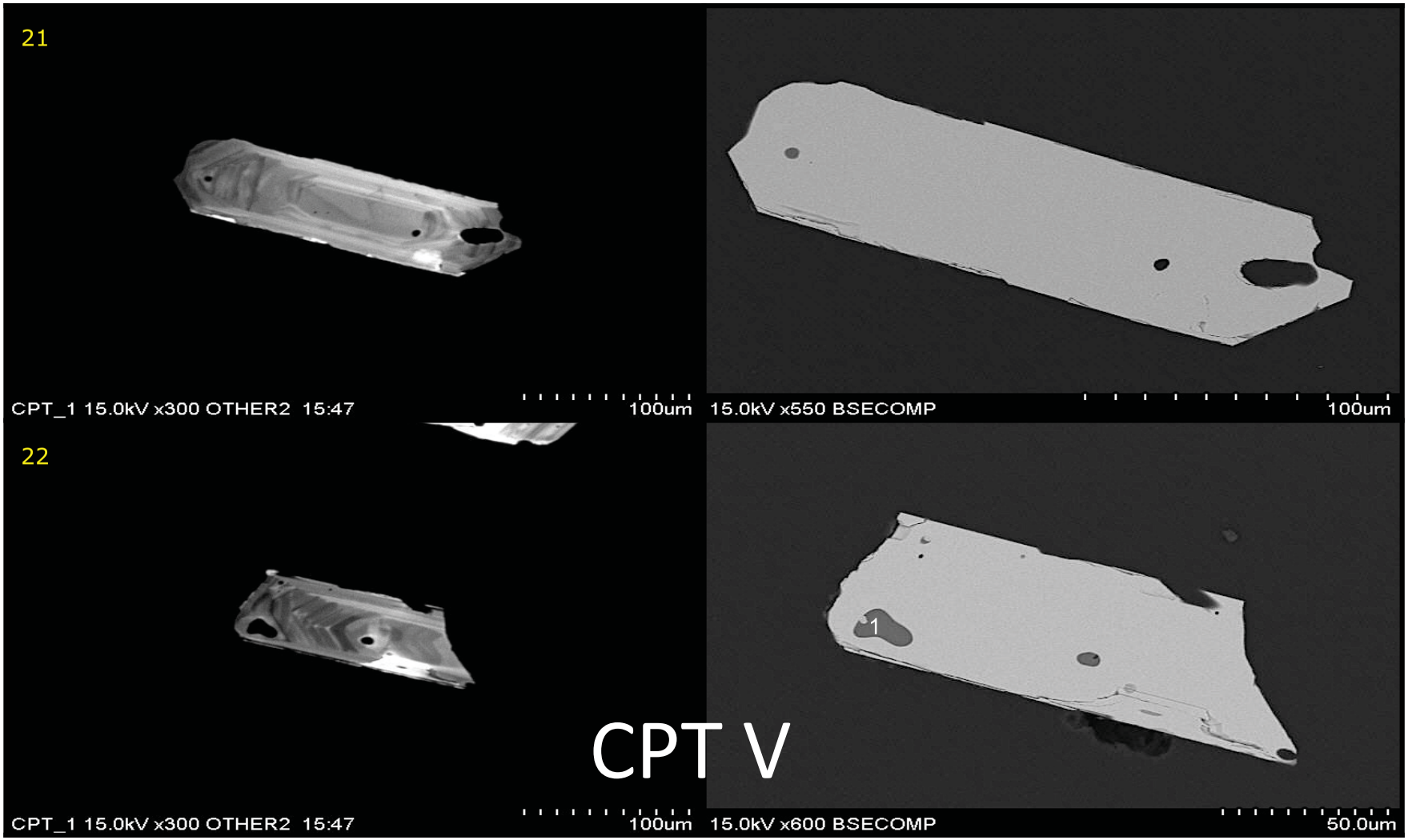
21
CPT_1 15.0kV x300 OTHER2 15:47
100um
15.0kV x550 BSECOMP
100um
22
CPT_1 15.0kV x300 OTHER2 15:47
100um
1
15.0kV x600 BSECOMP
50.0um
CPT V

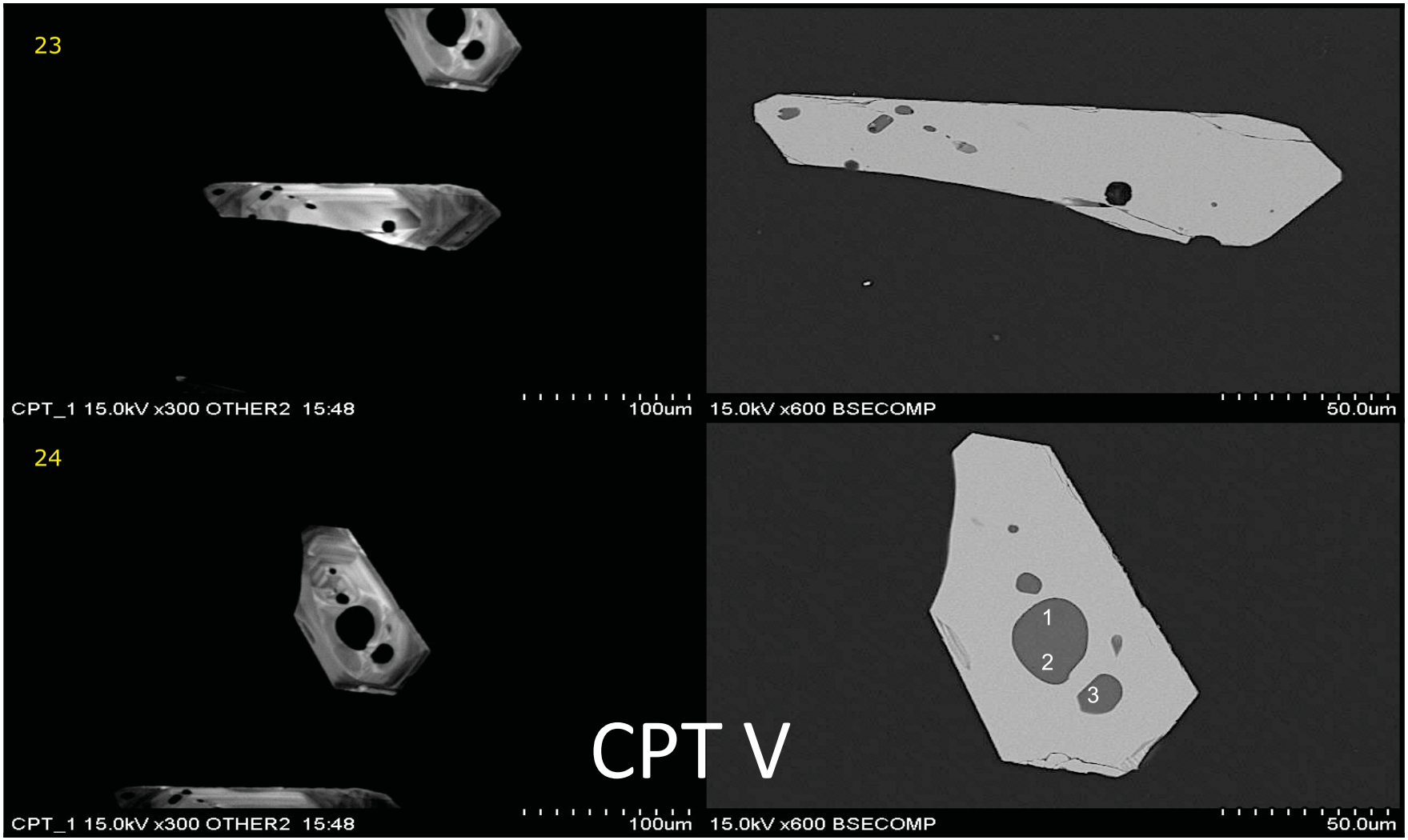
23
CPT_1 15.0kV x300 OTHER2 15:48
100um
15.0kV x600 BSECOMP
50.0um
24
CPT_1 15.0kV x300 OTHER2 15:48
100um
15.0kV x600 BSECOMP
50.0um
1
2
3
CPT V

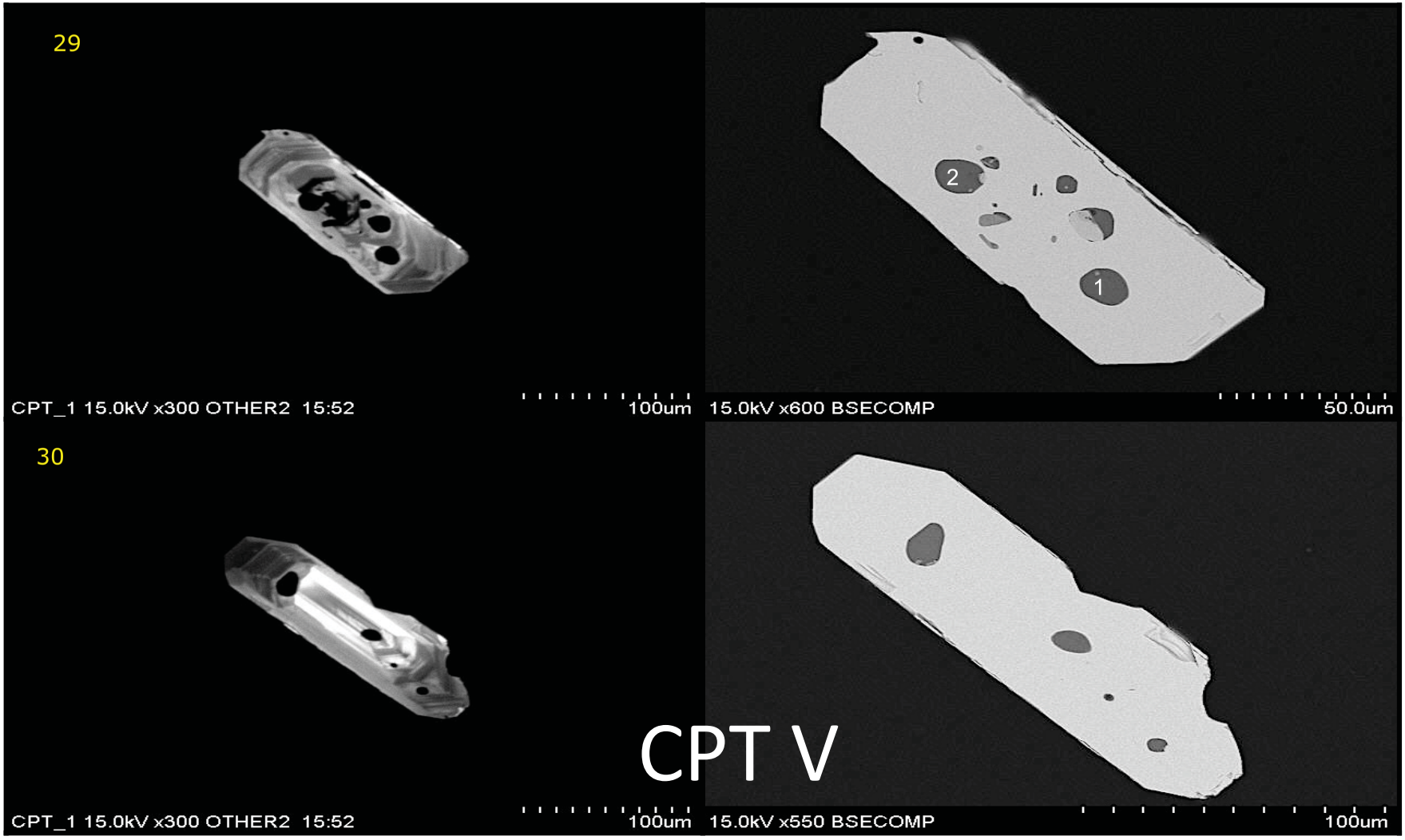
29
CPT_1 15.0kV x300 OTHER2 15:52
100um
2
1
15.0kV x600 BSECOMP
50.0um
30
CPT_1 15.0kV x300 OTHER2 15:52
100um
15.0kV x550 BSECOMP
100um
CPT V

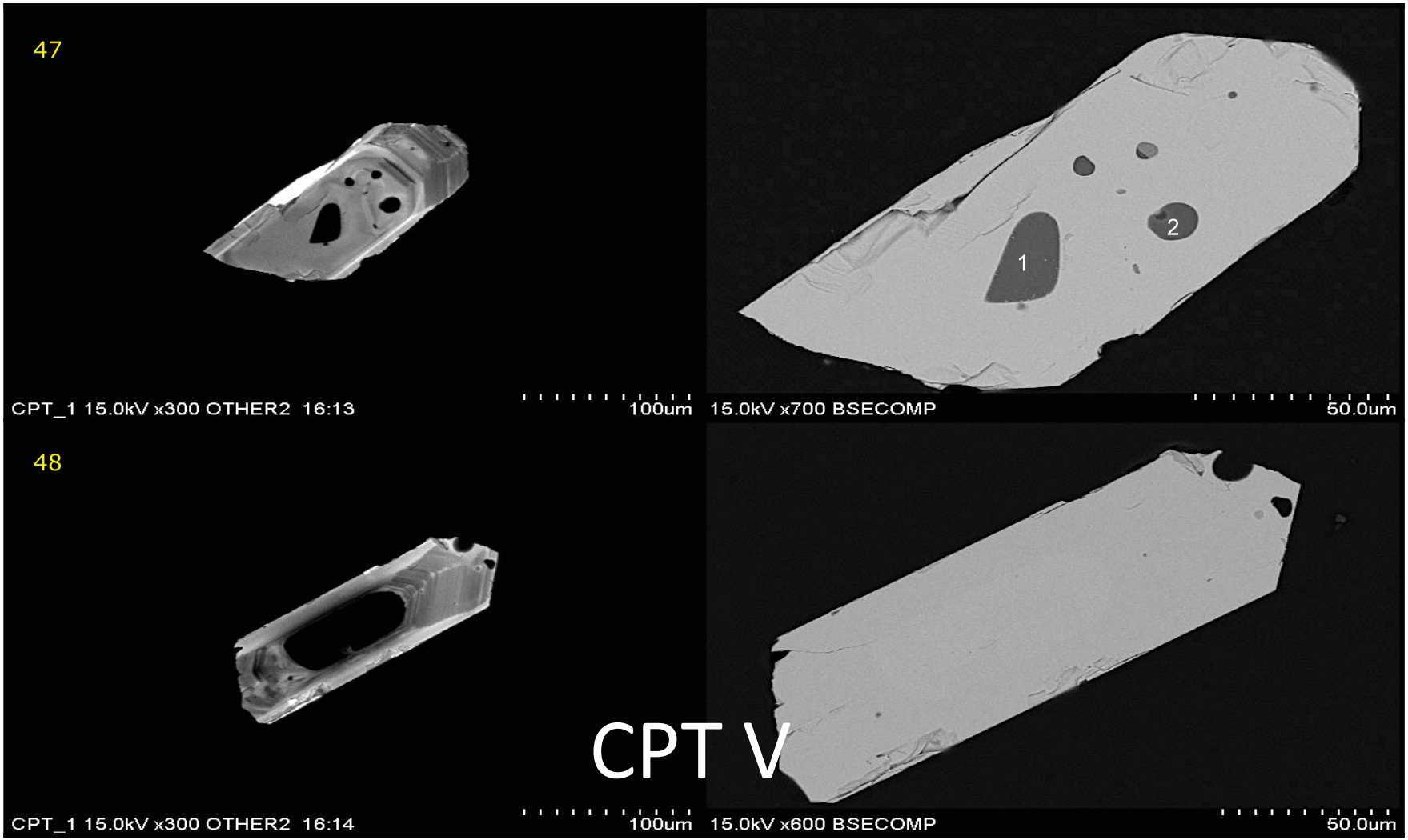
47
CPT_1 15.0kV x300 OTHER2 16:13
100um
1
2
15.0kV x700 BSECOMP
50.0um
48
CPT_1 15.0kV x300 OTHER2 16:14
100um
15.0kV x600 BSECOMP
50.0um

CPT V

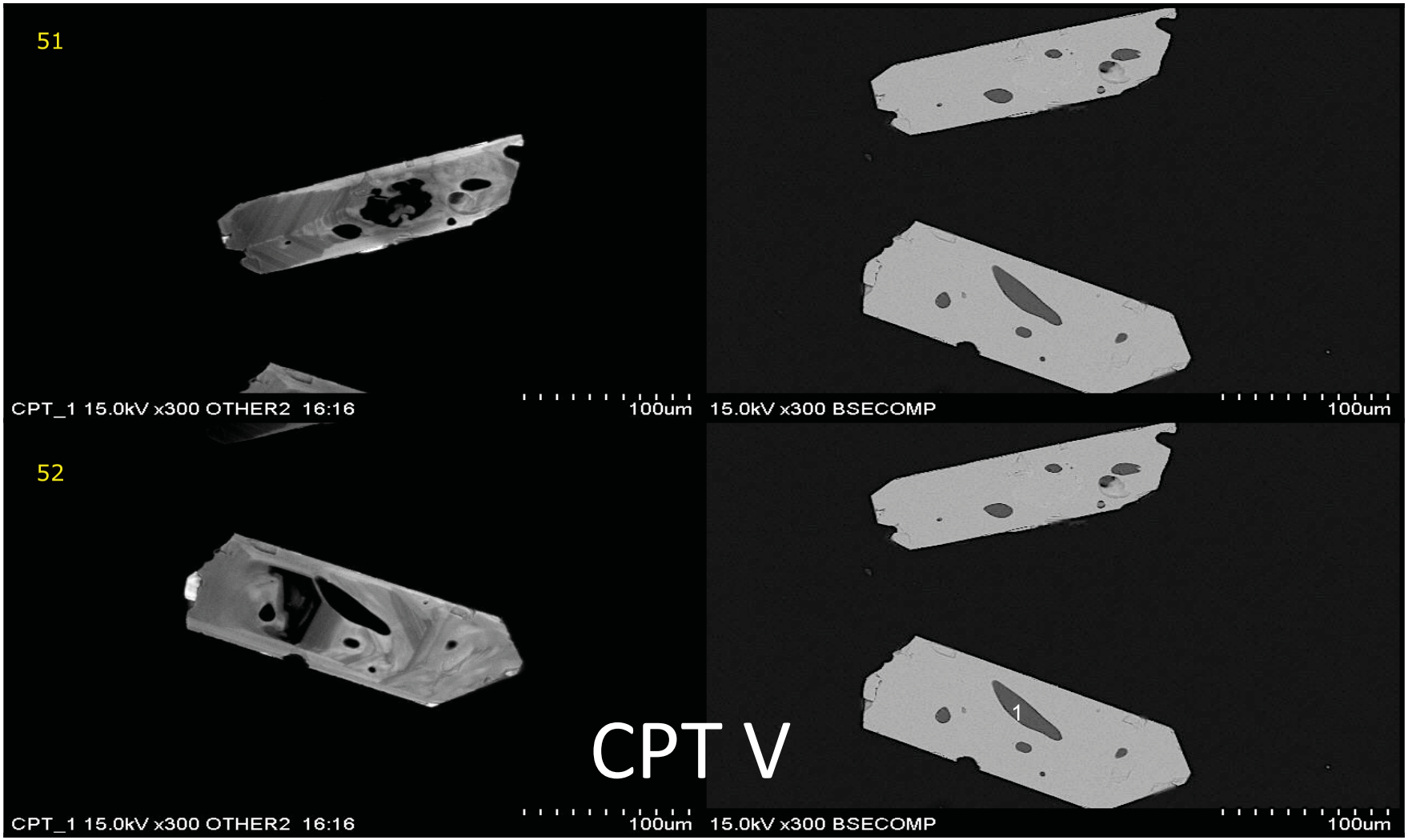
51
CPT_1 15.0kV x300 OTHER2 16:16
100um
15.0kV x300 BSECOMP
100um
52
CPT_1 15.0kV x300 OTHER2 16:16
100um
15.0kV x300 BSECOMP
100um
1
CPT V

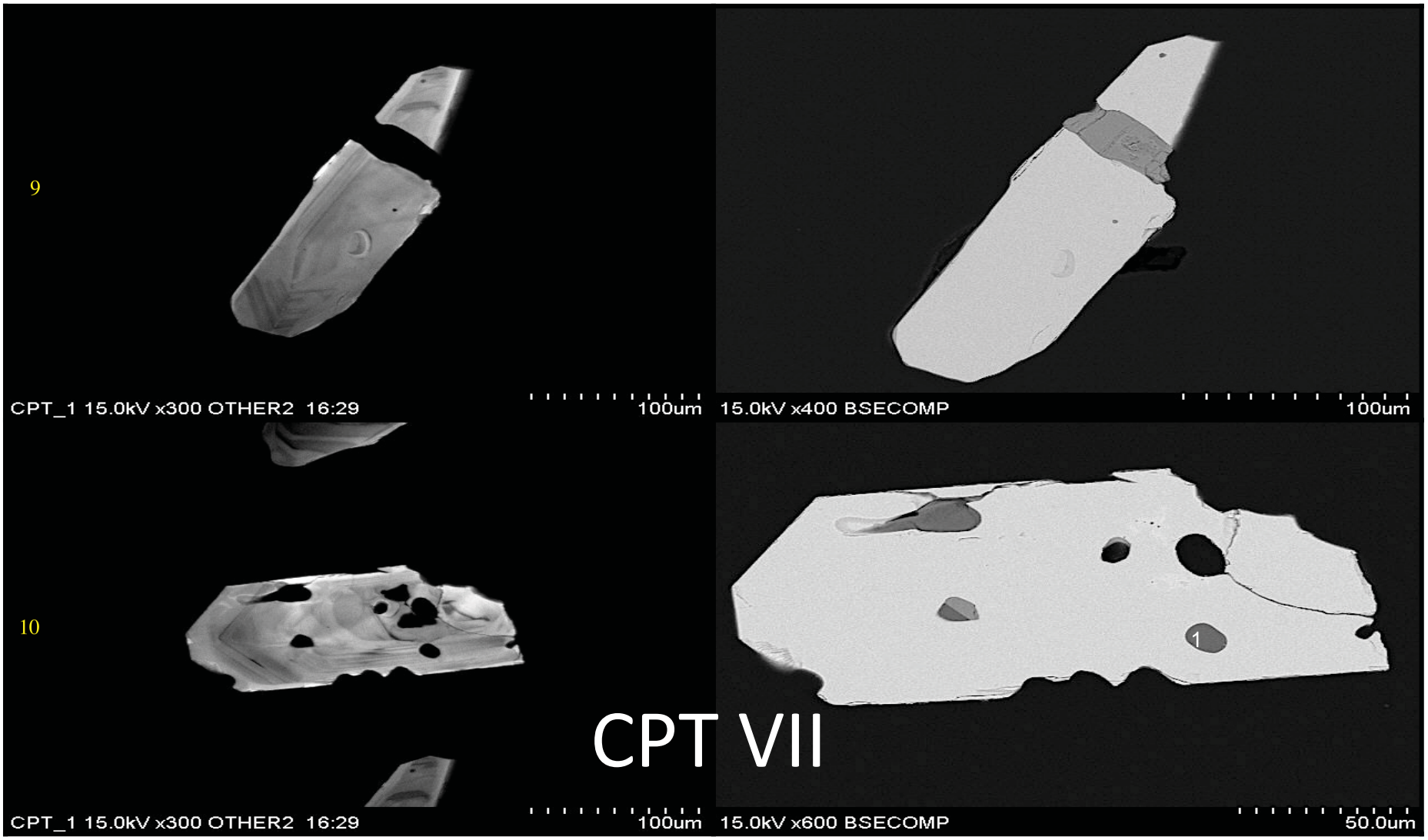
9
CPT_1 15.0kV x300 OTHER2 16:29
100um
15.0kV x400 BSECOMP
100um
10
CPT_1 15.0kV x300 OTHER2 16:29
100um
1
15.0kV x600 BSECOMP
50.0um

CPT VII

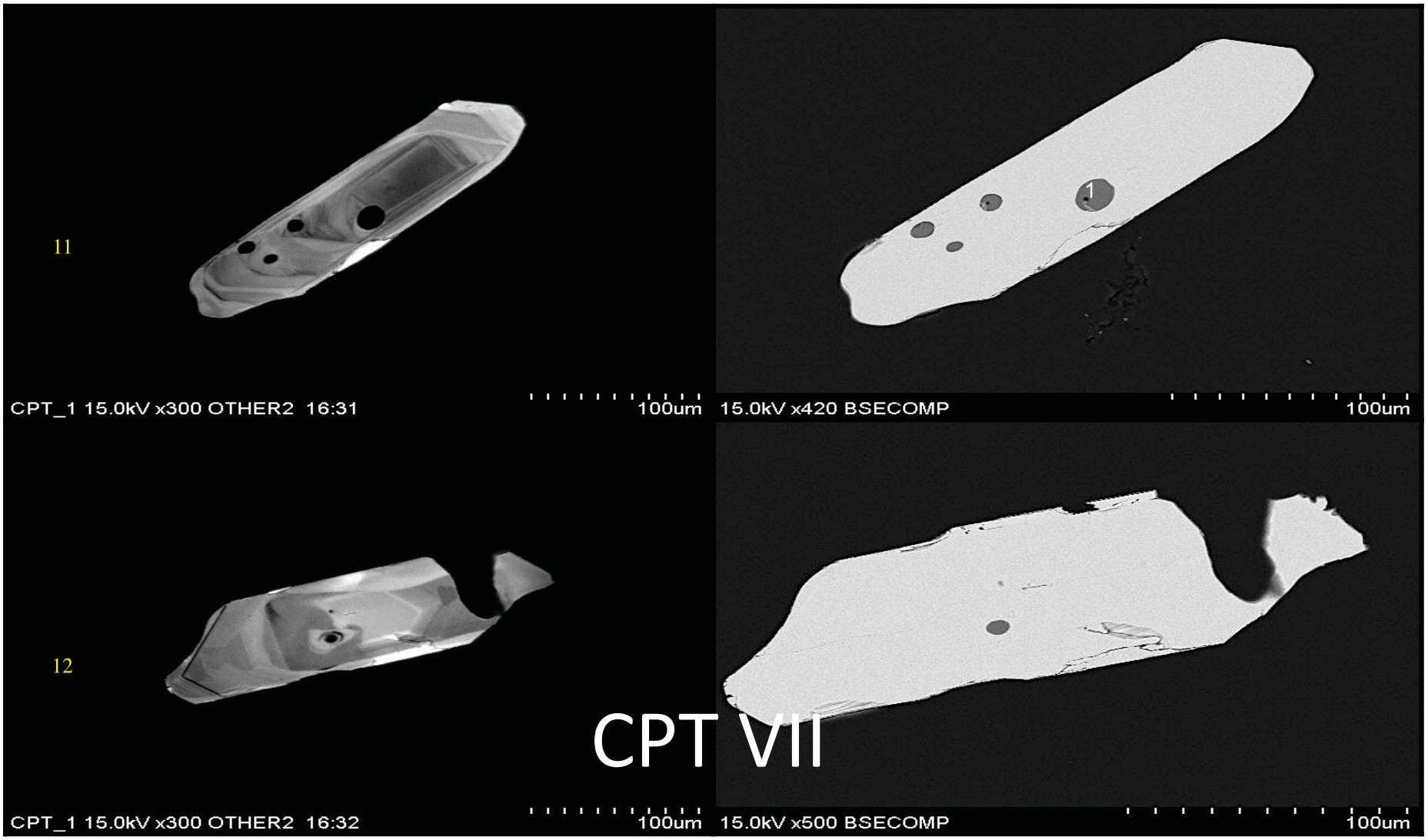
11
CPT_1 15.0kV x300 OTHER2 16:31
100um
1
15.0kV x420 BSECOMP
100um
12
CPT_1 15.0kV x300 OTHER2 16:32
100um
15.0kV x500 BSECOMP
100um

CPT VII

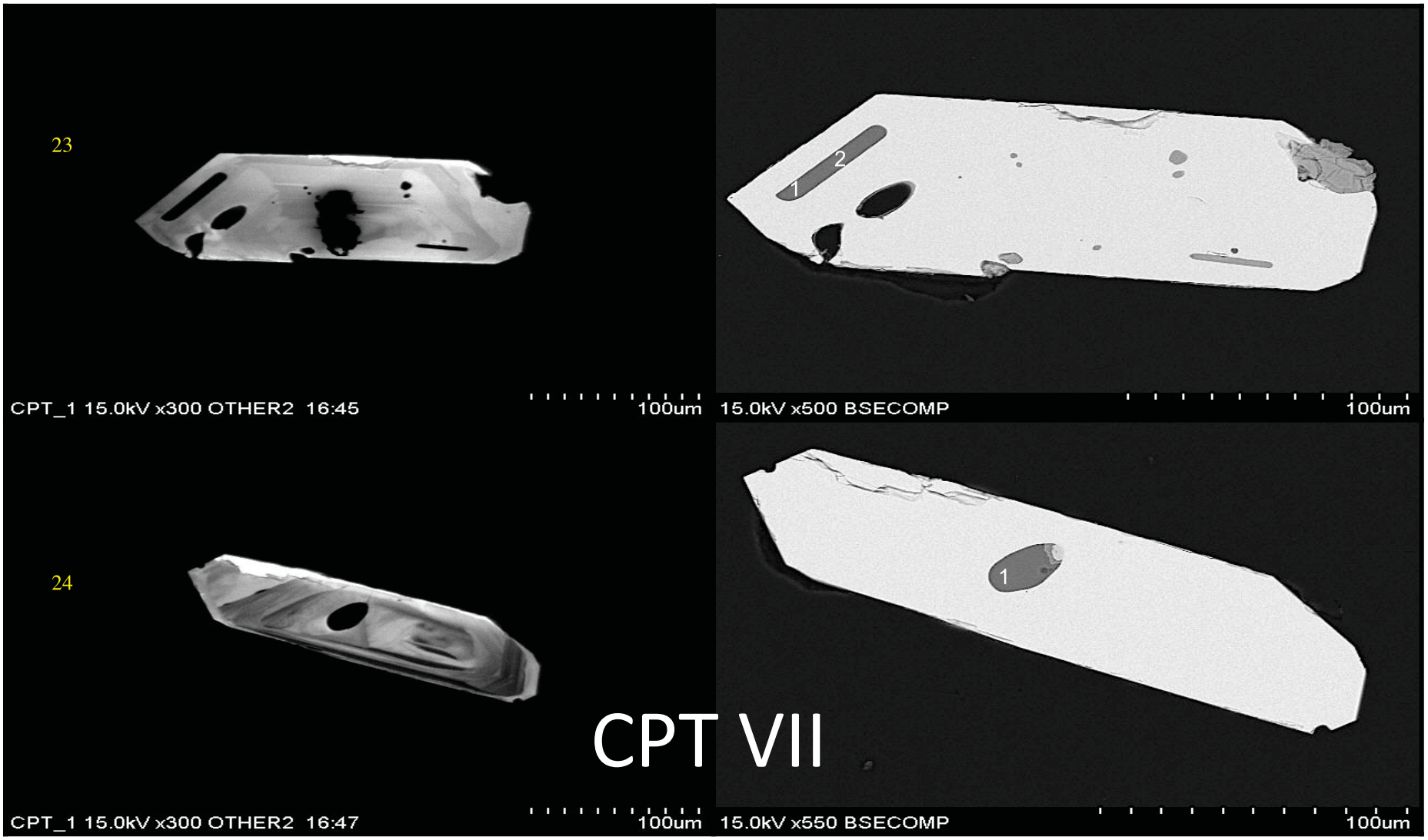
23
CPT_1 15.0kV x300 OTHER2 16:45
100um
2
1
15.0kV x500 BSECOMP
100um
24
CPT_1 15.0kV x300 OTHER2 16:47
100um
1
15.0kV x550 BSECOMP
100um

CPT VII

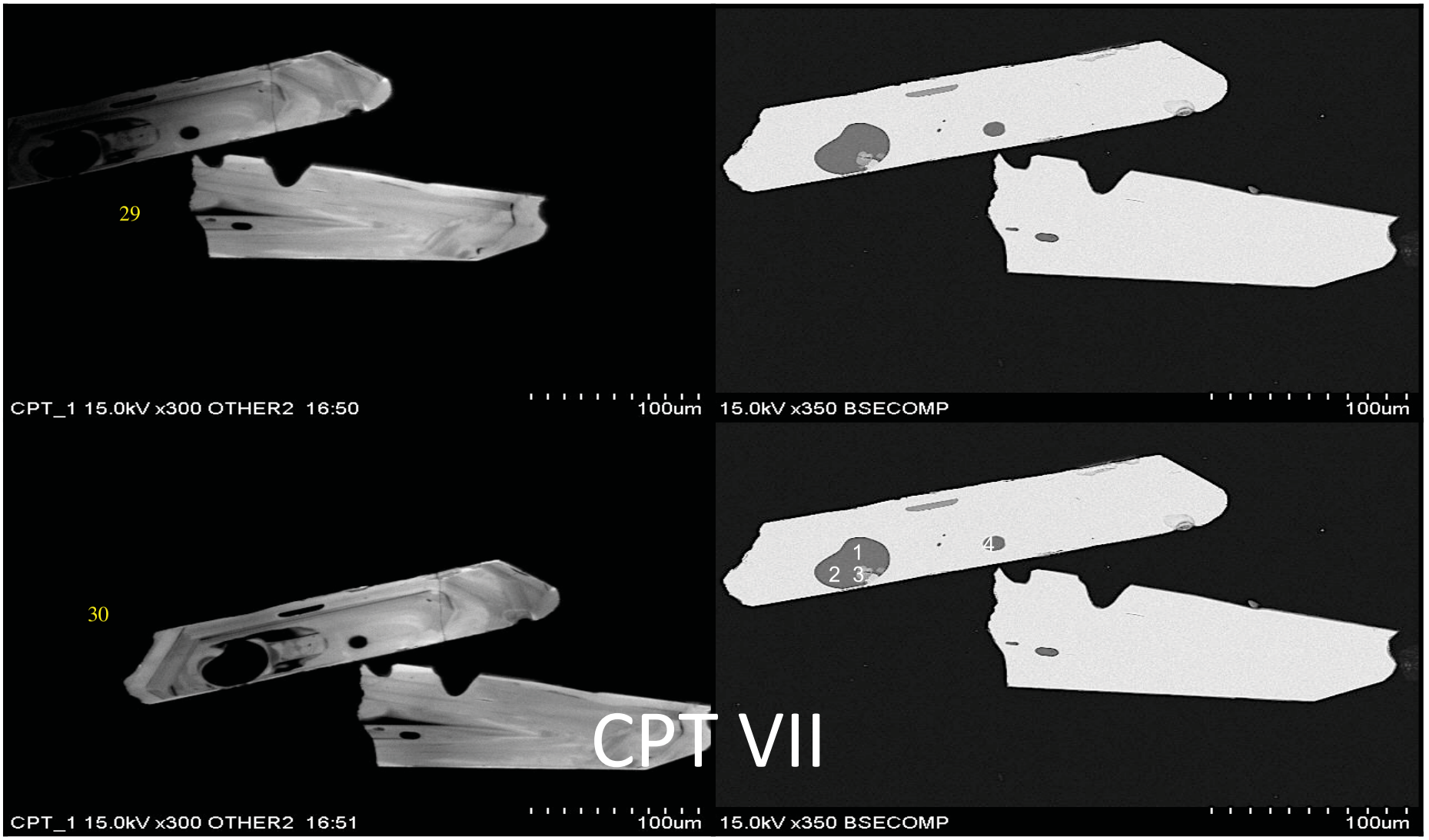
29
CPT_1 15.0kV x300 OTHER2 16:50
100um
15.0kV x350 BSECOMP
100um
30
1
2 3
4
CPT VII
CPT_1 15.0kV x300 OTHER2 16:51
100um
15.0kV x350 BSECOMP
100um


45
CPT_1 15.0kV x300 OTHER2 17:03
100um
15.0kV x370 BSECOMP
100um
46
CPT VII
CPT_1 15.0kV x300 OTHER2 17:04
100um
1
15.0kV x450 BSECOMP
100um

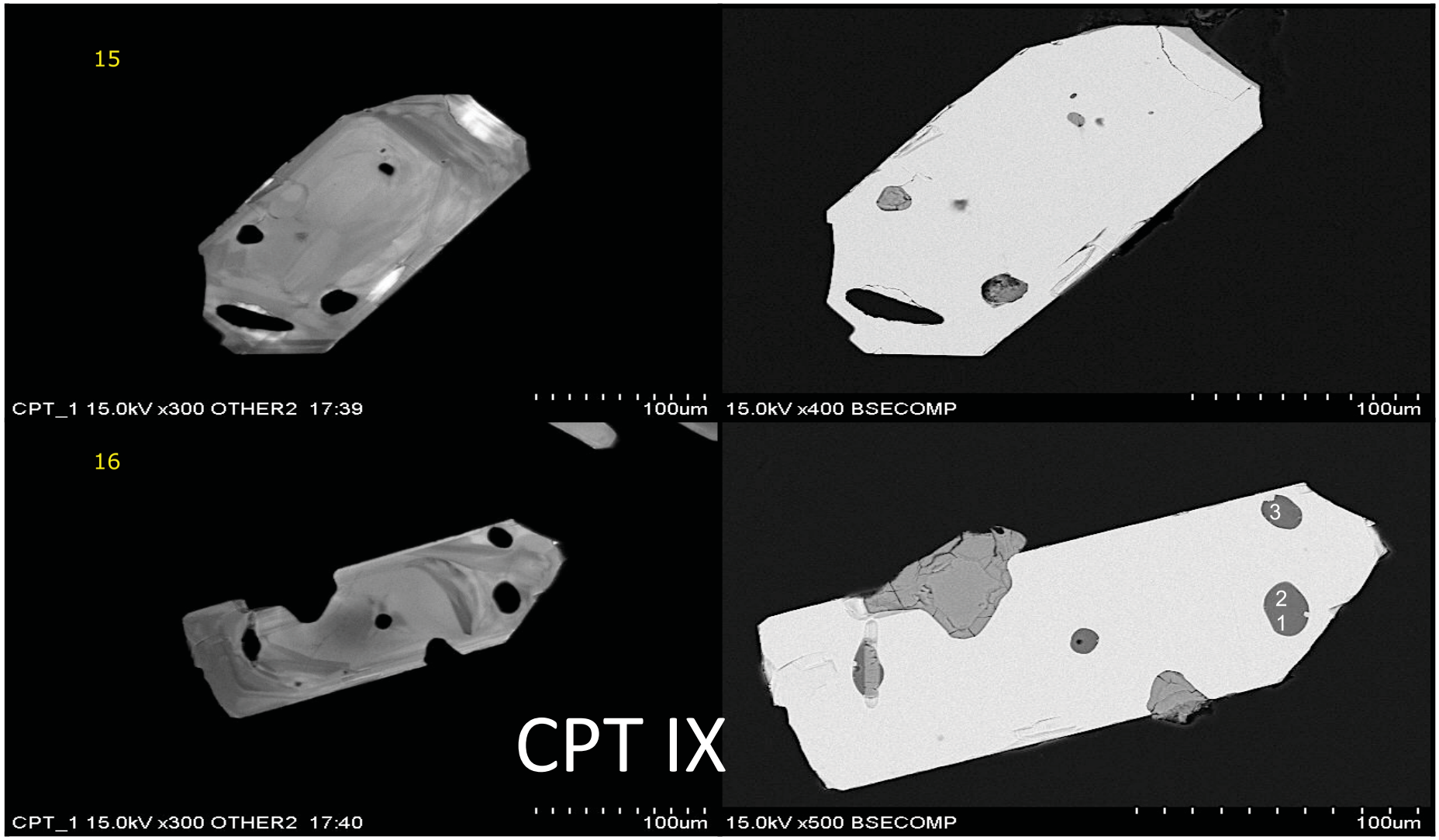
15
CPT_1 15.0kV x300 OTHER2 17:39
100um
15.0kV x400 BSECOMP
100um
16
CPT_1 15.0kV x300 OTHER2 17:40
100um
3
2
1
15.0kV x500 BSECOMP
100um

CPT IX

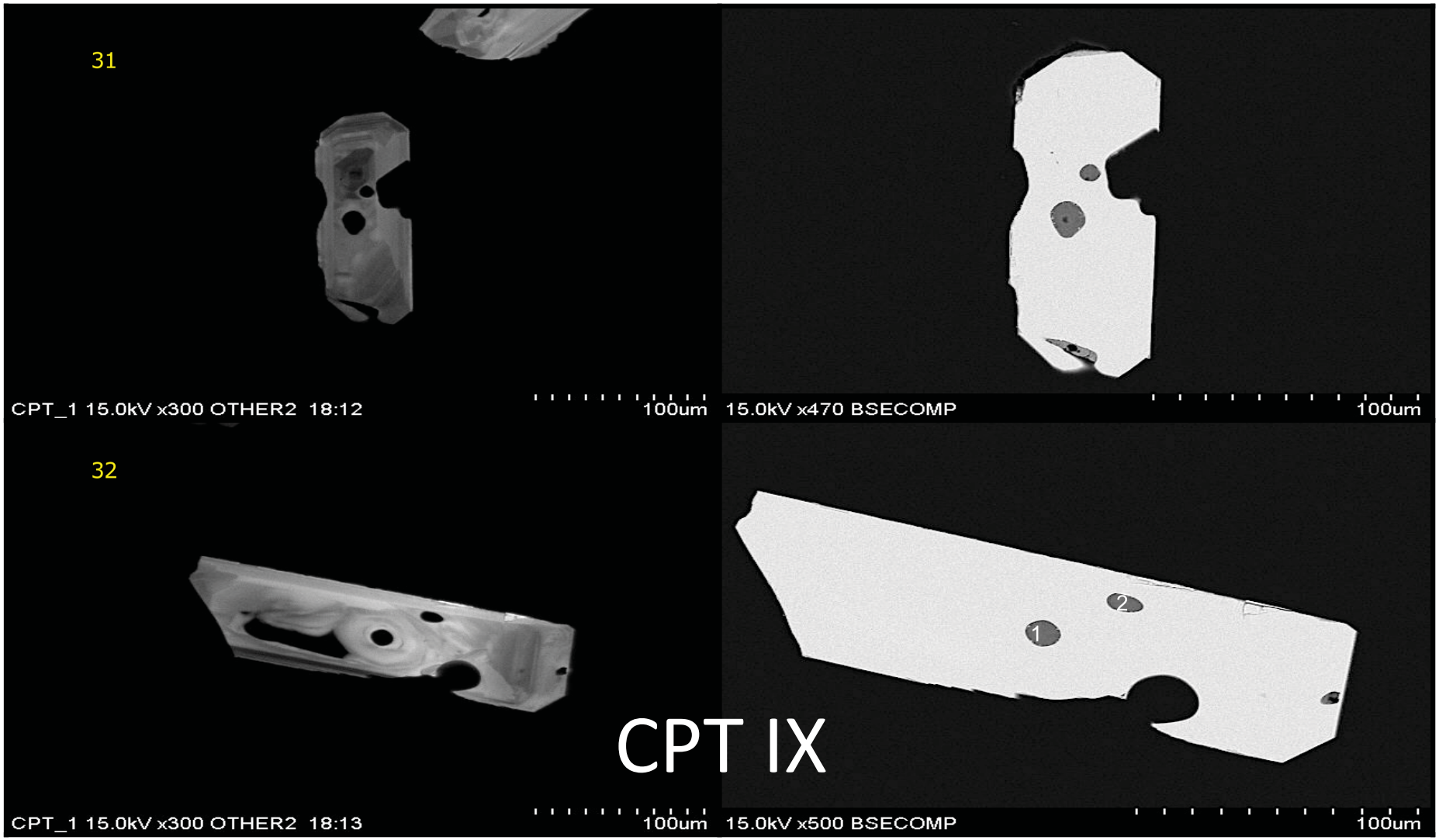
31
CPT_1 15.0kV x300 OTHER2 18:12
100um
15.0kV x470 BSECOMP
100um
32
CPT_1 15.0kV x300 OTHER2 18:13
100um
1
2
15.0kV x500 BSECOMP
100um

CPT IX

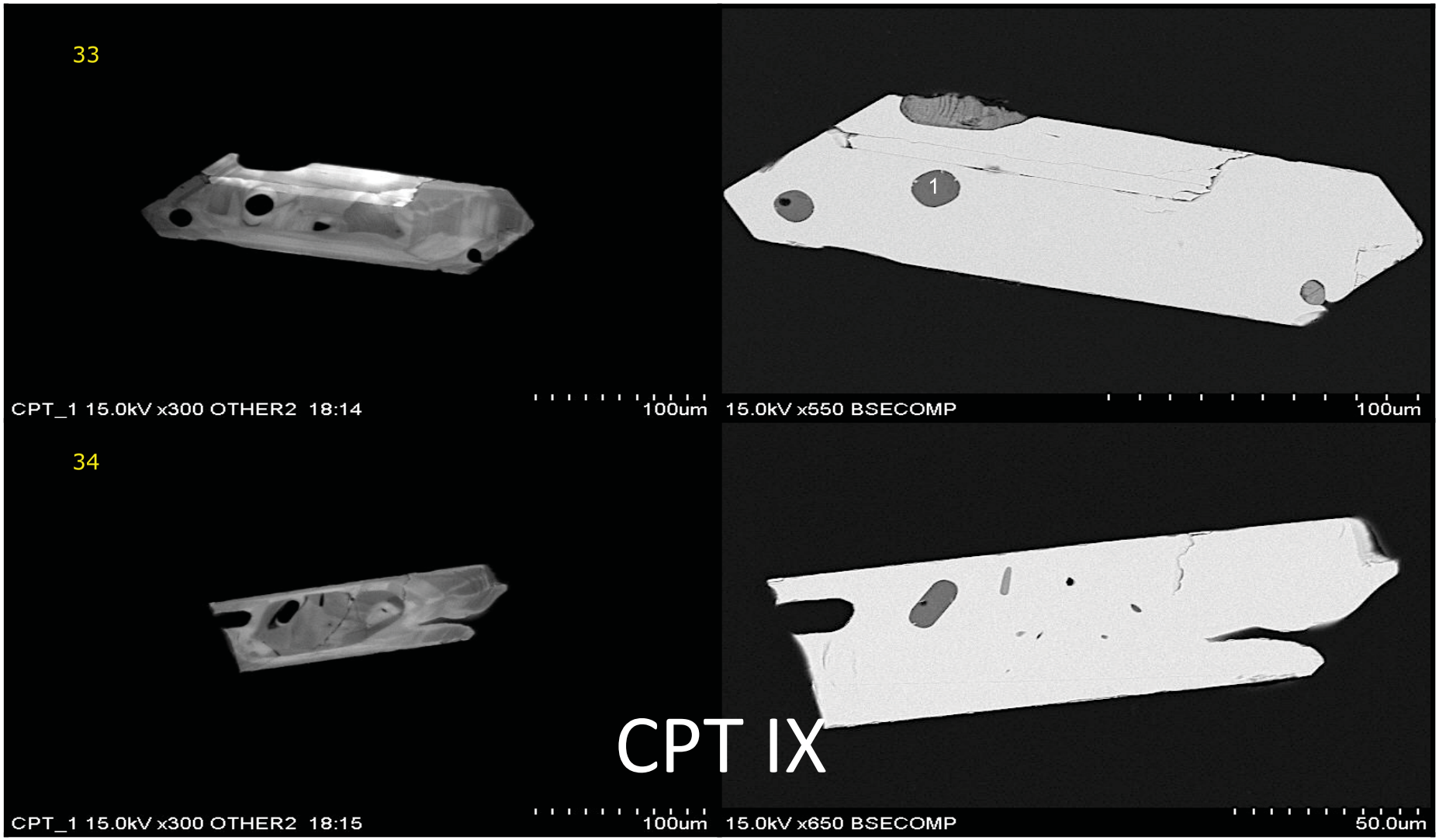
33
CPT_1 15.0kV x300 OTHER2 18:14
100um
1
15.0kV x550 BSECOMP
100um
34
CPT_1 15.0kV x300 OTHER2 18:15
100um
15.0kV x650 BSECOMP
50.0um

CPT IX

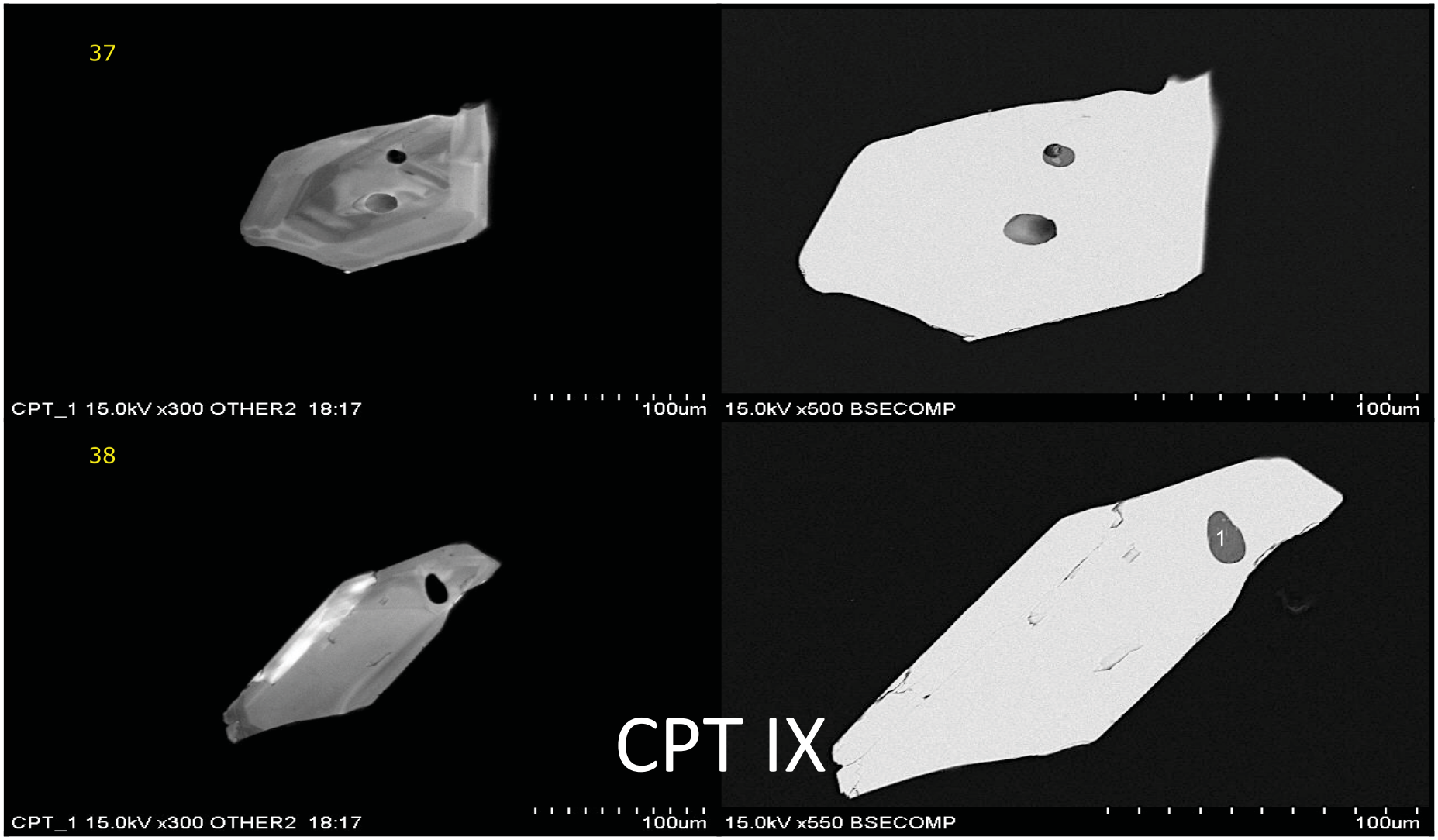
37
CPT_1 15.0kV x300 OTHER2 18:17
100um
15.0kV x500 BSECOMP
100um
38
CPT_1 15.0kV x300 OTHER2 18:17
100um
1
15.0kV x550 BSECOMP
100um

CPT IX

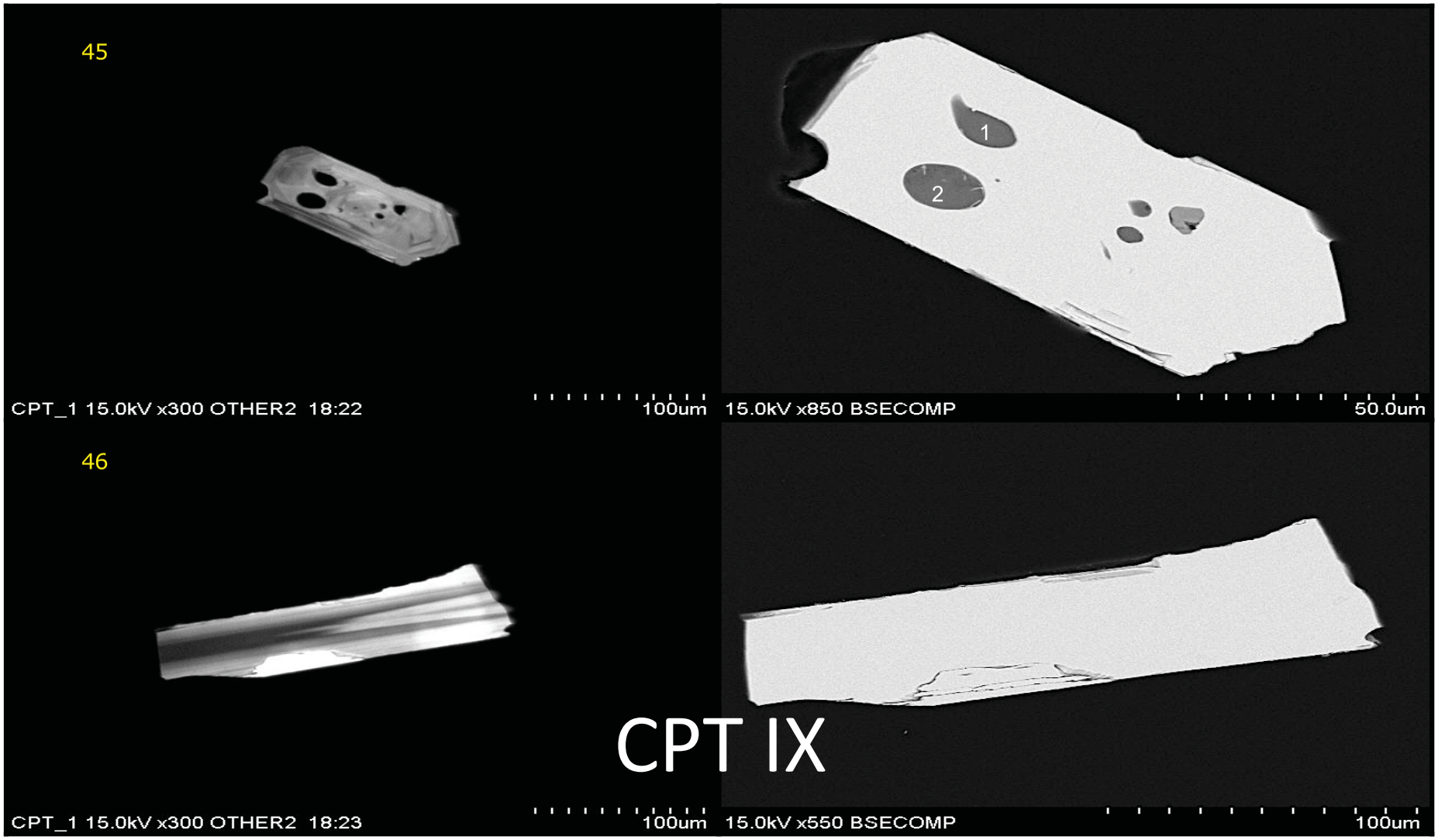
45
CPT_1 15.0kV x300 OTHER2 18:22
100um
1
2
15.0kV x850 BSECOMP
50.0um
46
CPT_1 15.0kV x300 OTHER2 18:23
100um
15.0kV x550 BSECOMP
100um

CPT IX

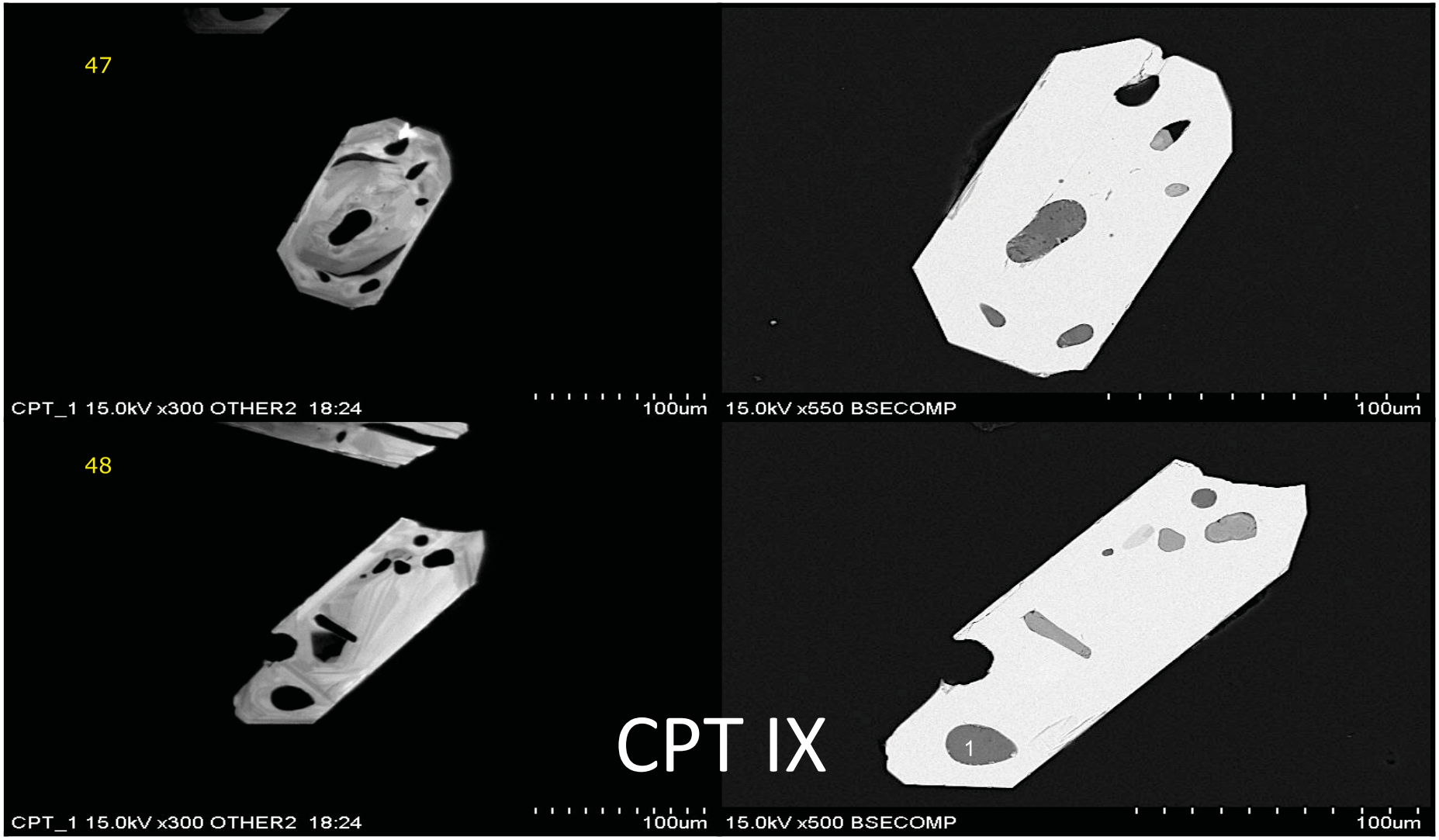
47
CPT_1 15.0kV x300 OTHER2 18:24
100um
15.0kV x550 BSECOMP
100um
48
CPT_1 15.0kV x300 OTHER2 18:24
100um
1
15.0kV x500 BSECOMP
100um

CPT IX

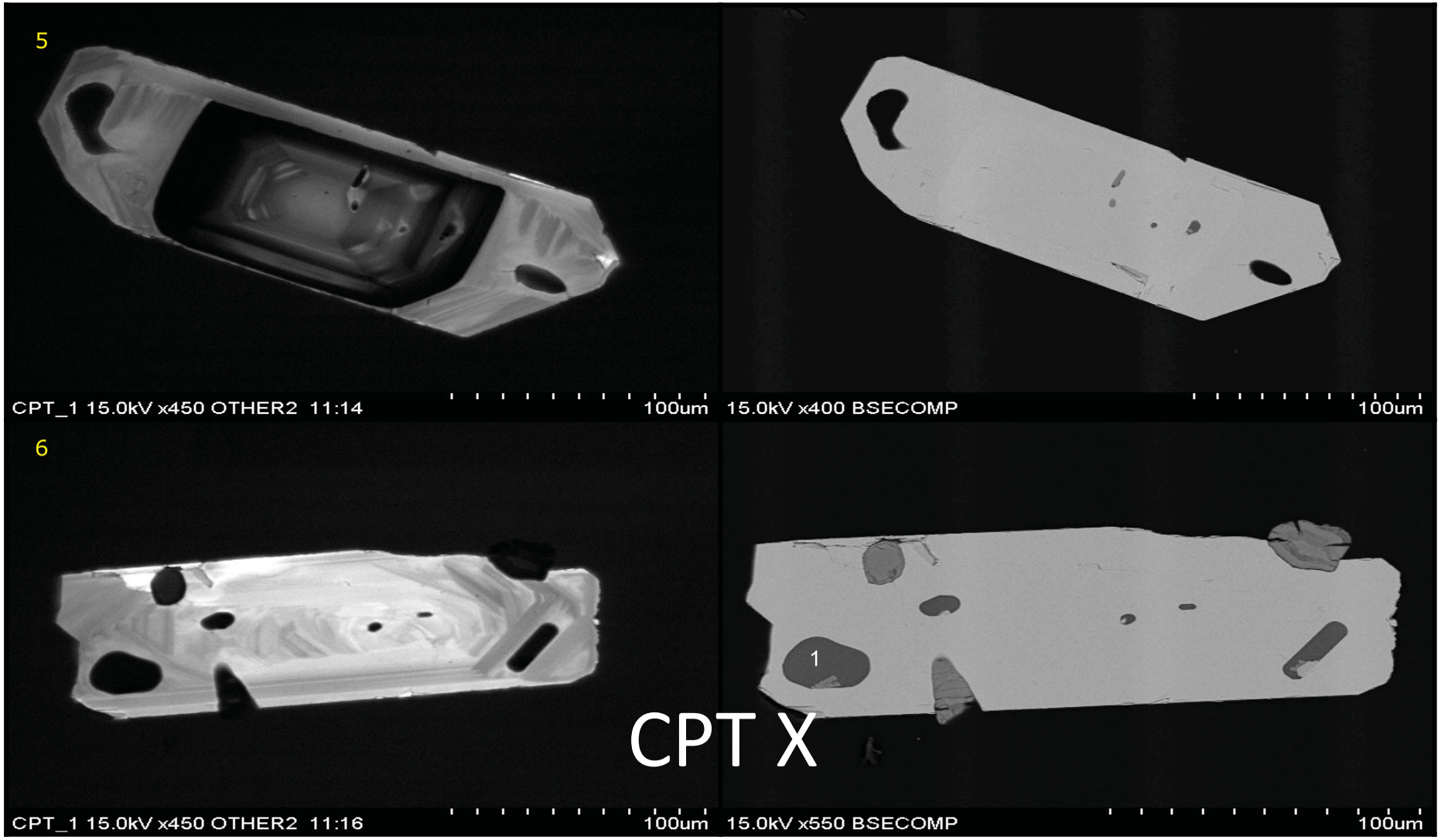
5
CPT_1 15.0kV x450 OTHER2 11:14
100um
15.0kV x400 BSECOMP
100um
6
CPT_1 15.0kV x450 OTHER2 11:16
100um
1
15.0kV x550 BSECOMP
100um
CPT X

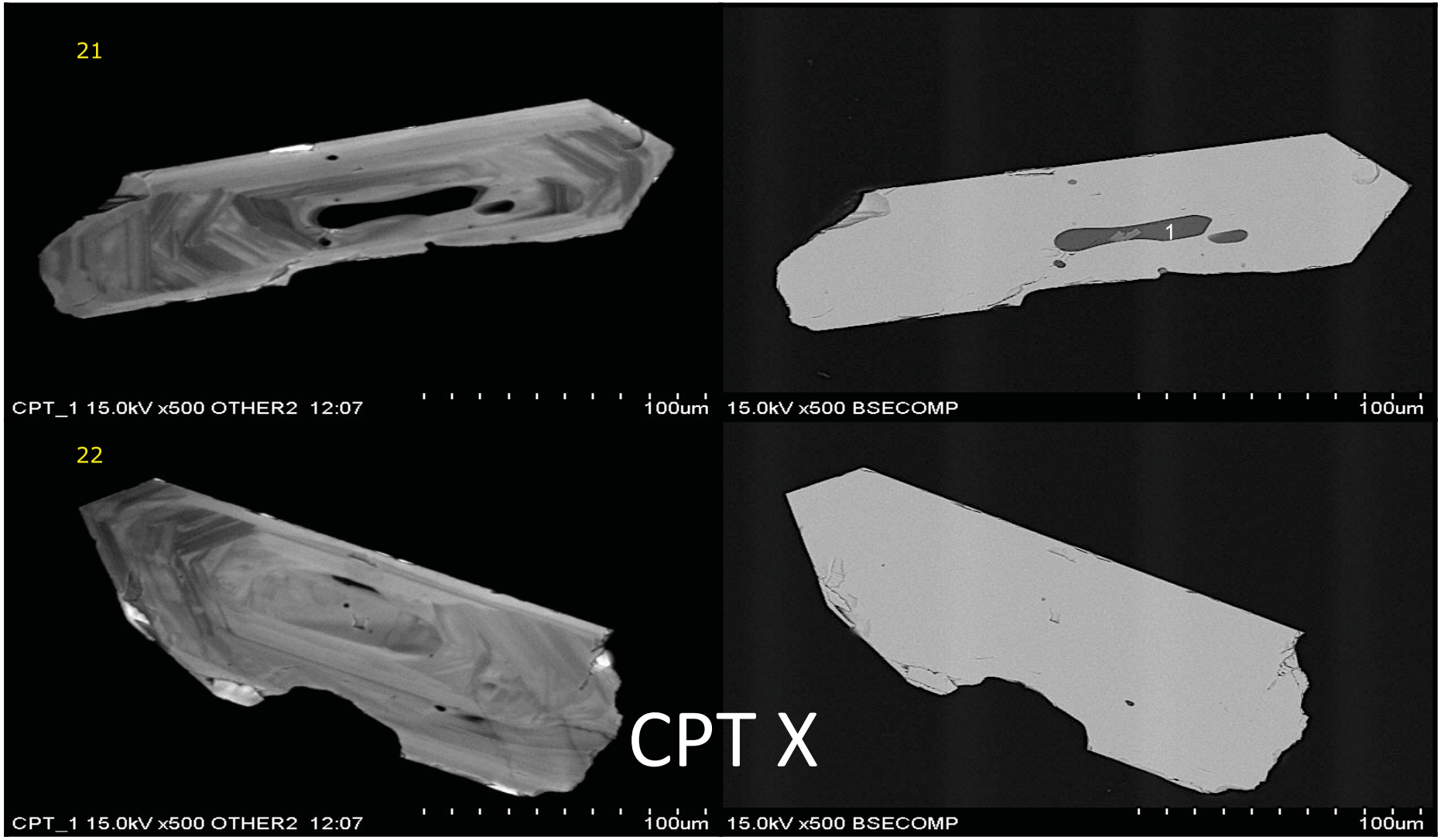
21
CPT_1 15.0kV x500 OTHER2 12:07
100um
1
15.0kV x500 BSECOMP
100um
22
CPT_1 15.0kV x500 OTHER2 12:07
100um
15.0kV x500 BSECOMP
100um
CPT X

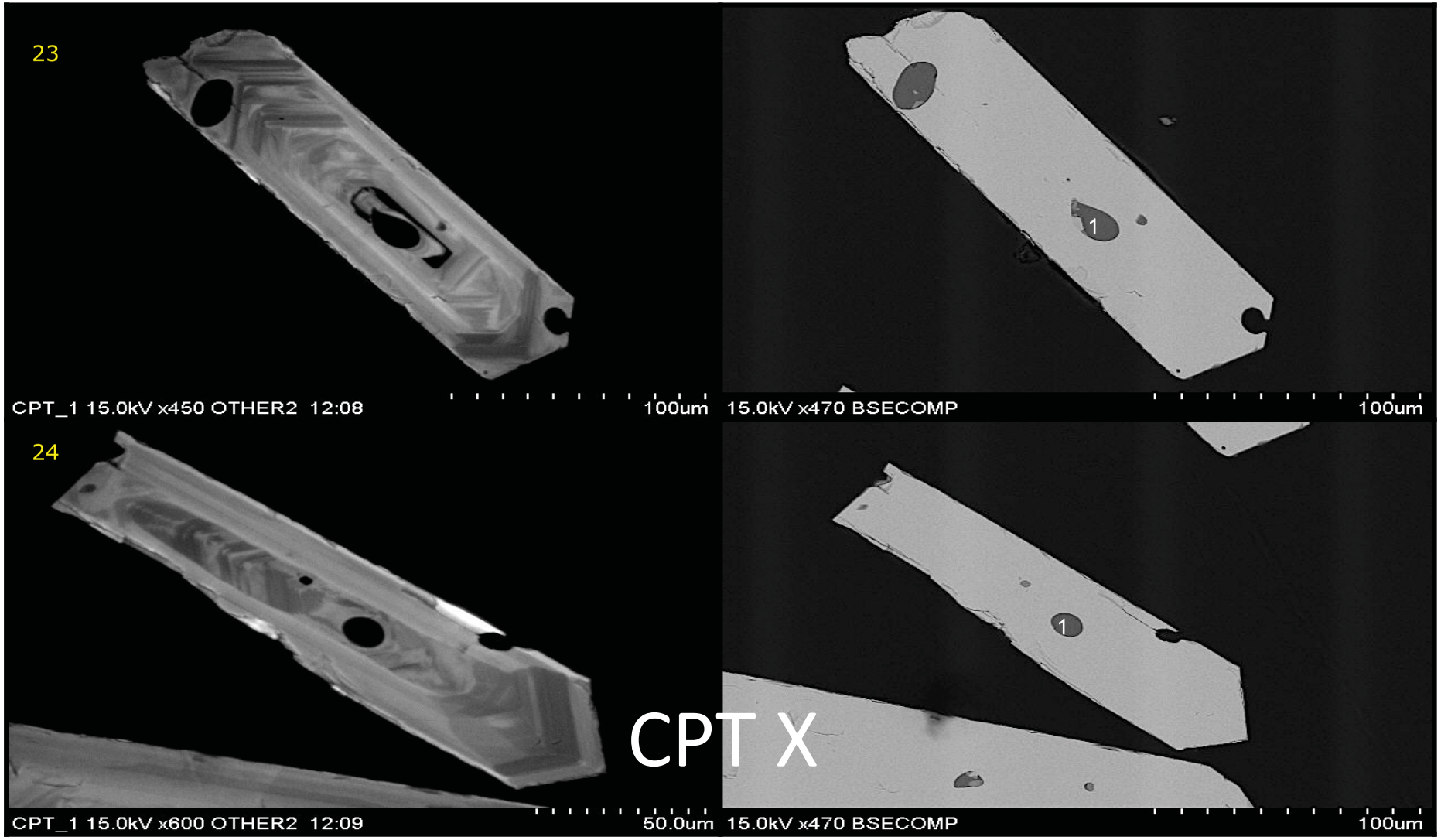
23
CPT_1 15.0kV x450 OTHER2 12:08
100um
1
15.0kV x470 BSECOMP
100um
24
CPT_1 15.0kV x600 OTHER2 12:09
50.0um
CPT X
1
15.0kV x470 BSECOMP
100um

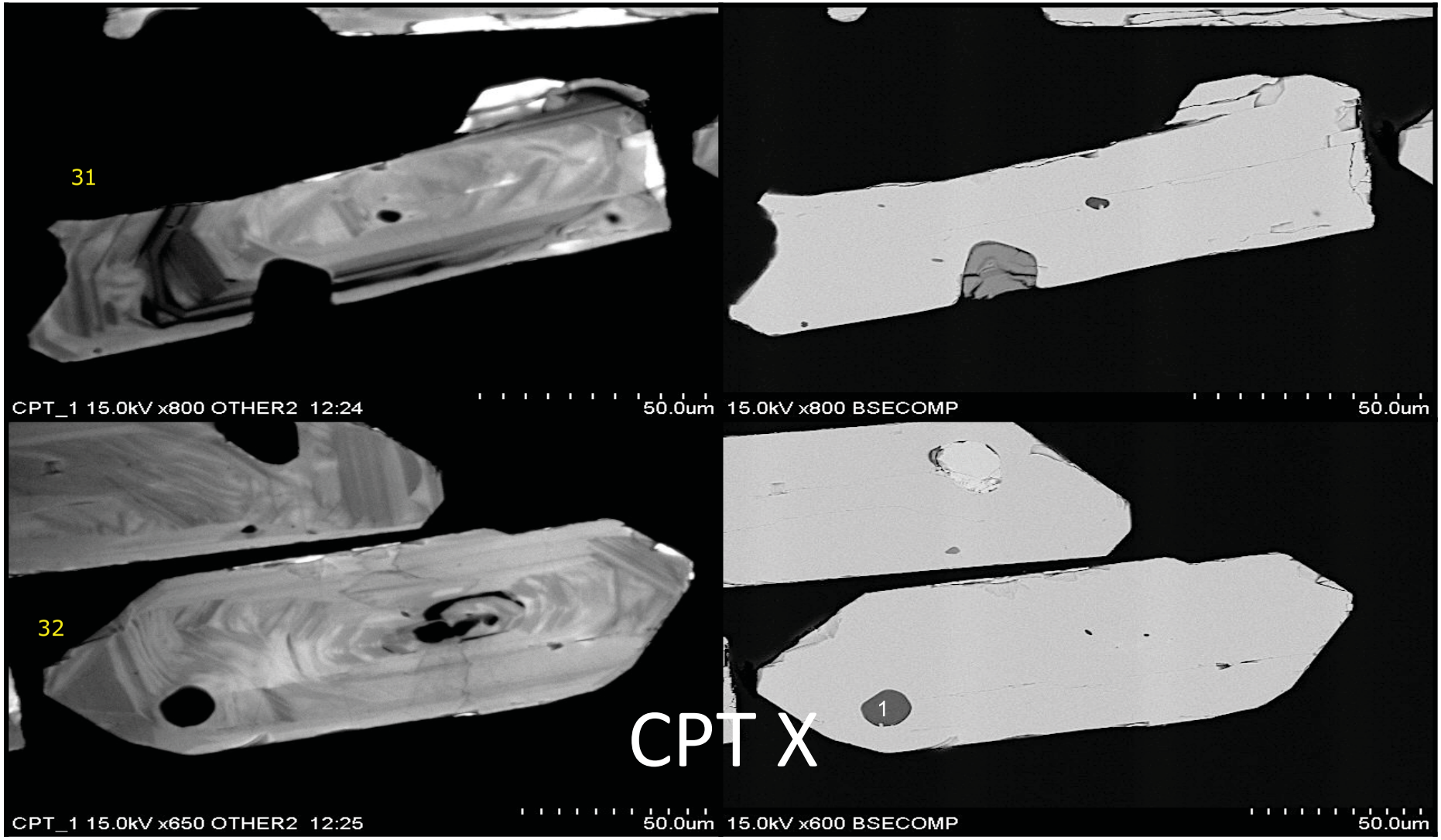
31
CPT_1 15.0kV x800 OTHER2 12:24
50.0um
15.0kV x800 BSECOMP
50.0um
32
CPT_1 15.0kV x650 OTHER2 12:25
50.0um
1
15.0kV x600 BSECOMP
50.0um
CPT X

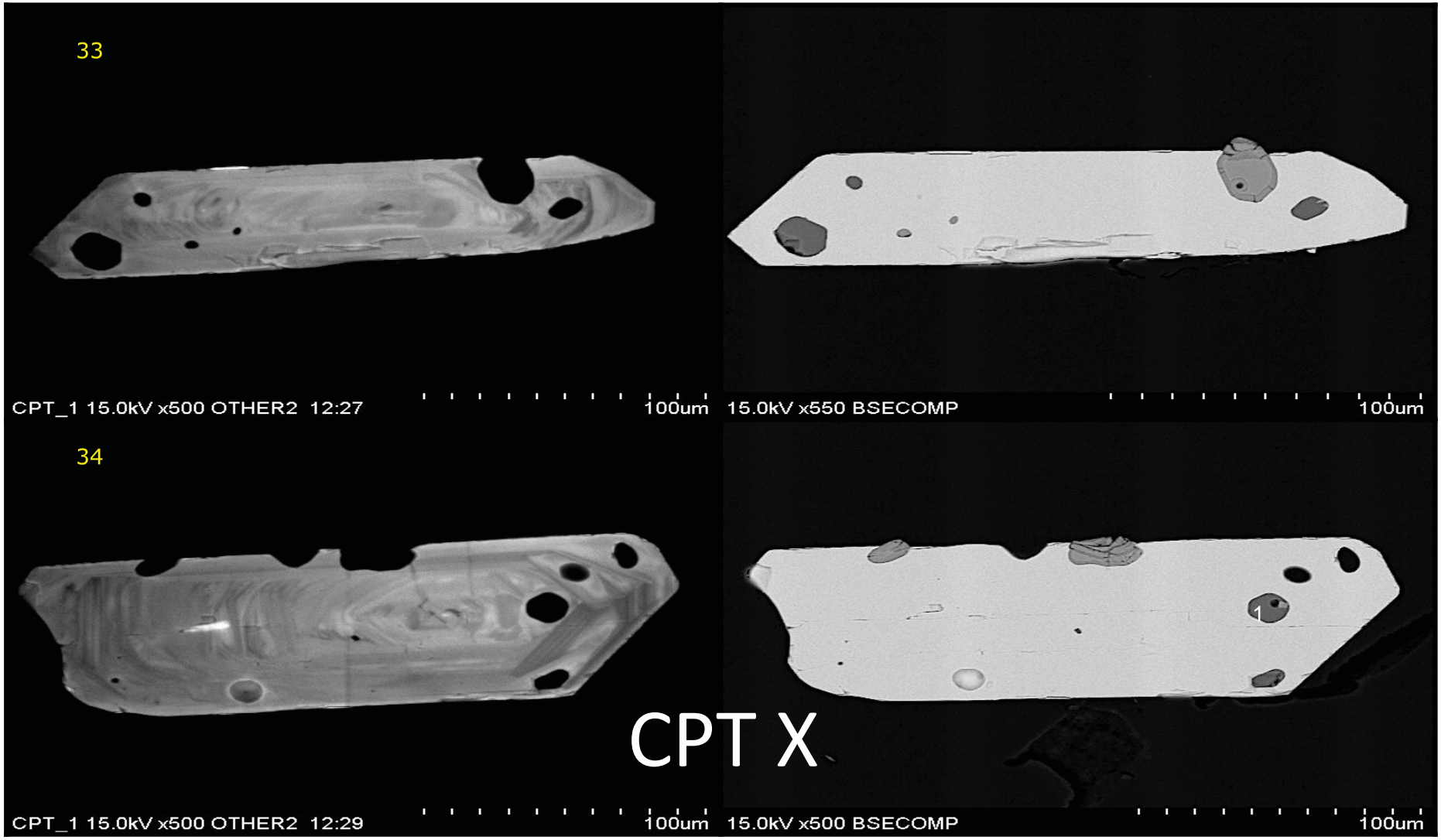
33
CPT_1 15.0kV x500 OTHER2 12:27
100um
15.0kV x550 BSECOMP
100um
34
CPT_1 15.0kV x500 OTHER2 12:29
100um
15.0kV x500 BSECOMP
100um

CPT X

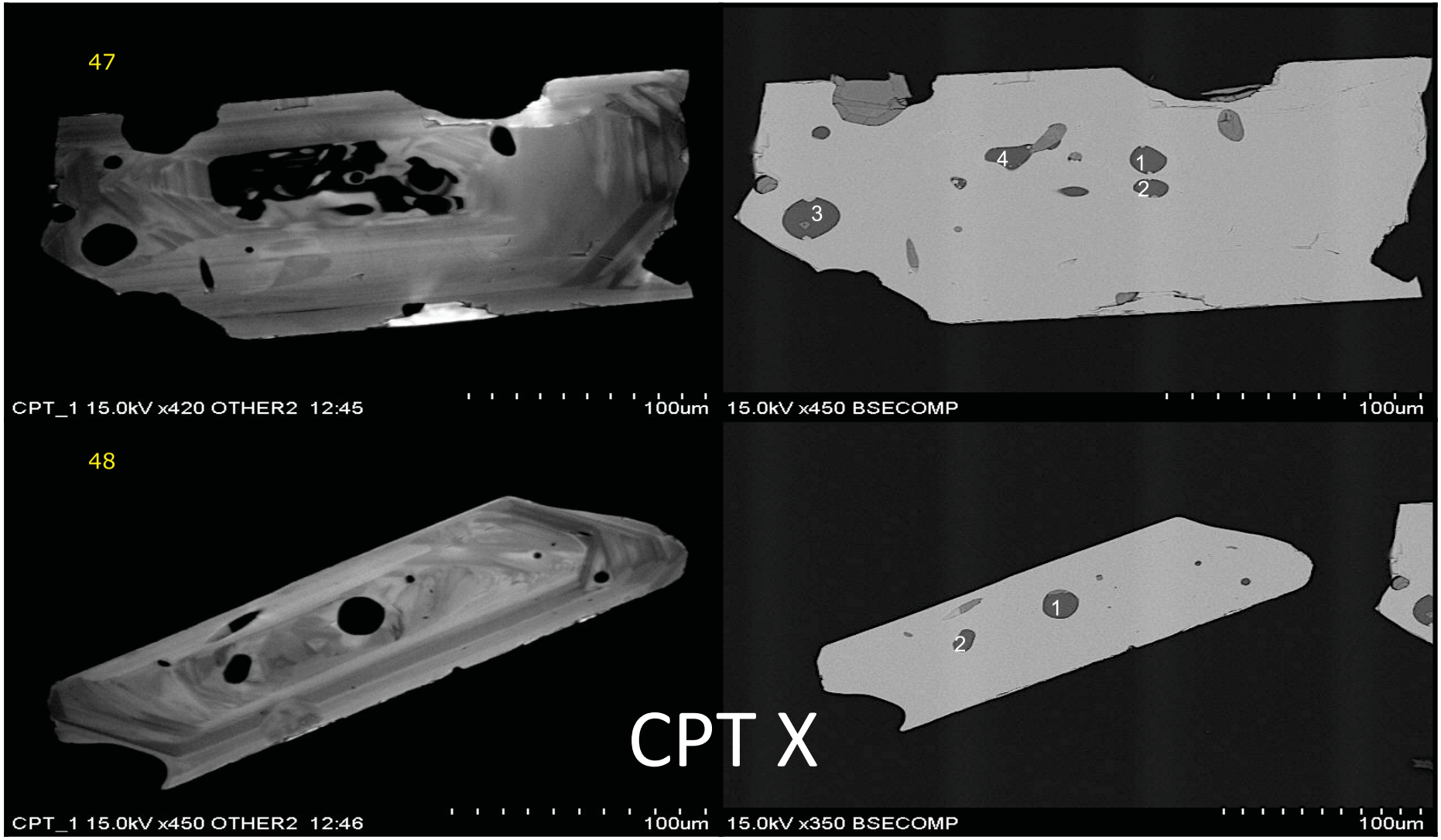
47
CPT_1 15.0kV x420 OTHER2 12:45
100um
4
1
2
3
15.0kV x450 BSECOMP
100um
48
CPT_1 15.0kV x450 OTHER2 12:46
100um
1
2
15.0kV x350 BSECOMP
100um
CPT X

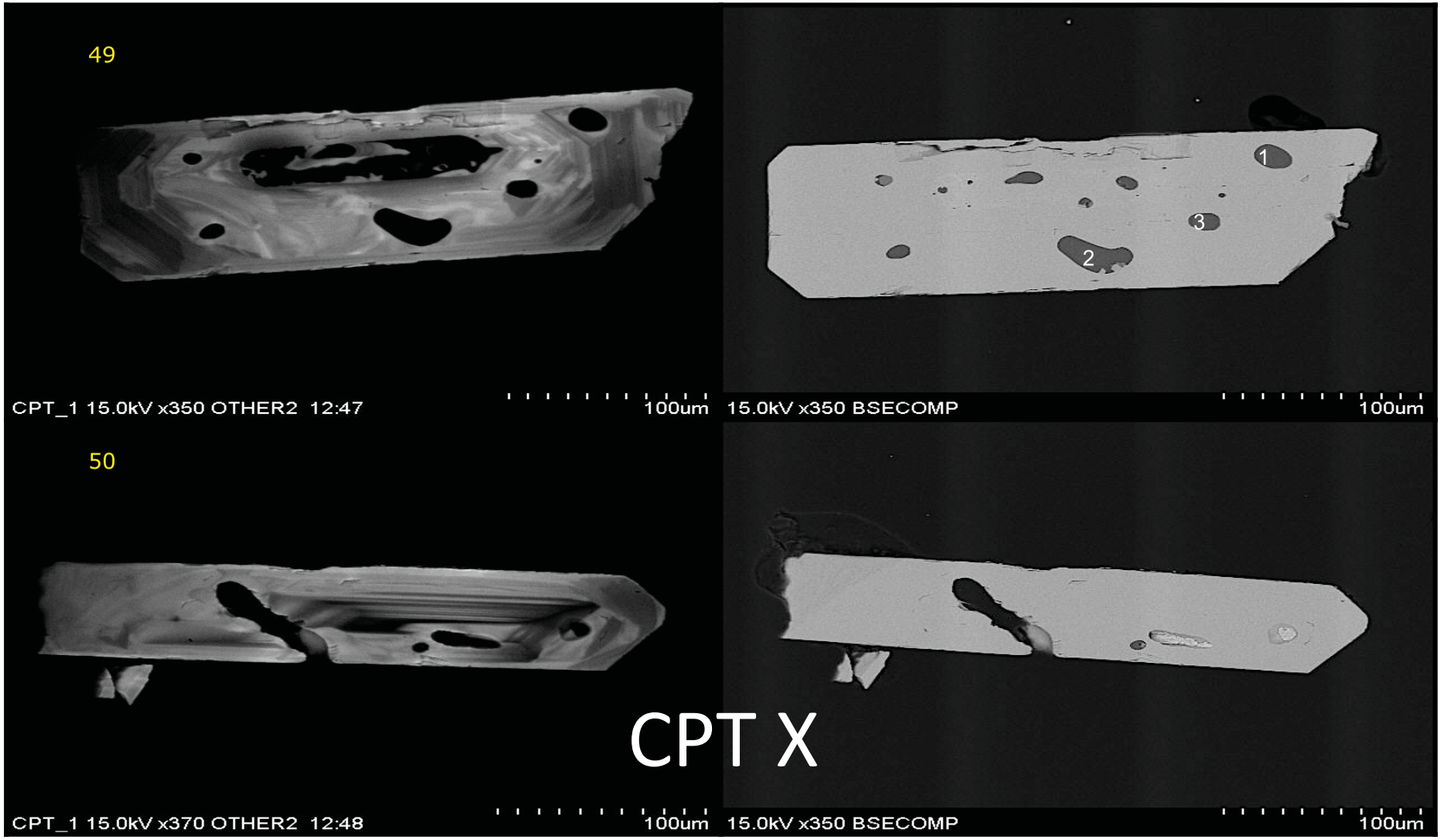
49
CPT_1 15.0kV x350 OTHER2 12:47
100um
1
3
2
15.0kV x350 BSECOMP
100um
50
CPT_1 15.0kV x370 OTHER2 12:48
100um
15.0kV x350 BSECOMP
100um

CPT X

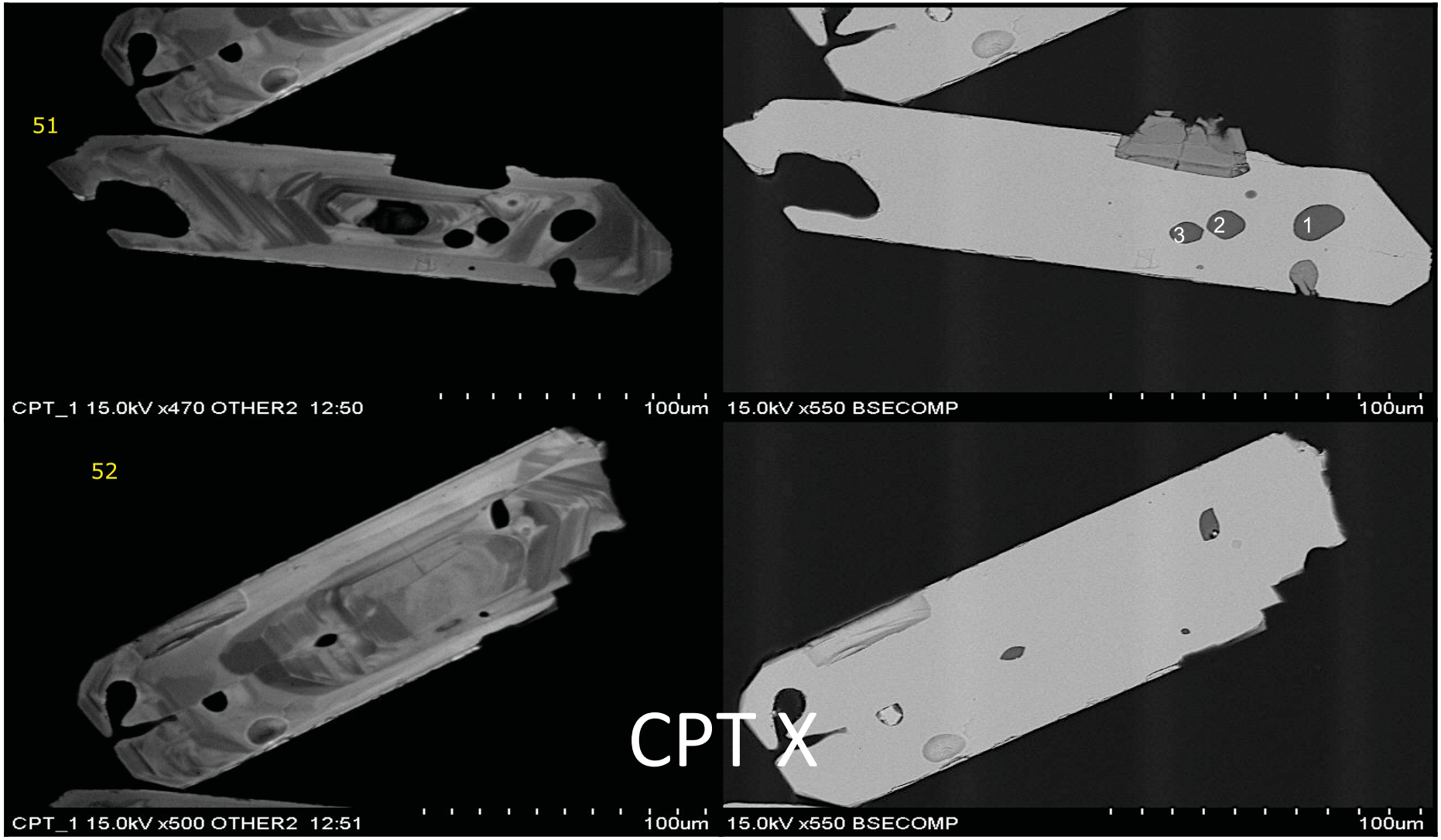
51
CPT_1 15.0kV x470 OTHER2 12:50
100um
3
2
1
15.0kV x550 BSECOMP
100um
52
CPT_1 15.0kV x500 OTHER2 12:51
100um
15.0kV x550 BSECOMP
100um
CPT X

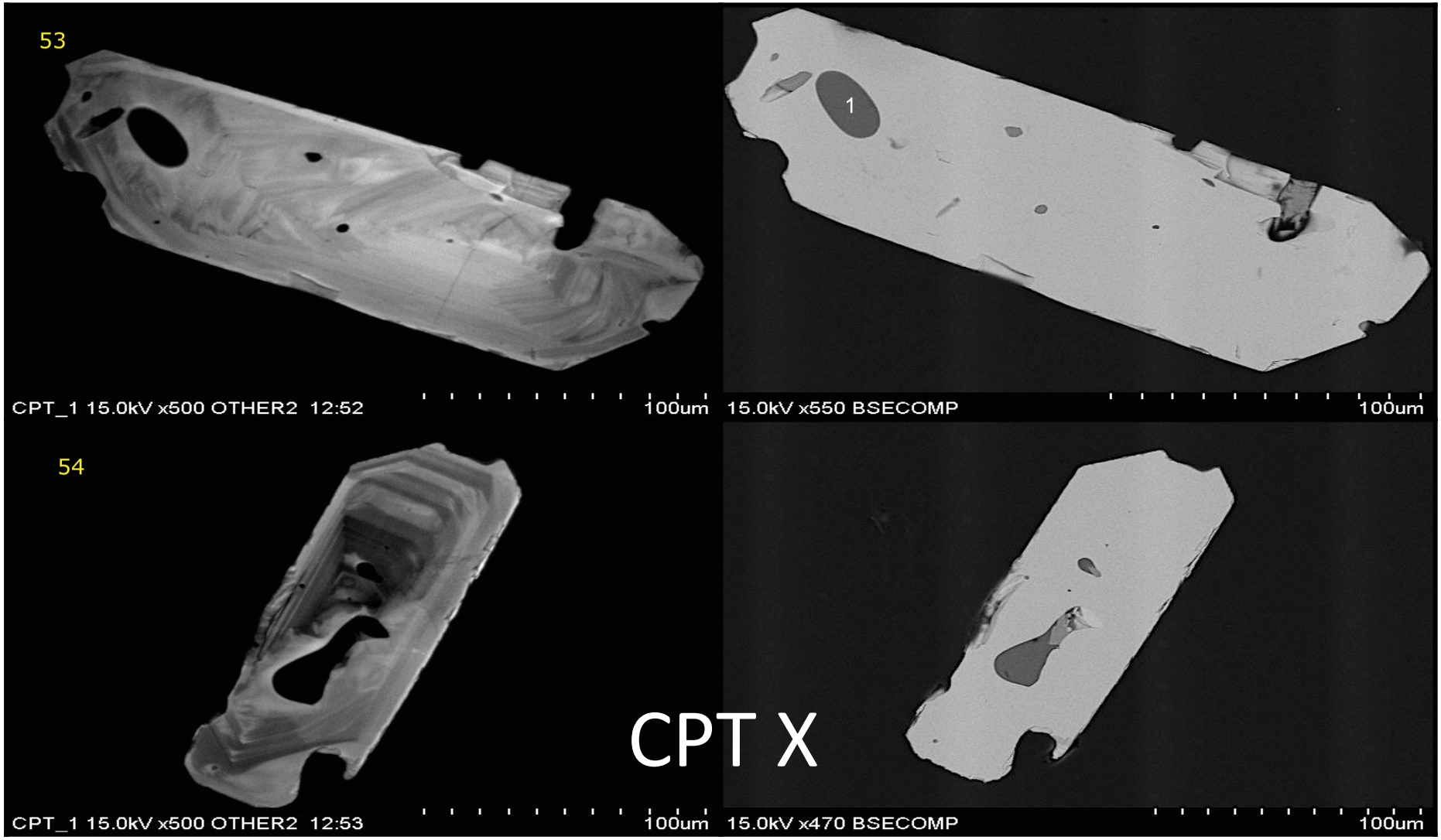
53
CPT_1 15.0kV x500 OTHER2 12:52
100um
1
15.0kV x550 BSECOMP
100um
54
CPT_1 15.0kV x500 OTHER2 12:53
100um
15.0kV x470 BSECOMP
100um

CPT X

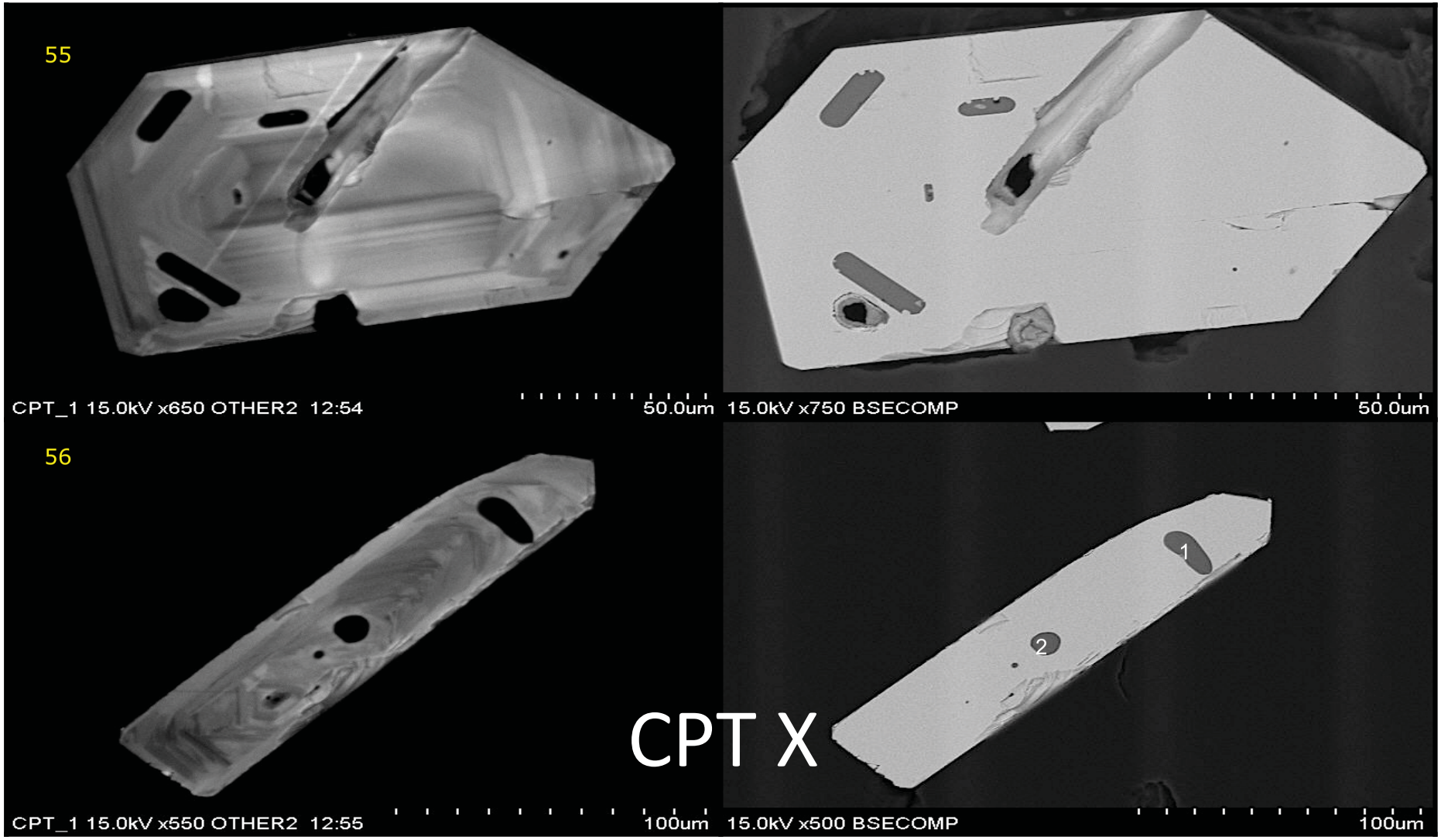
55
CPT_1 15.0kV x650 OTHER2 12:54
50.0um
15.0kV x750 BSECOMP
50.0um
56
CPT_1 15.0kV x550 OTHER2 12:55
100um
1
2
15.0kV x500 BSECOMP
100um
CPT X

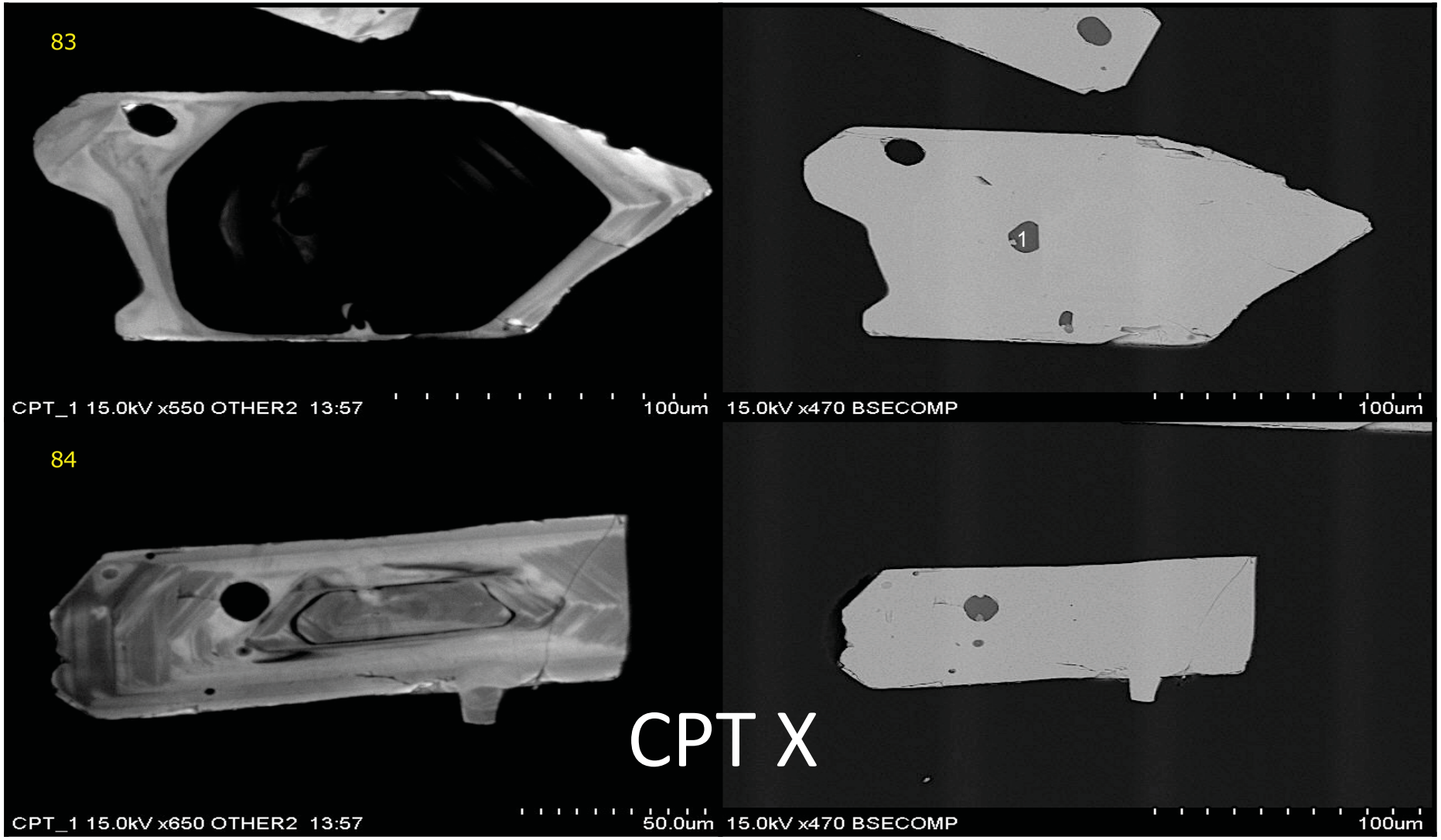
83
CPT_1 15.0kV x550 OTHER2 13:57
100um
1
15.0kV x470 BSECOMP
100um
84
CPT_1 15.0kV x650 OTHER2 13:57
50.0um
15.0kV x470 BSECOMP
100um
CPT X

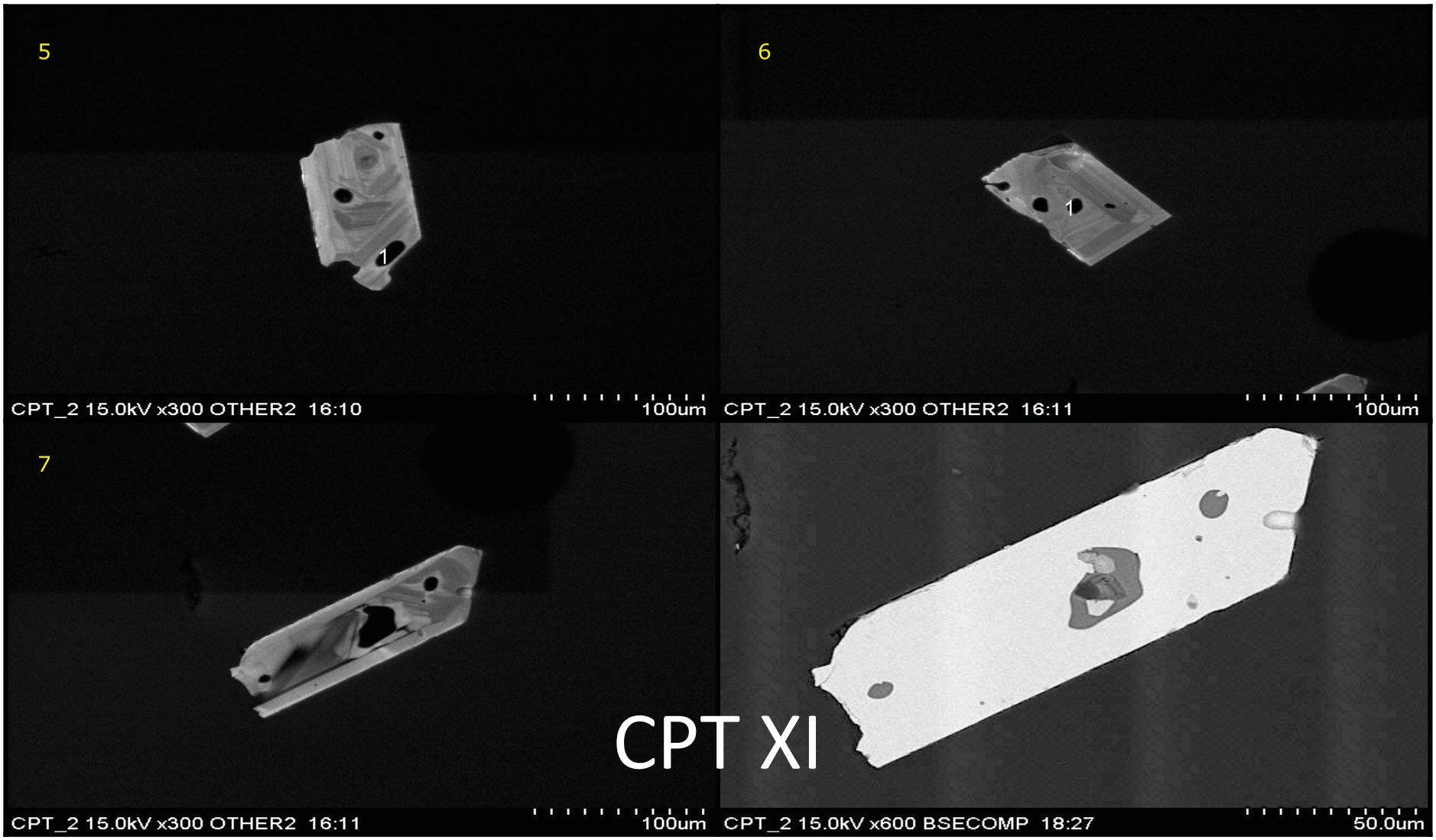
5
1
CPT_2 15.0kV x300 OTHER2 16:10
100um
6
1
CPT_2 15.0kV x300 OTHER2 16:11
100um
7
CPT_2 15.0kV x300 OTHER2 16:11
100um
CPT_2 15.0kV x600 BSECOMP 18:27
50.0um

CPT XI

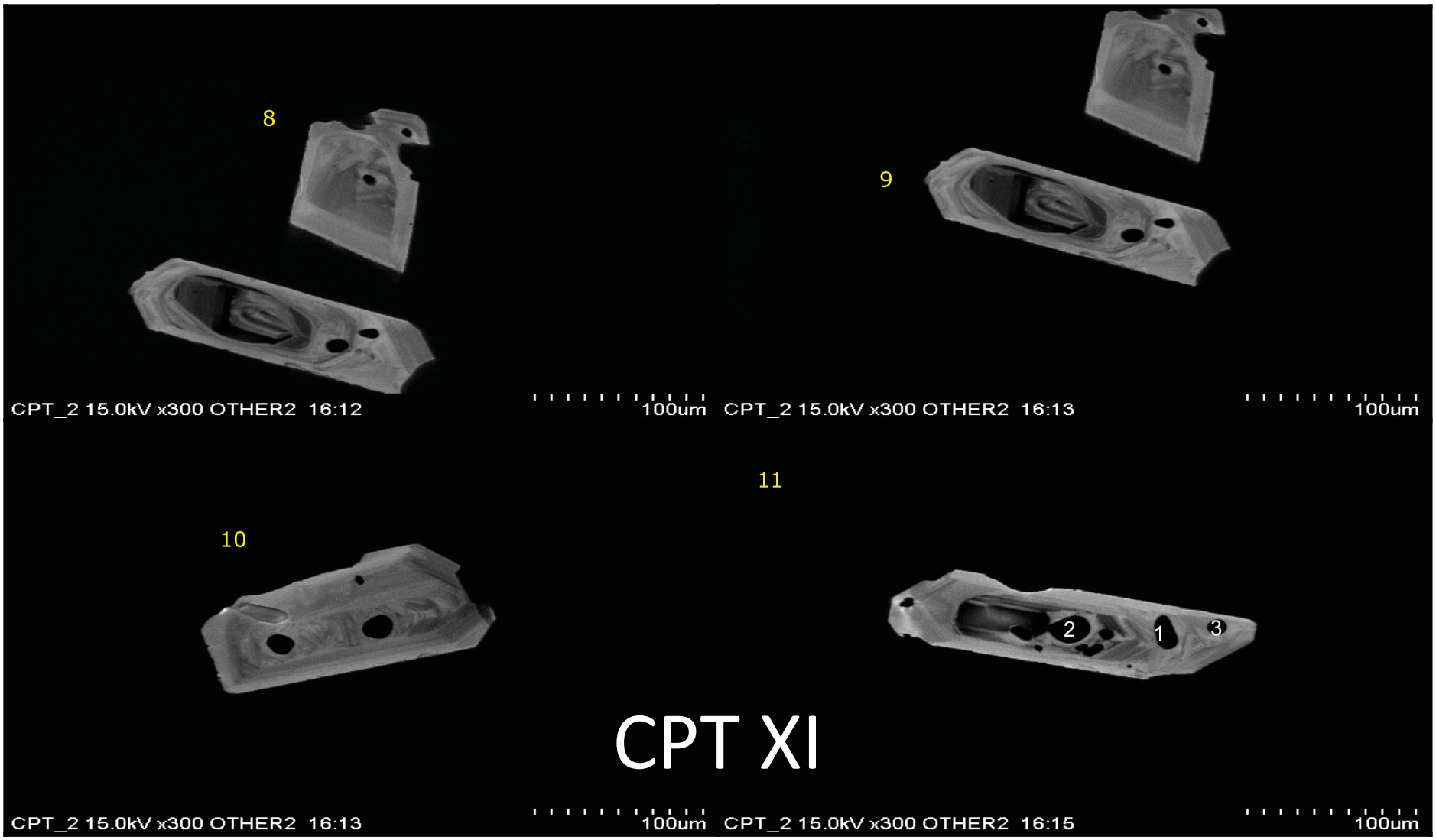
8
CPT_2 15.0kV x300 OTHER2 16:12
100um
9
CPT_2 15.0kV x300 OTHER2 16:13
100um
10
CPT_2 15.0kV x300 OTHER2 16:13
100um
11
2
1
3
CPT_2 15.0kV x300 OTHER2 16:15
100um
CPT XI

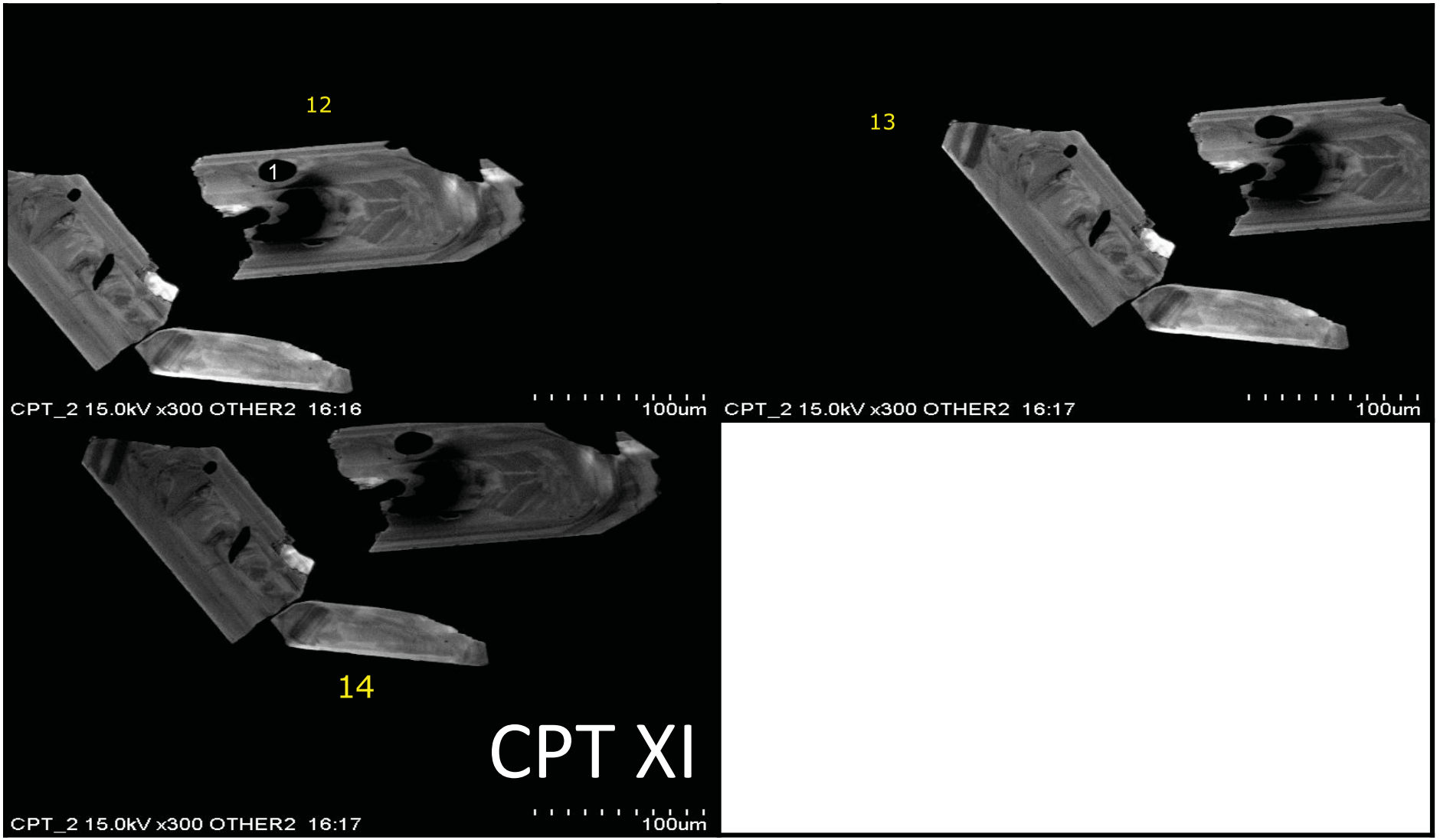
12
1
CPT_2 15.0kV x300 OTHER2 16:16
100um
13
CPT_2 15.0kV x300 OTHER2 16:17
100um
14
CPT XI
CPT_2 15.0kV x300 OTHER2 16:17
100um

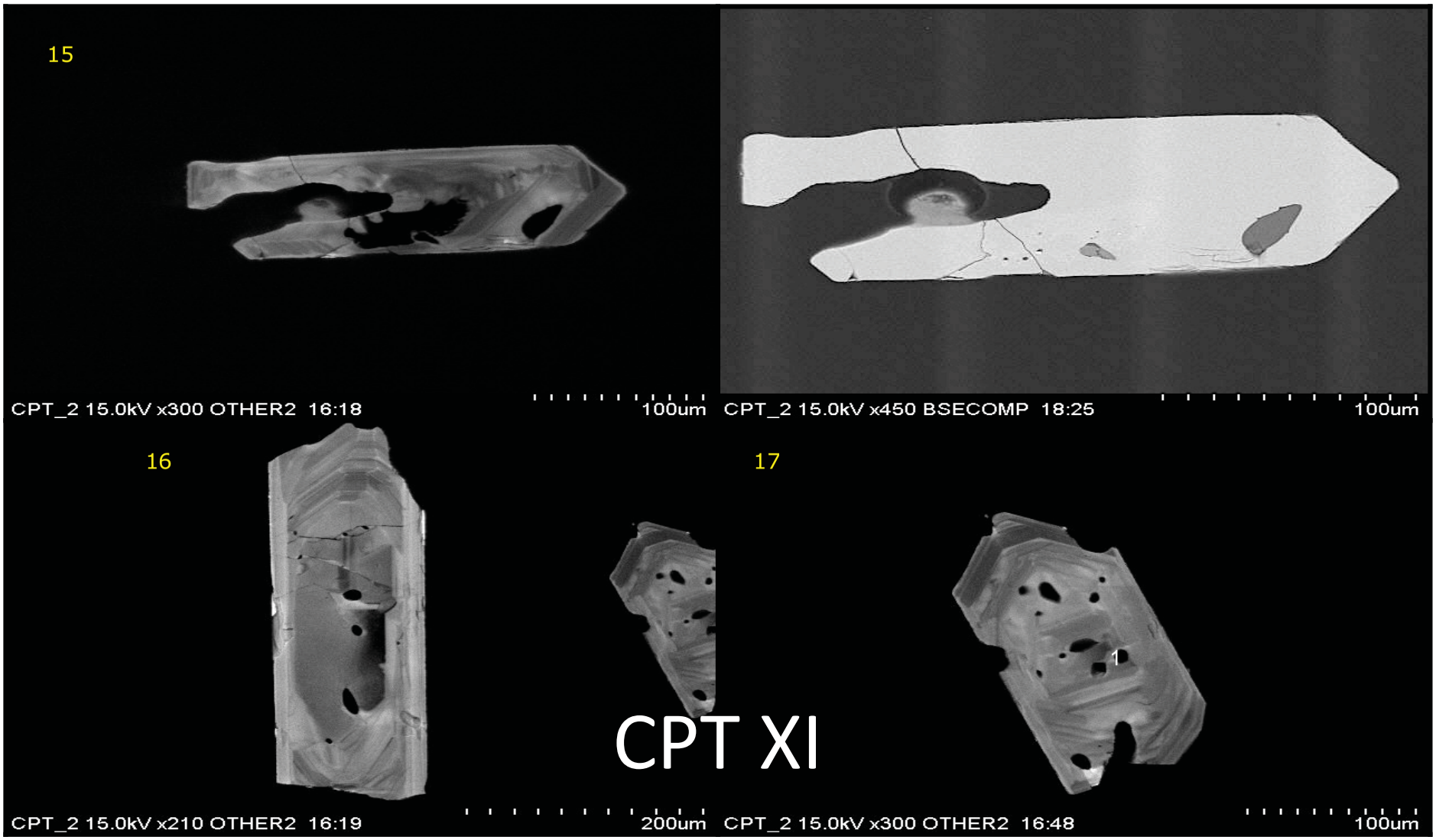
15
CPT_2 15.0kV x300 OTHER2 16:18
100um
CPT_2 15.0kV x450 BSECOMP 18:25
100um
16
CPT_2 15.0kV x210 OTHER2 16:19
200um
17
1
CPT_2 15.0kV x300 OTHER2 16:48
100um
CPT XI


18
1
CPT_2 15.0kV x300 OTHER2 16:49
100um
19
CPT_2 15.0kV x300 OTHER2 16:49
100um
20
CPT_2 15.0kV x300 OTHER2 16:50
100um
21
CPT_2 15.0kV x300 OTHER2 16:52
100um
CPT XI

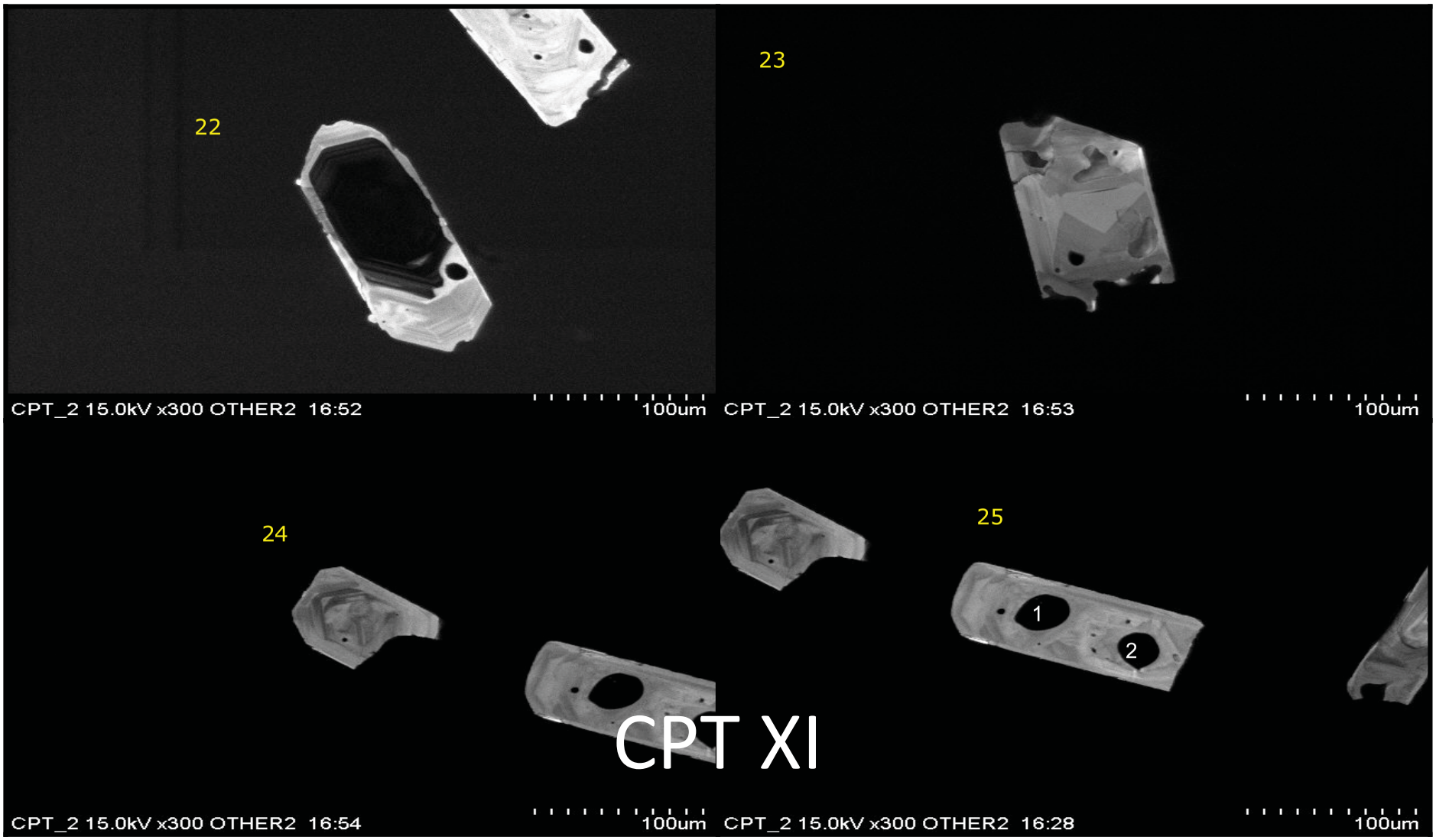
22
CPT_2 15.0kV x300 OTHER2 16:52
100um
23
CPT_2 15.0kV x300 OTHER2 16:53
100um
24
CPT_2 15.0kV x300 OTHER2 16:54
100um
25
1
2
CPT_2 15.0kV x300 OTHER2 16:28
100um
CPT XI


26
1
CPT_2 15.0kV x300 OTHER2 16:29
100um
27
CPT_2 15.0kV x300 OTHER2 16:30
100um
28
CPT_2 15.0kV x300 OTHER2 16:31
100um
29
1
2
CPT_2 15.0kV x300 OTHER2 16:31
100um

CPT XI

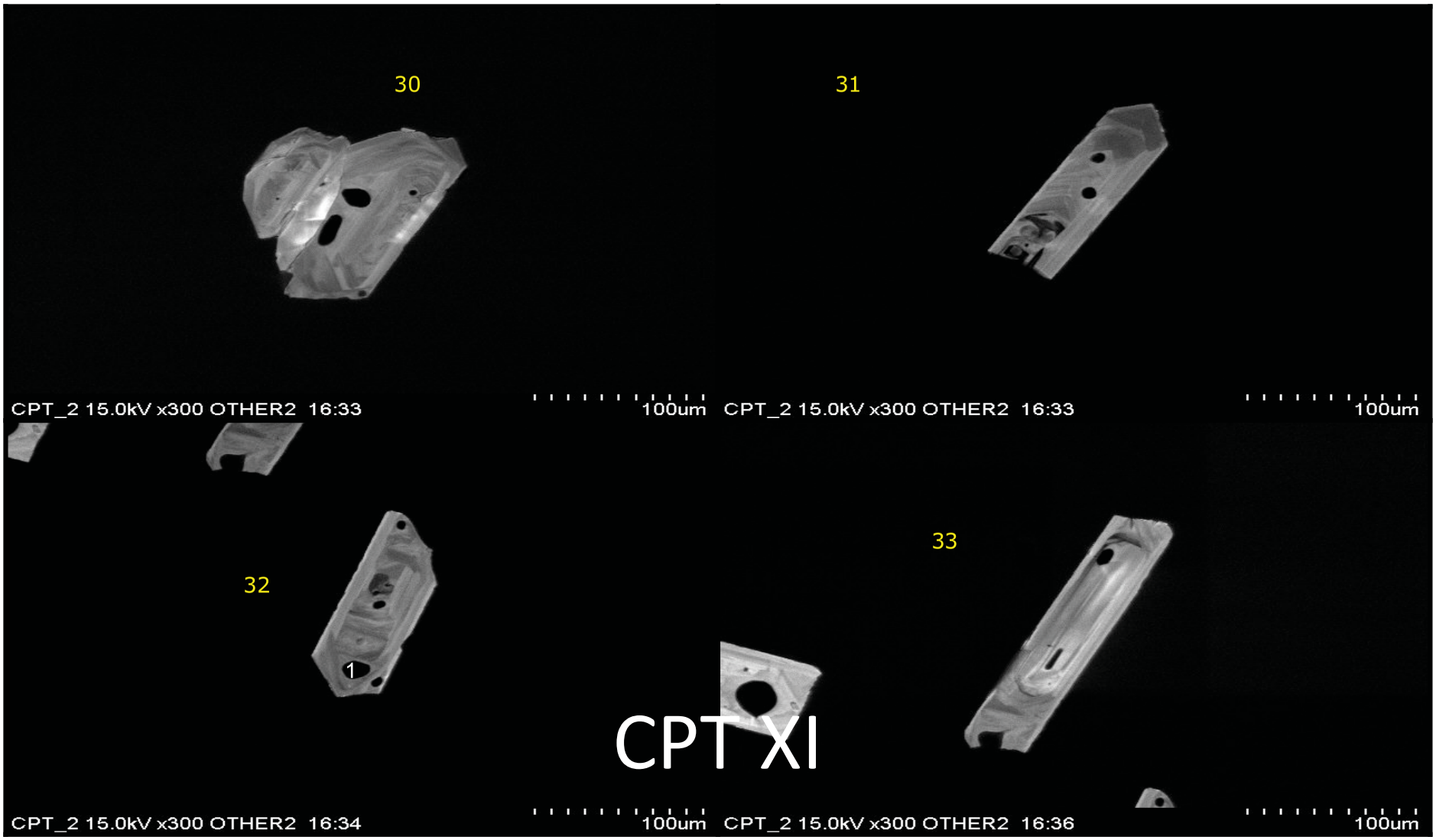
30
CPT_2 15.0kV x300 OTHER2 16:33
100um
31
CPT_2 15.0kV x300 OTHER2 16:33
100um
32
1
CPT_2 15.0kV x300 OTHER2 16:34
100um
33
CPT_2 15.0kV x300 OTHER2 16:36
100um
CPT XI

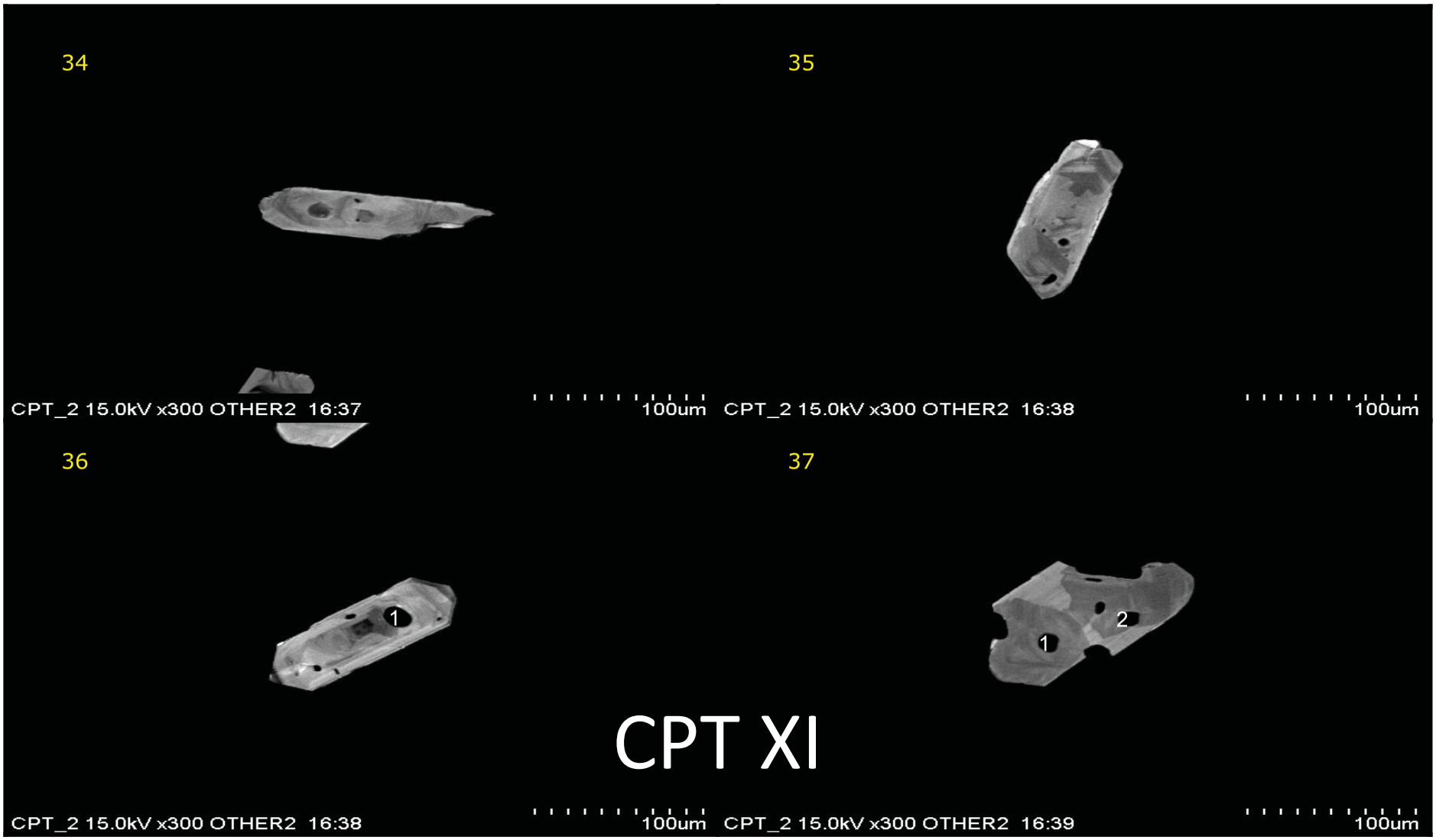
34
CPT_2 15.0kV x300 OTHER2 16:37
100um
35
CPT_2 15.0kV x300 OTHER2 16:38
100um
36
1
CPT_2 15.0kV x300 OTHER2 16:38
100um
37
1
2
CPT_2 15.0kV x300 OTHER2 16:39
100um
CPT XI

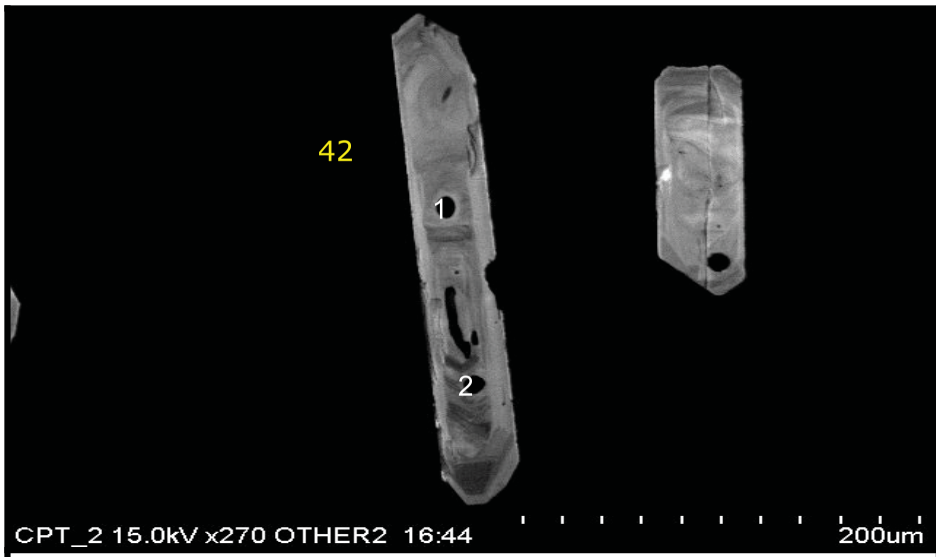
42
1
2
CPT_2 15.0kV x270 OTHER2 16:44
200um

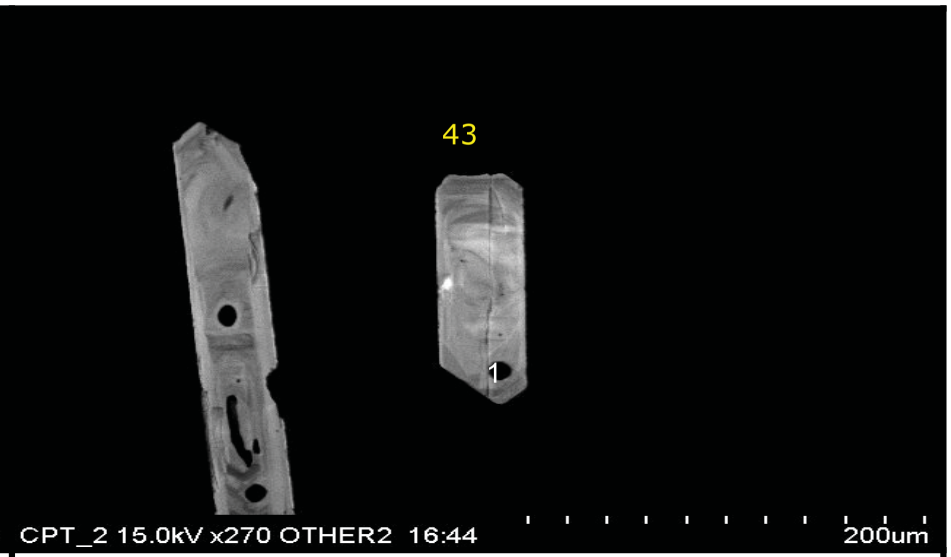
43
1
CPT_2 15.0kV x270 OTHER2 16:44
200um

CPT XI

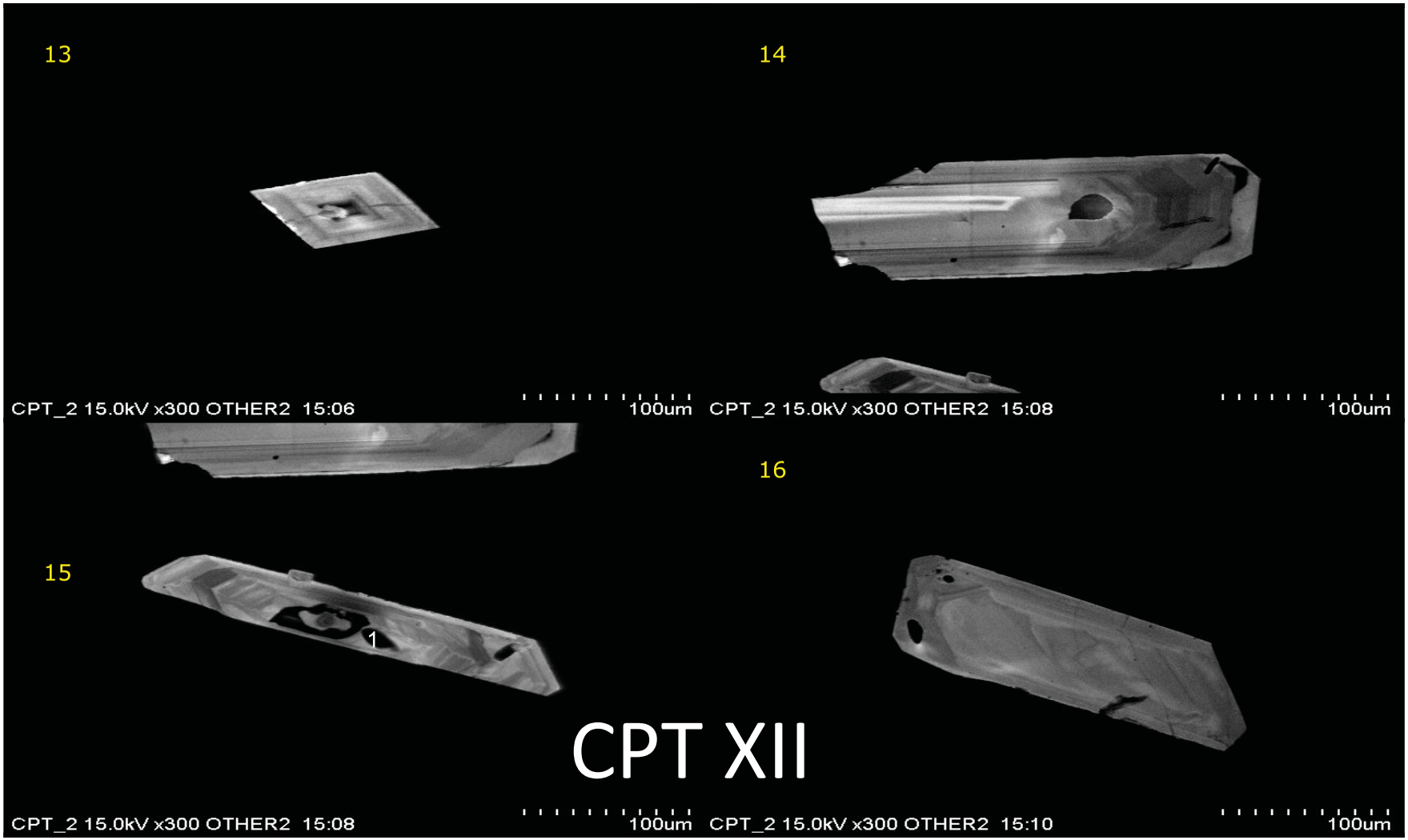
13
CPT_2 15.0kV x300 OTHER2 15:06
100um
14
CPT_2 15.0kV x300 OTHER2 15:08
100um
16
15
1
CPT XII
CPT_2 15.0kV x300 OTHER2 15:08
100um
CPT_2 15.0kV x300 OTHER2 15:10
100um

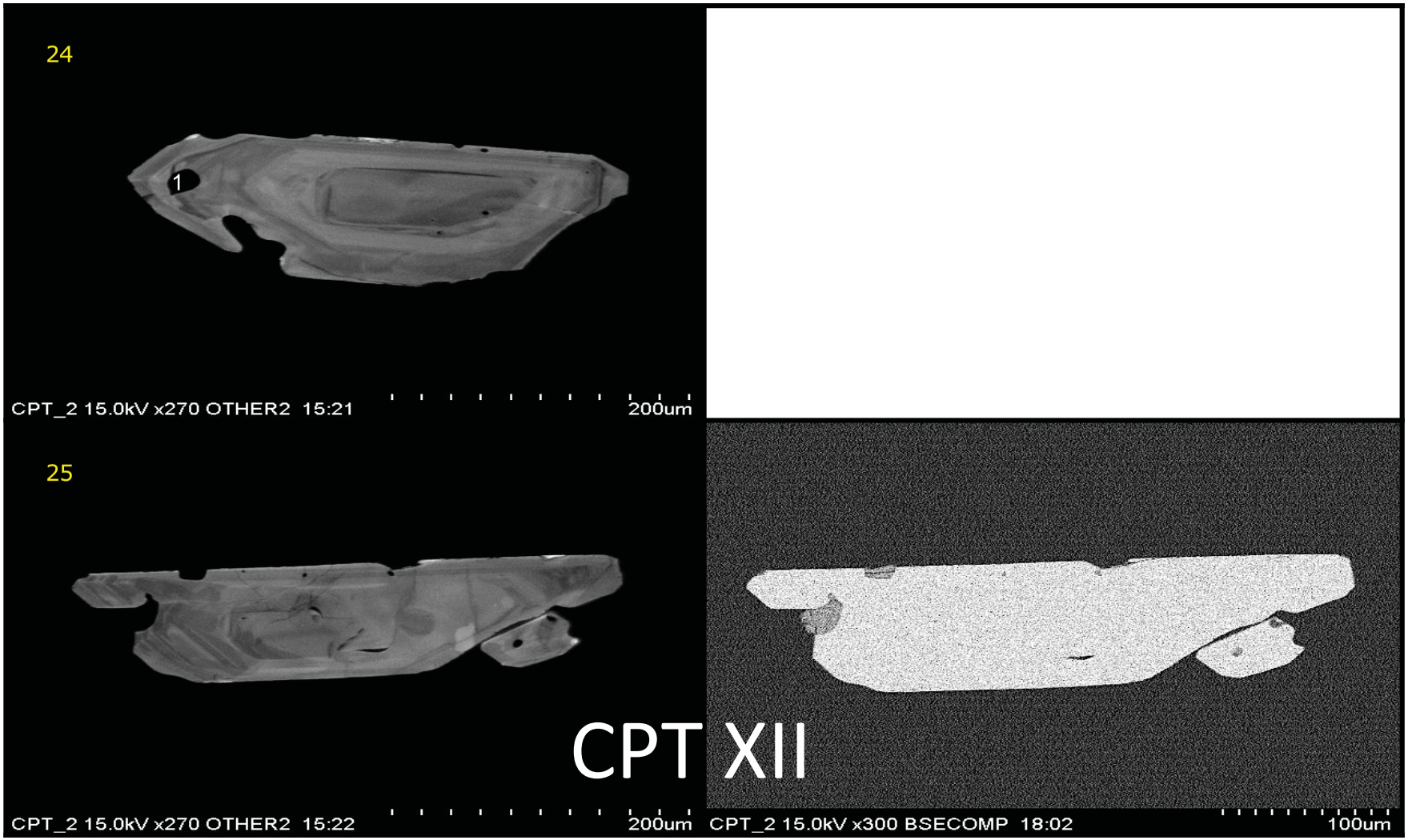
24
1
CPT_2 15.0kV x270 OTHER2 15:21
200um
25
CPT_2 15.0kV x270 OTHER2 15:22
200um
CPT XII
CPT_2 15.0kV x300 BSECOMP 18:02
100um

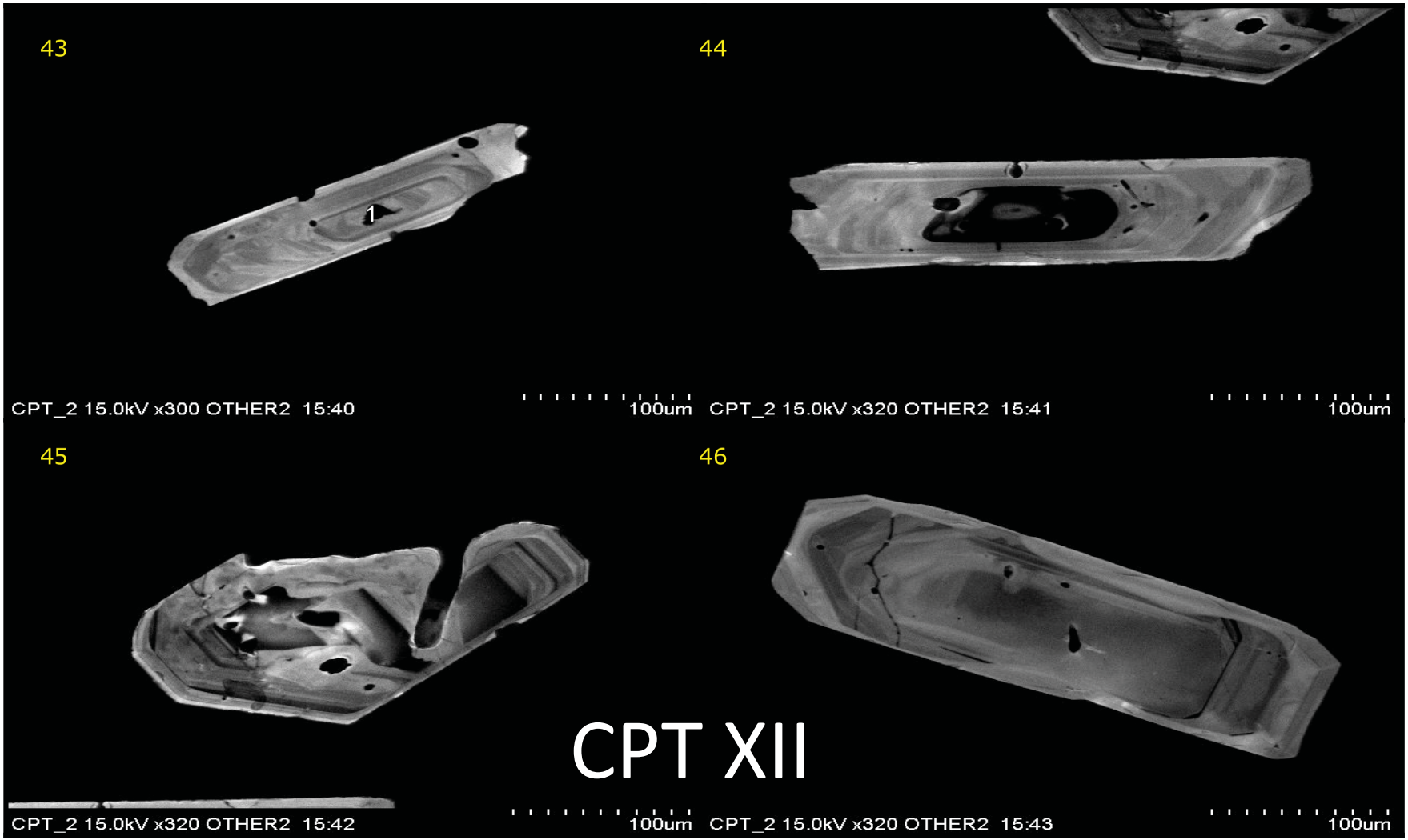
43
1
CPT_2 15.0kV x300 OTHER2 15:40
100um
44
CPT_2 15.0kV x320 OTHER2 15:41
100um
45
CPT_2 15.0kV x320 OTHER2 15:42
100um
46
CPT_2 15.0kV x320 OTHER2 15:43
100um
CPT XII

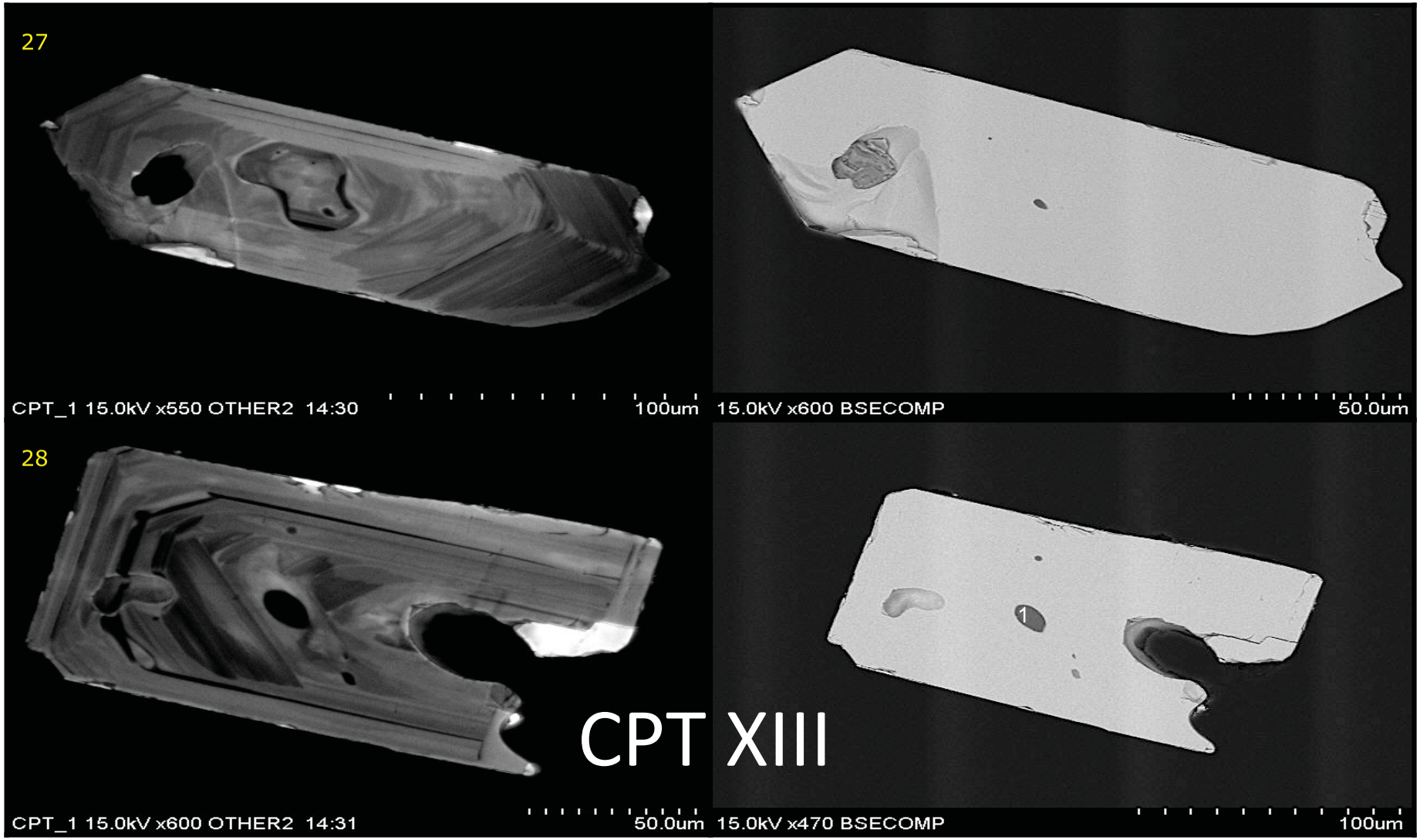
27
CPT_1 15.0kV x550 OTHER2 14:30
100um
15.0kV x600 BSECOMP
50.0um
28
CPT_1 15.0kV x600 OTHER2 14:31
50.0um
15.0kV x470 BSECOMP
100um
CPT XIII

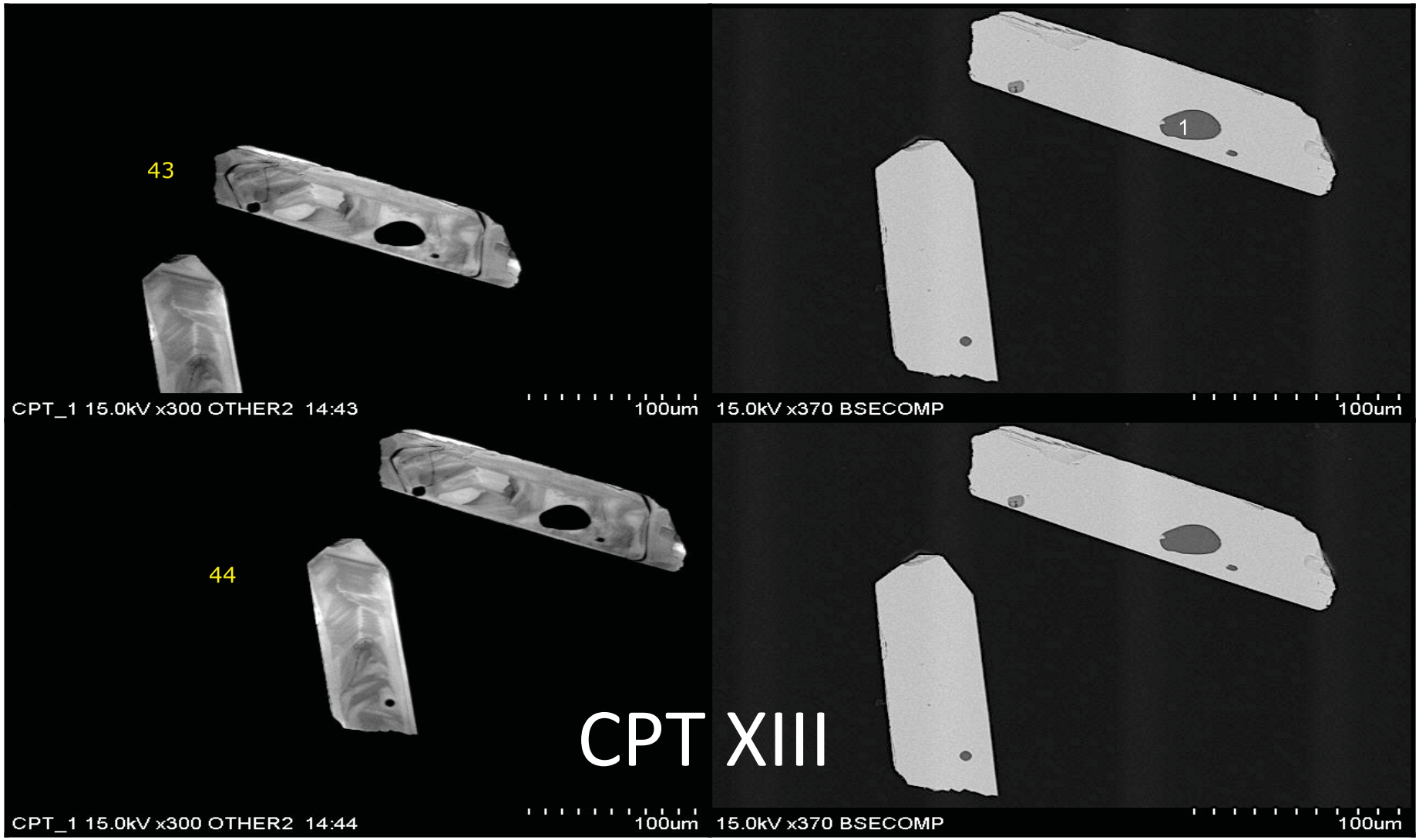
43
CPT_1 15.0kV x300 OTHER2 14:43
100um
1
15.0kV x370 BSECOMP
100um
44
CPT_1 15.0kV x300 OTHER2 14:44
100um
15.0kV x370 BSECOMP
100um
CPT XIII

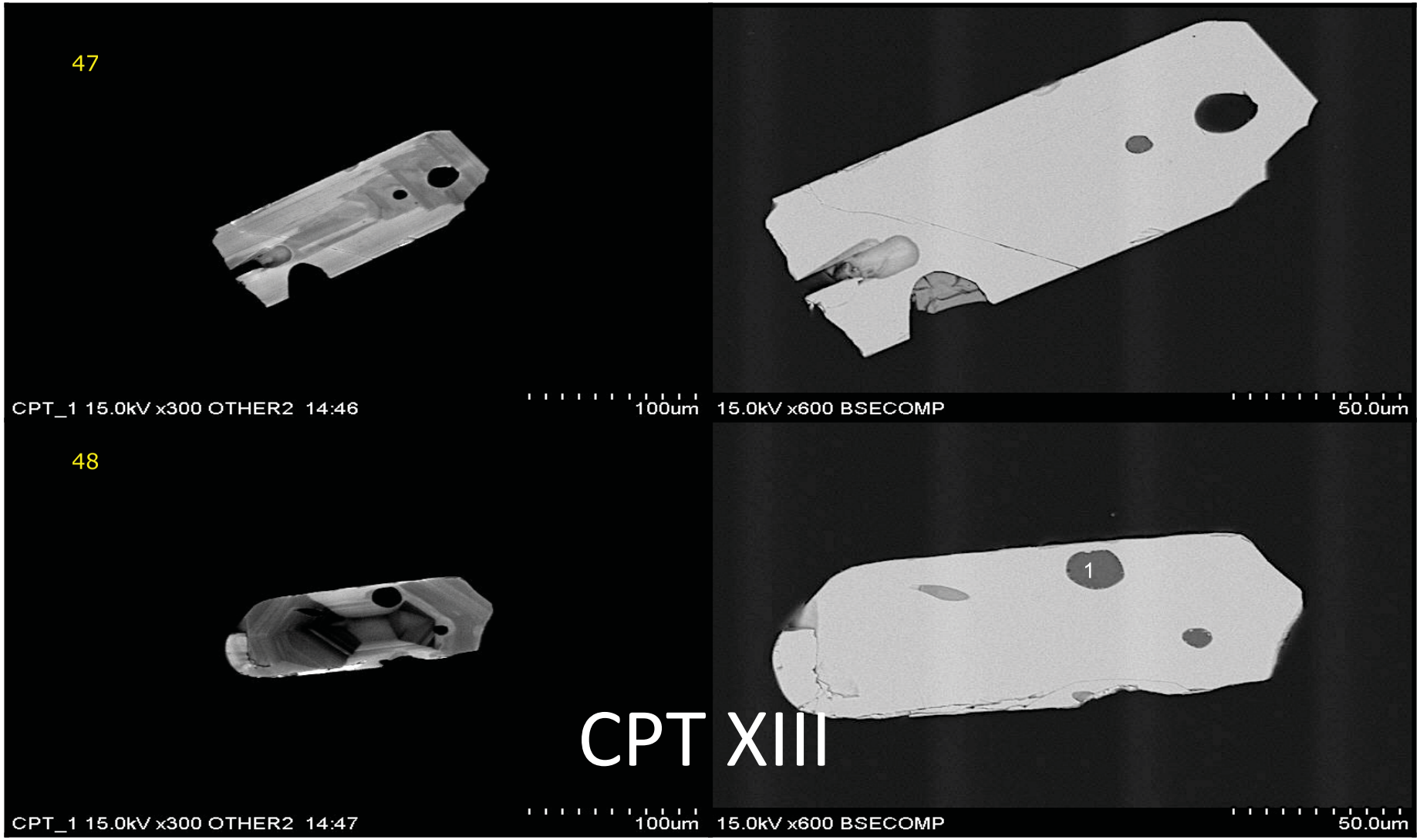
47
CPT_1 15.0kV x300 OTHER2 14:46
100um
15.0kV x600 BSECOMP
50.0um
48
1
CPT_1 15.0kV x300 OTHER2 14:47
100um
15.0kV x600 BSECOMP
50.0um

CPT XIII

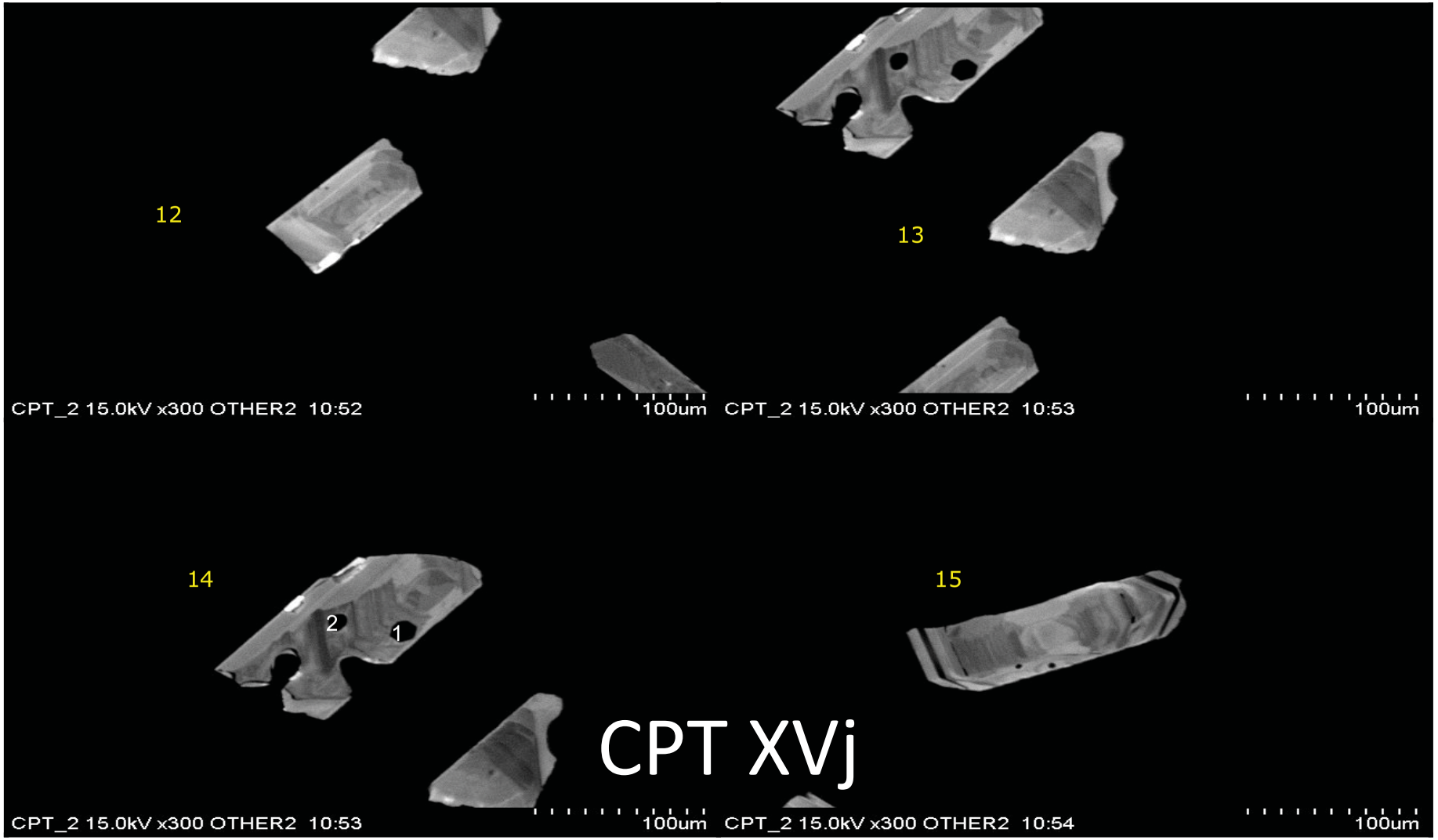
12
CPT_2 15.0kV x300 OTHER2 10:52
100um
13
CPT_2 15.0kV x300 OTHER2 10:53
100um
14
2
1
CPT_2 15.0kV x300 OTHER2 10:53
100um
15
CPT_2 15.0kV x300 OTHER2 10:54
100um
CPT XVj

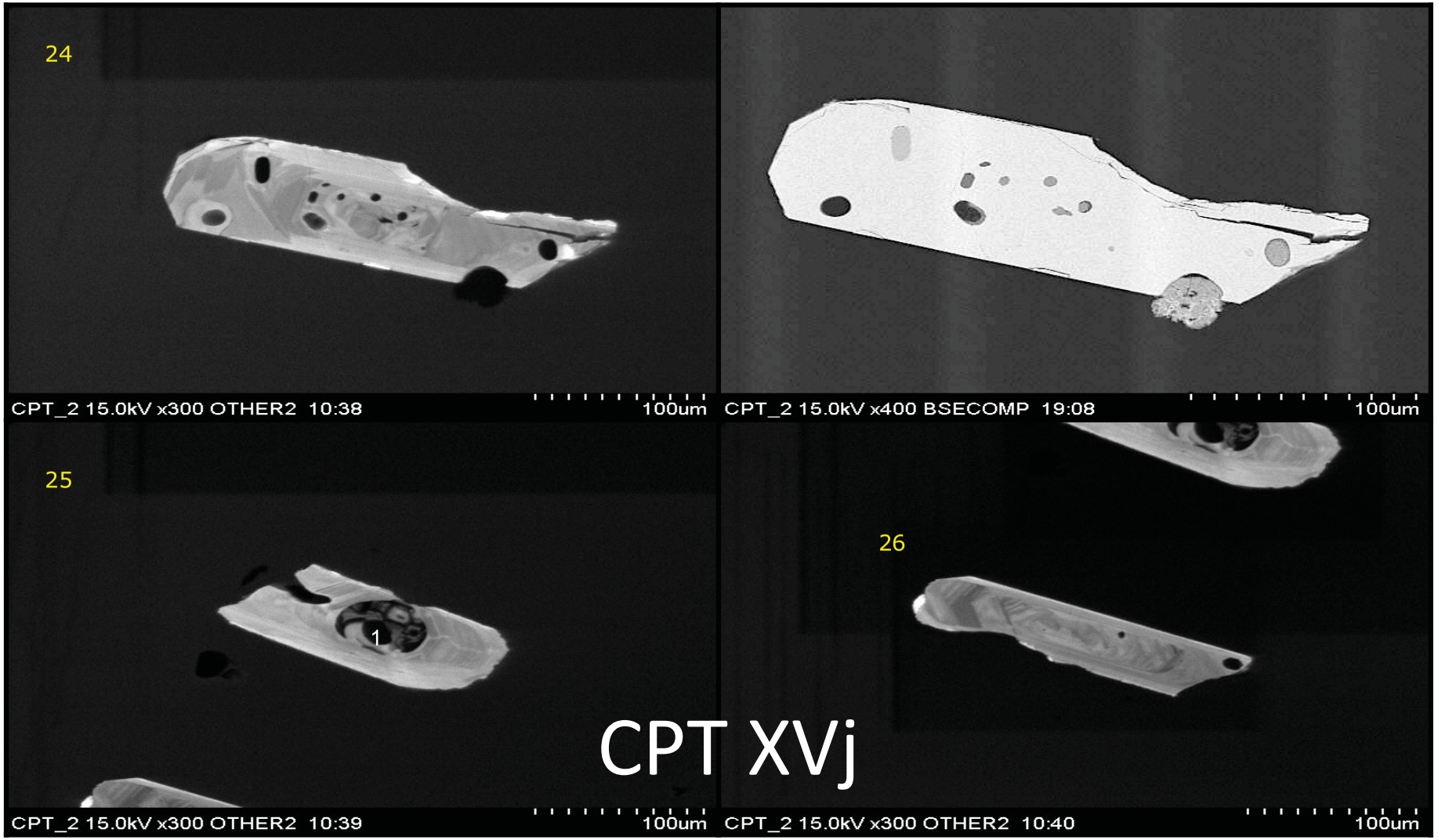
24
CPT_2 15.0kV x300 OTHER2 10:38
100um
CPT_2 15.0kV x400 BSECOMP 19:08
100um
25
1
CPT_2 15.0kV x300 OTHER2 10:39
100um
26
CPT_2 15.0kV x300 OTHER2 10:40
100um

CPT XVj

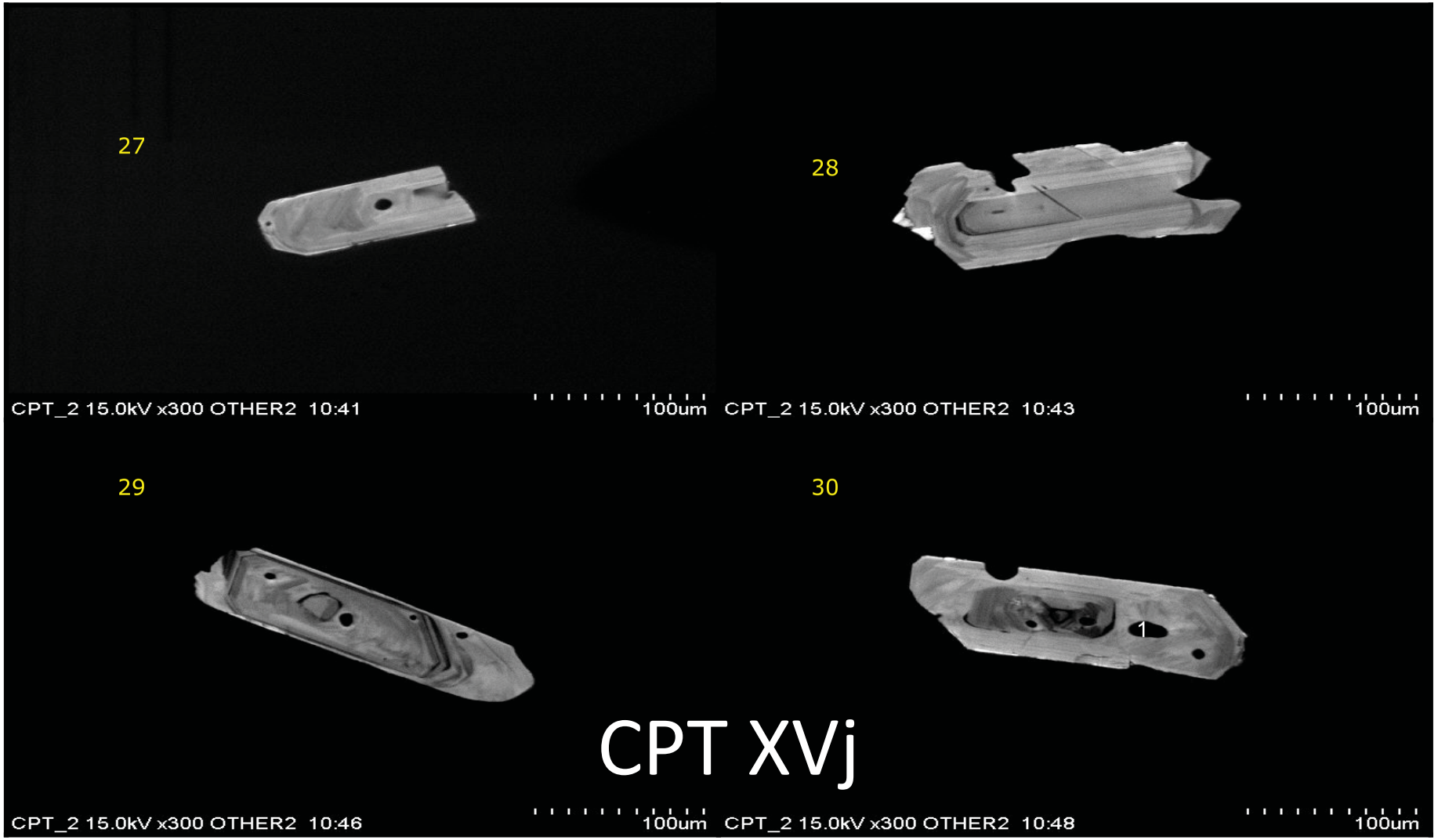
27
CPT_2 15.0kV x300 OTHER2 10:41
100um
28
CPT_2 15.0kV x300 OTHER2 10:43
100um
29
CPT_2 15.0kV x300 OTHER2 10:46
100um
30
1
CPT_2 15.0kV x300 OTHER2 10:48
100um
CPT XVj

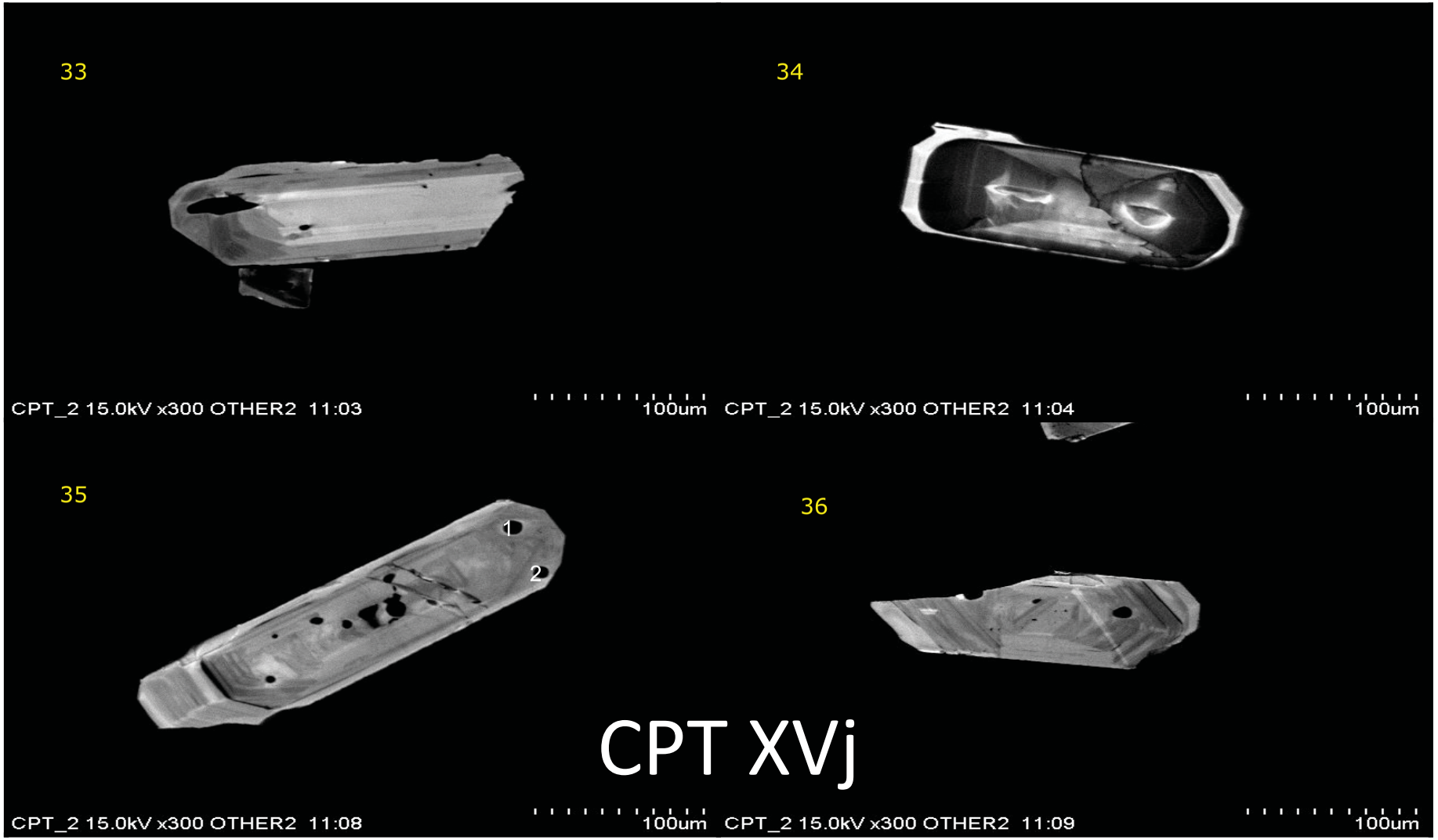
33
CPT_2 15.0kV x300 OTHER2 11:03
100um
34
CPT_2 15.0kV x300 OTHER2 11:04
100um
35
1
2
CPT_2 15.0kV x300 OTHER2 11:08
100um
36
CPT_2 15.0kV x300 OTHER2 11:09
100um
CPT XVj

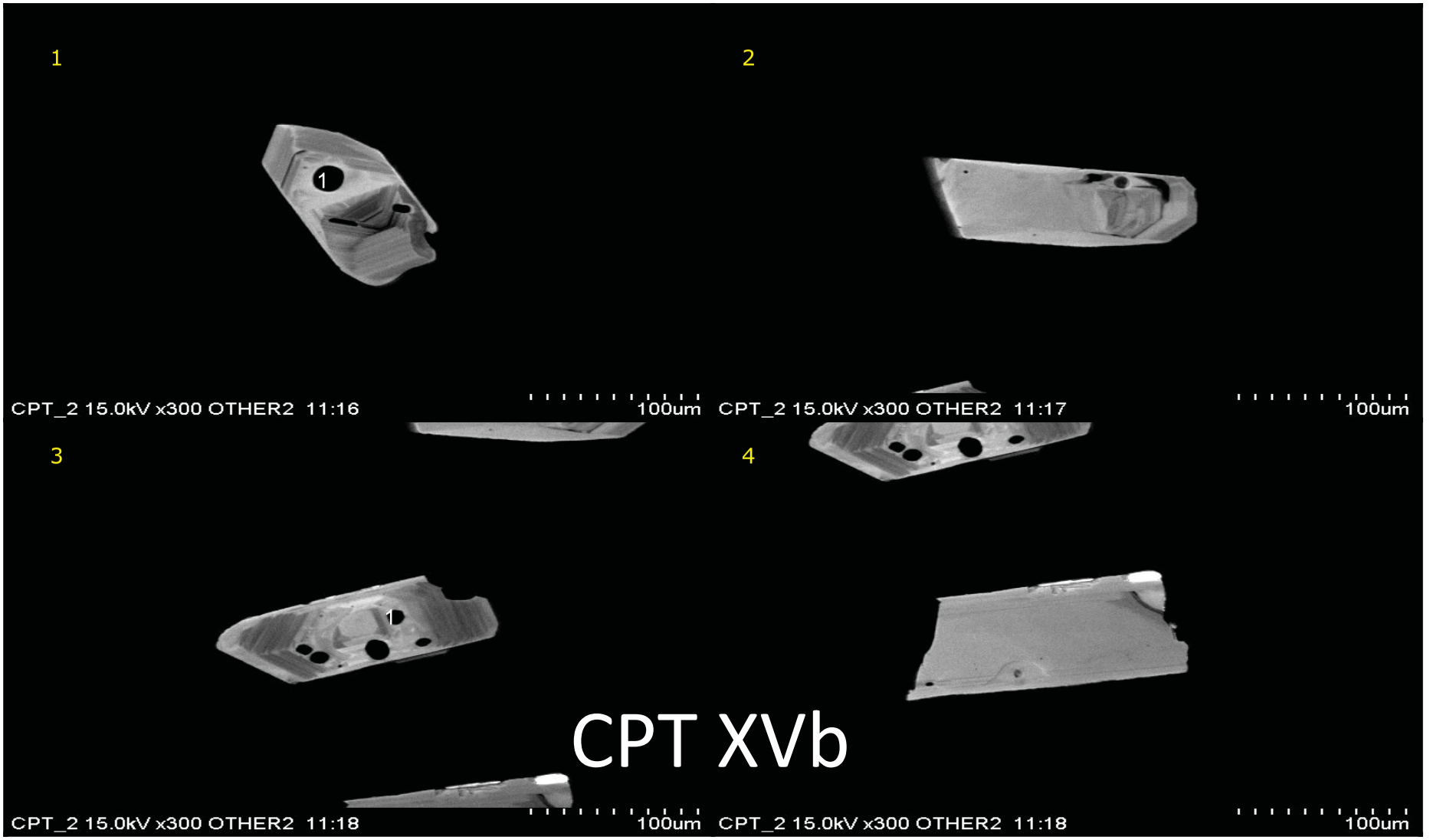
1
1
CPT_2 15.0kV x300 OTHER2 11:16
100um
2
CPT_2 15.0kV x300 OTHER2 11:17
100um
3
1
CPT_2 15.0kV x300 OTHER2 11:18
100um
4
CPT_2 15.0kV x300 OTHER2 11:18
100um
CPT XVb

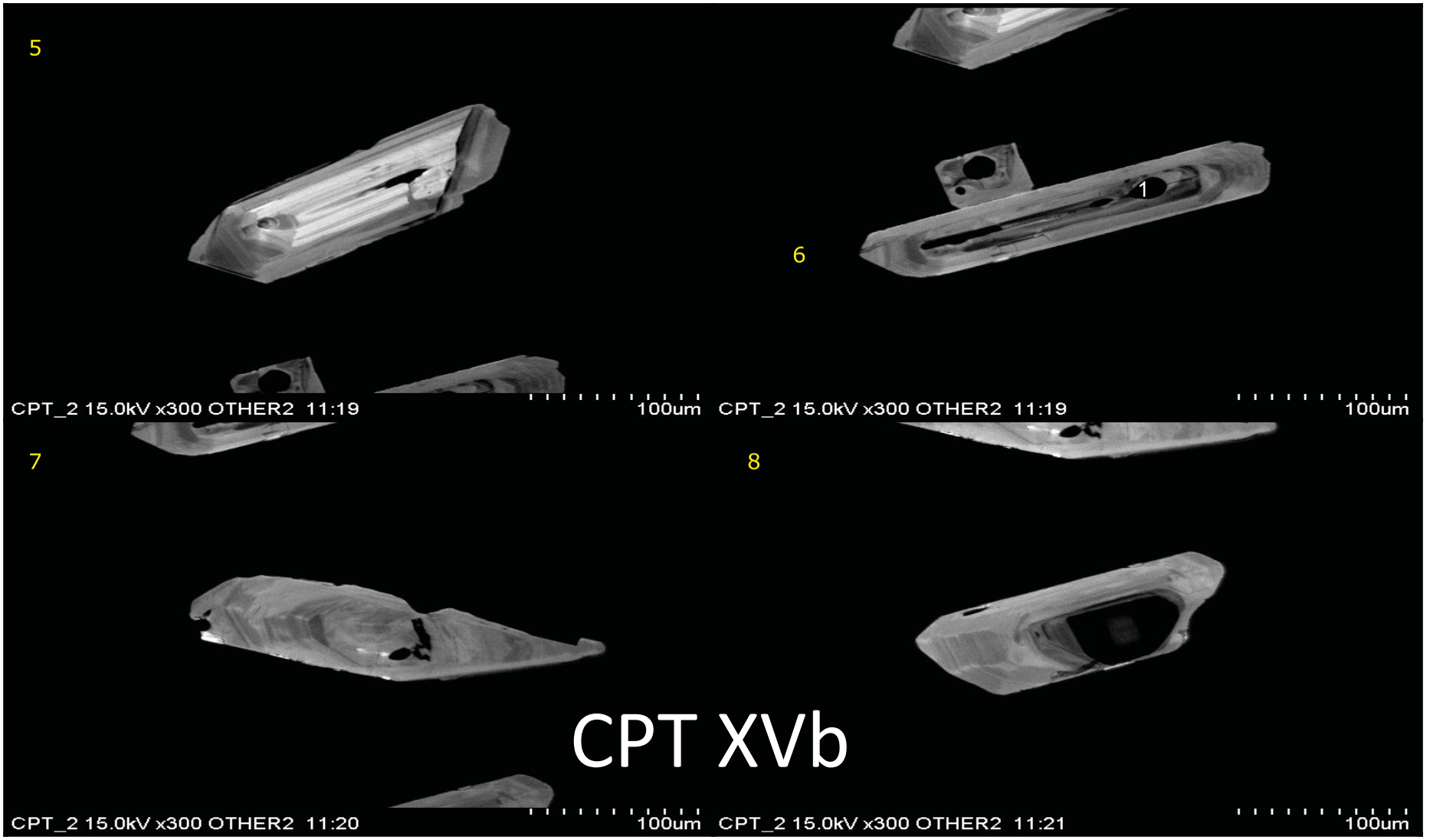
5
CPT_2 15.0kV x300 OTHER2 11:19
100um
6
1
CPT_2 15.0kV x300 OTHER2 11:19
100um
7
CPT_2 15.0kV x300 OTHER2 11:20
100um
8
CPT_2 15.0kV x300 OTHER2 11:21
100um

CPT XVb

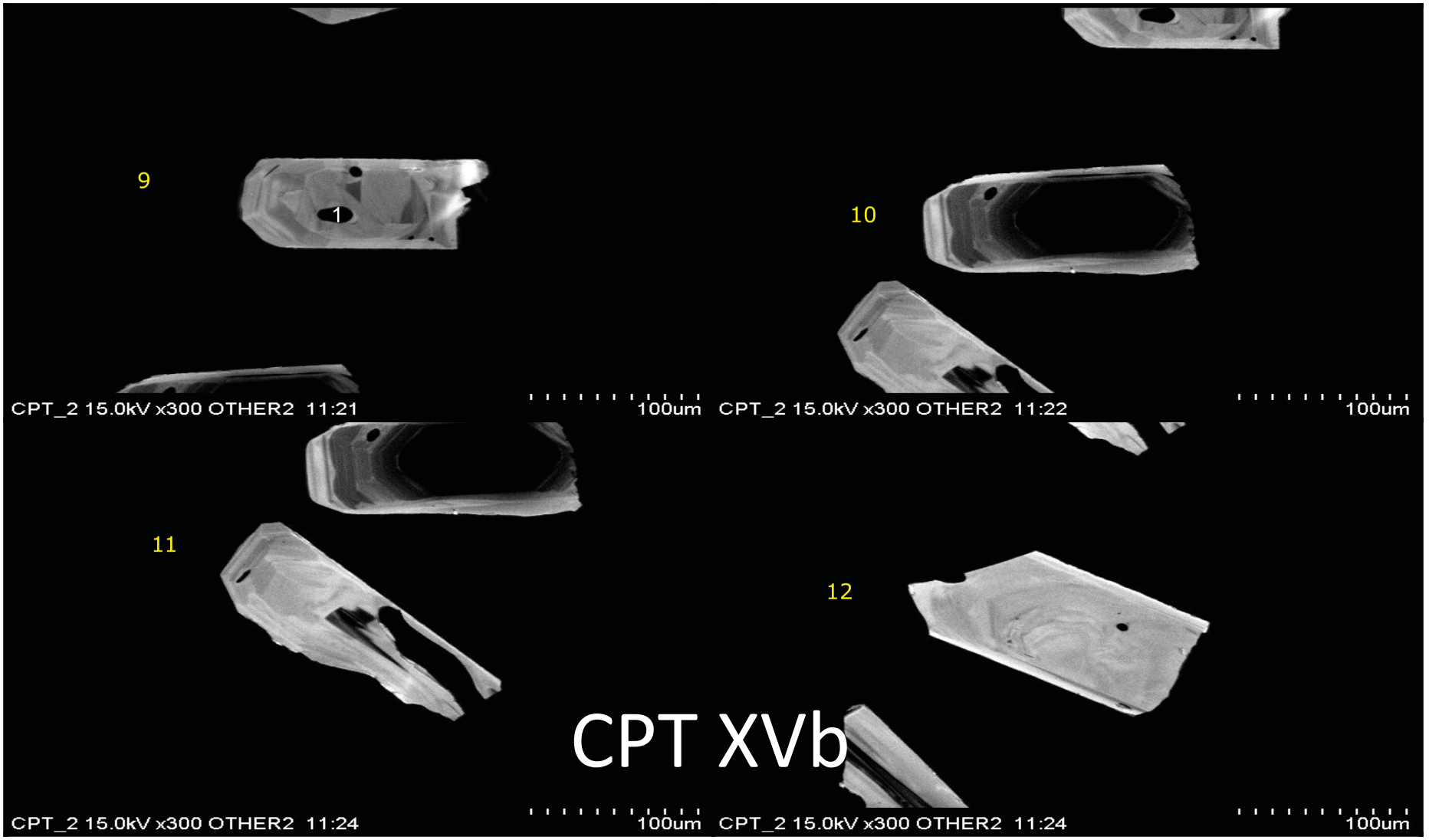
9
1
CPT_2 15.0kV x300 OTHER2 11:21
100um
10
CPT_2 15.0kV x300 OTHER2 11:22
100um
11
CPT_2 15.0kV x300 OTHER2 11:24
100um
12
CPT_2 15.0kV x300 OTHER2 11:24
100um
CPT XVb

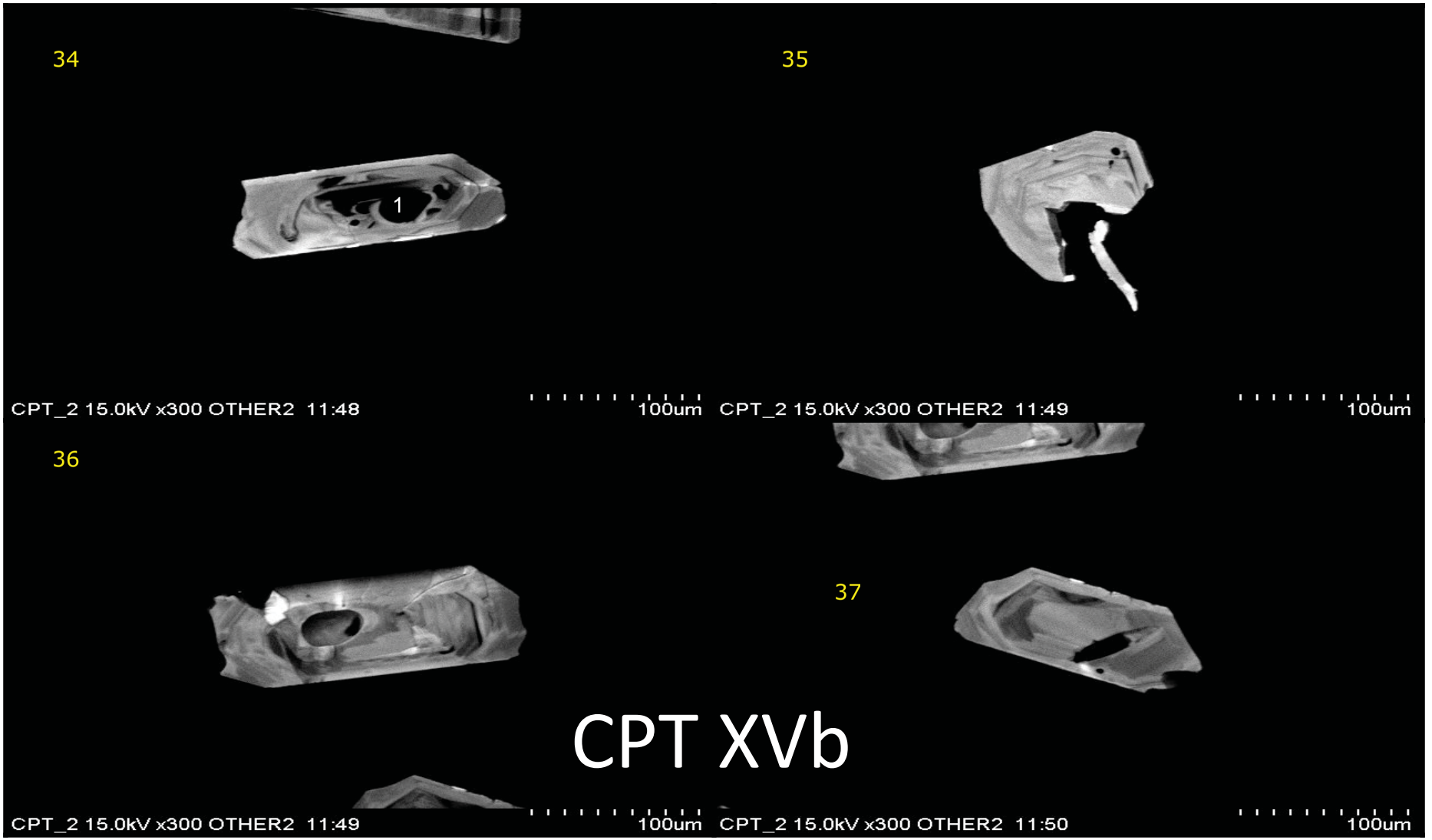
34
1
CPT_2 15.0kV x300 OTHER2 11:48
100um
35
CPT_2 15.0kV x300 OTHER2 11:49
100um
36
CPT_2 15.0kV x300 OTHER2 11:49
100um
37
CPT_2 15.0kV x300 OTHER2 11:50
100um
CPT XVb

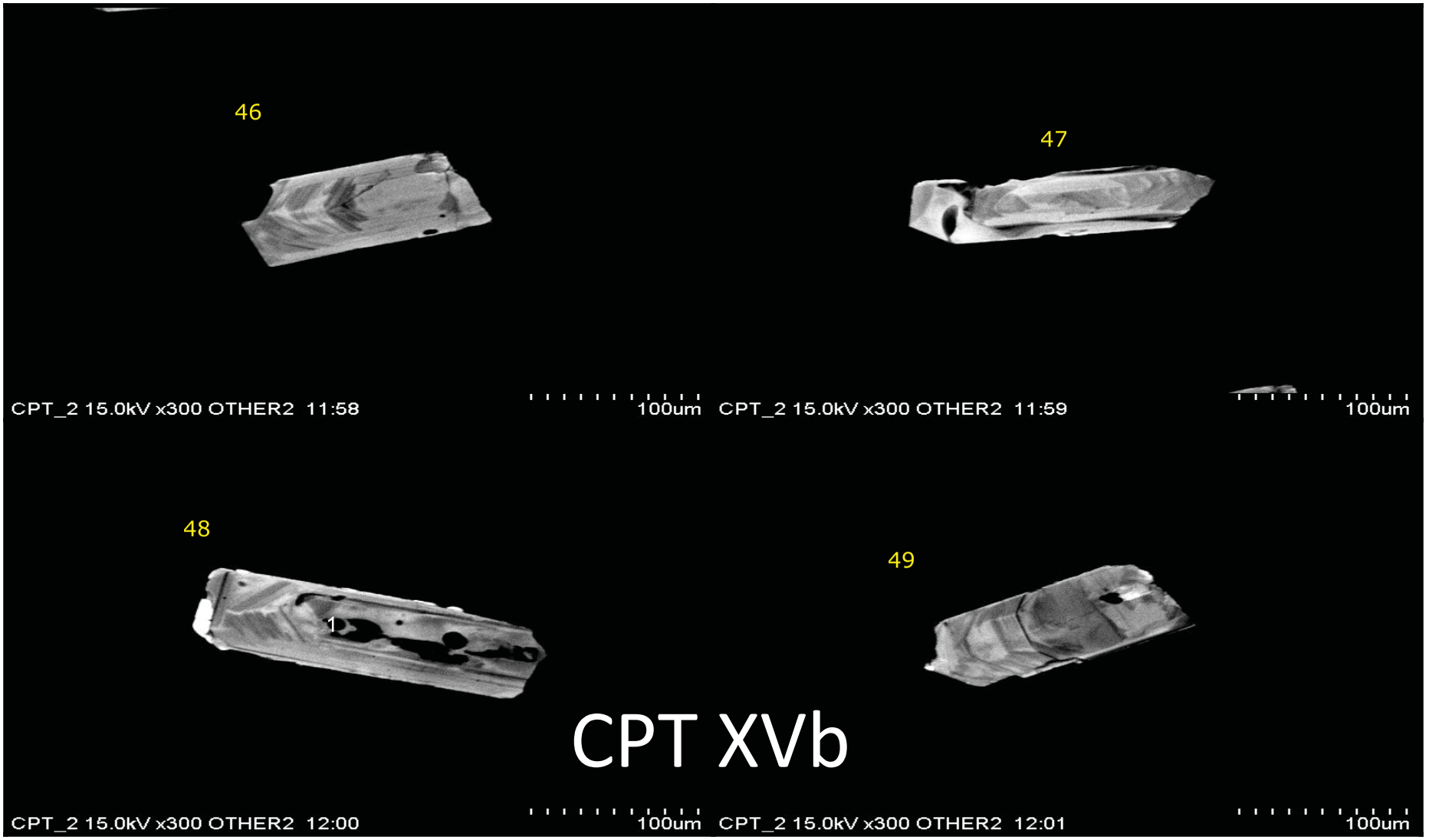
46
CPT_2 15.0kV x300 OTHER2 11:58
100um
47
CPT_2 15.0kV x300 OTHER2 11:59
100um
48
1
CPT_2 15.0kV x300 OTHER2 12:00
100um
49
CPT_2 15.0kV x300 OTHER2 12:01
100um
CPT XVb

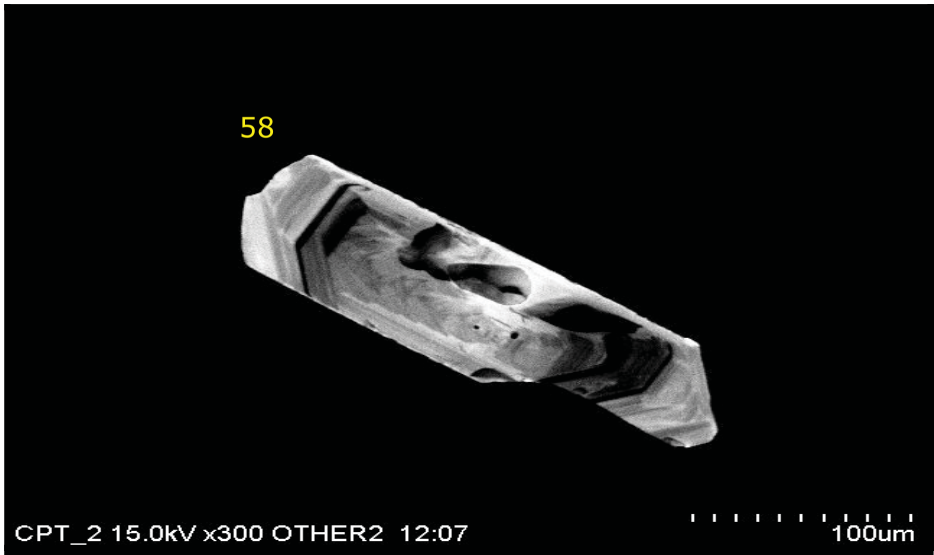
58
CPT_2 15.0kV x300 OTHER2 12:07
100um

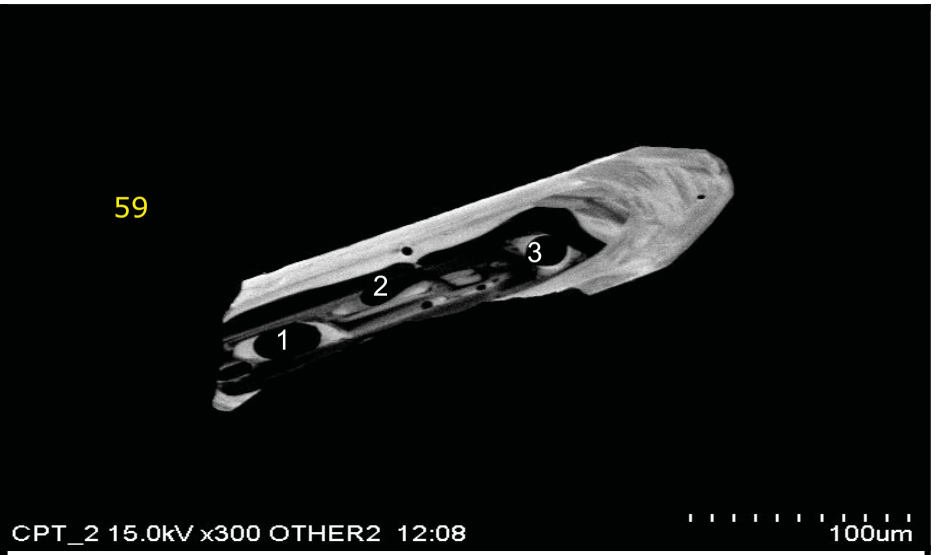
59
1
2
3
CPT_2 15.0kV x300 OTHER2 12:08
100um

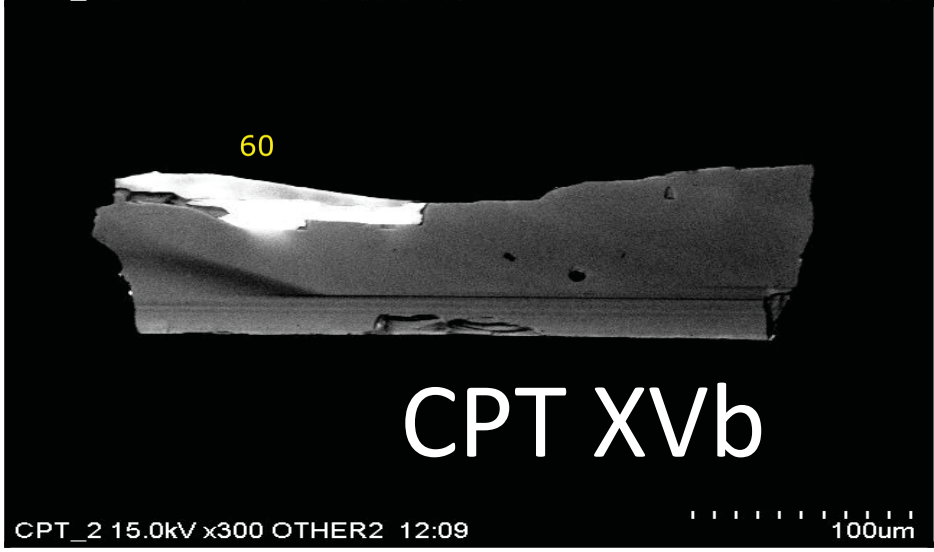
60
CPT XVb
CPT_2 15.0kV x300 OTHER2 12:09
100um


61
CPT_2 15.0kV x300 OTHER2 12:10
100um
CPT_2 15.0kV x350 BSECOMP 18:55
100um
62
1
2
63
CPT XVb
CPT_2 15.0kV x300 OTHER2 12:10
100um
CPT_2 15.0kV x300 OTHER2 12:11
100um


72
1
CPT_2 15.0kV x300 OTHER2 12:20
100um
73
CPT_2 15.0kV x300 OTHER2 12:21
100um
74
1
CPT_2 15.0kV x300 OTHER2 12:21
100um
75
CPT_2 15.0kV x300 OTHER2 12:22
100um
CPT XVb